DOC.20041118.0006

QA: QA

ANL-WIS-PA-000001 REV 01

November 2004

EBS Radionuclide Transport Abstraction

Prepared for:
U.S. Department of Energy
Office of Civilian Radioactive Waste Management
Office of Repository Development
1551 Hillshire Drive
Las Vegas, Nevada 89134-6321

Prepared by:
Bechtel SAIC Company, LLC
1180 Town Center Drive
Las Vegas, Nevada 89144

Under Contract Number
DE-AC28-01RW12101

QA: QA

EBS Radionuclide Transport Abstraction

ANL-WIS-PA-000001 REV 01

November 2004

OCRWM	MODEL SIGNATURE PAGE/CHANGE HISTORY	Page iii 1. Total Pages: 532

2. Type of Mathematical Model

☐ Process Model ☒ Abstraction Model ☐ System Model

Describe Intended Use of Model

The abstraction for flow and transport of radionuclides in the Engineered Barrier System (EBS) will be incorporated into the GoldSim model for TSPA-LA.

3. Title

EBS Radionuclide Transport Abstraction

4. DI (including Rev. No., if applicable)

ANL-WIS-PA-000001 REV 01

5. Total Appendices	6. No. of Pages in Each Appendix
Nine (9)	A - 8; B - 28; C - 16; D - 18; E - 18; F - 40; G - 12; H - 81 - 8.

	Printed Name	Signature	Date
7. Originator	James D. Schreiber	James D. Schreiber	11/18/2004
8. Independent Technical Reviewer	Rob Howard	[illegible]	18 Nov 04
9. Checker	Joshua S. Stein (Lead)	Joshua S. Stein	11/18/2004
10. QER	Darrell Svalstad	[illegible]	11/18/2004
11. Responsible Manager/Lead	M. Kathryn Knowles	[illegible]	11/18/04
12. Responsible Manager	Ernest L. Hardin	[illegible]	11/18/04

13. Remarks

This revision addresses TER-02-0068, which is now CR 155, and TER-02-0038, which is now CR 143.

* Incorporated Management comments and addressed an error documented in CR 3980.

Change History

14. Revision No.	15. Description of Change
REV 00	Initial issue.
REV 00, ICN 01	Changed functional dependence of diffusion coefficient on liquid saturation and porosity.
REV 00, ICN 02	Modified EBS flow and transport abstraction to include an EBS design without backfill; modified thermal and mechanical response of drip shield to reflect new drip shield design and rockfall analyses.
REV 01	Complete revision. Revisions are too extensive to use change lines. Modified flux splitting model, incorporating experimental data; added model validation. Added in-package retardation and diffusion models, with validation. Modified invert diffusion properties model and added data qualification and validation. Included general mathematical description of EBS transport. Expanded treatment of colloid-facilitated transport. Updated YMRP Acceptance Criteria and FEPs list. Modified flow pathways and flow and transport abstractions. Added alternative conceptual models, including dual-continuum invert. Added DIRS numbers to references. Added summary of barrier capability. Added discussion of parameter and model uncertainty. Added list of nomenclature. Added appendices describing spreadsheets used to develop and validate models. Added output DTN. Added sorption in the invert. Revised and expanded discretization of EBS RT Abstraction. Added UZ input parameters for EBS-UZ boundary condition model. Addressed an error documented in CR 3980.

INTENTIONALLY LEFT BLANK

CONTENTS

CONTENTS (Continued)

Page

CONTENTS (Continued)

Page

CONTENTS (Continued)

Page

CONTENTS (Continued)

INTENTIONALLY LEFT BLANK

FIGURES

Page

INTENTIONALLY LEFT BLANK

TABLES

Page

TABLES (Continued)

Page

TABLES (Continued)

Page

INTENTIONALLY LEFT BLANK

ACRONYMS AND ABBREVIATIONS

ASTM	American Society for Testing and Materials
BSC	Bechtel SAIC Company LLC
BWR	boiling water reactor
CDSP	codisposal
CP	corrosion products
CSNF	commercial spent nuclear fuel
DOE	U.S. Department of Energy
DSNF	defense spent nuclear fuel
EBS	engineered barrier system
EPA	U.S. Environmental Protection Agency
EPRI	Electric Power Research Institute
FEP	features, events, and processes
FHH	Frenkel-Halsey-Hill adsorption isotherm equation
HLW	high-level radioactive waste
IED	information exchange drawing
LA	license application
LA-ICP-MS	laser ablation coupled with inductively coupled plasma-mass spectrometry
NRC	U.S. Nuclear Regulatory Commission
RH	relative humidity
SNF	spent nuclear fuel
SR	Site Recommendation
TSPA	total system performance assessment
TWP	technical work plan
UZ	unsaturated zone
WE	Westinghouse Electric
YMP	Yucca Mountain Project

INTENTIONALLY LEFT BLANK

1. PURPOSE

The purpose of this analysis model report is to develop and analyze the engineered barrier system (EBS) radionuclide transport abstraction model, consistent with Level I and Level II model validation, as identified in *Technical Work Plan for: Near-Field Environment and Transport: Engineered Barrier System: Radionuclide Transport Abstraction Model Report Integration* (BSC 2004 [DIRS 170775]). The EBS radionuclide transport abstraction (or *EBS RT Abstraction*) is the conceptual model used in the total system performance assessment for the license application (TSPA-LA) to determine the rate of radionuclide releases from the EBS to the unsaturated zone (UZ).

The *EBS RT Abstraction* conceptual model consists of two main components—a flow model and a transport model. Both models are developed mathematically from first principles in order to show explicitly what assumptions, simplifications, and approximations are incorporated into the models used in the TSPA-LA.

The flow model defines the pathways for water flow in the EBS and specifies how the flow rate is computed in each pathway. The input to this model is the seepage flux into a drift. The seepage flux is potentially split by the drip shield, with some (or all) of the flux being diverted by the drip shield and some passing through breaches in the drip shield that might result from corrosion or seismic damage. The flux through drip shield breaches is potentially split by the waste package, with some (or all) of the flux being diverted by the waste package and some passing through waste package breaches that might result from corrosion or seismic damage. The flow model is validated in an independent model validation technical review. The drip shield and waste package flux splitting algorithms are developed and validated using experimental data.

The transport model considers advective transport and diffusive transport from a breached waste package. Advective transport occurs when radionuclides that are dissolved or sorbed onto colloids or both are carried from the waste package by the portion of the seepage flux that passes through waste package breaches. Diffusive transport occurs as a result of a gradient in radionuclide concentration and may take place while advective transport is also occurring, as well as when no advective transport is occurring. Diffusive transport is addressed in detail because it is the sole means of transport when there is no flow through a waste package, which is postulated to predominate during the regulatory compliance period in the nominal and seismic cases. The advective transport rate, when it occurs, is generally greater than the diffusive transport rate. Colloid-facilitated advective and diffusive transport is also modeled and is presented in detail in Appendix B of this model report.

Additional submodels and model parameters developed in this model report include:

- Diffusion inside a waste package—The time-dependent quantity of corrosion products inside a breached waste package is estimated; this enables the surface area available for adsorption of water to be approximated, which in turn gives the water saturation through which diffusion of radionuclides may occur.
- Sorption onto stationary corrosion products in a breached waste package.

- Diffusion in the invert, accounting for the dependence of diffusion on porosity, saturation, and temperature.
- Sorption in the invert.
- EBS-UZ interface submodel—implementation in the TSPA-LA includes this submodel to provide a realistic concentration boundary condition.

Parameter uncertainty associated with each model and submodel is discussed. The transport model and the EBS-UZ interface submodel are validated using corroborative data and models as well as an independent model validation technical review.

Alternative conceptual models considered include:

- A "bathtub" flow model in which water must fill a breached waste package before any can flow out, as opposed to the flow-through model that is used.
- Models that show the effect of limitations on diffusion of water vapor and oxygen into a breached waste package and consequential delays in releases of radionuclides.
- A dual-continuum invert flow and transport submodel.
- Alternative invert diffusion coefficient submodels.

Output from the *EBS RT Abstraction* includes:

- The flow model—the algorithms for computing the flow in each flow path within the EBS, with parameter values or sources for those parameters used in the model.
- The transport model—a model for advective and diffusive transport, specifying the computational procedure for both commercial spent nuclear fuel (CSNF) and codisposal waste packages in both seep and no-seep environments, with parameter values or sources for those parameters used in the model.
- Ranges and distributions for parameters that are uncertain and are sampled in the TSPA-LA implementation of the *EBS RT Abstraction.*

The scope of this abstraction and report is limited to flow and transport processes. Specifically, this report provides the algorithms that are implemented in TSPA-LA for transporting radionuclides using the flow geometry and radionuclide concentrations determined by other elements of the TSPA-LA model. The *EBS RT Abstraction* also identifies the important processes that are evaluated with process-level or component-level using analytical or numerical solutions.

This model report was prepared to comply with the U.S. Nuclear Regulatory Commission (NRC) rule for high-level radioactive waste (HLW), 10 CFR Part 63 [DIRS 158535], which requires the U.S. Department of Energy (DOE) to conduct a performance assessment to demonstrate compliance with postclosure performance objectives. The results from this conceptual model allow Bechtel SAIC Company LLC (BSC) to address portions of the acceptance criteria presented in *Yucca Mountain Review Plan, Final Report* (NRC 2003 [DIRS 163274]).

The following reports provide input to the *EBS RT Abstraction*:

- *Probability Analysis of Corrosion Rates for Waste Package Materials*
- *Multiscale Thermohydrologic Model*
- *Unsaturated Zone and Saturated Zone Transport Properties (U0100)*
- *Thermal Conductivity of the Potential Repository Horizon*
- *Calibrated Properties Model*
- *UZ Flow Models and Submodels*
- *Radionuclide Transport Models Under Ambient Conditions*
- *Analysis of Hydrologic Properties Data*
- *Drift-Scale Radionuclide Transport.*

The following documents use output from the *EBS RT Abstraction* as direct input:

- *In-Package Chemistry Abstraction*
- *Total System Performance Assessment (TSPA) Model/Analysis for the License Application.*

INTENTIONALLY LEFT BLANK

2. QUALITY ASSURANCE

Development of this model report and the supporting analyses have been determined to be subject to the Office of Civilian Radioactive Waste Management quality assurance program (BSC 2004 [DIRS 170775], Section 8). Approved quality assurance procedures identified in Section 4 of the technical work plan have been used to conduct and document the activities described in this model report. Section 8 of the technical work plan also identifies the methods used to control the electronic management of data during the analysis and documentation activities.

This model report provides models for evaluating the performance of the engineered barrier system, including the drip shields, waste packages, and invert, which are classified in the *Q-List* (BSC 2004 [DIRS 168361]) as Safety Category because they are important to waste isolation, as defined in AP-2.22Q, *Classification Analyses and Maintenance of the Q-List*. The results of this report are important to the demonstration of compliance with the postclosure performance objectives prescribed in 10 CFR Part 63 [DIRS 158535]. The report contributes to the analysis data used to support performance assessment; the conclusions do not directly impact engineered features important to safety, as defined in AP-2.22Q. This report was prepared in accordance with AP-SIII.10Q, *Models*.

INTENTIONALLY LEFT BLANK

3. USE OF SOFTWARE

3.1 MICROSOFT EXCEL

Microsoft Excel 2002 "Add Trendline" capability was used to perform a statistical analysis of diffusion coefficient values reported in Section 6.3.4.1.1. Microsoft Excel 2002 was also used to analyze experimental data used to develop and validate the drip shield and waste package flux splitting submodels (Sections 6.5.1.1.2.4, 6.5.1.1.3, and 7.1.1). A calculation of the potential mass of corrosion products in fully degraded waste packages, summarized in Table 6.3-4, is described in Appendix A. A sample calculation to demonstrate the solution procedure used in the colloid transport model, described in Appendix B, was also carried out using Microsoft Excel 2002. A complete description of the formulas, inputs, and outputs used in the Microsoft Excel analysis of the drip shield experimental data is provided in Appendices C (the drip shield flux splitting submodel), D (the waste package flux splitting submodel), and E (validation of the flux splitting submodels). The formulas, inputs, and outputs used in Microsoft Excel to perform the sample colloid transport calculation are presented in Appendix F, and the invert diffusion properties model analysis is described in Appendix G.

3.2 GOLDSIM

GoldSim V8.01 Service Pack 1 (STN: 10344-8.01 SP1-00) (Golder Associates 2003 [DIRS 166572]) is run on Microsoft Windows 2000 on Dell workstation with Intel Xeon processor and was developed to perform dynamic, probabilistic simulations. GoldSim V8.01 was used in accordance with LP-SI.11Q-BSC, *Software Management*. GoldSim calculations were done in support of validation of models developed in the *EBS RT Abstraction* (see Section 7.3.1). GoldSim calculations were also run to verify an alternative model implementation in Section 6.6.4.4. GoldSim V8.01 is used in these validation calculations because it is used in the TSPA-LA model. This software was used within the range of validation and was obtained from Configuration Management.

INTENTIONALLY LEFT BLANK

4. INPUTS

4.1 DIRECT INPUT

4.1.1 Data

Inputs in this section are used as direct input data for the models and analyses presented in Section 6. Tables 4.1-1 through 4.1-6 and Figure 4.1-1 summarize the relevant input data and the sources for these values. Data in this section are presented as found in the source documents; unit conversions and manipulation of data are not done in this section, but are performed as needed in Section 6.

Data uncertainty is addressed in Section 6. In particular, corrosion rates of carbon and stainless steels are listed in Table 6.5-13 as model input with ranges and distributions determined from the data in Table 4.1-1. The breached drip shield experimental test data in Tables 4.1-2 through 4.1-6 and Figure 4.1-1 are evaluated in Section 6.5.1, resulting in uncertain model input parameters listed in Table 6.5-13.

Table 4.1-1. Input Data for *EBS RT Abstraction*

Model Input	Value		Source
	Rate (μm yr^{-1})	*ECDF*	
Rate of corrosion of A 516 and A 27 carbon steels in simulated dilute well J-13 water at 60°C, long term (≥ 1 yr); ECDF	65.77	0.042	DTN: MO0409SPAACRWP.000 [DIRS 172059]; Spreadsheet "ECDF_metals2.xls"; Worksheet "A516-Carbon Steel", Columns B & C, Rows 5–30
	66.75	0.083	
	69.84	0.125	
	70.00	0.167	
	71.25	0.208	
	72.21	0.250	
	72.64	0.292	
	72.87	0.333	
	72.89	0.375	
	73.47	0.417	
	74.29	0.458	
	74.51	0.500	
	74.60	0.542	
	75.41	0.583	
	77.31	0.625	
	79.29	0.667	
	80.00	0.708	
	80.87	0.750	
	83.26	0.792	
	83.66	0.833	
	83.74	0.875	
	85.68	0.917	
	90.97	0.958	
	106.93	1.000	

Table 4.1-1. Input Data for *EBS RT Abstraction* (Continued)

Model Input	Value		Source
	Rate (μm yr^{-1})	*ECDF*	
Rate of corrosion of 316L stainless steel in fresh water at 50–100°C; ECDF	0.037 0.1016 0.109 0.1524 0.154 0.1778 0.2032 0.2286 0.254 0.2794 0.51	0.063 0.125 0.188 0.250 0.313 0.375 0.438 0.563 0.750 0.813 1.000	DTN: MO0409SPAACRWP.000 [DIRS 172059]; Spreadsheet "ECDF_metals2.xls"; Worksheet "316 ss", Columns L & M, Rows 5–15

ECDF= empirical cumulative distribution function

Table 4.1-2. Atlas Breached Drip Shield Experiments on Smooth Drip Shield Surface – Dripping on Crown – Flow into Breaches

Drip Location	Water Input Mass (g)		Breach Where Water Was Collected	Water Collection Mass (g)	
	Tare	Final		Initial	Final
Single Patch Q(film) Tests (DTN: MO0207EBSATBWP.023 [DIRS 163402])					
8 cm right of Patch 4 centerline	-50.32	-228.52	B4	107.60	129.62
Patch 5 centerline	-12.66	-176.40	B5	109.40	130.52
4 cm left of Patch 5 centerline	-210.48	-344.27	B5	109.18	118.28
Patch 4 centerline	52.77	-135.86	B4	107.57	129.82
Multiple Patch Tests (DTN: MO0207EBSATBWP.024 [DIRS 163401])					
27 cm right of drip shield center	-0.51	-276.65	B5	109.10	113.59
27 cm left of drip shield center	710.10	433.27	B4	107.77	110.40
81 cm left of drip shield center	755.52	529.3	B4	107.18	110.63
81 cm right of drip shield center	768.79	547.67	B5	107.99	111.53
Bounding Flow Rate Tests (DTN: MO0207EBSATBWP.025 [DIRS 163403])					
54 cm left of drip shield center	853.83	516.11	B4	107.35	153.76
54 cm left of drip shield center	769.21	680.32	B4	107.73	115.61
27 cm left of drip shield center	857.57	524.88	B4	107.22	110.57
27 cm left of drip shield center	872.20	771.25	B4	107.00	107.65
27 cm right of drip shield center	907.84	529.11	B5	109.81	112.26
27 cm right of drip shield center*	782.29	644.57	B5	109.55	114.00

*Drip location shown incorrectly as 7 cm in DTN: MO0207EBSATBWP.025 [DIRS 163403]; correct value of 27 cm obtained from Howard 2002 [DIRS 161522], p. 33.

ECDF= empirical cumulative distribution function

Table 4.1-3. Atlas Breached Drip Shield Experiments on Smooth Drip Shield Surface – Dripping on Crown – Rivulet Spread Data – 33° from Crown

Drip Location	Left (cm)	Right (cm)	Relevant Patch
Single Patch Q(film) Tests (DTN: MO0207EBSATBWP.023 [DIRS 163402])			
8 cm right of Patch 4 centerline	15.0	28.5	4
Patch 5 centerline	28.0	0	5
4 cm left of Patch 5 centerline	Not recorded	21	5
Patch 4 centerline	11.0	26.5	4
Multiple Patch Tests (DTN: MO0207EBSATBWP.024 [DIRS 163401])			
27 cm right of drip shield center	13.0	29.0	5
27 cm left of drip shield center	21.0	21.5	4
81 cm left of drip shield center	17.0	23.5	4
81 cm right of drip shield center	20.0	18.0	5
Bounding Flow Rate Tests (DTN: MO0207EBSATBWP.025 [DIRS 163403])			
54 cm left of drip shield center (High Flow Rate)	22.0	32.0	4
54 cm left of drip shield center (Low Flow Rate)	10.5	30.0	4
27 cm left of drip shield center (High Flow Rate)	24	19	4
27 cm left of drip shield center (Low Flow Rate)	10.0	8.0	4
27 cm right of drip shield center (High Flow Rate)	24.0	16.5	5
27 cm right of drip shield center (Low Flow Rate)*	20.0	13.5	5

*Drip location shown incorrectly as 7 cm in DTN: MO0207EBSATBWP.025 [DIRS 163403]; correct value of 27 cm obtained from Howard 2002 [DIRS 161522], p. 33.

Table 4.1-4. Atlas Breached Drip Shield Experiments on Smooth Drip Shield Surface – Dripping on Crown – Splash Radius Tests

No. Drips	Splash Radius (cm)		Comments
	Left	Right	
Splash Radius Test #1 (DTN: MO0207EBSATBWP.022 [DIRS 163400])			
1	1.6	1.6	Measured at outer fringe
2	26.5	18.4	Measured outer fringe
5	37.5	18.4	Measured outer fringe
13	37.5	27.8	Measured outer fringe
21	37.5	31.5	Measured outer fringe
27	52.8	35.0	Measured outer fringe
38	59.9	54.2	Measured outer fringe
49	25.0	29.0	Measured inner cluster
49	72.0	63.2	Measured outer fringe
60	40.0	40.0	Measured inner cluster
60	72.5	54.2	Measured outer fringe
90	48.0	43.0	Measured inner cluster
Single Patch Q(film) Tests (DTN: MO0207EBSATBWP.023 [DIRS 163402])			
—	—	54.5	Patch 5, center, crown
—	—	82	Patch 4, center, crown
—	—	86	Patch 4, 8 cm right of center, crown

NOTE: — indicates no measurements were made.

Table 4.1-5. Atlas Breached Drip Shield Experiments on Smooth Drip Shield Surface – Dripping at Off-Crown Locations – Flow into Breaches

Drip Location	Water Input Mass (g)		Breach Where Water Was Collected	Water Collection Mass (g)	
	Tare	Final		Initial	Final
Single Patch Q(splash) Tests (DTN: MO0207EBSATBWP.023 [DIRS 163402])					
P5, 17.5 cm left of center, 33°	529.45	439.68	B5	108.57	108.86
P4, center, 33°	685.41	548.20	B4	106.86	216.70
P4, 17.5 cm right of center, 33°	670.30	538.88	B4	106.75	115.71
P4, 17.5 cm right of center, 16.5°	667.12	516.36	B4	106.80	108.59
P4, centerline, 16.5°	669.72	529.82	B4	106.98	191.33
P5, 17.5 cm left of center, 16.5°	661.50	474.00	B5	109.13	111.79
P6, 35.5 cm left of center, 16.5°	661.82	519.54	B4	107.31	108.90
P5, centerline, 16.5°	676.13	551.39	B5	108.60	199.16
P6, 36.5 cm left of center, between crown and 16.5°	660.40	531.13	B4	107.60	113.69
Single Patch Q(film) Tests (DTN: MO0207EBSATBWP.023 [DIRS 163402])					
P4, 8 cm right of center, 16.5°	-0.90	-173.28	B4	107.16	199.69
P2, 15 cm right of center, 16.5°	36.10	-141.12	B5	109.40	109.79
P5, 4 cm left of center, 16.5°	-37.20	-210.37	B5	117.40	301.94
P4, 8 cm right of center, 33°	53.74	-83.70	B4	114.89	222.27
Bounding Flow Rate Tests (DTN: MO0207EBSATBWP.025 [DIRS 163403])					
54 cm left of drip shield center, 16.5°	850.06	496.63	B4	107.44	277.21
54 cm left of drip shield center, 16.5°	822.71	715.70	B4	107.71	192.26
27 cm left of drip shield center, 16.5°	768.00	646.24	B5	109.21	109.79
27 cm left of drip shield center, 16.5°	868.59	498.18	B4	107.27	110.65
27 cm right of drip shield center, 16.5°	862.08	522.34	B5	109.33	113.57
27 cm right of drip shield center, 16.5°	808.93	713.52	B5	109.30	110.41
27 cm left of drip shield center, 33°	907.89	540.78	B4	107.17	108.13
27 cm right of drip shield center, 33°	835.68	518.08	B5	109.94	113.52
54 cm left of drip shield center, 33°	890.39	561.54	B4	107.28	294.13
54 cm left of drip shield center, 33°	685.39	584.26	B4	107.32	190.42
27 cm left of drip shield center, 33°	-1.99	-98.20	B4	109.88	111.06
27 cm right of drip shield center, 33°	-121.69	-217.44	B5	110.83	110.96

Table 4.1-6. Atlas Breached Drip Shield Experiments on Smooth Drip Shield Surface – Dripping off Crown – Rivulet Spread Data – 33° from Crown and at Transition

Drop Location	At 33°		At Transition	
	Right (cm)	Left (cm)	Right (cm)	Left (cm)
Q(film) Single Patch Tests (DTN: MO0207EBSATBWP.023 [DIRS 163402])				
P4, 8 cm right of center, 16.5°	5.5	3.5	13.5	N/A
P2, center, 16.5°	7.5	4.5	19.5	22.0
P2, 15 cm right of center, 16.5°	11.5	9.0	18.0	15.0
P5, 4 cm left of center, 16.5°	8.5	8.5	N/A	N/A
Bounding Flow Rate Tests (DTN: MO0207EBSATBWP.025 [DIRS 163403])				
54 cm left of drip shield center, 16.5°	31.0	46.0	35.0	46.0
54 cm left of drip shield center, 16.5°	8.5	10.0	19.0	27.0
27 cm left of drip shield center, 16.5°	6.0	8.0	17.0	16.0
27 cm left of drip shield center, 16.5°	18.0	24.0	22.0	19.0
27 cm right of drip shield center, 16.5°	13.0	27.0	14.0	23.0
27 cm right of drip shield center, 16.5°	12.0	17.0	16.0	19.0
27 cm left of drip shield center, 33°	N/A	N/A	11.0	17.0
27 cm right of drip shield center, 33°	N/A	N/A	15.0	17.0
54 cm left of drip shield center, 33°	N/A	N/A	17.0	17.0
27 cm left of drip shield center, 33°	N/A	N/A	9.0	9.5
27 cm right of drip shield center, 33°	N/A	N/A	8.5	10.0

NOTE: N/A indicates that rivulet spread measurements at drop location are not applicable to this analysis.

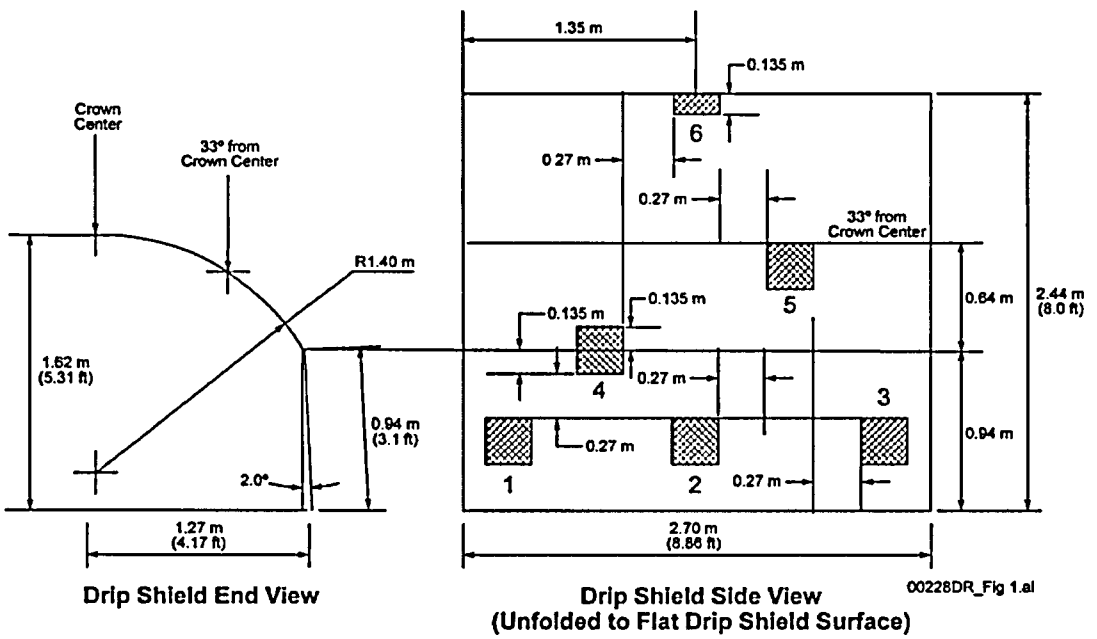

Source: Howard 2002 [DIRS 161516], p. 14.

NOTE: Figure modified from reference by labeling patches (1–6).

Figure 4.1-1. Dimensions of Drip Shield Mock-Up Used in Breached Drip Shield Experiments on Smooth Drip Shield Surface

4.1.2 Parameters and Other Technical Information

Parameters in Tables 4.1-7 through 4.1-14 are used as inputs for the analyses in Section 6. Uncertainty in certain parameters is discussed in Section 6. Specifically, sorption distribution coefficients (K_d values) in Tables 4.1-11 and 4.1-12 are evaluated in Section 6.3.4.2 in determining ranges and distributions for use in modeling retardation in the waste package; Tables 6.3-6 and 6.5-13 list the K_d values and their associated uncertainty.

Parameters in Table 4.1-7 are from American Society for Testing and Materials (ASTM) codes and from various editions of the *CRC Handbook of Chemistry and Physics* (Weast 1985 [DIRS 111561]). Input parameters in Table 4.1-8 were developed on the Yucca Mountain Project (YMP). Input parameters in Table 4.1-9 are from various outside sources, such as journals and text books. A description of each parameter is given following Table 4.1-9, together with the justification for its use. These inputs thus are considered qualified for their intended use within this report.

Table 4.1-7. Parameters for *EBS RT Abstraction* (Established Fact)

Model Input	Value	Source
Avogadro's number, N_A	$6.0221419947 \times 10^{23}$ mol^{-1}	Lide 2002 [DIRS 160832], p. 1-7
Water density: at 25°C at 50°C	997.0449 kg m^{-3} 988.0363 kg m^{-3}	Weast 1985 [DIRS 111561], p. F-5
Water viscosity at 25°C	0.890 mPa-s	Lide 2000 [DIRS 162229], p. 6-180
Density of hematite (α-Fe_2O_3)	5240 kg m^{-3}	Weast 1985 [DIRS 111561], p. B-104
Density of A 516 carbon steel	7850 kg m^{-3}	ASTM A 20/A20M-99a [DIRS 147578]
Density of 6061 aluminum	2700 kg m^{-3}	ASTM G 1-90 [DIRS 103515], p. 7, Table X1
Molecular weight of water (H_2O)	0.01801528 kg mol^{-1}	Lide 2002 [DIRS 160832], p. 6-4
Molecular weight of hematite (Fe_2O_3)	0.15969 kg mol^{-1}	Weast 1985 [DIRS 111561], p. B-104
Atomic weight of iron (Fe)	0.055847 kg mol^{-1}	Weast 1985 [DIRS 111561], p. B-102
Atomic weight of molybdenum (Mo)	0.09594 kg mol^{-1}	Weast 1985 [DIRS 111561], p. B-116
Atomic weight of chromium (Cr)	0.051996 kg mol^{-1}	Weast 1985 [DIRS 111561], p. B-88
Atomic weight of nickel (Ni)	0.05869 kg mol^{-1}	Weast 1985 [DIRS 111561], p. B-118
Atomic weight of aluminum (Al)	0.02698154 kg mol^{-1}	Weast 1985 [DIRS 111561], p. B-68

NOTE: Dependence of viscosity on temperature, T (°C), 20°C $\leq T \leq$ 100°C, reference temperature = 20°C (Weast and Astle 1981 [DIRS 100833], p. F-42):

$$\log_{10}\left(\frac{\eta_T}{\eta_{20}}\right) = \frac{1.3272(20-T) - 0.001053(T-20)^2}{T+105}.$$

Table 4.1-8. Parameters for *EBS RT Abstraction* (Project Sources)

Model Input	Value	Source
Density of Stainless Steel Type 316	8000 kg m^{-3}	DTN: MO0003RIB00076.000 [DIRS 153044]
Modulus of elasticity for Alloy 22 at 204°C	196 Gpa	DTN: MO0107TC239753.000 [DIRS 169973]
Size of patches in Breached Drip Shield Experiments drip shield mockup	0.27 m × 0.27 m	Howard 2002 [DIRS 161516], p. 13
Outer lid surface hoop stress	385.0522 MPa	BSC 2004 [DIRS 172203], Table 6-9
Porosity of TSw35 tuff rock matrix	0.131 m^3 pore vol. m^{-3} bulk vol.	DTN: LB0207REVUZPRP.002 [DIRS 159672]; Spreadsheet "Matrix_Props.xls", Row 20, Column C
Porosity of crushed tuff invert ballast	0.45 m^3 pore vol. m^{-3} bulk vol.	BSC 2004 [DIRS 169565], Appendix X
Unsaturated zone fracture frequency for TSw35	Mean = 3.16 m^{-1} Std Dev = 2.63 m^{-1} Log-normal	BSC 2004 [DIRS 170040], Appendix A, Table A-1
Unsaturated zone fracture porosity for TSw35	Range: 0 – 1 Distribution: Beta Mean = 9.6 × 10^{-3} Std Dev = 2.82 × 10^{-3}	BSC 2004 [DIRS 170040], Appendix D, Table D-1
Unsaturated zone matrix porosity for TSw35	Range: 0 – 1 Distribution: Beta Mean = 0.131 Std Dev = 0.031	BSC 2004 [DIRS 170040], Appendix D, Table D-1
Unsaturated zone fracture saturation	Uniform sampling from 433 locations for each infiltration case	DTN: LB0307FMRADTRN.001 [DIRS 165451], Folder U0230_excel_files.zip, Spreadsheet "Flow and Saturation Data from UZ Flow Model.xls", Column D
Unsaturated zone fracture residual saturation	Uniform sampling from 433 locations	DTN: LB0307FMRADTRN.001 [DIRS 165451], Folder U0230_excel_files.zip, Spreadsheet "Fracture Residual Saturation.xls", Column E
Unsaturated zone fracture percolation flux	Uniform sampling from 433 locations for each infiltration case	DTN: LB0307FMRADTRN.001 [DIRS 165451], Folder U0230_excel_files.zip, Spreadsheet "Flow and Saturation Data from UZ Flow Model.xls", Column C
Unsaturated zone fracture interface area	9.68 m^2 m^{-3}	DTN: LB0205REVUZPRP.001 [DIRS 159525]; Spreadsheet "FRACTURE_PROPERTY.xls," Row 20, Column R
Unsaturated zone active fracture parameter for TSw35 for all three infiltration cases	Low = 0.476 Mean = 0.569 High = 0.570	DTN: LB03013DSSCP3I.001 [DIRS 162379]; (BSC 2004 [DIRS 169861], Table A-1, A-2, and A-3)
Unsaturated zone fracture aperture	1.5 × 10^{-4} m	DTN: LB0205REVUZPRP.001 [DIRS 159525]; Spreadsheet "FRACTURE_PROPERTY.xls," Row 20, Column L
Unsaturated zone fracture diffusion coefficient	Function of matrix water content and effective permeability; same as matrix diffusion coefficient	BSC 2004 [DIRS 170040], Equation 6-52

Table 4.1-8. Parameters for *EBS RT Abstraction* (Project Sources) (Continued)

Model Input	Value	Source
Unsaturated zone matrix saturation	Uniform sampling from 433 locations for each infiltration case	DTN: LB0307FMRADTRN.001 [DIRS 165451], Folder U0230_excel_files.zip, Spreadsheet "Flow and Saturation Data from UZ Flow Model.xls", Column G
Unsaturated zone matrix percolation flux	Uniform sampling from 433 locations for each infiltration case	DTN: LB0307FMRADTRN.001 [DIRS 165451], Folder U0230_excel_files.zip, Spreadsheet "Flow and Saturation Data from UZ Flow Model.xls", Column F
Unsaturated zone matrix diffusion coefficient	Function of matrix water content and effective permeability	BSC 2004 [DIRS 170040], Equation 6-52
Unsaturated zone matrix effective permeability	Function of matrix permeability and relative permeability	BSC 2004 [DIRS 170040], Equation 6-57
Unsaturated zone matrix permeability for TSw35 for all three infiltration cases	Low = 2.33×10^{-18} m^2 Mean = 4.48×10^{-18} m^2 High = 8.55×10^{-18} m^2	DTNs: LB0208UZDSCPLI.002 [DIRS 161788]; LB0208UZDSCPMI.002 [DIRS 161243]; and LB0302UZDSCPUI.002 [DIRS 161787]; BSC 2004 [DIRS 170040], Table 4-6
Unsaturated zone matrix relative permeability	Uniform sampling from 433 locations for each infiltration case	DTN: LB0307FMRADTRN.001 [DIRS 165451], Folder U0230_excel_files.zip, Spreadsheet "Flow and Saturation Data from UZ Flow Model.xls", Column H
Unsaturated zone dry matrix density for TSw35 (stratigraphic unit Tptpll)	1.9793 g cm^{-3}	DTN: SN0404T0503102.011 [DIRS 169129], File "ReadMe.doc," Table 7-10
Unsaturated zone fracture percolation flow-focusing factor	Uniform sampling from 433 locations for each infiltration case	DTN: LB0307FMRADTRN.001 [DIRS 165451], Folder U0230_excel_files.zip, Spreadsheet "Fracture Flux and Water Content with Flow Focusing r1.xls", Column D

UZ = unsaturated zone

Table 4.1-9. Parameters for *EBS RT Abstraction* (Various Sources)

Model Input	Value	Source
Self-diffusion coefficient of water at 25°C	2.299×10^{-9} m^2 s^{-1}	Mills 1973 [DIRS 133392], Table III
Parameter *k* in FHH water vapor adsorption isotherm for Fe_2O_3	1.1 (dimensionless)	Jurinak 1964 [DIRS 154381], p. 486
Parameter *s* in FHH water vapor adsorption isotherm for Fe_2O_3	2.45 (dimensionless)	Jurinak 1964 [DIRS 154381], p. 486
Water molecule cross-sectional area, A_w	10.6 $Å^2$	McCafferty and Zettlemoyer 1970 [DIRS 154382], p. 454
Cementation factor (exponent on porosity in Archie's law)	1.3 (dimensionless)	Bear 1988 [DIRS 101379], p. 116
Saturation exponent in Archie's law	2 (dimensionless)	Bear 1988 [DIRS 101379], p. 116
Specific surface area of natural hematite (Fe_2O_3)	1.8 m^2 g^{-1}	Langmuir 1997 [DIRS 100051], Table 10.2 (natural hematite)
Specific surface area of hematite (Fe_2O_3)	21.4 m^2 g^{-1}	Briand et al. 2001 [DIRS 161617], Table 4
Density of Neutronit A 978 steel	7760 kg m^{-3}	Kügler 1996 [DIRS 107760], p. 17
Fuel rod outside diameter (WE 17 × 17)	0.374 in.	DOE 1992 [DIRS 102588], Volume 1, p. 2A-30

Table 4.1-9. Parameters for *EBS RT Abstraction* (Various Sources) (Continued)

Model Input	Value	Source
Fuel rod length (WE 17 × 17)	151.560 in.	DOE 1992 [DIRS 102588], Volume 1, p. 2A-30
Fuel rods per assembly (WE 17 × 17)	264	DOE 1992 [DIRS 102588], Volume 1, p. 2A-30

FHH = Frenkel-Halsey-Hill adsorption isotherm equation; WE = Westinghouse Electric; DOE = U.S. Department of Energy

Fuel rod dimensions–The fuel rod dimensions for assembly Westinghouse Electric (WE) 17 × 17 are given in *Characteristics of Potential Repository Wastes* (DOE 1992 [DIRS 102588]). This four-volume report is the definitive compilation of the characteristics of potential repository wastes. The concerns raised by *Deficiency Report VAMO-98-D-132* (DOE 1998 [DIRS 123628] regarding inconsistencies between data reported in *Characteristics of Potential Repository Wastes* (DOE 1992 [DIRS 102588] and its data sources do not impact the data used in this analysis with regard to the WE 17 × 17 fuel rods; thus, these data are considered reliable and are justified as suitable for intended use in this analysis. The WE 17 × 17 fuel assembly is used as the representative fuel assembly because; (1) Westinghouse fuel assemblies comprise a large fraction (about 21 percent) of all fuel assemblies, (2) the 17 × 17 configuration comprises about 34 percent of discharged fuel assemblies (Faruque 1993 [DIRS 170706]), and (3) 21-pressurized water reactor (PWR) waste packages that will contain the WE 17 × 17 fuel assemblies are the most common type of waste package, nominally comprising 4299 of the 11,184 waste packages planned for the repository (BSC 2004 [DIRS 169472], Table 11).

The fuel rod length is reported in *Characteristics of Potential Repository Wastes* (DOE 1992 [DIRS 102588], Volume 1, p. 2A-30) as ranging from 151.560 in. to 151.635 in. Because no distribution for length is given in the reference (which would give some guidance on selecting a single representative value for length) and because the range is small (less than 0.05 percent variation from minimum to maximum), the minimum length is used as representative of the range.

Water molecule cross-sectional area–The cross-sectional area of the water molecule is taken from the paper "Adsorption of Water Vapour on Alpha-Fe_2O_3" (McCafferty and Zettlemoyer 1970 [DIRS 154382]). The paper was published in *Discussions of the Faraday Society*, a publication started in 1947 and continuing to this day as the *Faraday Discussions* under the sponsorship of the Royal Society of Chemistry. The Royal Society of Chemistry is the largest organization in Europe for advancing the chemical sciences and is supported by a network of 45,000 members worldwide. The McCafferty and Zettlemoyer paper is directly relevant to the Yucca Mountain repository because hematite (Fe_2O_3) will be the predominant form of iron oxide in a degrading waste package, and hematite will comprise the bulk of the corrosion products in the waste package.

The value of 10.6 $Å^2$ per molecule reported by McCafferty and Zettlemoyer (1970 [DIRS 154382], p. 454) is corroborated by Holmes et al. (1974 [DIRS 154379], p. 368), who also use a value of 10.6 $Å^2$ for the cross-sectional area of a water molecule. Jurinak (1964 [DIRS 154381]) assumes a cross-sectional area of 10.8 $Å^2$ for a water molecule. Gregg and Sing (1982 [DIRS 153010], p. 188) state that a "close-packed" monolayer of water corresponds to a figure of 10.5 $Å^2$ for the cross-sectional area of a water molecule.

Self-diffusion coefficient of water at 25°C–The value for the self-diffusion coefficient of water at 25°C is 2.299×10^{-9} m^2 s^{-1} and comes from the paper "Self-diffusion in Normal and Heavy Water in the Range 1-45°" (Mills 1973 [DIRS 133392]) in the *Journal of Physical Chemistry*. The *Journal of Physical Chemistry* has been published since 1896. Articles are reviewed by experts in the field, so this coefficient can be considered reliable.

Parameter *k* in Frenkel-Halsey-Hill adsorption isotherm equation (FHH) water vapor adsorption isotherm for Fe_2O_3–The value of the parameter *k* in the FHH water vapor adsorption isotherm for Fe_2O_3 is 1.1 and comes from the paper, "Interaction of Water with Iron and Titanium Oxide Surfaces: Goethite, Hematite, and Anatase" (Jurinak 1964 [DIRS 154381]) in the *Journal of Colloid Science*. The *Journal of Colloid Science*, now the *Journal of Colloid and Interface Science*, has been published since 1947 and is a refereed journal; therefore, the data in the articles can be considered reliable.

Parameter *s* in FHH water vapor adsorption isotherm for Fe_2O_3–The value of the parameter *s* in the FHH water vapor adsorption isotherm for Fe_2O_3 is 2.45 and comes from the paper "Interaction of Water with Iron and Titanium Oxide Surfaces: Goethite, Hematite, and Anatase" (Jurinak 1964 [DIRS 154381]) in the *Journal of Colloid Science*. The *Journal of Colloid Science*, now the *Journal of Colloid and Interface Science*, has been published since 1947 and is a refereed journal; therefore, the data in the paper can be considered reliable.

Cementation factor (exponent on porosity in Archie's law)–The value of 1.3 for the porosity exponent in Archie's law for unconsolidated sand is taken from the book *Dynamics of Fluids in Porous Media* (Bear 1988 [DIRS 101379], p. 116). The value 1.3 is corroborated by the *Handbook of Well Log Analysis for Oil and Gas Formation Evaluation* (Pirson 1963 [DIRS 111477]).

Saturation exponent in Archie's law–The value 2.0 for the saturation exponent in Archie's law for unconsolidated sand is taken from the book *Dynamics of Fluids in Porous Media* (Bear 1988 [DIRS 101379], p. 116). The value 2.0 is corroborated by *Electrical Methods in Geophysical Prospecting*, Volume 10 of *International Series in Electromagnetic Waves* (Keller and Frischknecht 1966 [DIRS 111470]).

Density of Neutronit A 978 steel–The density of Neutronit A 978 steel is 7,760 kg m^{-3} (at 20°C) from Böhler Bleche GmbH (Kügler 1996 [DIRS 107760]). Böhler Bleche is producer of plate steel products and is an outgrowth of the steel company Schoeller-Bleckmann AG founded in 1924. The company is a world-wide exporter of steel products and has a state-of-the-art research and development program to improve the material properties of steels. The company's expertise with steels makes the density value for Neutronit A 978 steel reliable.

Specific surface area of hematite–The specific surface area (surface area per unit mass) of hematite depends on several factors, including the source of the sample (whether natural or artificial), preparation of the sample, and the measurement technique. Because in the *EBS RT Abstraction* the specific surface area of hematite represents that of corrosion products, which will form under a wide range of conditions, this is a sample parameter in TSPA-LA. The values of specific surface area of hematite in Table 4.1-9 establish lower and upper bounds of the range to be sampled. The lower bound value, for natural hematite, is provided by Langmuir (1997

[DIRS 100051]), a widely used textbook on aqueous geochemistry by a reputable, extensively published author and environmental chemistry researcher. The upper bound value is provided by a study of catalytic behavior of metal oxides (Briand et al. 2001 [DIRS 161617]) published in the *Journal of Catalysis*, a reputable refereed journal. Further discussion and corroboration of the range of specific surface area of hematite is provided in Section 6.5.1.2.1.3.

Table 4.1-10. Elemental Composition (Weight Percent) of Waste Package Materials

Element	316 Stainless Steel[a]	A 516 Carbon Steel[b]	Neutronit A 978[c]	Aluminum 6061[d]
Fe	Balance	Balance	Balance	0.7
Mo	3.00	—	2.2	—
Cr	18.00	—	18.5	0.35
Ni	14.00	—	13.0	—
Al	—	—	—	Remainder
Co	—	—	0.20	—
W	—	—	—	—
Mn	2.00	1.30	—	0.15
C	0.08	0.26	0.04	—
P	0.045	0.035	—	—
S	0.030	0.035	—	—
Si	0.75	—	—	0.8
N	0.16	—	—	—
Cu	—	—	—	0.4
Mg	—	—	—	1.2
Zn	—	—	—	0.25
Ti	—	—	—	0.15
V	—	—	—	—
Residuals	—	—	—	0.15

NOTES: "—" indicates that the alloy chemical composition specification does not include this element. Compositions listed are the maximum specified for each element in the data source. "Balance" and "Remainder" are specified in the data source for the principal component of the alloy.

[a]DTN: MO0003RIB00076.000 [DIRS 153044].
[b]DTN: MO0107TC240032.000 [DIRS 169970].
[c]Kügler 1991 [DIRS 155761], p. 15 (vendor-supplied data).
[d]ASM 1979 [DIRS 154085], p. 115.

The data in Table 4.1-11, from DTN: LA0003AM831341.001 ([DIRS 148751], SEP table S00191_002), were developed in the analysis report *Unsaturated Zone and Saturated Zone Transport Properties (U0100)* (BSC 2001 [DIRS 160828], Section 6.4.2). This document has been cancelled because some of the output data, specifically, the transport properties of tuff, have been revised and updated in more recent YMP reports. However, the ranges and distributions of sorption distribution coefficients on iron oxide have not been revised, and they demonstrate the properties of interest for the analysis of sorption parameters for the waste package corrosion products, as discussed in Section 6.3.4.2.3. Corroborating data are available, and the values in Table 4.1-11 are compared with these data in Section 6.3.4.2.3 and Table 6.3-6. Accordingly, these factors justify these product output of the cancelled document as qualified input data suitable for application to modeling retardation in iron corrosion products in the *EBS RT Abstraction.*

Table 4.1-11 includes ranges and distributions of K_d values from DTN: LA0003AM831341.001 ([DIRS 148751], SEP table S00191_002) for 10 radionuclides for sorption onto "iron oxide," which is the "Rock type" specified in the reference, for unsaturated zone units.

In DTN: LA0003AM831341.001 [DIRS 148751], the K_d value for iodine and technetium is listed as zero for "all rock types" for unsaturated zone units; K_d values for sorption onto "iron oxide" are not listed. In DTN: LA0003AM831341.001 ([DIRS 148751] SEP table S00191_001), the K_d value for iodine in saturated zone units is listed as ranging from 0.32 to 0.63 ml g^{-1} with a uniform distribution for rock type "alluvium." reporting the same SEP table, the K_d value for technetium in saturated zone units is listed as ranging from 0.27 to 0.62 ml g^{-1} with a uniform distribution for rock type "alluvium." The data for iodine and technetium in saturated zone units for rock type "alluvium" are suitable for modeling retardation in corrosion products because they provide evidence that some small degree of sorption of these elements is possible onto unspecified mineral assemblages, yet the uncertainty is small because the maximum K_d values are small.

Input values for sorption distribution coefficient (K_d) ranges on devitrified tuff for unsaturated zone units are listed in Table 4.1-12. These data are used for calculating retardation in the invert. The data are appropriate for this use because the crushed tuff to be used in the invert is the same material that is mined from the drifts when the repository is constructed. The repository will be located primarily in the TSw35 horizon in which the host rock is devitrified tuff. These sorption distribution coefficient data are correlated using the correlation matrix in Table 4.1-13.

Diffusion coefficient data for granular materials are listed in Table 4.1-14. These data are used to develop an effective diffusion coefficient for the invert in Section 6.3.4.1.1. The data are qualified for use in this report in Appendix H.

Table 4.1-11. Sorption Distribution Coefficient (K_d) Ranges on Iron Oxide in Unsaturated Zone Units; All Distributions Are Uniform Except as Noted

Element	Minimum K_d (ml g^{-1})	Maximum K_d (ml g^{-1})
Actinium	1,000	5,000
Americium	1,000	5,000
Carbon	10	100
Cesium [a]	0	300
Neptunium	500	1,000
Plutonium	1,000	5,000
Protactinium	500	1,000
Radium [a]	0	500
Strontium [b]	0	20
Thorium	1,000	5,000
Uranium	100	1,000

Source: DTN: LA0003AM831341.001 ([DIRS 148751] SEP table S00191_002).

NOTES: $E(x)$ = expected value of the distribution; COV = coefficient of variance = $\sigma(x)/E(x)$; $\sigma(x)$ = standard deviation of the distribution.

[a] Distribution type: Beta; $E(x)$ = 30; COV = 1.0.
[b] Distribution type: Beta; $E(x)$ = 10; COV = 0.25.

Table 4.1-12. Sorption Distribution Coefficient (K_d) Ranges on Devitrified Tuff for Unsaturated Zone Units

Species[a]	Distribution Type	Coefficients Describing Distribution[b]
U	Cumulative	(0, 0) (0.2, 0.5) (4., 1.0)
Np	Cumulative	(0, 0) (0.5, 0.5) (6., 1.0)
Pu	Cumulative	(10., 0) (70., 0.5) (200., 1.0)
Am	Truncated Normal	Range = 1,000 – 10,000 ml g^{-1} Mean = 5,500 ml g^{-1} Std. Dev. = 1500 ml g^{-1}
Pa	Truncated Normal	Range = 1,000 – 10,000 ml g^{-1} Mean = 5,500 ml g^{-1} Std. Dev. = 1,500 ml g^{-1}
Cs	Uniform	1 – 15 ml g^{-1}
Sr	Uniform	10 – 70 ml g^{-1}
Ra	Uniform	100 – 1,000 ml g^{-1}
Th	Uniform	1,000 – 10,000 ml g^{-1}

[a] DTN: LA0408AM831341.001 [DIRS 171584].
[b] For cumulative distribution: (K_d value, ml g^{-1}; probability) and for uniform distribution: K_d range.

Table 4.1-13. Correlations for Sampling Sorption Distribution Coefficient (K_d) Probability Distributions for Devitrified Tuff

Element	Am	Cs	Np	Pa	Pu	Ra	Sr	Th	U
Am	100	—	—	—	—	—	—	—	—
Cs	0	100	—	—	—	—	—	—	—
Np	25	0	100	—	—	—	—	—	—
Pa	75	0	0	100	—	—	—	—	—
Pu	10	0	10	0	100	—	—	—	—
Ra	0	100	0	0	0	100	—	—	—
Sr	0	25	50	0	0	25	100	—	—
Th	0	0	50	0	0	0	75	100	—
U	0	0	0	0	0	0	0	0	100

DTN: LA0311AM831341.001 [DIRS 167015].

Table 4.1-14. Diffusion Coefficient for Granular Materials for Volumetric Moisture Content Between 1.5 Percent and 66.3 Percent

Sample	Volumetric Moisture Content (%)	Diffusion Coefficient ($cm^2 s^{-1}$)
1	1.50	1.39×10^{-8}
2	1.70	6.60×10^{-9}
3	1.90	8.60×10^{-9}
4	2.17	2.77×10^{-8}
5	2.20	3.63×10^{-8}
6	2.29	1.09×10^{-8}
7	2.50	2.50×10^{-8}
8	3.10	3.30×10^{-8}
9	3.14	3.06×10^{-8}
10	3.20	1.35×10^{-8}
11	3.27	2.79×10^{-8}
12	3.33	6.35×10^{-8}
13	3.34	2.60×10^{-8}
14	3.57	3.37×10^{-8}
15	3.70	3.70×10^{-8}
16	3.70	6.60×10^{-8}
17	4.00	5.22×10^{-8}
18	4.20	5.94×10^{-8}
19	4.60	6.21×10^{-8}
20	4.90	7.20×10^{-8}
21	5.10	1.32×10^{-7}
22	5.30	2.40×10^{-8}
23	5.40	7.60×10^{-8}
24	5.51	7.68×10^{-8}
25	5.83	1.23×10^{-7}
26	5.90	9.30×10^{-8}
27	6.00	8.92×10^{-8}
28	6.30	1.06×10^{-7}
29	6.90	6.00×10^{-8}
30	6.93	1.50×10^{-7}
31	7.30	1.60×10^{-7}
32	7.40	2.50×10^{-7}
33	7.60	2.60×10^{-7}
34	7.60	1.10×10^{-7}
35	7.60	2.69×10^{-7}
36	7.70	1.10×10^{-7}
37	8.00	1.98×10^{-7}
38	8.10	1.70×10^{-7}
39	8.32	4.10×10^{-7}
40	8.35	2.15×10^{-7}
41	8.60	3.20×10^{-7}
42	8.80	2.30×10^{-7}

Table 4.1-14. Diffusion Coefficient for Granular Materials for Volumetric Moisture Content Between 1.5 Percent and 66.3 Percent (Continued)

Sample	Volumetric Moisture Content (%)	Diffusion Coefficient ($cm^2 s^{-1}$)
43	9.24	2.55×10^{-7}
44	9.24	2.55×10^{-7}
45	9.56	3.00×10^{-7}
46	9.64	3.07×10^{-7}
47	9.75	3.20×10^{-7}
48	10.1	3.51×10^{-7}
49	10.1	3.62×10^{-7}
50	10.2	3.54×10^{-7}
51	10.2	3.30×10^{-7}
52	10.3	3.34×10^{-7}
53	10.3	2.10×10^{-7}
54	10.4	3.40×10^{-7}
55	10.9	3.62×10^{-7}
56	11.1	3.72×10^{-7}
57	11.1	4.22×10^{-7}
58	11.1	4.27×10^{-7}
59	11.2	4.19×10^{-7}
60	11.2	5.48×10^{-7}
61	11.4	4.27×10^{-7}
62	11.4	4.12×10^{-7}
63	11.6	5.40×10^{-7}
64	11.7	2.60×10^{-7}
65	11.8	4.80×10^{-7}
66	12.0	2.40×10^{-7}
67	12.0	4.47×10^{-7}
68	12.2	4.09×10^{-7}
69	12.3	5.05×10^{-7}
70	12.3	4.40×10^{-7}
71	12.3	3.60×10^{-7}
72	12.3	4.50×10^{-7}
73	12.5	2.90×10^{-7}
74	12.7	4.37×10^{-7}
75	12.7	4.90×10^{-7}
76	12.7	5.32×10^{-7}
77	13.1	4.77×10^{-7}
78	13.9	5.39×10^{-7}
79	13.9	7.80×10^{-7}
80	14.1	5.12×10^{-7}
81	14.2	5.52×10^{-7}
82	14.4	4.50×10^{-7}
83	14.4	5.20×10^{-7}
84	14.4	4.50×10^{-7}

Table 4.1-14. Diffusion Coefficient for Granular Materials for Volumetric Moisture Content Between 1.5 Percent and 66.3 Percent (Continued)

Sample	Volumetric Moisture Content (%)	Diffusion Coefficient ($cm^2 s^{-1}$)
85	14.6	6.82×10^{-7}
86	14.7	9.00×10^{-7}
87	14.8	6.54×10^{-7}
88	16.0	1.47×10^{-6}
89	16.1	6.82×10^{-7}
90	16.5	5.45×10^{-7}
91	16.7	6.60×10^{-7}
92	17.0	1.20×10^{-6}
93	17.1	8.20×10^{-7}
94	17.3	1.76×10^{-6}
95	17.5	1.10×10^{-6}
96	18.8	1.60×10^{-6}
97	18.9	8.19×10^{-7}
98	19.4	9.89×10^{-7}
99*	20.4	4.19×10^{-6}
100	20.8	3.58×10^{-6}
101	21.0	2.34×10^{-6}
102	21.5	1.23×10^{-6}
103	21.6	1.29×10^{-6}
104	23.1	2.40×10^{-6}
105	23.1	1.90×10^{-6}
106	24.0	2.90×10^{-6}
107*	25.3	5.82×10^{-6}
108	25.4	2.50×10^{-6}
109*	25.7	9.26×10^{-6}
110	28.2	3.50×10^{-6}
111	28.5	1.00×10^{-6}
112	30.9	1.51×10^{-6}
113*	31.7	1.23×10^{-5}
114	32.3	4.60×10^{-6}
115*	33.8	1.34×10^{-5}
116*	35.8	1.57×10^{-5}
117	38.5	4.33×10^{-6}
118*	39.3	1.36×10^{-5}
119*	39.5	1.13×10^{-5}
120	40.0	6.90×10^{-6}
121	42.0	5.80×10^{-6}

Table 4.1-14. Diffusion Coefficient for Granular Materials for Volumetric Moisture Content Between 1.5 Percent and 66.3 Percent (Continued)

Sample	Volumetric Moisture Content (%)	Diffusion Coefficient ($cm^2 s^{-1}$)
122	42.5	3.22×10^{-6}
123*	43.4	1.02×10^{-5}
124	49.0	6.09×10^{-6}
125	66.3	1.83×10^{-5}

NOTE: All values are from Conca and Wright 1992 [DIRS 100436], Figure 2, except for those indicated by an asterisk, which are from Conca et al. 1993 [DIRS 170709], Figure 2.

4.1.3 Design Information

Some of the information necessary for the model presented in this document consists of parameters and other descriptions based on the license application (LA) conceptual design of the repository. Included are dimensions, material amounts and properties, and physical configuration of the drifts and their contents, listed in Tables 4.1-15 through 4.1-17. For TSPA-LA analyses, this information was obtained from information exchange drawings (IEDs) and design drawings cited on IEDs.

In Table 4.1-17, the component materials in a 21-PWR waste package are obtained from *Design and Engineering, 21-PWR Waste Package Configuration* (BSC 2004 [DIRS 167394]), which is the design version preceding the current version (BSC 2004 [DIRS 170710]). Justification for using the previous design data and the impact on TSPA-LA calculations is provided in Section 6.3.4.2.3, where the impact is shown to be negligible.

In Table 4.1-17, the masses and numbers of components in a 5 DHLW/DOE - Short waste package are obtained from Revision 00B of *D&E/PA/C IED Typical Waste Package Components Assembly* (BSC 2004 [DIRS 167207]), which is the version of the information exchange drawing (IED) preceding Revision 00C (BSC 2004 [DIRS 169472]), used for the 21-PWR waste packages. Minor changes in component masses were made in the 5 DHLW/DOE - Short waste package from Revision 00B to Revision 00C, whereas no changes were made for the other waste package types. The impacts of the changes in component masses in the 5 DHLW/DOE - Short waste package are analyzed in Section 6.3.4.2.3 and are shown to be negligible.

Table 4.1-15. Design Information for EBS Components

Model Input	Value	Source
Diameter of the drift	5.5 m	BSC 2004 [DIRS 169503]
Length of drip shield	5805 mm	BSC 2004 [DIRS 169220], Table 1
Maximum depth of invert	2 ft 10 in	BSC 2004 [DIRS 169503]
21-PWR (Absorber Plate) Waste Package Characteristics		
Outer barrier outside diameter	1637 mm	BSC 2004 [DIRS 166953], Section B-B
Maximum outside diameter around trunnion collars	1718.3 mm	BSC 2004 [DIRS 166953]
Outer barrier inside diameter	1597 mm	BSC 2004 [DIRS 166953], Section B-B
Inner vessel inside diameter	1485.9 mm	BSC 2004 [DIRS 166953], Section B-B

Table 4.1-15. Design Information for EBS Components (Continued)

Model Input	Value	Source
Total outside length	5024.4mm	BSC 2004 [DIRS 166953], Section A-A
Inner vessel cavity length	4584.7 mm	BSC 2004 [DIRS 166953], Section A-A
Outer barrier thickness	20 mm	BSC 2004 [DIRS 169472], Table 1
Middle lid thickness	12.7 mm	BSC 2004 [DIRS 167394], Detail A
Middle lid to outer lid gap	30.16 mm	BSC 2004 [DIRS 169472], Detail A
Outer lid thickness	25.4 mm	BSC 2004 [DIRS 169472], Details A and B
Inner vessel bottom lid thickness	50.8 mm	BSC 2004 [DIRS 169472], Detail B
Inner vessel top lid thickness	50.8 mm	BSC 2004 [DIRS 169472], Detail A
Top lid lifting device thickness	25.4 mm	BSC 2004 [DIRS 169472], Detail C
Bottom skirt length	101.6 mm	BSC 2004 [DIRS 169472], Detail B
5 DHLW/DOE SNF - Short Waste Package Characteristics		
Nominal diameter	2126.0 mm	BSC 2004 [DIRS 169472], Table 1
Nominal length	3452.8 mm	BSC 2004 [DIRS 169472], Table 1
Outer barrier thickness	25.4 mm	BSC 2004 [DIRS 169472], Table 1
Outer barrier outside diameter	2044.7 mm	BSC 2004 [DIRS 166946], Section B-B
Outer barrier inside diameter	1993.9 mm	BSC 2004 [DIRS 166946], Section B-B
Total length	3452.8 mm	BSC 2004 [DIRS 166946], Section A-A

DHLW=defense high-level (radioactive) waste, SNF=spent nuclear fuel

Table 4.1-16. Component Dimensions in a 21-PWR (Absorber Plate) Waste Package

Component	Dimensions
Basket Side Guide	3/8 in. thickness
Basket Side Guide Stiffener	3/8 in. thickness
Basket End Side Guide	3/8 in. thickness
Basket End Guide Stiffener	3/8 in. thickness
Basket Corner Guide	3/8 in. thickness
Basket Corner Guide Stiffener	3/8 in. thickness
Fuel Basket A-Plate	7 mm thickness
Fuel Basket B-Plate	7 mm thickness
Fuel Basket C-Plate	7 mm thickness
Fuel Basket D-Plate	¼ in. thickness
Fuel Basket E-Plate	¼ in. thickness
Basket Tube	180 in. length; 9.12 in. interior dimension; 3/16 in. thickness

Sources: Thickness: BSC 2004 [DIRS 169472], Table 2.
Basket Tube Length: BSC 2004 [DIRS 166953], Section A-A.
Basket Tube Interior Dimension: BSC 2004 [DIRS 166953], Section B-B.

Table 4.1-17. Masses and Numbers of Components in Waste Packages

21-PWR (Absorber Plate) (BSC 2004 [DIRS 167394], material table; BSC 2004 [DIRS 169472], Table 2)			
Material	**Component**	**Mass (kg)**	**Number**
Carbon Steel Type A 516	Basket – Side Guide	24.9	16
	Basket – Side Guide Stiffener	0.615	32
	Basket – End Side Guide	32.7	32
	Basket End Side Guide Stiffener	1.38	64
	Basket Corner Guide	40.1	16
	Basket Corner Guide Stiffener	2.07	32
	Fuel Basket Tube	159	21
Neutronit A 978	Fuel Basket A - Plate	86.8	8
	Fuel Basket B - Plate	86.8	8
	Fuel Basket C - Plate	45.8	16
Al 6061	Fuel Basket D - Plate	27.4	8
	Fuel Basket E - Plate	27.4	8
Stainless Steel Type 316	Inner Vessel w/o Guides	9,920	1
	Inner Lid w/ LLF	739	1
	Interface Ring	35.6	1
	Spread Ring	25.3	1
	Total 316 Welds	81.0	—
Alloy 22	OCB with trunnion sleeves	5,730	1
	Middle Lid w/ LLF	226	1
	Outer Lid w/ LLF	445	1
	Total Alloy 22 Welds	51.8	—
5 DHLW/DOE – Short (BSC 2004 [DIRS 166947], material table; BSC 2004 [DIRS 167207], Table 5)			
Material	**Component**	**Mass (kg)**	**Number**
Carbon Steel Type A 516	Divider Plate Assembly	3,720	1
Stainless Steel Type 316	Inner Vessel	8,860	1
	Inner Lid w/ LLF	1,170	1
	Interface Ring	44.6	1
	Spread Ring	31.9	1
	Total 316 Welds	102	—
Alloy 22	OCB with trunnion sleeves	6,540	1
	Middle Lid w/ LLF	350	1
	Outer Lid w/ LLF	693	1
	Total Alloy 22 Welds	64.2	—

NOTE: — indicates number of welds is not specified in source IED.

BWR = boiling water reactor, DHLW = defense high-level (radioactive) waste, IED = information exchange drawing, LLF = lid lifting feature, PWR = pressurized water reactor; DOE = U.S. Department of Energy

4.2 CRITERIA

This report was prepared to comply with 10 CFR Part 63 [DIRS 158535]. Relevant requirements for performance assessment from Section 114 of that document are: "Any performance assessment used to demonstrate compliance with Sec. 113(b) shall: (a) Include data related to the geology, hydrology, and geochemistry ... used to define parameters and conceptual models used in the assessment. (b) Account for uncertainties and variabilities in parameter values and provide the technical basis for parameter ranges, probability distributions, or bounding values used in the performance assessment. ... (g) Provide the technical basis for models used in the performance assessment such as comparisons made with outputs of detailed process-level models ...."

Programmatic requirements for this document are listed in *Technical Work Plan for: Near-Field Environment and Transport: Engineered Barrier System: Radionuclide Transport Abstraction Model Report Integration* (BSC 2004 [DIRS 170775]). This technical work plan (TWP) specifies that this document and all analyses described herein must adhere to the requirements of AP-SIII.10Q, *Models*, and to the requirements mentioned in the *Project Requirements Document* (Canori and Leitner 2003 [DIRS 166275]). This TWP also specifies that *Yucca Mountain Review Plan, Final Report* (NRC 2003 [DIRS 163274]) acceptance criteria must be addressed.

4.2.1 Yucca Mountain Review Plan Criteria

The acceptance criteria that concern flow and transport related to the EBS are presented in Section 2.2.1.3 of the *Yucca Mountain Review Plan, Final Report* (NRC 2003 [DIRS 163274]). Of the 14 model abstraction sections in the review plan, Sections 2.2.1.3.3 and 2.2.1.3.4 are applicable to this abstraction. The pertinent acceptance criteria from those two sections are listed in Sections 4.2.1.1 and 4.2.1.2, respectively.

4.2.1.1 Applicable Acceptance Criteria from Section 2.2.1.3.3, "Quantity and Chemistry of Water Contacting Engineered Barriers and Waste Forms"

The following acceptance criteria, listed in Section 2.2.1.3.3.3 of *Yucca Mountain Review Plan, Final Report* (NRC 2003 [DIRS 163274]), apply to this abstraction. These acceptance criteria are based on meeting the requirements of 10 CFR 63.114(a)–(c) and (e)–(g) [DIRS 158535], relating to the quantity and chemistry of water contacting engineered barriers and waste forms model abstraction.

Acceptance Criterion 1–System Description and Model Integration Are Adequate.

(1) Total system performance assessment adequately incorporates important design features, physical phenomena, and couplings, and uses consistent and appropriate assumptions throughout the quantity and chemistry of water contacting engineered barriers and waste forms abstraction process.

(2) The abstraction of the quantity and chemistry of water contacting engineered barriers and waste forms uses assumptions, technical bases, data, and models, that are appropriate and consistent with other related U.S. Department of Energy abstractions. For example, the assumptions used for the quantity and chemistry of water contacting

engineered barriers and waste forms are consistent with the abstractions of "Degradation of Engineered Barriers" (NRC 2003 [DIRS 163274], Section 2.2.1.3.1); "Mechanical Disruption of Engineered Barriers" (NRC 2003 [DIRS 163274], Section 2.2.1.3.2); "Radionuclide Release Rates and Solubility Limits" (Section 2.2.1.3.4); "Climate and Infiltration" (NRC 2003 [DIRS 163274], Section 2.2.1.3.5); and "Flow Paths in the Unsaturated Zone" (NRC 2003 [DIRS 163274], Section 2.2.1.3.6). The descriptions and technical bases provide transparent and traceable support for the abstraction of quantity and chemistry of water contacting engineered barriers and waste forms.

(3) Important design features, such as waste package design and material selection, backfill, drip shield, ground support, thermal loading strategy, and degradation processes, are adequate to determine the initial and boundary conditions for calculations of the quantity and chemistry of water contacting engineered barriers and waste forms.

(4) Spatial and temporal abstractions appropriately address physical couplings (thermal-hydrologic-mechanical-chemical). For example, the U.S. Department of Energy evaluates the potential for focusing of water flow into drifts, caused by coupled thermal-hydrologic-mechanical-chemical processes.

(5) Sufficient technical bases and justification are provided for total system performance assessment assumptions and approximations for modeling coupled thermal-hydrologic mechanical-chemical effects on seepage and flow, the waste package chemical environment, and the chemical environment for radionuclide release. The effects of distribution of flow on the amount of water contacting the engineered barriers and waste forms are consistently addressed, in all relevant abstractions.

(6) The expected ranges of environmental conditions within the waste package emplacement drifts, inside of breached waste packages, and contacting the waste forms and their evolution with time, are identified. These ranges may be developed to include: (i) the effects of the drip shield and backfill on the quantity and chemistry of water (e.g., the potential for condensate formation and dripping from the underside of the shield); (ii) conditions that promote corrosion of engineered barriers and degradation of waste forms; (iii) irregular wet and dry cycles; (iv) gamma-radiolysis; and (v) size and distribution of penetrations of engineered barriers.

(7) The model abstraction for quantity and chemistry of water contacting engineered barriers and waste forms is consistent with the detailed information on engineered barrier design and other engineered features. For example, consistency is demonstrated for: (i) dimensionality of the abstractions; (ii) various design features and site characteristics; and (iii) alternative conceptual approaches. Analyses are adequate to demonstrate that no deleterious effects are caused by design or site features that the U.S. Department of Energy does not take into account in this abstraction.

(8) Adequate technical bases are provided, including activities such as independent modeling, laboratory or field data, or sensitivity studies, for inclusion of any thermal-hydrologic-mechanical-chemical couplings and features, events, and processes.

(9) Performance-affecting processes that have been observed in thermal-hydrologic tests and experiments are included into the performance assessment. For example, the U.S. Department of Energy either demonstrates that liquid water will not reflux into the underground facility or incorporates refluxing water into the performance assessment calculation, and bounds the potential adverse effects of alteration of the hydraulic pathway that result from refluxing water.

Acceptance Criterion 2–Data Are Sufficient for Model Justification.

(1) Geological, hydrological, and geochemical values used in the license application are adequately justified. Adequate description of how the data were used, interpreted, and appropriately synthesized into the parameters is provided.

(2) Sufficient data were collected on the characteristics of the natural system and engineered materials to establish initial and boundary conditions for conceptual models of thermal-hydrologic-mechanical-chemical coupled processes, that affect seepage and flow and the engineered barrier chemical environment.

(4) Sufficient information to formulate the conceptual approach(es) for analyzing water contact with the drip shield, engineered barriers, and waste forms is provided.

Acceptance Criterion 3–Data Uncertainty Is Characterized and Propagated Through the Model Abstraction.

(1) Models use parameter values, assumed ranges, probability distributions, and bounding assumptions that are technically defensible, reasonably account for uncertainties and variabilities, and do not result in an under representation of the risk estimate.

(2) Parameter values, assumed ranges, probability distributions, and bounding assumptions used in the total system performance assessment calculations of quantity and chemistry of water contacting engineered barriers and waste forms are technically defensible and reasonable, based on data from the Yucca Mountain region (e.g., results from large block and drift-scale heater and niche tests), and a combination of techniques that may include laboratory experiments, field measurements, natural analog research, and process-level modeling studies.

(3) Input values used in the total system performance assessment calculations of quantity and chemistry of water contacting engineered barriers (e.g., drip shield and waste package) are consistent with the initial and boundary conditions and the assumptions of the conceptual models and design concepts for the Yucca Mountain site. Correlations between input values are appropriately established in the U.S. Department of Energy total system performance assessment. Parameters used to define initial conditions, boundary conditions, and computational domain in sensitivity

analyses involving coupled thermal-hydrologic-mechanical-chemical effects on seepage and flow, the waste package chemical environment, and the chemical environment for radionuclide release, are consistent with available data. Reasonable or conservative ranges of parameters or functional relations are established.

(4) Adequate representation of uncertainties in the characteristics of the natural system and engineered materials is provided in parameter development for conceptual models, process-level models, and alternative conceptual models. The U.S. Department of Energy may constrain these uncertainties using sensitivity analyses or conservative limits. For example, the U.S. Department of Energy demonstrates how parameters used to describe flow through the engineered barrier system bound the effects of backfill and excavation-induced changes.

Acceptance Criterion 4–Model Uncertainty Is Characterized and Propagated Through the Model Abstraction.

(1) Alternative modeling approaches of features, events, and processes are considered and are consistent with available data and current scientific understanding, and the results and limitations are appropriately considered in the abstraction.

(2) Alternative modeling approaches are considered and the selected modeling approach is consistent with available data and current scientific understanding. A description that includes a discussion of alternative modeling approaches not considered in the final analysis and the limitations and uncertainties of the chosen model is provided.

(3) Consideration of conceptual model uncertainty is consistent with available site characterization data, laboratory experiments, field measurements, natural analog information and process-level modeling studies; and the treatment of conceptual model uncertainty does not result in an under-representation of the risk estimate.

(4) Adequate consideration is given to effects of thermal-hydrologic-mechanical-chemical coupled processes in the assessment of alternative conceptual models. These effects may include: (i) thermal-hydrologic effects on gas, water, and mineral chemistry; (ii) effects of microbial processes on the engineered barrier chemical environment and the chemical environment for radionuclide release; (iii) changes in water chemistry that may result from the release of corrosion products from the engineered barriers and interactions between engineered materials and ground water; and (iv) changes in boundary conditions (e.g., drift shape and size) and hydrologic properties, relating to the response of the geomechanical system to thermal loading.

Acceptance Criterion 5–Model Abstraction Output Is Supported by Objective Comparisons.

(1) The models implemented in this total system performance assessment abstraction provide results consistent with output from detailed process-level models and/or empirical observations (laboratory and field testings and/or natural analogs).

(2) Abstracted models for coupled thermal-hydrologic-mechanical-chemical effects on seepage and flow and the engineered barrier chemical environment, as well as on the chemical environment for radionuclide release, are based on the same assumptions and approximations demonstrated to be appropriate for process-level models or closely analogous natural or experimental systems. For example, abstractions of processes, such as thermally induced changes in hydrological properties, or estimated diversion of percolation away from the drifts, are adequately justified by comparison to results of process-level modeling, that are consistent with direct observations and field studies.

(3) Accepted and well-documented procedures are used to construct and test the numerical models that simulate coupled thermal-hydrologic-mechanical-chemical effects on seepage and flow, engineered barrier chemical environment, and the chemical environment for radionuclide release. Analytical and numerical models are appropriately supported. Abstracted model results are compared with different mathematical models, to judge robustness of results.

4.2.1.2 Applicable Acceptance Criteria from Section 2.2.1.3.4, "Radionuclide Release Rates and Solubility Limits"

The following acceptance criteria, listed in Section 2.2.1.3.4.3 of *Yucca Mountain Review Plan, Final Report* (NRC 2003 [DIRS 163274]), apply to this abstraction. These acceptance criteria are based on meeting the relevant requirements of 10 CFR 63.114(a)–(c) and (e)–(g) [DIRS 158535], as they relate to the radionuclide release rates and solubility limits model abstraction.

Acceptance Criterion 1–System Description and Model Integration Are Adequate.

(1) Total system performance assessment adequately incorporates important design features, physical phenomena, and couplings, and uses consistent and appropriate assumptions throughout the radionuclide release rates and solubility limits abstraction process.

(2) The abstraction of radionuclide release rates uses assumptions, technical bases, data, and models that are appropriate and consistent with other related U.S. Department of Energy abstractions. For example, the assumptions used for this model abstraction are consistent with the abstractions of "Degradation of Engineered Barriers" (NRC 2003 [DIRS 163274], Section 2.2.1.3.1); "Mechanical Disruption of Engineered Barriers" (NRC 2003 [DIRS 163274], Section 2.2.1.3.2); "Quantity and Chemistry of Water Contacting Engineered Barriers and Waste Forms" (NRC 2003 [DIRS 163274], Section 2.2.1.3.3); "Climate and Infiltration" (NRC 2003 [DIRS 163274],

Section 2.2.1.3.5); and "Flow Paths in the Unsaturated Zone" (NRC 2003 [DIRS 163274], Section 2.2.1.3.6). The descriptions and technical bases provide transparent and traceable support for the abstraction of radionuclide release rates.

(3) The abstraction of radionuclide release rates provides sufficient, consistent design information on waste packages and engineered barrier systems. For example, inventory calculations and selected radionuclides are based on the detailed information provided on the distribution (both spatially and by compositional phase) of the radionuclide inventory, within the various types of high-level radioactive waste.

(4) The U.S. Department of Energy reasonably accounts for the range of environmental conditions expected inside breached waste packages and in the engineered barrier environment surrounding the waste package. For example, the U.S. Department of Energy should provide a description and sufficient technical bases for its abstraction of changes in hydrologic properties in the near field, caused by coupled thermal-hydrologic-mechanical-chemical processes.

(5) The description of process-level conceptual and mathematical models is sufficiently complete, with respect to thermal-hydrologic processes affecting radionuclide release from the emplacement drifts. For example, if the U.S. Department of Energy uncouples coupled processes, the demonstration that uncoupled model results bound predictions of fully coupled results is adequate.

(6) Technical bases for inclusion of any thermal-hydrologic-mechanical-chemical couplings and features, events, and processes in the radionuclide release rates and solubility Review Plan for Safety Analysis Report limits model abstraction are adequate. For example, technical bases may include activities, such as independent modeling, laboratory or field data, or sensitivity studies.

Acceptance Criterion 2–Data Are Sufficient for Model Justification.

(1) Geological, hydrological, and geochemical values used in the license application are adequately justified. Adequate description of how the data were used, interpreted, and appropriately synthesized into the parameters is provided.

(2) Sufficient data have been collected on the characteristics of the natural system and engineered materials to establish initial and boundary conditions for conceptual models and simulations of thermal-hydrologic-chemical coupled processes. For example, sufficient data should be provided on design features, such as the type, quantity, and reactivity of materials, that may affect radionuclide release for this abstraction.

(4) The corrosion and radionuclide release testing program for high-level radioactive waste forms intended for disposal provides consistent, sufficient, and suitable data for the in-package and in-drift chemistry used in the abstraction of radionuclide release rates and solubility limits. For expected environmental conditions, the U.S. Department of Energy provides sufficient justification for the use of test results,

not specifically collected from the Yucca Mountain site, for engineered barrier components, such as high-level radioactive waste forms, drip shield, and backfill.

Acceptance Criterion 3–Data Uncertainty Is Characterized and Propagated Through the Model Abstraction.

(1) Models use parameter values, assumed ranges, probability distributions, and bounding assumptions that are technically defensible, reasonably account for uncertainties and variabilities, and do not result in an under representation of the risk estimate.

(2) Parameter values, assumed ranges, probability distributions, and bounding assumptions used in the abstractions of radionuclide release rates and solubility limits in the total system performance assessment are technically defensible and reasonable based on data from the Yucca Mountain region, laboratory tests, and natural analogs. For example, parameter values, assumed ranges, probability distributions, and bounding assumptions adequately reflect the range of environmental conditions expected inside breached waste packages.

(3) DOE uses reasonable or conservative ranges of parameters or functional relations to determine effects of coupled thermal-hydrologic-chemical processes on radionuclide release. These values are consistent with the initial and boundary conditions and the assumptions for the conceptual models and design concepts for natural and engineered barriers at the Yucca Mountain site. If any correlations between the input values exist, they are adequately established in the total system performance assessment. For example, estimations are based on a thermal loading and ventilation strategy; engineered barrier system design (including drift liner, backfill, and drip-shield); and natural system masses and fluxes that are consistent with those used in other abstractions.

(4) Uncertainty is adequately represented in parameter development for conceptual models, process models, and alternative conceptual models considered in developing the abstraction of radionuclide release rates and solubility limits, either through sensitivity analyses or use of bounding analyses.

(5) Parameters used to describe flow through and out of the engineered barrier, sufficiently bound the effects of backfill, excavation-induced changes, and thermally induced mechanical changes that affect flow.

(8) DOE adequately considers the uncertainties, in the characteristics of the natural system and engineered materials, such as the type, quantity, and reactivity of material, in establishing initial and boundary conditions for conceptual models and simulations of thermal-hydrologic-chemical coupled processes that affect radionuclide release.

Acceptance Criterion 4–Model Uncertainty Is Characterized and Propagated Through the Model Abstraction.

(1) Alternative modeling approaches of features, events, and processes are considered and are consistent with available data and current scientific understanding, and the results and limitations are appropriately considered in the abstraction.

(2) In considering alternative conceptual models for radionuclide release rates and solubility limits, DOE uses appropriate models, tests, and analyses that are sensitive to the processes modeled for both natural and engineering systems. Conceptual model uncertainties are adequately defined and documented, and effects on conclusions regarding performance are properly assessed. For example, in modeling flow and radionuclide release from the drifts, DOE represents significant discrete features, such as fault zones, separately, or demonstrates that their inclusion in the equivalent continuum model produces a conservative effect on calculated performance.

(3) Consideration of conceptual model uncertainty is consistent with available site characterization data, laboratory experiments, field measurements, natural analog information and process-level modeling studies; and the treatment of conceptual model uncertainty does not result in an under-representation of the risk estimate.

(4) The effects of thermal-hydrologic-chemical coupled processes that may occur in the natural setting, or from interactions with engineered materials, or their alteration products, on radionuclide release, are appropriately considered.

Acceptance Criterion 5–Model Abstraction Output Is Supported by Objective Comparisons.

(1) The models implemented in this total system performance assessment abstraction provide results consistent with output from detailed process-level models and/or empirical observations (laboratory and field testings and/or natural analogs);

(3) DOE adopts well-documented procedures that have been accepted by the scientific community to construct and test the numerical models, used to simulate coupled thermal-hydrologic-chemical effects on radionuclide release. For example, DOE demonstrates that the numerical models used for high-level radioactive waste degradation and dissolution, and radionuclide release from the engineered barrier system, are adequate representations; include consideration of uncertainties; and are not likely to underestimate radiological exposures to the reasonably maximally exposed individual and releases of radionuclides into the accessible environment; and

4.3 CODES, STANDARDS, AND REGULATIONS

The relevant codes, standards, and regulations for the development of the *EBS RT Abstraction* are listed in Section 9.2.

5. ASSUMPTIONS

5.1 ALL SEEPAGE FALLS ONTO DRIP SHIELD/WASTE PACKAGE

Assumption: It is assumed that the locations of seeps in the emplacement drifts are random with respect to waste package locations, but that once a seep occurs, its location does not change over time. It is also assumed that fragments of the drip shield that may rest on the waste package, or fallen rock that may rest on the drip shield or waste package, do not divert any seepage flux. In addition, it is assumed that all seepage into the drift falls on the crown of the drip shield, and in the absence of a drip shield, all seepage falls on the crown of the waste package. In the event of a breach in the drip shield, all the seepage that penetrates the drip shield contacts the waste package.

Basis: Once seepage occurs during cooldown, the fracture characteristics that control the location of seepage are not expected to change. If such changes occur, they are likely to be limited in extent, or to occur in a random manner for many waste packages such that there is no overall, significant effect on the interaction of seepage water with waste forms. The mean seepage for the degraded drift is greater than for the non-degraded case, but the factors controlling seep locations are still likely to occur in a random manner for many waste packages.

Confirmation Status: This assumption does not require confirmation because it maximizes the duration of seepage contact with drip shields and waste packages as represented in TSPA-LA. It also maximizes the flux of dripping water available to flow through breaches in the drip shield or waste package, once such flow is initiated as represented in the TSPA-LA.

Use in the Model: This assumption is used throughout Sections 6 and 7.

5.2 EVAPORATION FROM A DRIP SHIELD DOES NOT OCCUR

Assumption: It is assumed that there is no evaporation of seepage water from the surface of the drip shield.

Basis: The heat output from the waste package will cause the drip shield generally to be hotter than the drift wall from which seepage water is dripping. Some seepage water that drips onto the drip shield may be evaporated, thereby reducing the flux of water through the drip shield. A reduction in the quantity of water flux through the drip shield reduces the potential for advective transfer and subsequent release and transport of radionuclides from the waste packages. Ignoring the process of evaporation in this analysis therefore bounds (maximizes) the impacts of the seepage flux on waste packages.

Although some splashing or splattering can occur as water droplets impinge on the drip shield, the splash distance would be limited, and the water would effectively be redistributed over the top of the drip shield. If water droplets were to fall near the edge of the top plate, some splashes could fall onto the invert or lower walls of the drift and drain directly into the invert. This situation would minimize the degrading effects of water dripping on the drip shield and therefore is eliminated from consideration in order to bound the impacts of the seepage flux on waste packages.

Confirmation Status: This assumption does not require confirmation because it provides for a reasonable upper bound on the flux available to interact with the drip shield and waste package, and bounds (maximizes) the potential degrading effects of seepage water on the drift environment.

Use in the Model: This assumption is used in Sections 6.3.2.4, 6.5.1.1, and 7.2.1.

5.3 EVAPORATION FROM A WASTE PACKAGE DOES NOT OCCUR

Assumption: It is assumed that evaporation of water from the surface or interior of a waste package does not occur.

Basis: Although heat released by spent nuclear fuel (SNF) will evaporate seepage water that drips onto the surface of or flows into breaches in a waste package, this process is not included in the analysis. Advective transport within the EBS is not possible if evaporation eliminates liquid fluxes. Therefore, evaporative processes are eliminated from this analysis to maximize the potential for advective transport of radionuclides. In addition to maximizing the advective flux of radionuclides from a waste package, this assumption also allows the water saturation inside a failed waste package to be set at 100 percent (fully saturated) in a codisposal waste package or in the degraded waste rind inside a failed fuel rod in a CSNF waste package, thereby maximizing the amount of water available for dissolving radionuclides. This assumption comes into play only after the thermal peak period of roughly 1,000 years (BSC 2004 [DIRS 169565], Figure 6.3-67), since dripping onto a waste package will not occur until the drift has cooled sufficiently for liquid water to be present. Because the relative humidity in the drift is low during the thermal peak period, condensation on cooler waste packages is unlikely, precluding evaporation from those surfaces.

Confirmation Status: This assumption does not require confirmation because it is used to ensure the maximum potential for advective transport of radionuclides.

Use in the Model: This assumption is used in Sections 6.3.3, 6.5.1.1.3, and 7.2.2.

5.4 PRODUCTION OR CONSUMPTION OF WATER BY CHEMICAL REACTIONS DOES NOT OCCUR

Assumption: It is assumed that chemical reactions in the EBS neither produce nor consume water and therefore do not effect on the water mass balance in the EBS.

Basis: Chemical processes in the EBS could produce or consume water. This is generally a small effect. Although unlikely, water could possibly be produced by the decomposition of hydrated salts or minerals. However, this phenomenon would only occur at elevated temperatures where liquid water would not be present; this would result in the release of water vapor rather than liquid water, and therefore would not directly affect liquid water fluxes. Water absorption by hygroscopic salts deposited on the drip shield and waste package surfaces as dust or as precipitates from earlier drift seepage may lead to the formation of aqueous solutions when the relative humidity reaches the deliquescence point of the salts (BSC 2004 [DIRS 169863], Sections 6.3 and 6.6). While this phenomenon may have important implications for corrosion processes, the quantity of liquid potentially produced by deliquescence is minimal and thus

assumed to be negligible, limited by the amount of salts that can be deposited on the waste package and drip shield surfaces. It is therefore reasonable to neglect the formation of aqueous solutions due to water absorption by hygroscopic salts as a source of water for advective transport.

However, consumption of water, particularly by corrosion reactions, is likely to occur. Anoxic corrosion of iron inside a waste package is a prime example of a water-consuming process that can consume enough water to impact flow through a waste package. Formation of hydrated corrosion products may also consume negligibly small amounts of water. Water absorption by hygroscopic salts deposited on the drip shield and waste package surfaces as dust or as precipitates would consume water as long as the relative humidity remains below the deliquescence point of the salts, although the quantity of water consumed is likely to be negligible. Neglecting consumption of water in the EBS radionuclide transport analysis is a bounding assumption, providing more water for dissolution and transport of radionuclides, and potentially greater releases, than would otherwise occur.

Confirmation Status: This assumption does not require confirmation because it bounds (maximizes) the amount of water potentially available for advective transport and release of radionuclides.

Use in the Model: This assumption is used throughout Sections 6 and 7.

5.5 THIN WATER FILMS ALWAYS EXIST BELOW 100°C

Assumption: A thin film of adsorbed water is assumed always to exist on the surfaces of internal waste package components and corrosion products in a breached waste package. This water film is assumed to be continuous and to behave as bulk liquid insofar as allowing radionuclides to dissolve in and diffuse through it. At and above 100°C, the thin film is assumed to evaporate, and no transport of radionuclides takes place.

Basis: All surfaces exposed to water vapor will adsorb water. The amount of adsorbed water vapor depends principally on the nature of the sorbing material and the ambient relative humidity.

The first layers of adsorbed water often do not contain ions from the sorbing solid (Lee 1994 [DIRS 154380], p. 73). This indicates that multiple water layers are needed in order for solid species (such as radionuclides) to dissolve and diffuse. Thus, to assume that radionuclides will dissolve in and diffuse through the adsorbed water film regardless of its thickness will overestimate releases of radionuclides. It is also necessary to assume that the water film is continuous, i.e., there are no gaps in the film from one particle or surface to the next, so that radionuclides can diffuse throughout the waste package interior and through corrosion products.

Above the boiling point of water, the thin films are assumed to evaporate. Due to the lack of a continuous water film, transport cannot take place. The boiling point is nominally 100°C, but may vary due to the elevation of the repository or to dissolved salts in the water film. Temperatures above the boiling point will exist at least through the thermal peak period of

roughly 1,000 years (BSC 2004 [DIRS 169565], Figure 6.3-67), and may continue to exist on certain waste packages well beyond that time.

Confirmation Status: This assumption does not require confirmation because it allows for radionuclide transport due to the presence of a continuous thin film of water on the surfaces of internal waste package components and corrosion products.

Use in the Model: This assumption is used in Sections 6.3.4.

5.6 ALL CORROSION PRODUCTS ARE HEMATITE (Fe_2O_3)

Assumption: It is assumed that the products of the corrosion of all internal waste package components except for fuel rods and spent nuclear fuel (SNF) are Fe_2O_3 (hematite).

Basis: This is a necessary assumption for the purpose of calculating corrosion product surface area and the resulting potential adsorption of water. Establishing the mineralogical type of iron oxide corrosion product enables the amount of water adsorbed onto surfaces to be estimated. This assumption also allows for reasonable estimates of the void volume of the waste package under conditions when the waste package internal components are fully corroded.

The bulk of the mass of materials in a CSNF waste package, excluding the SNF and the outer corrosion barrier, consists of various types of steel. The iron content of these steels (Table 6.3-4) ranges from 61.935 weight percent (Type 316, used in the inner vessel; DTN: MO0003RIB00076.000 [DIRS 153044]) to 98.37 weight percent (A 516 carbon steel, used in the basket components; DTN: MO0107TC240032.000 [DIRS 169970]). It is thus reasonable to treat all corrosion products as iron oxide.

Geochemical analyses of the basket degradation process (YMP 1998 [DIRS 104441], p. C-23) have demonstrated that the iron oxide produced from corrosion of carbon steel and borated stainless steels will remain in the waste package as insoluble hematite. In addition to hematite, goethite (FeOOH) is expected to form. The water vapor adsorption isotherm (expressed as water layer thickness) for goethite is similar to that of hematite (Jurinak 1964 [DIRS 154381], p. 486), although at a given relative humidity, more water is adsorbed onto hematite than onto goethite. The specific surface area of goethite is generally greater than hematite (Langmuir 1997 [DIRS 100051], Table 10.2), meaning that the water content is greater and the potential for radionuclide sorption is greater for goethite than for hematite. However, measurements of rust on ancient iron artifacts indicate that the specific surface area of goethite and other iron oxides ranges from 6 to 15 $m^2\ g^{-1}$ (Dillmann et al. 2004 [DIRS 171480], p. 1421 and Table 7), comparable to that of hematite. Thus, insofar as affecting the mobility of radionuclides in corrosion products, the higher specific surface area of goethite is offset by the greater water adsorption on hematite and the indications that the minerals comprising corrosion products have a much lower specific surface area than pure goethite. Hematite sorption behavior has been studied more thoroughly than goethite sorption behavior, which provides greater confidence that its behavior is represented accurately; therefore, corrosion products are assumed to be hematite.

Confirmation Status: This assumption does not require confirmation because it is a reasonable approach in the absence of detailed compositional data, corrosion process information, and adsorption isotherms for the numerous other potential steel corrosion products.

Use in the Model: This assumption is used in Sections 6.3.4.

5.7 NO CORROSION PRODUCTS EXIST IN THE INVERT

Assumption: It is assumed that no corrosion products exist in the invert.

Basis: Neglecting the corrosion products in the invert is an assumption that maximizes the potential transport of radionuclides through the invert. The invert consists of a carbon steel structural frame supported on the lower drift walls, and of crushed tuff ballast placed below and between the steel frame members. The invert steel structure consists of transverse beams anchored at each end on the drift wall, and of three longitudinal beams which directly support the waste package pallet. When the invert steel beams corrode, most of the iron oxide corrosion products will end up in the crushed tuff component of the invert. In addition, communication cables will eventually corrode, leaving copper oxide corrosion products in the invert. The crushed tuff has little radionuclide sorptive capacity compared to the metal oxide corrosion products, which are capable of sorbing large amounts of radionuclides, potentially enhancing the barrier capability of the invert. However, the corrosion products in the invert will tend to be localized and widely separated. For example, the transverse support beams in the invert are spaced 1.524 m (5 ft 0 in.) apart (BSC 2004 [DIRS 169503]). Thus, the corrosion products of the support beams will reside in a strip a few centimeters wide separated by 1.524 m of crushed tuff containing little or no corrosion products. Compared with the length of a waste package [3.45 m (5 DHLW/DOE SNF - Short) to 5.84 m (Naval long) (BSC 2004 [DIRS 169472], Table 1)], the width of regions within the invert that would potentially contain corrosion products is small. Therefore, the chance of radionuclides being released from the waste package and passing through corrosion products in the invert is proportionately small. Although the invert will contain steel corrosion products, it is bounding in terms of radionuclide releases to neglect their presence.

Confirmation Status: This assumption does not require confirmation because it is a bounding assumption that reduces the potential effectiveness of the invert as a transport barrier; i.e., the potential for radionuclide sorption by steel corrosion products is ignored.

Use in the Model: This assumption is used in Sections 6.3.4.2.

INTENTIONALLY LEFT BLANK

6. MODEL DISCUSSION

6.1 MODELING OBJECTIVE

The objective of the *EBS RT Abstraction* is to provide the conceptual model used to determine the time-dependent flux of radionuclides from the EBS to the unsaturated zone in the TSPA-LA. In particular, this model is used to quantify such releases from a failed waste package and the subsequent transport of those radionuclides through the EBS to the emplacement drift wall/unsaturated zone interface. The basic time-dependent inputs to the *EBS RT Abstraction* in TSPA-LA calculations consist of the drift seepage influx, the environmental conditions in the drift (temperature, relative humidity, and water chemistry), and the degradation state of the EBS components. Outputs consist of the rates of radionuclide fluxes to the unsaturated zone as a result of advective and diffusive transport, radionuclide solubility, retardation, the degree of liquid saturation of the waste form and invert materials, and the impact of colloids on potential radionuclide transport. The *EBS RT Abstraction* is implemented directly into the TSPA-LA GoldSim model to compute the release rates; details of the implementation are provided in Section 6.5.3.

6.1.1 Engineered Barrier System Components

The EBS consists of the drip shield, the waste package on an emplacement pallet, and an invert constructed with steel supports and filled between the steel framework with crushed tuff. Each of the components of the EBS is designed to act as a barrier to prevent or delay the mobilization and release of radionuclides into the geologic environment (see Section 6.7 for a summary of barrier capabilities). For example, the drip shield is designed to redirect any seepage that flows into the drift away from the waste package. The invert supports the waste package and emplacement pallet. It acts as a barrier to diffusive transport of radionuclides in liquids if the liquid saturation in the crushed tuff is low. Figure 6.1-1 presents a typical cross-section of an emplacement drift and the major components of the EBS.

The drip shield is fabricated from titanium, a corrosion-resistant material to provide long-term effectiveness. The waste package outer corrosion barrier is comprised of Alloy 22. The major corrosive processes are stress corrosion cracking in the closure lid welds of the waste package, localized corrosion in the waste package outer corrosion barrier, and general corrosion for both the drip shield and waste package.

Once the drip shield fails (i.e., is initially breached), a portion of the total dripping flux can drip onto the waste package. It is possible for breaches to occur at the gap between adjacent waste packages, because the overlap between adjacent drip shields is located over the gap, and this overlap is a potential leakage pathway. If breaches in the drip shield occur at the gap between two drip shield segments, the dripping flux would fall directly to the invert, avoiding the waste package. The possibility that breaches in the drip shield can occur over a gap, allowing liquid to bypass the waste package, is not considered in the *EBS RT Abstraction*.

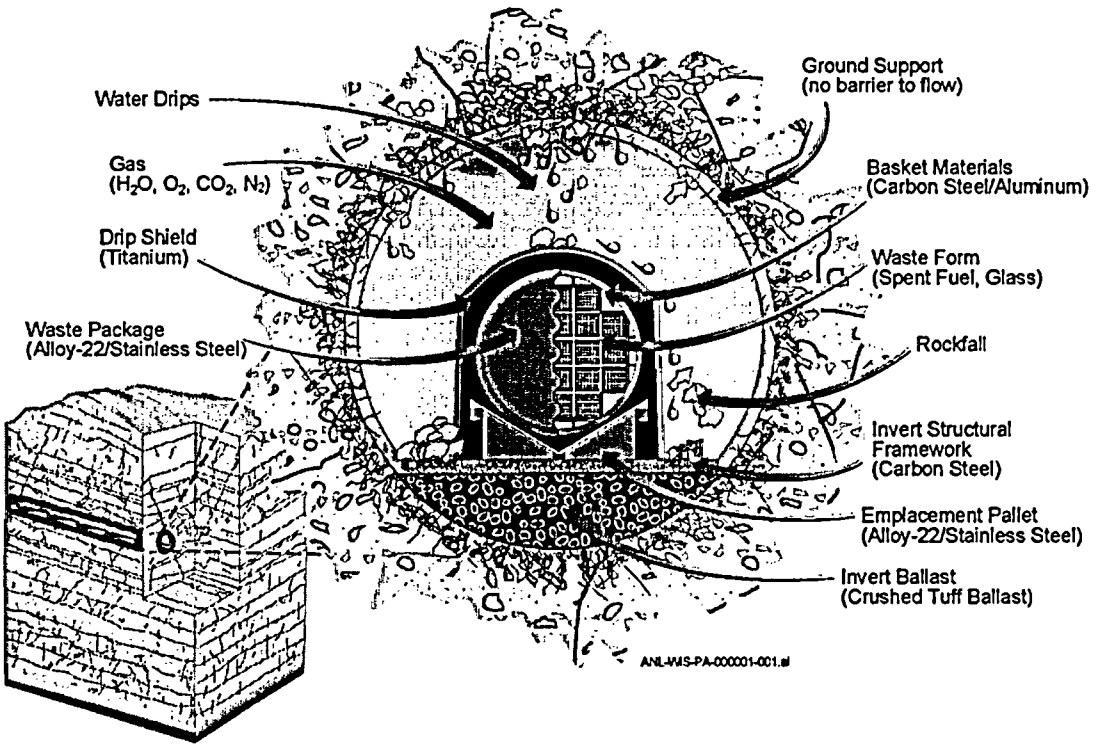

Figure 6.1-1. Schematic Diagram of a Typical Emplacement Drift and the Major Components of the EBS

After the waste package fails (breached by corrosion, seismic damage, or early failure mechanisms), a portion of the water that flows through the drip shield can enter the waste package, mobilizing radionuclides in any degraded waste form, and transporting these radionuclides into the unsaturated zone. Diffusion is the primary transport mechanism when the flux into the waste package is small or zero, or if stress corrosion cracks are the only penetrations through the waste package. Advective transport is important when the dripping flux occurs. In this case, advective fluxes can pass through the breaches in the drip shield and waste package.

6.1.2 Scenario Classes for TSPA-LA

A scenario is a well-defined, connected sequence of features, events, and processes (FEPs) that can be thought of as an outline of a possible future condition in the repository system. Scenarios can be designated as undisturbed, in which case the performance would be the expected or nominal performance of the system. Or, scenarios can be designated as disturbed, if altered by disruptive events, such as human intrusion, or by natural phenomena, such as volcanism or nuclear criticality. A scenario class is a set of related scenarios that share sufficient similarities to aggregate them usefully for the purposes of screening or analysis. The scenario classes

included in TSPA-LA are the nominal scenario class, igneous scenario class, and seismic scenario class.

Nominal Scenario Class–The nominal scenario class for TSPA-LA encompasses all of the FEPs that are screened in, except for those FEPs related to igneous or seismic activity. This scenario class therefore incorporates the important effects and system perturbations caused by climate change and repository heating that are projected to occur over the 10,000-year regulatory-compliance period. In addition, the nominal scenario class considers that the waste packages and drip shields will be subject to EBS environments and will degrade with time until they are breached and expose the waste forms to percolating groundwater. Then the waste forms will degrade, releasing and mobilizing radionuclides that subsequently will be transported out of the repository. Radionuclides released from the repository then will be transported to the saturated zone by the groundwater percolating through the unsaturated zone below the repository, and then transported to the accessible environment by water flowing in the saturated zone.

The nominal scenario class is represented by two modeling cases. The first is for those waste packages that degrade by corrosion (general corrosion, stress-corrosion cracking, and localized corrosion) under expected repository conditions. The second is for those waste packages that fail early due to manufacturing and material defects and pre-emplacement operations including improper heat treatment.

Igneous Scenario Class–The igneous scenario class describes performance of the repository system in the event of igneous activity that disrupts the repository and is represented by two modeling cases: (1) igneous intrusion into the repository emplacement drifts that results in release of radionuclides to the groundwater and (2) volcanic eruption through the repository resulting in release of radionuclides to the atmosphere. Both modeling cases assume that the igneous event consists of a magmatic penetration of the repository at some time after permanent closure.

The igneous intrusion modeling case assumes that an igneous dike intersects drifts of the repository and destroys drip shields and waste packages in those drifts intruded by magma, exposing the waste forms to percolating water and mobilizing radionuclides. The released radionuclides can then be transported out of the repository, and flow down through the unsaturated zone to the saturated zone, and then be transported through the saturated zone flow and transport system to the accessible environment. Radionuclide releases occur only as a result of igneous interactions with EBS components and not as a result of drip shield or waste package corrosion processes or early waste package failure.

The volcanic eruption modeling case assumes that the magma flow associated with a dike intersects the repository and destroys a limited number of waste packages, transports waste from the destroyed waste packages to the land surface through one or more eruptive conduits, and then discharges tephra and entrained waste into the atmosphere and transports it downwind.

Seismic Scenario Class–The seismic scenario class describes performance of the repository system in the event of low probability seismic activity capable of disrupting repository emplacement drifts and the engineered components of the EBS. This scenario class includes

potential damage to drip shields, waste packages, and CSNF cladding as a function of the magnitude of the event in addition to localized corrosion processes on the waste package outer corrosion barrier. Radionuclides are dissolved and mobilized and transported out of the repository, transported to the water table by the groundwater percolating through the unsaturated zone, and then transported to the accessible environment by water flowing in the saturated zone. Localized corrosion processes on the waste package outer corrosion barrier are included in the seismic scenario class because synergistic interactions between localized corrosion and ground motion damage to EBS components may be important.

The seismic scenario class is represented by two modeling cases. The first is for those waste packages that fail solely due to mechanical damage associated with the seismic event (i.e., vibratory ground motion or fault displacement). The second is for waste package localized corrosion initiated prior to and following the seismic event. This modeling case includes any mechanical damage, general corrosion and microbially influenced corrosion that also occurs along with the localized corrosion.

6.2 FEATURES, EVENTS, AND PROCESSES INCLUDED IN THE MODEL

The development of a comprehensive list of FEPs potentially relevant to postclosure performance of the Yucca Mountain repository is an ongoing, iterative process based on site-specific information, design, and regulations. The approach for developing an initial list of FEPs, in support of TSPA-Site Recommendation (SR) (CRWMS M&O 2000 [DIRS 153246]), was documented in *The Development of Information Catalogued in REV00 of the YMP FEP Database* (Freeze et al. 2001 [DIRS 154365]). The initial features, events and processes (FEP) list contained 328 FEPs, of which 176 were included in TSPA-SR models (CRWMS M&O 2000 [DIRS 153246], Tables B-9 through B-17). To support TSPA-LA, the FEP list was re-evaluated in accordance with *The Enhanced Plan for Features, Events, and Processes (FEPs) at Yucca Mountain* (BSC 2002 [DIRS 158966], Section 3.2), resulting in the LA FEP list (DTN: MO0407SEPFEPLA.000 [DIRS 170760]). Table 6.2-1 provides a list of FEPs that are included in TSPA-LA models described in this model document, summarizes the details of their implementation in TSPA-LA, and provides specific references to sections within this document. Screening arguments for both included and excluded FEPs are summarized in *Engineered Barrier System Features, Events, and Processes* (BSC 2004 [DIRS 169898]).

Table 6.2-1. Included FEPs for This Report

FEP No.	FEP Name/FEP Description	Section Where Disposition Is Described
2.1.06.06.0A	Effects of drip shield on flow	6.3.2.4 6.5.1.1
2.1.08.04.0A	Condensation forms on roofs of drifts (drift-scale cold traps)	6.3
2.1.08.05.0A	Flow through invert	6.3 6.5
2.1.08.06.0A	Capillary effects (wicking) in EBS	6.3 6.5

Table 6.2-1. Included FEPs for This Report (Continued)

FEP No.	FEP Name/FEP Description	Section Where Disposition Is Described
2.1.08.07.0A	Unsaturated flow in the EBS	6.3 6.5
2.1.09.05.0A	Sorption of dissolved radionuclides in EBS	6.3.4.2 6.5.1.2 6.5.3
2.1.09.08.0A	Diffusion of dissolved radionuclides in EBS	6.3.1.2 6.3.4.1 6.5.1.2 6.5.3.1
2.1.09.08.0B	Advection of dissolved radionuclides in EBS	6.3.1.2
2.1.09.19.0B	Advection of colloids in EBS	6.3.4.4 6.5.1.2 6.5.3
2.1.09.24.0A	Diffusion of colloids in EBS	6.3.4.4 6.5.1.2 6.5.3
2.1.11.09.0A	Thermal effects on flow in the EBS	6.3.1.1
2.2.07.06.0A	Episodic/pulse release from repository	6
2.2.07.06.0B	Long-term release of radionuclides from the repository	6

6.3 BASE CASE CONCEPTUAL MODEL

6.3.1 Introduction and Overview

6.3.1.1 EBS Flow Abstraction

The primary source of inflow to the EBS is the seepage flux that drips from the crown (roof) of the drift. This flux is driven by downward infiltration through the existing fracture system at Yucca Mountain. The seepage flux is conceptualized to flow from discrete fractures above the roof of the drift, falling vertically downward. The seepage flux is represented in the TSPA-LA model through *Abstraction of Drift Seepage* (BSC 2004 [DIRS 169131]). A secondary source of inflow to the EBS is imbibition into the invert crushed tuff particles from the surrounding UZ rock matrix. The inflow from these sources can flow through the EBS along eight pathways, as shown in Figure 6.3-1.

The eight pathways are (with the volumetric water flux through pathway j designated by F_j):

1. **Seepage flux (F_1)**–This is the seepage inflow (dripping flux) from the crown (roof) of the drift. Any condensation that may occur on the walls of the drift above the drift shield is included in this seepage flux.

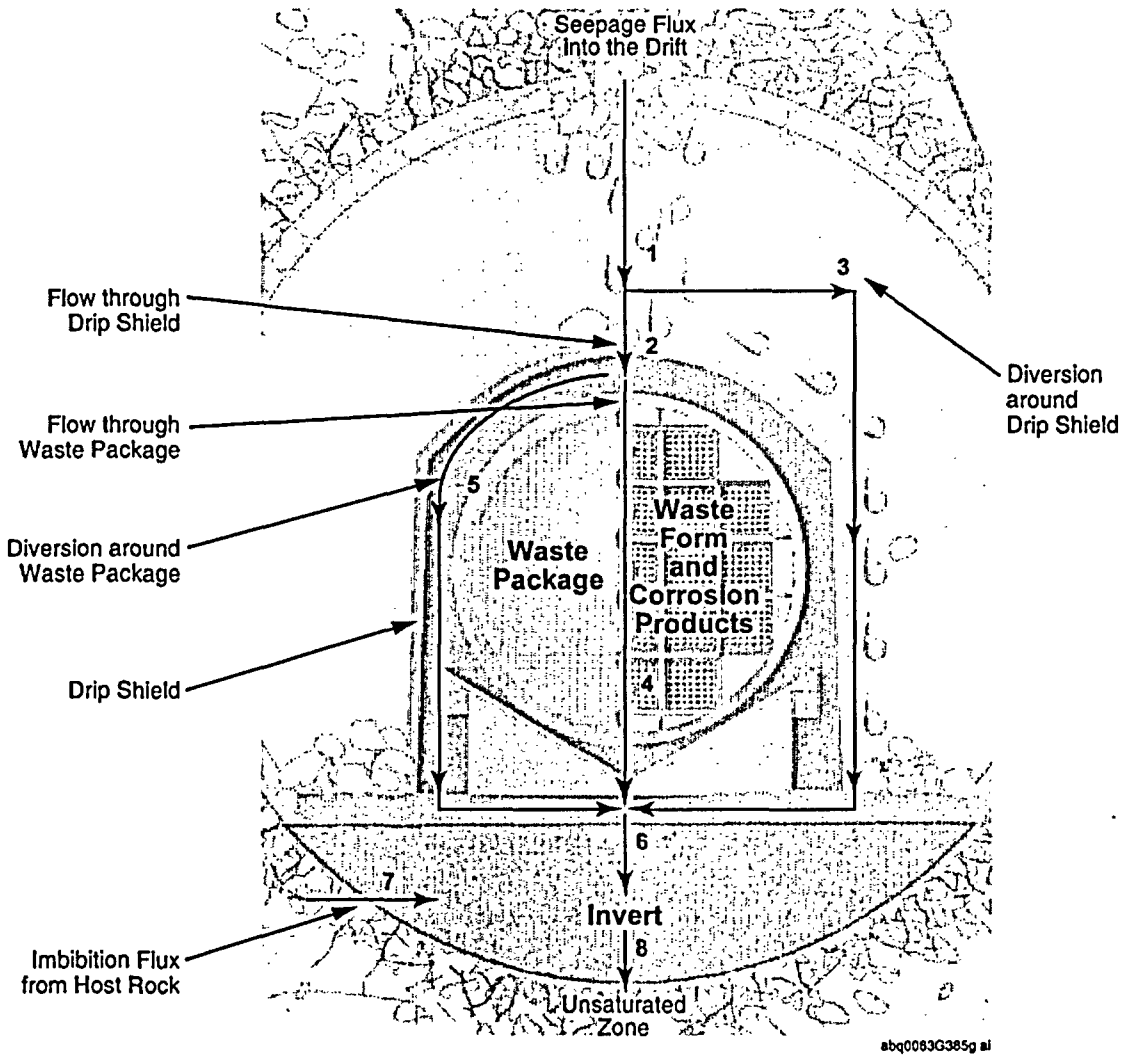

Figure 6.3-1. Schematic of the Potential Flow Pathways in the EBS

2. **Flux through the drip shield (F_2)**–The flux through the drip shield is based on the presence of patches due to general corrosion; localized corrosion and stress corrosion cracking on the drip shield are not expected to occur within the regulatory time period for repository performance (10,000 years) and are ignored (BSC 2004 [DIRS 169996], Section 7.2). The liquid flux through corrosion patches is proportional to the ratio of the axial length of the penetration(s) in the drip shield to the total axial length of a drip shield section (see Section 6.3.2.4). This flux splitting submodel for the drip shield should only be applied when there is a time-varying failure of the drip shield.

3. **Diversion around the drip shield (F_3)**–The portion of the flux that does not flow through the drip shield is assumed to flow directly into the invert.

4. **Flux through the waste package (F_4)**–The flux through the waste package is based on the presence of patches due to general corrosion and localized corrosion in the

waste package outer barrier. The number of patches in the waste package is calculated independently of the *EBS RT Abstraction* by the WAPDEG code (BSC 2004 [DIRS 169996]). The flux through waste package corrosion patches is proportional to the ratio of the axial length of the penetration(s) in the waste package to the total axial length of a waste package (see Section 6.3.3.2).

5. **Diversion around the waste package (F_5)**–The portion of the flux that does not flow into the waste package bypasses the waste form and flows directly into the invert.

6. **Flux into the Invert (F_6)**–All water flux from the waste package is modeled as flowing directly into the invert, independent of patch location on the waste package. In addition, the fluxes that were diverted around the waste package (F_5) and around the drip shield (F_3) flow into the invert. Only a portion of the total flux to the invert (the flux through the waste package, F_4) will contain radionuclides.

7. **Imbibition Flux to the Invert (F_7)**–Water can be imbibed from the host rock matrix into the invert.

8. **Flux from the Invert to the Unsaturated Zone (F_8)**–A portion of the advective flux from the invert equal to the total dripping flux (F_1) flows directly into the unsaturated zone (UZ) fractures. The portion of the advective flux from the invert equal to the imbibition flux to the invert (F_7) flows into the UZ matrix.

These pathways are time dependent, in the sense that total dripping flux, drip shield gaps, drip shield penetrations, and waste package penetrations will vary with time and local conditions in the repository.

The conceptual model for flow through the EBS includes three domains: the waste form (e.g., fuel rods or HLW glass), waste package corrosion products, and the invert. The first two domains are conceptualized to have concentric cylindrical geometry for volume calculations, with one-dimensional radial flow. The first domain (waste form) is part of the waste package that contains fuel rods or glass logs, which undergo alteration to form a rind. The thickness of the rind can be as much as the diameter of the fuel rod or glass log. The second domain (corrosion products from degradation of steel internal components) fills the inside of a waste package within the Alloy 22 outer corrosion barrier, so its thickness is uncertain and can be as much as the radius of the waste package. The third domain (invert) is in intimate contact with the waste package and has a thickness of 0.597 m (see Section 6.5.3). This is the average thickness of the invert directly beneath the waste package. This value is appropriate because flow out of the waste package is primarily vertically downward, and, ignoring splashing, it will not drip onto the surface of the invert beyond the edges of the waste package. Because the presence of the emplacement pallet is ignored, water and radionuclides pass directly from the waste package to the invert.

The waste form domain represents the source term for the TSPA-LA. Source term abstractions are defined in other model reports or design documents for radionuclide solubility (BSC 2004 [DIRS 169425]), HLW glass dissolution rate (BSC 2004 [DIRS 169988]), cladding response (BSC 2004 [DIRS 170023]), and inventory by waste package type (BSC 2004 [DIRS 169472],

Table 11). The source term represents input data or boundary conditions for the *EBS RT Abstraction* and is not discussed in this document.

The final output from the *EBS RT Abstraction* is the mass flux of radionuclides (kg yr^{-1}) from the EBS into the unsaturated zone. The parameters and formulas for calculating the water fluxes in the various pathways are summarized in Table 6.3-1.

Table 6.3-1. Summary of Parameters for EBS Flow Pathways

Flow Pathway, Pathway Flux F_i	Flow Parameters	Data Sources & Notes
1. Total dripping flux, F_1	Total dripping flux is a function of fracture properties, rock properties, and the percolation flux.	*Abstraction of Drift Seepage* (BSC 2004 [DIRS 169131]) provides time- and location-dependent values of total dripping flux.
2. Flux through the drip shield, F_2	L_{DS_Patch} is the axial half-length of each patch due to general corrosion of Ti. L_{DS} is the axial length of the drip shield. N_{bDS} is the number of corrosion patches of length L_{DS_Patch} in the drip shield. f'_{DS} is sampled uncertain parameter, Flux_Split_DS_Uncert. $F_2 = \min[F_1 N_{bDS} L_{DS\_Patch} f'_{DS}/L_{DS}, F_1]$	This flux splitting submodel for the drip shield should only be applied when there is a time-varying failure of the drip shield.
3. Diversion around drip shield, F_3	$F_3 = F_1 - F_2$.	Continuity of liquid flux.
4. Flux into the WP, F_4	L_{WP_Patch} is the axial half-length of each patch due to general corrosion of Alloy 22. L_{WP} is the axial length of the WP. N_{bWP} is the number of corrosion patches in the waste package. f'_{WP} is sampled uncertain parameter, Flux_Split_WP_Uncert. $F_4 = \min[F_2 N_{bWP} L_{WP\_Patch} f'_{WP}/L_{WP}, F_2]$	WAPDEG (BSC 2004 [DIRS 169996]) provides the number of patches and stress corrosion cracks on the WP. No flow through stress corrosion cracks due to plugging (BSC 2004 [DIRS 172203], Section 6.3.7). Steady state flow through WP (outflow = inflow in steady state; this is bounding for release).
5. Diversion around the WP, F_5	$F_5 = F_2 - F_4$	Continuity of liquid flux.
6. Flux to the invert, F_6	$F_6 = F_5 + F_4 + F_3$ $= F_1$	All advective flux enters the invert. Only F_4 can transport radionuclides into the invert.
7. Imbibition flux from the host rock matrix into the invert, F_7	F_7 is an input to the EBS flow model.	Imbibition flux is provided by *Multiscale Thermohydrologic Model* calculations (BSC 2004 [DIRS 169565]).
8. Flux from the invert into to the unsaturated zone, F_8	$F_8 = F_6 + F_7$ $= F_1 + F_7$	Total dripping flux portion (F_1) of advective flux from the invert flows into the UZ fractures, imbibition flux (F_7) flows into the UZ matrix.

WP=waste package; UZ=unsaturated zone

6.3.1.2 EBS Transport Abstraction

The waste form is the source of all radionuclides considered for the EBS. Radionuclides can be transported downward, through the invert and into the unsaturated zone. Transport can occur through advection when there is a liquid flux through the waste package and invert, via pathways 6 and 8 in Figure 6.3-1. Transport can also occur by diffusion in the waste form, in stress corrosion cracks in the lid of the waste package, and in the invert, even in the absence of a liquid flux, because it is assumed (Assumption 5.5) that there is a continuous liquid pathway via thin films. Diffusive transport may occur via flow pathways 6 and 8 even when no advection occurs on those pathways in the EBS flow model.

A detailed mathematical description of transport in the EBS is presented in Section 6.5.1.2. Retardation of radionuclides occurs in the waste package. Transport occurs by diffusion and by advection. Table 6.3-2 summarizes the modes and parameters for the transport pathways in the EBS.

Lateral and longitudinal dispersion are neglected in modeling radionuclide transport in the EBS. Because the EBS radionuclide transport model is a one-dimensional model, the lateral dispersion effects cannot be considered. This also maximizes the concentration in a given domain for greater mass flux. Longitudinal dispersion could potentially be considered in the invert, where advection is expected to occur due to imbibition flux, even when there is no drift seepage flux. However, the longitudinal dispersivity is uncertain, being dependent on the scale of transport (Anderson and Woessner 1992 [DIRS 123665], p. 326) and on porous media characteristics that are not well-defined. Since the thickness of the invert is less than one meter, longitudinal dispersion is expected to be small and to have negligible effect on the breakthrough times through the invert compared to the simulated time-steps considered in TSPA (tens of years). In addition, as shown in Section 6.3.4.1, the uncertainty in the invert diffusion coefficient ranges over a factor of 20 and essentially encompasses the variable breakthrough times that could occur from including the longitudinal dispersion. The dispersivity of the waste form and waste package corrosion product domains is also difficult to characterize; however, because the scale of these domains is comparable to that of the invert, and because the diffusion coefficients in these domains are similar (or larger) than those in the invert, it is reasonable to neglect dispersivity in these domains as well as in the invert.

There is no upward transport of radionuclides because there is no solid medium with a liquid pathway above the drip shield. After the drip shield is breached, upward diffusion is negligible in comparison to the downward advective flux through the drip shield.

Colloid-facilitated transport of radionuclides is included in the *EBS RT Abstraction.* Radionuclide transport from the waste package occurs in a liquid containing colloids and dissolved radionuclides. There are three types of colloids in the EBS: (a) waste form colloids from degradation of HLW glass, (b) iron oxyhydroxide colloids due to products from the corrosion of steel waste packages, and (c) groundwater or seepage water colloids. All three types of colloids may have reversibly sorbed radionuclides. The waste form colloids may have irreversibly attached (embedded) radionuclides and the corrosion products colloids may have reversibly attached (sorbed) radionuclides. However, some radionuclides, such as Pu and Am, can be so strongly sorbed onto iron oxyhydroxide that for modeling purposes they can be

considered to be irreversibly sorbed. Colloids may be transported by diffusion as well as by advection. The diffusion coefficient for colloids is less than that of dissolved species, but colloids are not excluded from diffusion due to size.

Table 6.3-2. Summary of Transport Modes and Parameters for the EBS Transport Pathways

Transport Pathway	Transport Modes	Transport Parameters and Data Sources
1. Waste form and corrosion products domains	Diffusion through stress corrosion cracks (no advective transport through stress corrosion cracks). Diffusion and advection through patches.	No lateral or forward dispersion. Colloidal particles will transport radionuclides. Diffusive area for each stress corrosion crack is 7.7×10^{-6} m^2 (see Section 6.3.3.1.2.1). Diffusive area for each patch is provided by WAPDEG (BSC 2004 [DIRS 169996]). Diffusion coefficient (all radionuclides): • 2.299×10^{-5} cm^2 s^{-1} at 25°C (Mills 1973 [DIRS 133392], Table III) • Modified for porosity and saturation (see Section 6.5.1.2.1.4) • Reduced by a factor of 100 if radionuclide is bound to a colloid (Section 6.3.4.4) The flow cross-sectional area is given by the interface between the waste package corrosion products domain and the invert domain. See Section 6.5.3 for further details.
2. Invert	Diffusion and advection (F_6) from corrosion products domain into the invert.	Liquid flux for advection = F_6 = F_5 (diverted by WP) + F_4 (flux through WP) + F_3 (diverted by drip shield). Diffusion coefficient (all radionuclides): • 2.299 × 10-5 cm^2 s^{-1} at 25°C (Mills 1973 [DIRS 133392], Table III) • Modified for porosity and saturation (see Section 6.3.4.1) • Temperature modification defined in Section 6.3.4.1.2; invert temperature is provided by *Multiscale Thermohydrologic Model* calculations (BSC 2004 [DIRS 169565]) • Reduced by a factor of 100 if radionuclide is bound to a colloid (Section 6.3.4.4) The flow cross-sectional area is the surface area between the invert and the drift wall contacting the invert. See Section 6.5.3 for further details.
3. Invert-UZ interface	Advection from the invert to UZ fractures (F_6) and UZ matrix (F_7); total flux is F_8. Diffusion from the invert to UZ fractures and matrix.	The invert diffusion calculation uses radionuclide concentrations in the WP corrosion products domain as the boundary condition at the top of the invert and a series of unsaturated zone computational cells below the invert that provide a gradient to a zero radionuclide concentration at some distance from the bottom of the invert (Section 6.5.3.6).

WP=waste package; UZ=unsaturated zone

The diffusion coefficient in the invert is based on the self-diffusion coefficient of water at 25°C as a bounding value for all radionuclides. The effects of variable porosity, liquid saturation, temperature, and uncertainty in the affect of these parameters are also included in calculating the diffusion coefficient.

The corrosion products from the waste package and SNFs have the potential to be strong sorbers for the actinides. Including sorption in the waste package and invert is beneficial to performance because this process can retain radionuclides in the EBS and delay release to the unsaturated zone. Because the waste package corrosion products are in intimate contact with or directly in the flow or diffusion path of the radionuclide source inside the waste package, retardation by corrosion products inside the waste package will occur. However, because corrosion products in the invert are more localized and not necessarily in any flow path from the waste package, sorption onto corrosion products in the invert is ignored (Assumption 5.7).

6.3.2 Water Flux through the Drip Shield (F_2)

6.3.2.1 Water Movement into and through a Drift (F_1 and F_3)

Water movement from the land surface and down through the unsaturated zone at Yucca Mountain is conceptualized to occur through a system of fractures (Liu et al. 1998 [DIRS 105729]). Simulations of water movement through the mountain yield estimates of percolation fluxes in the vicinity of the emplacement drifts that are a function of drift location, the geologic unit in which the drift resides, and the climate, which varies over time (BSC 2004 [DIRS 167652]). Consideration of the interactions between water moving through the mountain and the EBS form the basis of this abstraction for performance assessment.

The basic EBS design concept is shown in Figure 6.1-1 (Canori and Leitner 2003 [DIRS 166275], Figure 7-14). The drifts are 5.5 m in diameter. The bottom of the drift, commonly referred to as the invert, is filled with a ballast material of crushed tuff. The waste packages are to be placed on emplacement pallets that hold them in place above the invert. A titanium drip shield surrounds the waste packages. The space between the waste package and the drip shield, which is referred to as the axial space, is designed to remain air filled. The current repository design does not include an engineered backfill material (Canori and Leitner 2003 [DIRS 166275]); all of the analyses in this report reflect the no-backfill design.

At early times, any water that enters the drift is vaporized and expelled due to the heat output from the waste packages. According to modeling of water movement through the EBS using *Multiscale Thermohydrologic Model* (BSC 2004 [DIRS 169565]), much of the water that enters the drift remains as liquid once thermal output has subsided after approximately 2,000 years. Water that does seep into the drift can drip onto the drip shield and is diverted around the waste package, into the invert.

Water enters the drift by seepage from the roof of the drift. In this section, this mechanism is considered, followed by a discussion of water diversion around the drip shield.

6.3.2.1.1 Seepage Flux (F_1)

Seepage Model for PA Including Drift Collapse (BSC 2004 [DIRS 167652]) presents results of drift-scale UZ flow modeling of the interaction between host rock containing a fracture continuum and a drift for a variety of percolation flux rates and several sets of representative host rock hydraulic parameters. The seepage flux was found to be related to the percolation flux. However, the air-filled space beneath the roof of the drift acts as a capillary barrier that diverts water around the drift and limits seepage. These findings are consistent with the theory for seepage exclusion around cylindrical cavities introduced by Philip et al. (1989 [DIRS 105743]). Philip et al. showed that for given capillary properties of the host rock and a given drift diameter, there exists a critical percolation flux beneath which water will not enter the drift. The drift-scale unsaturated zone flow modeling results show a propensity for flow to diverge around the drifts.

Abstraction of Drift Seepage (BSC 2004 [DIRS 169131]) provides the rationale for calculating the seepage flux into the repository, accounting for thermal effects and spatial variability. The fraction of drifts that allow water seepage as a function of infiltration are given as a function of percolation rate. Across the range of percolation fluxes expected, a large majority of the drifts remain dry.

6.3.2.1.2 Diversion around the Drip Shield (F_3)

The drip shield has been designed to divert liquid water that may enter the drift away from the waste package. If the drip shield works as designed (this issue is discussed in detail below), it then acts as a no flow boundary. Any seepage that enters the drift moves downward under the force of gravity. As water migrates downward around the drip shield, it encounters the invert. The diversion around the drip shield occurs as droplets or rivulets, and any flow that enters the invert is concentrated at the sides of the drip shield while the drip shield is intact.

Once in the invert, water migrates quickly through into the unsaturated zone host rock at the bottom of the drift.

The algorithm for calculating the flux diversion around a breached drip shield is discussed in Section 6.3.2.4.

6.3.2.2 Drip Shield Effectiveness

Design drawings for the drip shield are given in *D&E / PA/C IED Interlocking Drip Shield and Emplacement Pallet* (BSC 2004 [DIRS 169220]) with details in drawings 000-M00-SSE0-00102-000-00B (BSC 2004 [DIRS 168067]), 000-M00-SSE0-02001-000-00A (BSC 2004 [DIRS 168326]), and other drawings cited on the information exchange drawing (IED). The drip shield has roughly the shape of the top of a mailbox with vertical sides and a top section that is curved for strength and to shed water. On one end, a drip shield connector guide is attached to the top of the curved section. The connector guide is a square rib, 50 mm wide (BSC 2004 [DIRS 168326]), that is attached to and extends across the curved top section. This connector guide provides extra stiffness to the end of the drip shield and can deflect seepage down the sides of the drip shield. On the other end of the drip shield, a connector plate is attached. The connector plate is 15 mm thick (BSC 2004 [DIRS 169220], Table 5) and also has a 50-mm-wide

square connector guide (BSC 2004 [DIRS 168326]) that is attached to the underside of the connector plate.

Adjacent drip shields are interlocked with one another. This is accomplished during installation by lowering the connector plate of one drip shield over the upward extending connector guide of the previously emplaced drip shield. The minimum overlap is the width of two connector guides, 100 mm (BSC 2004 [DIRS 168067]), and the maximum overlap between adjacent drip shields is 320 mm (BSC 2004 [DIRS 168067], Section A-A).

The gaps that exist between drip shields in this interlocking design can, potentially, provide a pathway for water to penetrate the drip shield system. The potential for such leakage under design conditions is considered here, followed by consideration of the ways in which the integrity of the drip shield might become compromised. This discussion is limited to considering the top of the drip shield because any water entering the contact between drip shields from the side would simply flow down the vertical sides of the drip shields, never contacting the waste.

Consider a system where the titanium walls of the drip shield form a barrier to flow. Water flux through the drip shield will now be limited to the gap where adjacent drip shields interlock. If high seepage flux conditions exist, then the flow can be driven into this gap. First, the water must travel laterally up to 320 mm to get beyond the overlap between the drip shields. As this water travels, it must remain precisely along the crown of this gap between the drip shields. If there is any deviation, the sloping sides of the drip shield impose gravity forces that will cause the water to flow down the sides and into the invert. Second, the upward extending drip shield connector guide provides a barrier to flow along the crown. Sufficient water pressure must be provided to push water up and over this barrier. Furthermore, the connector guides provide surfaces of contact with the drip shield and the connector plate. These contact surfaces maintain continuity down along the sloping sides of the top portion of the drip shield. These contacting surfaces will act akin to fractures in the sense that they impart capillarity and are able to transmit water. Any water reaching this point would run down the contact between the drip shields. Note also that the air-filled voids (having no capillarity) in between and beyond the connector guides provide an additional barrier to flow.

6.3.2.3 Drip Shield Breaching

The advective flow of water into the EBS has been shown to be effectively segregated from the waste packages as long as the integrity of the drip shield is maintained. Once corrosion patches form in the drip shield or adjacent drip shields separate, seepage can drip through the drip shield onto the waste package. The consequence of such drip shield failure is that a portion of the seepage water flux now migrates through the drip shield and comes into contact with the waste package. The thermal and mechanical response of the drip shield may produce gaps between adjacent sections of drip shield. These breaching mechanisms are screened out in *Engineered Barrier System Features, Events, and Processes* (BSC 2004 [DIRS 169898], Section 6.2.27, FEP 2.1.11.07.0A; Section 6.2.27, FEP 2.1.06.07.0B).

6.3.2.4 Water Flux through and around a Breached Drip Shield (F_2 and F_3)

Once the drip shield has been breached, a portion of the water flux (F_2) will pass through the drip shield and have access to the waste package. In this section, a flux splitting algorithm is developed to determine the fraction of the seepage flux that can pass through a degraded drip shield. A similar algorithm is developed in a later section to determine the fraction of the liquid flux through the drip shield that can enter a waste package. The flux splitting algorithm is important to TSPA-LA because the liquid flux into the waste package determines in part the transport of radionuclides by advection, an important release mechanism from the waste package and from the repository.

Once the flux through the drip shield is known, the flux diverted around the drip shield, F_3, is calculated using a quasi-static continuity of flow approach:

$$F_3 = F_1 - F_2 . \qquad \text{(Eq. 6.3.2.4-1)}$$

Key features of the drip shield flux splitting algorithm include: (1) the seepage flux into the drift falls as droplets from the top of the drift onto the crown of the drip shield (Assumption 5.1); (2) droplets fall randomly along the length of the drip shield; (3) only flow through general corrosion patches is considered; (4) evaporation from the drip shield is neglected (Assumption 5.2); all of the seepage flux either flows through corrosion patches or drains down the sides of the drip shield; and (5) all water that flows through breaches in the drip shield flows onto or into the waste package.

Some aspects of the flux splitting algorithm have been defined or clarified by experiments. The breached drip shield experiments (BSC 2003 [DIRS 163406]) were performed to validate the drip shield flux splitting algorithm and to examine in more detail the real behavior of seepage water impinging on and flowing over a drip shield. The tests were conducted by dripping water onto a mock-up portion of a full-scale drip shield made of stainless steel. The mockup section included slightly more than half of the shield from the top/center down the curvature to the side. The side was shortened along the longitudinal and vertical axes. Simulated corrosion patches-square holes 27 cm wide, the size of nodes in an earlier version of the WAPDEG corrosion model (CRWMS M&O 2000 [DIRS 151566], p. 36)–were cut into the drip shield at various locations to enable measurements of flow through breaches in the drip shield. Tests were performed with both smooth (machined stainless steel) and rough (silica anti-slip coating) surfaces. Data from the tests on the smooth surface were used to develop parameter values for the flux splitting submodel, whereas the rough surface test data were used to validate the submodel. Tests were conducted in a test chamber in an environment that would minimize evaporation (i.e., relative humidity of at least 80 percent). Water was dripped at various rates intended to cover the expected range of seepage rates within the repository. The dripping distance was the full-scale distance from the top of the drift to the crown of the drip shield, 2.17 m (BSC 2003 [DIRS 163406], Figure 10), based on repository design.

The tests that were conducted included (BSC 2003 [DIRS 163406]): (1) splash radius tests to determine the distance from the point of impact and a rough distribution of splattered water when drops impinge on the surface of the drip shield; (2) spread factor tests to determine the lateral rivulet spread distance from the drip impact point; (3) single patch splash tests to determine the

amount of water that enters targeted breaches as a result of splashing; (4) single patch flow tests to determine the amount of water that flows down the surface of the drip shield and into patches; (5) multiple patch tests to collect both splashed water and rivulet flows that entered all affected patches; and (6) bounding flow rate tests to provide data for extreme drift seepage conditions to compare with the nominal seepage rate.

Observations during the breached drip shield tests revealed that the primary mechanism for water to enter breaches is via rivulet flow that originates from an area around the point of drip impact. Following droplet impact at the crown, water splatters within some distance from the point of impact. The splattered water coalesces, forming beads that increase in size around the center of impact with each successive drop. After a time, the beads closest to the downhill curvature reach a critical mass and roll down the face of the drip shield in the form of a rivulet. The rivulet flow area spreads out in a delta formation (i.e., the maximum spread is located on the vertical section of the drip shield and the minimum spread is located at the point of impact). No film flow was observed during tests on the smooth or the rough drip shield surfaces.

Evaporation could occur in two forms during the test–from a freely falling drop and from a flow surface on the drip shield. The loss from a falling droplet is negligible; however, losses from the drip shield surface can be large. Experimental measurements included determination of evaporative losses. Although these data could be used to develop or validate a drip shield evaporation model, evaporation is not considered, which maximizes the potential for flow through breaches (Assumption 5.2).

For a given drip location onto the crown of the drip shield (see Assumption 5.1), the spreading of the rivulet flow is defined by a half-angle, α, formed with the vertical plane through the impact point (Figure 6.3-2). The lateral spread of the rivulet flow is given by $2x\tan\alpha$, where x is the arc length from the crown of the drip shield down to a location of interest (e.g., a corrosion patch). For N_b breaches in the drip shield of length L_{DS}, with each patch having a width of 2ℓ (m), the flux through the drip shield is given by:

$$F_2 = F_1 \frac{N_b \ell}{L_{DS}} \left(1 + \frac{\tan\alpha}{2}\right) f_{DS}. \qquad \text{(Eq. 6.3.2.4-2)}$$

For details of the mathematical development of this expression, see Section 6.5.1.1.2.4.

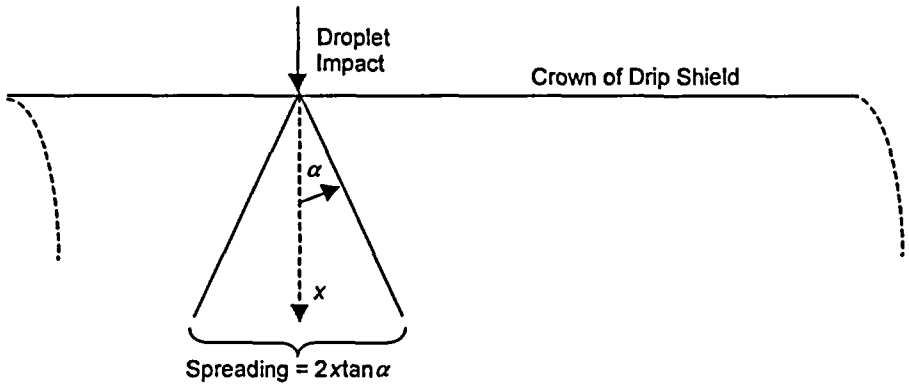

Figure 6.3-2. Illustration of Spreading for Rivulet Flow on the Drip Shield (Curvature not Shown)

The factor f_{DS} accounts for the uncertainty in the submodel and is a sampled parameter in TSPA-LA simulations. Sources of uncertainty include:

1. **Drip location with respect to the crown of the drip shield**–Drops that fall to either side of the crown will not divide exactly in half, as assumed by this submodel.

2. **Patch location**–Patches located on the crown will allow the entire dripping flux to pass through, whereas Equation 6.3.2.4-2 considers all patches to be located off the crown. For a given value of f_{DS}, Equation 6.3.2.4-2 underestimates the flux into crown patches because $f_{DS} < 1$, so $F_2 < F_1$, i.e., not all of the total dripping flux can flow through breaches. Since most of the randomly-located breaches occurring will not be located on the drip shield crown, this is a reasonable approximation, but not a bounding estimate of flow through drip shield breaches.

3. **Splattering distribution**–Although splattering of drops when they impinge on the drip shield is a random process, preferential directions or distributions could develop, for example, due to surface alteration as a result of corrosion or drift degradation (rockfall).

4. **Rivulet spread**–The breached drip shield experiments showed that a range of rivulet spread factors or spread angles can occur even on smooth surfaces. Surface roughness also affects the rivulet spread angle. Precipitation of salts or accumulation of dust on the drip shield surface could also affect rivulet flow.

5. **Interference among multiple patches**–Implicit in this submodel is that the patches do not interfere with each other, i.e., that no patch is lower on the drip shield surface than another patch. Patches located below another patch will see reduced or zero flux through the patch. By ignoring patch interference, water flux through the drip shield will be overestimated.

6. **Patches outside the footprint of the waste package**–Flux through these patches will pass directly to the invert. Since the conceptual model requires that all flow through

the drip shield goes onto or into the waste package, Equation 6.3.2.4-2 will overestimate that flow.

7. **Evaporation from the surface of the drip shield**–Evaporation is neglected (Assumption 5.2); if it occurs, the flux through the drip shield is less than predicted by Equation 6.3.2.4-2.

8. **Size of corrosion patches**–The WAPDEG model assumes a fixed size and shape for all corrosion patches. In reality, the patches will vary widely in size and shape randomly as well as over time.

Bounds and a distribution for f_{DS} must be established for use in TSPA-LA calculations. Because, under some of these uncertain conditions, the flux through the drip shield may be zero even when breaches exist, an appropriate lower bound on f_{DS} is zero. Under some other circumstances mentioned above, the entire seepage flux could flow through the drip shield. Thus, an upper bound on f_{DS} cannot be specified *a priori*, but should be given by:

$$f_{DS} = \frac{1}{\frac{N_b \ell}{L_{DS}}\left(1+\frac{\tan\alpha}{2}\right)}, \qquad \text{(Eq. 6.3.2.4-3)}$$

which makes $F_2 = F_1$. Since the number of patches, N_b, varies over time, f_{DS} should be a function of time, with a starting value of zero and potentially reaching a value equal to the total number of nodes in the WAPDEG corrosion model of the drip shield (BSC 2004 [DIRS 169996]). A uniform distribution is appropriate given that the uncertainty is difficult to quantify. To ensure that the flux through the drip shield is not greater than the seepage flux, the flux through the drip shield is computed as:

$$F_2 = \min\left[F_1 \frac{N_b \ell}{L_{DS}}\left(1+\frac{\tan\alpha}{2}\right) f_{DS}, F_1\right]. \qquad \text{(Eq. 6.3.2.4-4)}$$

The uncertainty in spread angle α can be lumped in with f_{DS} since both would otherwise be sampled independently. A lumped uncertainty factor f'_{DS} is defined as

$$f'_{DS} = \left(1+\frac{\tan\alpha}{2}\right) f_{DS}, \qquad \text{(Eq. 6.3.2.4-5)}$$

with the flux through the drip shield to be computed as:

$$F_2 = \min\left[F_1 \frac{N_b \ell}{L_{DS}} f'_{DS}, F_1\right]. \qquad \text{(Eq. 6.3.2.4-6)}$$

In Section 6.5.1.1.2.4, an upper bound on f'_{DS} is developed based on results of the breached drip shield experiments, and is used in the TSPA-LA model.

6.3.3 Water Flux through the Waste Package (F_4)

The conceptual model for the TSPA-LA is based on the assumed presence of continuous flow paths through the patches that penetrate the waste package. More specifically, in the TSPA-LA conceptual model, vertical flow of seepage into the waste package, through the waste form, and out of the waste package is not impeded by the location of patches on the surface of the waste package. In other words, there is no long-term build-up and retention of liquid within the waste package for flow and transport. (An alternative conceptual model in which water fills the waste package before any water flows out–the "bathtub" model–is evaluated in Section 6.4.1). There is also no resistance to the flow through the waste form. The TSPA-LA approach attempts to maximize the immediate release and mobilization of radionuclides, while retaining as much realism as justified by the data and understanding of the physical and chemical processes that take place.

Radionuclides cannot be released from the waste package if there is insufficient water or if there are no openings through either the wall or lid of the waste package. Section 6.3.3.1 describes the types of openings that can form, how and where they form, the timing of their formation, and the flow through these openings. The dimensions of these openings have implications for whether water is able to flow into and through the waste package or whether transport out of the waste package is by advection and/or diffusion. Section 6.3.3.2 describes the flux of liquid around or through the waste package. Section 6.3.3.3 describes the alternative pathway for liquid to reach the waste package; namely, evaporation from the invert and condensation on the inside of the drip shield can provide a source of liquid to the exterior of the waste package even when there are no openings in the drip shield. Section 6.3.3.4 describes the flux of liquid through the invert.

6.3.3.1 Breaching of the Waste Package

6.3.3.1.1 Waste Package Design

Ten waste package configurations are planned for the waste to be emplaced in the repository, where the nominal quantity for LA is shown in parentheses (BSC 2004 [DIRS 169472], Tables 1 and 11):

1. 21-PWR with absorber plates (4,299)
2. 21-PWR with control rods (95)
3. 12-PWR (163)
4. 44-BWR (2,831)
5. 24-BWR (84)
6. 5 DHLW/DOE SNF – Long (1,406)
7. 5 DHLW/DOE SNF – Short (1,147)
8. 2-MCO/2-DHLW (149)
9. Naval Short (144)
10. Naval Long (156).

Waste packages are broadly categorized as CSNF waste packages (21-PWR and 44-BWR are the most common), codisposal waste packages (5 DHLW/DOE SNF–Short and Long), and Naval Short and Long waste packages. Although waste packages vary depending on the waste form they contain, the majority of designs have features in common. These commonalties are described here. The waste package consists of a cylindrical inner stainless steel vessel, which is sealed with a stainless steel lid. The inner vessel is placed into an Alloy 22 outer corrosion barrier, which is sealed with a middle and outer lid. The inner vessel has 5-cm-thick walls and lid that provide structural integrity for the waste package. The Alloy 22 outer corrosion barrier has a wall approximately 2 cm thick, a middle lid approximately 13 mm thick, and a 2.5-cm-thick outer lid, that provide resistance to corrosion. Design information for waste packages is provided on IED, *D&E / PA/C IED Typical Waste Package Components Assembly* (BSC 2004 [DIRS 169472]), which identifies detailed design drawings, including drawings of the 21-PWR, 44-BWR, the 5 DHLW/DOE SNF - Short, and the Naval Short and Long waste packages, among others.

The stainless steel inner vessel of the waste package is modeled as having no resistance to corrosion as reflected in *WAPDEG Analysis of Waste Package and Drip Shield Degradation*, (BSC 2004 [DIRS 169996] Section 6.3), forming an immediate flow pathway once the outer (Alloy 22) corrosion barrier has been breached. Similarly, as modeled, the closure weld on the inner stainless steel lid, as part of the stainless steel inner vessel, has no resistance to corrosion, and the inner lid fails once the outer lids have failed.

6.3.3.1.2 Types of Openings

Three general types of openings can exist in the waste package due to corrosion. These are (1) radial stress corrosion cracks that penetrate the welds of the lids, (2) patches resulting from general corrosion, and (3) localized corrosion. Stress corrosion cracks and general corrosion patches are discussed in turn below. The opening area from localized corrosion is described in the *General Corrosion and Localized Corrosion of Waste Package Outer Barrier* (BSC 2004 [DIRS 169984], Section 8.3.1).

6.3.3.1.2.1 Radial Stress Corrosion Cracks in Lid Welds

Stress corrosion cracks can appear because of the residual tensile stresses generated during the process of welding the lids in place. It is not possible to anneal the final closure welds, although laser peening has been proposed as a means to mitigate residual stress in waste package closure lid welds (BSC 2004 [DIRS 172203], Section 6.4.4). Stress corrosion cracks will typically form along two orientations. Radial stresses can generate circumferential cracks while hoop stresses can generate radial cracks. Only radial stress corrosion cracks are considered in the *EBS RT Abstraction* because the formation of circumferential cracks that penetrate the thickness of the lids is unlikely. Cracks require the presence of tensile stress for initiation and propagation. Detailed finite-element analyses of the welding process demonstrate that only compressive radial stresses exist at the inner surface (BSC 2004 [DIRS 172203], Figure 6-11, Cross-Section 1-1). In this condition, circumferential cracks cannot propagate through the thicknesses of the lid welds and are therefore not considered in the *EBS RT Abstraction.*

Radial cracks are transverse to the weld and cannot be much longer than the weld width. A radial crack opening has an elliptical shape with length $2a$ and a gap width δ (BSC 2004 [DIRS 172203], Section 6.5.2). The equation given by Tada et al. (1973 [DIRS 118706], p. B.5) can be used to calculate the gap width, δ (m), for a crack with length $2a$ in an infinite sheet under plane stress load:

$$\delta = \frac{4a\sigma_a}{E}, \qquad \text{(Eq. 6.3.3.1-1)}$$

where E is the modulus of elasticity (Pa), $2a$ is the crack length (m), and σ_a is the applied stress (Pa). Values for E for Alloy 22 are given in DTN: MO0107TC239753.000 [DIRS 169973].

The residual hoop stress in the as-welded waste package outer lid is higher on the outside surface than on the inside surface (BSC 2004 [DIRS 172203], Table 6-9). The resulting shape of the crack is then an ellipsoidal cone where $2a$ is the length of the long axis, and short axis lengths δ_o and δ_i are the gap widths for the outside and inside surfaces, respectively. The depth d of the crack is taken to be the lid thickness. Figure 6.3-3 is a schematic diagram of the geometry of the ellipsoidal cone crack.

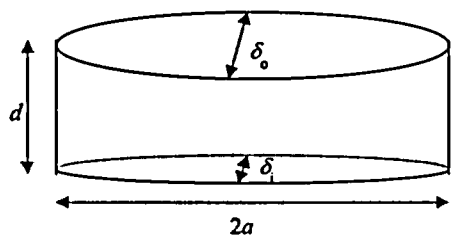

Figure 6.3-3. Schematic of the Dimensions for an Ellipsoidal Crack

A range of values of σ_a, the residual stress, and the maximum length $2a$ of a radial crack can be estimated. The region of high residual stress is identified from finite-element simulations (BSC 2004 [DIRS 172203], Section 6.4). The expected maximum length of a radial crack is approximately two times the lid thickness (BSC 2004 [DIRS 172203], Section 6.5.1). For an outer lid thickness of 25.4 mm (BSC 2004 [DIRS 167394]), the maximum crack length is approximately 50 mm. Table 6.3-3 gives the calculated gap width, based on Equation 6.3.3.1-1 and typical residual stresses at the inner and outer surface of the lid for a 21-PWR waste package (BSC 2004 [DIRS 172203], Table 6-9).

The cross-sectional area of the stress corrosion crack is important for transport by diffusion. The bounding (largest) cross-sectional area is defined by conditions at the outer surface of the 5-cm-long crack. The area of this ellipse is πab, where $2a$ is 5 cm and b is one-half of the larger gap width on the outer surface (in Table 6.3-3). The cross-sectional area of a single stress corrosion crack is then $\pi(0.025\text{ m})(9.82 \times 10^{-5}\text{ m})$ or $7.7 \times 10^{-6}\text{ m}^2$.

An updated analysis of stress corrosion cracking is given in *Stress Corrosion Cracking of the Drip Shield, the Waste Package Outer Barrier, and the Stainless Steel Structural Material* (BSC 2004 [DIRS 172203]). For the base conceptual model (BSC 2004 [DIRS 172203],

Appendix B, Table B-2), the estimated crack opening is smaller than the crack opening of 7.7×10^{-6} m^2 obtained in this section. Therefore, use of this value in TSPA-LA calculations when stress corrosion cracking occurs will overestimate the rate of release of radionuclides compared with the updated values in (BSC 2004 [DIRS 172203]).

Table 6.3-3. Calculated Gap Width for a Range of Residual Stresses at 400°F (Approximately 200°C) in a 21-PWR Container

Parameter	Inner Surface	Outer Surface
Hoop stress, σ_a (BSC 2004 [DIRS 172203], Table 6-9)	231.1380 MPa	385.0522 Mpa
Gap width for crack length $2a$ = 50 mm	118 μm	196 μm

Dripping water is capable of contacting a stress corrosion crack only if the waste package is tilted upward. A possible mechanism for tilting is emplacement pallet collapse due to corrosion that causes one end of the waste package to fall off its emplacement pallet. This maximum angle of tilt occurs when the lid end of the waste package is elevated to the height of the inside of the drip shield while the other end rests against the invert.

Advective flow of water through stress corrosion cracks can be neglected. This is bounding for several reasons. First, a film that completely spans the opening of a stress corrosion crack creates a differential in capillary forces that will prevent any further ingress of flowing water into the waste package. Second, the presence of corrosion products in the small stress corrosion crack may provide a capillary barrier for advective flux into the waste package. Third, in addition to a capillary barrier, corrosion products filling the corrosion cracks will provide resistance to flow, requiring a large head or pressure gradient that is unlikely to exist. Fourth, because corrosion patches are orders of magnitude larger in cross section and may appear in the same time frame, flow through corrosion cracks is negligibly small compared to flow through patches.

The potential for atmospheric pumping, hygroscopic salts in the waste package, and the uncertainty about film thickness make it difficult unequivocally to exclude liquid flow into the waste package. In any case, the more important question is how much liquid flows *out* of the waste package, advectively transporting radionuclides. Given the resistance to flow into the waste package through stress corrosion cracks, flow out is even less likely. The uncertainty in flow through corrosion cracks is compensated for at least in part by the assumption that a continuous water film is always present in corrosion cracks through which diffusion can occur (see Assumption 5.5) and by no restrictions on water vapor diffusing through the cracks, which provides a mechanism for water to enter a waste package once stress corrosion cracks exist.

6.3.3.1.2.2 Patches from General Corrosion

The waste package design consists of an inner stainless steel vessel placed inside an Alloy 22 outer corrosion barrier. No credit is taken for resistance to corrosion by the inner stainless steel vessel. The main corrosion mechanisms for the outer corrosion barrier are general corrosion and localized corrosion. The size and timing of patches resulting from general corrosion are predicted by the WAPDEG model (BSC 2004 [DIRS 169996]).

6.3.3.1.3 Impact of Heat Generation Inside Waste Package

Heat generated by the waste form has the potential to evaporate water within the waste package. In this situation, water cannot collect inside the waste package and cannot support advective transport of radionuclides. Preliminary estimates using *Multiscale Thermohydrologic Model* (BSC 2004 [DIRS 169565], Section 6.3) indicate that the available heat can evaporate incoming water for several thousand years. However, although evaporation is expected to occur, complexities in the internal geometry of the waste packages (particularly the response of any water pooled at the bottom of the package and the presence of small conduits for water vapor to escape through stress corrosion cracks) make it difficult to say definitively that all incoming water is evaporated. As a simplification, no transport is assumed to occur when the temperature in the waste package is above 100°C (Assumption 5.5), when a continuous film of water needed for transport is no longer expected to exist.

The expected evaporation in the waste package is ignored in the TSPA-LA. This approach is bounding because evaporation might eliminate advection as a transport mechanism. In addition, by ignoring evaporation from a waste package, it becomes possible to specify a water saturation of 1.0 (fully saturated) inside a failed waste package whenever dripping occurs. If evaporation were accounted for, the water saturation inside a waste package would generally be less than one, which would reduce the amount of radionuclides that could dissolve in the water and be advectively transported from the waste package. Lower water saturations would also reduce estimates of diffusive releases, since both the diffusion coefficient and the cross-sectional area for diffusion would be less. Thus, without these simplifying assumptions, the amount of radionuclides transported from a waste package would be expected to be much less.

6.3.3.2 Water Flux through and around the Breached Waste Package (F_4 and F_5)

The flux through (into and out of) the waste package, F_4, is conceptualized to be the flux through patches, which includes the flux thorough the drip shield (F_2). Advective flux of water through stress corrosion cracks is unlikely and therefore is neglected (Section 6.3.3.1.2.1). A quasi-steady state approach is used. The presence of a gap between adjacent waste packages is neglected in the TSPA-LA model. Dripping onto the waste package from condensation on the underside of the drip shield is screened out (BSC 2004 [DIRS 169898], Section 6.2.43).

A flux splitting algorithm analogous to the drip shield flux splitting algorithm (Section 6.3.2.4) is developed here. The analogy is appropriate based on similarities in geometry and assumptions regarding the source of liquid flux falling onto the waste package. The surface of the waste package is a horizontal cylinder, as is the top of the drip shield, the primary difference that impacts liquid flow on the curved surface being that the radius of curvature of the waste package is smaller than that of the drip shield. Thus, flow behavior on the surface of the waste package should be similar to that on the drip shield. In particular, if any water is available, it is expected to flow over the surface of the waste package in rivulets rather than as film flow, based on findings of the breached drip shield experiments (BSC 2003 [DIRS 163406]).

Whereas drip locations on the drip shield could reasonably be confined to the crown of the drip shield (because the drift seepage flux will most likely originate from the crown of the drift), the drip locations may be more widely dispersed on the waste package. This is the case for drips

that fall from breaches in the drip shield, which are randomly located on the drip shield. Since breaches (mainly general corrosion patches) in the waste package are also randomly located, the fraction of dripping flux falling on the waste package that flows into the waste package might be expected to be proportional to the total area of waste package patches. However, since drips that fall onto an intact waste package surface will drain down the surface, the flux of water, if any, entering a waste package is proportional to the total length of patches. Again, the analogy to the drip shield applies. Rivulets flowing down the surface of the waste package are intercepted in proportion to the lengths of the patches (ignoring interference by multiple patches).

Two other considerations reinforce the comparison with the drip shield. First, any condensation on the underside of the drip shield that falls onto the waste package will fall from the crown of the drip shield. Thus, for condensation at least, the geometry is completely analogous to that of the drip shield inside the drift. Second, due to uncertainty in the corrosion rate of the drip shield, the drip shield is modeled as a single entity and all drip shields in the repository fail by general corrosion at the same time for a given realization (BSC 2004 [DIRS 169996], Section 6.3). Once the drip shield is gone, the seepage flux will now fall directly from the drift crown onto the waste package crown, again completing the analogy with the drip shield under the drift crown. Since the corrosion rate of the titanium drip shield is higher than that of the Alloy 22 waste package outer corrosion barrier, the situation where a breached waste package lies unprotected under seepage from the drift crown should be more likely than a breached waste package underneath a breached but still partially effective drip shield. Therefore, within the uncertainty of the model, it is an appropriate simplification to assume that the flux impinging on the waste package falls entirely on the crown of the waste package. One implication of this assumption is that, as with the drip shield, half of this flux flows down each side of the waste package.

Based on these arguments, a flux splitting algorithm for the waste package can be given that is completely analogous to the drip shield flux splitting algorithm:

$$F_4 = \min\left[F_2\left(\frac{N_{bWP}\ell_{WP}}{L_{WP}}\right)\left(1+\frac{\tan\alpha}{2}\right)f_{WP}, F_2\right], \qquad \text{(Eq. 6.3.3.2-1)}$$

where F_4 is the flux through the waste package, F_2 is the flux through the drip shield, and L_{WP} is the total axial length of the waste package. N_{bWP} patches each of length $2\ell_{WP}$ comprise the breaches in the waste package. Flow through stress corrosion cracks is neglected as being unlikely to occur (see Section 6.3.3.1.2.1).

The factor f_{WP} accounts for the uncertainty in this algorithm. As with the corresponding factor f_{DS} for the drip shield, bounds can be established for f_{WP} based on the dimensions of the patches and the waste package and the uncertain rivulet spread angle. A lower bound of zero is necessary to account for the possibility that seepage through the drip shield is completely diverted by an intact portion of the waste package outer corrosion barrier.

For an upper bound on f_{WP}, the drip shield experiments (BSC 2003 [DIRS 163406]) provide some guidance. Since the radius of curvature of the waste packages is smaller than that of the drip shield, the rivulet spread angle on the waste packages would be expected to differ from, and

probably be smaller than, the spread angle on the drip shield. In some experiments, the drip location on the drip shield mockup was well away from the crown on more steeply inclined regions of the drip shield. Rivulets flowing from those drip locations may simulate more closely the behavior on a surface having a smaller radius, such as a waste package. Because the waste package has a smaller radius and more curvature than the drip shield surface, more of the surface is sloped to such a degree that water will readily flow down it by gravity. Only a larger cylindrical surface (the drip shield mockup) was available on which to observe gravity flow behavior. Observations away from the crown, where the slope is steep enough to initiate flow as readily as on a more highly curved surface, are appropriate analogs to measurements on an actual smaller cylinder. An analysis of drip shield experimental data for off-crown drip locations (Section 6.5.1.1.3) gives a mean spread angle of 13.7° and a range from 5.5° to 22.0°. In analogy to f_{DS}, an upper bound on f_{WP} can be obtained using the minimum rivulet spread angle α of 5.5° and the known values for N_{bWP} (BSC 2004 [DIRS 169996]), $2\ell_{WP}$, and L_{WP}:

$$f_{WP} = \frac{1}{\frac{N_{bWP}\ell_{WP}}{L_{WP}}\left(1+\frac{\tan\alpha}{2}\right)}. \qquad \text{(Eq. 6.3.3.2-2)}$$

As with the drip shield, the term $\left(1+\frac{\tan\alpha}{2}\right)$, which is uncertain itself, can be factored in with f_{WP} to simplify the model, resulting in:

$$F_4 = \min\left[F_2\left(\frac{N_{bWP}\ell_{WP}}{L_{WP}}\right)\left(1+\frac{\tan\alpha}{2}\right)f'_{WP}, F_2\right], \qquad \text{(Eq. 6.3.3.2-3)}$$

where

$$f'_{WP} = \left(1+\frac{\tan\alpha}{2}\right)f_{WP} \qquad \text{(Eq. 6.3.3.2-4)}$$

is assigned a uniform distribution. In Section 6.5.1.1.3, an upper bound on f'_{WP} is developed based on results of the breached drip shield experiments. The range for f'_{WP} based entirely on experimental results is used in TSPA-LA.

Finally, the flux that is diverted around the waste package, F_5, is calculated using continuity of the quasi-static flow around and into the waste package:

$$F_5 = F_2 - F_4. \qquad \text{(Eq. 6.3.3.2-5)}$$

6.3.3.3 Condensation on the Drip Shield

Condensation of water on the underside of the drip shield is excluded due to low consequence (BSC 2004 [DIRS 169898], Section 6.2.43, FEP Number 2.1.08.14.0A). A review of the temperature profiles calculated using the results described in *In-Drift Natural Convection and Condensation Model* (BSC 2004 [DIRS 164327], Section 6.3) indicates that the radial temperatures of the drip shield are highest at the crown of this component and slightly cooler on the sides. This temperature profile would support condensation of any water vapor convected upward from the invert along the sides of the drip shield. The condensate will be a weak carbonic acid solution (pH approximately 5) (BSC 2004 [DIRS 169860]), with condensation occurring when the drip shield temperatures drop below about 96°C. These conditions do not initiate corrosion of Alloy 22 (BSC 2004 [DIRS 169984]). Therefore, the presence of any condensate on the underside of the drip shield does not impact the barrier capability of the drip shield.

Condensate waters present on the underside of the drip shield have a small potential to drip onto exposed waste packages. Analysis of advective flux through stress corrosion cracks (BSC 2004 [DIRS 172203], Section 6.3.7), an analogous situation that similarly accounts for water on the underside of the drip shield, excludes this process on the basis of low consequence.

6.3.3.4 Flux into and through the Invert (F_6 and F_7)

The flux leaving the waste package is equal to the flux entering the waste package, F_4, by the quasi-steady-state flow assumption (the net effect of Assumptions 5.1 through 5.4 and 5.7). The total flux entering the invert is equal to the sum of the diversion around the waste package, F_5, and the flux leaving the waste package (equal to F_4), the diversion around the drip shield, F_3. The liquid flux leaving the invert, F_8, is equal to the total flux entering the invert plus the imbibition flux from the UZ matrix into the invert. That is,

$$F_6 = F_5 + F_4 + F_3, \qquad \text{(Eq. 6.3.3.4-1)}$$

and

$$F_8 = F_6 + F_7. \qquad \text{(Eq. 6.3.3.4-2)}$$

Only the flux leaving the waste package, F_4, can transport radionuclides to the invert.

The *Multiscale Thermohydrologic Model* (BSC 2004 [DIRS 169565]) determines the imbibition flux from the host rock matrix into the invert, F_7, as well as the water saturation in the invert. The advective flux through the invert exits the invert, flowing into the UZ fractures.

6.3.4 Transport through the EBS

The conceptual model for transport through the EBS consists of transport through three separate domains: (1) waste form, (2) waste package corrosion products, and (3) the invert. Transport through each of these domains occurs by advection and diffusion. Radionuclides travel in

sequence through each of these domains. In other words, all radionuclides entering the corrosion products domain come from the waste form domain, and all radionuclides exiting the corrosion products domain enter the invert domain. Advection in each domain is modeled as steady state flow; i.e., the flow rate may vary over time, but no accumulation occurs. Diffusion through each domain is considered to be transient.

The rate of diffusive transport through each domain is dependent upon the following parameters: the effective diffusion coefficient, the cross-sectional area available for diffusive transport, and the diffusion path length across which a concentration gradient exists. The effective diffusion coefficient for assumed transport through thin water films adsorbed to materials is taken as a bounding value to be the free-water diffusion coefficient, modified to account for porosity, saturation, and, in the case of the invert, temperature, and the uncertainty associated with the dependence on these parameters. The cross-sectional area for transport in each domain is dependent upon the geometry of the domain, the relative humidity, and the specific surface area and adsorption isotherm for the given material. A range of diffusion path lengths is determined from the geometry of the domain.

The waste form is the source of all radionuclides in the repository system. If sufficient water is available, radionuclides mobilized from the waste form can be transported out of the waste package, downward through the invert, and into the UZ, as shown in Figure 6.3-1. Transport out of the waste package can occur by advection, when there is a liquid flux through the waste package, and by diffusion through assumed continuous liquid pathways in the waste package, including thin films of adsorbed water. These two transport processes (diffusion and advection) are each a function of the type of penetrations through the drip shield and waste package and the local seepage conditions. Diffusion can occur through stress corrosion cracks or through general corrosion patches in the waste package both with and without liquid flux through the waste package. Advection is not considered through stress-corrosion cracks or through corrosion patches in the absence of liquid flux.

The diffusion coefficient for radionuclide transport is based on the self-diffusion coefficient of liquid water at 25°C. This is a bounding value for all radionuclides. The effects of porosity, liquid saturation, and uncertainty on the diffusion coefficient are incorporated using the formulation in Section 6.3.4.1.1. The effects of temperature on this bounding value are modified using the formulation in Section 6.3.4.1.2.

Advective transport is straightforward in the *EBS RT Abstraction.* In particular, mobilized radionuclides are transported with the local liquid flux from the waste package (F_4) through the invert (F_6) to the unsaturated zone (F_8). There are no modifications for dispersive effects (see Section 6.3.1.2); because the flow is modeled as one-dimensional vertically downward, lateral dispersion is not considered in the *EBS RT Abstraction.*

Diffusive transport depends on concentration gradients. The concentrations of radionuclides in the waste form domain are determined from the degree of waste form degradation and the solubility limit for each radionuclide. The concentrations in the waste package corrosion products domain take into account radionuclide solubility limits, sorption of radionuclides onto the corrosion products, sorption and desorption onto colloids, and colloid stability. The concentrations in the invert domain depend on the radionuclide solubility limits, colloid stability

in the invert, the transfer of radionuclides between the corrosion products domain and the invert, and the boundary concentrations at the invert-unsaturated zone interface. The boundary condition at the unsaturated zone interface is implemented by defining multiple grid cells in the unsaturated zone that provide a diffusive path length that is sufficiently long such that the concentration at the outlet of the farthest cell from the drift wall can realistically be assigned a value of zero (Section 6.5.3.6).

The emphasis in this *EBS RT Abstraction* is on transport of radionuclides through the EBS after the radionuclides are mobilized. This abstraction does not define elements of the TSPA-LA, such as corrosion processes, radionuclide solubility limits, waste form dissolution rates and concentrations of colloidal particles, that are generally represented as boundary conditions or input parameters for the *EBS RT Abstraction.* This abstraction provides the algorithms for determining radionuclide transport in the EBS using the flow and radionuclide concentrations determined by other elements of the TSPA-LA.

6.3.4.1 Invert Diffusion Submodel

The TSPA-LA model requires an abstraction for the effective diffusion coefficient in granular materials as a function of radionuclide, porosity, saturation, temperature, and concentration. This submodel is intended specifically to apply to the invert. The abstraction is as follows:

- Use the free water diffusion coefficient for self-diffusion of water, 2.299×10^{-5} cm^2 s^{-1} (Mills 1973 [DIRS 133392], Table III), as a bounding value for all radionuclides at 25°C.

- Modify the free water diffusion coefficient for the porosity and liquid saturation of the invert. The modification for porosity and saturation is based on Archie's law and experimental data for granular media, and is presented in Section 6.3.4.1.1.

- Further modify the diffusion coefficient for variation of the invert temperature using the formulation in Section 6.3.4.1.2. The invert temperature is provided by the *Multiscale Thermohydrologic Model* (BSC 2004 [DIRS 169565]).

- Ignore the increase in the diffusion coefficient with increasing ionic strength of concentrated solutions (see Section 6.3.4.1.2). The maximum modification for a highly concentrated solution of potassium iodide is a factor of 1.27. This factor is almost within the bounding approximation inherent in using the self-diffusion coefficient for all radionuclides. It is neglected for the TSPA-LA.

6.3.4.1.1 Modification of Diffusion Coefficient for Porosity and Saturation of the Invert

The modified diffusion coefficient for a partly saturated porous medium can be estimated from Archie's law and the relationship between electrical conductance and diffusivity in a liquid. Archie's law is an empirical function relating the electrical resistivity and porosity of a porous medium (Keller and Frischknecht 1966 [DIRS 111470], p. 21):

$$\rho_s = a\rho_w^e \phi^{-m}, \qquad \text{(Eq. 6.3.4.1.1-1)}$$

where ρ_s is the bulk resistivity (or specific resistance) of the fully water-saturated porous medium (Ω m), ρ_w^e is the resistivity of liquid water (Ω m), ϕ is the porosity (m^3 pore volume m^{-3} total volume), m is a cementation factor (dimensionless), and a is an empirical parameter (dimensionless) that, to a first approximation, may be assumed to have a value of 1 (Keller and Frischknecht 1966 [DIRS 111470], p. 21).

For a partially saturated porous medium, the resistivity is given by (Bear 1988 [DIRS 101379], p. 116; Keller and Frischknecht 1966 [DIRS 111470], p. 28; Pirson 1963 [DIRS 111477], p. 24):

$$\rho_t = \rho_s S_w^{-n}, \qquad \text{(Eq. 6.3.4.1.1-2)}$$

where ρ_t is the bulk resistivity (or specific resistance) of the partially saturated porous medium (Ω m), S_w is the water saturation (m^3 water m^{-3} pore volume), and n is a saturation exponent (dimensionless).

The cementation factor m "is somewhat larger than 2 for cemented and well-sorted granular rocks and somewhat less than 2 for poorly sorted and poorly cemented granular rocks" (Keller and Frischknecht 1966 [DIRS 111470], p. 21). For unconsolidated sand, a value of 1.3 has been reported for the cementation factor (Bear 1988 [DIRS 101379], p. 116; Pirson 1963 [DIRS 111477], p. 24). The invert, being composed of well-graded crushed tuff (BSC 2004 [DIRS 170559]), should have cementation characteristics similar to unconsolidated sand and poorly cemented granular rock, with a cementation factor of 1.3 or slightly higher, but less than 2.

For unconsolidated sand, a value of 2 is accepted for the saturation exponent n (Bear 1988 [DIRS 101379], p. 116; Keller and Frischknecht 1966 [DIRS 111470], p. 28; Pirson 1963 [DIRS 111477], p. 24).

Combining and simplifying Equations 6.3.4.1.1-1 and 6.3.4.1.1-2 results in an Archie's law formulation that gives the bulk resistivity of a partially saturated porous medium:

$$\rho_t = \rho_w^e \phi^{-m} S_w^{-n}. \qquad \text{(Eq. 6.3.4.1.1-3)}$$

The resistance of a porous medium of length L and cross-sectional area A is given by:

$$R_t = \rho_t L / A. \qquad \text{(Eq. 6.3.4.1.1-4)}$$

Since the electrical conductance, G ($S = \Omega^{-1}$), is defined as the reciprocal of resistance (Atkins 1990 [DIRS 111464], p. 750), Archie's law can be written for a partially saturated porous medium in terms of the conductance of the bulk porous medium, G_t (S) and the conductance of water, G_w (S):

$$G_t = G_w \phi^m S_w^n. \qquad \text{(Eq. 6.3.4.1.1-5)}$$

The last step is to rewrite Archie's law in terms of diffusion coefficients. The diffusion coefficient of an ion in solution is related to the conductance through the Nernst-Haskell equation (Perry and Chilton 1973 [DIRS 104946], p. 3-235) for diffusion in a binary electrolyte mixture at infinite dilution:

$$D = \frac{RT}{F^2}\left(\frac{l_+^0 l_-^0}{\Lambda_0}\right)\left(\frac{z_+ + z_-}{z_+ z_-}\right). \qquad \text{(Eq. 6.3.4.1.1-6)}$$

where:

D = diffusion coefficient ($m^2\ s^{-1}$)

R = molar gas constant = 8.314472 J mol^{-1} K^{-1} (Lide 2002 [DIRS 160832], p. 1-8)

T = temperature (K)

F = Faraday constant = 96485.3415 C mol^{-1} (Lide 2002 [DIRS 160832], p. 1-7)

l_+^0, l_-^0 = cationic and anionic conductance, respectively, at infinite dilution (S cm^2 $equivalent^{-1}$)

Λ_0 = equivalent electrolyte conductance at infinite dilution (S cm^2 $equivalent^{-1}$)

z_+, z_- = valence of cation and anion, respectively; magnitude only—no sign (dimensionless).

This equation can be simplified by making use of the average ionic conductance at infinite dilution, $\bar{l}$, where

$$\bar{l} = \frac{\Lambda_0}{2} = \frac{l_+^0 + l_-^0}{2}. \qquad \text{(Eq. 6.3.4.1.1-7)}$$

Since the ionic conductances l_+^0 and l_-^0 are non-negative numbers, $\bar{l}^2 \geq (l_+^0)(l_-^0)$, which can be seen as follows:

$$\begin{aligned}
\bar{l}^2 &= \left(\frac{l_+^0 + l_-^0}{2}\right)^2 \\
&= \frac{(l_+^0)^2 + 2(l_+^0)(l_-^0) + (l_-^0)^2}{4} \\
&= \frac{(l_+^0)^2 + (l_-^0)^2}{4} + \frac{(l_+^0)(l_-^0)}{2} \\
&= \frac{(l_+^0)^2 + (l_-^0)^2}{4} + \frac{(l_+^0)(l_-^0)}{2} + \frac{(l_+^0)(l_-^0)}{2} - \frac{(l_+^0)(l_-^0)}{2} \\
&= \frac{(l_+^0)^2 + (l_-^0)^2}{4} - \frac{(l_+^0)(l_-^0)}{2} + (l_+^0)(l_-^0) \\
&= \frac{1}{4}(l_+^0 - l_-^0)^2 + (l_+^0)(l_-^0) \\
&\geq (l_+^0)(l_-^0).
\end{aligned} \qquad \text{(Eq. 6.3.4.1.1-8)}$$

Thus, the square of the average ionic conductance can be substituted for the product of the individual conductances. This substitution will generally overestimate the diffusion coefficient given by Equation 6.3.4.1.1-6. At the same time, the valence of the ions z_+ and z_- are given a value one, because this, too, maximizes the diffusion coefficient. With these substitutions, Equation 6.3.4.1.1-5 simplifies to give the maximum diffusivity in a binary electrolyte mixture at infinite dilution:

$$\begin{aligned} D &= \frac{RT}{F^2}\left(\frac{\bar{l}^2}{2\bar{l}}\right)(2) \\ &= \frac{RT\,\bar{l}}{F^2} \\ &= \frac{RT\Lambda_0}{2F^2}. \end{aligned} \qquad \text{(Eq. 6.3.4.1.1-9)}$$

This shows that the diffusion coefficient for ions in an infinitely dilute binary mixture is proportional to the conductance of the electrolyte. For multicomponent solutions at other than infinite dilution, this equation represents an approximation with an associated uncertainty that can be estimated by comparison with experimental data, which is discussed later.

Using the conductance G_l for Λ_0 in the bulk porous medium and G_w for Λ_0 corresponding to the free water diffusivity D_0 (corresponding to the value of D when porosity and saturation are both 1.0), Archie's law (Equation 6.3.4.1.1-5) can be written in terms of the diffusivities of the bulk porous medium and the free water diffusivity:

$$D = D_0 \phi^m S_w^n. \qquad \text{(Eq. 6.3.4.1.1-10)}$$

This is the form of Archie's law that is generally applied for determination of the diffusion coefficient, D, as a function of porosity and saturation in a partly saturated, granular medium. Note that the diffusion coefficient, D, as introduced here and used throughout this section, is an effective value that implicitly includes the effects of porosity, saturation, and tortuosity. As such, it is defined differently from the coefficient D_{ml} defined in Section 6.5.1.2, which applies to a bulk liquid phase without modification for porosity, saturation, or tortuosity. With values of the cementation factor, m, of 1.3 and the saturation exponent, n, of 2 for unconsolidated sand, Archie's law becomes as:

$$D = D_0 \phi^{1.3} S_w^2. \qquad \text{(Eq. 6.3.4.1.1-11)}$$

Conca and Wright (1992 [DIRS 100436]) and Conca et al. (1993 [DIRS 170709]) measured the diffusion coefficient of unsaturated soil, gravel, bentonite, rock, and crushed tuff from Yucca Mountain over a broad range of water contents. These measured data are qualified in Appendix H and have been used to analyze the dependence of the diffusion coefficient on volumetric moisture content for a variety of granular materials. Figure 6.3-4 presents a summary of the diffusivity data for various granular media at volumetric moisture contents ranging between 1.5 percent and 66.3 percent.

Because these diffusion coefficients were measured as a function of volumetric water content, they have been analyzed using an alternative form of Archie's law in which the cementation factor and saturation exponent are equal (i.e., $n = m$). In effect, the diffusion coefficient is then a function of θ, the percent volumetric moisture content, defined as $\theta = 100\phi S_w$:

$$\begin{aligned} D &= D_0 \phi^n S_w^n \\ &= D_0 \left(\frac{\theta}{100} \right)^n . \end{aligned} \qquad \text{(Eq. 6.3.4.1.1-12)}$$

A statistical analysis using Microsoft Excel (Appendix G) produces an excellent fit to the diffusivity data (Conca and Wright 1992 [DIRS 100436], Figure 2; Conca et al. 1993 [DIRS 170709], Figure 2; listed in Table 4.1-14) using Equation 6.3.4.1.1-12 for moisture content in the range of 1.5 percent to 66.3 percent. The statistical fit to the diffusion coefficient, D, is based on a linearizing transformation to the variables X and Y, defined as:

$$\begin{aligned} Y &= \log_{10}(D / D_0) \\ X &= \log_{10} \theta - 2, \end{aligned} \qquad \text{(Eq. 6.3.4.1.1-13)}$$

where

D = the diffusion coefficient ($m^2\ s^{-1}$)
D_0 = free water diffusivity ($m^2\ s^{-1}$)
θ = volumetric moisture content (percent).

The slope of the X-Y relationship is found to be 1.863, leading to the following linear equation for Y as a function of X:

$$\begin{aligned} Y &= 1.863X \\ \log_{10}\left(\frac{D}{D_0} \right) &= 1.863(\log_{10} \theta - 2), \end{aligned} \qquad \text{(Eq. 6.3.4.1.1-14)}$$

or

$$\begin{aligned} D &= D_0 \phi^{1.863} S_w^{1.863} \\ &= D_0 \left(\frac{\theta}{100} \right)^{1.863} . \end{aligned} \qquad \text{(Eq. 6.3.4.1.1-15)}$$

The statistical fit for the diffusion coefficient has uncertainty, which is represented by the scatter of data points around the fit in Figure 6.3-4. This uncertainty is approximated by a normal distribution for the residuals (data–model) in log-log space. This normal distribution of residuals has a mean value of 0.033 and a standard deviation of 0.218. The uncertainty can be incorporated into the statistical fit as an additional factor on the full statistical fit.

$$D = D_0 \phi^{1.863} S_w^{1.863} 10^{ND(\mu=0.033, \sigma=0.218)}, \qquad \text{(Eq. 6.3.4.1.1-16)}$$

where *ND* represents a normal distribution with a mean, μ, of 0.033 and a standard deviation, σ, of 0.218. *ND* is in the exponent because the residuals are calculated in the log-log space of the statistical fit. This statistical fit is the submodel for the invert diffusion coefficient to be used for TSPA-LA. Since the normal distribution is theoretically unbounded, unrealistic values for the diffusion coefficient could potentially be obtained. To avoid this potential problem, the implementation in TSPA-LA will use a truncated normal distribution, limited to plus or minus three standard deviations from the mean.

Figure 6.3-4 presents the statistical fit (solid line) and the upper and lower bounds (dashed lines) at three standard deviations above and below the fit. The dashed lines encompass almost all the data points, because ± 3 standard deviations includes 99.7 percent of the area under a normal distribution. Equation 6.3.4.1.1-16, therefore, accurately represents the uncertainty in the diffusivity data for the TSPA-LA calculations.

Because the saturation exponent (1.863) is less than the generally accepted value (2), the fit to the data provides less of a bounding estimate for the diffusion coefficient than if the accepted value were used. However, the estimate using Equation 6.3.4.1.1-16 is realistic instead of simply bounding the diffusion coefficient because it is developed from measured data rather than using the general behavior of unconsolidated sand as its basis. Furthermore, being based on a large number of measured data, the uncertainty in diffusion coefficient using Equation 6.3.4.1.1-16 is quantified, which provides additional support for use of this equation instead of a more bounding approach using the accepted value for saturation exponent.

One element of the uncertainty in the diffusion coefficient is the uncertainty in the porosity of the invert. The bulk porosity of the invert crushed tuff is expected to vary between 0.27 and 0.39, with an average of 0.31 (BSC 2004 [DIRS 168138], Table 5). From Equation 6.3.4.1.1-16, the diffusion coefficient would vary due to variations in porosity by a factor of:

$$\frac{D_{max}}{D_{min}} = \frac{\phi_{max}^{1.863}}{\phi_{min}^{1.863}} = \left(\frac{0.39}{0.27}\right)^{1.863} = 1.98. \qquad \text{(Eq. 6.3.4.1.1-17)}$$

The range about the mean diffusion coefficient, $\overline{D}$, would be:

$$\frac{D_{min}}{\overline{D}} = \left(\frac{0.27}{0.31}\right)^{1.863} = 0.77 \qquad \text{(Eq. 6.3.4.1.1-18)}$$

to

$$\frac{D_{max}}{\overline{D}} = \left(\frac{0.39}{0.31}\right)^{1.863} = 1.53. \qquad \text{(Eq. 6.3.4.1.1-19)}$$

This range of uncertainty resulting from variation in the invert porosity is well within the range of the uncertain factor in Equation 6.3.4.1.1-16, which ranges from:

$$10^{0.033-3(0.218)} = 0.24 \qquad \text{(Eq. 6.3.4.1.1-20)}$$

to

$$10^{0.033+3(0.218)} = 4.86. \qquad \text{(Eq. 6.3.4.1.1-21)}$$

The uncertainty associated with the porosity of the invert is subsumed by the greater uncertainty associated with the measurements of the diffusion coefficient; thus the porosity uncertainty can be considered to be accounted for in the diffusion coefficient. The same conclusion is reached if the nominal value of intergranular porosity (0.45 as given in Tables 4.1-8, 6.6-2, and 8.2-4) is substituted for the mean, with the same spread for the uncertainty range.

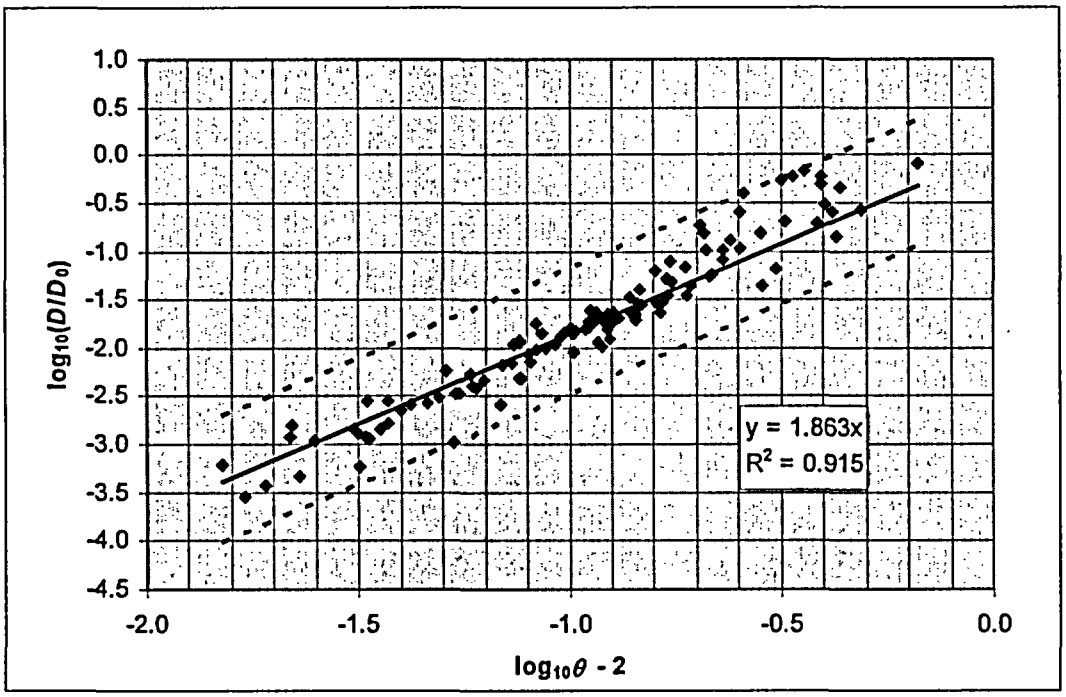

Source: Conca And Wright 1992 [DIRS 100436], Figure 2; Conca et al. 1993 [DIRS 170709], Figure 2.

NOTE: The dashed lines correspond to three standard deviations above and below the statistical fit to the data.

Figure 6.3-4. Uncertainty in the Statistical Fit for the Diffusion Coefficient

For each realization of the TSPA-LA calculations, the normal distribution is sampled, thereby incorporating the uncertainty of the experimental data into the diffusivity.

6.3.4.1.2 Modification for Temperature

The diffusivity D_T is proportional to absolute temperature and inversely proportional to viscosity η_T; i.e., $D_T \propto T/\eta_T$ (Cussler 1997 [DIRS 111468], p. 114). It follows that if the diffusivity is known at some temperature T_0, the diffusivity at temperature T can be found by:

$$\frac{D_T}{D_{T_0}} = \frac{\frac{T}{T_0}}{\frac{\eta_T}{\eta_{T_0}}}, \qquad \text{(Eq. 6.3.4.1.2-1)}$$

where D_T is the diffusion coefficient ($m^2 s^{-1}$) at temperature T (K), D_{T_0} is the diffusion coefficient ($m^2 s^{-1}$) at temperature T_0 (K), η_T is the viscosity of water (Pa s) at temperature T (K), and η_{T_0} is the viscosity of water (Pa s) at temperature T_0. The dependence of viscosity on temperature T (K) (293.15 K $\leq T \leq$ 373.15 K) is given by (Weast and Astle 1981 [DIRS 100833], p. F-42):

$$\log_{10}\left(\frac{\eta_T}{\eta_{20}}\right) = \frac{1.3272(293.15-T)-0.001053(T-293.15)^2}{T-168.15}, \qquad \text{(Eq. 6.3.4.1.2-2)}$$

where η_{20} is the viscosity of water at 20°C (293.15 K). Then

$$\frac{\eta_T}{\eta_{T_0}} = \frac{10^{\left[\frac{1.3272(293.15-T)-0.001053(T-293.15)^2}{T-168.15}\right]}}{10^{\left[\frac{1.3272(293.15-T_0)-0.001053(T_0-293.15)^2}{T_0-168.15}\right]}}, \qquad \text{(Eq. 6.3.4.1.2-3)}$$

and the diffusion coefficient at temperature T is given by:

$$\begin{aligned} D_T &= D_{T_0}\frac{T}{T_0}\frac{\eta_{T_0}}{\eta_T} \\ &= D_{T_0}\frac{T}{T_0}10^{\left[\frac{1.3272(293.15-T_0)-0.001053(T_0-293.15)^2}{T_0-168.15}\right]-\left[\frac{1.3272(293.15-T)-0.001053(T-293.15)^2}{T-168.15}\right]}. \end{aligned} \qquad \text{(Eq. 6.3.4.1.2-4)}$$

This equation is not valid above 100°C (373.15 K), where it is assumed that no transport occurs (Assumption 5.5). The invert temperature is provided by the *Multiscale Thermohydrologic Model* (BSC 2004 [DIRS 169565]).

6.3.4.1.3 Modification for Concentrated Aqueous Solutions

Data in *American Institute of Physics Handbook* (Gray 1972 [DIRS 138541], Table 2p-2) show that the majority of the diffusion coefficients increase with increasing solution strength. For example, the diffusion coefficient of sodium iodide increases from 1.616 in a dilute solution to 1.992 for a 3 M solution and the coefficient for potassium iodide increases from 2.00 in a dilute solution to 2.533 at 3.5 M. The percent increase for potassium iodide, 26.7 percent, is the greatest of any in Gray's Table 2p-2, (Gray 1972 [DIRS 138541]) excluding HCl. HCl has been excluded from consideration because, being volatile, it is not representative of the type of radionuclides released from the waste package.

Although the diffusion coefficients of aqueous solutions increase with increasing ionic strength, the self-diffusion coefficient of water is still higher. Therefore, using the self-diffusion coefficient for water is a bounding value for all radionuclides. The modification for concentrated aqueous solutions is therefore neglected in the TSPA-LA.

6.3.4.2 Retardation in the Engineered Barrier System

In this section, parameters are developed to enable the impact of sorption processes on radionuclide transport through the EBS to be quantified. Transport through the EBS is affected by the adsorption and desorption of radionuclides on the materials in the waste package and invert. Adsorption describes the uptake of a radionuclide by a solid surface when in contact with a radionuclide-laden aqueous solution. This uptake typically occurs when a bond is formed by surface sites that have a chemical affinity for the radionuclide. Progressive inflow of fluids with low radionuclide concentrations would thermodynamically favor desorption of the original population of sorbed radionuclides back into solution. The fully reversible sorption and desorption of radionuclides is often described by a linear isotherm, using a sorption distribution coefficient (K_d).

Irreversible sorption refers to the tendency in natural systems for desorption to be incomplete. In other words, the amount of sorbed contaminant available for desorption in natural systems is typically less than the total sorbed mass due to chemical and physical processes occurring at or beneath the mineral surface. Sorption processes are referred to as adsorption if the process occurs on the surface or absorption if the process occurs beneath the surface.

This section defines a conceptual model and parameters for transport through the degraded EBS, including appropriate ranges of K_d values for actinium, americium, carbon, cesium, iodine, neptunium, plutonium, protactinium, radium, strontium, technetium, thorium, and uranium, and the defensibility of irreversible sorption for these radionuclides.

The TSPA-SR transport model for the EBS assumed no sorption or retardation of dissolved species of radionuclides (CRWMS M&O 2000 [DIRS 153246], p. 3-134). This assumption was bounding for several reasons:

- A large mass of iron oxyhydroxides, including species such as hematite, is generated through corrosion of mild steel and stainless steels within the waste package and invert. The iron oxyhydroxides are known to be excellent sorbers (as indicated by their high K_d values) of many radionuclide species (Table 4.1-11).

- Some sorbed radionuclides, such as plutonium, appear not to desorb in many geologic environments (Brady et al. 1999 [DIRS 154421], Appendix VI). In effect, the sorption process appears partly irreversible, and a large percentage of sorbed radionuclides would appear to be permanently attached to the corrosion products in the EBS. But it is difficult to quantify irreversibility because the time scale for laboratory experiments or field observations is much shorter than repository time scales. In this situation, the short-term data may provide misleading information about long-term irreversibility. The net effect of irreversible sorption on EBS transport will depend on two competing effects: (1) irreversible sorption on the in-drift materials will decrease releases from the EBS, and (2) irreversible sorption to stable colloidal particles will increase transport through the EBS.

- Copper is present along the top of the invert as an electrical conductor. Two corrosion products produced by the alteration of elemental copper (copper oxide and copper sulfide) can strongly sorb iodine and technetium species (Balsley et al. 1998 [DIRS 154439], Tables 1 and 2), an important feature for decreasing releases of two elements that generally have minimal sorption in oxidizing environments.

Sorption distribution coefficients are typically measured for groundwaters and substrates at ambient or near ambient temperatures. There is little or no experimental data for sorption distribution coefficients at the elevated temperatures that may occur in the EBS with either the repository design and operating mode described in *Yucca Mountain Science and Engineering Report* (DOE 2001 [DIRS 153849]) or an alternative thermal operating mode. In this situation, the available data for sorption distribution coefficients have been used to define the ranges of K_d values for TSPA-LA analyses, but it is not possible to distinguish alternative thermal operating modes. The effect of temperature on sorption coefficients was reviewed by Meijer (1990 [DIRS 100780], p. 17). Measured sorption coefficients onto tuffs were higher at elevated temperature for all elements studied: Am, Ba, Ce, Cs, Eu, Pu, Sr, and U. The conclusion was drawn that sorption coefficients measured at ambient temperatures should be applicable and generally bounding when applied to describing aqueous transport from a hot repository. This conclusion must be tempered by the possibility that high temperatures could result in changes in the near-field mineralogy and water chemistry that are not predictable by short-term laboratory and field experiments.

6.3.4.2.1 Conceptual Model for the In-Drift Environment

The mild steel and stainless steel in the waste package and invert are expected to degrade to iron oxyhydroxides more rapidly than the corrosion-resistant materials in the EBS (e.g., Alloy 22 and titanium). The time sequence for corrosion of iron-based components in the EBS is:

- Mild steel in the invert (e.g., support beams, cap plate, and gantry rails) will begin to degrade after closure of the repository because the invert is directly exposed to the relative humidity and temperature environment within the drifts. Corrosion begins when the relative humidity becomes great enough to produce aqueous conditions on the surface, although the presence of deliquescent salts can result in aqueous conditions if the in-drift humidity is higher than the minimum deliquescent point of the salts (Campbell and Smith 1951 [DIRS 163817], p. 237).

  The steel and copper are in the top portion of the invert. More specifically, the longitudinal and transverse support beams are in the top half of the invert (BSC 2004 [DIRS 169776], Section A). The transverse support beams are spaced at 1.524-m intervals (BSC 2004 [DIRS 169503]), so the corrosion products from the beam will not always be directly beneath the emplacement pallet or stress corrosion cracks. Below and on either side of these beams, the invert is filled to depth with a granular ballast that does not contain any steel.

- Stainless steel rods in the emplacement pallet will corrode more slowly than mild steel (for mild carbon steel and stainless steel corrosion rates see DTN: MO0409SPAACRWP.000 [DIRS 172059]). Again, the rods are directly exposed

to the in-drift temperature and relative humidity after closure. The rods in the emplacement pallet are located directly beneath the waste package, in the anticipated flow path from the waste package.

- Mild steel (i.e., carbon steel Type A 516) inside the waste package can begin to degrade after stress corrosion cracks or general corrosion patches form in the waste package. Water vapor can enter the waste package once a crack forms, and this vapor will be adsorbed on the steel surfaces, providing an environment for corrosion within the waste package.

- Stainless steel inside the waste package can also corrode, albeit more slowly than mild steel, after a stress corrosion crack forms in the waste package lid weld or general corrosion patches form in the waste package.

Aluminum thermal shunts in 21-PWR and 44-BWR waste packages comprise less than two percent of the total mass of the waste package. Because the amount of aluminum is negligible, it is ignored in the *EBS RT Abstraction*. The Ni-Gd Alloy absorber plates in the CSNF waste package design are modeled as being composed of Neutronit, as in the waste package previous design; Neutronit is treated as having the same corrosion rate as stainless steel, resulting in corrosion products containing Fe_2O_3 in proportion to its iron content (see Section 6.3.4.2.3).

Because the corrosion rate of the carbon steel used for invert components is greater than that of the Alloy 22 waste package outer corrosion barrier, all mild steel components in the invert will degrade to iron oxyhydroxides by the time the first stress corrosion cracks or general corrosion patches form. In other words, iron oxyhydroxides will be present in the invert before any radionuclides are transported from the waste package. After stress corrosion cracks form, the mild steel internal components in the waste package will also degrade rapidly, adding iron oxyhydroxides to the in-package environment. Most iron-based in-package materials will degrade to corrosion products by 205,000 years, based on a thickness of the inner vessel of stainless steel of 50.8 mm (BSC 2004 [DIRS 169472]; BSC 2004 [DIRS 166953], Section B-B) and a mean corrosion rate of 0.248 $\mu m\ yr^{-1}$ (DTN: MO0409SPAACRWP.000 [DIRS 172059]), early in the waste package lifetime.

The degradation products in the waste package will include hydrous metal oxides from corrosion of steel and aluminum materials (YMP 1998 [DIRS 104441], p. C-23) and clays from degradation of HLW glass (BSC 2004 [DIRS 169988], Section 6.5.3.3). These corrosion products may form a residue that is similar to a highly iron-rich soil or sediment in terms of its bulk chemical properties for determining appropriate ranges of K_d. Because of their strong sorptive characteristics, the iron oxyhydroxides will dominate the sorptive properties of the corrosion products, although the aluminum oxides and manganese oxides are also highly sorptive.

The degradation products in the invert will include iron oxyhydroxides and other hydrous metal oxides from the corrosion of steels and copper-based materials, and minerals from the granular invert backfill. The invert corrosion products occur in the top portion of the invert because all steel and copper is located in the top half of the invert (BSC 2001 [DIRS 154441]).

The in-package degradation products are envisioned to be composed of unconsolidated particulates and larger agglomerations of clays, iron oxyhydroxides, and other mineral assemblages that slump to the bottom of the waste package. The invert degradation products are initially located near the top of the invert, but may move into the mass of granular invert backfill during thermal changes or seismic events. Any seepage through the waste package is expected to flow through this sludge at the bottom of the waste package.

The sludge of corrosion products is represented as a single porosity medium, a reasonable approach given the granularity of the corrosion products and the randomness of the slumping process. Channelized flow paths with no sorption, as in the discrete fractures of a dual porosity medium, are not anticipated to occur in this unconsolidated sludge. One conceptual model is for the radionuclides to have access to the mass of corrosion products in the waste package. An alternative conceptual model, with corrosion products that form a contiguous mass that has a low permeability and tight pore structure, would limit access to the full sorptive capacity of the corrosion products. The uncertainty in which the conceptual model is most representative can be implicitly acknowledged in the selection of broad distributions with small minimum values for the sorption distribution coefficients.

Descriptions of sorption based on a K_d are approximate because this approach is empirical, with little if any information about underlying mechanisms, and is therefore not easily extendable to different chemical environments and physical substrates (sorptive media). The use of a linear isotherm is also approximate because it does not predict saturation of the sorption sites with sorbed species that may include natural components of the groundwater. The mass of iron oxyhydroxides from waste package corrosion is large (Table 6.3-4), so each waste package provides many sites for sorption. For these reasons, the K_d approach is at best an order of magnitude measure of contaminant uptake in geologic environments (Davis and Kent 1990 [DIRS 143280]).

The use of the linear isotherm (K_d) approach to represent the subsequent release of radionuclides into fresh recharge (i.e., the desorption process) is often inconsistent with observations in geologic media. Typically, contaminants become more closely attached to a mineral surface after sorption, either adsorbed at high energy sites on the surface or absorbed through overcoating and buried due to other mineral surface reactions. The net result is that only a fraction of the original sorbed population remains available at the surface and able to react with adjacent solutions or be accessed by microorganisms. A linear isotherm (K_d) approach, on the other hand, assumes that all sorbed radionuclides are freely able to desorb from the substrate.

As an example, recent reviews of field and laboratory measurements indicate that the fraction of sorbed plutonium that is available for desorption rarely exceeds 1 percent (Brady et al. 1999 [DIRS 154421]; Davis and Kent 1990 [DIRS 143280]). Recognition of the strong role of irreversible sorption is implicit in models for watershed transport (Graf 1994 [DIRS 154419]) that focus solely on particulate transport. In these cases, desorption is ignored because it is rarely seen to occur with plutonium. However, as noted previously, the time scales for these observations are much shorter than the regulatory time period for repository performance (10,000 years), so the fraction of plutonium that is irreversibly sorbed in TSPA-LA calculations has a large uncertainty.

Table 6.3-4. Estimated Masses of Steels and Iron Content in Waste Packages and Equivalent Masses (kg) of Iron Corrosion Products (Fe_2O_3) for Use in Modeling Retardation in the Waste Package

Material	Fe Content[a] (%)	21-PWR		44-BWR		5-DHLW/DOE SNF - Short		Naval Long	
		Total Mass[b] (kg)	Fe Mass (kg)	Total Mass[c] (kg)	Fe Mass (kg)	Total Mass[d] (kg)	Fe Mass (kg)	Total Mass[e] (kg)	Fe Mass (kg)
Stainless Steel Type 316	61.935	10,800	6,690	11,120	6,890	10,160	6,300	14,420	8,930
A 516 Carbon Steel	98.37	5,600	5,510	6,800	6,690	3,720	3,660	—	—
Neutronit A 978	66.06	2,120	1,400	2,990	1,970	—	—	—	—
Total	—	18,520	13,600	20,910	15,550	13,880	9,960	14,420	8,930
Percentage of Total as iron	—	—	73.4	—	74.4	—	71.7	—	61.9
Equivalent Fe_2O_3 mass[f]	—	—	19,440	—	22,240	—	14,230	—	12,770

NOTE: Microsoft Excel calculation of equivalent Fe2O3 mass is described in Appendix A.

[a]Calculated "Balance" from Table 4.1-10 compositions: 100 – (sum of non-Fe constituents); see Appendix A.
[b]Total Mass in 21-PWR for each material in Table 4.1-17: sum of (mass × number) of each component (BSC 2004 [DIRS 169472], Table 2; Material Table in *Design and Engineering, 21-PWR Waste Package Configuration* (BSC 2004 [DIRS 167394]); see Appendix A.
[c]Total Mass in 44-BWR for each material: sum of (mass × number) of each component (BSC 2004 [DIRS 169472], Table 3; Material Table in *Design and Engineering, 44-BWR Waste Package Configuration* (BSC 2004 [DIRS 167555]); see Appendix A.
[d]Total Mass in 5-DHLW/DOE SNF – Short for each material in Table 4.1-17: sum of (mass × number) of each component (BSC 2004 [DIRS 167207], Table 5; Material Table in *Design & Engineering, 5 DHLW/DOE SNF - Short Waste Package Configuration* (BSC 2004 [DIRS 166947]). Interface Ring mass of 1 kg erroneously used (Figure A-2); correct mass is 44.6 kg (BSC 2004 [DIRS 167207], Table 5); see Appendix A.
[e]Total Mass in Naval Long for each material: sum of (mass × number) of each component (BSC 2004 [DIRS 169472], Table 4; Material Table in *Design and Engineering, Naval Long Waste Package Configuration* (BSC 2003 [DIRS 165159]); see Appendix A.
[f]Fe_2O_3 mass = (Fe mass, kg) × (molecular weight Fe_2O_3) × (1 mol Fe_2O_3/2 mol Fe) / (atomic weight Fe)
= (Fe mass, kg) × (0.15969 kg Fe_2O_3/mol) × (1 mol Fe_2O_3/2 mol Fe) / (0.055847 kg Fe/mol)
= 1.4297 × Fe mass.

BWR = boiling water reactor, DHLW = defense high-level (radioactive) waste, SNF = spent nuclear fuel; DOE = U.S. Department of Energy

6.3.4.2.2 Sorption Parameters for the Invert

Various conceptual models can be devised to quantify the uncertainty in retardation in the invert. Invert corrosion products will tend to be localized and widely spaced, with the possibility being that seepage from the waste package could completely miss corrosion products in the invert. In this case, even K_d values that would normally be considered to be small for corrosion products could overestimate the amount of retardation of radionuclides in the invert. At the same time, invert corrosion products will have a smaller sorptive capacity than waste package corrosion products simply because the masses of sorptive corrosion products in the invert are much less than in the waste packages. As a bounding treatment, sorption of radionuclides on corrosion products in the invert is ignored (Assumption 5.7).

Sorption onto the crushed tuff is included in the EBS transport abstraction. K_d values and distributions for 11 selected radionuclides are presented in Table 4.1-12 (DTN: LA0408AM831341.001 [DIRS 171584]); K_d values for sorption of carbon, iodine and technetium on tuff are zero. The ranges of K_d values for sorption onto devitrified tuff are used because the crushed tuff in the invert will be the same tuff that is removed when the drifts are bored; most of the repository will be developed in the TSw35 horizon, which is composed of devitrified tuff. The K_d values selected are summarized in Table 6.5-13. Correlations of K_d values among various radionuclides for sorption on tuff are given by a correlation matrix presented in Table 4.1-13. Invert K_d values are implemented in TSPA-LA by first computing unsaturated zone K_d values for devitrified tuff and then assigning those values to the invert.

Actinium and americium have similar chemistry in aqueous solution and sorption reactions (BSC 2001 [DIRS 160828], p. 64). Therefore, K_d values reported for americium in Table 4.1-12 are used for actinium in the invert.

6.3.4.2.3 Sorption Parameters for the Waste Package

This section presents and analyzes appropriate sorption parameters for the EBS. First, the mass of corrosion products (sorbers) is calculated for the repository design. Second, the available values for K_d are used to estimate the distributions of sorption distribution coefficients for the oxidizing in-drift environment in the waste package. Third, the available data on irreversible sorption of metals that are relevant to EBS transport are presented.

The mass of sorbing material in the waste package has been estimated using compositional information from Table 4.1-10 and numbers and masses of components listed in design drawings. The mass of sorbing material in the waste package is based on the iron contents of Stainless Steel Type 304L, Stainless Steel Type 316L, Stainless Steel Type 316 (these three types of stainless steel have similar iron contents), Carbon Steel Type A 516, Neutronit A 978, and the masses of these alloys in the four most common waste package types. The estimated masses of corrosion products are shown in Table 6.3-4 and described in Appendix A. The corrosion products are assumed to be Fe_2O_3 (Assumption 5.6), and, the mass of corrosion products is calculated based on the ratio of molecular weight of Fe_2O_3 to the atomic weight of Fe, accounting for stoichiometry (footnote f in Table 6.3-4). The results shown in Table 6.3-4 are based on an earlier version of the waste package design (IED 800-IED-WIS0-00202-000-00B, BSC 2004 [DIRS 167207]). Due to minor design changes for the 5 DHLW/DOE Short waste package (see Section 4.1.3, following Table 4.1-17), the mass of iron in that waste package is larger using the current design (IED 800-IED-WIS0-00202-000-00C, BSC 2004 [DIRS 169472], Table 5) than for the earlier design version (BSC 2004 [DIRS 167207], Table 5). In addition, in the calculation of the corrosion product mass (see Figure A-2), a mass of 1 kg for the Interface Ring for the 5 DHLW/DOE Short waste package is erroneously used; the correct value is 44.6 kg. Using the updated 5 DHLW/DOE Short waste package design data and correcting the Interface Ring mass result in an increase in the estimated mass of corrosion products, from 14,230 kg (Table 6.3-4) to 14,320 kg (updated, corrected value). The difference (0.6 percent) is negligible, so the earlier estimate of 14,230 kg shown in Table 6.3-4 is suitable for TSPA-LA calculations.

In a revision to the 21-PWR and 44-BWR waste package design (Anderson 2004 [DIRS 171637], BSC 2004 [DIRS 170710], BSC 2004 [DIRS 170838]), the Neutronit used for the absorber plates is replaced with a nickel-chromium-molybdenum-gadolinium alloy, N06464 (ASTM B 932-04 [DIRS 168403]), denoted as Ni-Gd Alloy. The mass of Neutronit in a 21-PWR waste package (2,120 kg; see Table 6.3-4) is replaced by 2400 kg of Ni-Gd Alloy. The mass of Neutronit in a 44-BWR waste package (2,990 kg; see Table 6.3-4) is replaced by 3,380 kg of Ni-Gd Alloy. Whereas Neutronit contains 66.06 percent iron (Kügler 1991 [DIRS 155761], p. 15), N06464 contains a maximum of 1.0 percent iron (ASTM B 932-04 [DIRS 168403]). In the analysis summarized in Table 6.3-4, only the iron in the waste package components contributes to the corrosion product mass that is used in water adsorption calculations in the in-package diffusion submodel, Section 6.5.1.2.1. This corrosion product mass also is used in the radionuclide sorption calculations. Using N06464 instead of Neutronit in a 21-PWR waste package would reduce the total iron mass from 13,600 kg to 12,220 kg; the equivalent mass of Fe_2O_3 would be reduced from 19,440 kg to 17,470 kg, a reduction of 10.1 percent. Using N06464 instead of Neutronit in a 44-BWR waste package would reduce the total iron mass from 15,550 kg to 13,610 kg; the equivalent mass of Fe_2O_3 would be reduced from 22,240 kg to 19,460 kg, a reduction of 12.5 percent.

For purposes of TSPA-LA calculations, iron and corrosion product mass estimates are based on the earlier waste package design. For a 21-PWR waste package, the calculations use Revision 00C of *Design and Engineering, 21-PWR Waste Package Configuration* (BSC 2004 [DIRS 167394]) rather than Revision 00D (BSC 2004 [DIRS 170710]). For a 5 DHLW/DOE Short waste package, the calculations use Revision 00B of *D&E/PA/C IED Typical Waste Package Components Assembly* (BSC 2004 [DIRS 167207], Table 5), instead of Revision 00C (BSC 2004 [DIRS 169472], Table 5). The estimated masses of corrosion products in 44-BWR and Naval Long waste packages shown in Table 6.3-4 are not used directly in TSPA-LA calculations.

This reduction in Fe_2O_3 mass compared with the previous waste package design has two competing effects on predicted releases of radionuclides from a breached waste package. First, the mass of sorbant of radionuclides is reduced, which could potentially increase predicted releases; however, as shown in Appendix B (p. B-25), the sorption capacity of a 21-PWR waste package is more than double the available radionuclide inventory of a waste package, so using the previous design with a 10-to-12 percent higher sorption capacity is inconsequential. Second, using the larger mass of Fe_2O_3 in the previous design results in a higher water saturation in a no-seep case (as given by the in-package diffusion submodel, Section 6.5.1.2.1), which will overestimate diffusive releases of radionuclides.

As discussed previously, the use of a linear isotherm is an empirical, order-of-magnitude description of mineral surface processes because it is not based on underlying physical or chemical mechanisms. In essence, a K_d value is valid only for the specific substrate and chemical conditions under which it is measured. More defensible models of contaminant uptake by mineral surfaces require a more comprehensive mechanistic understanding of the chemical reactions involved (Davis et al. 1998 [DIRS 154436]). In lieu of a more involved mechanistic treatment based on surface complexation that includes a provision for irreversible sorption, K_d values can provide a first-order picture of the sorption process, using generic ranges based on soils and iron oxyhydroxides. The rationale for this approach is described below.

Based on previous TSPA calculations, the pH of waste package fluids (CRWMS M&O 2000 [DIRS 153246], Tables 3.3-7 through 3.3-9) is expected to fall within the range observed in soils and groundwaters (pH values between 4 and 10). Although the composition of in-package fluids will vary with time due to degradation of the waste package components (primarily steels, Zircaloy cladding, SNF, and waste glass), major element characteristics (such as alkalinity and system redox state) will be controlled by equilibrium with atmospheric carbon dioxide and free oxygen. The primary reactive components in the degraded waste package environment are iron hydroxides, the same mineral phases that tend to dominate trace element sorption in soils. The only major element species that will be present in waste package fluids, but that tend to be scarcer in natural soils and groundwaters, are those containing uranium.

The trace element composition of waste package fluids will differ due to the presence of metal components and various radiogenic isotopes. On the other hand, the waste package environment is expected to contain greater volumes of iron hydroxides than all but the most iron-rich soils. Consequently, sorption calculations using ranges of K_d values measured on iron-containing soils or iron hydroxides provide a reasonable measure of sorption inside the waste package.

Sorption distribution coefficients often vary by at least an order of magnitude. Each range of K_d represents the compilation of many experimental measurements with wide variations in sorbant composition and characteristics, contaminant level, solution composition and temperature, and method of measurement.

Sorption distribution coefficient values for a linear, reversible isotherm can be interpreted physically (Stumm 1992 [DIRS 141778], Section 4.12) in terms of retarding the movement of a contaminant relative to the velocity of the water carrying it. If the average water velocity is $\bar{v}$ (m s^{-1}) and the front of the contaminant concentration profile has an average velocity v_c, the retardation of the front relative to the bulk mass of water is described by the relation:

$$R_f = \frac{\bar{v}}{v_c} = 1 + \frac{\rho_b}{\phi} K_d, \qquad \text{(Eq. 6.3.4.2.3-1)}$$

where R_f is the retardation factor (dimensionless ratio of water velocity to the concentration front velocity), ρ_b is the bulk density of the rock (kg m^{-3}) having a porosity ϕ (fraction). For example, a contaminant with a K_d of 1,000 ml g^{-1} will move at one ten-thousandth the rate of the carrier water for a rock porosity of 20 percent and a rock density of 2,000 kg m^{-3}. A contaminant with a K_d of 1 ml g^{-1} will move at one-eleventh the velocity of the carrier water, and a contaminant with a K_d of 0 moves at the velocity of the water, both for the same values of rock porosity and rock density. These effective transport velocities provide an estimate of the delay for first breakthrough of the contaminant; after the sorption sites are completely saturated, changes in mass flow rate will be delayed only by the water transport time through the system.

The corrosion product assemblage is predicted by the in-package chemistry model reaction path calculations to be made up primarily of iron oxyhydroxides (e.g., goethite, hematite, ferrihydrite) and aluminum oxides. Lesser amounts of manganese oxides, metal phosphates and clay minerals are anticipated. The integrated sorptive properties of the assemblage might therefore be approximated as being that of iron oxyhydroxides with some aluminum oxides. The latter

possess high specific surface areas and a strong chemical affinity for many radionuclides. Cesium primarily exchanges onto clay minerals. Strontium and radium tend to exchange onto clay lattices in soils, although strontium does sorb onto iron oxyhydroxides, particularly above pH 7. The fact that strontium and radium behave similarly in soils indicates that limited radium uptake by iron oxyhydroxides can be expected as well. Under oxidizing conditions technetium and iodide sorb negligibly to most soil components. However, reduction of technetium on solid surfaces containing reduced elements (e.g., iron metal) can cause strong retardation.

Table 6.3-5 summarizes the observations above by listing the components of soils that tend to control sorption. Iron oxyhydroxides are an important sorbing component of soils for all radioelements except iodine and technetium.

Table 6.3-5. Influences Over Radionuclide Sorption in Soils

Element	Important Solid Phase and Aqueous-Phase Parameters Influencing Contaminant Sorption*
Americium	[Clay Minerals], [Iron/Aluminum Oxide Minerals], pH
Cesium	[Aluminum/Iron Oxide Minerals], [Ammonium], Cation Exchange Capacity, [Clay Mineral], [Mica-like Clays], pH, [Potassium]
Iodine	[Dissolved Halides], [Organic Matter], Redox, Volatilization, pH
Neptunium	[Clay Minerals], [Iron/Aluminum Oxide Minerals], pH
Radium	$BaSO_4$ Coprecipitation, [Dissolved Alkaline Earth Elements], Cation Exchange Capacity, [Clay Minerals], Ionic Strength, [Iron-/Aluminum-Oxide Minerals], [Organic Matter], pH
Technetium	[Organic Matter], Redox
Plutonium	[Aluminum/Iron Oxide Minerals], [Carbonate, Fluoride, Sulfate, Phosphate], [Clay Mineral], [Organic Matter], pH, Redox
Strontium	Cation Exchange Capacity, [Calcium], [Carbonate], pH, [Stable Strontium]
Thorium	[Aluminum/Iron Oxide Minerals], [Carbonate], [Organic Matter], pH
Uranium	[Aluminum/Iron-Oxide Minerals], [Carbonate, Fluoride, Sulfate, Phosphate], [Clay Mineral], [Organic Matter], pH, Redox, [U]

Source: EPA (2004 [DIRS 172215]), Table 5.35.
EPA (1999 [DIRS 170376]), Table 5.20.
*Parameters listed in alphabetical order. Square brackets represent concentration.

Corrosion product K_d ranges have been compiled by Electric Power Research Institute (EPRI) (2000 [DIRS 154149], Table 6-9) from a literature review of iron oxyhydroxides sorption measurements. Ranges and distributions of K_d values for sorption of radionuclides onto iron oxide are also evaluated and compiled in DTN: LA0003AM831341.001 ([DIRS 148751] SEP table S00191_002); these are listed in Table 4.1-11. The U.S. Environmental Protection Agency (EPA) has compiled K_d values for soils for many of the same radionuclides (EPA 1999 [DIRS 170376]; EPA 2004 [DIRS 172215]). The large role of iron and aluminum oxyhydroxides minerals in controlling overall soil K_d values is explicitly recognized in the EPA documents. For this reason, one would expect EPA soil K_d values and EPRI iron oxyhydroxides K_d values to be similar and both to provide a reasonable approximation of retardation in the waste package corrosion products. There are some caveats, however, the most important one being that K_d values for a given material and radionuclide are approximate values that can vary widely depending on the specifics of the measurement (solid/solution ratio, radionuclide level, time allowed for equilibration). General coherence in an order-of-magnitude sense is the best

that can be expected as the K_d approach does a poor job of reproducing actual transport profiles; see, for example, Bethke and Brady (2000 [DIRS 154437]) and Reardon (1981 [DIRS 154434).

Table 6.3-6 gives K_d ranges describing retardation in the waste package corrosion products for the 12 radionuclides that are tracked in TSPA-LA, with the minimum K_d and maximum K_d being the ranges used in TSPA-LA. For all but iodine and technetium, the maximum K_d values are from DTN: LA0003AM831341.001 ([DIRS 148751] SEP table S00191_002). The maximum K_d value for iodine and technetium is chosen to be 0.6 ml g^{-1}, which is the approximate maximum K_d value for iodine and technetium specified for alluvium in saturated zone units in DTN: LA0003AM831341.001 ([DIRS 148751] SEP table S00191_001). The minimum K_d values for carbon, cesium, iodine, radium, strontium, and technetium are the minimum K_d values specified in DTN: LA0003AM831341.001 ([DIRS 148751] SEP table S00191_002). In order to provide a more bounding estimate of releases of radionuclides that have a large impact on dose, the minimum K_d values for actinium, americium, plutonium, and thorium are reduced by a factor of 10 from the minimum K_d values specified in DTN: LA0003AM831341.001 ([DIRS 148751] SEP table S00191_002). For the same reason, the minimum K_d value for protactinium is reduced by a factor of 5 from the minimum K_d value of 500 ml g^{-1} specified in DTN: LA0003AM831341.001 ([DIRS 148751] SEP table S00191_002); this minimum value is corroborated by *Evaluation of the Candidate High-Level Radioactive Waste Repository at Yucca Mountain Using Total System Performance Assessment, Phase 5* (EPRI 2000 [DIRS 154149], Table 6-9). The minimum K_d value for uranium is reduced by a factor of 100 from the minimum K_d value of 100 ml g^{-1} specified in DTN: LA0003AM831341.001 ([DIRS 148751] SEP table S00191_002); this minimum value is corroborated by *Review of Geochemistry and Available K_d Values for Cadmium, Cesium, Chromium, Lead, Plutonium, Radon, Strontium, Thorium, Tritium (^3H), and Uranium.* Volume II of *Understanding Variation in Partition Coefficient, K_d, Values* (EPA 1999 [DIRS 170376], Table 5.17). The minimum K_d value for neptunium is reduced by a factor of 500 from the minimum K_d value of 500 ml g^{-1} specified in DTN: LA0003AM831341.001 ([DIRS 148751] SEP table S00191_002); this minimum value is corroborated by *Evaluation of the Candidate High-Level Radioactive Waste Repository at Yucca Mountain Using Total System Performance Assessment, Phase 5* (EPRI 2000 [DIRS 154149], Table 6-9) and *Review of Geochemistry and Available K_d Values for Cadmium, Cesium, Chromium, Lead, Plutonium, Radon, Strontium, Thorium, Tritium (^3H), and Uranium.* Volume II of *Understanding Variation in Partition Coefficient, K_d, Values* (EPA 1999 [DIRS 170376], Table 5.17).

For cesium, radium, and strontium, a beta distribution as specified in DTN: LA0003AM831341.001 ([DIRS 148751] SEP table S00191_002), is used in TSPA-LA. For carbon, iodine, protactinium, and technetium, a uniform distribution as specified in DTN: LA0003AM831341.001 ([DIRS 148751] SEP table S00191_001) is used in TSPA-LA. Whereas DTN: LA0003AM831341.001 ([DIRS 148751] SEP table S00191_002) specified a uniform distribution for americium, neptunium, plutonium, thorium, and uranium, a log-uniform distribution is used in TSPA-LA, all of which have K_d values that range over more than an order of magnitude. A log-uniform distribution is specified to avoid the high-end bias that results from sampling from a uniform distribution that has a large range.

Table 6.3-6 also gives corroborating ranges and data source(s) described in recent literature. To capture the secondary role of iron oxyhydroxides in soil sorption of strontium, radium and

cesium, clay-poor soil K_d values from the EPA compilation are used in the comparison. In all cases the corroborating K_d ranges overlap the ranges used in TSPA-LA. Moreover, in most cases the TSPA-LA K_d values tend to be on the low end of the K_d range considered in aggregate.

Table 6.3-6. Summary of Partition Coefficient (K_d) Ranges and Distributions for Retardation in the Waste Package Corrosion Products

Element	Minimum K_d (ml g^{-1})	Maximum K_d (ml g^{-1})	Distribution Type	Corroborating K_d Range (ml g^{-1})	Corroborating K_d Range Source
Ac	100	5,000	Log-Uniform	1,000–20,000	EPRI 2000 [DIRS 154149], Table 6-9
Am	100	5,000	Log-Uniform	1,000–>100,000 1,000–20,000	EPA 2004 [DIRS 172215], Section 5.2.5.1; EPRI 2000 [DIRS 154149], Table 6-9
C	10	100	Uniform	0–100	EPRI 2000 DIRS 154149], Table 6-9
Cs	0	300	Beta $E(x)$=30 $\sigma(x)$=30	10–3,500 1–200	EPA 1999 [DIRS 170376], Table D.10 (low clay soils); EPRI 2000 [DIRS 154149], Table 6-9
I	0	0.6	Uniform	0–1	EPRI 2000 [DIRS 154149], Table 6-9
Np	1	1,000	Log-Uniform	0.16–929 10–1,000 (0.1–1,000)	EPA 2004 [DIRS 172215], Section 5.6.5.4; EPRI 2000 [DIRS 154149], Table 6-9 (reduced by factor of 100 for U site saturation)
Pa	100	1,000	Uniform	100–10,000	EPRI 2000 [DIRS 154149], Table 6-9
Pu	100	5,000	Log-Uniform	60–15,000 1,000–20,000	EPA 1999 [DIRS 170376], p. G-4 EPRI 2000 [DIRS 154149], Table 6-9
Ra	0	500	Beta $E(x)$=30 $\sigma(x)$=30	1–120 50–1,000	EPA 2004 [DIRS 172215] (Section 5.7.5.1: use Sr values) EPRI 2000 [DIRS 154149], Table 6-9
Sr	0	20	Beta $E(x)$=10 $\sigma(x)$=2.5	1–120 10–100	EPA 1999 [DIRS 170376], Table 5.13 EPRI 2000 [DIRS 154149], Table 6-9
Tc	0	0.6	Uniform	0–1,000	EPRI 2000 [DIRS 154149], Table 6-9
Th	100	5,000	Log-Uniform	20–300,000 1,000–20,000	EPA 1999 [DIRS 170376], Table 5.15 EPRI 2000 [DIRS 154149], Table 6-9
U	1	1,000	Log-Uniform	0–630,000 50–10,000	EPA 1999 [DIRS 170376], Table 5.17 EPRI 2000 [DIRS 154149], Table 6-9

EPA = Environmental Protection Agency

Irreversible uptake can be the dominant control over contaminant transport in soils. Evidence for soil sequestering of bomb-pulse plutonium and americium and of uranium, iodine, technetium, cesium, and strontium from ore processing and reactor operations has been extensively documented in the literature (Coughtrey et al. 1983 [DIRS 132164]).

Estimates of the mean fraction of irreversible sorption for various radionuclides on soil are derived in *Site Screening and Technical Guidance for Monitored Natural Attenuation at DOE Sites* (Brady et al. 1999 [DIRS 154421], Appendix VI). The value of the irreversible fraction for the EBS will differ from that for soils and will depend on the material that the specific radionuclide encounters, the speciation of the radionuclide, and other factors in the material and

chemical environment. Irreversible sorption is an important process for many radionuclides that potentially contribute to dose. For the TSPA-LA model, irreversible sorption of Pu and Am is included, with appropriate fractions of the total mass adsorbed being based on field observations. Details of the radionuclide sorption component of the EBS transport model are described in Sections 6.5.1.1.1 and 6.5.3.

6.3.4.2.4 Sorption Parameters for Corrosion Products in the Invert

To compare with the mass of sorbing material in the waste packages, the mass of sorbing material in the invert has been estimated using the data from *Repository Subsurface Emplacement Drifts Steel Invert Structure Sect. & Committed Materials* (BSC 2004 [DIRS 169776], Committed Materials table). The iron content of the steel invert support beams, stiffeners, base plates, gantry runway beams, runway beam cap plates, stub columns and top plates, miscellaneous stiffener plates, and the gantry rails is included in this calculation. The iron in the steel set ground support, the rock bolts, and the welded wire fabric steel has been ignored, even though the corrosion products from these components may fall on the invert. The mass of corrosion products is again estimated by assuming that iron converts to Fe_2O_3 during the corrosion process. The mass of A 588 carbon steel per unit length of drift in the invert is 893 kg m^{-1} (BSC 2004 [DIRS 169776], Committed Materials table), having an iron content of 859 kg m^{-1} (using an iron content of 96.16 percent for the composition of A 588 steel; ASTM A 588/A 588M-01 [DIRS 162724], Table 1). The mass of A 759 steel in the gantry rails is 134 kg m^{-1} (BSC 2004 [DIRS 169776], Committed Materials table), which has an iron content of 97.47 percent (ASTM A 759-00 [DIRS 159971]), or 131 kg m^{-1}. The total iron content of the invert is then 990 kg m^{-1}, which converts to 1,415 kg m^{-1} of Fe_2O_3. As a comparison, the average mass of Fe_2O_3 in the invert under a 21-PWR or 44-BWR waste package, having a nominal length of 5.02 m (BSC 2004 [DIRS 169472], Table 1), would be 6,820 kg, or approximately one-third the amount of iron corrosion products inside a waste package (Table 6.3-4). While not negligible, the sorptive capacity of the invert is small compared to that of the waste packages, so, not considering retardation by corrosion products in the invert (Assumption 5.7) will overestimate radionuclide transport.

The impact of copper in the invert on retarding iodine and technetium is discussed here to complete the analysis of neglecting retardation by corrosion products in the invert and thus overestimating radionuclide transport. The amount of elemental copper in the drift is given by the nominal weight of the solid copper conductor bar rail, 4.0 kg m^{-1} (BSC 2001 [DIRS 154441], Section 3.1.7), plus the copper in the communication cable, which is 50 percent by weight of the total cable weight of 2.00 kg m^{-1} (BSC 2001 [DIRS 154441], Sections 3.1.9 and 3.2.1.3). The total weight of elemental copper per meter of drift is then [4.0 + (0.5)(2.00)] or a total of 5.0 kg m^{-1}. These values are based on the nominal mass of elemental copper, rather than the upper bound values, to provide a bounding estimate. The mass of elemental copper is not explicitly represented in the TSPA-LA model, but its presence when oxidized is noted because of its role as a potential sorber for iodine and technetium.

The mass of copper is large relative to the mass of iodine and technetium. Using a waste package length of 5.024 m for the CSNF waste package (BSC 2004 [DIRS 169472], Table 1), there is 25.1 kg of elemental copper in the invert per CSNF waste package. This value (25.1 kg) can be compared to approximately 7.64 kg of technetium-99 and 1.75 kg of iodine-129 per

CSNF waste package (DTN: SN0310T0505503.004 [DIRS 168761]). Thus, there is more elemental copper than iodine or technetium using a mass or molar basis. Similarly, the 5 DHLW/DOE SNF - Short codisposal waste package has a length of 3.45 m (BSC 2004 [DIRS 169472], Table 3), implying that there is 17.3 kg of elemental copper per 5 DHLW/DOE SNF - Short waste package in the invert. This mass is greater than the approximately 0.156 kg of technetium-99 or the 0.0351 kg of iodine-129 in the codisposal waste packages (DTN: SN0310T0505503.004 [DIRS 168761]). Based simply on a gross comparison of masses, there is ample quantity of copper in the invert to adsorb all iodine and technetium that might be released from the waste packages. Nevertheless, because the presence of copper is highly localized, the probability of iodine or technetium released from the waste package actually contacting the copper is low. Therefore, iodine and technetium are assumed not to sorb onto corrosion products in the invert.

To summarize, no credit is taken for radionuclide sorption onto corrosion products of iron or copper contained in the invert (Assumption 5.7), through which radionuclides must be transported to reach the accessible environment. By ignoring sorption in the invert, there is added confidence that the radionuclide inventory actually transported is less than the calculated value used in assessing dose to the individual.

6.3.4.3 In-Package Diffusion Submodel for Commercial Spent Nuclear Fuel Waste Packages

This submodel provides a way to quantify the uncertainty in diffusive releases from CSNF waste packages when no seepage occurs, when the only water present is water vapor. The object of the submodel is to compute the effective diffusion coefficient, cross sectional area for diffusion, and the diffusion path length for diffusion of radionuclides by Fick's law. From these output parameters, the rate of diffusion of radionuclides from the waste package to the invert can be determined.

One way to picture a breached and degraded waste package is for the radionuclide inventory to be located just inside the thickness of the waste package outer corrosion barrier or lids from the invert, with a fully saturated porous medium separating the interior of the waste package from the invert. This scenario provides essentially no resistance to diffusion from the waste package and thus grossly overestimates diffusive releases of radionuclides. Compared to this picture, the present base submodel with in-package diffusion can potentially delay and reduce computed diffusive releases by providing a much more realistic estimate of the resistance to diffusion that occurs when little water is present. This is especially important if, as expected, much of the repository has no seepage into drifts.

The fundamental basis of this submodel is that the only liquid water present is the thin film of adsorbed water that covers all surfaces exposed to humid air (Assumption 5.5). In this submodel, all dissolution and diffusion of radionuclides occur in this thin film.

As the steel internal components corrode, the interior of the waste package becomes filled with a mass of porous corrosion products. Diffusion will occur on the thin films coating the surfaces of particles of corrosion products. The extent of corrosion will determine the amount of corrosion products and, in turn, the amount of adsorbed water that is present, from which the water

saturation is computed. Together with estimates of the porosity, the effective diffusion coefficient is calculated using Archie's law. A bulk cross sectional area for diffusion is estimated, and the length of the diffusion path is a sampled parameter for each leg of the path from the waste form domain to the corrosion products domain to the invert domain.

The extent of corrosion is taken to vary linearly over the lifetime of the waste package steels. The amount of water adsorbed is a function of the relative humidity. Consequently, the rate of diffusive releases varies over time. All internal steel components are considered to be iron that corrodes to form Fe_2O_3.

A number of uncertain parameters are associated with this submodel. The lengths of the various diffusive pathways are also uncertain because the location of the failed fuel rods and therefore the distance from the points of failure to the openings in the waste package outer corrosion barrier cannot be known. In addition, the surface area available for adsorption of water is uncertain because the condition of the corrosion products cannot be determined–they may be finely powdered with a high specific surface, or agglomerate into an impermeable mass with low specific surface area, all depending on unpredictable circumstances and material behaviors. Details of the in-package diffusion submodel for CSNF waste packages are presented in Section 6.5.1.2.1.

6.3.4.4 Colloidal Transport

Radionuclide transport from the waste package occurs as dissolved species at the appropriate solubility or dissolution rate limit and as colloidal particles. Three types of colloids are anticipated to exist in the EBS (BSC 2004 [DIRS 170025]): (a) waste form colloids from degradation of HLW glass, (b) iron oxyhydroxide colloids due to products from the corrosion of steel waste packages, and (c) groundwater or seepage water colloids. All three types of colloids may have reversibly sorbed radionuclides. The waste form colloids may have irreversibly attached (embedded) or reversibly attached (sorbed) radionuclides. The corrosion products colloids may have irreversibly attached (strongly sorbed) or reversibly attached (weakly sorbed) radionuclides. The stability and mass concentrations of colloids are functions of the ionic strength and pH of the groundwater or local liquid chemistry in the waste package and invert. Both groundwater and waste form colloids are stipulated to be smectite, and therefore K_d values associated with radionuclide sorption onto smectite colloids are used in the TSPA-LA model (BSC 2004 [DIRS 170025], Table 6-6).

The potential mass of radionuclides irreversibly attached (embedded) to the waste form colloids (BSC 2004 [DIRS 170025], Section 6.3.3.3) is determined from reactions within the waste package. The mass of radionuclides reversibly attached to all three types of colloids is determined primarily by three parameters:

- Mass concentration of dissolved (aqueous) radionuclide in the liquid
- Mass concentration of colloid material in the liquid
- Radionuclide distribution coefficient (K_d) of a specific radionuclide on a specific colloid mineralogical type.

The potential concentrations of colloids in the drifts and EBS have also been assessed (BSC 2004 [DIRS 170025]). In a DOE-funded research project at the University of Nevada at Las Vegas to evaluate the corrosion of scaled-down miniature waste packages, the data indicate a preponderance of amorphous corrosion products released as colloids, including magnetite (Fe_3O_4), lepidocrocite (FeOOH), and goethite (FeOOH) (DTN: MO0302UCC034JC.003 [DIRS 162871]; BSC 2004 [DIRS 170025], Section 6.3.1.3).

Colloidal transport of radionuclides occurs by advective and diffusive processes. Advective transport moves colloids (and the associated radionuclides) at approximately the same velocity as the liquid flux through the EBS. Longitudinal dispersion, which could potentially enable colloids to travel faster than the bulk average liquid velocity, is ignored because of the short travel distance through the EBS (see Section 6.3.1.2). Diffusive transport moves colloids due to the concentration gradient and the medium diffusive properties. In the absence of a rigorous theory of solute diffusion in liquids, order of magnitude estimates may be made on the basis of hydrodynamic theory. Based on the Stokes-Einstein equation (Bird et al. 1960 [DIRS 103524], p. 514, Equation 16.5-4), the diffusivity of a solute in a liquid is inversely proportional to the radius of the diffusing particles.

Rates of diffusion of colloidal particles can be estimated by scaling those experimentally determined free water diffusion coefficients for dissolved actinides to dissolved colloidal materials on the basis of size (Stokes-Einstein relationship) as follows:

$$D_{coll} = D_{ion}\left(\frac{r_{ion}}{r_{coll}}\right), \qquad \text{(Eq. 6.3.4.4-1)}$$

where

D_{coll} = diffusion constant for a colloidal actinide of radius r_{coll}

D_{ion} = diffusion constant for a dissolved actinide of radius r_{ion}

r_{coll} = radius of the colloidal actinide

r_{ion} = radius of the dissolved actinide.

For example, given an ionic radius $r_{ion} = 1$ Å (0.1 nm) and a colloidal particle radius $r_{coll} = 10$ nm, the free water diffusion coefficient for the colloidal particle would be that of the dissolved actinide reduced by a factor of 100 ($D_{coll} = D_{ion}[0.1\,\text{nm}/10\,\text{nm}] = D_{ion}/100$, from Equation 6.3.4.4-1). This approach is consistent with discussions in *Principles of Colloid and Surface Chemistry* (Hiemenz 1986 [DIRS 117358], p. 81).

Radionuclides may sorb onto stationary corrosion products from the degradation of waste package internal components (Section 6.5.3) as well as onto mobile colloids. This sorption process will compete with sorption onto colloids. A portion of plutonium and americium sorb irreversibly onto mobile colloids as well as onto stationary corrosion products in the waste package. In order to model both reversible and irreversible sorption of plutonium and americium onto iron oxyhydroxide colloids, the TSPA model reduces the upper bounds for the K_d values in Table 6.3-7 for plutonium and americium by a factor of 100 (BSC 2004 [DIRS 170025],

Section 6.3.3.2), which constrains the K_d values to the lower bound. This allows for more of the plutonium and americium to desorb from the iron oxyhydroxide colloids, thereby simulating reversible sorption.

The sorption distribution coefficients (K_d values) for colloids used in the TSPA-LA calculations are presented in Table 6.3-7. The ranges of K_d values used for colloids are different from those used for stationary corrosion products (Table 6.3-5) and are higher for all radionuclides that are considered. The rationale for this difference is that the specific surface area of colloids is generally greater than that of stationary corrosion products, largely because colloid particles are smaller. The specific surface area used for corrosion products ranges from about 0.4 to 22.4 $m^2 g^{-1}$ (Section 6.5.1.2.1.3.1). In contrast, the specific surface area of iron oxyhydroxide colloids ranges from 1.8 to 720 $m^2 g^{-1}$ with a log-uniform distribution (DTN: SN0309T0504103.010 [DIRS 165540]; BSC 2004 [DIRS 170025], Section 6.3.3.2).

Another reason for the disparities between stationary corrosion products K_d values and colloid K_d values is an intentional bias toward lower K_d values in each model so as to overestimate releases of radionuclides. In the case of stationary corrosion products, lower K_d values will tend to release more radionuclides from the waste packages. For colloids, predicted releases of radionuclides sorbed onto colloids are higher using higher K_d values, since the radionuclides then remain sorbed longer and are transported farther.

6.3.4.5 Transport through Stress Corrosion Cracks

Transport through stress corrosion cracks in the waste package is limited to diffusion. Once stress corrosion cracks form in the lid of the waste package, all surfaces inside the waste package are assumed to be coated with a thin film of water (per Assumption 5.5). This thin film provides the medium for diffusion from the waste form, through the stress corrosion crack, and out of the waste package. The diffusive area is calculated as the product of the area and number of cracks. The area of each crack is estimated from the data in Table 6.3-3. The maximum cross-sectional area of each crack for diffusive transport is calculated to be 7.7×10^{-6} m^2 (Section 6.3.3.1.2.1).

Table 6.3-7. Sorption Distribution Coefficient (K_d) Values and Interval Probabilities Used for Reversible Radionuclide Sorption on Colloids in TSPA-LA Calculations

Radionuclide	Colloid	K_d Value Range (ml g^{-1})	K_d Value Intervals (ml g^{-1})	K_d Value Interval Probabilities
Pu	Iron Oxyhydroxide	10^4 to 10^6	$<1 \times 10^4$ 1×10^4 to 5×10^4 5×10^4 to 1×10^5 1×10^5 to 5×10^5 5×10^5 to 1×10^6 $> 1 \times 10^6$	0 0.15 0.2 0.5 0.15 0
	Smectite	10^3 to 10^6	$< 1 \times 10^3$ 1×10^3 to 5×10^3 5×10^3 to 1×10^4 1×10^4 to 5×10^4 5×10^4 to 1×10^5 1×10^5 to 5×10^5 5×10^5 to 1×10^6 $> 1 \times 10^6$	0 0.04 0.08 0.25 0.2 0.35 0.08 0

Table 6.3-7. Sorption Distribution Coefficient (K_d) Values and Interval Probabilities Used for Reversible Radionuclide Sorption on Colloids in TSPA-LA Calculations (Continued)

Radionuclide	Colloid	K_d Value Range (ml g^{-1})	K_d Value Intervals (ml g^{-1})	K_d Value Interval Probabilities
Am, Th, Pa	Iron Oxyhydroxide	10^5 to 10^7	$< 1 \times 10^5$ 1×10^5 to 5×10^5 5×10^5 to 1×10^6 1×10^6 to 5×10^6 5×10^6 to 1×10^7 $> 1 \times 10^7$	0 0.15 0.2 0.55 0.1 0
	Smectite	10^4 to 10^7	$< 1 \times 10^4$ 1×10^4 to 5×10^4 5×10^4 to 1×10^5 1×10^5 to 5×10^5 5×10^5 to 1×10^6 1×10^6 to 5×10^6 5×10^6 to 1×10^7 $> 1 \times 10^7$	0 0.07 0.1 0.23 0.2 0.32 0.08 0
Cs	Iron Oxyhydroxide	10^1 to 10^3	$< 1 \times 10^1$ 1×10^1 to 5×10^1 5×10^1 to 1×10^2 1×10^2 to 5×10^2 5×10^2 to 1×10^3 $> 1 \times 10^3$	0 0.13 0.22 0.55 0.1 0
	Smectite	10^2 to 10^4	$< 1 \times 10^2$ 1×10^2 to 5×10^2 5×10^2 to 1×10^3 1×10^3 to 5×10^3 5×10^3 to 1×10^4 $> 1 \times 10^4$	0 0.2 0.25 0.5 0.05 0

DTN: SN0306T0504103.006 [DIRS 164131], Table 1.

NOTE: In engineered barrier system calculations, upper bound of Kd ranges for plutonium (Pu) and americium (Am) on iron oxyhydroxide reduced by a factor of 100 to be compatible with mechanistic sorption model described in *Waste Form and In-Drift Colloids-Associated Radionuclide Concentrations: Abstraction and Summary* (BSC 2004 [DIRS 170025], Section 6.3.3.2).

6.4 CONSIDERATION OF ALTERNATIVE CONCEPTUAL MODELS

Alternative conceptual models considered in the EBS radionuclide transport abstraction are discussed in this section. A summary of models that are analyzed is presented in Table 6.4-1.

Table 6.4-1. Alternative Conceptual Models Considered

Alternative Conceptual Models	Key Assumptions	Screening Assessment and Basis
Bathtub flow model (alternative to flow-through model)	Seepage water flowing into breached waste package accumulates until void volume is filled before water containing dissolved radionuclides flows out. Various cases, such as changing inflow rates and effect of solubility and dissolution rate limits, are evaluated.	Screened out in analysis in Section 6.6.1. For several of the most pertinent cases, the flow-through model is bounding with respect to releases of radionuclides.

Table 6.4-1. Alternative Conceptual Models Considered (Continued)

Alternative Conceptual Models	Key Assumptions	Screening Assessment and Basis
Water vapor diffusion limitations through stress corrosion cracks (alternative to unlimited access to water vapor)	If the rate of corrosion of steel components inside waste package is greater than the rate of diffusion of water vapor into waste package, a film of adsorbed water cannot form, which delays diffusive releases until all steel is fully corroded. Water vapor concentration inside waste package is assumed to be zero to maximize concentration gradient. Alternative cases consider stress corrosion cracks that are assumed to be (1) fully open and (2) filled with corrosion products but still permeable. Alternative corrosion stoichiometry is considered for formation of (1) Fe_2O_3 and (2) $Fe(OH)_2$. Alternative corrosion rates are considered assuming (1) only carbon steel corrodes, (2) all internal components corrode at carbon steel rate and at stainless steel rate, with mass of iron computed as in the in-package diffusion submodel.	Screened out. Potentially delays releases for hundreds to thousands of years, which requires unattainable reduction in model uncertainties. The assumption that no water is physically adsorbed until all steel is corroded is questionable, since adsorption is typically a fast process. On the other hand, if water consumption by corrosion keeps the relative humidity inside the waste package low, the effective water saturation, as computed in the in-package diffusion submodel, will be so low that bulk liquid phase behavior allowing dissolution and diffusion of dissolved radionuclides will not exist until corrosion is complete.
Oxygen diffusion limitations through stress corrosion cracks (alternative to unlimited access to oxygen)	Same as for water vapor diffusion limitation model, but less restrictive in that oxygen as well as water vapor can corrode steels, potentially reducing time needed for complete corrosion of internal components. Assumes that oxic corrosion occurs at the same rate as anoxic corrosion with water. Assumes oxygen and water vapor can diffuse independently of each other without interfering. Oxygen concentration inside waste package is assumed to be zero to maximize concentration gradient.	Screened out. Potentially delays releases, which is not justifiable in view of large model uncertainties. Comparative rates of oxic and anoxic corrosion should be considered. Competing diffusion with water vapor should also be addressed.
Dual-continuum invert model	Crushed tuff invert ballast is modeled as a dual-continuum material consisting of intergranular pore space and intragranular pore space. All seepage flow into the drift flows through the intergranular pore space and into the UZ fractures. Imbibition from UZ host rock into the invert flows through the intragranular pore space. Diffusion of radionuclides also occurs in both the intergranular and intragranular pore spaces, from the waste package corrosion products into UZ fractures and matrix, as well as between the two invert continua.	Screened out. Insufficient data to validate diffusion coefficients in individual continua. Insufficient data to confirm whether this is a bounding approach with respect to chemical behavior in the invert.
Invert diffusion coefficient model with lower limit on water content	As the water content of the crushed tuff ballast decreases, the water films that connect pore spaces become disconnected, and the effective diffusion coefficient drops more rapidly than predicted by Archie's law. Below some critical water content, the diffusion coefficient becomes zero. Based on models of diffusion in soils.	Screened out. Insufficient data to validate diffusive behavior at very low water contents. Does not provide upper bounds on diffusion coefficients.

6.4.1 Bathtub Model for the Waste Package

The bathtub model is an alternative conceptual EBS flow model in which seepage collects within the waste package before being released to the EBS. This is an alternative to the "flow-through" geometry, and is analyzed in Section 6.6.1. It is concluded that, with respect to releases of radionuclides, the flow-through model increases releases relative to the bathtub model and is therefore bounding for the following cases:

1. Primary case, in which the water inflow rate is constant, the rate of radionuclide dissolution is limited, and the radionuclide concentration is solubility-limited. Unlike the bathtub model, there is no delay in release of radionuclides in the flow-through model.

2. Secondary case 1, in which the inflow rate undergoes a step change. The response of the bathtub model is identical to the flow-through model for solubility-limited radionuclides. For dissolution-rate-limited radionuclides, the flow-through model overestimates releases of radionuclides for the case of decreasing inflow, or increasing concentration, which is of primary interest from a performance or regulatory standpoint.

3. Secondary case 2, a step change in groundwater chemistry. The flow-through model overestimates releases of radionuclides relative to the bathtub model when the solubility or dissolution rate increases because it has an instantaneous change to the higher equilibrium value, whereas the bathtub geometry delays the change. For decreasing solubility or dissolution rate, the bathtub overestimates releases of radionuclides, but this case is of no interest from a performance or regulatory point of view.

4. Secondary case 3, wherein a second corrosion patch opens instantaneously beneath the water level in the waste package in the bathtub model. The impact of this alternative flow path was screened out because of the potential mitigation from sorption and diffusion and because the variability of corrosion rates provides large uncertainty in radionuclide release rates from the waste package.

As a result of this analysis, the bathtub model has been screened out as an alternative conceptual model in order to overestimate radionuclide transport.

6.4.2 Limited Water Vapor Diffusion Rate into Waste Package

This alternative conceptual model accounts for the resistance to diffusion of water vapor *into* a waste package through stress corrosion cracks. In the base model, there is no limit to the amount of water vapor available to adsorb onto surfaces within a waste package, which creates a pathway for diffusive transport of radionuclides out of the waste package (This applies to the in-package diffusion submodel, Section 6.5.1.2.1.1.). However, the base model currently used for the TSPA to calculate dose overestimates releases of radionuclides, particularly at early times when the only breaches in a waste package are small stress corrosion cracks. If the diffusion rate is limited, the rate of steel corrosion is limited by the rate of diffusion of water vapor. The result is that no water is available to adsorb and form a thin liquid film on corrosion products, and no

water would be available for radionuclide transport. This is because all water is consumed by the corrosion process as quickly as it diffuses into the waste package. This prevents formation of a diffusive path until all of the internal steel components are fully corroded, which in turn delays diffusive releases until that time. Since this may take hundreds to thousands of years, the delay in releases of radionuclides from breached waste packages could be extensive. During this delay, radioactive decay will decrease the quantity of radionuclides in the waste package, ultimately reducing releases to the environment.

A mathematical description of this model is presented in Section 6.6.2.

6.4.3 Limited Oxygen Diffusion Rate into Waste Package

This alternative conceptual model is similar to the alternative conceptual model dealing with limited water vapor diffusion into a waste package through stress corrosion cracks described in Section 6.4.2. In both models, the rate of steel corrosion is limited by the rate of diffusion of reactive gases. They also imply that no adsorbed water film can form until all of the steel is corroded, as long as the rate of water consumption by corrosion is greater than the rate of diffusion of reactants into the waste package. The difference in this model is that oxygen in the waste package is also diffusion limited, yet oxygen also reacts readily with the steel internal components. Depending on how oxygen competes with water vapor in diffusing through stress corrosion cracks and reacting with steel, the time required for all internal components to react and stop consuming water would be shortened. Then diffusive releases through the film of adsorbed water (given by the in-package diffusion submodel, Section 6.5.1.2.1) can begin earlier than predicted by the water vapor limited diffusion model alone.

A mathematical description of this model is presented in Section 6.6.3.

6.4.4 Dual-Continuum Invert

This alternative conceptual model treats the crushed tuff in the invert as a dual continuum comprised of two pore spaces – intragranular pore space (tuff particle matrix) and intergranular pore space. Although radionuclide transport by both advection and diffusion can occur in both pore spaces, the dominant flow and transport processes in each of these two pore spaces is generally different. In order to simulate flow and transport through the invert accurately, the invert is conceptualized in this alternative conceptual model as overlapping dual continua using a dual-permeability approach, wherein flow and transport occur in both pore spaces, and mass transfer takes place between the two pore spaces.

A mathematical description of this model is presented in Section 6.6.4.

6.4.5 Alternative Invert Diffusion Coefficient Models

The following two alternative models for determining the diffusion coefficient in the invert are assessed: the single-continuum invert diffusion coefficient model and the dual-continuum invert diffusion coefficient model. In the single-continuum invert diffusion coefficient model, an alternative to the Archie's law approach for determination of the diffusion coefficient for the single-continuum crushed tuff invert ballast (Section 6.3.4.1) is modeled using an approach that has been applied to diffusion in soils. In the dual-continuum invert diffusion coefficient model,

the bulk diffusion coefficient is dominated by the intergranular diffusion coefficient above the critical bulk moisture content, while below this critical value, the intragranular diffusion coefficient dominates.

Mathematical descriptions of these models are presented in Section 6.6.5.

6.5 MODEL FORMULATION FOR BASE CASE MODEL

6.5.1 Mathematical Description of Base Case Conceptual Model

A solute transport model typically consists of two component models: a model to solve the flow equation and another to solve the transport equation (Anderson and Woessner 1992 [DIRS 123665], p. 327). The solution of the flow equation yields the flow velocities or flow rates. These flow rates are input to the transport model, which predicts the concentration distribution in time and space. Development of the EBS flow model and the EBS transport model are discussed separately in the next two subsections.

6.5.1.1 EBS Flow Model

The EBS flow model is essentially a mass balance on water in the EBS. Because the microscopic details of processes that occur in the EBS are not important on a drift or waste package scale, an appropriate starting point for developing the EBS flow model is a general macroscopic balance on water within a drift (Bird et al. 1960 [DIRS 103524], p. 686):

$$\frac{dm_w}{dt} = -\Delta w_w + w_w^m + r_w. \qquad \text{(Eq. 6.5.1.1-1)}$$

Here, m_w (kg) is the instantaneous total mass of water within the walls of a drift, which encompass the EBS. This equation states that the rate of change of water mass in the EBS is equal to the difference between the mass rate of flow into and out of the EBS (Δw_w [kg s^{-1}]), plus w_w^m (kg s^{-1}), the net mass flow rate of water across bounding surfaces by mass transfer (e.g., condensation or evaporation transfer water across a liquid surface, which is a boundary between gas-phase flow and transport and liquid-phase flow and transport), plus the rate of production of water by chemical reactions, r_w (kg s^{-1}). Per Assumption 5.4, production or consumption of water by chemical reactions is assumed to be zero, resulting in:

$$\frac{dm_w}{dt} = -\Delta w_w + w_w^m. \qquad \text{(Eq. 6.5.1.1-2)}$$

At steady state or when the mass of water in the EBS changes slowly, the time derivative can be set to zero:

$$-\Delta w_w + w_w^m = 0. \qquad \text{(Eq. 6.5.1.1-3)}$$

The alternative bathtub conceptual model, using Equation 6.5.1.1-2 for the waste package, is screened out as an alternative conceptual model in Section 6.6.1. By neglecting changes in the density of the water within a drift as it passes through the EBS, Equation 6.5.1.1-3 can be

divided by the density of water, ρ_w (kg m^{-3}), to transform it into a volume balance involving volumetric flow rates:

$$-\Delta F_w + F_w^m = 0, \qquad \text{(Eq. 6.5.1.1-4)}$$

where $F_w = w_w / \rho_w$ is the volumetric flow rate (m^3 s^{-1}), and the superscript m still refers to mass transfer processes. Since both $-\Delta F_w$ and F_w^m represent a net inflow minus outflow, Equation 6.5.1.1-4 simply states that outflow is equal to inflow. This is the general form of the water mass balance that is used for individual flow paths in the EBS in the *EBS RT Abstraction*. It is applicable to the EBS as a whole as well as to individual components of the EBS. In particular, the terms Δw_w and w_w^m can be broken down into the separate and distinct flow paths listed in Section 6.3.1.1.

The volumetric flow rate of water into the top of the EBS is referred to as the total dripping flux, designated F_1 in Table 6.3-1, and is comprised of seepage flux into the top of the drift and condensation on walls of the drift. The seepage flux is computed in the GoldSim TSPA model using *Abstraction of Drift Seepage* (BSC 2004 [DIRS 169131]); this is an input or source of inflow into the EBS flow model.

Over the entire EBS, Equation 6.5.1.1-4 becomes

$$F_1 + F_7 = F_8, \qquad \text{(Eq. 6.5.1.1-5)}$$

where F_1 is the total dripping flux into the top of the drift and F_7 is the imbibition flux into the invert; see Figure 6.3-1. F_8 is the flow rate of water leaving the invert and entering the unsaturated zone.

For the drip shield, the flux through corrosion breaches in the drip shield is F_2, and the flux of water diverted by the drip shield is F_3, so the water balance on the drip shield is:

$$F_1 = F_2 + F_3. \qquad \text{(Eq. 6.5.1.1-6)}$$

For the waste package, the water mass balance is:

$$F_2 = F_4 + F_5. \qquad \text{(Eq. 6.5.1.1-7)}$$

As modeled, there is no water storage in the waste package. Therefore, the flow rate of water from the waste package to the invert is equal to the flow into the waste package, F_4. The water balance over the invert includes this influx of water that has flowed through the waste package as well as water diverted around the waste package and water diverted around the drip shield. The total flow into the invert that originates from seepage flux (F_1), is:

$$\begin{aligned} F_6 &= F_3 + F_4 + F_5 \\ &= F_1. \end{aligned} \qquad \text{(Eq. 6.5.1.1-8)}$$

A water mass balance over the invert indicates that the sum of the seepage flux (F_1) and imbibition flux (F_7) flows out of the invert (Equation 6.5.1.1-5):

$$\begin{aligned} F_8 &= F_6 + F_7 \\ &= F_1 + F_7. \end{aligned} \qquad \text{(Eq. 6.5.1.1-9)}$$

6.5.1.1.1 Water Flux through a Breached Drip Shield

Key features of the drip shield flux splitting algorithm include: (1) the seepage flux into the drift falls as droplets from the top of the drift onto the crown of the drip shield (Assumption 5.1), (2) droplets fall randomly along the length of the drip shield, (3) only flow through general corrosion patches is considered, (4) evaporation from the drip shield is neglected (Assumption 5.2); all of the seepage flux either flows through corrosion patches or drains down the sides of the drip shield, (5) all water that flows through breaches in the drip shield flows onto the waste package.

In the conceptual model of the breached drip shield corrosion patches are represented by square holes, with dimensions specified in an earlier version of the WAPDEG corrosion model as approximately 27 cm in width (CRWMS M&O 2000 [DIRS 151566], p. 36, where the patch area is specified to be 7.214×10^4 mm^2). The breached drip shield experiments (BSC 2003 [DIRS 163406]) were designed using holes of this size.

Consider first some simple cases with idealized behavior, in which drops falling onto the drip shield either fall straight through corrosion patches or, after impacting the drip shield surface, flow straight down the sides of the drip shield. These will provide bounding cases for comparison as more realism is added to the flux splitting submodel. Let 2ℓ be the width (m) of a square corrosion patch, L_{DS} the axial length (m) of the drip shield, and N_b the number of patches on the drip shield, assumed to not overlap each other.

In the simplest case, N_b patches are located on the crown of the drip shield, none off the crown. Since all of the seepage flux F_1 falls on the crown of the drip shield, the amount that passes straight through breaches in the drip shield (F_2) is simply the ratio of the total length of the N_b patches to the total length of the drip shield multiplied by the seepage flux:

$$F_2 = F_1 \frac{2\ell N_b}{L_{DS}}. \qquad \text{(Eq. 6.5.1.1.1-1)}$$

Next, suppose a single patch exists, randomly located on the top of the drip shield, but fully off the crown so that none of the seepage flux falls directly through the patch, but instead lands on the drip shield crown and then flows straight down the surface. Ideally, exactly half of the seepage flux drains down one side of the drip shield, and half down the other side. The reality is not far removed from the ideal: when drops strike the drip shield, they splatter in a random pattern; the region where splattered droplets fall is roughly circular. After a large number of drops have fallen, on average half of the droplets will have landed on each of the two sides of the drip shield. Since only half of the seepage flux drains down one side of the drip shield, a single

patch can only capture $2\ell / L_{DS}$ of the flow down one side $(F_1/2)$, so the flux through a single patch in the drip shield is:

$$F_2 = F_1 \frac{\ell}{L_{DS}}. \qquad \text{(Eq. 6.5.1.1.1-2)}$$

If two patches exist, with one patch on each side of the drip shield, the total flux will clearly be twice what flows through a single patch:

$$F_2 = F_1 \frac{2\ell}{L_{DS}}. \qquad \text{(Eq. 6.5.1.1.1-3)}$$

If two patches are located on one side of the drip shield, away from the crown, and located randomly except that they do not interfere with each other (i.e., one patch is not upstream from another where it would intercept flow that would be captured by a lower patch), then a fraction $2\ell / L_{DS}$ of the flow down one side $(F_1/2)$ will enter each patch. The total flux through the drip shield in this case is:

$$F_2 = 2\left(\frac{F_1}{2}\right)\frac{2\ell}{L_{DS}} = F_1 \frac{2\ell}{L_{DS}}. \qquad \text{(Eq. 6.5.1.1.1-4)}$$

In the general case where N_b patches are randomly distributed on the drip shield, off the crown and not interfering with each other, Equation 6.5.1.1.1-4 becomes:

$$F_2 = F_1 \frac{N_b \ell}{L_{DS}}. \qquad \text{(Eq. 6.5.1.1.1-5)}$$

Different behavior is clearly seen depending on whether the patch is located directly on the crown such that drops fall straight through it, or whether the seepage is split by falling on the drip shield first, causing half of the dripping flux to flow down each side of the drip shield. If N_c patches are located on the crown $(N_c \le N_b)$, the most general form of the flux splitting algorithm for this idealization is:

$$\begin{aligned} F_2 &= F_1 \frac{\ell}{L_{DS}}\left[2N_c + (N_b - N_c)\right] \\ &= F_1 \frac{(N_b + N_c)\ell}{L_{DS}}. \end{aligned} \qquad \text{(Eq. 6.5.1.1.1-6)}$$

Although this equation is general, it requires a distinction between patches on the crown and off the crown. However, the location of patches is completely random, so the location cannot be specified *a priori*. To account for the different flux through crown patches, note that crown patches occur within a distance $\pm 2\ell$ from the crown, or over an area $4\ell L_{DS}$. The total surface area of a drip shield is $W_{DS} L_{DS}$, where W_{DS} is the total unfolded width of the drip shield (m) as

measured from the bottom edge of one side, over the top, and down to the bottom of the other side. Then the probability of a patch occurring on the crown is:

$$\frac{4\ell L_{DS}}{W_{DS}L_{DS}} = \frac{4\ell}{W_{DS}}. \qquad \text{(Eq. 6.5.1.1.1-7)}$$

Equation 6.5.1.1.1-6 can be rewritten to account for the probability of seepage flux falling into a crown patch or onto intact drip shield, and for the flux through a single crown patch being twice the flux through an off-crown patch for a given seepage flux:

$$\begin{aligned} F_2 &= F_1\left(\frac{2N_b\ell}{L_{DS}}\right)\left(\frac{4\ell}{W_{DS}}\right) + F_1\left(\frac{N_b\ell}{L_{DS}}\right)\left(1-\frac{4\ell}{W_{DS}}\right) \\ &= F_1\frac{N_b\ell}{L_{DS}W_{DS}}(4\ell + W_{DS}) \qquad \text{(Eq. 6.5.1.1.1-8)} \\ &= F_1\frac{N_b\ell}{L_{DS}}\left(\frac{4\ell}{W_{DS}}+1\right). \end{aligned}$$

For a patch size of $2\ell = 27\,\text{cm}$ and a total drip shield width of $W_{DS} = 6.94\,\text{m}$, the term $4\ell/W_{DS} = 0.078$. Then, to provide a good approximation, the term $4\ell/W_{DS}$ can be assumed to be zero, yielding:

$$F_2 = F_1\frac{N_b\ell}{L_{DS}}, \qquad \text{(Eq. 6.5.1.1.1-9)}$$

which is identical to Equation 6.5.1.1.1-5. This result indicates that, although the flux is higher through crown patches, the probability of patches occurring on the crown is small ($2\ell/W_{DS}$, or 3.9 percent) and may be ignored in light of the uncertainties discussed in Section 6.3.2.4.

The simple model presented thus far assumes ideal drops that do no splatter and that run down the drip shield in straight, nondiverging paths. Next, realism is added to the flux splitting submodel by taking into account observations and data from breached drip shield experiments, which account for drop splattering and the nature of rivulet flow along the surface of the drip shield.

6.5.1.1.2 Breached Drip Shield Experiments

The breached drip shield experiments (BSC 2003 [DIRS 163406]) are described in Section 6.3.2.4. The tests were performed at three different drip rates, which represent the range of expected liquid water influx rates over a single drip shield. The bulk of the tests were performed at a drip rate of 2 $m^3\ yr^{-1}$. Additional bounding flow rate tests were performed at a lower rate of 0.2 $m^3\ yr^{-1}$ and a higher rate of 20 $m^3\ yr^{-1}$. The tests were performed by dripping water at specified drip locations, one location at a time for a period that allowed a measurable amount of liquid to be collected through breaches in the drip shield (typically 30-60 min at 2 $m^3\ yr^{-1}$, 10 min at 20 $m^3\ yr^{-1}$, and 5-5½ hr at 0.2 $m^3\ yr^{-1}$).

Four basic types of tests were performed: (1) "q(splash)" test, in which the splash distance was measured when a drop falls onto the drip shield surface; (2) "q(film)" tests, where the primary goals were to measure rivulet spread and the amount of flow into a single breach in the drip shield; (3) multiple breach tests, which were similar to the q(film) tests, except that multiple breaches existed in the drip shield mockup; and (4) bounding flow rate tests, which repeated the q(film) and multiple breach tests using different drip rates. Most of the tests were performed on both a smooth drip shield and a rough drip shield.

The dripping distance was based on design parameters and carried out at full scale. Thus the dripping distance used for dripping onto the crown of the drip shield was 2.173 m (BSC 2003 [DIRS 163406]). The splash radius on the drip shield was measured for both the smooth surface (DTN: MO0207EBSATBWP.022 [DIRS 163400]) and the rough surface (DTN: MO0207EBSATBWP.021 [DIRS 163399]). The maximum lateral splash radius observed in Splash Radius Test #1 on the smooth surface was 72.5 cm after 60 drops; in Test #2, the maximum splash radius was 53.0 cm after 66 drops. On the rough surface, the maximum lateral splash radius in the five tests that were conducted was 106.5 cm after 203 drops. In addition to the splash radius tests, splash distances were recorded for some of the single patch q(film) rivulet flow tests; a maximum splash distance of 86 cm (DTN: M0207EBSATBWP.023 [DIRS 163402]) was observed for drip location Patch 4, 8 cm right of center, onto the crown of the drip shield. The distribution of droplet formation on the surface as a function of distance from the impact location was not measured, although an approximate determination was made to distinguish an "inner cluster" of droplets from an "outer fringe," where the droplets were noticeably smaller (Table 4.1-4). It was observed that the outer splashes on the fringe tended to be smaller and less frequent on the rough surface than on the smooth surface.

Observations during the breached drip shield tests revealed that the primary mechanism for water to enter breaches is via rivulet flow that originates from an area around the point of drip impact. Following droplet impact at the crown, beads formed and increased in size around the center of impact with each successive drop. After a time, the beads closest to the downhill curvature would reach a critical mass and roll down the face of the drip shield in the form of a rivulet. The rivulet flow area spreads out in a delta formation (i.e., the maximum spread was located on the vertical section of the drip shield and the minimum spread was located at the point of impact). No film flow was observed during tests on the smooth or the rough drip shield surfaces.

For a given drip location onto the crown of the drip shield (Assumption 5.1), the spreading of the rivulet flow is defined by a half-angle, α, formed with the vertical plane through the impact point. The lateral spread of the rivulet flow is given by $2x\tan\alpha$, where x is the arc length from the crown of the drip shield down to a location of interest. These definitions are illustrated in Figure 6.3-2. The curvature/shape of the drip shield is not shown in Figure 6.3-2 for simplicity and clarity.

The spread of rivulets from drips onto the crown of the experimental drip shield is reported in DTNs: MO0207EBSATBWP.023 [DIRS 163402], MO0207EBSATBWP.024 [DIRS 163401], and MO0207EBSATBWP.025 [DIRS 163403] and summarized in Table 4.1-6. The data are analyzed in Microsoft Excel spreadsheet: Flux Split Drip Shield Model, Worksheet: Spread angles, which is documented in Appendix C. The average spread at 33° from the crown in 26 measurements was 20.1 cm, corresponding to an average spread angle of about 13.2°. The

range of spread angles, from one standard deviation smaller and greater than the mean, was about 8.9° to 17.3°. The distribution for spread angle is not clearly defined by the experimental data, and therefore a uniform distribution is considered appropriate.

The initial simple model wherein drips flow straight down the curved top of the drip shield is made more realistic by incorporating the random spread of rivulets over an angle α as they flow down the drip shield surface. The spreading of rivulets increases the probability that they will flow into a breach (corrosion patch). Three cases are considered, two for a centrally located breach at different distances from the crown such that different proportions of the rivulet spread will encounter a breach, and one for a breach at the end of the drip shield.

6.5.1.1.2.1 Drip Shield Flux for a Centrally Located Breach, Case 1

Consider a breach that is centrally located on the drip shield. The breach is centrally located if Points A and B (defined below) are located on the same segment of the drip shield as the breach itself. In other words, the ends of the drip shield lie beyond Point A and Point B. Figure 6.5-1 illustrates the location and geometry for potential rivulet flows into a breach with length 2ℓ and whose top edge is located a distance of x from the crown. For simplicity in evaluating coordinates, the zero point of the y-axis is coincident with the center of the breach.

In Case 1, $\ell > x\tan\alpha$; in other words, the breach is wider than the rivulet spread at the top of the breach.

Points A and B are defined as follows:

- Point A corresponds to the leftmost point from which the edge of the fan from the rivulet can enter the left side of the breach.
- Point B corresponds to the leftmost point from which all rivulets will enter the top edge of the breach. Point B lies between $-\ell$ (left side of the breach) and the origin, $y = 0$.
- Point C corresponds to the rightmost point from which all rivulets will enter the top edge of the breach. Point C lies between the origin and $+\ell$ (right side of the breach).
- Point D corresponds to the rightmost point at which the edge of the fan from the rivulet can enter the right side of the breach.

Rivulets originating between Point A and Point $-\ell$ can flow into the left side or the top of the breach. Symmetrically, rivulets originating between Point $+\ell$ and Point D can flow into the right side or the top of the breach. All rivulets originating between Point $-\ell$ and $+\ell$ flow only into the top of the breach, not into the sides. The y-coordinates of Points A through D are:

$$\begin{aligned} y_A &= -\ell - (x + 2\ell)\tan\alpha \\ y_B &= -\ell + x\tan\alpha \\ y_C &= \ell - x\tan\alpha \\ y_D &= \ell + (x + 2\ell)\tan\alpha. \end{aligned} \qquad \text{(Eq. 6.5.1.1.2-1)}$$

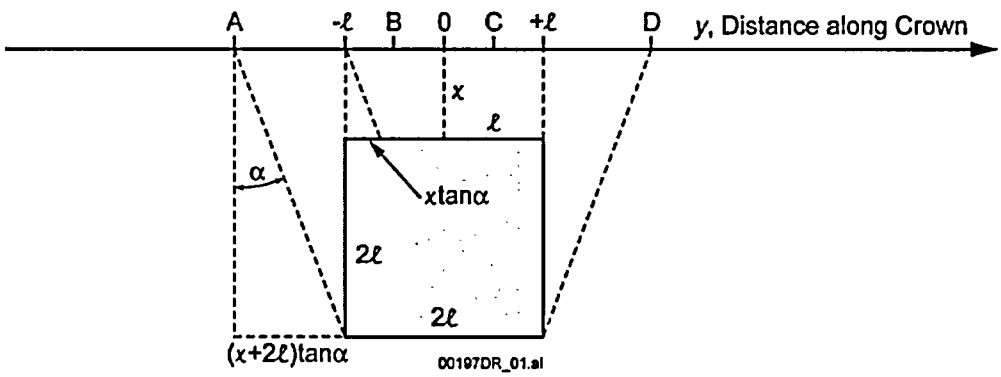

Figure 6.5-1. Geometry and Nomenclature for a Centrally Located Breach with $\ell > x \tan \alpha$

The fraction f of the random rivulet flow that enters the breach depends on the origin y of the rivulet:

- For $y \le y_A$, $f_{A-} = 0$.
- For $y_A < y \le -\ell$,

$$f_{A\ell} = \frac{y + \ell + (x + 2\ell)\tan\alpha}{2(x + 2\ell)\tan\alpha} \qquad \text{(Eq. 6.5.1.1.2-2)}$$

- For $-\ell < y < y_B$,

$$f_{\ell B} = \frac{y + \ell + x\tan\alpha}{2x\tan\alpha} \qquad \text{(Eq. 6.5.1.1.2-3)}$$

- For $y_B \le y \le y_C$,

$$f_0 = 1 \qquad \text{(Eq. 6.5.1.1.2-4)}$$

- For $y_C < y < \ell$,

$$f_{C\ell} = \frac{-y + \ell + x\tan\alpha}{2x\tan\alpha} \qquad \text{(Eq. 6.5.1.1.2-5)}$$

- For $\ell \le y < y_D$,

$$f_{\ell D} = \frac{-y + \ell + (x + 2\ell)\tan\alpha}{2(x + 2\ell)\tan\alpha} \qquad \text{(Eq. 6.5.1.1.2-6)}$$

- For $y \ge y_D$, $f_{D+} = 0$.

In this context, f is essentially a probability distribution function (i.e., the probability that a rivulet will intersect the square corrosion patch). Integrating f over the full length of the drip shield (from $-L_{DS}/2$ to $+L_{DS}/2$) gives the total water flux through a breach of width 2ℓ. Then the fraction F $(=F_2/F_1)$ of seepage flux passing through the breach is:

$$F=\frac{1}{2L_{DS}}\int_{-L_{DS}/2}^{L_{DS}/2} f(y)dy \qquad \text{(Eq. 6.5.1.1.2-7)}$$

$$=\frac{1}{2L_{DS}}\left[\int_{y_A}^{-\ell} f_{A\ell}(y)dy+\int_{-\ell}^{y_B} f_{\ell B}(y)dy+\int_{y_B}^{y_C} f_0 dy+\int_{y_C}^{+\ell} f_{C\ell}(y)dy+\int_{+\ell}^{y_D} f_{\ell D}(y)dy\right] \qquad \text{(Eq. 6.5.1.1.2-8)}$$

$$=\frac{\ell}{L_{DS}}+\frac{\ell\tan\alpha}{2L_{DS}}. \qquad \text{(Eq. 6.5.1.1.2-9)}$$

The factor of 2 in the denominator starting in Equation 6.5.1.1.2-7 accounts for the seepage flux being split in two when it drips onto the crown of the drip shield, and half of the flux flows down each side.

The result is independent of x, the distance from the crown. The amount of seepage flux that flows into a breach is, however, dependent on the rivulet spread angle α. This is reasonable because a wider spread angle allows rivulets from a wider span of the crown to access the breach. In effect, the width of the drip shield crown from which rivulets can flow into a breach is expanded from 2ℓ to $2\ell+\ell\tan\alpha$. Flow into the sides of the breach contributes only a small amount to the total if the spread angle is small. If, for example, $\alpha=13.2°$ (the mean spread angle from the drip shield experiments), the total flow into a breach, from Equation 6.5.1.1.2-9, is $(\ell/L_{DS})(1+0.117)$, so only about 0.117/1.117 ≈ 1/10 of the total breach flow enters through the sides of the breach.

As a check on this result, consider the case where the rivulets do not spread out over an angle α, but instead flow straight down (i.e., $\alpha=0=\tan\alpha$). Then Equation 6.5.1.1.2-9 becomes:

$$F=\frac{\ell}{L_{DS}}, \qquad \text{(Eq. 6.5.1.1.2-10)}$$

or

$$F_2=F_1\frac{\ell}{L_{DS}}. \qquad \text{(Eq. 6.5.1.1.2-11)}$$

Equation 6.5.1.1.2-11 is identical to Equation 6.5.1.1.1-2, which was obtained from simple logic arguments.

As a further check on the validity of Equation 6.5.1.1.2-9, consider a single patch located adjacent to the crown, just far enough away from the crown that the dripping seepage flux can impinge on the crown and flow down both sides (i.e., $x\approx 0$, about the width of a drop). Water

flowing from the crown toward the patch will immediately enter the patch, since the spread over the angle α is negligible. Seepage flux dripping onto the drip shield crown to the left and right of the patch will flow down the drip shield in rivulets, fanning out over the angle α. In this case, $y_A = -\ell - 2\ell \tan\alpha$; similarly, $y_B = \ell + 2\ell \tan\alpha$. The fractions of the rivulet flow down one side of the drip shield into the patch are:

- For $y \le y_A$, $f_{A-} = 0$.
- For $y_A < y < -\ell$,

$$f_{A\ell} = \frac{y + \ell + 2\ell \tan\alpha}{4\ell \tan\alpha} \qquad \text{(Eq. 6.5.1.1.2-12)}$$

- For $-\ell \le y \le \ell$,

$$f_0 = 1 \qquad \text{(Eq. 6.5.1.1.2-13)}$$

- For $\ell < y < y_B$,

$$f_{\ell B} = \frac{-y + \ell + 2\ell \tan\alpha}{4\ell \tan\alpha} \qquad \text{(Eq. 6.5.1.1.2-14)}$$

- For $y \ge y_B$, $f_{B+} = 0$.

Moving right from $y = y_A$, where $f = 0$, f increases linearly until $y = -\ell^-$ (on the left side of $-\ell$), where $f = 1/2$; because half of the rivulet fan is directed away from the patch at that point, at most half of the rivulet will enter the patch. Between $-\ell$ and $+\ell$, all of the rivulets flow directly into the patch, so $f = 1$. As on the left side of the patch, to the right of the patch, from $y = \ell$ to $y = y_B = \ell + 2\ell \tan\alpha$, f decreases linearly from ½ to 0. Performing the same integration as in Equations 6.5.1.1.2-7 and 6.5.1.1.2-8 results in:

$$F = \frac{\ell}{L_{DS}} + \frac{\ell \tan\alpha}{2L_{DS}}, \qquad \text{(Eq. 6.5.1.1.2-15)}$$

which is again identical to Equation 6.5.1.1.2-9. Since, as seen earlier, the flow into the top edge of the patch is ℓ / L_{DS}, the term $\ell \tan\alpha / (2L_{DS})$ accounts for rivulet flow into the sides of the patch.

Multiple patches increase the flow into patches in direct proportion to the number of patches, assuming that patches do not interfere:

$$F = N_b \left[\frac{\ell}{L_{DS}} + \frac{\ell \tan\alpha}{2L_{DS}} \right], \qquad \text{(Eq. 6.5.1.1.2-16)}$$

or

$$F_2 = F_1 N_b \left[\frac{\ell}{L_{DS}} + \frac{\ell \tan\alpha}{2L_{DS}} \right]. \qquad \text{(Eq. 6.5.1.1.2-17)}$$

If patches are located below other patches, the rivulets are intercepted by the higher patches, and none or less flows into lower patches. In that case, the flux through the drips shield, F_2, is less than predicted by Equation 6.5.1.1.2-17. However, to neglect interference among multiple patches and use Equation 6.5.1.1.2-17 overestimates releases of radionuclides.

6.5.1.1.2.2 Drip Shield Flux for a Centrally Located Breach, Case 2

In Case 2, $\ell < x \tan\alpha$; in other words, the breach is narrower than the rivulet spread at the top of the breach (see Figure 6.5-2). In Case 1, over some range of y centered at $y = 0$, all of the rivulet flow enters the top edge of the breach $(f_0 = 1)$. In contrast, in Case 2, the rivulet spread is too wide for all of the rivulet flow to enter the breach at any point $(f_0 < 1)$.

Points A and B are defined as follows:

- Point A corresponds to the leftmost point from which the edge of the fan from the rivulet can enter the left side and top of the breach.
- Point B corresponds to the leftmost point from which rivulets will enter only the top edge of the breach. Point B lies between $-\ell$ (left side of the breach) and the origin, $y = 0$. Rivulets originating between $-\ell$ and Point B enter only a portion of the top edge of the breach.
- Point C corresponds to the rightmost point from which all rivulets will enter the top edge of the breach. Point C lies between the origin and $+\ell$ (right side of the breach). Rivulets originating between Point C and $+\ell$ enter only a portion of the top edge of the breach. Rivulets originating between Point B and Point C can enter the entire top edge of the breach.
- Point D corresponds to the rightmost point at which the edge of the fan from the rivulet can enter the right side and top of the breach.

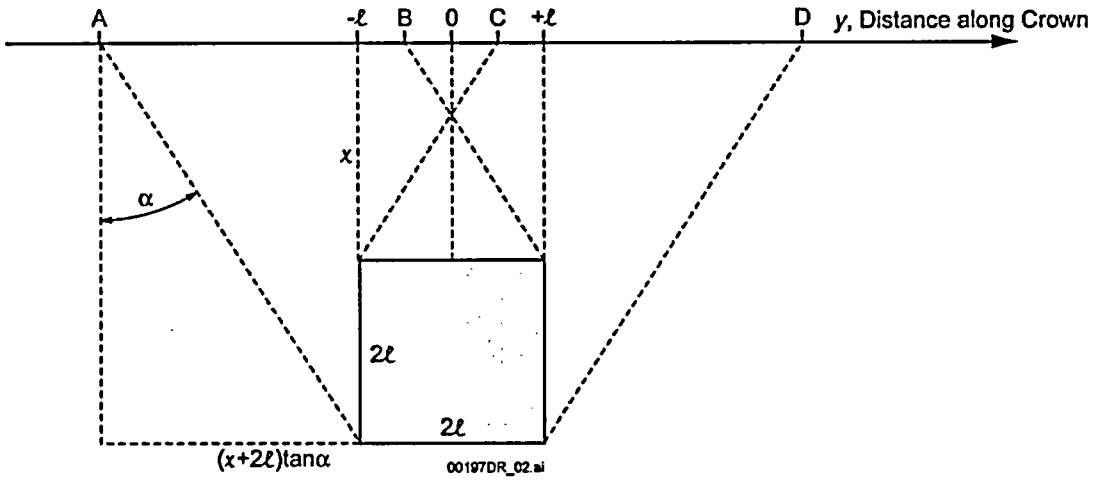

Figure 6.5-2. Geometry and Nomenclature for a Centrally Located Breach with $\ell < x \tan \alpha$

As in Case 1, rivulets originating between Point A and Point $-\ell$ can flow into the left side or the top of the breach. Symmetrically, rivulets originating between Point $+\ell$ and Point D can flow into the right side or the top of the breach. All rivulets originating between Point $-\ell$ and $+\ell$ flow only into the top of the breach, not into the sides. The y-coordinates of Points A through D are:

$$\begin{aligned} y_A &= -\ell - (x + 2\ell)\tan\alpha \\ y_B &= \ell - x\tan\alpha \\ y_C &= -\ell + x\tan\alpha \\ y_D &= \ell + (x + 2\ell)\tan\alpha. \end{aligned} \qquad \text{(Eq. 6.5.1.1.2-18)}$$

The central region boundaries, y_B and y_C, are different for Case 2 than for Case 1.

The fraction f of the random rivulet flow that enters the breach depends on the origin y of the rivulet. These fractions are identical for corresponding regions to those in Case 1 except for the region $y_B \le y \le y_C$, where now $f_0 < 1$ instead of $f_0 = 1$.

- For $y \le y_A$, $f_{A-} = 0$.
- For $y_A < y \le -\ell$,

$$f_{A\ell} = \frac{y + \ell + (x + 2\ell)\tan\alpha}{2(x + 2\ell)\tan\alpha} \qquad \text{(Eq. 6.5.1.1.2-19)}$$

- For $-\ell < y < y_B$,

$$f_{\ell B} = \frac{y + \ell + x\tan\alpha}{2x\tan\alpha} \qquad \text{(Eq. 6.5.1.1.2-20)}$$

- For $y_B \le y \le y_C$,

$$f_0 = \frac{2\ell}{2x\tan\alpha} \qquad \text{(Eq. 6.5.1.1.2-21)}$$

- For $y_C < y < \ell$,

$$f_{C\ell} = \frac{-y+\ell+x\tan\alpha}{2x\tan\alpha} \qquad \text{(Eq. 6.5.1.1.2-22)}$$

- For $\ell \le y < y_D$,

$$f_{\ell D} = \frac{-y+\ell+(x+2\ell)\tan\alpha}{2(x+2\ell)\tan\alpha} \qquad \text{(Eq. 6.5.1.1.2-23)}$$

- For $y \ge y_D$, $f_{D+} = 0$.

Integrating f over the full length of the drip shield (from $-L_{DS}/2$ to $+L_{DS}/2$), as in Case 1, gives the total water flux through a breach of width 2ℓ. The fraction F $(=F_2/F_1)$ of seepage flux passing through the breach is:

$$F = \frac{1}{2L_{DS}} \int_{-L_{DS}/2}^{L_{DS}/2} f(y)dy \qquad \text{(Eq. 6.5.1.1.2-24)}$$

$$= \frac{1}{2L_{DS}}\left[\int_{y_A}^{-\ell} f_{A\ell}(y)dy + \int_{-\ell}^{y_B} f_{\ell B}(y)dy + \int_{y_B}^{y_C} f_0 dy + \int_{y_C}^{+\ell} f_{C\ell}(y)dy + \int_{+\ell}^{y_D} f_{\ell D}(y)dy\right] \qquad \text{(Eq. 6.5.1.1.2-25)}$$

$$= \frac{\ell}{L_{DS}} + \frac{\ell\tan\alpha}{2L_{DS}}. \qquad \text{(Eq. 6.5.1.1.2-26)}$$

For Case 2, the seepage flux passing through the breach is identical to Case 1 (Equation 6.5.1.1.2-9). This is reasonable considering that F is independent of x. In other words, the breach can be located at any distance from the crown, and the same fraction of seepage flux will flow into it. The two cases are really a single case where the breach in Case 2 is simply located further from the crown than in Case 1.

6.5.1.1.2.3 Drip Shield Flux for an End-Located Patch

The drip shield design (BSC 2004 [DIRS 168275], Sheet 1) includes a connector guide at one end and a connector plate at the other end that, being thicker than the plates comprising the top and sides of the drip shield, should survive intact longer than the plates. These components will prevent any rivulets from flowing off the ends of the drip shield. This will alter the fraction of rivulet flow that enters patches that are located at the ends of the drip shield. If the patch is located a short distance from the end, the space between the patch and the connector guide will allow water diverted by the guide to flow down the drip shield instead of into the patch. This distance is unknown, but for simplicity is chosen to be zero (i.e., if the patch is not coincident with the connector guide, it behaves as a centrally located patch).

Consider a breach that is located at one end of the drip shield. Figure 6.5-3 illustrates the location and geometry for potential rivulet flows into a breach with length 2ℓ and whose top edge is located a distance of x from the crown. For simplicity in evaluating coordinates, the zero point of the y-axis is again coincident with the center of the patch, and the end of the patch as well as the drip shield are at $y = -\ell$.

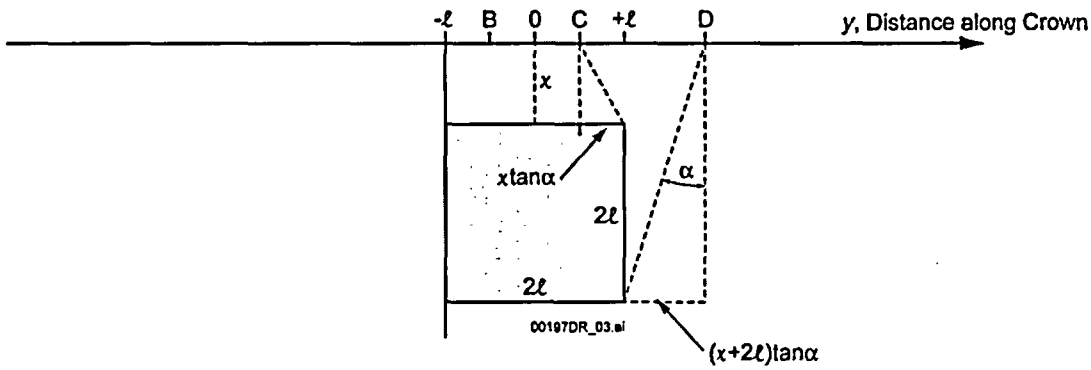

Figure 6.5-3. Geometry and Nomenclature for an End-Located Breach with $\ell > x \tan \alpha$

The Points A through D are defined as above for Case 1, except that y_A is beyond the end of the drip shield. Distinguishing Point B is unimportant, because all rivulets originating to the left of Point C flow completely into the breach.

$$\begin{aligned} y_B &= -\ell + x \tan \alpha \\ y_C &= \ell - x \tan \alpha \\ y_D &= \ell + (x + 2\ell) \tan \alpha. \end{aligned} \qquad \text{(Eq. 6.5.1.1.2-27)}$$

Consider first the case where $\ell > x \tan \alpha$, corresponding to Case 1 above. It is shown that the result is independent of x, as seen above for the centrally located breach. Therefore, a second analysis corresponding to Case 2 above is not necessary. The fraction f of rivulet flow into the patch over ranges of y are:

- For $y \le -\ell = -L_{DS}/2$, $f = 0$.
- For $-\ell \le y \le y_C$,

$$f_0 = 1 \qquad \text{(Eq. 6.5.1.1.2-28)}$$

- For $y_C < y < \ell$,

$$f_{C\ell} = \frac{-y + \ell + x \tan \alpha}{2x \tan \alpha} \qquad \text{(Eq. 6.5.1.1.2-29)}$$

- For $\ell \le y < y_D$,

$$f_{\ell D} = \frac{-y+\ell+(x+2\ell)\tan\alpha}{2(x+2\ell)\tan\alpha} \qquad \text{(Eq. 6.5.1.1.2-30)}$$

- For $y \ge y_D$, $f_{D+} = 0$.

Integrating f over the full length of the drip shield (from $-L_{DS}/2$ to $+L_{DS}/2$) gives the total water flux through a breach of width 2ℓ. The fraction F $(=F_2/F_1)$ of seepage flux passing through the breach is:

$$F = \frac{1}{2L_{DS}} \int_{-L_{DS}/2}^{L_{DS}/2} f(y)dy \qquad \text{(Eq. 6.5.1.1.2-31)}$$

$$= \frac{1}{2L_{DS}} \left[\int_{-\ell}^{y_C} f_0 dy + \int_{y_C}^{+\ell} f_{C\ell}(y)dy + \int_{+\ell}^{y_D} f_{\ell D}(y)dy \right] \qquad \text{(Eq. 6.5.1.1.2-32)}$$

$$= \frac{\ell}{L_{DS}} + \frac{\ell \tan\alpha}{4L_{DS}}. \qquad \text{(Eq. 6.5.1.1.2-33)}$$

Thus, the seepage flux fraction F for breaches at the end of the drip shield is independent of the distance x from the crown. The only difference from centrally located breaches is the term that accounts for flow into the side of a breach $[\ell \tan\alpha/(4L_{DS})]$. Since only one side of the breach is accessible to rivulet flow, the flow through the one side of the breach at the end of the drip shield is just half of the flow through two sides in a centrally located breach.

As seen above, for a small rivulet spread angle, the portion of the flow into a breach that enters through the side is small. For an end breach, that fraction is even smaller. In the example given in Section 6.5.1.1.2.1, for a mean spread angle of $\alpha = 13.2°$, flow through the sides of the breach accounts for only about 1/10 of the total. For an end breach, based on Equation 6.5.1.1.2-31, side flow will account for only 6 percent in this example. In Section 6.5.1.1.2, experimental results are discussed that show the spread angle is approximately 13.2° and that the amount of seepage flux that actually enters a breach varies widely. Differences of 6 percent are negligible. Since the end-located breach model (Equation 6.5.1.1.2-31) applies only to breaches that are exactly at the ends of the drip shield, which will be an infrequent occurrence, it is reasonable to ignore the distinction between end breaches and centrally located breaches.

Then the flux through one patch in the drip shield is:

$$F_2 = F_1 \frac{\ell}{L_{DS}} \left(1 + \frac{\tan\alpha}{2}\right). \qquad \text{(Eq. 6.5.1.1.2-34)}$$

6.5.1.1.2.4 Analysis of Breached Drip Shield Experiments

The breached drip shield experiments (BSC 2002 [DIRS 158193]; BSC 2003 [DIRS 163406]) provide estimates of the rivulet spread factor from which the spread angle α can be determined (DTN: MO0207EBSATBWP.022 [DIRS 163400]), the splash radius from drops falling from the roof of the drift to the crown of the drip shield (DTN: MO0207EBSATBWP.022 [DIRS 163400]), and the flow into breaches from a number of discrete drip locations (DTN: MO0207EBSATBWP.023 [DIRS 163402]). In addition, the tests characterized the flow behavior on the drip shield surface, determining that flow occurs as rivulets rather than as film flow.

In Splash Radius Test #1 (DTN: MO0207EBSATBWP.022 [DIRS 163400]), water was dripped onto the drip shield crown, and the distance that the water splattered was measured. In 12 separate sets of measurements (Table 4.1-4), using from 1 to 90 drips, splash distances to the right ranged from 1.6 cm (single drip) to 63.2 cm (49 drips); splash distances to the left ranged from 1.6 cm (single drip) to 72.5 cm (60 drips). Tests using larger numbers of drips tended to result in larger maximum splash distances. "Outer fringe" measurements using more than 20 drips ranged from 31.5 cm to 72.5 cm, whereas "inner cluster" measurements using more than 20 drips ranged from 25.0 cm to 48.0 cm. The definition of the grouping as "outer fringe" and "inner cluster" was not specified, but the results indicate a distribution of splashed water heavily weighted to a median radius of about 40 cm.

The splash radius is useful for providing a distribution of rivulet origins based on limited experimental data. In the flow tests, water was dripped onto the drip shield in only a few discrete locations. In order to make greater use of the data to determine the uncertainty in applying the drip shield flux splitting submodel (Equation 6.5.1.1.2-34), the distribution of splattered water can be treated as multiple drip locations in comparing Equation 6.5.1.1.2-34 to the experimental data.

Rivulet spread was measured in single patch q(film) tests (DTN: MO0207EBSATBWP.023 [DIRS 163402]), multiple patch tests (DTN: MO0207EBSATBWP.024 [DIRS 163401]), and in bounding flow rate tests (DTN: MO0207EBSATBWP.025 [DIRS 163403]). Table 4.1-3 summarizes the maximum rivulet spread to the left and right of a straight line down the drip shield from the drip impact point. The rivulet spread data are analyzed in Microsoft Excel spreadsheet: Flux Split Drip Shield Model, Worksheet: Spread angles, which is documented in Appendix C. The results–the mean and range of spread angles–are reported in Section 6.5.1.1.2.

Rivulet spread measurements at the top edge of patches in the drip shield mockup are used. The distance x from the drip location on the crown of the drip shield to the point of measurement is determined from the drawing of the drip shield mockup shown in Figure 4.1-1, which is reproduced from Howard (2002 [DIRS 161516], p. 14). Various dimensions used in the Microsoft Excel spreadsheet analysis of the data are listed in Table 6.5-1. Because the drip shield top surface is a circular arc (Figure 4.1-1), the 16.5° line is at half the distance from the crown to the 33° line, or 0.43 m from the crown.

Table 6.5-1. Dimensions Used in the Analysis of Breached Drip Shield Experiments, Based on Dimensions Shown in Figure 4.1-1

Dimension	Calculation	Distance (m)
Crown to 33° line	2.44 m – 0.94 m – 0.64 m	0.86
Crown to 16.5° line	½ distance from Crown to 33° line	0.43
Crown to top edge of Patch 4	2.44 m – 0.94 m – 0.135 m	1.365
Crown to top edge of Patch 5	2.44 m – 0.94 m – 0.64 m	0.86
Crown to transition line	2.44 m – 0.94 m	1.50
16.5° line to transition line	0.43 m (Crown to 16.5° line)+ 0.64 m	1.07
16.5° line to 33° line	½ distance from Crown to 33° line	0.43
16.5° line to Patch 4	0.43 m (Crown to 16.5° line)+ 0.64 m – 0.135 m	0.935
16.5° line to Patch 5	½ distance from Crown to 33° line	0.43
33° line to Patch 4	0.64 m – 0.135 m	0.505
33° line to transition line	0.64 m	0.64
½ distance between Crown and 16.5° line to Patch 4	½(0.43 m [Crown to 16.5° line]) + 0.43 m (Crown to 16.5° line) + 0.64 m -0.135 m	1.15

Source: Howard 2002 [DIRS 161516], p. 14.

Since the experiments involved dripping at a few discrete locations, it is not possible to calculate the flux through the drip shield as given by Equation 6.5.1.1.2-34 using experimental data. Instead, the fraction f of dripping flux at an individual drip location that flows into a given breach can be computed for the tests and compared with the fraction expected using one of the Equations 6.5.1.1.2-1 to 6.5.1.1.2-6 (Case 1) or 6.5.1.1.2-19 to 6.5.1.1.2-23 (Case 2). The appropriate equation to be used depends on the drip location relative to the breach. The variability in the experimental values (f_{expt}) and comparisons with calculated values (f_{calc}) show the range of uncertainty in the drip shield flux ratio $F = F_2 / F_1$. The values of f_{expt} and f_{calc} are calculated in Microsoft Excel spreadsheet: Flux Split Drip Shield Model, Worksheet: f calculations, which is documented in Appendix C.

Experimental data from two breaches are pertinent to this analysis–Breach 4 and Breach 5. Breach 4 straddled the transition line between the top of the drip shield and the vertical side, with the top edge 136.5 cm from the crown. Breach 5 was located on the top of the drip shield, about half way between the crown and the transition line, with the top edge 86 cm from the crown.

Table 6.5-2 shows the fraction of the total dripping flux that entered a breach in each of 14 tests. The data sources are single patch q(film) test results (DTN: MO0207EBSATBWP.023 [DIRS 163402]), multiple patch test results (DTN: MO0207EBSATBWP.024 [DIRS 163401]), and bounding flow rate test results (DTN: MO0207EBSATBWP.025 [DIRS 163403]), and are given in Table 4.1-2. The results are compared with calculated fractions for the mean spread angle as well as for the spread angles corresponding to plus or minus one standard deviation from the mean rivulet spread angle. The experimentally observed fractions, f_{expt}, were calculated assuming that the water that flowed down the side of the drip shield where the breaches were located was half of the total dripping flux. This is necessary for f_{expt} to be consistent with the fractions in Sections 6.5.1.1.2.1 and 6.5.1.1.2.2, which are the fractions of flow down one side of the drip shield that enters a breach.

Table 6.5-2. Comparison of Experimental Breach Inflow Fractions with Model Calculations from Appendix C

Drip Location (Test Description)	Breach No.	*y*, Drip Location Relative to Breach Center (cm)	*x*, Vertical Distance from Crown (drip) to Top of Breach (cm)	f_{expt}	f_{calc}		
					α=8.9°	α=13.2°	α=17.3°
8 cm right of Patch 4 centerline (Q[film] Test)	4	8	136.5	0.247	0.629	0.423	0.318
Patch 5 centerline (Q[film] Test)	5	0	86.0	0.258	1.000	0.672	0.504
4 cm left of Patch 5 centerline (Q[film] Test)	5	-4	86.0	0.136	0.854	0.680	0.504
Patch 4 centerline (Q[film] Test)	4	0	136.5	0.236	0.634	0.423	0.318
27 cm right of drip shield center (Multiple Patch Test)	5	-27	86.0	0.033	0.117	0.244	0.504
27 cm left of drip shield center (Multiple patch test)	4	27	136.5	0.019	0.236	0.323	0.318
81 cm left of drip shield center (Multiple Patch Test)	4	-27	136.5	0.031	0.236	0.323	0.318
81 cm right of drip shield center (Multiple Patch Test)	5	27	86.0	0.032	0.117	0.244	0.504
54 cm left of drip shield center (High Flow Rate Test)	4	0	136.5	0.275	0.634	0.423	0.318
54 cm left of drip shield center (Low Flow Rate Test)	4	0	136.5	0.177	0.634	0.423	0.318
27 cm left of drip shield center (High Flow Rate Test)	4	27	136.5	0.020	0.236	0.323	0.318
27 cm left of drip shield center (Low Flow Rate Test)	4	27	136.5	0.013	0.236	0.323	0.318
27 cm right of drip shield center (High Flow Rate Test)	5	-27	86.0	0.013	0.117	0.244	0.504
27 cm right of drip shield center (Low Flow Rate Test)	5	-27	86.0	0.065	0.117	0.244	0.504
Mean				0.111	0.414	0.380	0.398
Std. Dev.				0.106	0.305	0.144	0.096
Median				0.049	0.236	0.323	0.318
Minimum				0.013	0.117	0.244	0.318
Maximum				0.275	1.000	0.680	0.504

DTNs: MO0207EBSATBWP.023 [DIRS 163402]; MO0207EBSATBWP.024 [DIRS 163401]; MO0207EBSATBWP.025 [DIRS 163403].

The experimentally observed fraction of drip seepage flowing into a breach varies widely. This variability is primarily due to the drip location–when the drip location is centered over the breach, much of the flow enters the breach, and when the drip is far off to the side of a breach, little of it enters the breach. However, the variability also includes differences in drip rate, the distance from the crown to the breach, evaporation from the drip shield surface, and random variability in drop splashing and rivulet flow behavior.

The fraction of drip seepage flowing into a breach calculated from the model is found always to be higher than observed experimentally, particularly when the drip location is far from the breach. When the drip location is well away from the patch center, and little water flows into the breaches (f_{expt} less than about 0.1), the model overestimates the experimental fraction increasingly as the estimated spread angle increases (see Table 6.5-3). In contrast, the model predicts that ever-increasing amounts of water flow into a breach as the spread angle increases. This can be seen in Equation 6.5.1.1.2-34, which shows that the flow into breaches is proportional to $(1 + \frac{1}{2} \tan \alpha)$, so as the spread angle α increases, so does the flow into breaches. Evaporation also plays a part. The model assumes no evaporative losses (Assumption 5.2), whereas evaporation from the drip shield occurred in the experiments because the relative humidity was less than 100 percent. Using a larger spread angle in the model results in increased predicted flow into a breach, whereas evaporation consistently reduces the experimentally measured inflow. Thus, ignoring the observed occurrence of evaporation in the development of the drip shield flux splitting submodel will overestimate the transport of radionuclides.

When the drip location is directly above the breach, the model agrees more closely with experiments as the spread angle increases. Again, the model generally overestimates the flow into breaches. In this case, as the estimated spread angle increases, less flow into breaches is predicted, so the model agrees more closely with experiments.

A major reason for the differences between the flux splitting submodel calculations and the experimental results is that splashing of the drops when they impinged on the drip shield resulted in a dispersed source of rivulets. In contrast, the model supposes that the entire dripping flux flows down the drip shield from the point of impact. Splattering spreads the dripping flux over a wide span of the drip shield crown. The splash radius tests recorded splashes that extended up to 72.5 cm from the drip location, with an "inner cluster" radius of 25 to 48 cm (DTN: MO0207EBSATBWP.022 [DIRS 163400]). In three of the q(film) rivulet flow tests, lateral splash distances ranging from 54.5 cm to 86 cm from the drip point on the crown were observed (DTN: MO0207EBSATBWP.023 [DIRS 163402], Drip Location: Patch 5, center, crown; Patch 4, center, crown; and Patch 4, 8 cm right of center, crown). Since a large portion of the dripping flux in the tests splattered beyond the range of rivulet flow into individual breaches, the flow into breaches was much less than predicted by the model. Thus, ignoring the observed occurrence of splattering in the development of the drip shield flux splitting submodel will overestimate the transport of radionuclides.

Table 6.5-3. Additional Comparisons of Experimental Breach Inflow Fractions with Model Calculations from Appendix C

Drip Location (Test Description)	f_{expt}	$f_{calc} - f_{expt}$			f_{calc} / f_{expt}		
		α=8.9°	α=13.2°	α=17.3°	α=8.9°	α=13.2°	α=17.3°
8 cm right of Patch 4 centerline (Q[film] Test)	0.247	0.382	0.176	0.071	2.545	1.713	1.286
Patch 5 centerline (Q[film] Test)	0.258	0.742	0.414	0.246	3.876	2.604	1.955
4 cm left of Patch 5 centerline (Q[film] Test)	0.136	0.718	0.544	0.368	6.277	4.998	3.707
Patch 4 centerline (Q[film] Test)	0.236	0.398	0.187	0.082	2.686	1.794	1.347
27 cm right of drip shield center (Multiple Patch Test)	0.033	0.085	0.212	0.472	3.606	7.515	15.507
27 cm left of drip shield center (Multiple patch test)	0.019	0.217	0.304	0.299	12.393	17.016	16.722
81 cm left of drip shield center (Multiple Patch Test)	0.031	0.205	0.293	0.287	7.720	10.600	10.417
81 cm right of drip shield center (Multiple Patch Test)	0.032	0.085	0.212	0.472	3.662	7.632	15.750
54 cm left of drip shield center (High Flow Rate Test)	0.275	0.359	0.148	0.043	2.306	1.540	1.156
54 cm left of drip shield center (Low Flow Rate Test)	0.177	0.456	0.246	0.140	3.574	2.387	1.792
27 cm left of drip shield center (High Flow Rate Test)	0.020	0.215	0.303	0.298	11.693	16.055	15.777
27 cm left of drip shield center (Low Flow Rate Test)	0.013	0.223	0.310	0.305	18.286	25.108	24.673
27 cm right of drip shield center (High Flow Rate Test)	0.013	0.104	0.231	0.491	9.064	18.888	38.978
27 cm right of drip shield center (Low Flow Rate Test)	0.065	0.053	0.180	0.440	1.815	3.781	7.804
Mean	0.111	0.303	0.269	0.287	6.393	8.688	11.205
Std. Dev.	0.106	0.221	0.107	0.155	4.885	7.672	11.033
Median	0.049	0.220	0.239	0.298	3.769	6.256	9.110
Minimum	0.013	0.053	0.1484	0.043	1.8145	1.540	1.156
Maximum	0.275	0.742	0.5439	0.491	18.286	25.108	38.978

Table 6.5-4. Water Collected in Drip Shield Experiment Q(film); Drip Location: Patch 4, 8 cm Right of Center, Crown

Collection Station	Initial Mass (g)	Final Mass (g)	Net Water Mass (g)	Water Collected In Each Group of Collection Stations (g)
Input Water	-50.32	-228.52	-178.20	178.20
Gutter 1-1	7.652	16.434	8.782	36.351
Gutter 3-1	7.611	8.677	1.066	
Gutter 3-2	7.600	23.213	15.613	
Gutter 3-3	7.612	8.899	1.287	
Gutter 3-4	7.521	17.124	9.603	
Breach 2	107.02	109.00	1.98	24.00
Breach 4	107.60	129.62	22.02	
Drip Shield OUT 1	7.634	8.738	1.104	72.685
Drip Shield OUT 2	7.578	19.681	12.103	
Drip Shield OUT 3	7.574	34.446	26.872	
Drip Shield OUT 4	7.702	40.308	32.606	

DTN: MO0207EBSATBWP.023 [DIRS 163402].

One other cause for the discrepancies between experimental and predicted flow fractions is that, in the model, all dripping flux flows down the drip shield surface. In the experiments, a large amount of water remained on the drip shield as splattered drops that had not yet grown large enough to flow down the surface. For example, Table 6.5-4 shows the amount of water collected in the first experiment listed in Table 6.5-2. Of the 178.2 g of water that was dripped onto the surface, only 60.35 g was collected from the breaches or drainage gutters, whereas 72.685 g, or 41 percent, that remained on the surface ("Drip Shield OUT" entries). This is a source of uncertainty in the experimental results that could be reduced by increasing the duration of the experiment far beyond the one-hour length of the test, but is inherent in the experiment and cannot be eliminated. The result is that less of the dripping flux actually flowed down the drip shield surface than is predicted by the model. This also causes the model to overestimate the fraction that flows into breaches, and, therefore, overestimates the transport of radionuclides.

Results presented in Table 6.5-2 and Table 6.5-3 show a large uncertainty in the fraction of rivulet flow that enters breaches. The integrated fraction of flow into breaches, which is the desired result, is not readily discerned from the uncertainty in the inflow fractions, even though the flows obtained experimentally are more clearly quantified.

Another approach, which is used to develop an uncertainty factor for use in TSPA-LA, is to apply the integrated flow fraction approach to a drip shield whose length is about as wide as the splash diameter. If the rivulet source is dispersed along the crown, the integrated flow into a breach, Equation 6.5.1.1.2-34, can be applied. However, instead of the full drip shield length, the splash diameter is used for L_{DS}. Thus, for the breached drip shield experiments, L_{DS} has a range that is double the measured range for "inner cluster" splash radius (25 to 48 cm, as discussed at the beginning of this section, Section 6.5.1.1.2.4), or 50 to 96 cm.

The uncertainty in the effective drip shield length and in the spread angle is accounted for in a parameter f_{DS}, and the fraction of seepage flux that enters a breach F_2/F_1, is written as in Equation 6.3.2.4-2:

$$F_2/F_1 = \frac{N_b \ell}{L_{DS}}\left(1+\frac{\tan\alpha}{2}\right) f_{DS}. \qquad \text{(Eq. 6.5.1.1.2-35)}$$

In this approach, the uncertainty factor f_{DS} is obtained by replacing F_2/F_1 with f_{expt}, the experimental fraction of drip flow that enters a breach:

$$\begin{aligned} f_{DS} &= \frac{F_2/F_1}{\frac{\ell}{L_{DS}}\left(1+\frac{\tan\alpha}{2}\right)} \\ &= \frac{f_{expt}}{\frac{\ell}{L_{DS}}\left(1+\frac{\tan\alpha}{2}\right)}. \end{aligned} \qquad \text{(Eq. 6.5.1.1.2-36)}$$

The range of values for f_{DS} is obtained by evaluating it with the appropriate minimum and maximum values of L_{DS} and α so as to minimize and maximize f_{DS}. The minimum value of f_{DS}, using $L_{DS} = 50$ cm and $\alpha = 17.3°$, is $f_{DS} = 3.205 f_{expt} = 0.356$ using the mean value of 0.111 for f_{expt}. The maximum value of f_{DS}, using $L_{DS} = 96$ cm and $\alpha = 8.9°$, is $f_{DS} = 6.5947 f_{expt} = 0.732$ using the mean value of 0.111 for f_{expt}. Because zero must be the low end of the range of f_{DS}, these estimates are regarded as a range for the maximum value of f_{DS}. By treating the experimental drip shield as a segment whose length is the splash diameter, a maximum value of 0.36 to 0.73 for the flux splitting uncertainty factor f_{DS} is obtained.

It is also reasonable to use the median value for f_{expt} (0.0486) instead of the mean to define the range for f_{DS}. In this case, f_{DS} would range from 0.16 to 0.32, a factor of 2.3 lower than when the mean is used, which gives some indication of the degree of uncertainty in the experimental measurements and the resulting flux splitting submodel.

The drip shield flux splitting submodel, Equation 6.3.2.4-4, includes the rivulet spread angle, α. As discussed in Section 6.3.2.4, this equation can be simplified by lumping the uncertainty in α with the range in f_{DS}. In Section 6.5.1.1.2, α was found based on experiments to range from about 8.9° to 17.3°. The uncertainty in α appears as a factor $(1+\tan\alpha/2)$, ranging from 1.08 to 1.16, which multiplies f_{DS}, resulting in a range for the product $f'_{DS} = (1+\tan\alpha/2) f_{DS}$. The maximum for f'_{DS} based on experimental results is (1.16)(0.73) = 0.85 (using the maximum spread angle of 17.3° in the factor $(1+\tan\alpha/2)$ and the minimum spread angle of 8.9° to define f_{DS}).

The sampled parameter is then f'_{DS}, and the drip shield flux splitting algorithm is:

$$F_2 = \min\left[F_1 \frac{N_b \ell}{L_{DS}} f'_{DS}, F_1\right], \qquad \text{(Eq. 6.5.1.1.2-37)}$$

which is identical to Equation 6.3.2.4-6. Using the higher value of maximum for f'_{DS} of 0.85 is both more reliable, being based on experimental data, and overestimates releases of radionuclides by predicting a higher water flow rate through the drip shield. The range for f'_{DS} to be used in TSPA-LA is 0 to 0.85. A uniform distribution is appropriate for f'_{DS} because insufficient data are available to define any other distribution.

6.5.1.1.3 Water Flux through a Breached Waste Package

The submodel for flow through a breached waste package is conceptually identical to the submodel for flow through a breached drip shield. Key features listed at the start of Section 6.5.1.1.1 apply to both the drip shield and waste package cases. The waste package and drip shield flow submodels differ in two important respects: (1) the radius of curvature of the waste package is less than that of the drip shield; and (2) the nominal corrosion patch size as modeled by WAPDEG (BSC 2004 [DIRS 169996]) is smaller for a waste package than for the drip shield. These differences have no affect on the formulation of the waste package flow model. However, they have an affect on the values of uncertainty parameters that are part of the model. Because experiments were performed on a breached drip shield but not on a breached waste package, application of drip shield data to the waste package flow model introduces additional uncertainty in development of the model; however, these uncertainties cannot be quantified.

The water flux through a breached waste package, F_4, as developed in Section 6.3.3.2, is given by:

$$F_4 = \min\left[F_2 \frac{N_{bWP} \ell_{WP}}{L_{WP}} f'_{WP}, F_2\right], \qquad \text{(Eq. 6.5.1.1.3-1)}$$

where F_2 is the flux through the breached drip shield. This is a simplification of a slightly more rigorous expression:

$$F_4 = \min\left[F_2 \frac{N_{bWP} \ell_{WP}}{L_{WP}} \left(1 + \frac{\tan\alpha}{2}\right) f_{WP}, F_2\right], \qquad \text{(Eq. 6.5.1.1.3-2)}$$

which explicitly accounts for the rivulet spread angle α. Because α is an uncertainty parameter itself, it can be lumped in with the parameter f_{WP} to give f'_{WP}. Equation 6.5.1.1.3-2 is considered first in order to examine the dependence on α.

As with the drip shield model, the primary mechanism for water to enter breaches is via rivulet flow that originates from an area around the point of drip impact. The rivulets spread out in a delta formation from the point of impact defined by a half-angle, α, and the lateral spread of the rivulet flow is given by $2x\tan\alpha$, where x is the distance from the crown to the top edge of the breach. The smaller radius of curvature of the waste package would be expected to result in a smaller spread angle, although the difference may be lost in the variability and uncertainty of rivulet flow. The radius of curvature of the drip shield is 1.40 m, whereas waste package radii range from 0.859 m for a 21-PWR (BSC 2004 [DIRS 169472], Table 1) to 1.063 m for a 5 DHLW/DOE SNF - Short (BSC 2004 [DIRS 169472], Table 1).

Rivulet spread measurements at the 16.5° line, at the 33° line, and at the transition line between the curved top surface and the vertical side of the drip shield are used. The distance x from the drip location to the point of measurement is determined from the drawing of the drip shield mockup shown in Figure 4.1-1, which is reproduced from Howard (2002 [DIRS 161516], p. 14); various dimensions used in analyzing the data are listed in Table 6.5-1. The rivulet spread angle data are analyzed in Microsoft Excel spreadsheet: Flux Split Waste Package Model, Worksheet: Spread angles, which is documented in Appendix D.

To capture some of the effect of the smaller radius, namely the steeper incline closer to the crown, the data from drip locations that are off the crown of the smooth drip shield surface experiments are used to develop parameters for the waste package model. The results varied widely. In 20 measurements at the 33° line with drips at the 16.5° line, the mean spread angle was 17.0° (±11.2° = one standard deviation). In 17 measurements at the transition line with drips at the 16.5° line, the mean spread angle was 11.1° (±4.1°). In 10 measurements at the transition line with drips at the 33° line, the mean spread angle was 11.5° (±3.3°). For all 47 measurements the mean spread angle was 13.7° (±8.2°), which is just slightly larger than the spread angle measured for drips on the crown of the drip shield, although the variability is greater (standard deviation of 8.2°, compared with 4.1° for drips from the crown). Utilizing all of the data available, the spread angle for rivulet flow on the waste package can be assigned a mean value of about 13.7° and a range (± one standard deviation) from 5.5° to 22.0°.

The splash distance is uncertain for drip locations off the crown. In four of the q(film) rivulet flow tests, maximum lateral splash distances ranging from 56 cm to 122 cm from the drip point were observed (DTN: MO0207EBSATBWP.023 [DIRS 163402], pp. 14, 16, 18, and 20) for drip locations at the 16.5° line. However, no further observations indicated any change in the "inner cluster" splash distance range of 50 cm to 96 cm from Splash Radius Test #1 (DTN: MO0207EBSATBWP.022 [DIRS 163400]).

An uncertainty factor f_{WP} that can be obtained by replacing the fraction F_4 / F_2 with f_{expt}:

$$f_{WP} = \frac{F_4 / F_2}{\frac{\ell}{L_{WP}}\left(1+\frac{\tan\alpha}{2}\right)} = \frac{f_{expt}}{\frac{\ell}{L_{WP}}\left(1+\frac{\tan\alpha}{2}\right)}. \qquad \text{(Eq. 6.5.1.1.3-3)}$$

The range of values for f_{WP} is obtained by evaluating it with the appropriate minimum and maximum values of L_{WP} and α so as to minimize and maximize f_{WP}. The half-width of the patch used in the experiments ($\ell = 13.5$ cm) is used to evaluate f_{WP}. The minimum value of f_{WP}, using $L_{WP} = 50$ cm and $\alpha = 22.0°$, is $f_{WP} = 3.081 f_{expt} = 0.909$ using the mean value of 0.295 for f_{expt}. The maximum value of f_{WP}, using $L_{WP} = 96$ cm and $\alpha = 5.5°$, is $f_{WP} = 6.784 f_{expt} = 2.001$ using the mean value of 0.295 for f_{expt}.

A much lower range could also be justified by using the median inflow fraction of 0.014 instead of the mean (0.295) to define f_{WP}. In this case, f_{WP} would range from 0.043 to 0.095, which demonstrates the large degree of uncertainty in the experimental measurements and the resulting flux splitting submodel. The values for f_{WP} discussed in this section actually represent a range for the maximum value of f_{WP}, since the minimum must be zero.

If the factor (1 + ½ tan α) that accounts for the rivulet spread angle is lumped in with f_{WP}, the sampled uncertain factor f'_{WP} has an upper bound (using the maximum rivulet spread angle, $\alpha = 22°$) of 2.41. The range for f'_{WP} to be used in TSPA-LA is 0 to 2.41. f'_{WP} is assigned a uniform distribution.

6.5.1.2 EBS Transport Model

The EBS transport model consists of mass balances on radionuclides. The transport model is more complex than the flow model for two basic reasons. First, the transport model is necessarily transient because the mass of each radionuclide at any particular location is dependent on its history (i.e., how far it has traveled, the quantity remaining at the source, and the extent of radioactive decay or ingrowth). Second, several complex interacting processes occur in transport, including dissolution and precipitation, sorption, advective transport, diffusion, and colloid-facilitated transport. The term "colloid-facilitated transport" includes numerous phenomena, including adsorption and desorption of radionuclides onto mobile and immobile colloids, capture of colloids by solid surfaces and the air-water interface, filtering, dispersion, and diffusion. Transport can take place at any degree of water saturation greater than zero, so the model has to account for water saturation. Dissolution and precipitation may occur at finite rates or sufficiently fast to reach equilibrium. Solubility limits that determine whether,

or to what extent, these processes occur are dependent on the chemical environment of the EBS. The EBS transport model applies to the waste package, the invert, and the invert/UZ interface.

Mass Balance for Dissolved and Reversibly and Irreversibly Sorbed Radionuclides in the Aqueous Phase

As with the flow model, the details of pore structure within the EBS are not important, and macroscopic mass balances using phenomenological rate expressions are appropriate. The starting point is the equation of continuity, or mass balance equation, for each *dissolved* radionuclide species *i* (Bird et al. 1960 [DIRS 103524], p. 561):

$$\frac{\partial \rho_i}{\partial t} = -\nabla \cdot J_i + Q_i^m + r_i . \qquad \text{(Eq. 6.5.1.2-1)}$$

Here, ρ_i is the mass concentration of dissolved radionuclide species *i* (kg *i* m^{-3} bulk volume), J_i is the mass flux vector (or mass specific discharge) (kg m^{-2} s^{-1}) of dissolved radionuclide species *i* in the mobile water phase and accounts for advection, hydrodynamic dispersion, and diffusion of the dissolved radionuclide species *i*. The term Q_i^m is the net rate on a bulk volume basis (kg m^{-3} s^{-1}) of the various mass transfer processes, including reversible and irreversible sorption onto solid stationary materials in the EBS, dissolution and precipitation, and the various colloid-facilitated transport processes. The reaction term, r_i, accounts for radioactive decay and ingrowth on a bulk volume basis (i.e., production by decay of the parent of *i*) (kg m^{-3} s^{-1}). Each of these terms is expanded and described in more detail below, then simplified as appropriate for application in the TSPA-LA model.

It is convenient to develop the transport model following the approach normally taken in the literature (Corapcioglu and Jiang 1993 [DIRS 105761], pp. 2217 to 2219; Choi and Corapcioglu 1997 [DIRS 161621], p. 306), with an emphasis on colloid-facilitated transport, since the complexity of those processes tends to dominate the analysis. First, Equation 6.5.1.2-1 is rewritten in terms of concentrations of radionuclides in an unsaturated porous medium. The density, or mass concentration, of dissolved radionuclide species *i* is given by:

$$\rho_i = C_i \phi S_w , \qquad \text{(Eq. 6.5.1.2-2)}$$

where C_i is the concentration on a water volume basis of radionuclide species *i* (kg m^{-3}), ϕ is the porosity (m^3 void m^{-3} EBS) of a representative elemental volume of EBS, and S_w is the water saturation (m^3 water m^{-3} void). The expression for ρ_i is inserted into Equation 6.5.1.2-1, resulting in

$$\frac{\partial(\phi S_w C_i)}{\partial t} = -\nabla \cdot J_i + Q_i^m + r_i . \qquad \text{(Eq. 6.5.1.2-3)}$$

The concentration C_i is constrained by the solubility limit, C_{si}, which is defined in *Dissolved Concentration Limits of Radioactive Elements* (BSC 2004 [DIRS 169425], Table 8-3) for each of 14 elements (U, Np, Pu, Am, Ac, Th, Tc, C, I, Ra, Pa, Pb, Cs, and Sr). The solubility limits for

U, Np, Pu, Th, Am, Ac, and Pa are given as functions of pH, CO_2 fugacity, and fluoride concentration.

The mass flux vector is expressed as

$$J_i = -\phi S_w D_i \nabla C_i + q_w C_i, \qquad \text{(Eq. 6.5.1.2-4)}$$

where D_i is the hydrodynamic dispersion coefficient of species i ($m^2\ s^{-1}$), and q_w is the specific discharge vector, or Darcy velocity, of water ($m\ s^{-1}$). The specific discharge vector is related to the water flow rates F_j ($m^3\ s^{-1}$) in each pathway j of the EBS flow model (Section 6.5.1.1) by:

$$q_w = \frac{F_j}{A} i, \qquad \text{(Eq. 6.5.1.2-5)}$$

where A is the spatially dependent cross sectional flow area within the pathway j (m^2), and i is a unit vector in the direction of the flow path. Because of the complex flow geometry in the EBS, assigning a value to A is not always straightforward; for example, for pathway 4 (Section 6.5.1.1), flow through the waste package, A can be the cross sectional area of corrosion patches or some fraction of the cross sectional area of a waste package.

The hydrodynamic dispersion coefficient, D_i, can be expressed in terms of two components (Freeze and Cherry 1979 [DIRS 101173], pp. 389 to 390):

$$\alpha \bar{v} + D_{mi}, \qquad \text{(Eq. 6.5.1.2-6)}$$

where α is the dispersivity (m), $\bar{v}$ is the average interstitial water velocity ($m\ s^{-1}$), and D_{mi} is the effective molecular diffusion coefficient ($m^2\ s^{-1}$). The dispersivity can be further broken down into lateral and longitudinal dispersivities. However, the dispersivity in the EBS is ignored (see Section 6.3.1.2). Consequently, the hydrodynamic dispersion is accounted for solely by molecular diffusion. The free water diffusion coefficient for self-diffusion of water, D_0, is used as a bounding value of the molecular diffusion coefficient for all radionuclides in the EBS. Modifications to the diffusion coefficient D_{mi} for the porosity, saturation, temperature and uncertainty within the invert are described in Section 6.3.4.1. Modifications to the diffusion coefficient for the porosity and saturation within the waste package are described in Section 6.5.1.2.1. The effects of concentrated solutions are ignored. Throughout the mathematical description of the radionuclide transport, D_i represents the effective diffusion coefficient for species i.

The term Q_i^m ($kg\ m^{-3}\ s^{-1}$) in Equation 6.5.1.2-3 is expanded to account for individual contributions of different processes to radionuclide transport:

$$Q_i^m = Q_{id} - Q_{iprecip} - Q_{is}^{rev} - Q_{is}^{irrev} - Q_{icm}^{rev} - Q_{icm}^{irrev} - Q_{icc} - Q_{icc}^{int} \pm Q_{imi} - Q_{icm}^{embed}. \qquad \text{(Eq. 6.5.1.2-7)}$$

The first term is the source term, Q_{id}, accounting for the rate of dissolution of species *i*, and $Q_{iprecip}$ is the rate of precipitation of species *i*. If the concentration of species *i* is below the solubility limit, then $Q_{iprecip} = 0$; otherwise, the precipitation rate is determined from the mass balance so as to honor the solubility limit.

The next six terms in Equation 6.5.1.2-7 account for sorption-related processes. Q_{is}^{rev} is the net rate of reversible sorption of radionuclide species *i* onto the stationary solid matrix (internal waste package corrosion products and invert matrix). Q_{is}^{irrev} is the net rate of irreversible sorption of radionuclide species *i* onto the stationary solid matrix (internal waste package corrosion products). Q_{icm}^{rev} is the net rate of reversible sorption of radionuclide species *i* onto mobile colloid surfaces. Development of this term requires assumptions regarding the reversibility of radionuclide sorption onto colloids and is discussed below. Q_{icm}^{irrev} is the net rate of irreversible sorption of radionuclide species *i* onto mobile colloid surfaces.

Q_{icc} and Q_{icc}^{int} are the net rates of sorption of radionuclide species *i* onto immobile colloid surfaces captured by the stationary solid matrix and by the air-water interface, respectively. Wan and Wilson (1994 [DIRS 124994]) found that "particle transport was tremendously retarded by the air-water interface acting as a strong sorption phase" (Choi and Corapcioglu 1997 [DIRS 161621], p. 301). However, as a bounding assumption (BSC 2004 [DIRS 170025], Assumption 5.4), sorption by the air-water interface is assumed not to occur ($Q_{icc}^{int} = 0$). Distribution coefficients for sorption onto the stationary solid matrix and onto immobile colloid surfaces will generally be different. However, it is difficult to distinguish among various types of matrixes and immobile colloids. Therefore, no distinction is made, and the term Q_{icc} (sorption onto immobile colloids) is lumped in with Q_{is}^{rev} or Q_{is}^{irrev} (sorption onto the stationary solid matrix). Sorption and retardation in the waste package is discussed in more detail in Section 6.3.4.2.

Q_{imt} is the net rate of interface transfer of dissolved mass between the continua in a dual continuum. The sign of this transfer term is determined by the sign of the concentration difference between the media and which medium is associated with the mass balance equation. This term is included even though it is zero in the single-continuum domains that represent the EBS in the *EBS RT Abstraction* in order to keep the mass balance equations as generally applicable as possible. In particular, the equations apply in the dual-continuum invert model presented as an alternative conceptual model in Section 6.6.4.

Q_{icm}^{embed} is the rate of mass conversion from dissolved state to embedded state onto waste form colloids for radionuclide species *i*. Radionuclides become embedded only in waste form colloids, not in iron oxyhydroxide or groundwater colloids. The conversion rate to embedded species is represented by a first order conversion of the species in solution:

$$Q_{icm}^{embed} = \lambda_i^{embed} C_i, \qquad \text{(Eq. 6.5.1.2-8)}$$

where is the λ_i^{embed} is the first order rate constant (s^{-1}) for mass conversion from the dissolved state to the embedded state onto waste form colloids for radionuclide species *i*.

Decay and ingrowth are expressed as:

$$r_i = \lambda_{ip} r_{ip}^M \phi S_w C_{ip} - \lambda_i \phi S_w C_i . \qquad \text{(Eq. 6.5.1.2-9)}$$

Radionuclide species *i* is produced by the decay of its parent species at a rate proportional to the concentration of the parent, C_{ip} (kg m^{-3}), and the parent species decay constant, λ_{ip} (s^{-1}). The decay constant is related to the half-life, $t_{1/2,ip}$ (s), of the radionuclide by:

$$\lambda_{ip} = \frac{\ln(2)}{t_{1/2,ip}} . \qquad \text{(Eq. 6.5.1.2-10)}$$

Similarly, species *i* is lost by decay at a rate $\lambda_i C_i$ (kg m^{-3} s^{-1}), where λ_i is the decay constant for species *i* (s^{-1}), defined analogously to λ_{ip}. The term r_{ip}^M in the production rate is the dimensionless ratio of the mass (kg) of species *i* produced by decay of the parent species to the mass (kg) of the parent species lost by decay. This is equal to the ratio of the atomic weight of species *i* to that of its parent for species that have just one parent. In TSPA-LA, each radionuclide is modeled as having at most one parent, which is implied in Equation 6.5.1.2-9.

Transport of dissolved and reversibly sorbed radionuclide species *i* in the aqueous phase is then given by:

$$\begin{aligned} \frac{\partial(\phi S_w C_i)}{\partial t} = {} & \nabla \cdot (\phi S_w D_i \nabla C_i) - \nabla \cdot q_w C_i \\ & + Q_{id} - Q_{iprecip} - Q_{is}^{rev} - Q_{is}^{irrev} - Q_{icm}^{rev} - Q_{icm}^{irrev} \\ & \pm Q_{imt} - Q_{icm}^{embed} + \phi S_w \left(\lambda_{ip} r_{ip}^M C_{ip} - \lambda_i C_i\right), \end{aligned} \qquad \text{(Eq. 6.5.1.2-11)}$$

which is essentially identical to Equations 19 and 20 by Choi and Corapcioglu (1997 [DIRS 161621], p. 306), with the addition of decay and ingrowth terms and a dissolution source term, Q_{idp}. A further modification of the equations by Choi and Corapcioglu involves the diffusive term, $\nabla \cdot (\phi S_w D_i \nabla C_i)$, which Choi and Corapcioglu write as $\nabla \cdot [D_i \nabla (\phi S_w C_i)]$. This form of the term incorrectly allows diffusion to occur in the absence of a concentration gradient as long as the water content, ϕS_w, varies.

The source term for radionuclide species *i* reversibly sorbed onto the stationary solid matrix (corrosion products or invert matrix) is given by:

$$Q_{is}^{rev} = \frac{\partial(\rho_b K_{dis} C_i)}{\partial t} - \rho_b \left(\lambda_{ip} r_{ip}^M K_{dips} C_{ip} - \lambda_i K_{dis} C_i\right), \qquad \text{(Eq. 6.5.1.2-12)}$$

where ρ_b is the dry bulk density of the stationary solid matrix (kg m^{-3} bulk volume). A linear adsorption isotherm is used for the relationship between the aqueous and solid phase equilibrium concentration, expressed in terms of a sorption distribution or distribution coefficient of the dissolved species *i*, K_{dis} (m^3 water kg^{-1} solid [more typically reported in units of ml g^{-1}]). K_{dis} depends both on the radionuclide species *i* being sorbed and on the solid substrate, either stationary iron oxyhydroxide corrosion products or invert material or both, in this case.

The source term for radionuclide species *i* irreversibly sorbed onto the stationary solid iron oxyhydroxide corrosion products is given by:

$$Q_{is}^{irrev} = \rho_b \bar{s}_{CP} k_i C_i, \qquad \text{(Eq. 6.5.1.2-13)}$$

where $\bar{s}_{CP}$ is the specific surface area of iron oxyhydroxide corrosion products [m^2 CP kg^{-1} CP], and k_i is the irreversible forward rate constant (m^3 water m^{-2} CP s^{-1}). The reaction is modeled as first order in the solution concentration.

The source term for radionuclide species *i* reversibly sorbed onto the mobile colloids is given by:

$$\begin{aligned} Q_{icm}^{rev} = & \frac{\partial[\phi S_w (K_{dicWF} C_{cWF} + K_{dicFeOx} C_{cFeOx} + K_{dicGW} C_{cGW}) C_i]}{\partial t} \\ & + \nabla \cdot (J_{icWF} + J_{icFeOx} + J_{icGW}) \\ & - \phi S_w [\lambda_{ip} r_{ip}^{M} (C_{ipcWF} + C_{ipcFeOx} + C_{ipcGW}) - \lambda_i (C_{icWF} + C_{icFeOx} + C_{icGW})], \end{aligned} \qquad \text{(Eq. 6.5.1.2-14)}$$

where C_{icWF}, C_{icFeOx}, and C_{icGW} are the concentrations on a water volume basis of radionuclide species *i* reversibly sorbed onto the mobile waste form, iron oxyhydroxide (FeOx), and groundwater (GW) colloids, respectively (kg *i* m^{-3} water). The subscript *ip* refers to the parent of radionuclide species *i*. The terms C_{cWF}, C_{cFeOx}, and C_{cGW} are the concentrations on a water volume basis of mobile waste form, iron oxyhydroxide, and groundwater colloids, respectively (kg colloid m^{-3} water). The K_d values of radionuclide species *i* for the respective colloids are K_{dicWF}, $K_{dicFeOx}$, and K_{dicGW} (typical units: ml g^{-1}).

The vectors for mass fluxes of colloids, J_{icWF}, J_{icFeOx}, and J_{icGW}, are:

$$J_{icWF} = -\phi S_w D_c \nabla (K_{dicWF} C_{cWF} C_i) + q_w K_{dicWF} C_{cWF} C_i \qquad \text{(Eq. 6.5.1.2-15)}$$

$$J_{icFeOx} = -\phi S_w D_c \nabla (K_{dicFeOx} C_{cFeOx} C_i) + q_w K_{dicFeOx} C_{cFeOx} C_i \qquad \text{(Eq. 6.5.1.2-16)}$$

$$J_{icGW} = -\phi S_w D_c \nabla (K_{dicGW} C_{cGW} C_i) + q_w K_{dicGW} C_{cGW} C_i. \qquad \text{(Eq. 6.5.1.2-17)}$$

The source term for radionuclide species *i* irreversibly sorbed onto the mobile iron oxyhydroxide corrosion products colloids is given by:

$$Q_{icm}^{irrev} = \phi S_w C_{cFeOx} \bar{s}_c k_i C_i, \qquad \text{(Eq. 6.5.1.2-18)}$$

where $\bar{s}_c$ is the specific surface area of mobile corrosion products colloids (m^2 colloids kg^{-1} colloids), and k_i is the forward rate constant for irreversible sorption (m^3 water m^{-2} FeOx colloids s^{-1}). k_i for mobile iron oxyhydroxide corrosion products colloids is the same as for stationary iron oxyhydroxide corrosion products. The reaction is modeled as first order in the solution concentration. Irreversible sorption onto mobile colloids occurs only onto mobile iron oxyhydroxide corrosion products colloids, not onto mobile waste form or mobile groundwater colloids. As discussed earlier, radionuclides may become embedded in waste form colloids, which has a similar net effect as irreversible sorption but is modeled as a distinctly separate process.

The term Q_{imt} is the net rate of interface transfer of dissolved and reversibly sorbed mass between the continua in a dual continuum material (as in the dual continuum invert alternative conceptual model; see Section 6.6.4) on a bulk volume basis ($kg\ m^{-3}\ s^{-1}$]). It is given by (Corapcioglu and Wang 1999 [DIRS 167464], p. 3265; Gerke and van Genuchten 1996 [DIRS 167466], p. 345):

$$\begin{aligned} Q_{imt} = {} & \gamma_d\left[(C_i)_{intra} - (C_i)_{inter}\right] \\ & + \gamma_c\left[(C_{icWF})_{intra} - (C_{icWF})_{inter}\right. \\ & \left. + (C_{icFeOx})_{intra} - (C_{icFeOx})_{inter} + (C_{icGW})_{intra} - (C_{icGW})_{inter}\right]. \end{aligned} \qquad \text{(Eq. 6.5.1.2-19)}$$

In a single-continuum material, $Q_{imt} = 0$. The dissolved and colloid mass transfer coefficients, γ_d and γ_c, respectively, depend on which continuum the mass balance represents. For the dissolved mass transfer term:

$$\gamma_d = \alpha\phi_{intra} S_{w\_intra}, \text{ for the intragranular mass balance,} \qquad \text{(Eq. 6.5.1.2-20)}$$

$$\gamma_d = \alpha\phi_{intra} S_{w\_intra}\left(\frac{1 - w_{inter}}{w_{inter}}\right), \text{ for the intergranular mass balance,} \qquad \text{(Eq. 6.5.1.2-21)}$$

where α is the first-order mass transfer coefficient of the form:

$$\alpha = \frac{\beta}{d^2} D_{ie}, \qquad \text{(Eq. 6.5.1.2-22)}$$

β is a dimensionless geometry-dependent coefficient, d is a characteristic length (m) of the matrix structure (e.g., half the aggregate width or half the fracture spacing), and D_{ie} is an effective diffusion coefficient ($cm^2\ s^{-1}$) that represents the diffusion properties of the interface between the two continua for radionuclide species i. Because the intergranular continuum is open pore space, diffusion is expected to be controlled by the diffusive properties of the intragranular continuum. Thus, D_{ie} is taken to be the effective diffusion coefficient in the intragranular continuum. The colloid coefficient γ_c is evaluated similarly to the dissolved

coefficient, but uses an effective colloid diffusion coefficient to evaluate α in Equation 6.5.1.2-22. The mass transfer function between the two invert continua is described in Section 6.6.4.1.

In a dual-continuum material, the intergranular porosity ϕ_{inter} and intragranular porosity ϕ_{intra} are defined as follows. Let V_p be the total volume of pore space in the bulk material, which has a total volume of V_t. The intergranular pore space has a total volume designated by V_{t_inter} and a pore volume of V_{p_inter}. Similarly, the intragranular pore space has a total volume designated by V_{t_intra} and a pore volume of V_{p_intra}. $V_p = V_{p\_intra} + V_{p\_inter}$ and $V_t = V_{t\_intra} + V_{t\_inter}$. The porosities are defined as:

$$\phi_{inter} = \frac{V_{p\_inter}}{V_t} \qquad \text{(Eq. 6.5.1.2-23)}$$

and

$$\phi_{intra} = \frac{V_{p\_intra}}{V_t}. \qquad \text{(Eq. 6.5.1.2-24)}$$

The total bulk porosity of the material is:

$$\phi_t = \frac{V_p}{V_t} = \phi_{inter} + \phi_{intra}. \qquad \text{(Eq. 6.5.1.2-25)}$$

The parameter w_{inter} is the ratio of the intergranular continuum volume to the total bulk volume:

$$w_{inter} = \frac{V_{t\_inter}}{V_t}. \qquad \text{(Eq. 6.5.1.2-26)}$$

Then $\left(\frac{1-w_{inter}}{w_{inter}}\right)$ is the ratio of intragranular continuum volume to intergranular continuum volume:

$$\frac{1-w_{inter}}{w_{inter}} = \frac{1-\frac{V_{t\_inter}}{V_t}}{\frac{V_{t\_inter}}{V_t}} = \frac{V_t - V_{t\_inter}}{V_{t\_inter}} = \frac{V_{t\_intra}}{V_{t\_inter}}. \qquad \text{(Eq. 6.5.1.2-27)}$$

Mass Balance for Irreversibly Adsorbed Radionuclides on Iron Oxyhydroxide Corrosion Products and Colloids

The mass balance for irreversibly adsorbed radionuclides on mobile iron oxyhydroxide colloids, which originate in the corrosion products, accounts for advection, diffusion, and decay and is given by:

$$\frac{\partial\left(\phi S_w C_{icFeOx}^{irrev}\right)}{\partial t} = -\nabla\cdot\left(J_{icFeOx}^{irrev}\right) + Q_{icm}^{irrev} \pm Q_{imt}^{irrev} + \phi S_w\left(\lambda_{ip} r_{ip}^{M} C_{ipcFeOx}^{irrev} - \lambda_i C_{icFeOx}^{irrev}\right), \quad \text{(Eq. 6.5.1.2-28)}$$

where

$$Q_{imt}^{irrev} = \gamma_c\left[\left(C_{icFeOx}^{irrev}\right)_{intra} - \left(C_{icFeOx}^{irrev}\right)_{inter}\right], \quad \text{(Eq. 6.5.1.2-29)}$$

$$J_{icFeOx}^{irrev} = -\phi S_w D_c \nabla\left(C_{icFeOx}^{irrev}\right) + q_w C_{icFeOx}^{irrev}. \quad \text{(Eq. 6.5.1.2-30)}$$

C_{icFeOx}^{irrev} is the concentration of radionuclide species i irreversibly adsorbed onto iron oxyhydroxide colloids on a water volume basis (kg i m^{-3} water). The source term for radionuclide species i irreversibly sorbed onto the mobile corrosion products colloids, Q_{icm}^{irrev}, is given by Equation 6.5.1.2-18.

The mass balance for irreversibly adsorbed radionuclides on stationary iron oxyhydroxide corrosion products accounts for decay and is given by:

$$\frac{\partial\left(\phi S_w C_{iCPFeOx}^{irrev}\right)}{\partial t} = Q_{is}^{irrev} + \phi S_w\left(\lambda_{ip} r_{ip}^{M} C_{ipCPFeOx}^{irrev} - \lambda_i C_{iCPFeOx}^{irrev}\right), \quad \text{(Eq. 6.5.1.2-31)}$$

where $C_{iCPFeOx}^{irrev}$ is the concentration of radionuclide species i irreversibly adsorbed onto iron oxyhydroxide corrosion products on a water volume basis (kg i m^{-3}). The source term for radionuclide species i irreversibly sorbed onto the solid stationary iron oxyhydroxide corrosion products, Q_{is}^{irrev}, is given by Equation 6.5.1.2-13.

Mass Balance for Waste Form Colloid Particles

The waste form colloids are generated in the waste form domain and are transported in accordance with an advective/diffusive mass balance. The waste form colloid concentration is subject to stability constraints based on the local domain chemistry. The iron oxyhydroxide and ground water colloids both exist in the corrosion products and invert domains, and their concentrations are dependent on the local domain chemistry (BSC 2004 [DIRS 170025]). Hence, no transport mass balance equations are required for iron oxyhydroxide and ground water colloids.

The mass balance for waste form colloidal particles suspended in the aqueous phase can be expressed as (Choi and Corapcioglu 1997 [DIRS 161621], p. 302):

$$\frac{\partial(\phi S_w C_{cWF})}{\partial t} = -\nabla \cdot J_{cWF} - Q_{cWF} - Q_{cWF}^{int} - Q_{cWFfg} + Q_{cWFs} \pm Q_{cWFmt}. \quad \text{(Eq. 6.5.1.2-32)}$$

C_{cWF} is the concentration of suspended waste form colloids in the aqueous phase (kg waste form colloids m^{-3} water), and J_{cWF} is the mass flux vector of waste form colloids (kg m^{-2} s^{-1}). Q_{cWF} (kg m^{-3} s^{-1}) is the net rate of waste form colloid capture on the solid surface, with Q_{cWF}^{int} (kg m^{-3} s^{-1}) representing capture at the air-water interface. As mentioned earlier, the latter is neglected. The term Q_{cWFfg} is the net rate of waste form colloid removal from suspension (kg m^{-3} s^{-1}) by means of physical filtering (pore clogging, sieving, and straining) and by gravitational settling. Both of these processes are neglected as bounding assumptions (BSC 2004 [DIRS 170025], Section 6.3.1). Although colloid capture is akin to sorption and a different process from physical filtration, the net effect is indistinguishable from physical filtration, and it is also, too, is neglected ($Q_{cWF} = 0$).

With these assumptions, Equation 6.5.1.2-32 simplifies to:

$$\frac{\partial(\phi S_w C_{cWF})}{\partial t} = -\nabla \cdot J_{cWF} + Q_{cWFs} \pm Q_{cWFmt}. \quad \text{(Eq. 6.5.1.2-33)}$$

The source term, Q_{cWFs} (kg m^{-3} s^{-1}), in Equation 6.5.1.2-33 represents the formation or degradation of waste form colloids. Colloid formation may be rate limited, or it may be instantaneous, with equilibrium between the colloids and their dissolved components. In either case, colloid stability is strongly dependent on the chemical environment, specifically on the pH and ionic strength of the aqueous phase. The colloid source term is the subject of *Waste Form and In-Drift Colloids-Associated Radionuclide Concentrations: Abstraction and Summary* (BSC 2004 [DIRS 170025]), and is discussed further below.

Q_{cWFmt} is the net rate of interface transfer of waste form colloidal mass between the intergranular and intragranular continua in a dual continuum model, such as the dual continuum invert alternative conceptual model (Section 6.6.4). For a single continuum, $Q_{cWFmt} = 0$. The sign of this transfer term is determined by the sign of the waste form colloid concentration difference between the media and which medium is associated with the mass balance equation. This is just the colloid transfer term in Equation 6.5.1.2-32:

$$Q_{cWFmt} = \gamma_c \left[(C_{cWF})_{intra} - (C_{cWF})_{inter} \right]. \quad \text{(Eq. 6.5.1.2-34)}$$

Since Equation 6.5.1.2-34 is for the waste form colloid particles themselves, as opposed to radionuclides sorbed onto the particles, there are no decay or ingrowth terms.

The mass flux vector for waste form colloids is expressed as (Choi and Corapcioglu 1997 [DIRS 161621], p. 303, Equation 4):

$$\begin{aligned} J_{cWF} &= J_{cB} + J_{cMD} + q_w C_{cWF} \\ &= -\phi S_w D_B \nabla C_{cWF} - \phi S_w D_{MD} \nabla C_{cWF} + q_w C_{cWF} \\ &= -\phi S_w D_c \nabla C_{cWF} + q_w C_{cWF}, \end{aligned} \qquad \text{(Eq. 6.5.1.2-35)}$$

where subscript B refers to Brownian diffusion, and MD refers to mechanical dispersion. The mechanical dispersion and Brownian diffusion terms can be lumped together in a colloid hydrodynamic dispersion term with a colloid dispersion or diffusion coefficient D_c ($m^2\ s^{-1}$). The diffusion coefficient of colloids is estimated to be a factor of 100 less than that of the free water diffusivity (Section 6.3.4.4) (i.e., $D_c = D_0/100$). The mass balance on waste form colloid particles, Equation 6.5.1.2-33, then becomes:

$$\begin{aligned} \frac{\partial(\phi S_w C_{cWF})}{\partial t} &= \nabla\cdot(\phi S_w D_c \nabla C_{cWF}) - \nabla\cdot(q_w C_{cWF}) + Q_{cWFs} \\ &\quad \pm \gamma_c\left[(C_{cWF})_{intra} - (C_{cWF})_{inter}\right]. \end{aligned} \qquad \text{(Eq. 6.5.1.2-36)}$$

Mass Balance for Embedded Mass on Waste Form Colloids

The mass balance for the radionuclide species i embedded on waste form colloids is:

$$\begin{aligned} \frac{\partial(\phi S_w C_i^{embed})}{\partial t} &= \nabla\cdot(\phi S_w D_c \nabla C_i^{embed}) - \nabla\cdot(q_w C_i^{embed}) \\ &\quad + \phi S_w\left(\lambda_{ip} r_{ip}^M C_{ip}^{embed} - \lambda_i C_i^{embed}\right) + \phi S_w Q_{icm}^{embed}, \end{aligned} \qquad \text{(Eq. 6.5.1.2-37)}$$

where C_i^{embed} and C_{ip}^{embed} are the concentrations of species i and the parent of species i, respectively, embedded on waste form colloids.

Inserting the source terms into Equation 6.5.1.2-11 gives the equation for the transport of radionuclides dissolved in the aqueous phase and reversibly sorbed:

$$\begin{aligned} \frac{\partial}{\partial t}\left[\phi S_w R_{fi} C_i\right] &= \nabla\cdot(\phi S_w D_i \nabla C_i) \\ &\quad + \nabla\cdot\{\phi S_w D_c \nabla[(K_{dcWF} C_{cWF} + K_{dcFeOx} C_{cFeOx} + K_{dcGW} C_{cGW}) C_i]\} \\ &\quad - \nabla\cdot[q_w(1 + K_{dcWF} C_{cWF} + K_{dcFeOx} C_{cFeOx} + K_{dcGW} C_{cGW}) C_i] \\ &\quad + Q_{id} - Q_{iprecip} - (\rho_b \bar{s}_{CP} + \phi S_w C_{cFeOx} \bar{s}_c) k_i C_i - \lambda_i^{embed} C_i \\ &\quad \pm \gamma_d\left[(C_i)_{intra} - (C_i)_{inter}\right] \\ &\quad \pm \gamma_c\left[(C_{icWF} + C_{icFeOx} + C_{icGW})_{intra} - (C_{icWF} + C_{icFeOx} + C_{icGW})_{inter}\right] \\ &\quad + \phi S_w\left[\lambda_{ip} r_{ip}^M R_{fip} C_{ip} - \lambda_i R_{fi} C_i\right], \end{aligned} \qquad \text{(Eq. 6.5.1.2-38)}$$

where

$$R_{fi} = 1 + \frac{\rho_b K_{dis}}{\phi S_w} + K_{dicWF} C_{cWF} + K_{dicFeOx} C_{cFeOx} + K_{dicGW} C_{cGW}, \quad \text{(Eq. 6.5.1.2-39)}$$

and R_{fip} is the corresponding factor for the parent species *ip* of radionuclide species *i*:

$$R_{fip} = 1 + \frac{\rho_b K_{dips}}{\phi S_w} + K_{dipcWF} C_{cWF} + K_{dipcFeOx} C_{cFeOx} + K_{dipcGW} C_{cGW}. \quad \text{(Eq. 6.5.1.2-40)}$$

In Equation 6.5.1.2-38, the left side of the equation represents the accumulation of dissolved and reversibly sorbed radionuclide species *i*. The term in brackets is the mass of species *i* present in a unit bulk volume of EBS, so the equation units are mass of species *i* per unit bulk volume of EBS per time. The first term on the right side represents the rate of diffusion of dissolved species *i* in the aqueous phase. The second term accounts for diffusion of mobile colloids on which species *i* is adsorbed. The third term is the rate at which species *i* dissolved mass and mass reversibly sorbed to mobile colloids is transported by advection. The fourth and fifth terms represent the net rate of dissolution and precipitation of species *i*, respectively. The sixth term is the conversion rate due to irreversible sorption on both iron oxyhydroxide corrosion products and colloids. The seventh term is the rate of irreversible capture of species *i* by embedding in waste form colloids. The eighth and ninth terms represent respectively the mass flux of dissolved and reversibly sorbed species *i* between the continua in a dual-continuum material; for a single-continuum material, these terms are omitted. The last (tenth) term accounts for ingrowth, or production of species *i* by decay of the parent of *i*, and decay of species *i*, as dissolved species and as sorbed onto colloids and immobile matrix.

Inserting the source terms into Equation 6.5.1.2-28, the mass balance for irreversibly adsorbed radionuclides on iron oxyhydroxide corrosion product colloids becomes:

$$\begin{aligned} \frac{\partial\left(\phi S_w C_{icFeOx}^{irrev}\right)}{\partial t} &= \nabla \cdot \left[\phi S_w D_c \nabla\left(C_{icFeOx}^{irrev}\right)\right] - \nabla \cdot \left(q_w C_{icFeOx}^{irrev}\right) \\ &+ \phi S_w C_{cFeOx} \bar{s}_c k_i C_i \pm \gamma_c \left[\left(C_{icFeOx}^{irrev}\right)_{intra} - \left(C_{icFeOx}^{irrev}\right)_{inter}\right] \quad \text{(Eq. 6.5.1.2-41)} \\ &+ \phi S_w \left(\lambda_{ip} r_{ip}^M C_{ipcFeOx}^{irrev} - \lambda_i C_{icFeOx}^{irrev}\right). \end{aligned}$$

The source term in Equation 6.5.1.2-41, $\phi S_w C_{cFeOx} \bar{s}_c k_i C_i$, couples this equation to Equation 6.5.1.2-38.

The mass balance for irreversibly adsorbed radionuclides on iron oxyhydroxide corrosion products accounts for decay and is given by:

$$\frac{\partial\left(\phi S_w C_{iCPFeOx}^{irrev}\right)}{\partial t} = \rho_b \bar{s}_{CP} k_i C_i + \phi S_w \left(\lambda_{ip} r_{ip}^M C_{ipCPFeOx}^{irrev} - \lambda_i C_{iCPFeOx}^{irrev}\right). \quad \text{(Eq. 6.5.1.2-42)}$$

The source term in Equation 6.5.1.2-42, $\rho_b \bar{s}_{CP} k_i C_i$, couples this equation to Equation 6.5.1.2-38.

For a single continuum medium with no colloids or corrosion products present, Equation 6.5.1.2-38 reduces to the conventional advection/diffusion transport equation (with source and sink terms):

$$\frac{\partial(\phi S_w R_{fi} C_i)}{\partial t} = \nabla \cdot (\phi S_w D_i \nabla C_i) - \nabla \cdot (q_w C_i) + Q_{id} - Q_{iprecip} + \phi S_w \left(\lambda_{ip} r_{ip}^M C_{ip} R_{fip} - \lambda_i C_i R_{fi}\right) \quad \text{(Eq. 6.5.1.2-43)}$$

with the conventional retardation factors for radionuclide species *i* and parent species *ip*, respectively:

$$R_{fi} = 1 + \frac{\rho_b K_{dis}}{\phi S_w} \quad \text{(Eq. 6.5.1.2-44)}$$

and

$$R_{fip} = 1 + \frac{\rho_b K_{dips}}{\phi S_w}. \quad \text{(Eq. 6.5.1.2-45)}$$

Equations 6.5.1.2-38 (mass balance for dissolved and reversibly sorbed radionuclide species *i*), 6.5.1.2-41 (mass balance for radionuclide species *i* irreversibly sorbed to iron oxyhydroxide colloids) and 6.5.1.2-42 (mass balance radionuclide species *i* irreversibly sorbed to iron oxyhydroxide corrosion products) are solved simultaneously for all radionuclides to obtain the dependent variables, C_i, C_{icFeOx}^{irrev}, and $C_{iCPFeOx}^{irrev}$, the concentration of dissolved radionuclide species *i*, the concentration of species *i* irreversibly sorbed to iron oxyhydroxide colloids, and species *i* irreversibly sorbed to iron oxyhydroxide corrosion products, respectively.

The initial conditions are $C_i = C_{icFeOx}^{irrev} = C_{iCPFeOx}^{irrev} = 0$ for all *i*. Upstream of the waste form domain, all radionuclide concentrations are zero. Consequently, the upstream boundary maintains a zero flux condition. Radionuclide concentrations will remain zero until a waste package failure occurs. A treatment of the zero concentration boundary within the UZ is provided in Section 6.5.3.6. The radionuclides are released or mobilized within the waste form domain. Flow is expected to be predominately downward. Then the resulting transport will be in a downward direction from the waste form to the corrosion products, which will accumulate in the bottom of the waste container. From the corrosion products, the radionuclide will migrate down to the invert, and from there it will enter the UZ. The representation for the radionuclide transport is consequently a one-dimensional mass balance equation for radionuclide species. For the one-dimensional EBS radionuclide transport model (in the downward +*z*-direction), the specific discharge (Darcy velocity) vector, q_w, is in the downward +*z*-direction only and is denoted by $q_w = q_{wz} \boldsymbol{i}$, where $\boldsymbol{i}$ is a unit vector in the *z*-direction, and q_{wz} is the scalar specific discharge in the *z*-direction (zero in the other two directions). In one dimension, the mass balance equations can be written as scalar equations and are summarized as follows.

The one-dimensional mass balance equation describing transport of dissolved and reversibly sorbed radionuclide species *i* in (from Equation 6.5.1.2-38) is:

$$\begin{aligned}\frac{\partial}{\partial t}\left[\phi S_w R_{fi} C_i\right] = & \frac{\partial}{\partial z}\left(\phi S_w D_i \frac{\partial C_i}{\partial z}\right) \\ & + \frac{\partial}{\partial z}\left(\phi S_w D_c \frac{\partial}{\partial z}\left[\left(K_{dicWF} C_{cWF} + K_{dicFeOx} C_{cFeOx} + K_{dicGW} C_{cGW}\right) C_i\right]\right) \\ & - \frac{\partial}{\partial z}\left[q_{wz}\left(1 + K_{dicWF} C_{cWF} + K_{dicFeOx} C_{cFeOx} + K_{dicGW} C_{cGW}\right) C_i\right] \\ & + Q_{id} - Q_{ipreclp} - \left(\rho_b \bar{s}_{CP} + \phi S_w C_{cFeOx} \bar{s}_c\right) k_i C_i - \lambda_i^{embed} C_i \\ & \pm \gamma_d \left[\left(C_i\right)_{intra} - \left(C_i\right)_{inter}\right] \\ & \pm \gamma_c \left[\left(C_{icWF} + C_{icFeOx} + C_{icGW}\right)_{intra} - \left(C_{icWF} + C_{icFeOx} + C_{icGW}\right)_{inter}\right] \\ & + \phi S_w \left[\lambda_{ip} r_{ip}^M R_{fip} C_{ip} - \lambda_i R_{fi} C_i\right].\end{aligned} \qquad \text{(Eq. 6.5.1.2-46)}$$

Similarly, the one-dimensional mass balance equation for irreversibly sorbed radionuclide species *i* on iron oxyhydroxide colloids (from Equation 6.5.1.2-41) is:

$$\begin{aligned}\frac{\partial\left(\phi S_w C_{icFeOx}^{irrev}\right)}{\partial t} = & \frac{\partial}{\partial z}\left(\phi S_w D_c \frac{\partial}{\partial z}\left(C_{icFeOx}^{irrev}\right)\right) - \frac{\partial}{\partial z}\left(q_{wz} C_{icFeOx}^{irrev}\right) \\ & + \phi S_w C_{cFeOx} \bar{s}_c k_i C_i \pm \gamma_c \left[\left(C_{icFeOx}^{irrev}\right)_{intra} - \left(C_{icFeOx}^{irrev}\right)_{inter}\right] \\ & + \phi S_w \left(\lambda_{ip} r_{ip}^M C_{ipcFeOx}^{irrev} - \lambda_i C_{icFeOx}^{irrev}\right).\end{aligned} \qquad \text{(Eq. 6.5.1.2-47)}$$

The one-dimensional mass balance equation for irreversibly sorbed radionuclide species *i* on iron oxyhydroxide corrosion products is the same as Equation 6.5.1.2-42, since there is no advection or diffusion of corrosion products:

$$\frac{\partial\left(\phi S_w C_{iCPFeOx}^{irrev}\right)}{\partial t} = \rho_b \bar{s}_{CP} k_i C_i + \phi S_w \left(\lambda_{ip} r_{ip}^M C_{ipCPFeOx}^{irrev} - \lambda_i C_{iCPFeOx}^{irrev}\right). \qquad \text{(Eq. 6.5.1.2-48)}$$

The one-dimensional mass balance equation for waste form colloid transport (from Equation 6.5.1.2-36) is:

$$\begin{aligned}\frac{\partial\left(\phi S_w C_{cWF}\right)}{\partial t} = & \frac{\partial}{\partial z}\left(\phi S_w D_c \frac{\partial}{\partial z} C_{cWF}\right) - \frac{\partial}{\partial z}\left(q_w C_{cWF}\right) \\ & + Q_{cWFs} \pm \gamma_c \left[\left(C_{cWF}\right)_{intra} - \left(C_{cWF}\right)_{inter}\right].\end{aligned} \qquad \text{(Eq. 6.5.1.2-49)}$$

Within the waste package, the media supporting transport are represented as single continua. In the UZ, however, the bulk medium is conceptualized as a dual continuum, characterized by two sets of local-scale properties unique to each continuum. Transport in the dual continuum media is represented by a mass balance equation for each continuum. The single invert continuum interfaces a dual continuum (fracture/matrix) UZ medium. Advective transport from the invert enters both the UZ fracture and matrix continua.

The diffusive fluxes to the dual UZ continua are determined from the flux continuity at the interface. This requirement states that the diffusive flux exiting the invert domain is equal to the sum of the diffusive fluxes entering the two UZ continua. The diffusive flux split will depend on the diffusive properties in the invert domain and both UZ continua together with the concentration gradients across the interface.

For discussion of the diffusive flux treatment at the invert/UZ interface consider a diffusive flux term, either aqueous or colloid flux, within the transport mass balance equation. Let $z_{interface}$ denote the spatial location of the invert/UZ interface. Then for $z < z_{interface}$, the diffusive flux for radionuclide species i at a location within the invert domain is:

$$\phi_I S_{wI} D_{iI} \frac{\partial C_{iI}}{\partial z}, \qquad \text{(Eq. 6.5.1.2-50)}$$

where ϕ_I is the porosity of the single-continuum invert domain.

For $z > z_{interface}$, the diffusive fluxes within the UZ matrix and UZ fracture media are, respectively,

$$\phi_m S_{wm} D_{im} \frac{\partial C_{im}}{\partial z}, \qquad \text{(Eq. 6.5.1.2-51)}$$

$$\phi_f S_{wf} D_{if} \frac{\partial C_{if}}{\partial z}. \qquad \text{(Eq. 6.5.1.2-52)}$$

For the case with no advection, the mass transport via diffusion across this interface is coupled by the flux continuity condition at the interface:

$$\phi_I S_{wI} D_{iI} \frac{\partial C_{iI}}{\partial z^-} = \phi_m S_{wm} D_{im} \frac{\partial C_{im}}{\partial z^+} + \phi_f S_{wf} D_{if} \frac{\partial C_{if}}{\partial z^+}, \qquad \text{(Eq. 6.5.1.2-53)}$$

where

$$\frac{\partial}{\partial z^-} \text{ and } \frac{\partial}{\partial z^+}$$

are the derivative from the left and the derivative from the right, respectively, at the interface.

The waste form colloids are generated in the waste form domain and are transported in accordance with an advective/diffusive mass balance. The waste form colloid concentration is subject to stability constraints based on the local domain chemistry. The waste form colloids transport both reversibly sorbed radionuclide mass and embedded (irreversibly sorbed) radionuclide mass. The iron oxyhydroxide colloids exist in the corrosion products and invert domains, and their concentrations are dependent on the local domain chemistry. The iron oxyhydroxide colloids transport both reversibly sorbed and irreversibly sorbed radionuclide

mass; the irreversibly sorbed radionuclides are sorbed onto the surface of these colloids, rather than being embedded within the colloid matrix, as are the radionuclides associated with the waste form colloids. The ground water colloids exist in the corrosion products and invert domains, and their concentrations are dependent on the local domain chemistry. The ground water colloids transport only reversibly sorbed radionuclide mass. The iron oxyhydroxide corrosion products are immobile and found only in the corrosion products domain. These corrosion products support both reversibly sorbed and irreversibly sorbed radionuclide mass. Since corrosion products are immobile, all radionuclide mass sorbed to corrosion products is not transported but is retarded.

All of the features of the EBS radionuclide transport abstraction are accounted for in Equations 6.5.1.2-38, 6.5.1.2-36, 6.5.1.2-41, and 6.5.1.2-42 (or the one-dimensional versions of these equations, Equations 6.5.1.2-46, 6.5.1.2-49, 6.5.1.2-47, and 6.5.1.2-48, respectively), including invert diffusion, retardation in the waste package, in-package diffusion, and transport facilitated by reversible and irreversible colloids. Implementation of these equations into TSPA-LA involves additional simplifications and restrictions that are discussed in Section 6.5.3.

6.5.1.2.1 Mathematical Description of In-Package Diffusion Submodel for Commercial Spent Nuclear Fuel Waste Packages

The objective of the in-package diffusion submodel is to quantify the uncertainty in the effective diffusion coefficient for diffusion of radionuclides through a breached waste package. Transport within the waste package can occur through advective or diffusive mechanisms. Advective transport occurs when a radionuclide, either as a dissolved species in an aqueous solution or attached to a colloidal particle, moves with a flowing fluid. Diffusive transport occurs when a radionuclide, either as a dissolved species in aqueous solution or attached to a colloidal particle, moves from a region of high concentration to a region of lower concentration in water that may be stagnant or flowing. Both advective and diffusive transport occur for those waste packages exposed to a seep environment in the repository. Only diffusive transport is anticipated to occur in those waste packages in the dry (no-seep) regions of the repository. In-package diffusion is an important process for release of radionuclides from the waste package, especially if no seepage occurs in large portions of the repository. This section provides a model to enable the impact of in-package diffusion on repository performance to be quantified.

The focus in this submodel is on diffusive releases from CSNF waste packages in no-seep regions of the repository. In a no-seep environment, the water saturation inside the CSNF waste package is computed as a function of relative humidity. In a seep environment, the water saturation in a CSNF waste package is set to 1.0, and is not dependent on the relative humidity in the waste package. For HLW packages, the water saturation is set to 1.0 in both seep and no-seep environments independently of the relative humidity in the waste package. HLW packages are treated differently from CSNF waste packages because the hygroscopic nature of HLW glass will result in a comparatively high water saturation at lower relative humidities than for CSNF.

In the EBS transport base model, the waste package is considered to be adjacent to the invert for purposes of calculating diffusive releases. This eliminates any resistance to diffusion between the waste package and the invert and maximizes estimated releases. If the first breaches are

stress corrosion cracks in the lid welds, the earliest diffusive path is through these cracks. The length of the diffusive path is taken to be the distance through the multiple lids on the waste package. This implies that the entire radionuclide inventory of the waste package is modeled as lying at the inside surface of the lid, which provides the maximum concentration gradient over a short distance, thereby maximizing calculated diffusive releases.

In reality, the internal components of the waste package will degrade slowly over thousands of years, keeping much of the radionuclides suspended within a crumbling framework, but nevertheless well dispersed throughout much of the interior of the canister. Even in its fully degraded state, when all internal components are completely corroded, the interior will consist of a large mass of porous corrosion products slumped in the bottom of the breached waste package, with radionuclides dispersed throughout. This dispersion inside a waste package is simply the result of the steel baskets, side guides, and inner vessel corroding at a faster rate than the Zircaloy fuel rods and assemblies. Thus, the actual diffusive path length can be greater than just the thickness of the lids, which reduces the rate of diffusive releases in comparison to the model where the radionuclide source is modeled as being adjacent to the interior surface of the waste package.

In a no-seep environment, the interior of a breached waste package will generally not be fully saturated with water. In this case, the only water present may be a thin film of adsorbed water that offers only a small diffusive area, which further hinders diffusive releases from the waste package.

These two conditions–a longer diffusive path length and a much smaller cross sectional area for diffusion–can delay or reduce the rate of predicted diffusive releases of radionuclides from the waste packages, relative to the EBS transport base model.

6.5.1.2.1.1 Conceptual Model for the Commercial Spent Nuclear Fuel In-Package Environment

Fuel rods are expected to be robust because the Zircaloy cladding around the fuel pellets is corrosion-resistant; at 100°C, the cladding remains intact for at least 100,000 years (CRWMS M&O 2000 [DIRS 136058], p. 48) barring damage from rockfalls. However, some fuel rods may be damaged while in use or during handling and shipping to the repository. A number of mechanisms cause fuel rod failure inside a reactor core, including damage from debris striking the rods, manufacturing defects, radiation-enhanced corrosion resulting in splitting of the rods, localized corrosion, and chafing where the rods contact the assembly spacer grids. Fuel rod cladding that has not failed (i.e., become perforated) is predicted to remain intact for the regulatory period (BSC 2004 [DIRS 170023], Section 1). Cladding that has failed is assumed to undergo instantaneous axial splitting after a waste package is breached (BSC 2004 [DIRS 170023], Assumption 5.3), exposing the fuel to the environment. These failed rods release radionuclides through diffusion once a waste package is breached, when a continuous film of liquid water is assumed (Assumption 5.5) to cover all the internal components of the waste package.

Baskets and guides support fuel rod assemblies inside a waste package for CSNF. These support components are fabricated from carbon steel and will begin to corrode once the waste package is

breached. Corrosion begins when the relative humidity is sufficient to produce aqueous conditions on the surface. The presence of deliquescent salts can result in aqueous conditions if the in-drift humidity is higher than the minimum deliquescent point of the salts (Campbell and Smith 1951 [DIRS 163817], p. 237). As the support components become thinner due to corrosion, they will weaken and eventually allow fuel rod assemblies to fall to the bottom of the waste package.

Corrosion of the internal support components will increase the surface area for adsorption of water and increase the area for diffusive transport, resulting in greater diffusive releases from the waste package. The fuel rods could also be bent if sections of the support components fail sooner than other parts. This could result in enhanced rod failure rates, with a greater mass of radionuclides available to diffuse out of a waste package.

The waste package inner vessel, made of Stainless Steel Type 316, has a long lifetime as computed from known general corrosion rates. However, the potential performance credit of the stainless steel inner vessel is not included in the nominal TSPA-LA analysis. As with the baskets and other waste form components (except for the fuel rods), the degradation of the inner vessel will provide additional surface area for adsorption of water and additional cross-sectional area for diffusion of radionuclides through the water film.

6.5.1.2.1.2 Adsorption of Water Vapor in Commercial Spent Nuclear Fuel Waste Packages

All surfaces exposed to water vapor will adsorb water. The amount of adsorbed water vapor depends principally on the nature of the material and the relative humidity. In many cases, the first layer of water adsorbed is chemically bound to the surface (McCafferty and Zettlemoyer 1971 [DIRS 154378], p. 239) and is difficult to remove except at high temperatures, higher than will exist in the repository. Subsequent layers are less tightly bound, being attracted simply by van der Waals forces to lower water layers. The first few layers of water often form an ice-like structure with little mobility. As the relative humidity approaches 100 percent, the outer layers of water begin to behave more like bulk liquid; at 100 percent relative humidity, bulk condensation of water occurs, forming a liquid phase.

Except for inert metals such as gold and platinum, most metals form a passivating oxide surface layer when exposed to oxygen or water. Oxygen diffuses slowly through the oxide layer; the resistance to oxygen diffusion protects the metal underneath. In the case of Alloy 22, stainless steel, Zircaloy, and aluminum–metals found in the waste package or waste form–the surface oxide layer is passivating. Thus, all metals in a waste package contain a surface oxide layer on which water adsorption takes place.

Adsorption isotherms define the amount of water adsorbed as a function of relative humidity or relative pressure, provided sufficient time is allowed for equilibrium to be achieved. Extensive measurements have been made for a few substances, such as iron oxide and titanium oxide, but adsorption isotherms are only available for a few materials. Isotherms for metal oxides found in waste packages have been measured for NiO, Fe_2O_3, and ZrO_2. Isotherms for other major components of stainless steel, such as Cr_2O_3 and Mo_2O_3, are not readily available. However, the oxides of iron, nickel, and zirconium make up the bulk of oxides in a package and are representative of in-package materials. Figure 6.5-4 presents the adsorption isotherms for Fe_2O_3, NiO, and ZrO_2.

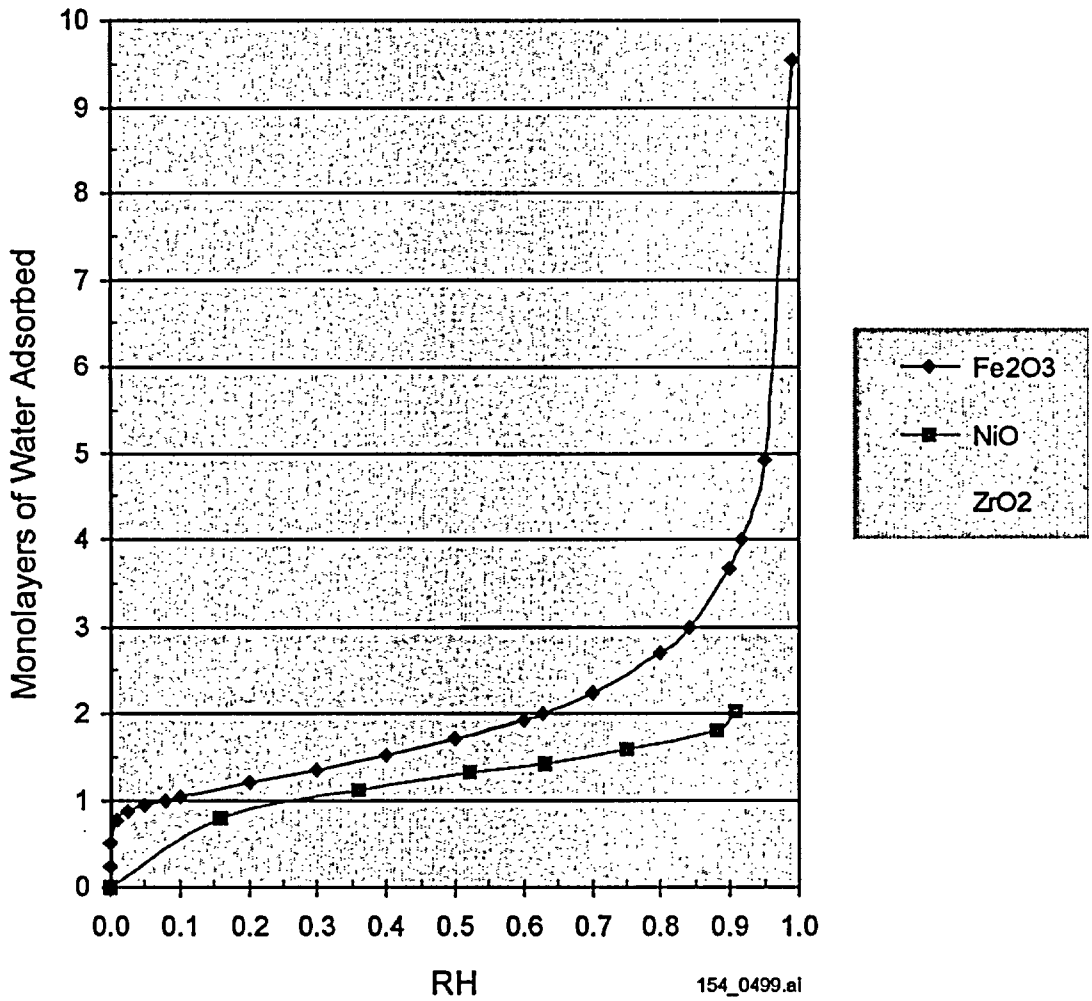

Sources: Jurinak 1964 [DIRS 154381]; Lee 1994 [DIRS 154380]; Holmes et al. 1974 [DIRS 154379].

Figure 6.5-4. Comparison of Adsorption Isotherms for Water Vapor on Fe_2O_3, NiO, and ZrO_2

6.5.1.2.1.2.1 Iron Oxide Isotherm

The isotherm for adsorption of water onto α-Fe_2O_3, a form of hematite, has been extensively measured and reported in the literature (McCafferty and Zettlemoyer 1970 [DIRS 154382]; Jurinak 1964 [DIRS 154381]). These measurements are directly relevant to the repository because (1) hematite will be the predominant form of iron oxide in a degrading waste package (YMP 1998 [DIRS 104441], p. C-23), and (2) hematite will comprise the bulk of the corrosion products in the waste package, because iron is the largest constituent of waste package internal components, as shown in Table 6.5-9 for the three major types of steel used in the 21-PWR waste package components. The contents of Table 6.5-9 are derived from compositional data presented in Table 4.1-10.

Jurinak (1964 [DIRS 154381], p. 486) provides a functional relationship for the coverage (i.e., number of monolayers of water adsorbed) as a function of relative humidity based on the Frenkel-Halsey-Hill (FHH) equation for multilayer adsorption:

$$\log_{10}\left(p_w / p_w^\circ\right) = -\frac{k}{\left(V / V_m\right)^s}, \qquad \text{(Eq. 6.5.1.2.1-1)}$$

where

p_w = partial pressure of water (Pa)
p_w° = vapor pressure of water (Pa)
k = FHH adsorption isotherm fitting parameter (dimensionless)
s = FHH adsorption isotherm fitting parameter (dimensionless)
V = volume of water vapor adsorbed at reference conditions (m^3 H_2O kg^{-1} Fe_2O_3)
V_m = volume of adsorbed water vapor that provides a one-monolayer coverage on the surface (m^3 H_2O kg^{-1} Fe_2O_3).

The ratio of water vapor partial pressure to vapor pressure is the relative humidity (RH). The ratio of V to V_m is the number of monolayers of water (i.e., the number of layers of individual water molecules) adsorbed on the surface, assuming complete and uniform coverage. Letting $\theta_a = V / V_m$ and $RH = p_w / p_w^\circ$, and making use of the relationship to convert base 10 logarithms to natural logarithms ($\log_{10} RH = \log_{10} e^{\ln RH} = \ln RH \log_{10} e$), Jurinak's correlation may be written in general terms with parameters k and s:

$$\ln(RH) = -\frac{k}{\theta_a^s \log_{10} e}, \qquad \text{(Eq. 6.5.1.2.1-2)}$$

or

$$\theta_a = \left(\frac{k}{\log_{10} e}\right)^{\frac{1}{s}} \left[-\ln(RH)\right]^{-1/s}. \qquad \text{(Eq. 6.5.1.2.1-3)}$$

For Fe_2O_3, $k = 1.1$ and $s = 2.45$ (Jurinak 1964 [DIRS 154381], p. 486):

$$\ln(RH) = -2.5328\theta_a^{-2.45} \qquad \text{(Eq. 6.5.1.2.1-4)}$$

or

$$\theta_a = 1.461296\left[-\ln(RH)\right]^{-0.40816}. \qquad \text{(Eq. 6.5.1.2.1-5)}$$

This isotherm is plotted in Figure 6.5-4.

The average thickness of a monolayer of water can be computed from the cross-sectional area of a water molecule. Holmes et al. (1974 [DIRS 154379], p. 368) use a value of 10.6 $Å^2$ for the cross-sectional area of a water molecule. Jurinak (1964 [DIRS 154381]) assumes a

cross-sectional area of 10.8 Å^2 for a water molecule. McCafferty and Zettlemoyer (1970 [DIRS 154382], p. 453) report a single value of 10 m^2 g^{-1} for "nominal argon surface area" and assume a cross-sectional area of the water molecule of 10.6 Å^2. Gregg and Sing (1982 [DIRS 153010], p. 188) state that a "close-packed" monolayer of water corresponds to a figure of 10.5 Å^2 for the cross-sectional area of a water molecule. In this report, a value for the cross-sectional area of a water molecule of $A_w = 10.6$ Å^2 per molecule (McCafferty and Zettlemoyer 1970 [DIRS 154382], p. 454) is used. Using a water density at 25°C of $\rho_w = 997.0449$ kg m^{-3} (Weast 1985 [DIRS 111561], p. F-5), the thickness of a water monolayer, t_f, is:

$$t_f = \frac{M_w}{A_w \rho_w N_A}$$

$$= \frac{18.01528\times10^{-3}\ \frac{\text{kg}}{\text{mol}}}{\left(10.6\times10^{-20}\ \frac{\text{m}^2}{\text{molec}}\right)\left(997.0449\ \frac{\text{kg}}{\text{m}^3}\right)\left(6.02214199\times10^{23}\ \frac{\text{molec}}{\text{mol}}\right)} \qquad \text{(Eq. 6.5.1.2.1-6)}$$

$$= 2.83\times10^{-10}\ \text{m},$$

where N_A is Avogadro's number (Lide 2002 [DIRS 160832], p. 1-7), and M_w is the molecular weight of water (kg mol^{-1}).

At 50°C, the density of water is 988.0363 kg m^{-3} (Weast 1985 [DIRS 111561], p. F-5) and the adsorbed water monolayer thickness is 2.85 × 10^{-10} m, which shows that the monolayer thickness sensitivity to temperature is small.

The adsorption isotherm for water vapor on ZrO_2 at 25°C (Holmes et al. 1974 [DIRS 154379], p. 367, Figure 3) is shown in Figure 6.5-4 as monolayers of water adsorbed; Table 6.5-5 lists the same data, taken from Figure 3 of Holmes et al. and given in units of mg water adsorbed g^{-1} ZrO_2. The conversion from mg g^{-1} to monolayers adsorbed is made using 14.5 m^2 g^{-1} for specific surface area (Holmes et al. 1974 [DIRS 154379], p. 368; average of 2 values):

$$\frac{\left(14.5\ \frac{\text{m}^2}{\text{g ZrO}_2}\right)\left(18.01528\times10^{3}\ \frac{\text{mg H}_2\text{O}}{\text{mol}}\right)}{\left(10.6\times10^{-20}\ \frac{\text{m}^2}{\text{molecule}}\right)\left(6.0221419947\times10^{23}\ \frac{\text{molecule}}{\text{mol}}\right)} = 4.092\ \frac{\text{mg H}_2\text{O}}{\text{g ZrO}_2}/\text{monolayer}.$$

(Eq. 6.5.1.2.1-7)

Table 6.5-5. Adsorption of Water on ZrO_2 at 25°C, Outgassed at 500°C

RH	Water Adsorbed on ZrO_2 (mg g^{-1})
0.010	5.54
0.050	6.92
0.100	7.76
0.150	8.53
0.200	9.12
0.300	10.4
0.400	11.52
0.500	12.80
0.600	14.56
0.658	16.00
0.700	17.81
0.784	24.00
0.840	32.00
0.880	40.00
0.917	48.00
0.947	56.00

Source: Holmes et al. 1974 [DIRS 154379], p. 367; taken from "Adsorption" curve on Figure 3.

6.5.1.2.1.2.2 Behavior of Thin Water Films

In this section, the behavior of thin films of water is described. It is assumed in the *EBS RT Abstraction* that continuous thin films of adsorbed water will cover all surfaces inside a breached waste package and that these films behave the same as bulk liquid (Assumption 5.5). In order to understand the bounding nature of this assumption and how it leads to overestimating releases of radionuclides from the EBS, it is necessary to understand the actual behavior of thin films.

Water at solid surfaces varies in nature from a highly structured form on hydrophilic substrates to a loose, entropic form on more hydrophobic substrates possessing hydrophilic sites (Lee 1994 [DIRS 154380], p. 74). The adsorption of water on solids depends on the capacity of the surface to orient the water dipoles, usually with the proton outward. Near polar surfaces of solids such as metal and oxides, the cause of the orientation of water molecules at the interface could be either hydrogen bonding or dipole-dipole interactions, depending on the chemical nature of the solid. Depending on the dissimilarity between the ordered (dipole-dipole), induced structure near the interface and the bulk structure, various thicknesses of the ordered layers are possible (Lee 1994 [DIRS 154380], p. 75).

The structure of liquid water is considered to consist of unbonded molecules and of molecules hydrogen-bonded in clusters that have a mean size of about 90 molecules at 0°C (Lee 1994 [DIRS 154380], p. 79). At hydrophilic surfaces, such as oxides, the structure of water resembles that of ice (McCafferty and Zettlemoyer 1971 [DIRS 154378], p. 239). This behavior is attributed to the existence of a monolayer in which the adsorbed water is held rigidly to the solid surface at fixed sites. The first layer is localized by double hydrogen bonding of a single water molecule to two surface hydroxyls. This highly constrained first layer relaxes in the next layers,

where the water molecules start to possess a rotational degree of freedom, being singly hydrogen-bonded. The second layer becomes more ordered when hydrogen bonds to a third layer, and so on, until the ordering effect of the surface is overcome and bulk liquid layers form farther from the surface. On a hydrophobic surface, such as silica, different behavior is observed. When half of the surface hydroxyls on silica are occupied by water, the water starts to agglomerate into clusters instead of adsorbing uniformly over the surface.

Layers of water adsorbed on an oxide surface can promote lateral ion movement, which sets up localized electrochemical cells due to inhomogeneities in the underlying metal (Lee 1994, [DIRS 154380] p. 141). Such cells promote localized corrosion. Surface water dipoles may act to shield oxygen ions from an internal field that promotes ion movement. On the other hand, the gel-like structure of a metal oxyhydroxide may not support the charge separation that normally accounts for the field-driven process. Instead, ion movement may take place under the influence of a concentration gradient. The first layers of adsorbed water often do not contain ions from the solid (Lee 1994 [DIRS 154380], p. 73). This says that multiple water layers are needed in order for solid species (such as radionuclides) to dissolve and diffuse.

6.5.1.2.1.3 Specific Surface Areas of Component Materials

6.5.1.2.1.3.1 Specific Surface Area for Metal Oxides

Most studies of the nature of adsorbed water at solid surfaces have been done with solid powders whose specific surface area is at least 5 $m^2 g^{-1}$. Such high interfacial areas are required for sufficient sensitivity in the measurements of adsorbed mass using routine gravimetric techniques. However, the use of surface areas of 10 to 20 $m^2 g^{-1}$ typical of the samples used in adsorption studies for Fe_2O_3 and ZrO_2 results in predicted quantities of adsorbed water being larger than might be realistically expected for materials with lower specific surface area such as hematite corrosion products, resulting in an overestimation of the amount of radionuclides released by purely diffusive mechanisms.

Values for the specific surface area of α-Fe_2O_3 (hematite) shown in Table 6.5-6 range from 1.8 to 21.4 $m^2 g^{-1}$. At the low end is "natural" hematite, with a specific surface area of 1.8 $m^2 g^{-1}$ (Langmuir 1997 [DIRS 100051], Table 10.2). At the high end is a sample of Fe_2O_3 used in an analysis of its catalytic activity (Briand et al. 2001 [DIRS 161617], Table 4). Morimoto et al. (1969 [DIRS 162877], Table I) and Tamura et al. (1999 [DIRS 161625], Table 1) each report two values for Fe_2O_3 samples prepared by different methods that differ by factors of 1.5 and 2.8, respectively. These results illustrate how the method of preparation can have a large effect on the specific surface area of a material. Gregg and Sing (1982 [DIRS 153010], p. 188) report surface area measurements of a material identified only as "iron oxide" by mercury porosimetry and by nitrogen adsorption.

Jurinak (1964 [DIRS 154381], p. 480) measured surface area of Fe_2O_3 by nitrogen adsorption ranging from 9.60 to 9.70 $m^2 g^{-1}$, whereas water adsorption surface areas ranged from 6.52 to 9.10 $m^2 g^{-1}$. It was concluded that about one-third of the Fe_2O_3 is covered with chemisorbed water that, unless removed by activation (i.e., heating to at least 425°C), blocks water adsorption sites on the surface. The latter value (9.10 $m^2 g^{-1}$) is used in sample calculations in the *EBS RT Abstraction,* because it is consistent with the water adsorption isotherm of Jurinak that is used.

The value of 10.0 $m^2 g^{-1}$ reported by McCafferty and Zettlemoyer (1970 [DIRS 154382], p. 453) is close to that of Jurinak and is consistent with their water adsorption isotherm, which is used in Section 7.2.1 to corroborate the isotherm of Jurinak (1964 [DIRS 154381]).

The specific surface area of Fe_2O_3 plays an important role in the EBS radionuclide transport abstraction because all corrosion products are assumed to be hematite (Assumption 5.6). It is appropriate to account for the uncertainty in the measured values of the specific surface area by sampling the value. A range from 1.0 $m^2 g^{-1}$ to 22 $m^2 g^{-1}$ covers the range of observed values. A uniform distribution is assigned to this parameter in order to achieve an unbiased sampling of the full range of variability.

In example calculations in Section 6.5.1.2.1 (e.g., Tables 37 and 38), a value of 9.1 $m^2 g^{-1}$ obtained by Jurinak (1964 [DIRS 154381], p. 480) is generally used in order to be consistent with the water vapor adsorption isotherm of Jurinak that is used in the in-package diffusion submodel. However, it is appropriate in the in-package diffusion submodel to use any value of specific surface area for Fe_2O_3 within the range specified for this uncertain parameter.

Table 6.5-6. Specific Surface Area of Fe_2O_3

Specific Surface Area ($m^2 g^{-1}$)	Source
9.1	Jurinak 1964 [DIRS 154381], p. 480
10	McCafferty and Zettlemoyer 1970 [DIRS 154382], p. 453
13.3 – 14.3	Gregg and Sing 1982 [DIRS 153010], Table 3.17
21.4	Briand et al. 2001 [DIRS 161617], Table 4
14.5	Morimoto et al. 1969 [DIRS 162877], Table I (treated at 250°C; from calcinations of $FeSO_4.7H_2O$)
21.2	Morimoto et al. 1969 [DIRS 162877], Table I (treated at 250°C; from calcinations of α-FeOOH)
15.9	Tamura et al. 1999 [DIRS 161625], Table 1 (NaOH method)
5.60	Tamura et al. 1999 [DIRS 161625], Table 1 (Grignard method)
1.8	Langmuir 1997 [DIRS 100051], Table 10.2 (natural hematite)
3.1	Langmuir 1997 [DIRS 100051], Table 10.2 (synthetic hematite)

For ZrO_2, Holmes et al. (1974 [DIRS 154379], pp. 367 to 368) measured specific surface areas by nitrogen adsorption and by argon adsorption; the average value was 14.5 $m^2 g^{-1}$.

The products of the corrosion of all internal waste package components except for fuel rods and SNF are assumed to be Fe_2O_3 (hematite) (Assumption 5.6). The bulk of the mass of materials in a CSNF waste package, excluding the SNF itself and the outer corrosion barrier of the waste package, consists of various types of steel. The iron content of these steels (see Table 6.5-9 below) ranges from 61.935 weight percent (Type 316, used in the inner vessel; DTN: MO0003RIB00076.000 [DIRS 153044]) to 98.37 weight percent (A 516 carbon steel, used in the basket components; DTN: MO0107TC240032.000 [DIRS 169970]). It is thus reasonable to treat all corrosion products as iron oxide, specifically Fe_2O_3 (hematite), for which specific surface area and adsorption data are readily available. The specific surface areas of some other waste package component corrosion products are shown in Table 6.5-7, which demonstrates that the bulk of corrosion products exhibit similar adsorption characteristics.

Table 6.5-7. Specific Surface Area of Various Waste Package Corrosion Products

Corrosion Product	Specific Surface Area ($m^2 g^{-1}$)	Source
Cr_2O_3	3.0	Briand et al. 2001 [DIRS 161617], Table 4
	1.09	Tamura et al. 1999 [DIRS 161625], Table 1
	12.0	Nagao et al. 1995 [DIRS 162878], p. 222
NiO	1.1	Briand et al. 2001 [DIRS 161617], Table 4
	22.4	Matsuda et al. 1992 [DIRS 154383], p. 1839 [for NiO(II)]
CoO	0.4	Briand et al. 2001 [DIRS 161617], Table 4
MoO_3	5.0	Briand et al. 2001 [DIRS 161617], Table 4
UO_2 (SNF)	0.4	BSC 2004 [DIRS 167618], Table 6-9 (Group 8b)
TiO_2	9.94	Morimoto et al. 1969 [DIRS 162877], Table I
ZrO_2	14.5	Holmes et al. 1974 [DIRS 154379], p. 368; average of 2 values
	39.0	Briand et al. 2001 [DIRS 161617], Table 4

6.5.1.2.1.3.2 Interior Surface Area for Commercial Spent Nuclear Fuel Waste Package

The internal surface area of an as-emplaced waste package (i.e., in an undegraded state) containing CSNF can be approximated if the dimensions and numbers of fuel rods, baskets, side guides, and other support components are known. Since the surface area will increase by orders of magnitudes as the waste package components degrade, the initial surface area is useful only as a limiting value, but one that can be estimated accurately (unlike the surface area of corrosion products). Typical measurements for a 21-PWR waste package are used (BSC 2004 [DIRS 169472], Table 1). The surface areas of fuel assembly spacer grids and end connections are ignored. The total internal surface area of a 21-PWR waste package as emplaced is approximately 1061 m^2. The surface area of basket components is computed as shown in Table 6.5-8 (footnote h) by dividing the total mass of each component by the density of the material (which gives the volume of material), then dividing by the thickness of the component. This results in the area of component material as though it were a plate, ignoring the area of edges. To account for both sides of the component being exposed to air and able to adsorb water, the area is multiplied by two.

The calculation of pore volume for a CSNF waste package is also summarized in Table 6.5-8. From these results, the initial porosity of an average 21-PWR waste package is determined to be 5.63/9.62 = 0.58.

Table 6.5-8. Characteristics of a 21-PWR Waste Package

Component	Dimensions[a]	Qty. in WP[b]	Mass[b] (kg)	Density (kg m^{-3})	Total Surface Area (m^2)	Total Volume[j] (m^3)
Fuel Rods	0.94996 cm OD[c]; 384.962 cm length[c]	5,544	—	—	636.93	1.513
Basket Side Guide	9.525 mm thickness	16	24.9	7,850[d]	10.66[h]	0.051
Basket Side Guide Stiffener	9.525 mm thickness	32	0.615	7,850[d]	0.53[h]	0.003
Basket End Side Guide	9.525 mm thickness	32	32.7	7,850[d]	27.99[h]	0.133
Basket End Guide Stiffener	9.525 mm thickness	64	1.38	7,850[d]	2.36[h]	0.011
Basket Corner Guide	9.525 mm thickness	16	40.1	7,850[d]	17.16[h]	0.082
Basket Corner Guide Stiffener	9.525 mm thickness	32	2.07	7,850[d]	1.77[h]	0.008
Fuel Basket A-Plate	7 mm thickness	8	86.8	7,760[e]	25.57[h]	0.089
Fuel Basket B-Plate	7 mm thickness	8	86.8	7,760[e]	25.57[h]	0.089
Fuel Basket C-Plate	7 mm thickness	16	45.8	7,760[e]	26.98[h]	0.094
Fuel Basket D-Plate	6.35 mm thickness	8	27.4	2,700[f]	25.57[h]	0.081
Fuel Basket E-Plate	6.35 mm thickness	8	27.4	2,700[f]	25.57[h]	0.081
Basket Tube	4,572 mm length[l]; 231.648 mm interior dimension[k]; 241.173 mm exterior dimension[m]	21	159	7,850[d]	181.59	0.425
Inner Vessel	1.4859 m ID[k]; 1.5875 m OD[k]; 4.5847 m cavity length[l]	1	9,920	8,000[g]	49.10	1.240
Inner Lid	1.4859 m vessel ID[k] 0.0508 m thickness[n]	1	739	8,000[g]	3.37	0.088
Total Surface Area					**1,061**	—
Total Volume[i]					—	**9.62**
Total Solids Volume					—	**3.99**
Total Void Volume					—	**5.63**

[a] Thicknesses from BSC 2004 [DIRS 169472], Table 2.
[b] Quantity (number) and mass of components in a 21-PWR waste package from BSC 2004 [DIRS 169472], Table 2.
[c] DOE 1992 [DIRS 102588], Volume 1, p. 2A-30. 264 rods/assembly. W1717WL chosen as average assembly.
[d] ASTM A 20/A20M-99a [DIRS 147578] (A 516 carbon steel).
[e] Kügler 1996 [DIRS 107760], p. 17 (Neutronit A 978).
[f] ASTM G 1-90 [DIRS 103515], p. 7, Table X1 (Al 6061).
[g] DTN: MO0003RIB00076.000 [DIRS 153044] (316 stainless steel).
[h] Surface Area = $2mN/(\rho\Delta x)$; m = mass (kg); N = quantity; ρ = density (kg m^{-3}); Δx = thickness (m); "2" accounts for 2 sides of a plate; edges ignored.
[i] Volume enclosed by Alloy 22 outer corrosion barrier having an inside diameter of 1.597 m (BSC 2004 [DIRS 166953], Section B-B) and inside length of 4.80374 m = 5,024.4 mm (total length, BSC 2004 [DIRS 166953], Section A-A) – 25.4 mm (lid lifting device thickness, BSC 2004 [DIRS 167394], Detail C) – 101.6 mm (bottom skirt, BSC 2004 [DIRS 167394], Detail B) – 25.4 mm (top outer lid thickness, BSC 2004 [DIRS 167394], Detail A) – 25.4 m (bottom outer lid thickness, BSC 2004 [DIRS 167394], Detail B) – 30.16 mm (middle lid to outer lid gap, BSC 2004 [DIRS 167394], Detail A) – 12.7 mm (middle lid, BSC 2004 [DIRS 167394], Detail A).
[j] Except for fuel rod volume, Volume = mN/ρ. See footnote h for nomenclature.
[k] BSC 2004 [DIRS 166953], Section B-B.
[l] BSC 2004 [DIRS 166953], Section A-A.
[m] Outside dimension = inside dimension + 2 × thickness = 9.12 in. (BSC 2004 [DIRS 166953], Section B-B) + 2 × 3/16 in(BSC 2004 [DIRS 169472], Table 2) = 231.648 mm + 2 (4.7625 mm) = 241.173 mm.
[n] BSC 2004 [DIRS 167394], Details A and B.
ID = inside diameter; OD = outside diameter; WP = waste package

An estimate of the waste package porosity in a fully degraded state can be obtained using the total potential equivalent mass of Fe_2O_3 in a 21-PWR from the corrosion of non-SNF components as shown in Table 6.3-4. The 19,440 kg equivalent mass of corrosion products from the iron comprising the steel internal components has a volume of (density of Fe_2O_3 from Weast (1985 [DIRS 111561], p. B-104):

$$\frac{19440\,\text{kg}\,Fe_2O_3}{5240\,\dfrac{\text{kg}\,Fe_2O_3}{\text{m}^3\,Fe_2O_3}} = 3.710\,\text{m}^3\,Fe_2O_3. \qquad \text{(Eq. 6.5.1.2.1-7a)}$$

The internal volume of a 21-PWR waste package outer corrosion barrier, with an inside diameter of 1.597 m and length of 4.8038 m, is 9.62 m^3 (from Table 6.5-8). The 5,544 fuel rods have a total volume of 1.513 m^3. Then the void volume that can be occupied by corrosion products is 8.110 m^3. If the corrosion products are uniformly dispersed throughout that volume, their porosity is: 1 - (3.710/8.110) = 0.54.

Lamination and flaking of corrosion products is expected to redistribute this material within the waste package pore space (Knight 1982 [DIRS 106733], p. 50), rather than leave it uniformly distributed throughout the waste package void volume. If the oxide settles to the bottom of a waste package, the physical geometry of the granular iron oxide that has settled can be represented by that of tightly packed sand, which has a solid content of 58 percent (Brown and Richards 1970 [DIRS 131479], Table 2.2), or a porosity of 0.42 (CRWMS M&O 1997 [DIRS 102824], p. 29). This value (0.42) for corrosion products porosity within a waste package has been used in criticality studies (CRWMS M&O 1997 [DIRS 102824], p. 29) and in an independent performance assessment of the Yucca Mountain repository (EPRI 2000 [DIRS 154149], p. 6-21 to 6-22). A porosity of 0.4 has been used in other criticality studies (YMP 1998 [DIRS 104441], p. C-23 to C-25) and in a model of diffusive releases from breached waste packages (Lee et al. 1996 [DIRS 100913], p. 5-67). A value of 0.4 is used for porosity of corrosion products in TSPA-LA.

In the calculation shown in Table 6.5-8, all the fuel rods are intact. The surface area of intact fuel rods accounts for about 62 percent of the total initial surface area. SNF pellets are generally highly fractured and can contribute to the surface area available for adsorption when a waste package is first breached. However, water adsorbed on the fuel itself constitutes the "rind" water (i.e., water in the conceptual waste form domain). It does not directly affect diffusion to the exterior of the waste package because the fuel is the source, rather than part of the corrosion products that comprise the diffusive path to the exterior.

Over time, the surface area of steel corrosion products would be expected to increase relative to the surface area of ZrO_2, since the cladding is predicted to degrade and fail at a slower rate than iron-based materials. In principle, the surface area inside a waste package can be computed as a function of time, if the degradation rates of the basket components and the stainless steel inner vessel and the failure rate of fuel rods are known. The calculation is complicated by the different compositions of each component of the waste package. Spatial variability in degradation rates due to variations in accessibility to water vapor further complicate the picture. For example, the fuel rod assemblies in 44-BWR waste packages are enclosed in flow tubes that provide added

protection from corrosion over 21-PWR fuel rod assemblies. However, an average corrosion rate for a 21-PWR waste package provides a reasonable approximation from which surface areas and quantities of adsorbed water can be computed.

The complete degradation of a 21-PWR waste package gives an estimated upper bound on the surface area available for adsorption. For this bounding estimate, the assumption is made that all corrodible material inside a 21-PWR waste package completely oxidizes to Fe_2O_3. The mass of each major component for four types of waste package is listed in Table 6.3-4. The amounts and composition of each waste package component are converted to total moles of material in Table 6.5-9.

The masses of materials differ little between the two types of waste packages for commercial SNF (21-PWR and 44-BWR), and all other types of packages comprise a much smaller fraction of the total waste in the repository. Therefore, the calculation is performed for the 21-PWR waste package as representative of all packages in the repository. Suppose that the stainless steel inner vessel fully corrodes, but that the Alloy 22 outer corrosion barrier remains intact (except for breaches, the sizes of which are neglected). Also suppose that the Zircaloy fuel claddings and assembly grid spacers do not degrade because the Zircaloy will remain uncorroded for tens of thousands of years after the steel has fully corroded.

Based on the elemental composition of each material shown in Table 6.5-9, the mass of each material listed in Table 6.5-8 is converted to moles by element. The moles of material, now considered to be iron, are summed, and the stoichiometrically equivalent amount of Fe_2O_3 in the waste package is determined. Using the measured surface area of Fe_2O_3, the total surface area for adsorption is calculated for the basket materials and inner vessel. This value provides an upper bound estimate for the surface area for adsorption in a completely degraded waste package.

The total amount of material in a 21-PWR waste package (treated as though it were iron) is 346,330 mol (see lower right-hand entry in Table 6.5-9). This iron will oxidize to 27,700 kg Fe_2O_3. Using a specific surface area of 9.1 $m^2\ g^{-1}$ for the oxide (Jurinak 1964 [DIRS 154381], p. 480), the estimated upper bound for total surface area for adsorption in a 21-PWR waste package is 2.5×10^8 m^2/package.

This approach differs from that used to estimate retardation in the waste package in that the latter used only the actual iron content of waste package components to determine the adsorptive capacity of corrosion products. Both approaches are bounding for their intended purposes. For the retardation calculation, the mass of sorbant in the waste package is underestimated, which in turn underestimates the amount of retardation that occurs in the waste package, maximizing the releases of radionuclides. For in-package diffusion, the surface area for adsorption of water is overestimated, resulting in an overestimation of diffusive releases. The higher estimate of total corrosion products mass is used in this section to analyze the relationship between corrosion products mass and waste package water saturation. However, for consistency, the mass developed for modeling in-package retardation (19,440 kg; see Table 6.3-4) is used in the EBS transport abstraction.

The surface area of the interior of a waste package at any particular time is estimated by interpolating between the surface area when the waste package is initially breached and the area at the time when the internal components are fully corroded. The latter is the estimated lifetime of each component that is determined by dividing the thickness of each component by the corrosion rate of the material that makes up the component under some given conditions.

For simplicity, the components are considered to be composed of either stainless steel or carbon steel. The maximum thickness of stainless steel in the interior of a waste package is 5 cm, which is the thickness of the inner vessel (BSC 2004 [DIRS 169472], Table 1; BSC 2004 [DIRS 166953], Section B-B). The maximum thickness of any carbon steel component is 10 mm (BSC 2004 [DIRS 169472], Table 1).

The corrosion rates for the two types of steel are known with some uncertainty, as shown by the data presented in Table 4.1-1 for carbon steel and for stainless steel (DTN: MO0409SPAACRWP.000 [DIRS 172059]). The data set used is for corrosion rates at 60°C in simulated dilute well J-13 water. The average corrosion rate for carbon steel is 77.43 $\mu m\ yr^{-1}$, with a standard deviation of 8.83 $\mu m\ yr^{-1}$ (DTN: MO0409SPAACRWP.000 [DIRS 172059]). An empirical cumulative distribution function developed in DTN: MO0409SPAACRWP.000 [DIRS 172059] is used for parameter CS_Corrosion_Rate to be sampled in TSPA-LA. The TSPA-LA implementation in GoldSim requires that the cumulative distribution functions (CDFs) cover the entire range of probabilities of 0.0 to 1.0. To accommodate this, another row for the zeroth percentile is added using a corrosion rate that is slightly lower than the minimum in the empirical cumulative distribution function (ECDF); this row is 65.76 $\mu m\ yr^{-1}$ and zero probability.

The mean corrosion rate for Stainless Steel Type 316L is 0.248 $\mu m\ yr^{-1}$, with a standard deviation of 0.146 $\mu m\ yr^{-1}$ (DTN: MO0409SPAACRWP.000 [DIRS 172059]). The data set used is for corrosion rates in fresh water for the temperature range of 50°C to 100°C. An ECDF developed in DTN: MO0409SPAACRWP.000 [DIRS 172059] is used for parameter SS_Corrosion_Rate to be sampled in TSPA-LA. As with carbon steel, the TSPA-LA implementation in GoldSim requires that the CDFs cover the entire range of probabilities of 0.0 to 1.0. To accommodate this, another row for the zeroth percentile is added using a corrosion rate that is slightly lower than the minimum in the ECDF; this row is 0.03699 $\mu m\ yr^{-1}$ and zero probability.

From these rates and the thicknesses of the steel components, the lifetime of each type of steel is computed. From Table 6.3-4 above, carbon steel comprises about one-third of the total mass of steel in a CSNF waste package (30 percent in a 21-PWR; 33 percent in a 44-BWR). Based on this fraction, the surface area is interpolated over time. More details of the implementation of this interpolation scheme are presented in Section 6.5.3.2.

Although this interpolation provides a reasonable means for approximating the surface area of the interior of a waste package over time as it degrades, there is still uncertainty as to the actual surface area. The corrosion rates themselves are uncertain. In addition, many factors affect the surface area of the corrosion products. The chemical and physical conditions under which corrosion takes place impacts the morphology of the corrosion products. Seismic occurrences and collapse of the internal components as they degrade will affect the surface area. The

hematite samples used in adsorption isotherm measurements are typically finely ground and highly purified, and have a higher specific surface area than typical corrosion products. At the same time, the morphology of corrosion products inside a waste package over the course of thousands of years is so uncertain that specific surface areas higher than purified hematite are possible.

Therefore, when the surface area of the corrosion products is computed, it is justifiable to factor in this uncertainty by using a sample specific surface area for corrosion products, ranging from 1.0 $m^2 g^{-1}$ to 22 $m^2 g^{-1}$. This range is large enough to reflect the uncertainty in the condition of the corrosion products. It reflects the uncertainty observed in measurements of the specific surface area of hematite (Table 6.5-6), as well as the fact that iron oxides do not adhere to the metal surface and may slough off in a finely divided state. Swelling as oxygen is incorporated into the crystal structure may provide a mechanism for breaking up the corrosion products more finely. Under certain conditions, iron oxyhydroxide colloid particles (0.001 to 1 μm) having a potentially enormous surface area may form in the waste package (BSC 2004 [DIRS 170025], Section 6.3.1.3). At the same time, in such a static environment as an enclosed waste package, where, as is the case here, no water is flowing through the waste package to stir up or erode the corrosion products, it is unlikely that such finely divided materials will form. The range attempts to account for the absence mechanisms that actively break up the mass of corrosion products, the lack of water with which to suspend and move particles apart, and the possibility that swelling against enclosures may agglomerate particles into low-surface-area masses.

Table 6.5-9. Elemental Composition of Each Waste Package Material in a 21-PWR

	Stainless Steel Type 316		A 516 Steel		Neutronit A 978		Aluminum 6061		Total
Material Mass	10,800 kg		5,600 kg		2,120 kg		440 kg		
	wt% [a]	mol	wt% [b]	Mol	wt% [c]	mol	wt% [d]	mol	mol
Fe	61.935	119,780	98.37	98,630	66.06	25,100	0.7	60	243,570
Mo	3.00	3,380	0	0	2.2	490	0	0	3,860
Cr	18.00	37,390	0	0	18.5	7,550	0.35	30	44,970
Ni	14.00	25,760	0	0	13.0	4,700	0	0	30,460
Al	0	0	0	0	0	0	95.85	15,570	15,570
Other	3.065	5,930	1.63	1,630	0.24	90	3.1	240	7,900
Total	100	192,240	100	100,260	100	37,930	100	15,900	346,330

Source: Material mass: Table 6.3-4.

NOTE: "Other" is treated as iron.

[a]Composition: DTN: MO0003RIB00076.000 [DIRS 153044].
[b]Composition: DTN: MO0107TC240032.000 [DIRS 169970].
[c]Composition: Kügler 1991 [DIRS 155761], p. 15.
[d]Composition: ASM 1979 [DIRS 154085], p. 115.

6.5.1.2.1.4 Cross-Sectional Areas, Diffusion Path Lengths, and Effective Diffusivity

6.5.1.2.1.4.1 Diffusion Coefficient in the Waste Package

The rate of diffusion of radionuclide species i, q_i (kg i s^{-1}), from a waste package to the exterior is given by:

$$q_i = -D_s A \frac{\partial C_i}{\partial x} \approx -D_s A \frac{\Delta C_i}{\Delta x}, \qquad \text{(Eq. 6.5.1.2.1-8)}$$

where

D_s = the effective diffusion coefficient (m^2 s^{-1})
A = the cross-sectional area of the diffusive pathway (m^2)
C_i = the concentration of the radionuclide (kg m^{-3})
x = the length of the path (m).

Note that the effective diffusion coefficient, D_s, as defined and used in this section, implicitly includes the effects of porosity, saturation, and tortuosity. The amount of water vapor that adsorbs on a surface is determined from the iron oxide adsorption isotherm discussed in Section 6.5.1.2.1.2.1. This provides the thickness of the water film. To calculate the cross-sectional area of the pathway, the width of the water film is also needed. Because of the difficulty in characterizing the waste, both initially and after it degrades, calculation of this width (and consequently, the cross-sectional area) is complex. The length of the diffusive path is also variable because the radionuclide sources may develop at random locations within a waste package and the path length will depend on the geometry of the film connecting the source to a breach. Finally, the effective diffusion coefficient itself depends on the complex interactions of source term composition, water chemistry, porosity, water saturation, and temperature, none of which can be characterized in a deterministic fashion. Thus, each term in the above equation–D_s, A, and Δx–needs to be sampled, and a reasonable range and distribution for each has to be determined. All three terms are interrelated through the geometry used for the waste package interior, and all are effectively a function of relative humidity and time.

Cross-Sectional Area of the Diffusive Pathway

This section describes alternative methods for computing the cross-sectional area of the diffusive pathway. The area used for TSPA-LA calculations is presented in Section 6.5.3.1.

In the simplest model, a single fuel rod fails in one location, a point source, and an adsorbed water film covers the fuel rod and provides direct connection to a breach. In this case, the cross-sectional area for diffusion, A_f, is that of the film uniformly covering the cylindrical fuel rod. The thickness of the film is obtained from the adsorption isotherm of water vapor adsorbed on ZrO_2 at the known relative humidity.

Thus,

$$A_f = \frac{\pi}{4}\left[\left(d_0 + 2t_f\right)^2 - d_0^2\right] = \pi t_f\left(d_0 + t_f\right), \qquad \text{(Eq. 6.5.1.2.1-9)}$$

where d_0 is the outer diameter of the fuel rod (m) and t_f is the adsorbed water film thickness (m). In this simple case, the minimum path length, Δx, would be the shortest distance along a solid surface from a fuel rod to the exterior of a waste package. This minimum length is 7 cm, which is the combined thickness of the waste package outer corrosion barrier and inner vessel. The maximum value for Δx would be the length of a fuel rod (151.560 in = 3.85 m; DOE 1992 [DIRS 102588], Volume 1, p. 2A-30) plus the maximum distance from a fuel rod to the exterior (approximately the inside diameter of a waste package outer corrosion barrier, 1.597 m; BSC 2004 [DIRS 166953], Section B-B), for a total of 3.85 m + 1.597 m = 5.45 m.

The adsorbed water film on ZrO_2, as shown in Figure 6.5-4, is 10 monolayers thick at about 88 percent relative humidity, the highest humidity value shown in Figure 6.5-4 for ZrO_2. From Equation 6.5.1.2.1-6, the thickness of a water monolayer is $t_f = 2.83 \times 10^{-10}$ m, so the water layer thickness at 88 percent relative humidity is 2.83×10^{-9} m, and the cross-sectional area on a 0.94996-cm diameter fuel rod is:

$$\begin{aligned} A &= \pi\left(2.83\times10^{-9}\ \text{m}\right)\left[9.4966\times10^{-3}\ \text{m} + 2.83\times10^{-9}\ \text{m}\right] \\ &= 8.44\times10^{-11}\ \text{m}^2 \\ &= 8.44\times10^{-5}\ \text{mm}^2. \end{aligned} \qquad \text{(Eq. 6.5.1.2.1-10)}$$

This is a small area through which radionuclides can diffuse, and releases from a single failed rod would be negligible on the basis of this area alone. Even if the average 2.2 rods per assembly (EPRI 2001 [DIRS 100444], p. 4-1), or 46.2 rods per 21-PWR waste package, have failed prior to emplacement, the total cross-sectional area of adsorbed water films on fuel rods for a waste package is only 3.9×10^{-3} mm^2. While this is small, it shows that a reasonable quantitative estimate of diffusive releases from a breached waste package can be obtained.

Another approach to determining the cross-sectional area is to ignore the dispersion of water over all surfaces within a waste package. Suppose that all the water adsorbed on surfaces is collected into a tube, connecting the source to the exterior surface. As shown in Table 6.5-8 above, the total initial surface area in a waste package is 1,061 m^2. Most of the surfaces are oxidized steel, so it is appropriate to use the Fe_2O_3 adsorption isotherm. From Equation 6.5.1.2.1-5, at an example 95 percent relative humidity, the amount of water adsorbed is 4.91 monolayers. Using a monolayer thickness of 2.83×10^{-10} m, the water film is 1.39×10^{-9} m thick. The total volume of adsorbed water is then 1.47×10^{-6} m^3. If the length of the diffusion pathway is the total outside length of a waste package (4.8974 m, see in Table 6.5-11, Note e), then the cross-sectional area for diffusion is 3.00×10^{-7} m^2 = 0.30 mm^2, equivalent to a square about 0.55 mm on a side. This is a large area for diffusion, considering that diffusion will take place for thousands of years. Porosity, saturation, and tortuosity are

factors that would retard radionuclide transport, and these factors have been neglected in this approach. This is therefore a bounding estimate for cross-sectional area.

At the other extreme in time and waste package condition, consider the cross-sectional area available when the interior of a waste package is fully degraded, at least to the extent that all iron-containing basket and inner vessel components have completely corroded. The Alloy 22 outer corrosion barrier should still be largely intact at this point; a number of general corrosion patches will have penetrated the waste package, but it will still provide some overall structural support. By this time, a large number of fuel rods will have failed by localized corrosion or axial splitting, but the Zircaloy spacer grids will provide enough support to hold assemblies together and support assemblies collapsed on top of them. Interspersed throughout the assemblies are porous corrosion products. Under this condition, the source is dispersed throughout the waste package interior. Diffusion will occur through the porous medium in which all surfaces are coated with the thin film of adsorbed water.

The cross-sectional area can be estimated for this degraded state. The fully degraded surface area is determined in Section 6.5.1.2.1.3.2 to be 2.5×10^8 m^2. At an example 95 percent relative humidity, the film thickness is 1.39×10^{-9} m, so the diffusion area over a path the length of a waste package is 0.071 m^2, equivalent to a square about 0.27 m on a side. This provides an upper bound on the cross-sectional area for diffusion in the waste package.

A more realistic estimate must take into account the saturation and porosity of the corrosion products. For porous media such as soils, the diffusion coefficient is reduced by a tortuosity factor (a function of porosity and saturation) to account for the increased path length and decreased cross-sectional area of the diffusing solute in an unsaturated porous medium. In the absence of an advective flux and negligible vapor phase transport, one-dimensional transient diffusion is given by Fick's second law of diffusion (Bird et al. 1960 [DIRS 103524], p. 558):

$$\frac{\partial C}{\partial t} = D_s \frac{\partial^2 C}{\partial x^2}, \qquad \text{(Eq. 6.5.1.2.1-11)}$$

where C is the concentration of a solute (kg m^{-3}), and D_s is the effective diffusion coefficient (m^2 s^{-1}).

Archie's Law

Archie's law, discussed in Section 6.3.4.1.1, gives the diffusion coefficient as a function of porosity and saturation in a partly saturated, granular medium as:

$$D_s = D_0 \phi^{1.3} S_w^2, \qquad \text{(Eq. 6.5.1.2.1-12)}$$

where ϕ is the porosity, and S_w is the liquid saturation of the porous medium, and D_0 is the free water diffusion coefficient. Diffusion coefficient D_s is an effective value that implicitly includes the effect of porosity, saturation, and tortuosity in a porous medium. As such, it is defined differently from the coefficient D_{mi} defined in Section 6.5.1.2, which applies to a bulk liquid phase without modification for porosity, saturation, or tortuosity. The exponents in Archie's law

are typical values, and will vary for different materials (Bear 1988 [DIRS 101379], p. 116). Whereas exponents of 1.863 are used for invert materials, based on experimental measurements of diffusion coefficients for crushed rock, the typical values (1.3 and 2) are used throughout this section to estimate in-package diffusion coefficients for corrosion products.

Effective Water Saturation

The effective water saturation, S_{we}, is obtained from adsorption isotherms as a function of relative humidity. Per Assumption 5.6, all corrosion products are assumed to be Fe_2O_3. The water saturation is given by:

$$S_{we} = \frac{V_w \left(\frac{s_{WP}}{s_{N_2}} \right)}{V_{WP}}, \qquad \text{(Eq. 6.5.1.2.1-13)}$$

where

V_w = the volume of water adsorbed (m^3 H_2O kg^{-1} Fe_2O_3)
V_{WP} = the pore volume of a waste package (m^3 pore volume)
s_{WP} = the surface area of a waste package (m^2)
s_{N_2} = the specific surface area of the porous degraded waste form (m^2 kg^{-1} Fe_2O_3).

Since V_w is normalized to the mass of Fe_2O_3, it must be multiplied by (s_{WP}/s_{N_2}) to obtain the volume of water in an entire waste package. V_w/s_{N_2} is the volume of water adsorbed per unit surface area, which is multiplied by the total surface area of the waste package to get the volume of water adsorbed in the entire waste package; it is divided by the pore volume of the waste package to obtain the saturation. V_w/s_{N_2} is obtained from an FHH multilayer adsorption isotherm model (Jurinak 1964 [DIRS 154381], p. 486), shown in Section 6.5.1.2.1.2.1, that gives the fractional surface coverage, or number of monolayers θ_a covering a surface (Equation 6.5.1.2.1-1 with terms rearranged):

$$\theta_a = \frac{V_w}{V_m} = \frac{m_a}{m_m} = \left(\frac{-1.1}{\log_{10} RH} \right)^{\frac{1}{2.45}}, \qquad \text{(Eq. 6.5.1.2.1-14)}$$

where

V_m = the volume of adsorbed water vapor that provides a one monolayer coverage on the surface (m^3 H_2O kg^{-1} Fe_2O_3)
m_a = the mass adsorbed per unit mass of adsorbent (kg H_2O kg^{-1} Fe_2O_3)
m_m = the specific mass of one monolayer of adsorbate per unit mass of adsorbent (kg H_2O kg^{-1} Fe_2O_3).

The specific mass of a monolayer adsorbate on Fe_2O_3 is:

$$
\begin{aligned}
m_m &= \frac{s_{N_2} M_w}{A_w N_A} \\
&= \frac{\left(9100 \frac{\mathrm{m}^2}{\mathrm{kg\,Fe_2O_3}}\right)\left(18.01528 \times 10^{-3} \frac{\mathrm{kg\,H_2O}}{\mathrm{mol}}\right)\left(\frac{1\ \mathrm{kg}}{1000\,\mathrm{g}}\right)}{\left(10.6 \times 10^{-20} \frac{\mathrm{m}^2}{\mathrm{molecule}}\right)\left(6.022 \times 10^{23} \frac{\mathrm{molecule}}{\mathrm{mol}}\right)} \\
&= 2.57 \frac{\mathrm{mg\,H_2O}}{\mathrm{g\,Fe_2O_3}}.
\end{aligned}
\qquad \text{(Eq. 6.5.1.2.1-15)}
$$

Suppose that bulk liquid properties apply to the adsorbed water, in particular that the density of adsorbed water is equal to that of liquid water. Then

$$m_a = \rho_w V_w \qquad \text{(Eq. 6.5.1.2.1-16)}$$

and

$$m_m = \rho_w V_m. \qquad \text{(Eq. 6.5.1.2.1-17)}$$

Combining these expressions with the definition of θ_a,

$$
\begin{aligned}
m_a &= m_m \theta_a \\
&= \frac{s_{N_2} M_w}{A_w N_A} \theta_a \\
&= \rho_w V_w.
\end{aligned}
\qquad \text{(Eq. 6.5.1.2.1-18)}
$$

Then the quantity $\left(V_w / s_{N_2}\right)$ needed for the saturation is:

$$
\begin{aligned}
\frac{V_w}{s_{N_2}} &= \frac{M_w}{\rho_w A_w N_A} \theta_a \\
&= \frac{M_w}{\rho_w A_w N_A} \left(\frac{-1.1}{\log_{10} RH}\right)^{\frac{1}{2.45}}.
\end{aligned}
\qquad \text{(Eq. 6.5.1.2.1-19)}
$$

Inserting this expression into S_{we} gives the effective water saturation of the entire waste package:

$$S_{we} = \frac{V_w}{s_{N_2}} \frac{s_{WP}}{V_{WP}}$$
$$= \frac{s_{WP}}{V_{WP}} \frac{M_w}{\rho_w A_w N_A} \left(\frac{-1.1}{\log_{10} RH} \right)^{\frac{1}{2.45}}. \qquad \text{(Eq. 6.5.1.2.1-20)}$$

The parameters used in this expression include the surface area and void volume of the waste package. The surface area can vary over five orders of magnitude, from an initial value of 1,061 m^2 to a fully degraded state value of 2.5×10^8 m^2. The initial void volume, as shown in Table 6.5-8, is 5.63 m^3. This void volume will decrease and the surface area will increase as corrosion products form, since the oxides occupy greater volume and have a greater surface area than the metals from which they are formed. However, the change depends on time and extent of corrosion, so for simplicity the initial void volume is used for all times. To give some idea of the effect of water saturation on surface area, some values of saturation are listed in Table 6.5-10 for various relative humidity values. The value used for the density of water is 988.0363 kg m^{-3} at 50°C. It is clear that the saturation can change enormously between the initial condition when the surface area is on the order of 1,000 m^2 to the time when the steel components are fully degraded.

Effective Diffusion Coefficient

Inserting S_{we} for S_w in the expression for the diffusion coefficient, Equation 6.5.1.2.1-12, and using water density at 50°C and the initial waste package porosity of 0.58 (Section 6.5.1.2.1.3.2,

$$D_s = \phi^{1.3} S_{we}^2 D_0$$
$$= \phi^{1.3} \left(\frac{s_{WP}}{V_{WP}} \frac{M_w}{\rho_w A_w N_A} \right)^2 \theta_a^2 D_0 \qquad \text{(Eq. 6.5.1.2.1-21)}$$

$$D_s = 1.29 \times 10^{-21} s_{WP}^2 \left(\frac{-1.1}{\log_{10} RH} \right)^{\frac{2}{2.45}} D_0 \qquad \text{(Eq. 6.5.1.2.1-22)}$$
$$= 1.39 \times 10^{-21} s_{WP}^2 \left(-\log_{10} RH \right)^{-0.816} D_0.$$

For consistency with other uses of adsorption models, natural logarithms are used instead of base 10 logarithms, using the relation:

$$-\log_{10} RH = -\log_{10} \left(e^{\ln RH} \right) = -\ln RH \log_{10} e. \qquad \text{(Eq. 6.5.1.2.1-23)}$$

Then the final expression for the diffusion coefficient is:

$$D_s = 2.75\times10^{-21} s_{WP}^2 \left(-\ln RH\right)^{-0.816} D_0 \qquad \text{(Eq. 6.5.1.2.1-24)}$$

Table 6.5-10 lists some values of D_s / D_0 using Equation 6.5.1.2.1-24 for initial and fully degraded state surface areas over a range of relative humidity values, showing the range of factors that impact the diffusion coefficient. Thus, initially, due to the low surface area available for water adsorption, the diffusion rate is negligibly small, whereas when the internal components of the waste package are fully corroded, the water saturation is sufficiently high that diffusive releases can be large.

Table 6.5-10. Values of Effective Water Saturation and Diffusion Coefficient Normalized to the Diffusion Coefficient in Water for Waste Package Surface Areas and Relative Humidities (*RH*) Using Equation 6.5.1.2.1-24

	s_{WP} = 1,061 m^2		s_{WP} = 2.5×10^8 m^2	
RH	S_{we}	D_s/D_0	S_{we}	D_s/D_0
0.1	5.6×10^{-8}	1.6×10^{-15}	0.013	8.7×10^{-5}
0.2	6.4×10^{-8}	2.1×10^{-15}	0.015	1.2×10^{-4}
0.3	7.2×10^{-8}	2.6×10^{-15}	0.017	1.5×10^{-4}
0.4	8.1×10^{-8}	3.3×10^{-15}	0.019	1.8×10^{-4}
0.5	9.1×10^{-8}	4.1×10^{-15}	0.021	2.3×10^{-4}
0.6	1.0×10^{-7}	5.3×10^{-15}	0.024	3.0×10^{-4}
0.7	1.2×10^{-7}	7.1×10^{-15}	0.028	4.0×10^{-4}
0.8	1.4×10^{-7}	1.0×10^{-14}	0.034	5.8×10^{-4}
0.9	2.0×10^{-7}	1.9×10^{-14}	0.046	1.1×10^{-3}
0.95	2.6×10^{-7}	3.5×10^{-14}	0.062	1.9×10^{-3}
0.99	5.1×10^{-7}	1.3×10^{-13}	0.12	7.3×10^{-3}

6.5.1.2.1.4.2 Diffusion Coefficient in General Corrosion Patches and Corrosion Products

If radionuclide sources (i.e., failed fuel rods) are distributed uniformly throughout a waste package, then the source can be thought of as residing at the inside surface of the waste package, particularly if the inside of the package is largely degraded. In this case, the diffusive path is short: the distance through the breach in the outer corrosion barrier. The cross-sectional area for diffusion is the area of the water film covering the material that fills the corrosion patch. If the corrosion patch is mostly empty space, then diffusion must occur through a much smaller area around the perimeter of the breach. This situation will occur if the corroded Alloy 22 falls away, leaving a gaping hole where the breach occurs. In any event, the size of the breach, rather than the diffusive path area inside the waste package, is the limiting factor for diffusion out of a waste package.

The nominal area of a single general corrosion patch is fixed in the current waste package degradation model, WAPDEG (BSC 2004 [DIRS 169996]). The diffusive area of the corrosion products domain is the total area of all waste package breaches, including corrosion patches and stress corrosion cracks and is determined differently for each scenario class, as discussed in Section 6.5.3.1.1.

The diffusion coefficient in the corrosion products is given by Archie's law, Equation 6.5.1.2.1-12, as a function of porosity and saturation. The water saturation within the corrosion products, $S_{we,CP}$, can be obtained as a function of RH using Equation 6.5.1.2.1-20, replacing the waste package pore volume, V_{WP}, with V_{CP}, the pore volume of the corrosion products, and replacing the waste package surface area, s_{WP}, with s_{CP}, the surface area of the corrosion products (m^2 Fe_2O_3), given by:

$$\begin{aligned} s_{CP} &= m_{CP}\bar{s}_{CP} \\ &= \rho_{FeOx}V_{CP}\bar{s}_{CP}\left(\frac{1-\phi_{CP}}{\phi_{CP}}\right). \end{aligned} \qquad \text{(Eq. 6.5.1.2.1-25)}$$

In this equation, m_{CP} is the mass of corrosion products (kg Fe_2O_3). The ratio of surface area to pore volume of the corrosion products can be expressed as:

$$\frac{s_{CP}}{V_{CP}} = \rho_{FeOx}\bar{s}_{CP}\left(\frac{1-\phi_{CP}}{\phi_{CP}}\right). \qquad \text{(Eq. 6.5.1.2.1-26)}$$

Using a solid density for Fe_2O_3 of ρ_{FeOx} =5,240 kg m^{-3} (Weast 1985 [DIRS 111561], p. B-104), the density of water at 50°C, the specific surface area of corrosion products ($\bar{s}_{CP}$) in units of m^2 kg^{-1}, and a porosity for corrosion products, ϕ_{CP}, of 0.4 (Section 6.5.1.2.1.3.2), the effective saturation of the corrosion products is given by:

$$\begin{aligned} S_{we,CP} &= \frac{s_{CP}}{V_{CP}}\frac{M_w}{\rho_w A_w N_A}\theta_a \\ &= \frac{\rho_{FeOx}\bar{s}_{CP}M_w}{\rho_w A_w N_A}\left(\frac{1-\phi_{CP}}{\phi_{CP}}\right)\left(\frac{-1.1}{\log_{10} RH}\right)^{\frac{1}{2.45}} \\ &= 3.28\times10^{-6}\bar{s}_{CP}\left(-\ln RH\right)^{-1/2.45}. \end{aligned} \qquad \text{(Eq. 6.5.1.2.1-27)}$$

The equivalent of Equation 6.5.1.2.1-24, which gives the effective diffusion coefficient based on Archie's law, can similarly be obtained for the corrosion products:

$$\begin{aligned} D_s &= \phi_{CP}^{1.3}S_{we,CP}^2 D_0 \\ &= (0.4)^{1.3}\left[3.28\times10^{-6}\bar{s}_{CP}\left(-\ln RH\right)^{-1/2.45}\right]^2 D_0 \\ &= 3.27\times10^{-12}\bar{s}_{CP}^2\left(-\ln RH\right)^{-0.816} D_0. \end{aligned} \qquad \text{(Eq. 6.5.1.2.1-28)}$$

Using RH = 0.95 and $\bar{s}_{CP} = 9.1 \times 10^3\ m^2\ kg^{-1}$ as an example, and with the self-diffusion coefficient for water (Section 6.3.4.1) of $D_0 = 2.299 \times 10^{-9}\ m^2 s^{-1}$, the effective diffusion coefficient for the corrosion products using Archie's law (Equation 6.5.1.2.1-28) is $D_s = 7.03 \times 10^{-12}\ m^2\ s^{-1}$, or $D_s / D_0 = 3.06 \times 10^{-3}$, for comparison with earlier estimates (Table 6.5-10). For the range of porosities of geologic media, 0.25 to 0.7 (Freeze and Cherry 1979 [DIRS 101173], p. 37), D_s ranges from $1.53 \times 10^{-11}\ m^2\ s^{-1}$ to $1.19 \times 10^{-12}\ m^2\ s^{-1}$.

6.5.1.2.1.4.3 Diffusion Coefficient in Stress Corrosion Cracks

When stress corrosion cracks first appear and are the only breaches in the package, the steel components will be largely intact. The surface area and diffusional cross-sectional areas of internal components will be small compared to the diffusional cross sectional area of stress corrosion cracks, resulting in a small diffusion coefficient. Since at this time this portion of the diffusion pathway will have both a smaller diffusion coefficient and a smaller cross sectional area, this pathway will control diffusive releases. Consider an example where 25 stress corrosion cracks per waste package appear (BSC 2004 [DIRS 169996], Figure 26), which is an upper bound estimate that occurs at approximately 300,000 years. With a cross sectional area of $7.7 \times 10^{-6}\ m^2$ for each crack (Section 6.3.3.1.2.1), the total area of stress corrosion crack openings in this example calculation is 1.93 cm^2. Since even the bounding estimate of initial cross-sectional area for diffusion within a package is $3.00 \times 10^{-7}\ m^2 = 3.00 \times 10^{-3}\ cm^2$, it is the adsorbed water film inside the package that controls diffusive releases because the diffusional cross-sectional area inside the waste package is much less than that of the stress corrosion cracks. This conclusion is appropriate when corrosion products fill the stress corrosion cracks, as they eventually will, and radionuclides diffuse through these products.

If the stress corrosion crack is not filled with corrosion products, diffusion can still occur through an adsorbed water film on the sides of the stress corrosion cracks. In this case, the cross-sectional area through the stress corrosion cracks is computed from the perimeter of the stress corrosion crack and the film thickness. The maximum length of a crack is about 5 cm (Section 6.3.3.1.2.1). Although a stress corrosion crack is theoretically ellipsoidal in shape, it is so narrow that the perimeter is approximately twice the length, or 10 cm. Using the example above with 25 stress corrosion cracks/package, the total width of the diffusive path is 250 cm. The water film thickness, assuming adsorption on Fe_2O_3 at RH = 95 percent, as an example, is 1.39×10^{-9} m (4.91 monolayers of thickness $t_f = 2.83 \times 10^{-10}$ m), so the cross-sectional area for diffusion on the sides of stress corrosion cracks is $3.5 \times 10^{-5}\ cm^2$, or a factor of 100 less than the high estimate for cross-sectional area inside the waste package ($3.00 \times 10^{-3}\ cm^2$). While it is not unreasonable for the actual diffusive area inside the waste package to be at least two orders of magnitude less than the high estimate, the area for diffusion along the walls of the stress corrosion cracks is at least as small as the diffusive area in the interior of the waste package, and may in fact be the controlling dimension. If the stress corrosion cracks are filled with corrosion products, then the cross-sectional area inside the waste package is more likely to be controlling, as discussed in the preceding paragraph.

Expressions for the effective saturation and diffusion coefficient based on Archie's law in a stress corrosion crack are identical to those obtained above for general corrosion patches, as long

as the same porous material properties are used. In Equation 6.5.1.2.1-27 (effective saturation), the ratio of the surface area to the pore volume of patches, s_{CP}/V_{CP}, is independent of the dimensions of the penetration, since, from Equation 6.5.1.2.1-26, $s_{CP}/V_{CP} = \bar{s}_{CP}\rho_{FeOx}(1-\phi_{CP})/\phi_{CP}$, where $\bar{s}_{CP}$ is the sampled specific surface area of Fe_2O_3 ($m^2\ kg^{-1}$), whose density is ρ_{FeOx} ($kg\ m^{-3}$), and porosity is ϕ_{CP}. Hence, the effective saturation and diffusion coefficient for a stress corrosion crack are identical to those for general corrosion patches if the same porous material properties are valid.

6.5.1.2.1.5 Diffusive Path Length

For stress corrosion cracks, the diffusion path length may be as long as the waste package or longer, depending on the tortuosity. It may also be only a few centimeters, the shortest distance from a fuel rod through a stress corrosion crack to the exterior of a waste package. The distance for corrosion patches is generally shorter, since by the time the general corrosion patches occur, the waste package should be filled with porous corrosion products through which a more direct path will exist from failed fuel rods to the exterior.

When a package is first breached and the interior components have not yet degraded (except for the few initially failed fuel rods), a range of path lengths can be estimated with some certainty. As the steel components inside a package corrode, the diffusion path will become more tortuous on a microscopic scale, but more direct on a larger scale. The uncertainty in cross-sectional area for diffusion increases, whereas the range and uncertainty in porosity, saturation, and path length remain small in comparison.

6.5.1.2.1.6 Comparison of Diffusive Release Estimates

In Table 6.5-11, the cross-sectional diffusion areas are summarized for the conditions described above. In addition, the quantity $D_s A/\Delta x = -q_l/\Delta C_l$ is computed to provide a consistent comparison among the different states and conditions for a waste package. Based on these results, the highest releases are predicted to occur when all the adsorbed water is consolidated into a single bulk water pathway in a package with fully degraded internal components. However, this result is based on the most extreme degradation state and on the bounding approach to calculating diffusive releases from a waste package. More realistic estimates for this quantity range from 10^{-15} to $10^{-11}\ m^3\ s^{-1}$.

Table 6.5-11. Summary and Comparison of Cross-Sectional Areas for Diffusion for Various Configurations at a Relative Humidity of 95 Percent

Component/ Configuration	Diffusive Path	Path Length[e] (m)	Cross-Sect. Area (mm^2)	Diffusion Coefficient[a] ($m^2 s^{-1}$)	$\frac{D_s A}{\Delta x}$ ($m^3 s^{-1}$)
Initial WP surface consolidated	Axially through full length of WP	4.90	0.297	2.299×10^{-9}	1.4×10^{-16}
Initial WP surface consolidated; 46.2 failed fuel rods	Axially through full length of WP	4.90	0.405	2.299×10^{-9}	1.9×10^{-16}
Initial WP surface consolidated; no cladding	Axially through full length of WP	4.90	14.0	2.299×10^{-9}	6.6×10^{-15}
Initial WP surface as porous medium	Axially through ½ length of WP	2.45	1.73×10^{6} [c]	8.00×10^{-23} [d]	5.7×10^{-23}
Stress corrosion cracks (filled with porous corrosion products)	Axially through stress corrosion cracks in lids	0.068[b]	193	7.03×10^{-12}	2.0×10^{-14}
Fully degraded WP surface consolidated	Axially through ½ length of WP	2.45	7.5×10^{4}	2.299×10^{-9}	7.0×10^{-11}
Fully degraded WP; porous medium	Axially through ½ length of WP	2.45	1.73×10^{6} [c]	4.46×10^{-12}	3.2×10^{-12}
Corrosion patch (1)	Radially outward through 1 patch in Alloy 22	0.02	2.346×10^{4}	7.03×10^{-12}	8.2×10^{-12}
Corrosion patches (10)	Radially outward through 10 patches in Alloy 22 outer corrosion barrier	0.02	2.346×10^{5}	7.03×10^{-12}	8.2×10^{-11}

[a]Self-diffusion coefficient of water (Mills 1973 [DIRS 133392], Table III) is used except for porous media in waste packages and in corrosion patches, which use effective diffusion coefficients.

[b]For 21-PWR; thickness of closure end lids plus the air gap between lids:

Middle lid thickness:	12.7 mm (BSC 2004 [DIRS 167394], Detail A).
Middle lid to outer lid gap:	30.16 mm (BSC 2004 [DIRS 167394], Detail A).
Outer lid thickness:	25.4 mm.
Total top lids thickness:	68.26 mm (BSC 2004 [DIRS 167394], Detail A).

[c]WP cross section; inner diameter = 1.4859 m (BSC 2004 [DIRS 169472]; BSC 2004 [DIRS 166953], Section B).

[d]$D_s/D_0 = 3.08\times10^{-14}$ (Equation 6.5.1.2.1-24, using initial surface area s_{WP} = 1,061 m^2/waste package).

[e]21-PWR outside waste package length is the distance from the outside of the top lid to the outside of the bottom lid, and is given by the overall length minus the length of the skirt around the bottom minus the thickness of the lifting device on the top lid:

Total length:	5,024.4 mm (BSC 2004 [DIRS 166953], Section A-A).
Bottom skirt length:	101.6 mm (BSC 2004 [DIRS 167394], Detail B).
Top lid lifting device thickness:	25.4 mm.
Total waste package length:	4,897.4 mm (BSC 2004 [DIRS 167394], Detail C).

WP = waste package

6.5.1.3 Nomenclature

Symbols used in Sections 6, 7, and 8 are summarized in Table 6.5-12.

Table 6.5-12. Nomenclature

Variable	Definition	Units	Where First Used
A	Cross sectional area of diffusive or flow pathway	m^2	Eq. 6.5.1.2-5
A_f	Cross sectional area for diffusion on exterior of an intact fuel rod	m^2	Eq. 6.5.1.2.1-9
A_f	Diffusive area of UZ fracture cell	m^2	Eq. 6.5.3.5-21
A_g	Surface area of crushed tuff granule	m^2	Section 6.6.4.1
A_I	Invert cross sectional area (circle segment)	m^2	Eq. 6.5.3.3-2
A_I	Diffusive area of invert cell	m^2	Eq. 6.5.3.5-21
A_{Is}	Intercepted flow area of a drift over the length of one waste package	m^2	Eq. 6.5.3.3-12
$A_{I/UZ}$	Diffusive area between invert and UZ cells	m^2	Eq. 6.5.3.3-4
A_m	Diffusive area of UZ matrix cell	m^2	Eq. 6.5.3.5-21
A_{scc}	Cross sectional area of stress corrosion crack	cm^2	Eq. 6.6.2-8
$A_{scc,eff}$	Effective cross sectional area of stress corrosion crack	cm^2	Section 6.6.2
A_{UZ}	Projected area of UZ normal to vertical flux	m^2	Eq. 6.5.3.6-1
A_w	Cross sectional area of water molecule	m^2	Table 4.1-9; Eq. 6.5.1.2.1-6
a	One-half the length of a stress corrosion crack	m	Eq. 6.3.3.1-1
a	Constant in equation for binary diffusion coefficient	dimensionless	Eq. 6.6.2-6
a	Empirical parameter in Archie's law	dimensionless	Eq. 6.3.4.1.1-1
a_g	Effective length of tuff granule matrix pore system	m	Section 6.6.4.1
b	One-half the stress corrosion crack gap width	m	Section 6.3.3.1.2.1
b	Exponent in equation for binary diffusion coefficient	dimensionless	Eq. 6.6.2-6
b	Slope of the $\ln\psi$ versus $\ln\theta$ curve	dimensionless	Eq. 6.6.5.1-2
C_{cFeOx}	Concentration of mobile iron oxyhydroxide (FeOx) colloids	$kg\ m^{-3}$	Eq. 6.5.1.2-14
C_{cGW}	Concentration of mobile groundwater (GW) colloids	$kg\ m^{-3}$	Eq. 6.5.1.2-14
C_{cWF}	Concentration of mobile waste form colloids	$kg\ m^{-3}$	Eq. 6.5.1.2-14
C_i	Concentration of radionuclide species i	$kg\ m^{-3}$	Eq. 6.5.1.2-2
C_i^{embed}	Concentration of radionuclide species i embedded on waste form colloids	$kg\ m^{-3}$	Eq. 6.5.1.2-37
C_{iI}	Concentration of radionuclide species i in the invert cell	$kg\ m^{-3}$	Eq. 6.5.3.5-11
$C_{iI/UZ}$	Concentration of radionuclide species i at the interface between the invert and UZ cells	$kg\ m^{-3}$	Eq. 6.5.3.5-11

Table 6.5-12. Nomenclature (Continued)

Variable	Definition	Units	Where First Used
C_{if}	Concentration of radionuclide species *i* in the UZ fracture cell	kg m^{-3}	Eq. 6.5.3.5-12
C_{im}	Concentration of radionuclide species *i* in the UZ matrix cell	kg m^{-3}	Eq. 6.5.3.5-13
$C_{i,new}$	"New" input concentration of radionuclide species *i*	kg m^{-3}	Eq. 6.6.1.2.1-1
$C_{i,old}$	"Old" input concentration of radionuclide species *i*	kg m^{-3}	Eq. 6.6.1.2.1-1
C_{ip}^{embed}	Concentration of parent *ip* of radionuclide species *i* embedded on waste form colloids	kg m^{-3}	Eq. 6.5.1.2-37
C_{icFeOx}	Concentration of radionuclide species *i* sorbed onto mobile iron oxyhydroxide (FeOx) colloids	kg m^{-3}	Eq. 6.5.1.2-14
C_{icFeOx}^{irrev}	Concentration of radionuclide species *i* irreversibly adsorbed onto iron oxyhydroxide (FeOx) colloids	kg m^{-3}	Eq. 6.5.1.2-28
C_{icGW}	Concentration of radionuclide species *i* sorbed onto mobile GW colloids	kg m^{-3}	Eq. 6.5.1.2-14
C_{iCP}	Concentration of dissolved radionuclide species *i* in corrosion products domain or cell	kg m^{-3}	Eq. 6.5.1.2-50
$C_{iCPFeOx}^{irrev}$	Concentration of radionuclide species *i* irreversibly adsorbed onto iron oxyhydroxide corrosion products	kg m^{-3}	Eq. 6.5.1.2-31
$C_{iCP/invint}$	Concentration of radionuclide species *i* at the interface between the corrosion products and invert cells	kg m^{-3}	Eq. 6.5.3.5-7
C_{icWF}	Concentration of radionuclide species *i* sorbed onto mobile waste form colloids	kg m^{-3}	Eq. 6.5.1.2-14
C_{iinter}	Concentration of dissolved radionuclide species *i* in invert intergranular continuum	kg m^{-3}	Eq. 6.5.1.2-51
C_{iintra}	Concentration of dissolved radionuclide species *i* in invert intragranular continuum	kg m^{-3}	Eq. 6.5.1.2-52
C_{ip}	Concentration of parent *ip* of radionuclide species *i*	kg m^{-3}	Eq. 6.5.1.2-9
$C_{ipcFeOx}$	Concentration of parent *ip* of radionuclide species *i* sorbed onto mobile iron oxyhydroxide (FeOx) colloids	kg m^{-3}	Eq. 6.5.1.2-14
$C_{ipcFeOx}^{irrev}$	Concentration of parent *ip* of radionuclide species *i* irreversibly adsorbed onto iron oxyhydroxide (FeOx) colloids	kg m^{-3}	Eq. 6.5.1.2-28
C_{ipcGW}	Concentration of parent *ip* of radionuclide species *i* sorbed onto mobile (GW) colloids	kg m^{-3}	Eq. 6.5.1.2-14
$C_{ipCPFeOx}^{irrev}$	Concentration of parent *ip* of radionuclide species *i* irreversibly adsorbed onto iron oxyhydroxide corrosion products	kg m^{-3}	Eq. 6.5.1.2-31
C_{ipcWF}	Concentration of parent *ip* of radionuclide species *i* sorbed onto mobile waste form colloids	kg m^{-3}	Eq. 6.5.1.2-14
C_{si}	Maximum concentration (solubility limit) of radionuclide species *i*	kg m^{-3}	Eq. 6.6.1.1.2-1
$C_{si,new}$	Maximum concentration (solubility limit) of radionuclide species *i* in "new" chemistry	kg m^{-3}	Eq. 6.6.1.2.2-9
$C_{si,old}$	Maximum concentration (solubility limit) of radionuclide species *i* in "old" chemistry	kg m^{-3}	Eq. 6.6.1.2.2-9
COV	Coefficient of variance [= $\sigma(x)/E(x)$]	dimensionless	Table 4.1-11

Table 6.5-12. Nomenclature (Continued)

Variable	Definition	Units	Where First Used
C_{O_2}	Molar concentration of oxygen in air	mol cm^{-3}	Eq. 6.6.3-2
C_{wv}	Molar concentration of water vapor in air	mol cm^{-3}	Eq. 6.6.2-5
D_{AB}	Binary diffusion coefficient	cm^2 s^{-1}	Eq. 6.6.2-6
D_B	Diffusion coefficient for Brownian motion	cm^2 s^{-1}	Eq. 6.5.1.2-35
D_c	Colloid dispersion or diffusion coefficient	m^2 s^{-1}	Eq. 6.5.1.2-35
$D_{c\_A/B}$	Interface diffusive conductance between cell *A* and cell *B*	cm^3 s^{-1}	Eq. 6.5.3.5-6
$D_{c\_B/C}$	Interface diffusive conductance between cell *B* and cell *C*	cm^3 s^{-1}	Eq. 6.5.3.5-8
D_{coll}	Colloid diffusion coefficient	m^2 s^{-1}	Eq. 6.3.4.4-1
D_i	Hydrodynamic dispersion coefficient, or effective diffusion coefficient, of radionuclide species *i*	m^2 s^{-1}	Eq. 6.5.1.2-4
D_{CP}	Diffusion coefficient in corrosion products domain	cm^2 s^{-1}	Eq. 6.6.4-1
$\hat{D}_{CP}$	Diffusive conductance in corrosion products cell	cm^3 s^{-1}	Eq. 6.6.4.2-1
$\hat{D}_{CP/CP-int}$	Diffusive conductance between corrosion products cell and corrosion products interface cell	cm^3 s^{-1}	Eq. 6.6.4.2-15
$\hat{D}_{CP-int/inter}$	Diffusive conductance between corrosion products interface cell and invert intergranular cell	cm^3 s^{-1}	Eq. 6.6.4.2-16
$\hat{D}_{CP-int/intra}$	Diffusive conductance between corrosion products interface cell and invert intragranular cell	cm^3 s^{-1}	Eq. 6.6.4.2-17
$\hat{D}_{CP/inter}$	Effective diffusive conductance between corrosion products cell and invert intergranular cell	cm^3 s^{-1}	Eq. 6.6.4.2-8
$\hat{D}_{CP/intra}$	Effective diffusive conductance between corrosion products cell and invert intragranular cell	cm^3 s^{-1}	Eq. 6.6.4.2-9
$\hat{D}_{intra/inter}$	Effective diffusive conductance between intragranular and invert intergranular cells	cm^3 s^{-1}	Eq. 6.6.4.2-10
D_e	Effective diffusion coefficient	cm^2 s^{-1}	Eq. 6.5.1.2-22
D_f	Effective diffusion coefficient within the UZ fracture cell	cm^2 s^{-1}	Eq. 6.5.3.5-12
D_I	Effective diffusion coefficient within the invert cell	cm^2 s^{-1}	Eq. 6.5.3.5-11
$\hat{D}_{If}$	Effective diffusive conductance between invert cell and UZ fracture cell	cm^3 s^{-1}	Eq. 6.5.3.5-18
$\hat{D}_{Im}$	Effective diffusive conductance between invert cell and UZ matrix cell	cm^3 s^{-1}	Eq. 6.5.3.5-19
$\hat{D}_{I/I-int}$	Diffusive conductance between the invert cell and the invert interface cell	cm^3 s^{-1}	Eq. 6.5.3.5-25
$\hat{D}_{I-int/f}$	Diffusive conductance between the invert interface cell and the UZ fracture cell	cm^3 s^{-1}	Eq. 6.5.3.5-26
$\hat{D}_{I-int/m}$	Diffusive conductance between the invert interface cell and the UZ matrix cell	cm^3 s^{-1}	Eq. 6.5.3.5-27

Table 6.5-12. Nomenclature (Continued)

Variable	Definition	Units	Where First Used
D_{inter}	Diffusion coefficient for invert intergranular continuum	$cm^2\ s^{-1}$	Eq. 6.6.4-2
$\hat{D}_{inter}$	Diffusive conductance in invert intergranular cell	$cm^3\ s^{-1}$	Eq. 6.6.4.2-2
$\hat{D}_{inter/inter-int}$	Diffusive conductance between the invert intergranular cell and the invert intergranular interface cell	$cm^3\ s^{-1}$	Eq. 6.6.4.2-19
$\hat{D}_{intra-int/UZm}$	Diffusive conductance between the invert intergranular cell and the invert intragranular interface cell	$cm^3\ s^{-1}$	Eq. 6.6.4.2-23
$\hat{D}_{intra-int/UZf}$	Diffusive conductance between the invert intergranular cell and the UZ fracture cell	$cm^3\ s^{-1}$	Eq. 6.6.4.2-24
D_{intra}	Diffusion coefficient for invert intragranular continuum	$cm^2\ s^{-1}$	Eq. 6.6.4-3
$\hat{D}_{intra}$	Diffusive conductance in invert intragranular cell	$cm^3\ s^{-1}$	Eq. 6.6.4.2-3
$\hat{D}_{intra/intra-int}$	Diffusive conductance between the invert intragranular cell and the UZ matrix cell	$cm^3\ s^{-1}$	Eq. 6.6.4.2-21
$\hat{D}_{inter-int/UZm}$	Diffusive conductance between the invert intragranular cell and the invert intragranular interface cell	$cm^3\ s^{-1}$	Eq. 6.6.4.2-20
$\hat{D}_{inter-int/UZf}$	Diffusive conductance between the invert intragranular cell and the UZ fracture cell	$cm^3\ s^{-1}$	Eq. 6.6.4.2-22
D_m	Effective diffusion coefficient within the UZ matrix cell	$cm^2\ s^{-1}$	Eq. 6.5.3.5-13
$\hat{D}_{mf}$	Effective diffusive conductance between UZ fracture and matrix cells	$cm^3\ s^{-1}$	Eq. 6.5.3.5-20
D_{ion}	Ion diffusion coefficient	$m^2\ s^{-1}$	Eq. 6.3.4.4-1
D_{limit}	Diffusion coefficient measurement limit	$cm^2\ s^{-1}$	Eq. 6.6.5.2-5
D_{MD}	Mechanical dispersion coefficient	$cm^2\ s^{-1}$	Eq. 6.5.1.2-35
D_{mi}	Molecular diffusion coefficient of species *i*	$m^2\ s^{-1}$	Eq. 6.5.1.2-6
D_{ms}	Diffusion coefficient for saturated tuff matrix	$cm^2\ s^{-1}$	Eq. 6.5.3.6-2
D_s	Effective diffusion coefficient	$m^2\ s^{-1}$	Eq. 6.5.1.2.1-8
D_T	Diffusion coefficient at temperature *T*	$m^2\ s^{-1}$	Eq. 6.3.4.1.2-1
D_{T_0}	Diffusion coefficient at temperature T_0	$m^2\ s^{-1}$	Eq. 6.3.4.1.2-1
D_{WF}	Diffusion coefficient in waste form domain	$cm^2\ s^{-1}$	Table 8.2-1
D_0	Free water diffusion coefficient	$m^2\ s^{-1}$	Eq. 6.3.4.1.1-10
D^*	Molecular diffusion coefficient	$cm^2\ s^{-1}$	Table 7.2-1, footnote a
d	Depth of stress corrosion crack	m	Figure 6.3-3
d	Characteristic length of the tuff matrix structure	m	Eq. 6.5.1.2-22
d_D	Diameter of drift	m	Eq. 6.5.3.6-1

Table 6.5-12. Nomenclature (Continued)

Variable	Definition	Units	Where First Used
d_g	Geometric particle diameter	mm	Eq. 6.6.5.1-3
d_0	Diameter of fuel rod	m	Eq. 6.5.1.2.1-9
E	Modulus of elasticity	Pa	Eq. 6.3.3.1-1
$E(x)$	Expected value of the K_d distribution	ml g^{-1}	Table 4.1-11
e	Elementary charge	C	Table 7.2-1, footnote a
e	Natural logarithm base	dimensionless	Eq. 6.5.1.2.1-2
F	Faraday constant	C mol^{-1}	Eq. 6.3.4.1.1.-6
F	Fraction of seepage flux onto drip shield or waste package that flows into a breach	dimensionless	Eq. 6.5.1.1.2-7
F_{alt}	Radionuclide release rate from waste package in alternative patch geometry model	kg s^{-1}	Eq. 6.6.1.2.3-2
F_{iCP}	Diffusive flux of radionuclide species *i* in corrosion products cell	kg s^{-1}	Eq. 6.6.4.2-1
F_{if}	Diffusive fluxes of radionuclide species *i* within the UZ fracture cell	kg s^{-1}	Eq. 6.5.3.5-12
F_{iI}	Diffusive fluxes of radionuclide species *i* within the invert cell	kg s^{-1}	Eq. 6.5.3.5-11
F_{iinter}	Diffusive flux of radionuclide species *i* in invert intergranular cell	kg s^{-1}	Eq. 6.6.4.2-2
F_{iintra}	Diffusive flux of radionuclide species *i* in invert intragranular cell	kg s^{-1}	Eq. 6.6.4.2-3
F_{im}	Diffusive fluxes of radionuclide species *i* within the UZ matrix cell	kg s^{-1}	Eq. 6.5.3.5-13
F_j	Volumetric flow rate or flux of water in flow path *j* (*j* = 1 to 8)	m^3 s^{-1}	Table 6.3-1; Eq. 6.5.1.1-5
F_{pri}	Radionuclide release rate from waste package in primary patch geometry model	kg s	Eq. 6.6.1.2.3-1
F_w	Volumetric flow rate of water	m^3 s^{-1}	Eq. 6.5.1.1-4
f_{At}	Theoretical fraction of dripping flux falling at Point $y<y_A$ that flows into a drip shield breach	dimensionless	Eq. 6.5.1.1.2-2
f_{A-}	Theoretical fraction of dripping flux falling between Points –I and B that flows into a drip shield breach	dimensionless	Eq. 6.5.1.1.2-2
f_{B+}	Theoretical fraction of dripping flux falling at Point $y>y_B$ that flows into a drip shield breach	dimensionless	Eq. 6.5.1.1.2-14
f_{Ct}	Theoretical fraction of dripping flux falling between Points C and +I that flows into a drip shield breach	dimensionless	Eq. 6.5.1.1.2-5
f_{calc}	Calculated fraction of dripping flux that flows into a drip shield breach	dimensionless	Section 6.5.1.1.2.4
f_{DS}	Uncertain drip shield flux splitting factor	dimensionless	Eq. 6.3.2.4-2
f'_{DS}	Sampled drip shield flux splitting factor that accounts for rivulet spread angle uncertainty	dimensionless	Eq. 6.3.2.4-5
f_{D+}	Theoretical fraction of dripping flux falling at Point $y>y_D$ that flows into a drip shield breach	dimensionless	Eq. 6.5.1.1.2-6
f_{expt}	Experimentally measured fraction of dripping flux that flows into a drip shield breach	dimensionless	Section 6.5.1.1.2.4

Table 6.5-12. Nomenclature (Continued)

Variable	Definition	Units	Where First Used
f_{tB}	Theoretical fraction of dripping flux falling between Points –I and B that flows into a drip shield breach	dimensionless	Eq. 6.5.1.1.2-3
f_{tD}	Theoretical fraction of dripping flux falling between Points –I and D that flows into a drip shield breach	dimensionless	Eq. 6.5.1.1.2-6
f_{VD}	Model validation uncertain drip shield flux splitting factor	dimensionless	Eq. 7.1.1.1-1
f'_{VD}	Model validation sampled drip shield flux splitting factor that accounts for rivulet spread angle uncertainty	dimensionless	Eq. 7.1.1.1-3
f_{VW}	Model validation uncertain waste package flux splitting factor	dimensionless	Eq. 7.1.1.2-1
f'_{VW}	Model validation sampled waste package flux splitting factor that accounts for rivulet spread angle uncertainty	dimensionless	Eq. 7.1.1.2-3
f_{WP}	Uncertain waste package flux splitting factor	dimensionless	Eq. 6.3.3.2-1
f'_{WP}	Sampled waste package flux splitting factor	dimensionless	Eq. 6.3.3.2-3
f_0	Theoretical fraction of dripping flux falling between Points B and C that flows into a drip shield breach	dimensionless	Eq. 6.5.1.1.2-4
G_t	Conductance of bulk porous medium	S	Eq. 6.3.4.1.1-5
G_w	Conductance of water	S	Eq. 6.3.4.1.1-5
H_m	Absolute humidity of air	kg kg^{-1}	Eq. 6.6.2-3
H_{mol}	Molal humidity of air	mol mol^{-1}	Eq. 6.6.2-4
I_s	Hydraulic head gradient in the invert	m m^{-1}	Eq. 6.5.3.3-12
$\boldsymbol{i}$	Unit vector in the *x*-direction or the direction of flow	dimensionless	Eq. 6.5.1.2-5
J_{cB}	Mass flux of waste form colloids due to Brownian motion	kg m^{-2} s^{-1}	Eq. 6.5.1.2-35
J_{cMD}	Mass flux of waste form colloids due to mechanical dispersion	kg m^{-2} s^{-1}	Eq. 6.5.1.2-35
J_{cWF}	Mass flux of waste form colloids	kg m^{-2} s^{-1}	Eq. 6.5.1.2-32
J_i	Mass flux (mass specific discharge) of radionuclide species *i*	kg m^{-2} s^{-1}	Eq. 6.5.1.2-1
J_{icFeOx}	Total mass flux of mobile iron oxyhydroxide (FeOx) colloids containing adsorbed radionuclide species *i*	kg m^{-2} s^{-1}	Eq. 6.5.1.2-14
J^{irrev}_{icFeOx}	Total mass flux of mobile iron oxyhydroxide (FeOx) colloids containing irreversibly adsorbed radionuclide species *i*	kg m^{-2} s^{-1}	Eq. 6.5.1.2-28
J_{icGW}	Total mass flux of mobile GW colloids containing adsorbed radionuclide species *i*	kg m^{-2} s^{-1}	Eq. 6.5.1.2-14
J_{icWF}	Total mass flux of mobile waste form colloids containing adsorbed radionuclide species *i*	kg m^{-2} s^{-1}	Eq. 6.5.1.2-14

Table 6.5-12. Nomenclature (Continued)

Variable	Definition	Units	Where First Used
K_d	Sorption distribution (or distribution) coefficient	ml g^{-1}	Table 4.1-11
$K_{dicFeOx}$	Sorption distribution (or distribution) coefficient of iron oxyhydroxide colloids containing adsorbed radionuclide species *i*	ml g^{-1}	Eq. 6.5.1.2-14
K_{dicGW}	Sorption distribution (or distribution) coefficient of groundwater colloids containing adsorbed radionuclide species *i*	ml g^{-1}	Eq. 6.5.1.2-14
K_{dicWF}	Sorption distribution (or distribution) coefficient of waste form colloids containing adsorbed radionuclide species *i*	ml g^{-1}	Eq. 6.5.1.2-14
K_{dips}	Sorption distribution (or distribution) coefficient of parent *ip* of radionuclide species *i*	ml g^{-1}	Eq. 6.5.1.2-12
K_{dis}	Sorption distribution (or distribution) coefficient of radionuclide species *i*	ml g^{-1}	Eq. 6.5.1.2-12
K_{us}	Unsaturated hydraulic conductivity of invert	m s^{-1}	Eq. 6.5.3.3-12
k	Boltzmann constant	J K^{-1}	Table 7.2-1, footnote a
k	Parameter in FHH adsorption isotherm	dimensionless	Eq. 6.5.1.2.1-2
k_i	Irreversible forward rate constant	m^3 m^{-2} s^{-1}	Eq. 6.5.1.2-13
k_m	Intrinsic permeability of saturated tuff matrix	m^2	Eq. 6.5.3.6-3
k_{me}	Effective permeability of tuff matrix	m^2	Eq. 6.5.3.6-2
k_{rm}	Relative permeability of tuff matrix	dimensionless	Eq. 6.5.3.6-3
L_A	Diffusive lengths from the cell centers to the cell interface within cell *A*	m	Eq. 6.5.3.5-5
L_B	Diffusive lengths from the cell centers to the cell interface within cell *B*	m	Eq. 6.5.3.5-5
L_{DS}	Axial length of drip shield	m	Table 6.3-1
L_{DS_Patch}	Axial half-length of each drip shield patch due to general corrosion	m	Table 6.3-1
L_f	Diffusive length within the UZ fracture cell	m	Eq. 6.5.3.5-12
L_I	Diffusive length within the invert cell	m	Eq. 6.5.3.5-11
L_{inter}	Diffusive length within the invert intergranular cell	m	Eq. 6.6.4.2-2
L_{intra}	Diffusive length within the invert intragranular cell	m	Eq. 6.6.4.2-3
L_m	Diffusive length within the UZ matrix cell	m	Eq. 6.5.3.5-13
L_{WP}	Length of waste package	m	Table 6.3-1
L_{WP_Patch}	Axial half-length of each drip waste package due to general corrosion	m	Table 6.3-1
$\bar{l}$	Average ionic conductance at infinite dilution	S cm^2 $equivalent^{-1}$	Eq. 6.3.4.1.1-7
l_+^0, l_-^0	Cationic and anionic conductance at infinite dilution	S cm^2 $equivalent^{-1}$	Eq. 6.3.4.1.1-6

Table 6.5-12. Nomenclature (Continued)

Variable	Definition	Units	Where First Used
ℓ	One-half width of corrosion patch in drip shield	m	Eq. 6.3.2.4-2
ℓ_{WP}	One-half width of corrosion patch in waste package	m	Eq. 6.3.3.2-1
M_A, M_B	Molecular weights of components *A* and *B*	g mol^{-1}	Eq. 6.6.2-6
M_a	Molecular weight of air	kg mol^{-1}	Eq. 6.6.2-3
M_w	Molecular weight of water	kg mol^{-1}	Eq. 6.5.1.2.1-6
m	Exponent on porosity in Archie's law	dimensionless	Eq. 6.3.4.1.1-1
m	Mass of waste package internal components	kg	Table 6.5-8, footnote h
m_a	Mass of water adsorbed per unit mass of adsorbent	kg kg^{-1}	Eq. 6.5.1.2.1-14
m_{CP}	Mass of corrosion products inside waste package; function of time *t*	kg	Eq. 6.5.1.2.1-25
m_{CPf}	Mass of corrosion products inside waste package from complete corrosion of all steel internal components	kg	Eq. 6.5.3.2-3
m_{CP1}	Mass of corrosion products inside waste package from corrosion of carbon steel	kg	Eq. 6.5.3.2-3
m_{CP2}	Mass of corrosion products inside waste package from corrosion of stainless steel	kg	Eq. 6.5.3.2-4
m_i	Mass of radionuclide species *i* in waste package	kg	Eq. 6.6.1.1.1-2
$\dot{m}_i$	Rate of release of radionuclide species *i* into water in waste package	kg s^{-1}	Eq. 6.6.1.1.1-1
m_m	Mass of one monolayer of adsorbate per unit mass of adsorbent	kg kg^{-1}	Eq. 6.5.1.2.1-14
m_w	Instantaneous total mass of water within the walls of a drift	kg	Eq. 6.5.1.1-1
N	Number of waste package internal components	dimensionless	Table 6.5-8, footnote h
N_A	Avogadro's number	molecules mol^{-1}	Eq. 6.5.1.2.1-6
N_b	Number of breaches (corrosion patches) in drip shield	dimensionless	Eq. 6.3.2.4-2
N_{bDS}	Number of breaches (corrosion patches) in drip shield	dimensionless	Table 6.3-1
N_{bWP}	Number of breaches (corrosion patches) in waste package	dimensionless	Table 6.3-1
N_c	Number of breaches (corrosion patches) on crown of drip shield	dimensionless	Eq. 6.5.1.1.1-6
ND	Normal distribution	dimensionless	Eq. 6.3.4.1.1-16
n	Exponent on saturation or water content in power law dependence of diffusion coefficient (e.g., Archie's law)	dimensionless	Eq. 6.3.4.1.1-2
n	Time step number	dimensionless	Eq. 6.5.3.5-1
p	Slope of the model function	dimensionless	Eq. 6.6.5.2-6
p	Total pressure	atm	Eq. 6.6.2-6
p_{cA}, p_{cB}	Critical pressure of components *A* and *B*	atm	Eq. 6.6.2-6

Table 6.5-12. Nomenclature (Continued)

Variable	Definition	Units	Where First Used
p_w	Partial pressure of water	Pa	Eq. 6.5.1.2.1-1
p_w^o	Vapor pressure of water	Pa	Eq. 6.5.1.2.1-1
Q_{cWF}	Net rate of waste form colloid capture on the solid surface	kg m^{-3} s^{-1}	Eq. 6.5.1.2-32
Q_{cWF}^{int}	Net rate of waste form colloid capture at the air-water interface	kg m^{-3} s^{-1}	Eq. 6.5.1.2-32
Q_{cWFfg}	Net rate of waste form colloid removal from suspension by means of physical filtering (pore clogging, sieving, and straining) and by gravitational settling	kg m^{-3} s^{-1}	Eq. 6.5.1.2-32
Q_{cWFmt}	Net rate of interface transfer of waste form colloidal mass between the continua in the dual continuum invert	kg m^{-3} s^{-1}	Eq. 6.5.1.2-32
Q_{cWFs}	Net rate of waste form colloid formation	kg m^{-3} s^{-1}	Eq. 6.5.1.2-32
Q_I	Volumetric discharge into the invert	m^3 s^{-1}	Eq. 6.5.3.3-12
Q_i^m	Net rate of various mass transfer process involving radionuclide species *i*	kg m^{-3} s^{-1}	Eq. 6.5.1.2-1
Q_{icc}	Net rate of sorption of radionuclide species *i* onto immobile colloid surfaces captured by the solid matrix	kg m^{-3} s^{-1}	Eq. 6.5.1.2-7
Q_{icc}^{int}	Net rate of sorption of radionuclide species *i* onto immobile colloid surfaces captured by the air-water interface	kg m^{-3} s^{-1}	Eq. 6.5.1.2-7
Q_{icm}^{embed}	Rate of mass conversion from dissolved state to embedded state onto waste form colloids for radionuclide species *i*	kg m^{-3} s^{-1}	Eq. 6.5.1.2-7
Q_{icm}^{irrev}	Net rate of irreversible sorption of radionuclide species *i* onto mobile colloid surfaces	kg m^{-3} s^{-1}	Eq. 6.5.1.2-7
Q_{icm}^{rev}	Net rate of reversible sorption of radionuclide species *i* onto mobile colloid surfaces	kg m^{-3} s^{-1}	Eq. 6.5.1.2-7
Q_{id}	Net rate of dissolution of radionuclide species *i*	kg m^{-3} s^{-1}	Eq. 6.5.1.2-7
Q_{imt}	Net rate of interface transfer of dissolved mass between the continua in the dual continuum invert	kg m^{-3} s^{-1}	Eq. 6.5.1.2-7
Q_{imt}^{irrev}	Net rate of interface transfer between the continua in the dual continuum invert of radionuclide species *i* irreversibly sorbed onto mobile colloids	kg m^{-3} s^{-1}	Eq. 6.5.1.2-28
$Q_{iprecip}$	Net rate of precipitation of radionuclide species *i*	kg m^{-3} s^{-1}	Eq. 6.5.1.2-7
Q_{is}^{irrev}	Net rate of irreversible sorption of radionuclide species *i* onto the solid matrix	kg m^{-3} s^{-1}	Eq. 6.5.1.2-7
Q_{is}^{rev}	Net rate of reversible sorption of radionuclide species *i* onto the solid matrix	kg m^{-3} s^{-1}	Eq. 6.5.1.2-7
Q_{wz}	Advective water volume flux per unit bulk volume	m^3 m^{-3} yr^{-1}	Eq. 6.5.3.5-3
q	Rate of diffusion of water vapor through air	mol s^{-1}	Eq. 6.6.2-8
q_i	Rate of diffusion of radionuclide species *i*	kg s^{-1}	Eq. 6.5.1.2.1-8

Table 6.5-12. Nomenclature (Continued)

Variable	Definition	Units	Where First Used
q_{in}	Rate of water flow into waste package	$m^3\ s^{-1}$	Section 6.6.1.1.1
$q_{in,new}$	"New" rate of water flow into waste package	$m^3\ s^{-1}$	Section 6.6.1.2.1
$q_{in,old}$	"Old" rate of water flow into waste package	$m^3\ s^{-1}$	Section 6.6.1.2.1
q_{out}	Rate of water flow out of waste package	$m^3\ s^{-1}$	Section 6.6.1.1.1
$q_{out,new}$	"New" rate of water flow out of waste package	$m^3\ s^{-1}$	Section 6.6.1.2.1
q_{wz}	Scalar specific discharge (Darcy velocity) of water in the downward +z-direction	$m\ s^{-1}$	Eq. 6.5.1.2-46
q_w	Specific discharge (Darcy velocity) of water	$m\ s^{-1}$	Eq. 6.5.1.2-4
R^2	Coefficient of determination	dimensionless	Figure 6.3-4
R_f	Retardation factor	dimensionless	Eq. 6.3.4.2.2-1
R_{fi}	Retardation factor for radionuclide species *i*	dimensionless	Eq. 6.5.1.2-38
R_{fip}	Retardation factor for parent *ip* of radionuclide species *i*	dimensionless	Eq. 6.5.1.2-38
RH	Relative humidity	$kg\ kg^{-1}$	Eq. 6.5.1.2.1-2
R_t	Resistance of a porous medium	Ω	Eq. 6.3.4.1.1-4
r_{coll}	Colloid particle radius	m	Eq. 6.3.4.4-1
r_{corr}	Steel corrosion rate	$mol\ yr^{-1}$	Table 6.6-1
r_D	Drift radius	m	Eq. 6.5.3.3-1
r_i	Reaction term accounting for decay and ingrowth of species *i*	$kg\ m^{-3}s^{-1}$	Eq. 6.5.1.2-1
r_{ion}	Ion radius	m	Eq. 6.3.4.4-1
r_{ip}^M	Ratio of the mass of radionuclide species *i* produced by decay of the parent species *ip* to the mass of the parent species lost by decay	$kg\ kg^{-1}$	Eq. 6.5.1.2-9
r_s	Dissolution rate of the waste form	$kg\ s^{-1}$	Eq. 6.6.1.1.1-1
r_w	Rate of production of water by chemical reactions	$kg\ s^{-1}$	Eq. 6.5.1.1-1
r_1	Sampled value for the corrosion rate of carbon steel	$\mu m\ yr^{-1}$	Eq. 6.5.3.2-1
r_2	Sampled value for the corrosion rate of stainless steel	$\mu m\ yr^{-1}$	Eq. 6.5.3.2-2
S_{ef}	Effective UZ fracture saturation	$m^3\ m^{-3}$	Eq. 6.5.3.6-4
S_w	Water saturation	$m^3\ m^{-3}$	Eq. 6.5.1.2-2
S_{we}	Effective water saturation	$m^3\ m^{-3}$	Eq. 6.5.1.2.1-13
$S_{we,CP}$	Effective water saturation within a corrosion patch or corrosion products	$m^3\ m^{-3}$	Eq. 6.5.1.2.1-27
S_{w_CP}	Water saturation in corrosion products domain	$m^3\ m^{-3}$	Eq. 6.6.4-1

Table 6.5-12. Nomenclature (Continued)

Variable	Definition	Units	Where First Used
S_{wf}	UZ fracture water saturation	$m^3\ m^{-3}$	Eq. 6.5.1.2-52
S_{wfr}	UZ fracture residual water saturation	$m^3\ m^{-3}$	Eq. 6.5.3.6-4
S_{wI}	Invert water saturation	$m^3\ m^{-3}$	Eq. 6.5.1.2-50
S_{w_inter}	Water saturation in invert intergranular continuum	$m^3\ m^{-3}$	Eq. 6.6.4-2
S_{w_intra}	Water saturation in invert intragranular continuum	$m^3\ m^{-3}$	Eq. 6.5.3.3-7
S_{wm}	UZ matrix water saturation	$m^3\ m^{-3}$	Eq. 6.5.1.2-51
s	Exponent in FHH adsorption isotherm	dimensionless	Eq. 6.5.1.2.1-2
s_{CP}	Surface area of corrosion products	m^2	Eq. 6.5.1.2.1-27
$\bar{s}_c$	Specific surface area of colloids	$m^2\ g^{-1}$	Eq. 6.5.1.2-18
$\bar{s}_{CP}$	Specific surface area of iron oxyhydroxide corrosion products	$m^2\ kg^{-1}$	Eq. 6.5.1.2-13
s_{N_2}	Specific surface area of porous material obtained by BET nitrogen adsorption measurements	$m^2\ kg^{-1}$	Eq. 6.5.1.2.1-13
s_{WP}	Internal surface area of waste package	m^2	Eq. 6.5.1.2.1-13
T	Temperature	K	Table 4.1-7
T_{cA}, T_{cB}	Critical temperatures of components *A* and *B*	K	Eq. 6.6.2-6
T_0	Reference temperature	K	Eq. 6.3.4.1.2-1
t	Time	s	Eq. 6.5.1.1-1
t_{corr}	Lifetime of steel	yr	Table 6.6-1
t_f	Thickness of a water monolayer	m	Eq. 6.5.1.2.1-6
t_{fill}	Time for a waste package to fill with water	s	Section 6.6.1.1
t_{f1}	Lifetime of carbon steel	yr	Eq. 6.5.3.2-1
t_{f2}	Lifetime of stainless steel	yr	Eq. 6.5.3.2-2
$t_{I,max}$	Maximum thickness of the invert	m	Eq. 6.5.3.3-1
$\bar{t}_I$	Average thickness of the invert	m	Eq. 6.5.3.5-5
t_0	Time of first breach of the waste package	yr	Eq. 6.5.3.2-3
$t_{1/2,ip}$	Half-life of parent *ip* of radionuclide species *i*	s	Eq. 6.5.1.2-10
u	Ion mobility	$cm^2\ s^{-1}\ V^{-1}$	Table 7.2-1, footnote a
V	Volume of water vapor adsorbed at reference conditions	$m^3\ kg^{-1}$	Eq. 6.5.1.2.1-1
$V(t)$	Volume of water within a waste package at time *t*	m^3	Section 6.6.1.1
V_B	Volume of cell *B*	m^3	Eq. 6.5.3.5-4
V_b	Bulk volume of UZ matrix cell	$m^3\ kg^{-1}$	Section 6.5.3.6

Table 6.5-12. Nomenclature (Continued)

Variable	Definition	Units	Where First Used
V_{CP}	Pore volume (water volume when fully saturated) of corrosion products	m^3	Eq. 6.5.1.2.1-25
V_{DSNF}	Volume of degraded DSNF	m^3	Table 8.2-1
V_g	Volume of crushed tuff granule	m^3	Section 6.6.4.1
V_m	Volume of water adsorbed that provides one monolayer coverage on the surface	$m^3\ kg^{-1}$	Eq. 6.5.1.2.1-1
V_{new}	Volume of "new" water in waste package	m^3	Section 6.6.1.2.2
V_{old}	Volume of "old" water in waste package	m^3	Section 6.6.1.2.1
V_p	Total volume of pore space in bulk invert	m^3	Eq. 6.5.1.2-23
V_{p_inter}	Intergranular pore space pore volume	m^3	Eq. 6.5.1.2-23
V_{p_intra}	Intragranular pore space pore volume	m^3	Eq. 6.5.1.2-24
V_t	Bulk invert total volume	m^3	Eq. 6.5.1.2-23
V_{t_inter}	Intergranular pore space total volume	m^3	Eq. 6.5.1.2-26
V_{t_intra}	Intragranular pore space total volume	m^3	Eq. 6.5.1.2-27
V_{tub}	Volume of water that can be retained within a waste package before it overflows	m^3	Section 6.6.1.1
V_w	Volume of water adsorbed	$m^3\ kg^{-1}$	Eq. 6.5.1.2.1-13
V_{wI}	Volume of water in invert	m^3	Eq. 6.5.3.3-3
V_{w_inter}	Volume of water in invert intergranular pore space	m^3	Eq. 6.5.3.3-6
V_{w_intra}	Volume of water in invert intragranular pore space	m^3	Eq. 6.5.3.3-6
V_{WP}	Pore volume of waste package	m^3	Eq. 6.5.1.2.1-13
v	Average water velocity	$m\ yr^{-1}$	Eq. 6.3.4.2.2-1
v_c	Average contaminant front velocity	$m\ yr^{-1}$	Eq. 6.3.4.2.2-1
W_{DS}	Total unfolded width of drip shield	m	Eq. 6.5.1.1.1-7
w_I	Width of top surface of invert	m	Eq. 6.5.3.3-1
w_{inter}	Volumetric ratio of the intergranular continuum volume to the total bulk invert volume	$m^3\ m^{-3}$	Eq. 6.5.1.2-26
w_w^m	Net mass flow rate of water across bounding surfaces by mass transfer	$kg\ s^{-1}$	Eq. 6.5.1.1-1
x	One-dimensional coordinate or distance	m	Figure 6.3-2
y	Distance along drip shield crown	m	Section 6.5.1.1.2.1
y_A	Distance along drip shield crown from center of breach – farthest point to the left from which rivulets can enter breach	m	Eq. 6.5.1.1.2-1
y_B	Distance along drip shield crown from center of breach – farthest point to the left from which rivulets can enter top of breach	m	Eq. 6.5.1.1.2-1

Table 6.5-12. Nomenclature (Continued)

Variable	Definition	Units	Where First Used
y_C	Distance along drip shield crown from center of breach – farthest point to the right from which rivulets can enter top of breach	m	Eq. 6.5.1.1.2-1
y_D	Distance along drip shield crown from center of breach – farthest point to the right from which rivulets can enter breach	m	Eq. 6.5.1.1.2-1
z	One-dimensional coordinate or distance	m	Eq. 6.5.1.2-46
z	Valence of an ion	dimensionless	Table 7.2-1, footnote a
$z_{interface}$	Spatial location of the corrosion products domain/invert interface	m	Section 6.5.1.2
z_+, z_-	Valence of cation and anion, respectively; magnitude only – no sign	dimensionless	Eq. 6.3.4.1.1-6
ΔC_i	Concentration difference	kg m^{-3}	Section 6.5.1.2.1.6
ΔC_{O_2}	Oxygen concentration difference	kg m^{-3}	Eq. 6.6.3-3
ΔC_{wv}	Water vapor concentration difference	kg m^{-3}	Eq. 6.6.2-8
ΔF_w	Difference between volumetric flow rate into and out of the EBS	m^3 s^{-1}	Eq. 6.5.1.1-4
Δt	Time to empty retained water in waste package	s	Eq. 6.6.1.2.3-2
Δt	Time step size from the nth to the $(n+1)^{th}$ time	s or yr	Eq. 6.5.3.5-1
Δw_w	Difference between mass rate of flow into and out of the EBS	kg s^{-1}	Eq. 6.5.1.1-1
Δx	Thickness or length of flow or diffusion path	m	Table 6.5-8, footnote h
Φ	Volumetric water content	percent	Eq. 7.2.1.2-1
Λ_0	Equivalent electrolyte conductance at infinite dilution	S cm^2 equivalent^{-1}	Eq. 6.3.4.1.1-6
Ω	Colloid flux out ratio	dimensionless	Eq. 6.5.3.4-1
α	Drip shield or waste package rivulet spread half angle	radian or degree	Eq. 6.3.2.4-2
α	Dispersivity	m	Eq. 6.5.1.2-6
α	First-order mass transfer coefficient	s^{-1}	Eq. 6.5.1.2-20
β	Geometry-dependent factor in expression for dual-continuum invert interface mass transfer coefficient	dimensionless	Eq. 6.5.1.2-22
β	Volume fraction of "old" water in total water volume of waste package	m^3 m^{-3}	Eq. 6.6.1.2.1-2
γ	UZ active fracture parameter	dimensionless	Section 6.5.3.6
γ_c	Colloid mass transfer coefficient	s^{-1}	Eq. 6.5.1.2-19
γ_d	Dissolved species mass transfer coefficient	s^{-1}	Eq. 6.5.1.2-19
δ	Stress corrosion crack gap width	m	Eq. 6.3.3.1-1
δ_i	Stress corrosion crack gap width, inner surface	m	Figure 6.3-3
δ_o	Stress corrosion crack gap width, outer surface	m	Figure 6.3-3
ζ	Dimensionless surface-area-to-volume ratio	dimensionless	Section 6.6.4.1
η_T	Viscosity of water at temperature T	Pa s	Table 4.1-7

Table 6.5-12. Nomenclature (Continued)

Variable	Definition	Units	Where First Used
η_{T_0}	Viscosity of water at temperature T_0	Pa s	Eq. 6.3.4.1.2-1
η_{20}	Viscosity of water at temperature T = 20°C	Pa s	Table 4.1-7
θ	Volumetric moisture content	percent	Eq. 6.3.4.1.1-12
θ_C	Critical volumetric moisture content	percent	Eq. 6.6.5.2-2
θ_a	Number of monolayers of adsorbed water	dimensionless	Eq. 6.5.1.2.1-2
θ_{inter}	Intergranular moisture content	percent	Eq. 6.6.5.1-5
θ_{intra}	Moisture content of invert intragranular continuum	percent	Eq. 6.6.5.2-5
θ_m	Moisture content of UZ matrix	percent	Eq. 6.5.3.6-2
θ_{min}	Minimum volumetric moisture content for diffusivity to be greater than limiting diffusivity	percent	Eq. 6.6.5.2-5
θ_s	Saturated moisture content	percent	Eq. 6.6.5.1-2
λ_i	Radioactive decay constant for species *i*	s^{-1} or yr^{-1}	Eq. 6.5.1.2-9
λ_{ip}	Radioactive decay constant for parent *ip* of species *i*	s^{-1} or yr^{-1}	Eq. 6.5.1.2-9
λ_i^{embed}	First order rate constant for mass conversion from dissolved state to embedded state onto waste form colloids for radionuclide species *i*	s^{-1} or yr^{-1}	Eq. 6.5.1.2-8
μ	Mean value	dimensionless	Eq. 6.3.4.1.1-16
$\bar{v}$	Average linear interstitial water velocity	$m\ s^{-1}$	Eq. 6.3.4.2.2-1
v_c	Average velocity of front of the contaminant concentration profile	$m\ s^{-1}$	Eq. 6.3.4.2.2-1
π	Ratio of circle circumference to diameter	dimensionless	Eq. 6.5.1.2.1-9
ρ	Density of waste package internal components	$kg\ m^{-3}$	Table 6.5-8, footnote h
ρ_b	Dry bulk density of the solid matrix	$kg\ m^{-3}$	Eq. 6.3.4.2.2-1
ρ_{FeOx}	Density of Fe_2O_3	$kg\ m^{-3}$	Eq. 6.5.1.2.1-25
ρ_i	Mass concentration of radionuclide species *i*	$kg\ m^{-3}$	Eq. 6.5.1.2-1
ρ_s	Electrical resistivity of a porous medium	Ω m	Eq. 6.3.4.1.1-1
ρ_t	Bulk resistivity of a partially saturated porous medium	Ω m	Eq. 6.3.4.1.1-2
ρ_w	Density of water	$kg\ m^{-3}$	Eq. 6.5.1.1-4
ρ_w^e	Electrical resistivity of liquid water	Ω m	Eq. 6.3.4.1.1-1
σ	Standard deviation	dimensionless	Eq. 6.3.4.1.1-16
$\sigma(x)$	Standard deviation of the K_d distribution	$ml\ g^{-1}$	Table 4.1-11
σ_a	Applied stress	Pa	Eq. 6.3.3.1-1
σ_g	Standard deviation of the pore size	mm	Eq. 6.6.5.1-4
σ_s	Sample standard deviation	dimensionless	Section 7.3.1.2

Table 6.5-12. Nomenclature (Continued)

Variable	Definition	Units	Where First Used
ϕ	Porosity	$m^3\ m^{-3}$	Eq. 6.3.4.2.2-1
ϕ_{CP}	Porosity of corrosion products	$m^3\ m^{-3}$	Eq. 6.5.1.2.1-25
ϕ_f	Porosity of UZ fractures	$m^3\ m^{-3}$	Eq. 6.5.1.2-52
ϕ_I	Bulk porosity of invert	$m^3\ m^{-3}$	Eq. 6.5.1.2-25
ϕ_{inter}	Porosity of invert intergranular continuum	$m^3\ m^{-3}$	Eq. 6.5.3.3-10
ϕ_{intra}	Porosity of invert intragranular continuum	$m^3\ m^{-3}$	Eq. 6.5.3.3-7
ϕ_m	Porosity of saturated tuff matrix	$m^3\ m^{-3}$	Eq. 6.5.1.2-51
Ψ	Moisture potential	$J\ kg^{-1}$	Eq. 6.6.5.1-2
Ψ_e	Air-entry moisture potential	$J\ kg^{-1}$	Eq. 6.6.5.1-2
Ψ_{es}	Air-entry moisture potential at a bulk density of 1,300 kg m^{-3}	$J\ kg^{-1}$	Eq. 6.6.5.1-3
ω_i	Mass fraction of radionuclide species *i* released per unit mass of waste form	$kg\ kg^{-1}$	Eq. 6.6.1.1.1-1
∇	Del operator: $i\frac{\partial}{\partial x}+j\frac{\partial}{\partial y}+k\frac{\partial}{\partial z}$, where *i*, *j*, and *k* are unit vectors in the *x*-, *y*-, and *z*-directions, respectively	m^{-1}	Eq. 6.5.1.2-1

BET = Brunauer, Emmett and Teller; CP = corrosion products; COV = coefficient of variance; DSNF = defense spent nuclear fuel; FHH = Frenkel-Halsey-Hill adsorption isotherm equation

6.5.2 Base Case Model Inputs

Table 6.5-13 summarizes model inputs used in the *EBS RT Abstraction* that are sampled in the TSPA-LA model calculations. The uncertainty associated with each parameter is indicated by the range and distribution shown for the parameter and is discussed in this section.

Table 6.5-13. Sampled Model Inputs Used in the EBS Radionuclide Transport Abstraction

Input Name	Input Description	Input Source	Range and Distribution	Type of Uncertainty
Invert_Diff_Coeff_Uncert	Invert diffusion coefficient uncertainty	Developed in Section 6.3.4.1.1, based on *Conca and Wright* (1992 [DIRS 100436], *Figure* 2), Conca et al. (1993 [DIRS 170709], Figure 2)	10ND; ND = Truncated *Normal Distribution;* Range: $10^{\pm 3\sigma}$ Mean μ = 0.033; Std. Dev. σ = 0.218	Epistemic
Kd_Ac_FeOx_CP	K_d of Ac on corrosion products	DTN: LA0003AM831341.001 ([DIRS 148751] SEP table S00191_002)	100–5,000 ml g^{-1} Log-uniform	Epistemic & Aleatoric
Kd_Am_FeOx_CP	K_d of Am on corrosion products	DTN: LA0003AM831341.001 ([DIRS 148751] SEP table S00191_002)	100–5,000 ml g^{-1} Log-uniform	Epistemic & Aleatoric
Kd_C_FeOx_CP	K_d of C on corrosion products	DTN: LA0003AM831341.001 ([DIRS 148751] SEP table S00191_002)	10–100 ml g^{-1} Uniform	Epistemic & Aleatoric
Kd_Cs_FeOx_CP	K_d of Cs on corrosion products	DTN: LA0003AM831341.001 ([DIRS 148751] SEP table S00191_002)	0–300 ml g^{-1}; Beta $E(x)$ = 30; $\sigma(x)$ = 30	Epistemic & Aleatoric
Kd_I_FeOx_CP	K_d of I on corrosion products	DTN: LA0003AM831341.001 ([DIRS 148751] SEP table S00191_001)	0.0–0.6 ml g^{-1} Uniform	Epistemic & Aleatoric
Kd_Np_FeOx_CP	K_d of Np on corrosion products	DTN: LA0003AM831341.001 ([DIRS 148751] SEP table S00191_002)	1–1,000 ml g^{-1} Log-uniform	Epistemic & Aleatoric
Kd_Pa_FeOx_CP	K_d of Pa on corrosion products	DTN: LA0003AM831341.001 ([DIRS 148751] SEP table S00191_002)	100–1,000 ml g^{-1} Uniform	Epistemic & Aleatoric
Kd_Pu_FeOx_CP	K_d of Pu on corrosion products	DTN: LA0003AM831341.001 ([DIRS 148751] SEP table S00191_002)	100–5,000 ml g^{-1} Log uniform	Epistemic & Aleatoric
Kd_Ra_FeOx_CP	K_d of Ra on corrosion products	DTN: LA0003AM831341.001 ([DIRS 148751] SEP table S00191_002)	0–500 ml g^{-1}; Beta $E(x)$ = 30; $\sigma(x)$ = 30	Epistemic & Aleatoric
Kd_Sr_FeOx_CP	K_d of Sr on corrosion products	DTN: LA0003AM831341.001 ([DIRS 148751] SEP table S00191_002)	0–20 ml g^{-1}; Beta $E(x)$ = 10; $\sigma(x)$ = 2.5	Epistemic & Aleatoric
Kd_Tc_FeOx_CP	K_d of Tc on corrosion products	DTN: LA0003AM831341.001 ([DIRS 148751] SEP table S00191_001)	0.0–0.6 ml g^{-1} Uniform	Epistemic & Aleatoric
Kd_Th_FeOx_CP	K_d of Th on corrosion products	DTN: LA0003AM831341.001 ([DIRS 148751] SEP table S00191_002)	100–5,000 ml g^{-1} Log-uniform	Epistemic & Aleatoric
Kd_U_FeOx_CP	K_d of U on corrosion products	DTN: LA0003AM831341.001 ([DIRS 148751] SEP table S00191_002)	100–1,000 ml g^{-1} Log-uniform	Epistemic & Aleatoric
Kd_Ac_Invert	K_d of Ac on crushed tuff in the invert	Developed in Section 6.3.4.2.2	Range = 1,000–10,000 ml g^{-1}; Mean = 5,500 ml g^{-1}; Std Dev. = 1,500 ml g^{-1}	Epistemic & Aleatoric
Kd_Am_Invert	K_d of Am on crushed tuff in the invert	DTN: LA0408AM831341.001 [DIRS 171584]	Range = 1,000–10,000 ml g^{-1}; Mean = 5,500 ml g^{-1}; Std Dev. = 1,500 ml g^{-1}	Epistemic & Aleatoric

Table 6.5-13. Sampled Model Inputs Used in the EBS Radionuclide Transport Abstraction (Continued)

Input Name	Input Description	Input Source	Range and Distribution		Type of Uncertainty
Kd_Cs_Invert	K_d of Cs on crushed tuff in the invert	DTN: LA0408AM831341.001 [DIRS 171584]	1–15 ml g^{-1}; Uniform		Epistemic & Aleatoric
Kd_Np_Invert	K_d of Np on crushed tuff in the invert	DTN: LA0408AM831341.001 [DIRS 171584]	(0,0) (0.5,0.5) (6.,1.0) Cumulative		Epistemic & Aleatoric
Kd_Pa_Invert	K_d of Pa on crushed tuff in the invert	DTN: LA0408AM831341.001 [DIRS 171584]	Range = 1,000–10,000 ml g^{-1}; Mean = 5,500 ml g^{-1}; Std. Dev. = 1,500 ml g^{-1}		Epistemic & Aleatoric
Kd_Pu_Invert	K_d of Pu on crushed tuff in the invert	DTN: LA0408AM831341.001 [DIRS 171584]	(10.,0) (70.,0.5) (200.,1.0) Cumulative		Epistemic & Aleatoric
Kd_Ra_Invert	K_d of Ra on crushed tuff in the invert	DTN: LA0408AM831341.001 [DIRS 171584]	100–1,000 ml g^{-1}; Uniform		Epistemic & Aleatoric
Kd_Sr_Invert	K_d of Sr on crushed tuff in the invert	DTN: LA0408AM831341.001 [DIRS 171584]	10–70 ml g^{-1}; Uniform		Epistemic & Aleatoric
Kd_Th_Invert	K_d of Th on crushed tuff in the invert	DTN: LA0408AM831341.001 [DIRS 171584]	1,000–10,000 ml g^{-1} Uniform		Epistemic & Aleatoric
Kd_U_Invert	K_d of U on corrosion products	DTN: LA0408AM831341.001 [DIRS 171584]	(0,0) (0.2,0.5) (4.,1.0) Cumulative		Epistemic & Aleatoric
SS_Corrosion_Rate	Stainless steel corrosion rate	DTN: MO0409SPAACRWP.000 [DIRS 172059]; Spreadsheet "ECDF_metals2.xls"; Worksheet "316 ss", Columns L & M, Rows 5–15 Empirical cumulative distribution function	Rate (μm yr^{-1})	ECDF	Epistemic & Aleatoric
			0.03699	0.000	
			0.037	0.063	
			0.1016	0.125	
			0.109	0.188	
			0.1524	0.250	
			0.154	0.313	
			0.1778	0.375	
			0.2032	0.438	
			0.2286	0.563	
			0.254	0.750	
			0.2794	0.813	
			0.51	1.000	

Table 6.5-13. Sampled Model Inputs Used in the EBS Radionuclide Transport Abstraction (Continued)

Input Name	Input Description	Input Source	Range and Distribution*		Type of Uncertainty
CS_Corrosion_Rate	Carbon steel corrosion rate	DTN: MO0409SPAACRWP.000 [DIRS 172059]; Spreadsheet "ECDF_metals2.xls"; Worksheet "A516-Carbon Steel", Columns B & C, Rows 5–30 Empirical cumulative distribution function	Rate ($\mu m\ yr^{-1}$)	ECDF	Epistemic & Aleatoric
			65.76	0.000	
			65.77	0.042	
			66.75	0.083	
			69.84	0.125	
			70.00	0.167	
			71.25	0.208	
			72.21	0.250	
			72.64	0.292	
			72.87	0.333	
			72.89	0.375	
			73.47	0.417	
			74.29	0.458	
			74.51	0.500	
			74.60	0.542	
			75.41	0.583	
			77.31	0.625	
			79.29	0.667	
			80.00	0.708	
			80.87	0.750	
			83.26	0.792	
			83.66	0.833	
			83.74	0.875	
			85.68	0.917	
			90.97	0.958	
			106.93	1.000	
Diff_Path_Length_CP_CSNF	Diffusive path length through corrosion products domain for CSNF packages	Developed in Section 6.5.3.1.1	0.02–0.859 m; Uniform		Epistemic & Aleatoric
Diff_Path_Length_CP_CDSP	Diffusive path length through corrosion products domain for codisposal waste packages	Developed in Section 6.5.3.1.1	0.025–1.063 m; Uniform		Epistemic & Aleatoric
Surface_Area_CP	Specific surface area of Fe2O3 corrosion products	Developed in Section 6.5.1.2.1.3.1	1.0–22 $m^2\ g^{-1}$; Uniform		Epistemic & Aleatoric

Table 6.5-13. Sampled Model Inputs Used in the EBS Radionuclide Transport Abstraction (Continued)

Input Name	Input Description	Input Source	Range and Distribution*	Type of Uncertainty
Flux_Split_DS_Uncert	DS flux splitting uncertainty factor	Developed in Section 6.5.1.1.2.4	0–0.85 (dimensionless); Uniform	Epistemic & Aleatoric
Flux_Split_WP_Uncert	WP flux splitting uncertainty factor	Developed in Section 6.5.1.1.3	0–2.41 (dimensionless); Uniform	Epistemic & Aleatoric
Fracture_Frequency	UZ fracture frequency	BSC 2004 [DIRS 170040], Appendix A, Table A-1	Mean = 3.16 m^{-1} Std. Dev. = 2.63 m^{-1} Log-normal	Epistemic
UZ_Fracture_Fraction	UZ fracture porosity	BSC 2004 [DIRS 170040], Appendix D, Table D-1	0–1 (fraction); Beta $E(x)=9.6 \times 10^{-3}$; $\sigma(x)=2.82 \times 10^{-3}$	Epistemic
UZ_Matrix_Porosity	UZ matrix porosity	BSC 2004 [DIRS 170040], Appendix D, Table D-1	0–1 (fraction); Beta $E(x) = 0.131$; $\sigma(x) = 0.031$	Epistemic
Fracture_Saturation	Unsaturated zone fracture saturation (DTN: LB0307FMRADTRN.001 [DIRS 165451])	Uniform sampling from 433 locations for each infiltration case	Provided in source DTN	Epistemic
Fracture_Residual_Sat	Unsaturated zone fracture residual saturation (DTN: LB0307FMRADTRN 001 [DIRS 165451])	Uniform sampling from 433 locations	Provided in source DTN	Epistemic
Fracture_Percolation_Flux	Unsaturated zone fracture percolation flux (DTN: LB0307FMRADTRN.001 [DIRS 165451])	Uniform sampling from 433 locations for each infiltration case	Provided in source DTN	Epistemic
Flow_Focus_Factor	Unsaturated zone fracture percolation flow-focusing factor (DTN: LB0307FMRADTRN 001 [DIRS 165451])	Uniform sampling from 433 locations for each infiltration case	Provided in source DTN	Epistemic
UZ_Matrix_Saturation	Unsaturated zone matrix saturation (DTN: LB0307FMRADTRN.001 [DIRS 165451])	Uniform sampling from 433 locations for each infiltration case	Provided in source DTN	Epistemic
Matrix_Percolation_Flux	Unsaturated zone matrix percolation flux (DTN: LB0307FMRADTRN 001 [DIRS 165451])	Uniform sampling from 433 locations for each infiltration case	Provided in source DTN	Epistemic
Matrix_Rel_Perm_Low, Matrix_Rel_Perm_Mean, Matrix_Rel_Perm_High	Unsaturated zone relative permeability for all three infiltration cases (DTN: LB0307FMRADTRN.001 [DIRS 165451])	Uniform sampling from 433 locations for each infiltration case	Provided in source DTN	Epistemic

*For distribution type beta, E(x) = expected value, σ(x) = standard deviation.

CP = corrosion products, CDSP = codisposal, WP = waste package, BET = Brunauer, Emmett and Teller, ECDF = empirical cumulative distribution function

6.5.2.1 Invert Diffusion Coefficient

The invert diffusion coefficient is used to calculate the rate of diffusion of radionuclides through the invert, after they have been released from the waste package. The uncertainty in the invert diffusion coefficient is epistemic. The values were derived from measured values of diffusion coefficients in various granular materials, including tuff. However, the data were scattered. This was particularly true at lower values of volumetric water content, where experimental difficulties are more pronounced – achieving uniform and consistent degrees of water saturation is difficult, resulting in uncertainties in the actual water content. The use of electrical conductivity measurements as an analog for diffusivity becomes more uncertain at low water content due to uncertainty in the electrical connectivity between electrodes and the porous material as well as between the particles themselves. The reported uncertainty approximates a normal distribution for the residuals in the statistical fit to the experimental data. Uncertainty in the porosity of the invert is subsumed by the greater uncertainty associated with the measurements of the diffusion coefficient; thus the porosity uncertainty can be considered to be accounted for in the diffusion coefficient.

6.5.2.2 Sorption Distribution Coefficients for Calculating In-Package Retardation

Sorption distribution coefficients (K_d values) are used to calculate sorption of radionuclides inside a breached waste package. Selection of K_d values for the 12 radionuclides listed in Table 6.5-13 is discussed in Section 6.3.4.2.2, where justification for the ranges is provided.

For iodine and technetium, the ranges are narrow (low uncertainty) because these elements have been found to be largely nonsorbing in most media, including the iron oxyhydroxides that will comprise the bulk of corrosion products. There is, however, still some uncertainty associated with these elements because they do sorb strongly onto certain substances, such as copper oxide and copper sulfide (Balsley et al. 1998 [DIRS 154439], Tables 1 and 2) and in oxidizing conditions (Onishi et al. 1981 [DIRS 154420], Table 8.96). Although the composition of the internal waste package components is known, the exact composition of the corrosion products over time is uncertain. Furthermore, the sorptive behavior of iodine and technetium in a mixture of corrosion products having a wide range of compositions is uncertain. Thus, assigning at least a small range of uncertainty is appropriate, as is a uniform distribution.

K_d values for the other elements (Am, C, Cs, Np, Pa, Pu, Ra, Sr, Th, and U) considered in calculating retardation in the EBS have been given wide ranges, reflecting the uncertainty in their values for sorption on corrosion products inside the breached waste package. Most of these elements are known to sorb strongly onto iron oxyhydroxides, as shown in Table 4.1-11. In particular, the ranges of values shown in Table 4.1-11 for sorption on iron oxide illustrates the large uncertainty in sorption distribution coefficients. One cause of this uncertainty is in the determination of the K_d values themselves, which are inherently inaccurate for high (and low) K_d values. When a great deal of sorption occurs, there can be large uncertainties associated with the measurement of the small amount of radioactivity left in solution after sorption (BSC 2001 [DIRS 160828], p. 50). This results in large uncertainties in the calculated K_d. Because of these uncertainties, most K_d values are only reported to one significant figure (BSC 2001 [DIRS 160828], p. 51). Distributions for sorption on iron oxide are uniform for C, I, Pa, and Tc,

and log-uniform for Am, Np, Pu, Th, and U. K_d values are assigned beta distributions for Cs, Ra, and Sr.

The K_d values for sorption on corrosion products for all radionuclides are sampled independently. Although K_d values for certain groups of elements may in reality be coupled or correlated due to their similar sorptive behavior and chemical response, the sparseness of data and the inherent approximations in the linear K_d approach preclude correlating K_d values for sorption on corrosion products.

Some aleatoric uncertainty exists for all of the K_d values in the uncertain chemistry of the water that might result from changes in seepage water conditions and thermal events and processes that could alter the concentration of dissolved species that affect sorption.

6.5.2.3 Sorption Distribution Coefficients for Calculating Invert Sorption

Sorption on crushed devitrified tuff in the invert also involves some epistemic uncertainty for most radionuclides. The exceptions are C, I, and Tc, which do not sorb measurably on tuff (K_d values are zero). As with K_d values for sorption on corrosion products, the invert K_d values also involve some aleatoric uncertainty due to the unpredictable chemistry of the seepage water and changes resulting from chemical processes that occur as EBS components degrade. Invert K_d values are correlated as shown in Table 4.1-13 (DTN: LA0311AM831341.001 [DIRS 167015]). In the implementation of sorption distribution coefficients in the invert in TSPA-LA, the devitrified tuff K_d values developed for the UZ submodel are assigned to the invert.

6.5.2.4 In-Package Diffusion Submodel

The corrosion rates for carbon steel and stainless steel are known with some uncertainty, as shown in the data presented in Table 4.1-1 (DTN: MO0409SPAACRWP.000 [DIRS 172059]). An empirical cumulative distribution function developed in DTN: MO0409SPAACRWP.000 [DIRS 172059] is used for parameter CS_Corrosion_Rate to be sampled in TSPA-LA. An empirical cumulative distribution function developed in DTN: MO0409SPAACRWP.000 [DIRS 172059] is used for parameter SS_Corrosion_Rate to be sampled in TSPA-LA. In view of the large range in the measured data even among multiple samples under identical conditions, some epistemic uncertainty exists in corrosion rates. In addition, the future physiochemical environment of the waste package interior will influence corrosion rates, as evidenced by the variability in rates under different conditions (DTN: MO0409SPAACRWP.000 [DIRS 172059]). Thus, aleatoric uncertainty also exists in the corrosion rates owing to the uncertain future waste package environment.

The parameters Diff_Path_Length_CP_CSNF and Diff_Path_Length_CP_CDSP are developed in Sections 6.5.3.1.1 and 6.5.3.1.2. These are the diffusion path lengths from the internal waste package corrosion products domain to the invert domain of the EBS transport abstraction for CSNF (e.g., 21-PWR and 44_BWR) and codisposal (CDSP) (e.g., 5 DHLW/DOE SNF – Short) waste packages, respectively. The radionuclide source (failed fuel rods or glass logs) and the porous corrosion products are treated as being uniformly distributed throughout the volume of the breached waste package. Breached fuel rods or glass logs may lie adjacent to the interior of a breach in the waste package or nearby. Some aleatoric uncertainty exists in the location of the

radionuclide source embedded in the corrosion products. The minimum path length is the thickness of the waste package outer corrosion barrier, 0.02 m for CSNF waste packages and 0.025 m for codisposal waste packages. The maximum is the radius of a waste package, 0.859 m for CSNF waste packages and 1.063 m for codisposal waste packages. A uniform distribution is appropriate for this parameter.

The parameter Surface_Area_CP, the specific surface area of corrosion products, is developed in Section 6.5.1.2.1.3.1, where uncertainties are discussed. This parameter accounts for the uncertainty in the computed surface area of corrosion products that is available for water adsorption inside a breached waste package. The calculated mass of corrosion products is multiplied by their specific surface area to compute the bulk surface area. The uncertainties are both aleatoric and epistemic. Unpredictable processes or events may occur that impact the morphology of corrosion products and alter their surface area, including seismic events, collapse of waste package internal structures, and changes in seepage rates. The nature of corrosion products formed under the conditions in a breached waste package in a humid environment, from a mixture of various types of steel, and their behavior in response to events and process that may occur is also uncertain. Due to the sparseness of the data for the specific surface area of corrosion products, only a uniform distribution can be justified for this parameter.

6.5.2.5 EBS-UZ Boundary Condition Implementation in TSPA-LA

The EBS-UZ boundary condition implementation, discussed in Section 6.5.3.6, is applied when the EBS transport abstraction is discretized and implemented in GoldSim. This model provides the radionuclide concentration boundary condition at the invert-UZ boundary such that the far-field concentration is approximately zero. To compute this boundary condition, a portion of the UZ is modeled, so input parameters for the UZ are used and therefore become EBS transport input parameters. The uncertainty in sampled parameters is discussed in this section; details about how UZ parameters are used are provided in Section 6.5.3.6.

Most of the parameters used for the EBS-UZ boundary condition implementation are taken from the output of *Drift-Scale Radionuclide Transport* (BSC 2004 [DIRS 170040]), in which specification of the ranges and distributions for the parameters is discussed. The parameters were developed for the discrete fracture-matrix partitioning model (BSC 2004 [DIRS 170040]). Although the modeling approach used in the *EBS RT Abstraction* is different, the parameter values remain unchanged. The parameter values are given in DTN: LB0307FMRADTRN.001 ([DIRS 165451], Folder: U0230_excel_files.zip). These parameters were developed for the lower, mean, and upper bound flow fields for the glacial transition climate and recommended for use in TSPA-LA for the entire duration of the simulation. The glacial transition lower, mean, and upper infiltration cases cover a range of conditions that encompass all of the monsoon climates and all but the present-day lower infiltration climate. Furthermore, most of the regulatory compliance period (2,000 to 10,000 years) is modeled as being under glacial transition climate. Because of the predominance in time and wide range of the glacial transition infiltration cases, these three cases are used as representative for the low, mean, and high infiltration cases for the entire compliance period.

6.5.2.5.1 Matrix and Fracture Percolation Fluxes

Similar to the approach taken in *Drift-Scale Radionuclide Transport* (BSC 2004 [DIRS 170040]), in the EBS-UZ interface submodel, the parameter uncertainty is included through uniform sampling of the 433 different repository locations that have been assigned model parameters such as fracture and matrix flux and water saturation values. These values have been taken from the output of the UZ flow model for the repository host rock; see Sections 6.4.5 and 6.4.6 of *Drift-Scale Radionuclide Transport* (BSC 2004 [DIRS 170040]) for additional information. The sampled parameters that are based on repository locations are sampled such that if a flux for a certain location is considered then the saturation for the same location is also used.

6.5.2.5.2 Fracture Frequency

The fracture frequency distribution for each UZ model layer is presented in Table A-1 of *Drift-Scale Radionuclide Transport* (BSC 2004 [DIRS 170040], Appendix A, Table A-1). Since approximately 80 percent of the waste emplacement drift area is occupied by the TSw35 (Topopah Spring welded tuff lower lithophysal) unit of the UZ model (Appendix H of *Drift-Scale Radionuclide Transport*, BSC 2004 [DIRS 170040]), and because of the small variation in fracture frequency among various units, it is sufficient to use the fracture frequency distribution for TSw35 as given in Table A-1 of *Drift-Scale Radionuclide Transport* (BSC 2004 [DIRS 170040], Appendix A, Table A-1).

6.5.2.5.3 Fracture Fraction

The average fraction of the UZ that is occupied by fractures (also referred to as fracture porosity) is given as a distribution in Table D-1 of *Drift-Scale Radionuclide Transport* (BSC 2004 [DIRS 170040], Appendix D). As with fracture frequency, the fracture porosity distribution for TSw35 given in Table D-1 of *Drift-Scale Radionuclide Transport* (BSC 2004 [DIRS 170040], Appendix D) is sufficient for modeling purposes.

6.5.2.5.4 Fracture Flow-Focusing Factor

The flow focusing of fracture flux at the drift scale is included through a flow-focusing factor. The sampled fracture flux is adjusted by multiplying it by the sampled flow-focusing factor (see *Drift Scale Radionuclide Transport,* BSC 2004 [DIRS 170040], Equation G-3 and Appendix C). A separate flow focusing factor is presented for each of the 433 repository locations.

6.5.2.5.5 Matrix Porosity

A distribution for matrix porosity for various UZ model layers is given in Table D-1 of *Drift-Scale Radionuclide Transport* (BSC 2004 [DIRS 170040], Appendix D, Table D-1). Matrix porosity distribution for TSw35 is used for modeling purpose.

6.5.2.5.6 Fracture Saturation

The physical saturation of the fracture is computed in *Drift-Scale Radionuclide Transport* (BSC 2004 [DIRS 170040], Appendix G, Equation G-6). This takes into account the effect of

flow focusing to account for sub-grid-block-scale heterogeneity for the mountain-scale flow fields in the fracture continuum. This value is calculated for the 433 repository locations for all three infiltration cases.

6.5.2.5.7 Fracture Residual Saturation

The fracture residual saturation is computed in *Drift-Scale Radionuclide Transport* (BSC 2004 [DIRS 170040], Appendix G). It is developed for 433 repository locations and does not vary by the infiltration case.

6.5.2.5.8 Matrix Relative Permeability

The matrix effective permeability to water is derived from *Drift-Scale Radionuclide Transport* (BSC 2004 [DIRS 170040], Equation 6-57), by multiplying the matrix intrinsic permeability by the matrix relative permeability. The matrix intrinsic permeability for all four UZ model layers at the repository horizon (TSw33, TSw34, TSw35, and TSw36) are given in *Drift-Scale Radionuclide Transport* (BSC 2004 [DIRS 170040], Table 4-6) for each infiltration case. The relative permeability is sampled for 433 repository locations and varies with the infiltration case; it is given in *Drift-Scale Radionuclide Transport* (BSC 2004 [DIRS 170040], Table B-1).

6.5.3 Summary of Computational Model

The object of the EBS radionuclide transport abstraction is to determine the rate of radionuclide releases from the EBS to the unsaturated zone. In the proposed EBS transport model, the EBS is spatially partitioned into the following domains: (1) waste form, consisting of for example, fuel rods or HLW glass; (2) waste package corrosion products; and (3) invert. In addition, the UZ immediately underlying the invert is conceptualized as a dual continuum consisting of (4) UZ matrix continuum and (5) UZ fracture continuum. The inclusion of a portion of the UZ is needed for an accurate calculation of the invert-to-UZ interface fluxes by providing a diffusive path length that is sufficiently long such that the concentration at the outlet of the UZ can realistically be assigned a value of zero.

In the waste form domain, degradation processes occur, including breaching and axial splitting of fuel rods, dissolution of SNF and HLW glass, and formation of waste form colloids wherever applicable. Dissolved species are transported by advection and/or diffusion to the waste package corrosion products domain. The primary interactions in the corrosion products domain involving radionuclide species are reversible and irreversible sorption of dissolved species onto iron oxyhydroxide colloids and stationary corrosion products, and reversible sorption onto groundwater colloids and waste form colloids (when present). In the invert domain, radionuclides released from the corrosion products domain are transported by advection and diffusion, and interact with the crushed tuff by adsorption processes. The properties of each domain, including the volume, porosity, water saturation, diffusion cross sectional area, and diffusive path length, affect the rate of advective and diffusive transport of radionuclides through the domain. The invert domain interfaces with both continua of the UZ. The properties of the domains are defined in the following sections.

6.5.3.1 Waste Form and Waste Package Diffusion Properties

This section summarizes the general approach, major assumptions, main steps in the computational algorithm, and the stochastic parameters for the in-package diffusion submodel for TSPA-LA sensitivity studies. The mathematical equations for the in-package diffusion submodel are described in Section 6.5.1.2.1.

The general approach for the commercial SNF (21-PWR and 44-BWR) waste packages is to consider two pathways for diffusion: (1) through porous waste form products inside the package, and (2) through porous corrosion products filling the bottom of the waste package. Starting from the time when a package is first breached, the extent of degradation is determined. This parameter is the basis for estimating the amount of corrosion products present inside a package, and allows the water saturation and effective diffusion coefficient to be computed.

Implementation of the three-domain EBS abstraction requires that properties be specified for each domain, including the volume, diffusive area, the diffusive path length, porosity, water saturation, and the procedure for calculating the diffusion coefficient. These properties must be specified for each type of waste package (CSNF and codisposal waste packages) and for the drip and no-seep environment.

6.5.3.1.1 CSNF Waste Packages Properties

This section discusses the CSNF waste package properties in the following two domains: CSNF waste form and CSNF corrosion products.

6.5.3.1.1.1 CSNF Waste Form Domain:

In CSNF waste packages, the waste form domain consists of fuel rods. Radionuclides are released only from failed rods. Although fuel rods initially fail either by perforations in the cladding as a result of corrosion or by damage in handling or in seismic events, it is assumed that the fuel rod cladding instantly splits along its length when the waste package fails (BSC 2004 [DIRS 170023], Assumption 5.3). Fuel rods split when the SNF reacts with the oxygen and moisture inside the waste package, forming metaschoepite. The resulting material, having a greater volume than SNF (mostly UO_2), causes the fuel rod to split open. The configuration of the failed rod is a mostly intact tube with the slit along the length exposing the SNF inside.

The reacted SNF constitutes a porous "rind" that is modeled as saturating quickly and completely with water, both in a seep and no-seep environment. The volume of the rind as a function of time and the rind porosity are provided by *Clad Degradation – Summary and Abstraction for LA* (BSC 2004 [DIRS 170023]). Radionuclides dissolve in the water that fully saturates the pore volume of the rind.

The diffusive area of the waste form domain is the total exposed surface area of the SNF in all of the axially split fuel rods, i.e., the area of the slit times the number of failed fuel rods. This area is provided by *Clad Degradation – Summary and Abstraction for LA* (BSC 2004 [DIRS 170023]).

The diffusive path length is the thickness of the rind, which is a function of time as the SNF reacts to form metaschoepite.

The diffusion coefficient is computed using Archie's law (Equation 6.5.1.2.1-12), with the porosity of the rind and the assigned water saturation of 1.0. As discussed in Section 6.5.3.5, the discretized mass balance equations use a diffusive conductance, which is a harmonic average of diffusion coefficient terms (including diffusivity, porosity, saturation, diffusive path length, and cross-sectional area for diffusion; see Equation 6.5.3.5-7), in this case, for the waste form and corrosion products domains. Since the TSPA-LA model, GoldSim (GoldSim Technology Group 2002 [DIRS 160579]) computes the diffusive conductance, only the diffusion coefficients need to be input, rather than the diffusive conductances themselves.

6.5.3.1.1.2 CSNF Corrosion Products Domain:

The second domain consists of the corrosion products inside the waste package. The mass of corrosion products (m_{CP}) is given as a function of time by Equation 6.5.3.2-5 below. In Section 6.5.1.2.1.3.2, a porosity (ϕ_{CP}) of 0.4 for corrosion products is shown to be appropriate. The corrosion products are assumed to be Fe_2O_3. With the known density of Fe_2O_3 (ρ_{FeOx}), the pore volume of the corrosion products domain is computed from:

$$V_{CP} = \frac{m_{CP}}{\rho_{FeOx}}\left(\frac{\phi_{CP}}{1-\phi_{CP}}\right). \qquad \text{(Eq. 6.5.3.1.1-1)}$$

In a seep environment, the water saturation (S_w) is assigned a value of 1.0. In a no-seep environment, the only water present is adsorbed water, and the saturation is the effective saturation of corrosion products given by Equation 6.5.1.2.1-27. Uncertainty in the water saturation of the corrosion products is provided for in the sampled specific surface area of the corrosion products.

In a seep environment, the effective diffusion coefficient for corrosion products is given by Archie's law (Equation 6.5.1.2.1-12), with the porosity ϕ_{CP}=0.4 and the assigned water saturation of 1.0.

In a non-seep environment, the effective diffusion coefficient is given by Eq. 6.5.1.2.1-28. The diffusive area of the corrosion products domain for diffusion to the invert domain is the total area of all waste package breaches, including corrosion patches and stress corrosion cracks. The breached area is determined differently for each scenario class:

- For the nominal scenario class:
  - Without early failure modeling cases and with no localized corrosion, the breached area is provided by the integrated waste package degradation model developed in *WAPDEG Analysis of Waste Package and Drip Shield Degradation* (BSC 2004 [DIRS 169996], Section 7.1.1.1).

- In the early failure modeling cases (no localized corrosion), the entire surface area of the waste package is breached (*WAPDEG Analysis of Waste Package and Drip Shield Degradation* [BSC 2004 (DIRS 169996), Section 6.3.8]).

- In the localized corrosion case, localized corrosion results from dust deliquescence only (i.e., no dripping flux), and the breached area is the entire lateral surface area of the waste package (*General Corrosion and Localized Corrosion of Waste Package Outer Barrier* [BSC 2004 (DIRS 169984), Section 8.3.1]). Values for the breached areas for CSNF and CDSP waste packages are provided by *WAPDEG Analysis of Waste Package and Drip Shield Degradation* (BSC 2004 [DIRS 169996], Section 6.3.2).

• For the seismic scenario class:

- With ground motion damage only (no localized corrosion), the breached area is provided by the *Seismic Consequence Abstraction* (BSC 2004 [DIRS 169183], Section 6.5.3). This breached area is applied to the thickness of the waste package outer shell only. For the rest of the corrosion products domain, the waste package plan area, equal to the waste package diameter times its length, is used.

- For the localized corrosion case, localized corrosion results from dust deliquescence as well as from seepage flux when seismic damage to the drip shield has occurred. The breached area is provided by the *General Corrosion and Localized Corrosion of Waste Package Outer Barrier* (BSC 2004 [DIRS 169984], Section 8.3.1).

• For the igneous scenario class:

- In the igneous intrusive scenario, the entire waste package is breached, and the waste package and cladding provide no further protection to the waste forms (BSC 2004 [DIRS 168960], Section 6.7.1).

- In the igneous eruptive scenario, the entire inventory of affected waste packages is made available for release to the air as ash. The EBS transport model does not apply.

The diffusive path length is a sampled parameter (see Table 6.5-13) ranging from 0.02 m (the thickness of the waste package outer corrosion barrier) to 0.859 m (the outside radius of a 21-PWR) (BSC 2004 [DIRS 169472], Table 1).

6.5.3.1.2 Codisposal Waste Packages Properties

Codisposal waste packages consist of five cylindrical canisters containing HLW glass (glass "logs") surrounding a central canister of defense spent nuclear fuel (DSNF). After the codisposal waste package is breached, the HLW glass eventually degrades to a clay-like material. However, the DSNF degrades almost instantaneously (within a single TSPA-LA time step) to uranium oxide (BSC 2004 [DIRS 167618], Section 8.1) after the waste package is breached, compared to the slower degradation of the HLW glass logs. Although the steel support framework inside the waste package corrodes, allowing the canisters of glass to collapse onto each other, the general cylindrical shape of the canisters is retained. With this assumption

of the internal configuration of a degraded codisposal waste package, the diffusive area between the conceptual waste form domain and the corrosion product domain is the sum of the initial surface area of the five glass logs. The DSNF is treated as part of the corrosion product domain, rather than part of the waste form domain, because degraded DSNF is conceptualized to be present corroded mass of uranium oxide, just as the iron corrosion products formed from the degradation of steel components inside the waste package.

The volume of the waste form domain is equal to the volume of degraded glass, which is determined from the degradation rate of the glass as provided by the defense HLW glass degradation model (BSC 2004 [DIRS 169988], Section 6.5).

The diffusive path length from the waste form domain to the corrosion products domain is the thickness of the degraded glass (the rind thickness), which is a function of time. This is determined from the degradation rate of the glass.

The diffusion coefficient of degraded glass is computed using Archie's law (Equation 6.5.1.2.1-12), with the porosity of the glass degradation products provided by the *Defense HLW Glass Degradation Model* (BSC 2004 [DIRS 169988], Table 8-1) and the assigned water saturation of 1.0.

The volume of corrosion products in a codisposal waste package is proportional to the mass of steel that has corroded. The mass of corrosion products is estimated as a function of time based on sampled corrosion rates for carbon and stainless steels. As shown in Table 6.3-4, the total mass of steel in a codisposal waste package (5 DHLW/DOE SNF – Short) is slightly less than in a 21-PWR. Using this mass and the porosity and density of corrosion products, the volume of the corrosion products domain in a codisposal waste package is computed using Equation 6.5.3.1.1-1. Because of the deliquescent nature of glass and glass degradation products, the corrosion products that surround those materials are considered to be fully saturated with water.

The degraded DSNF, considered to be part of the corrosion product domain, has water associated with it. The initial volume of DSNF in a codisposal waste package is given as 1 m^3 (BSC 2004 [DIRS 167618], Section 8.1). Because the degraded DSNF is conceptualized to be in a powdered form, it can be modeled as having a porosity of 0.2. The porosity is based on the porosity of unconsolidated sand, which ranges from 0.25 to 0.50 (Freeze and Cherry 1979 [DIRS 101173], Table 2.4); a value lower than this range is used to account for some consolidation. In addition, a smaller water volume results in higher radionuclide concentrations and hence overestimates releases. Just like corrosion products, the powdered DSNF can be considered fully saturated, yielding a water volume of 0.2 m^3. The water volume associated with the corrosion products is expected to dominate the water volume associated with DSNF due to the larger mass of steel. For this reason, the water volume associated with DSNF can be considered as the lower bound for the water volume in the corrosion product domain. Once the water volume associated with corrosion products exceeds the water volume associated with DSNF, then the corrosion product water volume is used.

The diffusive area between the corrosion products domain and the invert domain is the total area of all breaches in the Alloy 22 outer corrosion barrier of the waste package. The diffusive area is

dependent on the scenario class; the determination of diffusive areas as discussed in Section 6.5.3.1.1 for CSNF waste packages also applies to CDSP waste packages.

The diffusive path length is uncertain since the actual source of dissolved radionuclides inside the waste package may be located anywhere within the waste package at any given time. Thus, the path length is sampled, ranging from the thickness of the outer corrosion barrier (0.02 m) to the nominal radius of the 5 DHLW/DOE SNF - Short codisposal waste package, 1.063 m (BSC 2004 [DIRS 169472], Table 1).

The diffusion coefficient in codisposal waste package corrosion products is computed the same as for CSNF corrosion products using Archie's law (Equation 6.5.1.2.1-12), with the porosity of the corrosion products (ϕ_{CP}=0.4) and the assigned water saturation of 1.0.

6.5.3.2 Calculation of Corrosion Products Mass and Saturation

The major steps in the computational procedure are:

- Determine the extent of degradation of the iron-based internal components of the waste package and the resulting surface area available for adsorption of water vapor. This is a two-step process.

  First Step–Suppose the iron-based internal components have a lifetime equal to that of either the carbon steel components (maximum 10 mm thick) or the stainless steel inner vessel, which is 50 mm thick. Compute the lifetime by dividing the thickness by the corrosion rate for each type of steel. From Table 6.3-4, carbon steel comprises 30 percent of the total mass of steel in a 21-PWR and 33 percent in a 44-BWR. As an approximation, one-third of the iron-based internal components in all waste packages is carbon steel and two-thirds is stainless steel. Each type of steel corrodes at a different rate, determined by sampling its rate distribution. The lifetime of carbon steel (yr) is then given by:

$$t_{f1} = \frac{1000(\text{Max\_Thick\_CS})}{r_1}, \qquad \text{(Eq. 6.5.3.2-1)}$$

  where r_1 is the sampled value for the corrosion rate of carbon steel ($\mu m\ yr^{-1}$), and Max_Thick_CS is the maximum thickness of carbon steel components (mm). From *D&E/PA/C IED Typical Waste Package Components Assembly* (BSC 2004 [DIRS 169472], Table 2), the maximum thickness of a carbon steel waste package component is 3/8 in. = 9.525 mm, which is rounded to 10 mm for this parameter value. Similarly, the lifetime of stainless steel (yr) is given by:

$$t_{f2} = \frac{1000(\text{Max\_Thick\_SS})}{r_2}, \qquad \text{(Eq. 6.5.3.2-2)}$$

  where r_2 is the sampled value for the corrosion rate of stainless steel ($\mu m\ yr^{-1}$), and Max_Thick_SS is the maximum thickness of stainless steel components (mm). From

Design and Engineering, 21-PWR Waste Package Configuration (BSC 2004 [DIRS 167394], Detail A), the maximum thickness of a stainless steel in a waste package is the inner vessel thickness of 50.8 mm.

Second Step–One-third of the total mass of the internal components is assigned to carbon steel components and two-thirds are assigned to stainless steel components, similar to the assumption for the first step. When these components are fully corroded, the same proportions hold, but the rate of formation of corrosion products depends on the sampled rates of the two types of steel. The total mass of corrosion products when internal components are fully degraded, m_{CPf} (19,440 kg Fe_2O_3 in a 21-PWR; see Section 6.3.4.2.2), is based on data presented in Table 6.3-4. The initial mass of corrosion products is zero. For each type of steel, the mass of corrosion products present at time t (yr) is proportional to the fraction of the lifetime of each steel since the waste package was breached:

Carbon steel:
$$m_{CP1} = \begin{cases} \left(\dfrac{t-t_0}{t_{f1}}\right)\dfrac{1}{3}m_{CPf}, & t-t_0 \le t_{f1} \\ \dfrac{1}{3}m_{CPf}, & t-t_0 > t_{f1}, \end{cases} \qquad \text{(Eq. 6.5.3.2-3)}$$

Stainless steel:
$$m_{CP2} = \begin{cases} \left(\dfrac{t-t_0}{t_{f2}}\right)\dfrac{2}{3}m_{CPf}, & t-t_0 \le t_{f2} \\ \dfrac{2}{3}m_{CPf}, & t-t_0 > t_{f2}, \end{cases} \qquad \text{(Eq. 6.5.3.2-4)}$$

where t_0 is the time (yr) when the first breach appears in the waste package.

Then the total mass of corrosion products present is $m_{CP}(t) = m_{CP1} + m_{CP2}$. During the regulatory period:

Total corrosion products:
$$m_{CP}(t) = \frac{1}{3}m_{CPf}(t-t_0)\left(\frac{1}{t_{f1}} + \frac{2}{t_{f2}}\right), \qquad \text{(Eq. 6.5.3.2-5)}$$

The total surface area of corrosion products, s_{CP}, is obtained using the sampled value for the specific surface area of corrosion products, $\bar{s}_{CP}$:

Total surface area:
$$s_{CP} = \bar{s}_{CP} m_{CP}. \qquad \text{(Eq. 6.5.3.2-6)}$$

- Let the water saturation in the waste package corrosion products be 1.0 in the seep environment for both CSNF and codisposal waste packages and in the no-seep environment for codisposal waste packages. For CSNF waste packages in the no-seep environment, use the adsorption isotherm for Fe_2O_3 and compute the amount of water

vapor adsorbed (number of monolayers and film thickness) and the water saturation in the waste package corrosion products as follows (see Section 6.5.1.2.1.4.2):

$$S_{we,CP} = 3.28\times10^{-6}\,\bar{s}_{CP}\left(-\ln RH\right)^{-1/2.45} \qquad \text{(Eq. 6.5.3.2-7)}$$

- Compute the effective diffusion coefficient for steel corrosion products, D_s, using Archie's law with a fixed porosity of 0.4 (see Section 6.5.1.2.1.3.2) and the water saturation S_{we} obtained from the preceding bullet (either 1.0 or Equation 6.5.3.2-7).

6.5.3.3 Invert Domain Properties

The volume of the invert is equal to its cross sectional area (i.e., the area of a segment of a circle) times the axial length. Based on the drift diameter of 5.5 m (BSC 2004 [DIRS 169503]) (or drift radius $r_D = 2.75$ m) and maximum invert thickness of $t_{I,max} = 2$ ft 10 in. = 0.8636 m (BSC 2004 [DIRS 169503]), the width of the top surface of the invert is (Perry et al. 1963 [DIRS 119529], p. 2-6):

$$w_I = 2\sqrt{r_D^2 - \left(r_D - t_{I,max}\right)^2} = 4.00\,\text{m}. \qquad \text{(Eq. 6.5.3.3-1)}$$

The frontal cross sectional area of the invert is (Perry et al. 1963 [DIRS 119529], p. 2-6):

$$A_I = r_D^2\cos^{-1}\left(\frac{r_D - t_{I,max}}{r_D}\right) - \left(r_D - t_{I,max}\right)\sqrt{2r_D t_{I,max} - t_{I,max}^2} \qquad \text{(Eq. 6.5.3.3-2)}$$
$$= 2.39\,\text{m}^2.$$

The invert volume is this area (A_I) multiplied by the length of interest, for example, the length of a waste package, L_{WP}. The volume of water in the invert beneath a waste package of length L_{WP} is:

$$V_{wI} = \phi S_w A_I L_{WP}, \qquad \text{(Eq. 6.5.3.3-3)}$$

where ϕ is the porosity of the invert, and S_w is the water saturation of the invert.

For purposes of modeling flow and diffusion through the invert, the invert is regarded as having a rectangular cross section with a top surface being the actual top surface of the invert. The cross sectional area for flow or diffusion between the invert and the unsaturated zone is:

$$A_{I/UZ} = w_I L_{WP}. \qquad \text{(Eq. 6.5.3.3-4)}$$

The average thickness of the invert is given by:

$$\bar{t}_I = \frac{A_I}{w_I} = 0.597\,\text{m}. \qquad \text{(Eq. 6.5.3.3-5)}$$

Using this value preserves the top surface area and volume of the invert.

Sorption of radionuclides to the invert crushed tuff is modeled by applying the devitrified tuff K_d values from the UZ submodel to the invert. Ranges and distributions for these K_d values are shown in Table 4.1-12. The K_d values are correlated using the correlation matrix shown in Table 4.1-13.

The bulk water content in the invert, θ (fraction: m^3 water m^{-3} bulk volume), is used to compute the diffusion coefficient in the invert, Equation 6.3.4.1.1-16 (in which $\phi^{1.863}S_w^{1.863} = \theta^{1.863}$). The bulk water content in the invert is determined from the intragranular water saturation provided by *Multiscale Thermohydrologic Model* (BSC 2004 [DIRS 169565], Appendix X) and the seepage flux provided by the *Seepage Model for PA Including Drift Collapse* (BSC 2004 [DIRS 167652]).

The relationship between the bulk water content and the intergranular and intragranular water contents is based on the definitions of water content using the volumes of water, solids, and pore spaces:

$$\begin{aligned}\theta &= \frac{V_{w\_inter} + V_{w\_intra}}{V_t} = \frac{V_{w\_inter}}{V_t} + \frac{V_{w\_intra}}{V_t} \\ &= \theta_{inter} + \frac{V_{w\_intra}}{V_t},\end{aligned} \qquad \text{(Eq. 6.5.3.3-6)}$$

where V_{w_inter} is the volume of water in the intergranular pore space (m^3), V_{w_intra} is the volume of water in the intragranular (matrix) pore space (m^3), V_t is the total bulk invert volume (m^3), and θ_{inter} is the intergranular water content (a fraction here: m^3 water m^{-3} bulk volume; generally having units of percent throughout this report).

The ratio of water volume to total invert bulk volume, V_{w_intra}/V_t, is related to the porosity of the of the intragranular (tuff matrix) pore space, ϕ_{intra} (m^3 pore volume m^{-3} matrix volume):

$$\frac{V_{w\_intra}}{V_t} = \frac{V_{t\_intra}S_{w\_intra}}{V_t} = \frac{\phi_{intra}\left(V_t - V_{t\_inter}\right)S_{w\_intra}}{V_t}, \qquad \text{(Eq. 6.5.3.3-7)}$$

where S_{w_intra} is the water saturation of the matrix (m^3 water m^{-3} pore volume), V_{t_intra} is the total pore volume of the matrix (m^3), and V_{t_inter} is the total pore volume of the intergranular pore space (m^3). This expression makes use of the definition of matrix porosity, ϕ_{intra}, as the ratio of matrix pore volume to total matrix volume, where the latter is the difference between the bulk invert volume, V_t, and the intergranular pore volume, V_{t_inter}:

$$\phi_{intra} = \frac{V_{t\_intra}}{V_t - V_{t\_inter}}, \qquad \text{(Eq. 6.5.3.3-8)}$$

which can be rearranged to give:

$$V_{t\_intra} = \phi_{intra}\left(V_t - V_{t\_inter}\right). \qquad \text{(Eq. 6.5.3.3-9)}$$

Substituting the definitions of water content $\left(\theta_{intra} = \phi_{intra} S_{w\_intra}\right)$ and porosity of the intergranular pore space, $\left(\phi_{inter} = V_{t\_inter} / V_t\right)$, the ratio V_{w_intra} / V_t in Equation 6.5.3.3-6 can be written:

$$\frac{V_{w\_inter}}{V_t} = \theta_{intra}\left(1 - \phi_{inter}\right). \qquad \text{(Eq. 6.5.3.3-10)}$$

Inserting this into Equation 6.5.3.3-6 results in the expression for the bulk water content of the invert:

$$\theta = \theta_{inter} + \left(1 - \phi_{inter}\right)\theta_{intra}. \qquad \text{(Eq. 6.5.3.3-11)}$$

The intragranular water content, θ_{intra}, is calculated by multiplying the intragranular water saturation provided by the *Multiscale Thermohydrologic Model* (BSC 2004 [DIRS 169565]) with the intragranular porosity of ϕ_{intra} = 0.131 (DTN: LB0207REVUZPRP.002 [DIRS 159672]; Spreadsheet "Matrix_Props.xls", Row 20, Column C).

The intergranular water content, θ_{inter}, is evaluated indirectly from the seepage flux into the drift. The volumetric discharge into the invert, Q_I (m^3 water s^{-1}), which is equal to the seepage flux into the drift (see Equation 6.5.1.1-8, where $F_6 = F_1$), is given by:

$$Q_I = K_{us} I_s A_{Is} \qquad \text{(Eq. 6.5.3.3-12)}$$

where K_{us} is the unsaturated hydraulic conductivity of the invert (m s^{-1}), I_s is the hydraulic head gradient in the invert (m m^{-1}), and A_{Is} is the intercepted flow area of a drift over the length of one waste package, having a value of 28.05 m^2 (BSC 2004 [DIRS 167652], Section 6.3.1). For vertical one-dimensional flow, a hydraulic head gradient of unity $\left(I_s = 1\ \text{m/m}\right)$ is a bounding value for saturated rock with a free surface exposed to the open drift. Unsaturated crushed rock in the invert will have a lower head gradient, but by using a gradient of unity, Equation 6.5.3.3-12 simplifies and allows the unsaturated hydraulic conductivity of the invert to be evaluated given the seepage flux into the drift:

$$K_{us} = \frac{Q_I}{A_{Is}}. \qquad \text{(Eq. 6.5.3.3-13)}$$

The unsaturated hydraulic conductivity of the invert has been evaluated as a function of moisture potential, ψ (bar), in the *Multiscale Thermohydrologic Model* (BSC 2004 [DIRS 169565], Appendix X, Table X-6) for various particle sizes. The determination of intergranular water content uses a particle size of 3 mm (BSC 2004 [DIRS 169565], Section 6.3.11). Interpolating in Table X-6 of *Multiscale Thermohydrologic Model* (BSC 2004 [DIRS 169565]) for the

unsaturated hydraulic conductivity of the invert, K_{us}, as given by Equation 6.5.3.3-13, results in a value for the moisture potential, ψ, which is inserted into a van Genuchten fitting function (BSC 2004 [DIRS 169565], Equation X.4) to give the intergranular water content:

$$\theta_{inter} = \theta_r + \frac{(\theta_s - \theta_r)}{\left[1 + (\psi\alpha)^n\right]^m}, \qquad \text{(Eq. 6.5.3.3-14)}$$

Parameters in Equation 6.5.3.3-14 are:

θ_r = residual volumetric water content in the invert (fraction)
= 0.050 (BSC 2004 [DIRS 169565], Appendix X, Table X-7)

θ_s = saturated volumetric water content in the invert (fraction)
= 0.450 (BSC 2004 [DIRS 169565], Appendix X, Table X-7)

α = van Genuchten air-entry parameter (bar^{-1})
= 624. bar^{-1} (BSC 2004 [DIRS 169565], Appendix X, Table X-7)

n = van Genuchten n value (dimensionless)
= 8.013 (BSC 2004 [DIRS 169565], Appendix X, Table X-7)

m = van Genuchten m value (dimensionless)
= 0.875 (BSC 2004 [DIRS 169565], Appendix X, Table X-7)

With the algorithm and parameters described in this section, the bulk volumetric water content in the invert is obtained.

6.5.3.4 Irreversible Sorption onto Iron Oxyhydroxide Colloids and Stationary Corrosion Products

Irreversible sorption of Pu and Am onto iron oxyhydroxide colloids and stationary corrosion products in the corrosion product domain is considered. A linear forward rate constant is needed for modeling irreversible sorption. In the no-seep case or where iron oxyhydroxide colloids are unstable, the forward rate constant is randomly sampled from a range of 0.01 $m^3\ m^{-2}\ yr^{-1}$ to 0.24 $m^3\ m^{-2}\ yr^{-1}$, with a log-uniform distribution (DTN: SN0309T0504103.010 [DIRS 165540]).

For the seep case where colloids are stable, the forward rate constant k_f describing irreversible sorption to iron oxyhydroxide corrosion products and colloids (Equations 6.5.1.2-12 and 6.5.1.2-17) is computed as a fitting parameter to match a specified flux out ratio for the corrosion products domain (BSC 2004 [DIRS 170025], Section 6.3.3.2). The flux out ratio (Ω) is the ratio of radionuclide flux exiting the corrosion product domain that is transported by colloids to the total flux exiting the corrosion product domain (in dissolved state or sorbed onto colloids). The mass of radionuclides in the fluid exiting the corrosion products domain is expected to be proportioned such that the mass of radionuclide species *i* sorbed onto all colloids is some fraction of the total mass of radionuclide species *i* exiting the system in all forms–aqueous, reversibly sorbed, and irreversibly sorbed. Observations in nature, such as the transport of Pu from the

Benham test site (Kersting et al. 1999 [DIRS 103282]) indicate that this fraction is about 95 percent.

This is expressed as:

$$\Omega = \frac{\text{colloid mass flux out}}{\text{total mass flux out}} = 0.95 . \qquad \text{(Eq. 6.5.3.4-1)}$$

This flux out ratio value of 95 percent is uncertain with an uncertainty range of 0.9 to 0.99 associated with it (BSC 2004 [DIRS 170025], Table 6-12, p. 6-72). It also may be a function of time, since the observation time for the Benham test is only about 50 years. In TSPA-LA, irreversible sorption occurs only for Pu and Am.

The dependence of the forward rate constant on the flux out ratio is obtained from an analytical solution of a finite difference approximation of transport in the corrosion products domain. The function for evaluating the forward rate constant is given by Equation B-72 in Appendix B.

This treatment applies in a seep environment. The calculated forward rate constant is constrained to be less than or equal to the maximum value of the sampled range, 0.24 $m^3\ m^{-2}\ yr^{-1}$.

6.5.3.5 Discretization and Development of Computational Model for TSPA-LA

The continuum mass balance equations for EBS transport model are described and developed in Section 6.5.1.2. The one-dimensional mass balance equation describing transport of dissolved and reversibly sorbed radionuclide species *i* is provided by Equation 6.5.1.2-46. The one-dimensional mass balance equations for irreversibly sorbed radionuclide species *i* on iron oxyhydroxide colloids and corrosion products are given by Equations 6.5.1.2-47 and 6.5.1.2-48, respectively. The solution of these continuum-form mass balance equations is approximated for the purpose of numerical modeling by the solution of discrete forms of these equations using a finite-difference approach. This requires the discretization of the time derivative (or mass accumulation term) and the advective and diffusive terms for both dissolved and colloidal transport. All other source terms and decay terms do not require discretization in either time or space.

Numerical modeling of the EBS radionuclide transport is performed using the GoldSim software (Golder Associates 2003 [DIRS 166572]) cell pathway capability, available in the GoldSim Contaminant Transport Module. The cell pathway acts as a batch reactor, where radionuclide mass is assumed to be instantaneously and completely mixed and partitioned among all media (fluid or solid) within the cell. Both advective and diffusive transport mechanisms can be explicitly represented using the cell pathways. When multiple cells are linked together via advective and diffusive mechanisms, the behavior of the cell network is mathematically described using a coupled system of differential equations, and is mathematically equivalent to a finite difference network. GoldSim numerically solves the coupled system of equations to compute the radionuclide mass present in each cell and the mass fluxes between cells as a function of time. Both initial and boundary conditions for a cell can be defined explicitly, and systems of varying geometry can be modeled.

Within a computational cell network, each cell is allowed to communicate by advection and/or diffusion with any other cell. This concept is crucial in implementing the bifurcation of diffusive fluxes across an interface between a single continuum domain and a dual continuum domain, such as at the interface between the invert domain and the unsaturated zone. Each computational cell is provided with parameters describing water volumes, diffusive properties, and advective and diffusive flux links to other cells. Between any two cells, the diffusive flux can be bidirectional, depending on the concentration gradient, while the advective flux is unidirectional. The output of a cell is given in terms of the advective and diffusive mass fluxes for radionuclide species *i* and its concentration at the cell center.

The number of cells in the finite-difference network and the discretization of the cells is chosen in such a way as to capture the unique physical and chemical properties of the EBS components with respect to radionuclide transport. The abstractions are in the form of logic statements and stochastic distributions that provide a method for linking various cells in the network. Implementation of the EBS flow and transport model for TSPA-LA uses the output of the drift seepage model (BSC 2004 [DIRS 169131]), the models for drip shield and waste package degradation (BSC 2004 [DIRS 169996]), the EBS physical and chemical environment model (BSC 2004 [DIRS 169860]), the thermal-hydrologic environment model (BSC 2004 [DIRS 169565]), and the waste form degradation and mobilization model (BSC 2004 [DIRS 167618]); *Defense HLW Glass Degradation Model* (BSC 2004 [DIRS 169988]); and *CSNF Waste Form Degradation: Summary Abstraction* (BSC 2004 [DIRS 169987]). The flow through various cells is based on the continuity equations and conservation of mass, as discussed in Section 6.3. An overview of the computational model for TSPA-LA, as implemented using GoldSim, is provided below.

Radionuclide transport through the waste package is modeled by spatially discretizing the waste package into two domains: an upstream waste form domain and a downstream corrosion products domain. As implemented using GoldSim, a single waste form cell represents the entire volume of the waste form domain, while a single corrosion products cell represents the entire volume of the corrosion products domain. These are illustrated in Figure 6.5-5 below by the EBS portion of the cell network – waste form cell, corrosion products cell, and invert cell.

The waste form cell receives mass from a specialized GoldSim "Source" cell, which models the waste package failure, degradation of the waste form, and release of the inventory for possible transport through the EBS. The "Source" cell provides the specified flux boundary condition for solving the mass transport equations. Both advective and diffusive transport can occur from the waste form cell to the corrosion products cell. Reversible and irreversible sorption of radionuclides to the corrosion products along with colloid facilitated transport of radionuclides is modeled as described in Appendix B. Three types of colloids, namely, waste form colloids, iron oxyhydroxide colloids, and groundwater colloids, are considered that can facilitate the transport of radionuclides by reversible and/or irreversible sorption. The waste form colloids are generated in the waste form cell (for the co-disposal waste package only), while the iron oxyhydroxide colloids and groundwater colloids are modeled in the corrosion products cell. All three types of colloids can transport to the downstream cells by diffusion and advection.

The discretization of the invert domain, using GoldSim, consists of one cell. Both advective and diffusive flux communication exists between the corrosion products and invert cells. Advective flux due to imbibition from the host rock to the invert may enter the invert cell.

Below the invert, part of the near-field UZ is modeled by an array of cells. The inclusion of the UZ portion in the model serves to establish a far field zero-concentration boundary and an accurate representation of the flux at the invert-to-UZ interface. The EBS-UZ interface submodel is described in more detail in Section 6.5.3.6. The dual continuum approach for modeling the UZ is achieved by creating UZ matrix and fracture cells. The invert cell communicates with the UZ matrix and fracture cells directly below it in the UZ cell array (see Section 6.5.3.6).

The following description will focus on discretization of the mass balance equation for the dissolved and reversibly sorbed mass (Equation 6.5.1.2-46). Similar treatments apply to the mass balance transport equations for the irreversibly sorbed radionuclide species. In order to describe the time discretization, let the superscript n represent a solution at the nth time. The nth time step assumes the radionuclide concentrations are known at time level n, and the solution provides the concentrations at time level n+1. Over this time step, the accumulation term uses a first order backward in time discretization:

$$\frac{\partial}{\partial t}\left[\phi S_w R_{fl} C_i\right] \approx \frac{\phi S_w R_{fl}^n \left(C_i^{n+1} - C_i^n\right)}{\Delta t}, \qquad \text{(Eq. 6.5.3.5-1)}$$

where the adsorption retardation factor,

$$R_{fl} = 1 + \frac{\rho_b K_{dis}}{\phi S_w} + K_{dicWF} C_{cWF} + K_{dicFeOx} C_{cFeOx} + K_{dicGW} C_{cGW}, \qquad \text{(Eq. 6.5.3.5-2)}$$

and the cell water content are evaluated at the beginning of the time step, and Δt is the time step size from the nth to the $(n+1)^{th}$ time.

The advective transport is discretized with a first order backward (with respect to the flow direction) difference approximation. If the mass balance is applied to cell B, and the advective flux is from cell A to cell B with magnitude q_{wz} (m^3 water m^{-2} yr^{-1}), then

$$\begin{aligned}\frac{\partial}{\partial z}&\left[q_{wz}\left(1 + K_{dicWF} C_{cWF} + K_{dicFeOx} C_{cFeOx} + K_{dicGW} C_{cGW}\right) C_i\right] \approx \\ &\left[Q_{wz}^n \left(1 + K_{dicWF} C_{cWF} + K_{dicFeOx} C_{cFeOx} + K_{dicGW} C_{cGW}\right)^n C_i^{n+1}\right]_A \\ &- \left[Q_{wz}^n \left(1 + K_{dicWF} C_{cWF} + K_{dicFeOx} C_{cFeOx} + K_{dicGW} C_{cGW}\right)^n C_i^{n+1}\right]_B,\end{aligned} \qquad \text{(Eq. 6.5.3.5-3)}$$

where Q_{wz} (m^3 water m^{-3} cell B yr^{-1}) is the advective water volume flux per unit bulk volume. The advective flux and colloid concentrations are evaluated at the beginning of the time step.

The concentration of radionuclide species i is evaluated at the end of time step. The first term in the difference approximation is the advective mass flux entering cell B from cell A. The second term is the advective mass flux exiting cell B.

Consider the accumulation of solute mass in cell B due to diffusion. Suppose there is a diffusive flux link from cell A to cell B and from cell B to cell C. The dissolved mass diffusive flux accumulation in cell B is approximated by:

$$\frac{\partial}{\partial x}\left(\phi S_w D \frac{\partial C_i}{\partial x}\right) \approx \frac{F_{A/B} - F_{B/C}}{V_B}, \qquad \text{(Eq. 6.5.3.5-4)}$$

where $F_{A/B}$ is the diffusive mass flux (mass/time) across cells A and B interface. Similarly, $F_{B/C}$ is the diffusive mass flux (mass/time) across cells B and C interface. Consider the discretization of the diffusive flux at the A/B interface. A similar representation occurs at the B/C interface.

Apply Fick's First Law and assume continuity of flux at the interface. Then the flux entering the A/B interface from cell A must equal the flux exiting the A/B interface to cell B. This interface flux continuity condition is expressed as:

$$\begin{aligned} F_{A/B} &= \left(\frac{\phi S_w DA}{L}\right)_A \left([C_i^{n+1}]_A - [C_i^{n+1}]_{A/B}\right) \\ &= \left(\frac{\phi S_w DA}{L}\right)_B \left([C_i^{n+1}]_{A/B} - [C_i^{n+1}]_B\right), \end{aligned} \qquad \text{(Eq. 6.5.3.5-5)}$$

where C_i^{n+1} is the concentration at time step n+1 at the interface, as indicated by the subscript A/B, and D, A, and L are the cell effective diffusion coefficient, diffusive area, and diffusive length, respectively. If the A/B interface diffusive flux is expressed as an interface diffusive conductance times the concentration difference between cells A and B:

$$F_{A/B} = D_{c\_A/B}(C_A - C_B), \qquad \text{(Eq. 6.5.3.5-6)}$$

then the flux continuity condition provided by Equation 6.5.3.5-5 gives the interface diffusive conductance as:

$$D_{c\_A/B} = \frac{1}{\left(\frac{L}{\phi S_w DA}\right)_A + \left(\frac{L}{\phi S_w DA}\right)_B}. \qquad \text{(Eq. 6.5.3.5-7)}$$

The diffusive conductance is the harmonic average of $\frac{\phi S_w DA}{2L}$ between the two cells. At the *B/C* interface a similar expression gives:

$$D_{c\_B/C} = \frac{1}{\left(\frac{L}{\phi S_w DA}\right)_B + \left(\frac{L}{\phi S_w DA}\right)_C}. \qquad \text{(Eq. 6.5.3.5-8)}$$

The discretization of the accumulation of solute mass in cell *B* due to diffusive transport is:

$$\frac{\partial}{\partial x}\left(\phi S_w D \frac{\partial c}{\partial x}\right) \approx \frac{D_{c\_B/C}\left(\left[C_l^{n+1}\right]_C - \left[C_l^{n+1}\right]_B\right) - D_{c\_A/B}\left(\left[C_l^{n+1}\right]_B - \left[C_l^{n+1}\right]_A\right)}{V_B}. \qquad \text{(Eq. 6.5.3.5-9)}$$

The mass balance equations are discretized with the dependent concentration variable for the spatially dependent terms evaluated at the end of time step, C_l^{n+1}. This is stated explicitly in the discretization of the advective/diffusive terms. For other source terms, such as radionuclide decay, irreversible sorption reaction onto iron oxyhydroxide material and so forth, the concentration is evaluated at the end of the time step. In this sense, the mass balance equations are fully implicit and the discretization provides numerical stability. However, coefficient terms such as the moisture content are evaluated at the beginning of the time step. This formulation results in a linear system of equations that is solved for concentrations. If the coefficient dependence on concentrations were evaluated at the end of time step, then the resulting discretized algebraic equations would be nonlinear. The nonlinear system would require much more computational effort. Furthermore, the computational modeling tool (GoldSim) only solves linear systems. For this reason, all concentration dependent coefficient terms are evaluated explicitly at time level *n*.

The rate constant, λ_l^{embed}, for conversion of mass from solution to embedded mass on the waste form colloids, is calculated at each time step from information provided by the previous time step. Suppose that the solution for all radionuclide and colloid concentrations has been determined at time level *n* and the solution at time level (*n*+1) is required. At the known time level *n*, the concentration with respect to the water volume of the embedded radionuclide mass, $\left(C_l^{embed}\right)^n$, and the waste form colloid mass, $\left(C_{cWF}\right)^n$, are determined by the waste package chemistry as discussed in *Waste Form and In-Drift Colloids-Associated Radionuclide Concentrations: Abstraction and Summary* (BSC 2004 [DIRS 170025], Section 6.5.1.1, Step 1a). The ratio of the radionuclide concentration to the colloid concentration is the ratio of radionuclide mass to waste form colloid mass. The advective/diffusive mass rate of the waste form colloid mass, $\left(Q_{adv/diff}^{wfc}\right)^n$, is provided from the previous time step solution of the waste form colloid mass balance transport equation. The expression $\left(Q_{adv/diff}^{wfc} \frac{C_l^{embed}}{C_{cWF}}\right)^n$ represents the

advective/diffusive mass flux rate of embedded mass of species i for the previous time step. The discrete mass balance for embedded radionuclide mass is then expressed in the form:

$$\frac{\left(\phi S_w C_i^{embed}\right)^n - \left(\phi S_w C_i^{embed}\right)^{n-1}}{t_n - t_{n-1}} = \left(Q_{advl\,diff}^{wfc} \frac{C_i^{embed}}{C_{cWF}} \right)^n + \left(\phi S_w\right)^n \left(\lambda_{ip} r_{ip}^M C_{ip}^{embed} - \lambda_i C_i^{embed}\right) + \left(\phi S_w\right)^n \lambda_i^{embed} C_i^n .$$

(Eq. 6.5.3.5-10)

This equation is solved for the conversion rate λ_i^{embed}. This value, which is calculated from information at time level n, is then used as the conversion rate in the mass balance for the radionuclide concentration in solution at time level n+1.

The above diffusive flux discussion considers the diffusive flux communication from cells within a single continuum. For transport from the invert domain (single continuum) to the UZ (dual continuum), the flux continuity condition at the interface provides the diffusive flux bifurcation between the single continuum and the dual continuum.

The diffusive fluxes of radionuclide species i within the invert cell, the UZ fracture cell, and the UZ matrix cell are, respectively,

$$F_{il} = \frac{\phi S_w D_l A_{l\,lUZ}}{L_l}\left(C_{il} - C_{il\,lUZ}\right) = \hat{D}_l\left(C_{il} - C_{il\,lUZ}\right), \quad \text{(Eq. 6.5.3.5-11)}$$

$$F_{if} = \frac{\phi S_w D_f A_{l\,lUZ}}{L_f}\left(C_{il\,lUZ} - C_{if}\right) = \hat{D}_f\left(C_{il\,lUZ} - C_{if}\right), \quad \text{(Eq. 6.5.3.5-12)}$$

$$F_{im} = \frac{\phi S_w D_m A_{l\,lUZ}}{L_m}\left(C_{il\,lUZ} - C_{im}\right) = \hat{D}_m\left(C_{il\,lUZ} - C_{im}\right), \quad \text{(Eq. 6.5.3.5-13)}$$

where

D_l	= effective diffusion coefficient within the invert cell (cm^2 s^{-1}),
D_f	= effective diffusion coefficient within the UZ fracture cell (cm^2 s^{-1}),
D_m	= effective diffusion coefficient within the UZ matrix cell (cm^2 s^{-1}),
$A_{l\,lUZ}$	= diffusive area between the invert and UZ cells (m^2),
L_l	= diffusive length within the invert cell (m),
L_f	= diffusive length within the UZ fracture cell (m),

L_m = diffusive length within the UZ matrix cell (m) $= L_f$,

C_{il} = concentration of radionuclide species i in the invert cell (kg i m^{-3}),

C_{if} = concentration of radionuclide species i in the UZ fracture cell (kg i m^{-3}),

C_{im} = concentration of radionuclide species i in the UZ matrix cell (kg i m^{-3}),

$C_{il\,IUZ}$ = concentration of radionuclide species i at the interface between the invert and UZ cells (kg i m^{-3}),

and the $\hat{D} = \frac{\phi S_w DA}{L}$ are respective diffusive conductances (cm^3 s^{-1}).

The flux continuity at the interface requires:

$$F_{il} = F_{if} + F_{im}. \qquad \text{(Eq. 6.5.3.5-14)}$$

From the flux continuity, the interface concentration of radionuclide species i is determined as a function of the diffusive parameters and the cell concentrations as:

$$C_{il\,IUZ} = \frac{\hat{D}_l C_{il} + \hat{D}_f C_{if} + \hat{D}_m C_{im}}{\hat{D}_l + \hat{D}_f + \hat{D}_m}. \qquad \text{(Eq. 6.5.3.5-15)}$$

This provides the invert intergranular and intragranular diffusive fluxes of radionuclide species i, respectively, as:

$$F_{if} = \frac{\hat{D}_l \hat{D}_f}{\hat{D}_l + \hat{D}_f + \hat{D}_m}\left(C_{il} - C_{if}\right) + \frac{\hat{D}_f \hat{D}_m}{\hat{D}_l + \hat{D}_f + \hat{D}_m}\left(C_{im} - C_{if}\right) \qquad \text{(Eq. 6.5.3.5-16)}$$

$$F_{im} = \frac{\hat{D}_l \hat{D}_m}{\hat{D}_l + \hat{D}_f + \hat{D}_m}\left(C_{il} - C_{im}\right) - \frac{\hat{D}_f \hat{D}_m}{\hat{D}_l + \hat{D}_f + \hat{D}_m}\left(C_{im} - C_{if}\right). \qquad \text{(Eq. 6.5.3.5-17)}$$

The expression for the diffusive flux of radionuclide species i from the invert cell to the UZ fracture cell can be expressed as a diffusive conductance multiplied by a concentration difference of radionuclide species i between the invert cell and the UZ fracture cell plus a corrective flux between the UZ fracture and matrix cells. Similarly, the expression for the diffusive flux from the invert to the UZ matrix cell is expressed as a diffusive flux between the invert and the UZ matrix cell minus the same corrective flux between the UZ cells. The inclusion of the corrective flux term is explained as follows. The flux to both UZ cells should depend on the diffusive properties in the invert cell and the two UZ cells, together with the concentrations in these three cells. Therefore, the flux to the UZ fracture cell cannot be expressed only in terms of the concentration drawdown between the invert cell and the UZ fracture cell. The corrective term includes the dependence of the UZ fracture flux on the concentration of radionuclide species i in the UZ matrix cell. Further, the corrective flux term is not a true flux expression between the two UZ cells, since the diffusive conductance coefficient is dependent on the diffusive area between the invert and the UZ, and the diffusive lengths are the lengths with respect to flow from the invert cell to the UZ cells.

The UZ fluxes result in defining three diffusive conductances from the flux expressions:

$$\hat{D}_{If}\left(C_{Il}-C_{If}\right)=\frac{\hat{D}_I\hat{D}_f}{\hat{D}_I+\hat{D}_f+\hat{D}_m}\left(C_{Il}-C_{If}\right), \qquad \text{(Eq. 6.5.3.5-18)}$$

$$\hat{D}_{Im}\left(C_{Il}-C_{Im}\right)=\frac{\hat{D}_I\hat{D}_m}{\hat{D}_I+\hat{D}_f+\hat{D}_m}\left(C_{Il}-C_{Im}\right), \qquad \text{(Eq. 6.5.3.5-19)}$$

$$\hat{D}_{mf}\left(C_{Im}-C_{If}\right)=\frac{\hat{D}_m\hat{D}_f}{\hat{D}_I+\hat{D}_f+\hat{D}_m}\left(C_{Im}-C_{If}\right), \qquad \text{(Eq. 6.5.3.5-20)}$$

where

$\hat{D}_{If}$ = effective diffusive conductance between invert cell and UZ fracture cell ($cm^3\ s^{-1}$);

$\hat{D}_{Im}$ = effective diffusive conductance between invert cell and UZ matrix cell ($cm^3\ s^{-1}$);

$\hat{D}_{mf}$ = effective diffusive conductance between UZ fracture and matrix cells ($cm^3\ s^{-1}$).

In order to accommodate the GoldSim representation of diffusive conductance as a two-term expression, the diffusive conductances of radionuclide species *i* are written as:

$$\hat{D}_{If}=\frac{1}{\dfrac{L_I}{(\phi S_w DA)_I\left[\dfrac{(\phi S_w D)_f}{(\phi S_w D)_f+(\phi S_w D)_m}\right]}+\dfrac{L_f}{(\phi S_w DA)_f}}, \qquad \text{(Eq. 6.5.3.5-21)}$$

$$\hat{D}_{Im}=\frac{1}{\dfrac{L_I}{(\phi S_w DA)_I\left[\dfrac{(\phi S_w D)_m}{(\phi S_w D)_f+(\phi S_w D)_m}\right]}+\dfrac{L_m}{(\phi S_w DA)_m}}, \qquad \text{(Eq. 6.5.3.5-22)}$$

$$\hat{D}_{mf}=\frac{1}{\dfrac{L_f}{(\phi S_w DA)_f\left[\dfrac{L_I(\phi S_w D)_m}{L_I(\phi S_w D)_m+L_m(\phi S_w D)_I}\right]}+\dfrac{L_m}{(\phi S_w DA)_m}}. \qquad \text{(Eq. 6.5.3.5-23)}$$

Although the above approach is rigorous, it is complex and difficult to implement in the TSPA-LA model. A second approach that is easier to understand and simpler to implement,

while providing the same results as the above approach, is presented here. This approach requires introduction of an interface cell, located between the invert cell and the UZ cells. This interface cell provides an approximate interface concentration and the resulting flux split at the invert-to-UZ cell interface. The interface cell is conceptualized as a very thin slice of the invert cell. This implies the interface cell takes on the invert diffusive properties, with the exception of diffusive length. Let the diffusive length within the interface cell be some small fraction (a scale factor) of the invert diffusive length, say, Interface_Scale_Factor = 10^{-6}:

$$L_{I-int} = 10^{-6} L_I . \qquad \text{(Eq. 6.5.3.5-24)}$$

The diffusive conductance between the invert cell and the invert interface cell is calculated as the harmonic average:

$$\hat{D}_{I/I-int} = \frac{1}{\dfrac{L_I}{(\phi S_w DA)_I} + \dfrac{L_{I-int}}{(\phi S_w DA)_{I-int}}} . \qquad \text{(Eq. 6.5.3.5-25)}$$

For diffusion between the interface cell and the UZ fracture and matrix cells, the diffusive conductances of radionuclide species *i* are, respectively,

$$\hat{D}_{I-int/f} = \frac{1}{\dfrac{L_{I-int}}{(\phi S_w DA)_{I-int}} + \dfrac{L_{UZ}}{(\phi S_w DA)_f}} , \qquad \text{(Eq. 6.5.3.5-26)}$$

$$\hat{D}_{I-int/m} = \frac{1}{\dfrac{L_{I-int}}{(\phi S_w DA)_{I-int}} + \dfrac{L_{UZ}}{(\phi S_w DA)_m}} . \qquad \text{(Eq. 6.5.3.5-27)}$$

The interface cell concentration of radionuclide species *i* is computed as part of the cell network solution. Because the transport mass balance equations conserve mass, the mass flux leaving the interface cell must equal the sum of the mass fluxes entering the two UZ cells. The solution provides the flux continuity across the interface between the invert interface cell and UZ cells. This formulation expects the flux exiting the invert cell (or entering the interface cell) is approximately equal to the flux exiting the interface cell. This approximation is dependent on the diffusive length within the interface cell. The error in this approximate solution approaches zero as the diffusive length of the interface cell approaches zero.

6.5.3.6 EBS-UZ Boundary Condition Implementation in TSPA-LA

For TSPA-LA, a semi-infinite zero-concentration boundary condition is used for the EBS-UZ interface. This is approximated by applying an effective zero-concentration boundary at approximately three drift diameters below the invert-UZ boundary into the UZ. In an alternative approach, a zero-concentration boundary condition can be used at the interface between the invert and the UZ, which will result in an unrealistically high diffusive gradient through the

invert. By moving the zero-concentration boundary some distance below the invert, a more realistic diffusive gradient through the invert is achieved.

In the EBS-UZ interface submodel, the near-field UZ is modeled as a dual continuum of overlapping UZ-matrix and UZ-fracture media. This approach is consistent with the dual-permeability modeling approach used by the UZ transport model, as described in *Particle Tracking Model and Abstraction of Transport Processes* (BSC 2004 [DIRS 170041]). The matrix and fracture continua are represented in the *EBS RT Abstraction* by a two-dimensional vertical array of cells oriented parallel to a cross section of a drift and located immediately beneath a drift (Figure 6.5-5). This array consists of three columns or vertical zones, with each zone containing both a fracture cell and a matrix cell. The invert is in direct communication with the second or center zone of UZ matrix/fracture cells. Each zone is four layers deep in the vertical direction. Thus, the array consists of twelve pairs of matrix and fracture cells within the UZ. Laterally, each zone is one drift diameter wide, with the middle zone centered beneath the drift, so that each layer of the array extends one drift diameter on either side of the drift. In the longitudinal direction of a drift, the length of the array is equal to the length of the waste package being modeled.

The thickness of the first (top) layer of cells is 10 percent greater than the average invert thickness (0.597 m), or 0.6567 m. The thickness of the second layer is double that of the first layer, or 1.3134 m. The third and fourth layers are given an arbitrary thickness of 5 m and 10 m, respectively. A "collector cell" is placed beneath the fourth layer and is given a very large, numerically infinite, water volume (10^{10} m^3) to simulate an effective zero-concentration boundary. This collector cell acts as a sink for all the mass flow from the invert and UZ cells.

As depicted in Figure 6.5-5, each fracture cell interacts, via diffusive connection only, with the matrix cell of the same zone. The fracture cell also interacts via diffusive connection vertically with the fracture cell of underlying and overlying layers of the same zone. The matrix cell of each zone interacts via diffusive connection laterally with the matrix cells of adjacent zones and vertically with the matrix cell of underlying and overlying layers of the same zone. Radionuclides diffuse based on the concentration gradient between cells. Advection occurs downward only, from the fracture cell of one layer to the fracture cell of the underlying layer in the same zone, and from the matrix cell of one layer to the matrix cell of the underlying layer in the same zone; advection does not occur across zones. Each zone is spatially distinct. Each is one drift diameter in width. The only connection possible between adjacent zones is through the middle zone.

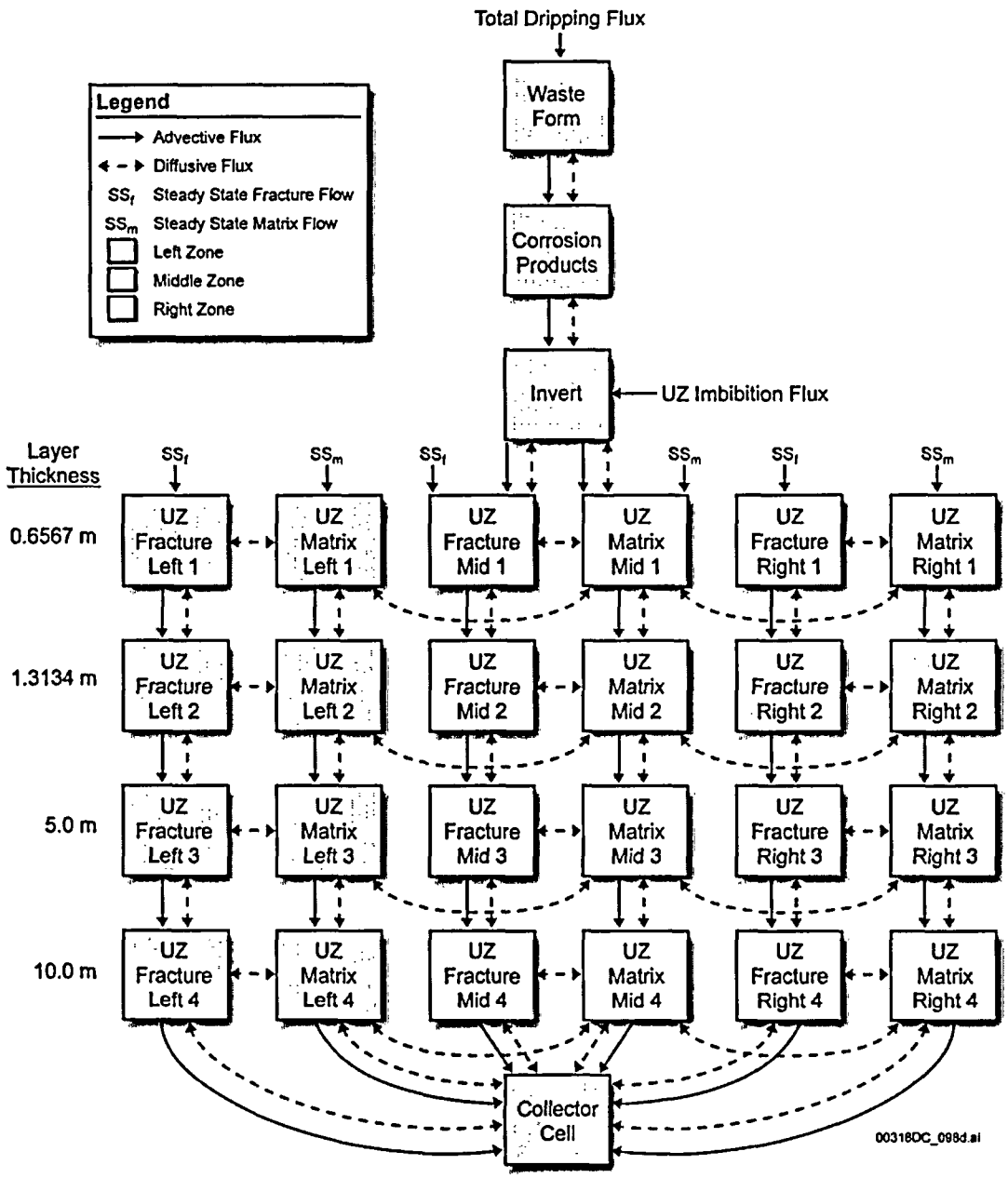

Figure 6.5-5. Computational Grid in the EBS-UZ Interface Submodel

The mass flux from the invert flows into the top layer of the middle zone in the UZ. The portion of the advective flux from the invert that is attributable to the total dripping flux (F_1) flows into the UZ fractures. The imbibition flux into the invert (F_7) flows out of the invert into the UZ matrix. The diffusive flux from the invert can go into both UZ continua based on the concentration gradient and effective diffusion coefficient. The advective flux flowing through the UZ fracture cells in the middle zone is given by the greater of the advective flux out of the invert (F_1) and the steady state UZ fracture flux. Because of the application of a flow focusing factor in the calculation of the total dripping flux (F_1), the flux going into UZ fractures in the EBS-UZ interface submodel can be greater than the steady state UZ fracture flux. The advective flux in the two outer zones is given by the steady state UZ flow in each continuum at the repository horizon; the drift shadow effects are ignored.

For the advective mass transport calculation shown in Equation 6.5.3.5-3, volumetric discharge for the fracture and matrix continua is needed. Since fracture and matrix percolation flux (described in Section 6.5.2 and provided by DTN: LB0307FMRADTRN.001 [DIRS 165451]) is given as specific discharge, the volumetric flux is calculated by multiplying the percolation flux for each continuum by the projected bulk area normal to the flux, where the projected area A_{UZ} is calculated as:

$$A_{UZ} = d_D L_{WP}, \qquad \text{(Eq. 6.5.3.6-1)}$$

where d_D is the drift diameter (m) and L_{WP} is the length of a waste package (m). This area is used for the diffusive and advective flux calculations between UZ cells. For the calculation between the invert and UZ, the area $A_{I/UZ}$ given by Equation 6.5.3.3.-4 is used.

The bulk volume calculation for each continuum is computed by multiplying the bulk volume for each discretized zone in each layer (based on the geometry) by either the fracture porosity (fracture fraction) or matrix porosity. Similarly, the water volume is calculated by multiplying the bulk volume of each continuum by its respective saturation.

For diffusive mass transport, in the calculation shown in Equation 6.5.3.5-5, the effective diffusion coefficient for the matrix continuum is calculated based on Equation 6-52 in *Drift-Scale Radionuclide Transport* (BSC 2004 [DIRS 170040]):

$$\log_{10} D_{ms} = -3.49 + 0.0138\theta_m + 0.165 \log_{10} k_{me}, \qquad \text{(Eq. 6.5.3.6-2)}$$

where D_{ms} is the effective UZ matrix diffusion coefficient ($cm^2\ s^{-1}$), θ_m is the matrix water content (percent), and k_{me} is the matrix effective permeability (m^2) (BSC 2004 [DIRS 170040], Equation 6-57):

$$k_{me} = k_{rm} k_m, \qquad \text{(Eq. 6.5.3.6-3)}$$

where k_{rm} is the relative permeability of unsaturated zone tuff matrix (dimensionless), and k_m is the intrinsic permeability of unsaturated zone tuff matrix (m^2). The same value of the diffusion coefficient is applied to the fracture diffusion coefficient as recommended by the *Drift-Scale*

Radionuclide Transport (BSC 2004 [DIRS 170040]). The sampling of the input parameters is described in Section 6.5.2.

The diffusive area between the fracture and matrix continua is computed by multiplying the bulk volume by the fracture interface area, which provides the connection area per unit bulk volume. This diffusive area is further reduced by the fracture-matrix interface reduction factor, given as $S_{ef}^{1+\gamma}$, where S_{ef} is the effective fracture saturation, and γ is the active fracture parameter (*UZ Flow Models and Submodels*, BSC 2004 [DIRS 169861]). The effective fracture saturation (S_{ef}) is computed as:

$$S_{ef} = \frac{S_{wf} - S_{wfr}}{1 - S_{wfr}}, \qquad \text{(Eq. 6.5.3.6-4)}$$

where S_{wf} is the fracture water saturation, and S_{wfr} is the fracture residual saturation. The mass flux of radionuclides from the invert domain to the dual continuum UZ, computed at the boundary of the EBS-UZ interface (between the invert cell and the adjacent UZ matrix and fracture cells), is passed to the UZ transport model for TSPA-LA calculations as described in *Particle Tracking Model and Abstraction of Transport Processes* (BSC 2004 [DIRS 170041]). In addition to the total mass flux, the relative fraction of the mass going into each of the fracture and the matrix cells at the EBS-UZ boundary is required by the UZ transport model. This fracture-matrix partitioning of mass is calculated on the basis of the mass fraction going into the fracture continuum (compared to the matrix continuum) from the invert domain in the EBS-UZ interface submodel. This partitioning is time dependent and captures the temporal processes active in the EBS, such as varying radionuclide concentrations in the waste form, corrosion products, and invert domains, and the changing water flux through various subcomponents of the EBS. Furthermore, this partitioning is computed by solving the mass transport equations for the EBS and part of the UZ as a coupled system with appropriate boundary conditions and adopting a modeling approach consistent with the *Multiscale Thermohydrologic Model* dual continuum model for the invert (BSC 2004 [DIRS 169565]) and the dual continuum transport model for the UZ (BSC 2004 [DIRS 170041]).

Sorption of radionuclides to the UZ matrix continuum is modeled by applying the devitrified tuff K_d values from the UZ submodel. For sorption calculations, the mass of UZ matrix continuum is calculated as: $V_b \rho_b (1 - \phi_f)$, where V_b is the bulk volume of the matrix cell considered (m^3), ϕ_f is the fracture porosity (fraction), and ρ_{bm} is the dry bulk density of TSw35 matrix (kg m^{-3}).

All three types of colloids are transported from the invert to the UZ cells. Groundwater colloids are present in all four layers. The iron oxyhydroxide and waste form colloids with reversibly sorbed radionuclides are modeled to be present in only the first two layers of the middle column, making the groundwater colloid the only type of colloid available for far-field transport, consistent with colloid-facilitated transport modeled in the UZ is covered in *Particle Tracking Model and Abstraction of Transport Processes* (BSC 2004 [DIRS 170041]).

6.6 MODEL FORMULATION FOR ALTERNATIVE CONCEPTUAL MODELS

6.6.1 Bathtub Flow Model

The conceptual model for the TSPA-LA is based on the presence of continuous flow paths through the patches and stress corrosion cracks that penetrate the waste package. More specifically, the TSPA-LA model conceptualizes that vertical flow of seepage into the waste package, through the waste form and out of the waste package is not impeded by the location of patches and stress corrosion cracks on the surface of the waste package. There is no long-term build-up and retention of liquid within the waste package for flow and transport. There is also no resistance to the flow through the waste form. The TSPA-LA approach attempts to maximize the immediate release and mobilization of radionuclides into the local groundwater environment. This approach is referred to as the "flow through" geometry.

An alternative conceptual model to the "flow through" geometry is the "bathtub" geometry (Mohanty et al. 1996 [DIRS 130419]). The bathtub geometry allows seepage to collect within the waste package before being released to the EBS. In theory, a bathtub geometry could result in the sudden release of a large pulse of radionuclides when a package overflows with liquid or when a second patch appears abruptly beneath the water line.

The "bathtub" effect would be most important during the period when only a few patches or cracks have penetrated the drip shield and waste package. In this situation, there may be penetrations through the top of the waste package while the bottom surface remains intact, leading to retention of liquid. At later times, the presence of multiple penetrations makes a "flow-through" geometry the more likely configuration.

The response of the bathtub geometry is evaluated for a primary case and for three secondary cases. The primary case includes consideration of two limiting conditions on radionuclide releases: dissolution rate limited and solubility limited. Tc is typical of dissolution rate limited radionuclides. The Tc released due to waste dissolution can always be dissolved in the available water because the solubility limit of Tc is high (BSC 2004 [DIRS 169425], Section 6.14). Np is typical of the solubility limited type of radionuclide, where all the release of Np from dissolution is limited by its low solubility (BSC 2004 [DIRS 169425], Section 6.6).

The results for the primary case are based on a closed form analytic solution with constant values of inflow rate, dissolution rate, and solubility. The three secondary cases consider a step change in inflow rate, such as would occur from a climatic change, a step change in water chemistry, or a step change in flow geometry, as would occur if a patch suddenly appeared beneath the waterline. The basic geometry and flow pattern for the primary bathtub model is shown in Figure 6.6-1 (from Mohanty et al. 1996 [DIRS 130419], Figure 2-7) q_{in} is identical to F_4 and in Section 6.3.1.1.

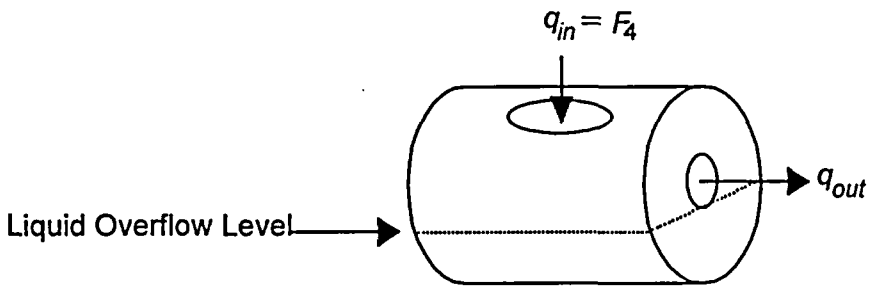

Figure 6.6-1. Schematic of the Bathtub Geometry for the Waste Package

6.6.1.1 Primary Case

6.6.1.1.1 Dissolution-Rate-Limited Radionuclide

In this case, the concentration of radionuclides is limited by the rate of dissolution. Consider the system shown in Figure 6.6-1, with a constant inflow rate, q_{in}, and let V_{tub} be the total volume of liquid that can be retained within the waste package before it overflows. The response of the waste package is a two step process. During Step 1, the package is filling with liquid and the outflow rate, q_{out}, is zero. This condition continues until the waste package fills with liquid at a time, t_{fill}, given by V_{tub}/q_{in}. Step 2 occurs after time t_{fill}; the amount of liquid inside the waste package remains constant, and $q_{out} = q_{in}$. This is a steady state condition, consistent with the assumption that q_{in} is constant and that liquid does not continue to accumulate within the package. The following analysis also supposes there is complete contact between the liquid and the waste form within the waste package, and that the dissolution rate is constant.

During Step 1, for time t such that $0 < t < t_{fill}$, the dissolution of a radioisotope into the water inside the waste package can be represented as:

$$\dot{m}_i = r_s \omega_i, \qquad \text{(Eq. 6.6.1.1.1-1)}$$

where

$\dot{m}_i$ = the rate of release of radionuclide into the liquid (kg s^{-1})

r_s = the dissolution rate of the waste form (kg s^{-1})

ω_i = the mass fraction of radioisotope i released per unit mass of waste form (dimensionless); ω_i is less than one for a waste form with multiple radionuclides.

During the fill period q_{out} is zero, so the mass, $m_i(t)$, of radioisotope dissolved within the liquid in the waste package at time t is given by:

$$m_i(t) = r_s \omega_i \, t, \qquad \text{(Eq. 6.6.1.1.1-2)}$$

because r_s and ω_i are constant. Similarly, the volume of liquid in the waste package at time t, $V(t)$, is given by:

$$V(t) = q_{in}t, \qquad \text{(Eq. 6.6.1.1.1-3)}$$

so the concentration of dissolved isotope i in the waste package, $C_i(t)$, is

$$C_i(t) = \frac{m_i(t)}{V(t)} = \frac{r_s\omega_i t}{q_{in}t} = \frac{r_s\omega_i}{q_{in}}. \qquad \text{(Eq. 6.6.1.1.1-4)}$$

The concentration, $C_i(t)$, is constant during the fill phase because the values of r_s, ω_i, and q_{in} are chosen to be constant. This condition is appropriate because the dissolved mass, m_i, and the volume of liquid, V, are linear functions of the time (and initially both are zero), so their ratio remains constant.

The result in Equation 6.6.1.1.1-4 holds for each dissolution-rate-limited radioisotope i in the waste form, although the numerical value of $C_i(t)$ differs because the mass fraction, ω_i, is different for each isotope.

During Step 2, when $t > t_{fill}$, the radioisotope mass within the waste package is a balance between the dissolution of radioisotope into the groundwater within the waste package and the loss of radioisotope due to outflow from the waste package:

$$\dot{m}_i = r_s\omega_i - q_{out}C_i(t). \qquad \text{(Eq. 6.6.1.1.1-5)}$$

Because the water inflow rate, waste form solubility, and mass fraction of radioisotope i all remain constant, the concentration $C_i(t)$ remains constant even when the solution is removed at a rate q_{out}. Therefore, at $t > t_{fill}$, the *net* rate of radionuclide release into the water inside the waste package is zero (i.e., the dissolution rate is exactly offset by the outflow rate):

$$\dot{m}_i = r_s\omega_i - q_{out}C_i(t) = 0. \qquad \text{(Eq. 6.6.1.1.1-6)}$$

For constant q_{in}, with $q_{out} = q_{in}$,

$$C_i(t) = \frac{r_s\omega_i}{q_{in}}. \qquad \text{(Eq. 6.6.1.1.1-7)}$$

The dissolved mass in the waste package is constant for $t > t_{fill}$. In addition, the concentration of dissolved radionuclide is constant for all time $t > 0$, as shown by Equations 6.6.1.1.1-4 and 6.6.1.1.1-7. These results are reasonable because the waste package is in steady state for $t > t_{fill}$. This means that the inflow rate equals the outflow rate and that any loss of dissolved

radionuclide mass in the outflow from the waste package is exactly balanced by the addition of dissolved radionuclide mass from dissolution of the waste form.

The response for the comparable flow-through model has the same radionuclide concentration, $C_i(t)$, and the same release flux, given by $C_i(t)q_{out}$, as the bathtub geometry. The sole difference between the flow-through and bathtub models is that the flux from the flow-through model starts from $t=0$ while the flux from the bathtub model is zero until time t_{fill}. The bathtub model introduces a delay in the response but does not change the concentration in the package or the mass flux out of the package.

Therefore, for the dissolution-rate-limited case, the flow-through model is bounding relative to the bathtub model for radionuclide releases from the waste package. This analysis considers advective transport with no sorption of radionuclides, whereas the current EBS transport model includes sorption onto stationary corrosion products (retardation in the waste package) as well as colloid-facilitated transport. In this analysis of alternative conceptual models, sorption onto stationary corrosion products inside the waste package would effectively reduce the dissolution rate. Since that rate is still constant and the same for both the flow-through and bathtub models, sorption would affect the concentrations of radionuclides in the outflow, but would have no impact on the conclusion that the bathtub model introduces a delay in releases compared to the flow-through model. Sorption onto colloids would have the opposite net effect of increasing the solubility and again would have no impact on the conclusions.

6.6.1.1.2 Solubility-Limited Radionuclide

The response for a solubility-limited radionuclide, in which the solubility limit of the radionuclide is instantaneous achieved, is similar to that for a dissolution-rate-limited radionuclide, in the sense that the bathtub model delays the release from the waste package but does not change the dose rate.

During Step 1, $0 < t < t_{fill}$, the amount of radionuclide dissolved in the groundwater in the waste package can be represented as:

$$\dot{m}_i = C_{si} q_{in}, \qquad \text{(Eq. 6.6.1.1.2-1)}$$

where C_{si} is the solubility limit of the radionuclide. If the groundwater chemistry is constant, the solubility is constant and the mass, m_i, of radioisotope retained in the waste package at time t is:

$$m_i(t) = C_{si} q_{in} t. \qquad \text{(Eq. 6.6.1.1.2-2)}$$

The volume of liquid in the waste package at time t, $V(t)$, is given by:

$$V(t) = q_{in} t, \qquad \text{(Eq. 6.6.1.1.2-3)}$$

so that the concentration of dissolved isotope in the waste package is:

$$C_i(t) = \frac{m_i(t)}{V(t)} = \frac{C_{si} q_{in} t}{q_{in} t} = C_{si}. \qquad \text{(Eq. 6.6.1.1.2-4)}$$

The concentration is constant during the fill phase and equal to the solubility limit, as would be expected. This is true for each radionuclide in the system, although the numerical values of the solubility limit vary.

For $t > t_{fill}$, the mass balance within the waste package is a steady state condition given by:

$$\dot{m}_i = C_{si} q_{in} - C_i(t) q_{out} = C_{si} q_{in} - \frac{m_i(t)}{V_{tub}} q_{out} = 0. \qquad \text{(Eq. 6.6.1.1.2-5)}$$

The solution to Equation 6.6.1.1.2-5 with $q_{out} = q_{in}$ is:

$$m(t) = C_{si} V_{tub}, \qquad \text{(Eq. 6.6.1.1.2-6)}$$

with

$$C_i(t) = C_{si}. \qquad \text{(Eq. 6.6.1.1.2-7)}$$

Again the dissolved mass in the waste package is constant for $t > t_{fill}$ and the concentration of dissolved radionuclide is constant at the solubility limit for all times $t > 0$.

The comparable flow-through model has the same radionuclide concentration, C_{si}, and the same release flux, given by $C_{si} q_{out}$, as the bathtub geometry. The sole difference is that the flux from the flow-through model starts from $t = 0$ while the flux from the bathtub model is zero until time t_{fill}. The bathtub model introduces a delay in the response but does not change the dose rate. Therefore, the flow-through model is again bounding relative to the bathtub model because radionuclides are released with no delay time to the EBS.

6.6.1.2 Secondary Cases

The secondary cases evaluate the response of the bathtub model when changes occur in the groundwater inflow rate, in inflow chemistry, or in the flow geometry.

6.6.1.2.1 Change in Inflow Rate

The response of a bathtub model to a change in inflow rate differs for a solubility-limited or a dissolution-rate-limited radionuclide. The solubility-limited case is simpler because of chemical equilibrium and is discussed first.

Consider a step change in inflow rate after the bathtub has filled for a *solubility-limited* radionuclide. Since kinetic effects are ignored, the chemical system is always at equilibrium and

the concentration within the waste package remains unchanged at the solubility limit. The only change in the system is that the radionuclide mass flux out of the waste package changes instantaneously from $C_l q_{out}$ to $C_l q_{out,new}$. This response is exactly the same as it would be for the flow-through model, so the response of the bathtub model is identical to that for the flow-through model.

Now consider a step change in inflow rate after the bathtub has filled for a *dissolution-rate-limited* radionuclide. In this case, the mass released per unit time remains constant because the dissolution rate remains constant, but the radionuclide concentration comes to a new equilibrium value. This new equilibrium value can be determined by Equation 6.6.1.1.1-7, with the product of concentration and liquid inflow remaining constant:

$$C_{l,new} q_{in,new} = C_{l,old} q_{in,old} = r_s \omega_l \ . \qquad \text{(Eq. 6.6.1.2.1-1)}$$

If the inflow rate decreases, the final concentration increases because the product of concentration and liquid inflow remains constant. A flow-through model has an instantaneous increase in concentration, whereas the bathtub model shows an exponential growth to the new concentration. Thus, the flow-through model is bounding for concentration released into the EBS because there is no delay in changing to the new increased radionuclide concentration.

The exponential growth to the new concentration can be seen as follows. The replacement of "old" inflow with concentration $C_{l,old}$ with "new" inflow with concentration $C_{l,new}$ is represented through a parameter, β, the volume fraction of old inflow to V_{tub}, the total liquid volume in the bathtub. The rate of change of the volume of old inflow, V_{old}, is given by:

$$\frac{dV_{old}}{dt} = -\beta\, q_{out,new} = -\beta\, q_{in,new}. \qquad \text{(Eq. 6.6.1.2.1-2)}$$

Equation 6.6.1.2.1-2 represents the loss of old inflow through outflow, with the factor β representing the (decreasing) volume fraction of old inflow that is lost. By definition,

$$\beta \equiv \frac{V_{old}}{V_{tub}}. \qquad \text{(Eq. 6.6.1.2.1-3)}$$

Substituting this definition into the left-hand side of Equation 6.6.1.2.1-2 gives:

$$\frac{d\beta}{dt} = -\frac{q_{in,new}}{V_{tub}}\beta. \qquad \text{(Eq. 6.6.1.2.1-4)}$$

The solution to Equation 6.6.1.2.1-4 with initial condition $\beta = 1$ at $t = 0$ is:

$$\beta = \exp\left(-\frac{q_{in,new}}{V_{tub}} t\right), \qquad \text{(Eq. 6.6.1.2.1-5)}$$

which corresponds to an exponential decay of C_i from $C_{i,old}$ to $C_{i,new}$.

If the inflow rate were to increase, the concentration would decrease. In a flow-through model, the concentration would instantaneously decrease, whereas in the bathtub model, the concentration would exponentially relax to the new concentration. The flow-through model is then not bounding for concentration released into the EBS. The mass of radionuclide mobilized is identical, as implied by Equation 6.6.1.2.1-1, but the dissolved concentration varies with the amount of fluid flowing through the system. However, the TSPA-LA model passes mass to the unsaturated zone, rather than concentration, so the difference between the flow through model and the bathtub model for this case is not critical to performance.

Finally, a change in inflow rate during the initial period, when the bathtub is filling, only affects the value of t_{fill} and hence the delay until the bathtub fills, after which it behaves as described in Section 6.6.1.1.

In summary, the response of the bathtub model to a change in inflow rate is identical to that of the flow-through model for solubility-limited radionuclides. For dissolution-rate-limited radionuclides, the response of the bathtub model is less bounding than the flow-through model when the inflow rate decreases (and concentration increases). If the inflow rate increases (resulting in a decrease in the outflow concentration of radionuclides), the bathtub model is more bounding than the flow-through model for dissolution-rate-limited radionuclides.

6.6.1.2.2 Change in Inflow Chemistry

Consider a step change in inflow chemistry after the bathtub has filled. Initially, there will be minor changes in concentration within the bathtub because the bulk of the water retains the original inflow composition. Eventually the "old" groundwater is flushed out and replaced with the "new" inflow, resulting in new concentrations within the bathtub.

As in the preceding section where a change in inflow rate was examined, the replacement of old with new inflow can be represented through a parameter β, representing the volume fraction of old inflow in V_{tub}, the total liquid volume in the bathtub. The rates of change of the volumes of old and new inflow are given by:

$$\frac{dV_{old}}{dt} = -\beta\, q_{out}, \qquad \text{(Eq. 6.6.1.2.2-1)}$$

and

$$\frac{dV_{new}}{dt} = q_{in} - (1-\beta) q_{out}, \qquad \text{(Eq. 6.6.1.2.2-2)}$$

where V_{old} and V_{new} represent the volumes of inflow with the old and new chemistries, respectively. Equation 6.6.1.2.2-1 represents the loss of old inflow through outflow, with the factor β representing the volume fraction of old inflow that is lost. Equation 6.6.1.2.2-2

represents the addition of new inflow and its partial loss through outflow. Remembering that $q_{out} = q_{in}$ because of the steady state assumption, it follows that:

$$\frac{dV_{old}}{dt} = -\beta\, q_{in}; \quad \frac{dV_{new}}{dt} = +\beta\, q_{in}. \qquad \text{(Eq. 6.6.1.2.2-3)}$$

By definition:

$$\beta \equiv \frac{V_{old}}{V_{tub}}. \qquad \text{(Eq. 6.6.1.2.2-4)}$$

Substituting this definition into the left-hand equation in 6.6.1.2.2-3, it follows that:

$$\frac{d\beta}{dt} = -\frac{q_{in}}{V_{tub}}\beta = -\frac{1}{t_{fill}}\beta. \qquad \text{(Eq. 6.6.1.2.2-5)}$$

The solution to Equation 6.6.1.2.2-5 with the initial condition $\beta(0) = 1$ is given by:

$$\beta(t) = e^{-\frac{t}{t_{fill}}}. \qquad \text{(Eq. 6.6.1.2.2-6)}$$

It follows that the old and new volumes of inflow are given by:

$$V_{old} = V_{tub} e^{-\frac{t}{t_{fill}}} \qquad \text{(Eq. 6.6.1.2.2-7)}$$

and:

$$V_{new} = V_{tub}\left(1 - e^{-\frac{t}{t_{fill}}}\right). \qquad \text{(Eq. 6.6.1.2.2-8)}$$

These equations say that the volume fraction of inflow with the old chemistry decays exponentially with the characteristic time t_{fill}. Alternatively, the volume fraction of new inflow increases to 1.0 with a characteristic time of t_{fill} for the exponential growth given by Equation 6.6.1.2.2-8.

The impact of changing inflow chemistry on dissolution rate or solubility is much more difficult to predict analytically because chemical interactions are nonlinear. More specifically, the pH of mixtures of inflows is not proportional to β because the pH scale is proportional to the log of the hydrogen ion concentration and inherently nonlinear and because potential chemical interactions in mixtures, such as buffering, produce a nonlinear response. In addition, solubility and dissolution rate are often complex nonlinear functions of the pH.

Nonlinear response makes it particularly difficult to predict the time-dependent response for solubility; however, the starting state and the ending state, for $t >> t_{fill}$, are well defined and can be approximated to first order by:

$$C_{si}(t) \approx C_{si,old} e^{-\frac{t}{t_{fill}}} + C_{si,new}\left(1 - e^{-\frac{t}{t_{fill}}}\right). \qquad \text{(Eq. 6.6.1.2.2-9)}$$

Consider the response when $C_{si,new} >> C_{si,old}$. This condition can easily occur for the actinides, where solubility increases by several orders of magnitude as pH changes from between 7 and 8 to a value below 6 or above 10. In the limit of large $C_{si,new}$, Equation 6.6.1.2.2-9 becomes:

$$(C_{si,new} >> C_{si,old}): \qquad C_{si}(t) \approx C_{si,new}\left(1 - e^{-\frac{t}{t_{fill}}}\right). \qquad \text{(Eq. 6.6.1.2.2-10)}$$

In effect the initial solubility is negligible compared to $C_{si,new}$, and solubility at late times increases to $C_{si,new}$ from below. Alternatively, if $C_{si,new} << C_{si,old}$,

$$(C_{si,new} << C_{si,old}): \qquad C_{si}(t) \approx C_{si,old} e^{-\frac{t}{t_{fill}}} + C_{si,new}. \qquad \text{(Eq. 6.6.1.2.2-11)}$$

Here the solubility decays towards a much smaller value in the new inflow mixture.

While the details of the time-dependent behavior are unknown, the starting and ending states must be accurate and Equations 6.6.1.2.2-10 and 6.6.1.2.2-11 provide a simplified approximation to the transition from one chemical regime to another. The dissolution rate could replace solubility in Equations 6.6.1.2.2-9 through 6.6.1.2.2-11, and the same general conclusions would hold.

In summary, the response of the bathtub model to a change in inflow chemistry is slower than that of a flow-through model, where the solubility or dissolution rate changes abruptly with a step change in inflow chemistry. The bathtub dampens or delays the response to a change in inflow chemistry over a time scale on the order of t_{fill} to $7t_{fill}$. The upper estimate of $7t_{fill}$ corresponds to an exponential factor of e^{-7} or 0.0009, at which point Equation 6.6.1.2.2-11 has reached an asymptote of $C_{si,new}$. The analytic models cannot predict the precise time dependence because of the nonlinear effects of mixing on pH and of pH on solubility and dissolution rate.

The flow-through model overestimates radionuclide releases compared to the bathtub model when solubility increases because the bathtub geometry delays the increase in radionuclide concentrations and mass fluxes from the waste package to the EBS. The case of increasing solubility or increasing dissolution rate is important because it will increase the peak dose rate. The fact that the flow-through model is not bounding when solubility or dissolution rate

decreases is therefore of less importance for performance assessment and is of secondary importance in selecting the conceptual model for flow through the waste package.

6.6.1.2.3 Change in Patch Geometry

The geometry for the bathtub model allows seepage to collect within the waste package before being released to the EBS. In the primary model (Figure 6.6-1), the patch is positioned such that release is governed by the condition $q_{out} = q_{in}$ after the package fills with liquid.

As an alternative to the primary patch model, consider a waste package that does not have an existing (outflow) patch on the side of the package, but instead has a second patch open abruptly beneath the water line. While the radionuclide concentration within the waste package is unchanged by the alternative location, failure results in the sudden release of a larger pulse of radionuclide mass at the time the second patch opens. Mathematically, the flux of radionuclides leaving the waste package in the primary model, F_{pri}, is given by:

$$F_{pri} = C_l q_{out} = C_l q_{in} = C_l \frac{V_{tub}}{t_{fill}}, \qquad \text{(Eq. 6.6.1.2.3-1)}$$

and the flux of radionuclides leaving the waste package in the alternative model, F_{alt}, is given by:

$$F_{alt} = C_l \frac{V_{tub}}{\Delta t}, \qquad \text{(Eq. 6.6.1.2.3-2)}$$

where Δt is the time to empty the retained liquid through the second patch. In theory, it is possible that $\Delta t << t_{fill}$, so that $F_{alt} >> F_{pri}$.

Equations 6.6.1.2.3-1 and 6.6.1.2.3-2 have the same value for radionuclide concentration, C_l, in the retained liquid because the chemistry of the groundwater is independent of patch location. Implicit in Equations 6.6.1.2.3-1 and 6.6.1.2.3-2 is that the second patch in the alternative conceptual model occurs when the volume of liquid is identical to the capacity of the waste package in the primary model.

The flow-through model produces an average release continuously, while the bathtub model with the alternative flow path produces zero release initially, followed by a high pulse that soon returns to the same flux as the flow-through model. In other words, the flow-through model represents a time average of the response of the bathtub model. From this viewpoint, the potential difference between F_{alt} and F_{pri} is partly mitigated by the sorption and diffusion processes in the unsaturated and saturated zones. The potential difference between F_{alt} and F_{pri} is also small if the second patch appears shortly after the first penetration because there is less retained liquid.

This alternative can also be thought of as being equivalent to the appearance of additional penetrations in the waste package. This analogy is appropriate because additional penetrations in

the waste package increase the inflow flux into the waste form, resulting in higher releases to the EBS. The main effect of the alternative patch geometry model is to generate this increase earlier. This is not considered a major difference because there is a wide range of variability in corrosion rates for the TSPA-LA model (BSC 2004 [DIRS 169996]). The effect of the alternative patch geometry model can then be reasonably considered to be captured within this variability.

The results and observations in this section (6.6.1.2.3) and throughout Section 6.6.1 are appropriate for the general boundary conditions considered here. In other words, this comparison is based on the full fluid flux into the waste package having access to all radioisotopes in the waste. The model implemented in TSPA-LA, in which radionuclides are mobilized in a mass of corrosion products around the fuel pellets, partly mitigates the differences discussed here. This mitigation occurs because a large fluid flux will not transport radionuclides at the solubility limit if the mass in solution is limited by the pore volume in a mass of corrosion products. The situation is then similar to that mentioned at the end of Section 6.6.1.2.1, where mass transfer to the unsaturated zone is the dominant issue, rather than dissolved concentration.

6.6.1.3 Summary

The response of the bathtub geometry has been evaluated for a primary case, with constant boundary conditions and material properties, and for three secondary cases. Analyses for the three secondary cases consider a step change in inflow rate, a step change in inflow chemistry, and a change in flow geometry, as would occur if a patch suddenly appeared beneath the waterline. All cases include consideration of two types of radionuclide release mechanisms: dissolution-rate-limited and solubility-limited. The comparisons are based on closed form analytic solutions.

The key conclusions from the evaluation follow:

- The bathtub model introduces a time delay in the release of radionuclides from the waste package to the EBS in comparison to the flow-through model for the primary case. The flow-through model overestimates releases of radionuclides in relation to the bathtub geometry for the primary case because there is no delay in release of radionuclides to the EBS.

- The response of the bathtub model to a step change in inflow rate (secondary case 1) is identical to the flow-through model for solubility-limited radionuclides. The response of the bathtub model for dissolution-rate-limited radionuclides is to delay the change in concentration and mass flux associated with the new inflow rate. The flow-through model overestimates releases of radionuclides with respect to the bathtub geometry for the case of decreasing inflow, when the concentration of radionuclide increases. The case of increasing radionuclide concentration is of primary interest from a performance or regulatory viewpoint since this case will result in greater releases.

- The response of the bathtub model to a step change in inflow chemistry (secondary case 2) is to delay the change in concentration and mass flux associated with the new inflow chemistry. Analytical models cannot define the exact time delay, which are sensitive to nonlinear chemical effects when inflows mix. Limiting cases, when

solubility increases or decreases by several orders of magnitude, have been examined to define a first order approximation to the response of the chemical system.

The flow-through model overestimates releases of radionuclides relative to the bathtub geometry when solubility or dissolution rate increase with changing inflow chemistry. The flow-through model has an instantaneous change to the higher equilibrium value while the bathtub geometry delays the change until the initial inflow is flushed out of the waste package. Increases in radionuclide concentrations and fluxes are of primary interest from a performance or regulatory viewpoint, so the underestimation of releases of radionuclides in the flow-through model for decreasing solubility or dissolution rate can reasonably be excluded from the TSPA-LA.

- The response of the bathtub model when a second patch opens instantaneously beneath the water level in the waste package (secondary case 3) has also been analyzed. The impact of the instantaneous opening is to release a pulse of radionuclides in comparison to the flow-through model. The impact of this alternative conceptual model is mitigated by the time delays introduced through sorption and diffusion in the unsaturated and saturated zones. In addition, the higher mass flux from the alternative flow path is similar to the impact from additional patches opening in the waste package. There is a wide range of variability in corrosion rates for the TSPA-LA model, and the impact from the instantaneous opening is encompassed in the uncertainty in corrosion rates.

  The impact of this alternative flow model has therefore been screened out of TSPA-LA analyses because of the potential mitigation from sorption and diffusion and because the variability of corrosion rates provides large uncertainty in radionuclide release rates from the waste package.

6.6.2 Limited Water Vapor Diffusion Rate into Waste Package

In this alternative conceptual model, a film of adsorbed water cannot form on the surface of corrosion products if the water consumption rate is greater than the rate of diffusion of water vapor into the waste package. Until a film of water forms on internal corrosion products surfaces, diffusive releases of radionuclides through the adsorbed water cannot occur (according to the in-package diffusion submodel). Thus, the resistance to diffusion of water vapor through stress corrosion cracks delays releases until all of the corrodible materials inside a waste package are fully degraded. It is implicit in this alternative conceptual model that stress corrosion cracks appear before general corrosion patches form; this will not necessarily be the outcome of TSPA-LA calculations.

The objective is to determine the length of time required to complete the corrosion of internal component steels, which is equivalent to the delay from the time a waste package is first breached by stress corrosion cracks until diffusive releases can first take place. This delay can potentially be important since it provides additional time for decay to reduce the concentration of radionuclides before they are released from a waste package. The rate of diffusion of water vapor through stress corrosion cracks into the waste package is estimated and compared with the rate of consumption of water by corrosion of steel internal components to show that diffusion rates are less than corrosion rates. Then, at the rate limited by diffusion, the time needed to

corrode the steels completely is calculated to give the delay before diffusive releases of radionuclides can occur.

An example calculation is presented for a typical set of conditions in the drift and waste package to estimate the time lag between appearance of stress corrosion cracks and the earliest times when an adsorbed water film can first form through which radionuclides can diffuse. Suppose that the temperature of the waste package and drift air is 50°C, the relative humidity in the drift is 95 percent, and the relative humidity is zero inside the waste package. Letting the humidity be zero inside the waste package maximizes the water vapor concentration gradient between the exterior and interior of the waste package. The diffusion distance is $\Delta x = 2.54$ cm, the thickness of waste package outer lid (BSC 2004 [DIRS 169472]; BSC 2004 [DIRS 167394], Detail A). This is the outer closure lid, made of Alloy 22, with a circumferential weld in which stress corrosion cracks may develop. The average diffusive distance is greater – half the length of the waste package interior, or about 240 cm for a 21-PWR (Note i in Table 6.5-8) – but the cross sectional area is less in the stress corrosion cracks than in the waste package, or about 1.93 cm^2 in the example calculation shown in Section 6.5.1.2.1.4.3 vs. 20,030 cm^2 (cross-sectional area of the inside of the outer corrosion barrier in a 21-PWR having a diameter of 1,597 mm; BSC 2004 [DIRS 166953], Section B-B), so diffusion through the cracks is the limiting segment of the path.

To calculate the diffusion rate, the concentration of water vapor in humid air is obtained from psychrometric data. Equations for the determination of psychrometric properties are given by Singh et al. (2002 [DIRS 161624]). At relative humidity RH (fraction) and temperature T (°C), the partial pressure of water p_w (Pa) is:

$$p_w = RH \cdot p_w^\circ, \qquad \text{(Eq. 6.6.2-1)}$$

where p_w° (Pa) is the vapor pressure of water at T (°C), given by:

$$p_w^\circ = \begin{cases} 610.78 \exp\left[\dfrac{17.269T}{237.3+T}\right] & (0^\circ\text{C} < T < 63.0^\circ\text{C}) \\ 610.78 \exp\left[\dfrac{17.269T}{236.3+1.01585T}\right] & (63.0^\circ\text{C} < T < 110^\circ\text{C}). \end{cases} \qquad \text{(Eq. 6.6.2-2)}$$

The absolute humidity H_m (kg water kg^{-1} dry air) is then:

$$H_m = \left(\frac{M_w}{M_a}\right)\left(\frac{p_w}{p - p_w}\right), \qquad \text{(Eq. 6.6.2-3)}$$

where p is the total pressure, chosen to be one atmosphere (101325 Pa), M_w is the molecular weight of water (0.01801528 kg mol^{-1}), and M_a is the molecular weight of air (0.028964 kg mol^{-1}) (Weast 1985 [DIRS 111561], p. F-150).

At 50°C and a relative humidity in the drift of 95 percent, the vapor pressure of water, from Equation 6.6.2-2, is $p_w^\circ = 12{,}334$ Pa, so the partial pressure at $RH = 0.95$ is $p_w = 11{,}717$ Pa. Then the absolute humidity is 0.0815 kg water kg^{-1} dry air.
The molal humidity is:

$$H_{mol} = \frac{H_m M_a}{M_w} = \frac{p_w}{p - p_w} = 0.1308 \text{ mol H}_2\text{O mol}^{-1} \text{ dry air}, \qquad \text{(Eq. 6.6.2-4)}$$

or 0.1156 mol H_2O mol^{-1} wet air. Assuming ideal gas behavior, with an ideal gas molar volume of 22,414 cm^3 mol^{-1} (at 0°C and 1 atm pressure) (Weast 1985 [DIRS 111561], p. F-194), the concentration of water vapor in air at 50°C and 95 percent relative humidity is:

$$C_{wv} = \frac{\left(0.1156 \dfrac{\text{mol H}_2\text{O}}{\text{mol air}}\right)}{\left(22414 \dfrac{\text{cm}^3}{\text{mol}}\right)\left(\dfrac{323.15\text{ K}}{273.15\text{ K}}\right)} = 4.361 \times 10^{-6} \text{ mol H}_2\text{O cm}^{-3}. \qquad \text{(Eq. 6.6.2-5)}$$

To calculate the binary diffusion coefficient, the following equation is used (Bird et al. 1960 [DIRS 103524], Equation 16.3-1):

$$D_{AB} = a\left(\frac{T}{\sqrt{T_{cA}T_{cB}}}\right)^b (p_{cA}p_{cB})^{1/3}(T_{cA}T_{cB})^{5/12}\left(\frac{1}{M_A} + \frac{1}{M_B}\right)^{1/2} p^{-1}, \qquad \text{(Eq. 6.6.2-6)}$$

where:

D_{AB} = the diffusion coefficient (cm^2 s^{-1}) for water (A) in air (B)
T = absolute temperature (K)
p = pressure (atm)
M = molecular weight (g mol^{-1})
a = 3.640×10^{-4} for H_2O with a nonpolar gas
b = 2.334 for H_2O with a nonpolar gas

subscript c refers to critical properties.

For water (A), T_{cA} = 374.1°C = 647.25 K, p_{cA} = 218.3 atm (Weast 1985 [DIRS 111561], p. F-64), and $M_A = 18.01528$ g mol^{-1}; for air (B), $T_{cB} = 132$ K, $p_{cB} = 36.4$ atm (Bird et al. 1960 [DIRS 103524], Table B-1), and $M_B = 28.964$ g mol^{-1} (Weast 1985 [DIRS 111561], p. F-150). Substituting these values into the above equation, the binary diffusion coefficient for water vapor in air is:

$$D_{AB} = \left(3.640 \times 10^{-4}\right)\left(\frac{323.15}{\sqrt{(647.25)(132.)}}\right)^{2.334} [(218.3)(36.4)]^{1/3} \cdot$$
$$[(647.25)(132.)]^{5/12}\left(\frac{1}{18.01528} + \frac{1}{28.964}\right)^{1/2} (1.0)^{-1} \qquad \text{(Eq. 6.6.2-7)}$$
$$= 0.3126\,\text{cm}^2\,\text{s}^{-1}.$$

For diffusion of water vapor through stagnant air in the stress corrosion cracks, the rate of diffusion is, from Fick's first law (Bird et al. 1960 [DIRS 103524], p. 503) for a binary system with constant molar density:

$$q = D_{AB} A_{scc} \frac{\partial C_{wv}}{\partial x}$$
$$= D_{AB} A_{scc} \frac{\Delta C_{wv}}{\Delta x} = D_{AB} A_{scc} \frac{C_{wv}}{\Delta x}$$
$$= \left(0.3126 \frac{\text{cm}^2}{\text{s}}\right) A_{scc} \left(\frac{4.361 \times 10^{-6} \frac{\text{mol}}{\text{cm}^3}}{1\,\text{cm}}\right) \qquad \text{(Eq. 6.6.2-8)}$$
$$= 1.363 \times 10^{-6}\,\text{mol}\,\text{cm}^{-2}\,\text{s}^{-1} \cdot A_{scc},$$

where A_{scc} is the cross-sectional area (cm^2) of stress corrosion cracks through which water vapor can diffuse. The typical cross-sectional area of a stress corrosion crack is 7.7×10^{-6} m^2 per stress corrosion crack (Section 6.3.3.1.2.1). Using the example from Section 6.5.1.2.1.4.3 of 25 stress corrosion cracks per waste package (BSC 2004 [DIRS 169996], Figure 26), $A = 1.93 \times 10^{-4}$ m^2 = 1.93 cm^2, and the rate of diffusion of water vapor is $q = 2.63 \times 10^{-6}$ mol s^{-1} = 83.0 mol H_2O yr^{-1}. Assuming a stoichiometry of 3 mol H_2O/2 mol Fe (to form Fe_2O_3), this water diffusion rate allows carbon steel to corrode at a rate of 55.3 mol Fe yr^{-1}.

When stress corrosion cracks first appear, water vapor that diffuses through will probably be consumed by corrosion of the most reactive materials within a waste package, namely the A 516 carbon steel that makes up the baskets. These steel components have an average corrosion rate of 77.43 μm yr^{-1} (DTN: MO0409SPAACRWP.000 [DIRS 172059]; Spreadsheet "aqueous-A516.xls"; Worksheet "Freshwater", 1-year data at 60°C) and a maximum thickness of 3/8 in. (9.525 mm) (BSC 2004 [DIRS 169472], Table 1), for an average lifetime of about 123 yr. From Table 6.5-9, the total A 516 steel in a 21-PWR waste package is 100,260 mol (assumed to be Fe; hence, all corrosion products are Fe_2O_3). The rate of iron consumption over the average

lifetime of this steel is about 815 mol Fe yr^{-1}. Two simplified reaction stoichiometries are considered:

$$2\,Fe + 3\,H_2O = Fe_2O_3 + 3\,H_2$$
$$Fe + 2\,H_2O = Fe(OH)_2 + H_2.$$

Anoxic corrosion of iron will typically result in $Fe(OH)_2$; however, to be consistent with the in-package diffusion submodel, the first reaction is also assumed to occur, producing Fe_2O_3 as the corrosion product. Assuming a stoichiometry of 3 mol H_2O/2 mol Fe (to form Fe_2O_3), corrosion of 815 mol Fe yr^{-1} of A 516 carbon steel consumes 1,220 mol H_2O yr^{-1}, which is a factor of 15 greater than the rate of diffusion of water vapor through stress corrosion cracks. Another estimate uses the stoichiometry for the formation of $Fe(OH)_2$ (i.e., 2 mol H_2O mol^{-1} Fe), which gives a water consumption rate of 1,630 mol H_2O yr^{-1}, a factor of 20 greater than the diffusion rate of water vapor through stress corrosion cracks.

If the stress corrosion cracks are filled with porous corrosion products, the cross sectional area for diffusion is less. For a porosity ϕ_{scc} of the stress corrosion crack, the effective cross sectional area is $A_{scc,eff} = \phi_{scc} A_{scc}$. For a porosity of 0.4, $A_{scc,eff} = 0.4(1.93\,cm^2) = 0.77\,cm^2$. The corrosion rates given above are now higher than the diffusion rate by an additional factor of $1/\phi_{scc}$, or a factor of 37 higher than the diffusion rate for Fe_2O_3 formation and a factor of 49 higher for $Fe(OH)_2$ formation.

Another way to show the effect of the corrosion rate being limited by the rate of diffusion of water vapor is to calculate the time required to corrode all of the steel in a waste package. As shown above, the lifetime of the carbon steel components is 130 yr when *not* limited by the availability of water. When the corrosion rate is limited by the water vapor diffusion rate, the lifetime is greater than 130 years. The diffusion rate of 83.0 mol H_2O yr^{-1} allows 55.3 mol Fe yr^{-1} to corrode to Fe_2O_3, thereby requiring 100,260 mol Fe/(55.3 mol Fe yr^{-1}) = 1,810 years for all A 516 steel components to degrade fully once stress corrosion cracks appear. To degrade to $Fe(OH)_2$, where the stoichiometry is 1 mol Fe/2 mol H_2O, and the diffusion limited corrosion rate is 41.5 mol Fe yr^{-1}, would require 2,420 yr. Accounting for a typical 40 percent porosity in the corrosion products increases these estimates to 4,530 yr and 6,040 yr, respectively.

A further refinement of these estimates includes corrosion of the stainless steel components in addition to the carbon steel. Suppose that all internal components corrode, and the composition of the component materials is treated as in Section 6.5.1.2.1.3.2 and Table 6.5-9, in which all elemental components of the metals are treated as though they were iron, on a molar basis. Effectively 346,330 mol Fe are to be corroded at a rate limited by water diffusion through stress corrosion cracks. Then 6,260 yr are required to consume all of the material to Fe_2O_3, at the water vapor diffusion-limited rate of 55.3 mol Fe yr^{-1}. At the mean stainless steel corrosion rate of 0.248 μm yr^{-1} (DTN: MO0409SPAACRWP.000 [DIRS 172059]; Spreadsheet "aqueous-316L.xls"; Worksheet "freshwater", 50-100°C data), the 50.8-mm-thick inner vessel (BSC 2004 [DIRS 169472]; BSC 2004 [DIRS 167394], Detail A) has a lifetime of 205,000 yr. Assuming that all 10,800 kg of the 316 stainless steel listed in Table 6.3-4 is part of the inner vessel or lids, and that this is equivalent to 192,240 mol Fe (Table 6.5-9), the mean molar corrosion rate is 192,240 mol/205,000 yr = 0.94 mol yr^{-1}. A stoichiometrically equivalent rate of water

consumption due to stainless steel corrosion to Fe_2O_3 is 1.4 mol H_2O yr^{-1}, which is a factor of 59 less than the rate of diffusion of water vapor through open stress corrosion cracks (83.0 mol H_2O yr^{-1}). In this case, water vapor diffusion through the stress corrosion cracks does not control the rate of corrosion and water consumption. If the cracks are filled with corrosion products to a porosity of 0.4, the rate of water vapor diffusion is less, as discussed earlier, and may then control the rate of corrosion.

In Table 6.6-1, the time required to corrode all of the carbon steel or all of the stainless steel is shown for various assumptions and conditions (temperature, relative humidity in the drift). If no diffusive path can form until all of the steels are fully corroded, the time needed to corrode the steel is effectively the time lag between the first appearance of stress corrosion cracks and the first diffusive releases from the breached waste package. Depending on conditions and assumptions, this delay can range from 630 yr (at 70°C) to more than 34,000 yr (at 30°C) even at 100 percent relative humidity in the drift. At lower relative humidities, the delay can be longer, for example, more than 43,000 yr at 30°C and 80 percent relative humidity. In this table, the water vapor concentration, C_{wv}, is obtained from Equations 6.6.2-4 and 6.6.2-5 as a function of relative humidity and temperature. The water vapor flux through stress corrosion cracks, q, is given by Equation 6.6.2-8. The corrosion rate, r_{corr}, is the stoichiometrically equivalent rate of iron consumption that occurs when limited by the water vapor influx, q. The release delay is the time, t_{corr}, required to corrode through 10 mm of carbon steel or 50.8 mm of stainless steel at the rate, r_{corr}.

Table 6.6-1. Summary of Release Delays Resulting from Limitations on Diffusion of Water Vapor Through Stress Corrosion Cracks

Drift *RH*	0.8	0.9	0.95	0.99	1.00
T = 50°C, D_{AB} = 0.313 cm^2 s^{-1}					
C_{wv} (mol cm^{-3})	3.67×10^{-6}	4.13×10^{-6}	4.36×10^{-6}	4.54×10^{-6}	4.59×10^{-6}
q (mol H_2O yr^{-1})	69.9	78.6	83.0	86.5	87.3
r_{corr} (mol Fe yr^{-1})	46.6	52.4	55.3	57.6	58.2
t_{corr}, Carbon steel only, Fe_2O_3 stoichiometry, open stress corrosion cracks (yr)	2,150	1,910	1,810	1,740	1,720
t_{corr}, Carbon steel only, $Fe(OH)_2$ stoichiometry, open stress corrosion cracks (yr)	2,870	2,550	2,420	2,320	2,300
t_{corr}, Carbon steel only, Fe_2O_3 stoichiometry, ϕ_{scc} = 0.4 (yr)	5,380	4,780	4,530	4,350	4,310
t_{corr}, Carbon steel only, $Fe(OH)_2$ stoichiometry, ϕ_{scc} = 0.4 (yr)	7,180	6,380	6,040	5,800	5,740
t_{corr}, All steel as stainless steel, Fe_2O_3 stoichiometry, open stress corrosion cracks (yr)	4,130	3,670	3,480	3,340	3,300
t_{corr}, All steel as stainless steel, $Fe(OH)_2$ stoichiometry, open stress corrosion cracks (yr)	5,500	4,890	4,630	4,450	4,400

Table 6.6-1. Summary of Release Delays Resulting from Limitations on Diffusion of Water Vapor Through Stress Corrosion Cracks (Continued)

Drift *RH*	0.8	0.9	0.95	0.99	1.00
$T = 50°C$, $D_{AB} = 0.313\ cm^2\ s^{-1}$					
t_{corr}, All steel as stainless steel, Fe_2O_3 stoichiometry, $\phi_{scc} = 0.4$ (yr)	10,320	9,170	8,690	8,340	8,250
t_{corr}, All steel as stainless steel, $Fe(OH)_2$ stoichiometry, $\phi_{scc} = 0.4$ (yr)	13,760	12,230	11,590	11,120	11,010
$T = 70°C$, $D_{AB} = 0.360\ cm^2\ s^{-1}$					
C_{wv} (mol cm^{-3})	8.75×10^{-6}	9.84×10^{-6}	1.04×10^{-5}	1.08×10^{-5}	1.09×10^{-5}
q (mol H_2O yr^{-1})	192	215	227	237	239
r_{corr} (mol Fe yr^{-1})	128	144	152	158	160
t_{corr}, Carbon steel only, Fe_2O_3 stoichiometry, open stress corrosion cracks (yr)	790	700	660	630	630
t_{corr}, Carbon steel only, $Fe(OH)_2$ stoichiometry, open stress corrosion cracks (yr)	1,050	930	880	850	840
t_{corr}, Carbon steel only, Fe_2O_3 stoichiometry, $\phi_{scc} = 0.4$ (yr)	1,960	1,750	1,650	1,590	1,570
t_{corr}, Carbon steel only, $Fe(OH)_2$ stoichiometry, $\phi_{scc} = 0.4$ (yr)	2,620	2,330	2,200	2,120	2,090
t_{corr}, All steel as stainless steel, Fe_2O_3 stoichiometry, open stress corrosion cracks (yr)	1,510	1,340	1,270	1,220	1,200
t_{corr}, All steel as stainless steel, $Fe(OH)_2$ stoichiometry, open stress corrosion cracks (yr)	2,010	1,780	1,690	1,620	1,610
t_{corr}, All steel as stainless steel, Fe_2O_3 stoichiometry, $\phi_{scc} = 0.4$ (yr)	3,760	3,350	3,170	3,040	3,010
t_{corr}, All steel as stainless steel, $Fe(OH)_2$ stoichiometry, $\phi_{scc} = 0.4$ (yr)	5,020	4,460	4,230	4,060	4,020
$T = 30°C$, $D_{AB} = 0.269\ cm^2\ s^{-1}$					
C_{wv} (mol cm^{-3})	1.35×10^{-6}	1.51×10^{-6}	1.60×10^{-6}	1.67×10^{-6}	1.68×10^{-6}
q (mol H_2O yr^{-1})	22.1	24.8	26.2	27.3	27.6
r_{corr} (mol Fe yr^{-1})	14.7	16.6	17.5	18.2	18.4
$T = 30°C$, $D_{AB} = 0.269\ cm^2\ s^{-1}$					
t_{corr}, Carbon steel only, Fe_2O_3 stoichiometry, open stress corrosion cracks (yr)	6,820	6,060	5,740	5,510	5,450
t_{corr}, Carbon steel only, $Fe(OH)_2$ stoichiometry, open stress corrosion cracks (yr)	9,090	8,080	7,650	7,340	7,270
t_{corr}, Carbon steel only, Fe_2O_3 stoichiometry, $\phi_{scc} = 0.4$ (yr)	17,040	15,140	14,350	13,770	13,630
t_{corr}, Carbon steel only, $Fe(OH)_2$ stoichiometry, $\phi_{scc} = 0.4$ (yr)	22,720	20,190	19,130	18,360	18,170

Table 6.6-1. Summary of Release Delays Resulting from Limitations on Diffusion of Water Vapor Through Stress Corrosion Cracks (Continued)

Drift *RH*	0.8	0.9	0.95	0.99	1.00
t_{corr}, All steel as stainless steel, Fe_2O_3 stoichiometry, open stress corrosion cracks (yr)	13,070	11,620	11,000	10,560	10,450
t_{corr}, All steel as stainless steel, $Fe(OH)_2$ stoichiometry, open stress corrosion cracks (yr)	17,420	15,490	14,670	14,080	13,940
t_{corr}, All steel as stainless steel, Fe_2O_3 stoichiometry, $\phi_{scc} = 0.4$ (yr)	32,670	29,040	27,510	26,400	26,140
t_{corr}, All steel as stainless steel, $Fe(OH)_2$ stoichiometry, $\phi_{scc} = 0.4$ (yr)	43,560	38,720	36,680	35,200	34,850

6.6.3 Limited Oxygen Diffusion Rate into Waste Package

Dry air oxidation under atmospheric conditions can also proceed once stress corrosion cracks appear (CRWMS M&O 2000 [DIRS 135968], p. 14). Therefore, the rate of oxygen diffusion through cracks should also be considered, since oxygen diffusion may limit the corrosion rate.

The mean corrosion rate of Stainless Steel Type 316L under atmospheric conditions, 0.113 $\mu m\ yr^{-1}$ (DTN: MO0312SPAPCEML.003 [DIRS 167409], Spreadsheet: atmospheric.xls, Worksheet: 316) is lower than under aqueous conditions, 0.248 $\mu m\ yr^{-1}$ (DTN: MO0409SPAACRWP.000 [DIRS 172059]; Spreadsheet "aqueous-316L.xls"; Worksheet "freshwater", 50-100°C data). To compare the corrosion rate with the oxygen diffusion rate, the lifetime of the waste package inner vessel is estimated, since this is the thickest component of a waste package and will provide the longest component lifetime. The inner vessel is 50.8 mm thick (BSC 2004 [DIRS 169472]; BSC 2004 [DIRS 167394], Detail A); with unlimited oxygen availability, its lifetime is $50.8\ mm/(0.113 \times 10^{-3}\ mm\ yr^{-1}) = 4.50 \times 10^5$ yr. An estimate of the molar corrosion rate can be obtained by letting the effective Fe content of the Stainless Steel Type 316 listed in Table 6.5-9 be inner vessel and lid material. Then the corrosion rate is $192240\ mol/(4.5\times10^5\ yr) = 0.43\ mol\ Fe\ yr^{-1}$. Accounting for the stoichiometry to produce Fe_2O_3 (3 mol O_2/4 mol Fe):

$$4\ Fe + 3\ O_2 \rightarrow 2\ Fe_2O_3.$$

This is equivalent to an oxygen consumption rate of 0.32 mol $O_2\ yr^{-1}$.

For nonpolar gas pairs, parameters a and b in the diffusion coefficient expression, Equation 5.4.2-6, are 2.745×10^{-4} and 1.823, respectively (Bird et al. 1960 [DIRS 103524], Equation 16.3-1). Using the appropriate parameters for oxygen (A) diffusing in air, T_{cA} = 154.58 K, p_{cA} = 5.043 MPa = 49.77 atm (Weast 1985 [DIRS 111561], p. F-62), and M_A =31.9988 g mol^{-1}, it follows that:

$$D_{AB} = \left(2.745\times10^{-4}\right)\left(\frac{323.15}{\sqrt{(154.58)(132.)}}\right)^{1.823}[(49.7)(36.4)]^{1/3}$$
$$[(154.58)(132.)]^{5/12}\left(\frac{1}{31.9988}+\frac{1}{28.964}\right)^{1/2}(1.0)^{-1} \qquad \text{(Eq. 6.6.3-1)}$$
$$= 0.2374\ \text{cm}^2\ \text{s}^{-1}.$$

Let the oxygen concentration in air in a drift outside a waste package be the same as in the atmosphere: 20.946 volume-percent (Weast 1985 [DIRS 111561], p. F-156) or 0.20946 mol O_2 mol^{-1} air. As an example, suppose the temperature is a uniform 50°C. With 22,414 cm^3 mol^{-1}, the O_2 concentration is:

$$C_{O_2} = \frac{\left(0.20946\,\frac{\text{mol}\,O_2}{\text{mol air}}\right)}{\left(22414\,\frac{\text{cm}^3}{\text{mol}}\right)\left(\frac{323.15}{273.15}\right)} \qquad \text{(Eq. 6.6.3-2)}$$
$$= 7.899\times10^{-6}\ \text{mol}\,O_2\ \text{cm}^{-3}\ \text{air}.$$

Inside a waste package, suppose the oxygen concentration is essentially zero. For an example with 25 stress corrosion cracks (Section 6.5.1.2.1.4.3) with a total cross-sectional area of 1.93 cm^2, the rate of diffusion of oxygen is:

$$q = D_{AB}A\frac{\Delta C_{O_2}}{\Delta x}$$
$$= \left(0.2375\,\frac{\text{cm}^2}{\text{s}}\right)\left(1.93\,\text{cm}^2\right)\left(\frac{7.899\times10^{-6}\,\frac{\text{mol}\,O_2}{\text{cm}^3}}{1\,\text{cm}}\right)\left(3.1556926\times10^7\,\frac{\text{s}}{\text{yr}}\right) \qquad \text{(Eq. 6.6.3-3)}$$
$$= 114\ \text{mol}\,O_2\ \text{yr}^{-1}.$$

In this case, the corrosion rate is limited by the reaction kinetics, rather than the rate of diffusion of oxygen, since the oxygen diffusion rate is about 360 times greater than the oxygen consumption rate due to stainless steel corrosion under atmospheric conditions (114 mol yr^{-1} vs. 0.32 mol yr^{-1}). If corrosion products fill the stress corrosion cracks to a porosity of, say 0.4, the diffusion rate is still 140 times greater than the oxygen consumption rate due to stainless steel corrosion.

Accounting for the stoichiometry to produce Fe_2O_3 (3 mol O_2/4 mol Fe), the oxygen diffusion rate is equivalent to an iron consumption rate of 152 mol Fe yr^{-1}. At the same temperature (50°C), water vapor diffusion allows, at most, 58.2 mol Fe yr^{-1} (Table 6.6-1, $RH = 1.0$) to be consumed, primarily because the water vapor concentration in air is much less than the oxygen concentration, so the gradient into the waste package is smaller. However, the reaction rate of iron with oxygen is lower than that of iron with water, so the steel components inside a waste package have a lesser affinity for oxygen than for water.

These calculations indicate that a more accurate mass balance for water and oxygen inside a waste package could reduce predicted releases of radionuclides to the invert, and thus releases to the accessible environment. Releases could be delayed for several thousand years compared with current estimates as the corrosion of fuel baskets and inner vessel components scavenges water and oxygen that diffuse through small stress corrosion cracks (providing general corrosion patches do not form first). Formation of a diffusive pathway could then be delayed until corrosion of iron-based materials is largely completed.

Despite the potential for delays in releases of radionuclides predicted by these models, uncertainty exists in the processes that are modeled. The assumption that no water is physically adsorbed until all steel is corroded is questionable, since adsorption is typically a fast process. On the other hand, if water consumption by corrosion does keep the relative humidity lower inside the waste package than outside, the effective water saturation could be less than when calculated using the humidity of the drift. If this occurs, calculated diffusion coefficients are simply lower than given by the in-package diffusion submodel, rather than zero, but for the time required for the internal components to corrode. The net effect is similar to what these alternative conceptual models predict. The corrosion rates that have been used are for aqueous conditions, which might exist on a microscopic scale. However, to be consistent with the assumption here that no adsorbed water film forms, rates in a low-humidity gaseous environment should be used. This increased realism would increase the time required for complete corrosion of the steel.

6.6.4 Dual-Continuum Invert

The LA invert design (BSC 2004 [DIRS 169503]) uses crushed tuff as the invert ballast material. This material is actually comprised of two pore spaces – intragranular pore space (tuff particle matrix) and intergranular pore space. Although radionuclide transport by both advection and diffusion can occur in both pore spaces, the dominant flow and transport processes in each of these two pore spaces is generally different. In order to simulate flow and transport through the invert accurately, the invert may be conceptualized as overlapping dual continua and modeled using a dual-permeability approach (Šimůnek et al. 2003 [DIRS 167469], p. 22), wherein flow and transport occur in both pore spaces, and mass transfer takes place between the two pore spaces.

Transport through the drift invert can occur either through the intergranular porosity of the invert ballast material or through the intragranular porosity. Advective transport depends upon the liquid flux through each of these porosities. Diffusive transport through each of these porosities depends upon the diffusive properties associated with each pathway. For this alternative conceptual model, the invert is modeled as overlapping dual continua in which one continuum is

represented by the intergranular porosity and the other continuum is represented by the intragranular porosity, as shown in Figure 6.6-2.

Whereas the single-continuum invert model, as shown in Figure 6.3-1, has a single advective flow path (Pathway 8) from the invert to the unsaturated zone, the dual-continuum invert has two potential advective flow pathways, as shown in Figure 6.6-2:

Pathway 8 **Flux from the Intragranular Invert Continuum to the Unsaturated Zone** – Advective flux from the invert intragranular continuum flows directly into the UZ matrix.

Pathway 9 **Flux from the Intergranular Invert Continuum to the Unsaturated Zone** – All advective flux from the invert intergranular continuum flows directly into the UZ fractures.

In this model, no advective flux occurs between the two invert continua. Thus, the flux through pathway 8 is identical to the imbibition flux, pathway 7: $F_8 = F_7$.

Ignoring three-dimensional effects (e.g., flow along the axis of the drift), the quasi-steady state flux through the intergranular invert continuum is equal to the seepage flux: $F_9 = F_1$.

This alternative conceptual model for flow and transport through the EBS includes five domains: the waste form (e.g., fuel rods or HLW glass), waste package corrosion products, the intergranular invert continuum, the intragranular invert continuum, and the invert/UZ interface domain. The first two domains are the same as in the base case model. The third domain (the intergranular invert continuum) is in intimate contact with the waste package and has an average thickness of 0.597 m (Section 6.5.3). The fourth domain (the intragranular invert continuum) is also in intimate contact with the waste package and has the same average thickness, 0.597 m, as the intergranular invert continuum.

Table 6.6-2 summarizes the transport modes and transport parameters for the transport pathways in the EBS when the invert is modeled as a dual continuum.

The diffusive fluxes to the dual invert continua are determined from the flux continuity at the interface between the corrosion products domain and the invert continua. This requirement states that the diffusive flux exiting the corrosion products domain is equal to the sum of the diffusive fluxes entering the two invert continua. The diffusive flux split will depend on the diffusive properties in the corrosion products domain and both invert continua together with the concentration gradients across the corrosion products domain/invert interface.

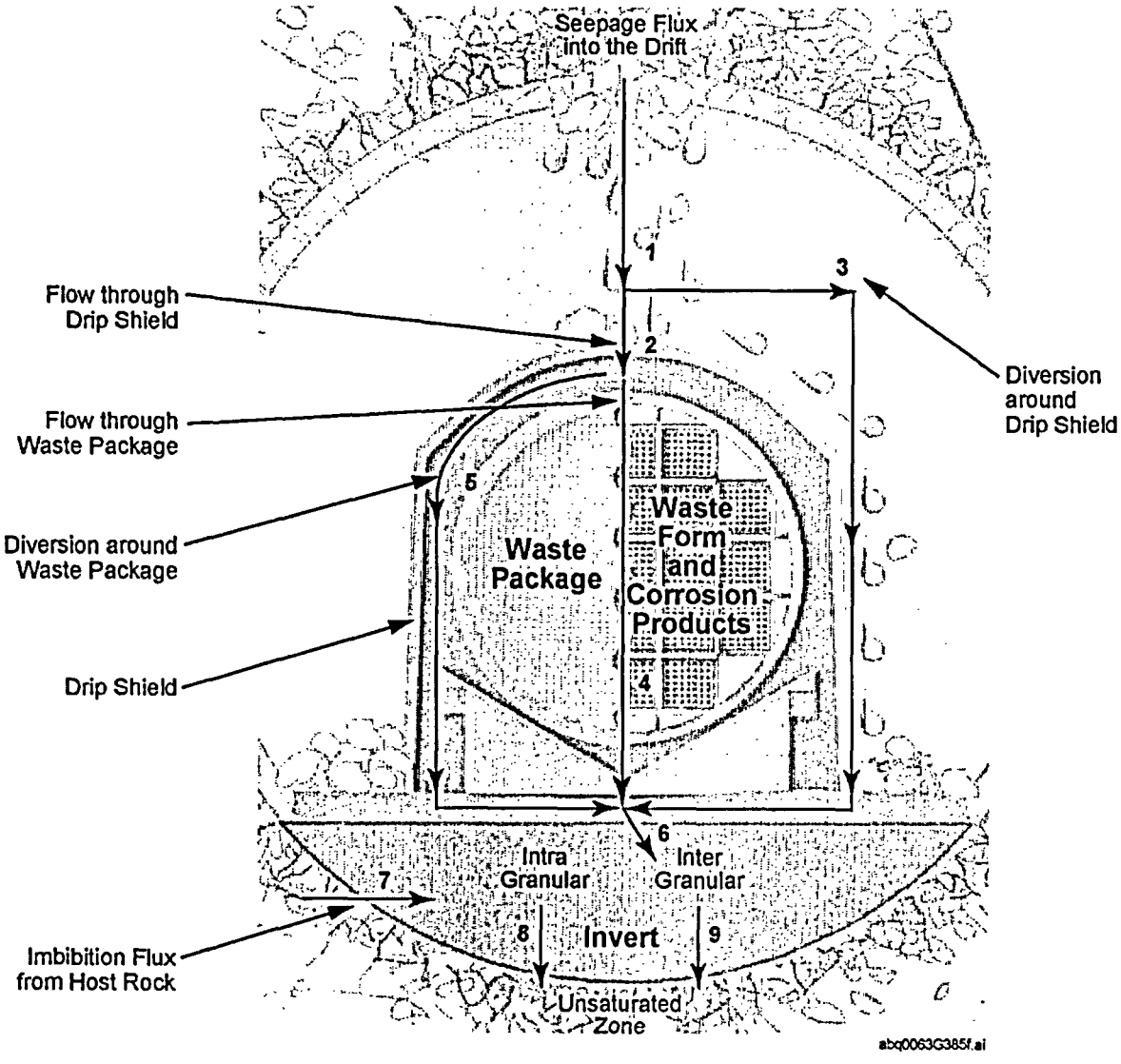

Figure 6.6-2. Schematic of the Potential Flow Pathways in the EBS

Table 6.6-2. Summary of Transport Modes and Parameters for the EBS Transport Pathways with Dual-Continuum Invert

Transport Pathway	Transport Modes	Transport Parameters and Data Sources
1. Waste form and corrosion products domains	Diffusion through stress corrosion cracks (no advective transport through stress corrosion cracks). Diffusion and advection through patches.	No lateral or forward dispersion. Colloidal particles will transport radionuclides. Diffusive area for each stress corrosion crack is 7.7×10^{-6} m^2 (see Section 6.3.3.1.2.1). Diffusive area for each patch is provided by WAPDEG (BSC 2004 [DIRS 169996]). Diffusion coefficient (all radionuclides): • 2.299×10^{-5} cm^2 s^{-1} at 25°C (Mills 1973 [DIRS 133392], Table III) • Modified for porosity and saturation (see Section 6.5.1.2.1.4) • Reduced by a factor of 100 if radionuclide is bound to a colloid (see Section 6.3.4.4). The cross-sectional area $A_{CP/invert}$ for radionuclide transport is given by the interface between the waste package corrosion products domain and the invert domain. See Section 6.5.3 for further details.
2. Intragranular invert continuum	Diffusion from corrosion products domain into the invert intragranular continuum.	No advection from corrosion products domain into invert intragranular continuum Diffusion coefficient (all radionuclides): • 2.299×10^{-5} cm^2 s^{-1} at 25°C (Mills 1973 [DIRS 133392], Table III) • Modified for porosity and saturation (see Section 6.3.4.1) • Temperature modification defined in Section 6.3.4.1.2 • Reduced by a factor of 100 if radionuclide is bound to a colloid (see Section 6.3.4.4). Flow cross-sectional areas given by the top surface area of the invert, A_{IVIZ} (Equation 6.5.3.3-4).
3. Intergranular invert continuum	Diffusion and advection (F_6) corrosion products domain into the invert intergranular continuum.	Liquid flux for advection = $F_6 = F_5$ (diverted by WP) + F_4 (flux through WP) + F_3 (diverted by drip shield). Diffusion coefficient (all radionuclides): • 2.299×10^{-5} cm^2 s^{-1} at 25°C (Mills 1973 [DIRS 133392], Table III) • Modified for porosity and saturation (see Section 6.3.4.1) • Temperature modification defined in Section 6.3.4.1.2; invert temperature is provided by *Multiscale Thermohydrologic Model* calculations (BSC 2004 [DIRS 169565] • Reduced by a factor of 100 if radionuclide is bound to a colloid (see Section 6.3.4.4). The cross-sectional area A_{IVIZ} for radionuclide transport is the top surface area of the invert (Equation 6.5.3.3-4).

Table 6.6-2. Summary of Transport Modes and Parameters for the EBS Transport Pathways with Dual-Continuum Invert (Continued)

Transport Pathway	Transport Modes	Transport Parameters and Data Sources
4. Invert intragranular – intergranular interface	Diffusion between the invert intergranular continuum and the intragranular continuum.	Mass transfer coefficient uses (see Section 6.6.4.1): • Diffusion coefficient of the intragranular continuum • Sampled geometry-dependent factor, β (Invert_Geometry_Coef) • Diffusive path length equal to mean invert tuff particle radius, 5 mm. Parameters are dependent on discretization of the invert model; see Section 6.5.3.5 for discretization and implementation details.
5. Invert-UZ interface	Advection from the invert intragranular continuum to UZ matrix (F_8). Advection from the invert intergranular continuum to UZ fractures (F_9). Diffusion from the invert intragranular continuum to UZ fractures and matrix. Diffusion from the invert intergranular continuum to UZ fractures and matrix.	The invert diffusion calculation uses radionuclide concentrations in the WP corrosion products domain as the boundary condition at the top of the invert and a series of unsaturated zone computational cells below the invert that provide a gradient to a zero radionuclide concentration at some distance from the bottom of the invert. See Section 6.5.3.6.

WP = waste package

For discussion of the diffusive flux treatment at the corrosion products domain/invert interface consider a diffusive flux term, either aqueous or colloid flux, within the transport mass balance equation. Let $z_{interface}$ denote the spatial location of the corrosion products domain/invert interface. Then for $z < z_{interface}$, the diffusive flux for radionuclide species i at a location within the corrosion products domain is:

$$\phi_{CP} S_{w\_CP} D_{CP} \frac{\partial C_{iCP}}{\partial z}, \qquad \text{(Eq. 6.6.4-1)}$$

where ϕ_{CP} is the porosity of the single-continuum corrosion products domain.

For $z > z_{interface}$, the diffusive fluxes within the intergranular invert and intragranular invert media are, respectively,

$$\phi_{inter} S_{w\_inter} D_{inter} \frac{\partial C_{iinter}}{\partial z}, \qquad \text{(Eq. 6.6.4-2)}$$

$$\phi_{intra} S_{w\_intra} D_{intra} \frac{\partial C_{iintra}}{\partial z}. \qquad \text{(Eq. 6.6.4-3)}$$

The mass transport across this interface is coupled by the flux continuity condition at the interface:

$$\phi_{CP} S_{w\_CP} D_{CP} \frac{\partial C_{iCP}}{\partial z^-} = \phi_{inter} S_{w\_inter} D_{inter} \frac{\partial C_{iinter}}{\partial z^+} + \phi_{intra} S_{w\_intra} D_{intra} \frac{\partial C_{iintra}}{\partial z^+}, \quad \text{(Eq. 6.6.4-4)}$$

where

$$\frac{\partial}{\partial z^-} \text{ and } \frac{\partial}{\partial z^+}$$

are the derivative from the left and the derivative from the right, respectively, at the interface.

A similar flux continuity condition for each invert continuum is applied at the invert/UZ interface.

6.6.4.1 Invert Dual Continuum Interface Transfer

If a gradient exists in the concentration of dissolved radionuclide species *i* or of colloids that contain radionuclide species *i*, mass will be transferred across the interface between the two continua. The mass transfer coefficients for dissolved species and colloids, α (given by Equation 6.5.1.2-22), are dependent on the geometry and diffusivity in the neighborhood of the interface.

Mass will also be transferred with advective flow across the interface as a result of head or pressure gradients between the two continua, for example, when imbibition into the tuff matrix (i.e., intragranular continuum) occurs. This effect is ignored in the invert since it should be a short term and infrequent occurrence.

When advective interface mass transfer is neglected, the mass transfer coefficient has the form (Gerke and van Genuchten 1996 [DIRS 167466], p. 345; Corapcioglu and Wang 1999 [DIRS 167464], p. 3263; Šimůnek et al. 2003 [DIRS 167469], pp. 28 and 30):

$$\alpha = \frac{\beta}{d^2} D_e, \quad \text{(Eq. 6.6.4.1-1)}$$

where β is a dimensionless geometry-dependent coefficient, d is a characteristic length (m) of the matrix structure (e.g., half the aggregate width or half the fracture spacing), and D_e is an effective diffusion coefficient ($cm^2\ s^{-1}$) that represents the diffusion properties of dissolved species at the interface between the two continua for radionuclide species *i*. For colloids containing sorbed radionuclides, D_e represents the diffusion properties of those colloids at the interface between the two continua. Since the self diffusion coefficient of water is used as a bounding value for all radionuclides, the subscript on the diffusion coefficient in Equation 6.5.1.2-22 can be dropped in Equation 6.6.4.1-1.

Mass transfer coefficients obtained analytically using Laplace transform comparisons derived values for β of 3 for rectangular slabs, 8 for solid cylinders, and 15 for spheres (Gerke and van Genuchten 1996 [DIRS 167466], p. 345). Values of β have also been obtained (Gerke and van Genuchten 1996 [DIRS 167466]) by directly matching analytical solutions of the diffusion models to results obtained with the first-order model such as Equation 6.5.1.2-18. Gerke and van Genuchten (1996 [DIRS 167466]) derived an empirical expression to estimate β for complex and mixed types of structural geometry. A dimensionless surface-area-to-volume ratio of a particle, $\zeta = \frac{A_g}{V_g} a_g$, is defined, where a_g is the effective length of the matrix pore system; for example, for a cylinder, a_g is the radius; for a cube, a_g is half the length of a side; for a sphere, a_g is the radius. Thus, for a cylinder, $\zeta = 2$, and for a sphere and a cube, $\zeta = 3$. For values $2 < \zeta \leq 10$, Gerke and van Genuchten (1996 [DIRS 167466], p. 354) give the following fitted empirical expression:

$$\beta = 11.4275 - 7.4438\zeta + 3.5473\zeta^2 . \qquad \text{(Eq. 6.6.4.1-2)}$$

For cubes and spheres, Equation 6.6.4.1-2 gives a value for β of 21.0, and for a cylinder, $\beta = 10.7$. Since the geometry of crushed tuff invert particles is uncertain, these estimates of β help to establish a range of values over which β can be sampled.

The crushed tuff invert material will be produced by a tunnel boring machine that will excavate the drifts for the repository. The cuttings from TBMs can be characterized as generally well graded material containing large flat and elongated chips and moderate excess of fines (Gertsch et al. 1993 [DIRS 107880], p. 20). Tests done on samples of TSw2 tuff using a linear cutting machine produced cuttings that, in the plus inch fraction, were elongated and flat, while the finer particles were more cubic (Gertsch et al. 1993 [DIRS 107880], p. 42-43). The operating parameters expected to be utilized in the Yucca Mountain Project tunnel boring machine will reduce the maximum particle size and result in the particles being more cubic (Gertsch et al. 1993 [DIRS 107880], p. 44). Particle sizes for the invert material will range from 0.075 mm (No. 200 sieve) to 50 mm, with 50 percent of the particles passing a 10-mm sieve (BSC 2004 [DIRS 170559], Sheet 2). Therefore, the average diameter for invert crushed tuff particles (spherical or cylindrical) is 10 mm; if the particles are treated as cubes, the average length of a side is 10 mm. The characteristic length *d* (Diff_Length_Inv_Inter_Intra) is the radius or half the distance through a cube, or 5 mm.

The invert material will be composed of particles that are roughly spherical or cubic, along with elongated particles that can be considered roughly cylindrical. For cylinders, cubes, and spheres, estimates of β (Invert_Geometry_Coef) range from 8 to 21. A particle shape distribution is not available; therefore, a uniform distribution for β is appropriate.

The model for the mass transfer between overlapping continua is represented by the diffusion of solute on a macroscopic control volume scale, i.e., between two entire domains or computational cells, rather than on the elemental volume scale used to formulate the mass balance equations in Section 6.5.1.2. Consequently, the mass transfer between the two invert continua is not written

as a gradient of diffusive mass flux with respect to the coordinate dimensions. In the discrete formulation, this flux is modeled as a diffusive flux between two invert cells. For the discrete realization of the invert continua mass transfer, the diffusive length within the intergranular continuum is taken to be zero. This is a result of the water within the intergranular continuum consisting of a film of negligible thickness on the surface of the intragranular materials. The diffusive length within the intragranular continuum depends on some mean diffusive length within the crushed tuff material. This diffusive length is taken as a mean radius of spherical particles, 5 mm. The diffusive area is estimated as the surface area of all spherical particles necessary to fill the invert volume. Therefore, the characteristic length parameter, d, is identified as the diffusive length (5 mm) within the intragranular continuum.

6.6.4.2 Discretization of Dual-Continuum Invert Alternative Computational Model

Discretization of the continuum mass balance equations for EBS transport model is described in Section 6.5.3.5 for a single-continuum invert. Numerical modeling of the EBS radionuclide transport is performed using the GoldSim software (Golder Associates 2003 [DIRS 166572]) cell pathway capability. The cell pathway acts as a batch reactor, where radionuclide mass is assumed to be instantaneously and completely mixed and partitioned among all media (fluid or solid) within the cell. When multiple cells are linked together in a cell network via advective and diffusive mechanisms, GoldSim numerically solves the coupled system of equations to compute the radionuclide mass present in each cell and the mass fluxes between cells as a function of time.

Within a computational cell network, each cell is allowed to communicate by advection and/or diffusion with any other cell. This concept is crucial in implementing the bifurcation of diffusive fluxes across an interface between a single continuum domain and a dual continuum domain, such as at the interface between the corrosion products domain and the dual continuum invert domains. Each computational cell is provided with parameters describing water volumes, diffusive properties, and advective and diffusive flux links to other cells. Between any two cells, the diffusive flux can be bidirectional, depending on the concentration gradient, while the advective flux is unidirectional. The output of a cell is given in terms of the advective and diffusive mass fluxes for radionuclide species i and its concentration at the cell center.

In this alternative conceptual model, the invert is conceptualized as a dual continuum domain of intergranular and intragranular continua. The discretization of the invert domain, using GoldSim, consists of two cells – one representing the invert intergranular continuum and the other representing the invert intragranular continuum.

Between the corrosion products and invert domains, an advective flux communication exists from the corrosion products cell to the invert intergranular cell only; none enters the intragranular invert cell. Any advective flux due to imbibition from the host rock to the invert enters the intragranular cell only. The advective exchange from the intergranular continuum to the intragranular continuum is excluded by capillary pressure differences. Diffusive flux communication exists between the single continuum corrosion products and dual continuum invert. It is shown subsequently in this section how the diffusive flux bifurcation at this interface satisfies the flux continuity condition (Equation 6.5.1.2-53). The mass balance transport equations for the dual continuum invert cells are coupled by the radionuclide mass transfer flux

(Section 6.6.4.1), which is represented within GoldSim as a diffusive flux link between the intergranular and intragranular invert cells.

Below the invert, part of the near-field UZ is modeled by an array of cells, which serves to establish a far field zero-concentration boundary and an accurate representation of the flux at the invert-to-UZ interface. The EBS-UZ interface submodel is described in more detail in Section 6.5.3.6. The dual continuum approach for modeling the UZ is considered by creating UZ matrix and fracture cells. The two invert cells communicate with the UZ matrix and fracture cells directly below them in the UZ cell array (Section 6.5.3.6).

For transport from the corrosion products domain (single continuum) to the invert domain (dual continuum), the flux continuity condition at the interface provides the diffusive flux bifurcation between the single continuum and the dual continuum.

The diffusive fluxes of radionuclide species *i* within the corrosion products cell, the invert intergranular cell, and the invert intragranular cell are, respectively,

$$F_{iCP} = \frac{(\phi S_w DA)_{CP}}{L_{CP}}(C_{iCP} - C_{iCP/invint}) = \hat{D}_{CP}(C_{iCP} - C_{iCP/invint}), \quad \text{(Eq. 6.6.4.2-1)}$$

$$F_{iinter} = \frac{(\phi S_w DA)_{inter}}{L_{inter}}(C_{iCP/invint} - C_{iinter}) = \hat{D}_{inter}(C_{iCP/invint} - C_{iinter}), \quad \text{(Eq. 6.6.4.2-2)}$$

$$F_{iintra} = \frac{(\phi S_w DA)_{intra}}{L_{intra}}(C_{iCP/invint} - C_{iintra}) = \hat{D}_{intra}(C_{iCP/invint} - C_{iintra}), \quad \text{(Eq. 6.6.4.2-3)}$$

where

D_{CP} = effective diffusion coefficient of radionuclide species *i* within the corrosion products cell ($cm^2\ s^{-1}$)

D_{inter} = effective diffusion coefficient of radionuclide species *i* within the invert intergranular cell ($cm^2\ s^{-1}$)

D_{intra} = effective diffusion coefficient of radionuclide species *i* within the invert intragranular cell ($cm^2\ s^{-1}$)

L_{CP} = diffusive length within the corrosion products cell (m)

L_{inter} = diffusive length within the invert intergranular cell (m)

L_{intra} = diffusive length within the invert intragranular cell (m)
= L_{inter}

C_{iCP} = concentration of radionuclide species i in the corrosion products cell (kg i m^{-3})

C_{iinter} = concentration of radionuclide species i in the invert intergranular cell (kg i m^{-3})

C_{iintra} = concentration of radionuclide species i in the invert intragranular cell (kg i m^{-3})

$C_{iCP/Invint}$ = concentration of radionuclide species i at the interface between the corrosion products and invert cells (kg i m^{-3})

and the $\hat{D} = \frac{\phi S_w DA}{L}$ are respective diffusive conductances (cm^3 s^{-1}).

The flux continuity at the interface requires:

$$F_{iCP} = F_{iinter} + F_{iintra}. \qquad \text{(Eq. 6.6.4.2-4)}$$

From the flux continuity, the interface concentration of radionuclide species i is determined as a function of the diffusive parameters and the cell concentrations as:

$$C_{iCP/Invint} = \frac{\hat{D}_{CP} C_{iCP} + \hat{D}_{inter} C_{iinter} + \hat{D}_{intra} C_{iintra}}{\hat{D}_{CP} + \hat{D}_{inter} + \hat{D}_{intra}}. \qquad \text{(Eq. 6.6.4.2-5)}$$

This provides the invert intergranular and intragranular diffusive fluxes of radionuclide species i, respectively, as:

$$F_{iinter} = \frac{\hat{D}_{CP}\hat{D}_{inter}}{\hat{D}_{CP} + \hat{D}_{inter} + \hat{D}_{intra}}(C_{iCP} - C_{iinter}) + \frac{\hat{D}_{inter}\hat{D}_{intra}}{\hat{D}_{CP} + \hat{D}_{inter} + \hat{D}_{intra}}(C_{iintra} - C_{iinter}) \qquad \text{(Eq. 6.6.4.2-6)}$$

$$F_{iintra} = \frac{\hat{D}_{CP}\hat{D}_{intra}}{\hat{D}_{CP} + \hat{D}_{inter} + \hat{D}_{intra}}(C_{iCP} - C_{iintra}) - \frac{\hat{D}_{inter}\hat{D}_{intra}}{\hat{D}_{CP} + \hat{D}_{inter} + \hat{D}_{intra}}(C_{iintra} - C_{iinter}). \qquad \text{(Eq. 6.6.4.2-7)}$$

The expression for the diffusive flux of radionuclide species i from the corrosion products cell to the invert intergranular cell can be expressed as a diffusive conductance multiplied by a concentration difference of radionuclide species i between the corrosion products cell and the invert intergranular cell plus a corrective flux between the invert intergranular and intragranular cells. Similarly, the expression for the diffusive flux from the corrosion products to the invert intragranular cell is expressed as a diffusive flux between the corrosion products and the invert intragranular cell minus the same corrective flux between the invert cells. The inclusion of the corrective flux term is explained as follows. The flux to both invert cells should depend on the

diffusive properties in the corrosion products cell and the two invert cells, together with the concentrations in these three cells. Therefore, the flux to the invert intergranular cell cannot be expressed only in terms of the concentration drawdown between the corrosion products cell and the invert intergranular cell. The corrective term includes the dependence of the invert intergranular flux on the concentration of radionuclide species *i* in the invert intragranular cell. Further, the corrective flux term is not a true flux expression between the two invert cells, since the diffusive conductance coefficient is dependent on the diffusive area between the corrosion products and the invert, and the diffusive lengths are the lengths with respect to flow from the corrosion products cell to the invert cells.

The invert fluxes result in defining three diffusive conductances from the flux expressions:

$$\hat{D}_{CP/inter}\left(C_{iCP}-C_{iinter}\right)=\frac{\hat{D}_{CP}\hat{D}_{inter}}{\hat{D}_{CP}+\hat{D}_{inter}+\hat{D}_{intra}}\left(C_{iCP}-C_{iinter}\right), \qquad \text{(Eq. 6.6.4.2-8)}$$

$$\hat{D}_{CP/intra}\left(C_{iCP}-C_{iintra}\right)=\frac{\hat{D}_{CP}\hat{D}_{intra}}{\hat{D}_{CP}+\hat{D}_{inter}+\hat{D}_{intra}}\left(C_{iCP}-C_{iintra}\right), \qquad \text{(Eq. 6.6.4.2-9)}$$

$$\hat{D}_{intra/inter}\left(C_{iintra}-C_{iinter}\right)=\frac{\hat{D}_{intra}\hat{D}_{inter}}{\hat{D}_{CP}+\hat{D}_{inter}+\hat{D}_{intra}}\left(C_{iintra}-C_{iinter}\right), \qquad \text{(Eq. 6.6.4.2-10)}$$

where

$D_{CP/inter}$ = effective diffusive conductance between corrosion products cell and invert intergranular cell ($cm^3\ s^{-1}$)

$\hat{D}_{CP/intra}$ = effective diffusive conductance between corrosion products cell and invert intragranular cell ($cm^3\ s^{-1}$)

$\hat{D}_{intra/inter}$ = effective diffusive conductance between intragranular and invert intergranular cells ($cm^3\ s^{-1}$).

In order to accommodate the GoldSim representation of diffusive conductance as a two-term expression, the diffusive conductances of radionuclide species *i* are written as:

$$\hat{D}_{CP/inter}=\frac{1}{\dfrac{L_{CP}}{(\phi S_w DA)_{CP}\left[\dfrac{(\phi S_w DA)_{inter}}{(\phi S_w DA)_{inter}+(\phi S_w DA)_{intra}}\right]}+\dfrac{L_{inter}}{(\phi S_w DA)_{inter}}}, \qquad \text{(Eq. 6.6.4.2-11)}$$

$$\hat{D}_{CP/intra}=\frac{1}{\dfrac{L_{CP}}{(\phi S_w DA)_{CP}\left[\dfrac{(\phi S_w DA)_{intra}}{(\phi S_w DA)_{inter}+(\phi S_w DA)_{intra}}\right]}+\dfrac{L_{intra}}{(\phi S_w DA)_{intra}}}, \qquad \text{(Eq. 6.6.4.2-12)}$$

$$\hat{D}_{intra/inter} = \frac{1}{\dfrac{L_{inter}}{(\phi S_w DA)_{inter}\left[\dfrac{L_{CP}(\phi S_w DA)_{intra}}{L_{CP}(\phi S_w DA)_{intra} + L_{intra}(\phi S_w DA)_{CP}}\right]} + \dfrac{L_{intra}}{(\phi S_w DA)_{intra}}}. \quad \text{(Eq. 6.6.4.2-13)}$$

Another approach to discretizing the dual-continuum invert requires introduction of an interface cell, located between the corrosion products cell and the invert cells. This interface cell provides an approximate interface concentration and the resulting flux split at the corrosion products to invert cell interface. The interface cell is conceptualized as a very thin slice of the corrosion products cell.

This implies the interface cell takes on the corrosion products diffusive properties, with the exception of diffusive length. Let the diffusive length within the interface cell be some small fraction (an Interface_Scale_Factor) of the corrosion products diffusive length, say, Interface_Scale_Factor = 10^{-6}:

$$L_{CP-int} = 10^{-6} L_{CP}. \quad \text{(Eq. 6.6.4.2-14)}$$

The use of a Interface_Scale_Factor of 10^{-6} is examined in Section 6.6.4.4.

The diffusive conductance between the corrosion products cell and the corrosion products interface cell is calculated as the harmonic average:

$$\hat{D}_{CP/CP-int} = \frac{1}{\dfrac{L_{CP}}{(\phi S_w DA)_{CP}} + \dfrac{L_{CP-int}}{(\phi S_w DA)_{CP}}}. \quad \text{(Eq. 6.6.4.2-15)}$$

For diffusion between the interface cell and the invert intergranular and intragranular cells, the diffusive conductances are, respectively,

$$\hat{D}_{CP-int/inter} = \frac{1}{\dfrac{L_{CP-int}}{(\phi S_w DA)_{CP}} + \dfrac{L_{invert}}{(\phi S_w DA)_{inter}}}, \quad \text{(Eq. 6.6.4.2-16)}$$

$$\hat{D}_{CP-int/intra} = \frac{1}{\dfrac{L_{CP-int}}{(\phi S_w DA)_{CP}} + \dfrac{L_{invert}}{(\phi S_w DA)_{intra}}}. \quad \text{(Eq. 6.6.4.2-17)}$$

The interface cell concentration of radionuclide species i is computed as part of the cell network solution. Because the transport mass balance equations conserve mass, the mass flux leaving the interface cell must equal the sum of the mass fluxes entering the two invert cells. The solution provides the flux continuity across the interface between the corrosion products interface cell and invert cells. This formulation expects the flux exiting the corrosion products cell (or entering the interface cell) is approximately equal to the flux exiting the interface cell. This approximation is

dependent on the diffusive length within the interface cell. The error in this approximate solution will approach zero as the diffusive length of the interface cell approaches zero.

At the invert-to-UZ interface, there is diffusive transport between both the invert cells and the UZ matrix and fracture cells. This implies four connections: from invert intergranular to UZ matrix, from invert intergranular to UZ fracture, invert intragranular to UZ matrix, and from invert intragranular to UZ fracture. An analysis similar to that for the diffusive conductances between the corrosion products cell and the dual invert cells (Equations 6.6.4.25-11 through 6.6.4.2-13) would provide expressions for diffusive conductances for each of the four diffusive flux links. However, for the TSPA-LA, the approximation provided by introducing an interface cell when diffusing from a single to a dual continuum exits is used. An approximate solution is obtained by the introduction of two interface cells at the invert-UZ interface. This approach is identical to that used above for the interface between the corrosion products cell and the invert dual continuum cells. One interface cell represents a thin slice of the invert intergranular cell, and the other represents a thin slice of the invert intragranular cell. Let the length of both invert interface cells be a fraction (an Interface_Scale_Factor) of the invert diffusive length, say, Interface_Scale_Factor = 10^{-6}:

$$L_{invert\_int} = 10^{-6} L_{invert}. \qquad \text{(Eq. 6.6.4.2-18)}$$

The use of an Interface_Scale_Factor of 10^{-6} is examined in Section 6.6.4.4.

The diffusive conductance between the invert intergranular cell and the invert intergranular interface cell is:

$$\hat{D}_{inter/inter-int} = \frac{1}{\dfrac{L_{invert}}{(\phi S_w DA)_{inter}} + \dfrac{L_{invert\_int}}{(\phi S_w DA)_{inter}}}, \qquad \text{(Eq. 6.6.4.2-19)}$$

while the diffusive conductance between the invert intragranular cell and the invert intragranular interface cell is:

$$\hat{D}_{intra/intra-int} = \frac{1}{\dfrac{L_{invert}}{(\phi S_w DA)_{intra}} + \dfrac{L_{invert\_int}}{(\phi S_w DA)_{intra}}}. \qquad \text{(Eq. 6.6.4.2-20)}$$

The fluxes of radionuclide species i from the invert intergranular boundary cell to the matrix-fracture UZ cells are computed with diffusive conductances:

$$\hat{D}_{inter-int/UZm} = \frac{1}{\dfrac{L_{invert\_int}}{(\phi S_w DA)_{inter}} + \dfrac{L_{UZ}}{(\phi S_w DA)_{UZm}}}, \qquad \text{(Eq. 6.6.4.2-21)}$$

$$\hat{D}_{inter-int/UZf} = \frac{1}{\frac{L_{invert\_int}}{(\phi S_w DA)_{inter}} + \frac{L_{UZ}}{(\phi S_w DA)_{UZf}}}. \qquad \text{(Eq. 6.6.4.2-22)}$$

Similarly, the fluxes of radionuclide species i from the invert intragranular boundary cell to the matrix-fracture UZ cells are computed with diffusive conductances:

$$\hat{D}_{intra-int/UZm} = \frac{1}{\frac{L_{invert\_int}}{(\phi S_w DA)_{intra}} + \frac{L_{UZ}}{(\phi S_w DA)_{UZm}}}, \qquad \text{(Eq. 6.6.4.2-23)}$$

$$\hat{D}_{intra-int/UZf} = \frac{1}{\frac{L_{invert\_int}}{(\phi S_w DA)_{intra}} + \frac{L_{UZ}}{(\phi S_w DA)_{UZf}}}. \qquad \text{(Eq. 6.6.4.2-24)}$$

One last term to be discussed is the mass transfer term, Q_{imt}, between the two invert continua given by Equation 6.5.1.2-19. This term appears in the mass balance for the transport of radionuclides dissolved in the aqueous phase and reversibly sorbed (Equation 6.5.1.2-38, or, for the one-dimensional case, Equation 6.5.1.2-46), and in Equation 6.5.1.2-27 (Equation 6.5.1.2-47 in one dimension), the mass balance for irreversibly adsorbed radionuclides on iron oxyhydroxide colloids. In these equations, the mass transfer between overlapping continua is represented by the diffusion of solute on a macroscopic control volume scale. Consequently, the mass transfer between the two invert continua is not written as a gradient of diffusive mass flux with respect to the coordinate dimensions, and the treatment described above for diffusive conductances does not directly apply. For the discrete realization of the invert continua mass transfer, the diffusive length within the intergranular continuum is taken to be zero. This is a result of the water within the intergranular continuum consisting of a thin film on the surface of the intragranular materials. The diffusive length within the intragranular continuum depends on some mean diffusive length within the crushed tuff material. This diffusive length is taken as a mean radius of spherical particles. The effective diffusive area is estimated as the surface area of all spherical particles necessary to fill the invert volume. Therefore, the characteristic length parameter, d, is identified as the diffusive length within the intragranular continuum and the diffusive area to length ratio with transfer term included as mentioned in Equation 6.5.1.2-19 is:

$$\left(\frac{A}{L}\right)_{inter/intra} = \frac{\beta\theta_{intra}V_{t\_intra}}{d^2}, \qquad \text{(Eq. 6.6.4.2-25)}$$

where V_{t_intra} is the volume of the invert intragranular continuum, and β is the sampled geometry-dependent factor, Invert_Geometry_Coef. The effective diffusive conductance is:

$$\hat{D}_c = D_{intra}\left(\frac{A}{L}\right)_{inter/intra}. \qquad \text{(Eq. 6.6.4.2-26)}$$

6.6.4.3 Dual-Continuum EBS-UZ Boundary Condition

The EBS-UZ boundary condition implementation described in Section 6.5.3.6 is used to obtain a realistic concentration boundary condition at the invert-UZ interface. For the dual-continuum invert alternative model, the boundary condition implementation is modified to account for diffusive fluxes from each invert continuum to both UZ fractures and matrix. This implementation is represented in Figure 6.6-3.

The mass flux from either invert continuum flows into the top layer of the middle zone in the UZ. The intergranular invert advective flux flows into the top middle UZ fracture cell, while the intragranular invert advective flux flows into the top middle UZ matrix cell. Transfer of water between the two continua is ignored. The diffusive flux from each of the invert continua can go into both UZ continua based on the concentration gradient and effective diffusion coefficient. The advective flux flowing through the UZ fracture cells in the middle zone is given by the greater of the advective flux out of the invert and the steady state UZ fracture flux. The advective flux in the two outer zones is given by the steady state UZ flow in each continuum at the repository horizon; the drift shadow effects are ignored.

The mass flux from the dual continuum invert domain to the dual continuum UZ, computed at the boundary of the EBS-UZ interface, is passed to the UZ transport model, which is described in *Particle Tracking Model and Abstraction of Transport Processes* (BSC 2004 [DIRS 170041]). In addition to the total mass flux, the relative fraction of the mass going into each of the fracture and the matrix cells at the EBS-UZ boundary is required by the UZ transport model. This fracture-matrix partitioning of mass is calculated on the basis of the mass fraction going into the fracture continuum (compared to the matrix continuum) from the dual continuum invert domain in the EBS-UZ interface submodel. This partitioning is time dependent and captures the temporal processes active in the EBS, such as varying radionuclide concentrations in the waste form, corrosion products, and invert domains and changing water flux through various subcomponents of the EBS.

6.6.4.4 Verification of Dual Invert/Dual UZ Diffusive Flux Bifurcation

In this section, calculation of the diffusive flux from a single cell (corrosion products) to dual invert cells (intergranular invert and intragranular invert) and then to two UZ cells (UZ matrix and UZ fracture) is tested. These tests show that the approximations in the GoldSim implementation using an Interface_Scale_Factor of 1.0×10^{-6} are correct and that the implementation in GoldSim agrees with Microsoft Excel calculations.

As modeled, there is no diffusive communication between the dual invert cells and between the UZ matrix/fracture cells. The corrosion products cell provides a diffusive flux to the dual invert cells. Each invert cell provides a diffusive flux to both the UZ matrix and fracture cells. For this verification, at time zero, an initial mass of one gram is released in the corrosion products cell, while all other cells have initial mass of zero. Parameters controlling diffusion through this test network were not determined strictly from TSPA-LA data, but were set so that measurable mass transport to all cells within the network occurs in a reasonable time frame. No parameters were assigned a value of one (other than the initial mass in the waste form cell), because any mistake in multiplication or division by a unit parameter would not be readily detectable.

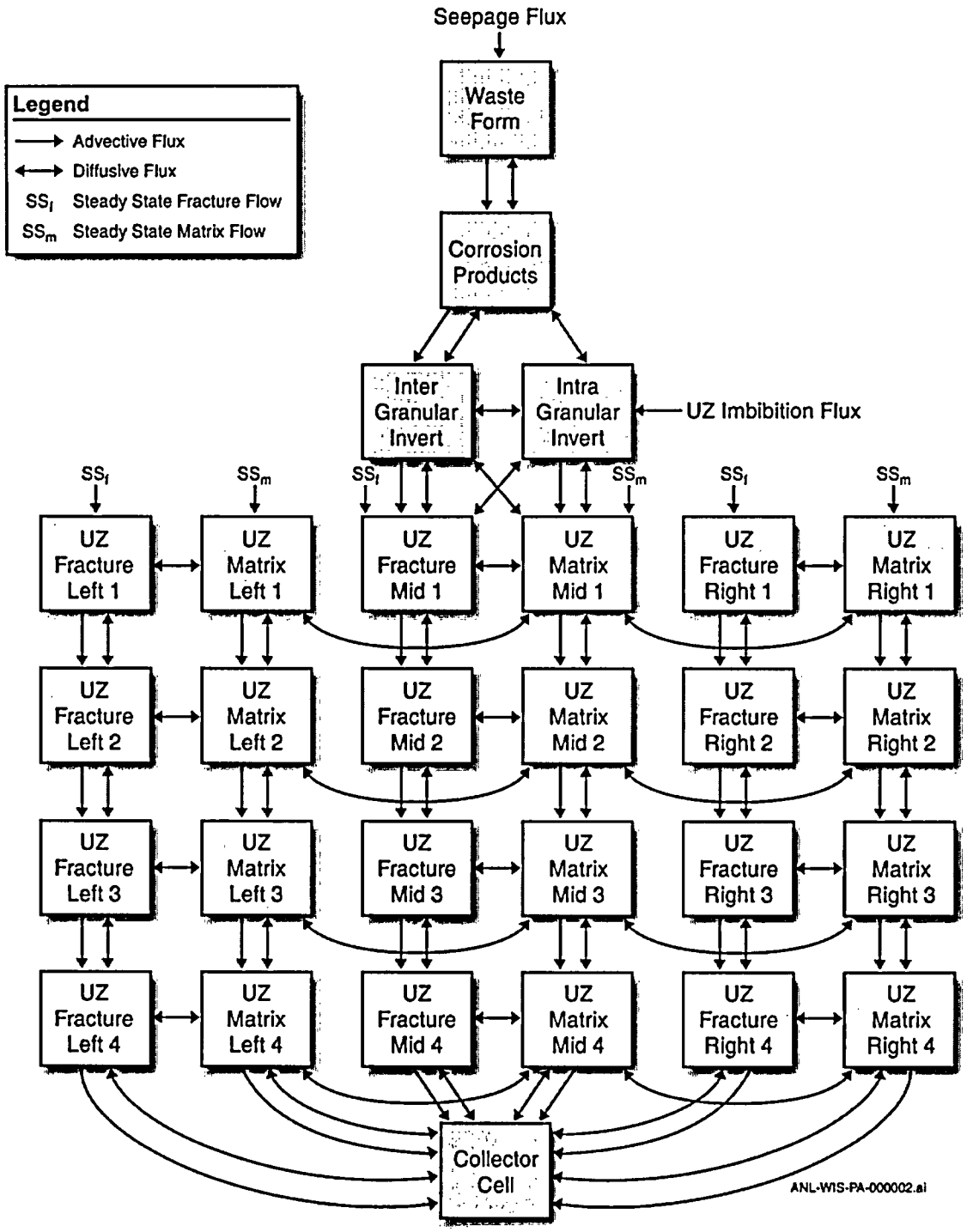

Figure 6.6-3. Computational Grid in the EBS-UZ Interface Submodel (Dual-Continuum Invert)

Two analytical approaches (A1 and A2) to the flux bifurcation can be taken when diffusion occurs from a single cell to dual cells:

A1: The first approach computes diffusive conductances between the single cell and each dual continuum cell; an auxiliary conductance is required between the dual continuum cells. This formulation presents the appearance of a diffusive flux communication between the dual continuum cells, when physically there is no such flux. This approach requires a five-cell network and provides an exact representation of the fluxes.

A2: The second approach incorporates an interface cell between cells where diffusion bifurcates from a single continuum cell to dual continuum cells. The interface cell provides an approximate concentration at the flux bifurcation interface. For diffusion from a single continuum cell to dual continuum cells, the interface cell is conceptualized as a thin slice of the single continuum cell. This implies that, for the proposed cell network, an interface cell is located between the corrosion products cell and the dual invert continuum cells. This cell is assigned representative properties of the corrosion products cell, with the exception of the diffusive length. The diffusive length for the interface cell is taken to be an Interface_Scale_Factor times the diffusive length of the corrosion products cell. Between the intergranular invert cell and the dual UZ cells, an intergranular invert interface cell is introduced with diffusive properties of the intergranular invert and a diffusive length of the Interface_Scale_Factor times the diffusive length of the invert. Similarly, between the intragranular invert cell and the dual UZ cells, an intragranular invert interface cell is introduced. This conceptualization requires an eight-cell network (five cells of A1 plus three interface cells) and provides an approximate solution.

Three solutions to the diffusion problem are presented:

S1: The first solution is an Excel calculation using A1 approach. This provides an exact solution for the transport network.

S2: The second solution is an Excel calculation using A2 approach. This provides an approximate solution dependent on the Interface_Scale_Factor parameter. A successive refinement of the Interface_Scale_Factor demonstrates the convergence of the approximate solution (S2) to the exact solution (S1).

S3: The third solution is a GoldSim stand-alone calculation using the A2 approach. This solution is compared with solution S2 to verify the GoldSim implementation of the model within the EBS transport abstraction.

The convergence of the approximate solution S2 to the exact solution S1 with refinement of the Interface_Scale_Factor is shown in Figure 6.6-4, where the relative error of the mass in place for each network cell is plotted as a function of the Interface_Scale_Factor. Figure 6.6-4 shows that the solution S2 converges to the exact solution S1 (i.e., a relative error of zero) with first order convergence rate with respect to the Interface_Scale_Factor. The error in the UZ matrix cell is not observed in Figure 6.6-4, since it is overlain by the error in the UZ fracture cell.

Figure 6.6-5 presents the GoldSim solution S3 and the Microsoft Excel solution S2. The Microsoft Excel solution S2 and GoldSim solution S3 use an Interface_Scale_Factor of

1.0×10^{-6}. Figure 6.6-5 shows the mass in place for each of the five cells and demonstrates the excellent agreement between the Microsoft Excel solution and GoldSim solution. After 2 years, the maximum relative error for the corrosion products cell and the two invert cells is 0.2 percent, and the maximum relative error for the two UZ cells is 1.5 percent.

These results confirm that the bifurcation of diffusive flux from a single continuum (corrosion products domain) to a dual continuum (invert domain) and then to another dual continuum (UZ) is accurate and properly implemented in GoldSim.

6.6.5 Alternative Invert Diffusion Coefficient Models

The following two alternative models for determining the diffusion coefficient in the invert are assessed in this section: the single-continuum invert diffusion coefficient model and the dual-continuum invert diffusion coefficient model.

6.6.5.1 Alternative Single-Continuum Invert Diffusion Coefficient Model

As an alternative to the Archie's law approach for determination of the diffusion coefficient for the single-continuum invert (Section 6.3.4.1), diffusion through the crushed tuff invert ballast is modeled using an approach that has been applied to diffusion in soils. Studies generally show that the bulk diffusion coefficients of soils at high water content decline with the moisture content and that a Millington-Quirk power law developed for high moisture content overpredicts the diffusion coefficient at low moisture content (Nye 1979 [DIRS 167377]; Olesen et al. 1999 [DIRS 154588]). The studies also show that, below a critical moisture content, the diffusion coefficient for granular materials becomes negligible (So and Nye 1989 [DIRS 170588]).

Olesen et al. (1996 [DIRS 155700]) found the best description of the bulk diffusion coefficient of granular soils is the following:

$$D = 0.0045 D_0 \theta \frac{(\theta - 2.2b)}{(100\phi - 2.2b)}, \qquad \theta \geq 2.2b$$
$$D = 0, \qquad \theta < 2.2b, \qquad \text{(Eq. 6.6.5.1-1)}$$

where D, θ, and ϕ are the bulk diffusion coefficient ($cm^2\ s^{-1}$), moisture content (percent), and bulk porosity of the soil (fraction), respectively, D_0 is the free water diffusion coefficient for self-diffusion of water, $2.299 \times 10^{-5}\ cm^2\ s^{-1}$ at 25°C (Mills 1973 [DIRS 133392], Table III), and the term $2.2b$ (percent) corresponds to the critical moisture content for these soils. In this expression, the parameter b corresponds to the dimensionless slope of the Campbell moisture retention curve on a log-log plot that varies with the pore and grain size distribution of the soil (Olesen et al. 1996 [DIRS 155700]).

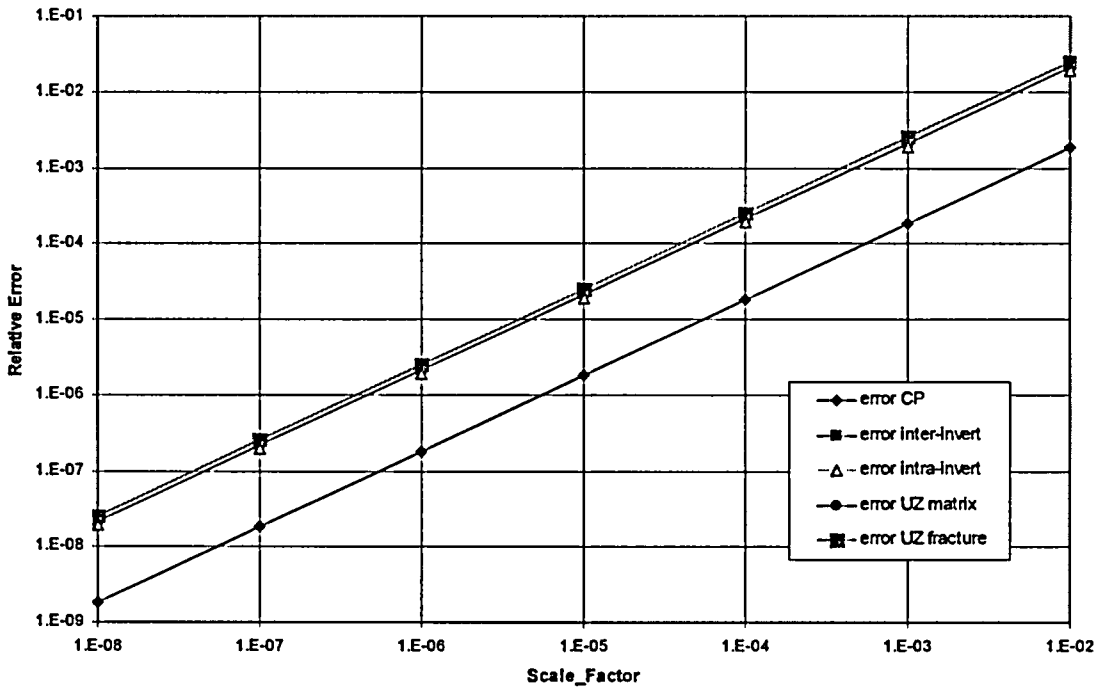

Figure 6.6-4. Relative Error of Mass-in-Place for Microsoft Excel Approximate Solution

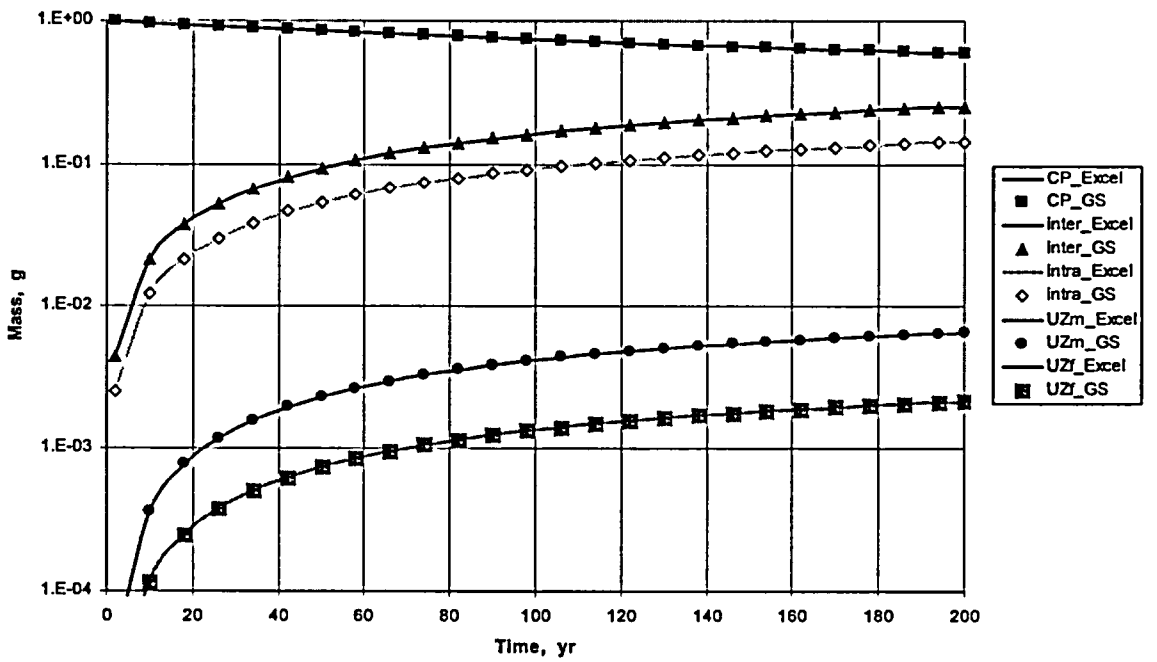

Figure 6.6-5. Comparison of Microsoft Excel and GoldSim Flux Bifurcation Solutions

This behavior for granular materials is generally explained (Olesen et al. 1999 [DIRS 154588]) in terms of a picture in which:

- Above the critical moisture content, the bulk diffusion coefficient of granular materials is dominated by diffusion coefficient in films of moisture on the grain surfaces
- The diffusion coefficient declines as the moisture content decreases and the tortuosity associated with these films increases
- Below the critical moisture content, diffusion by the surface films cannot be supported and the diffusion coefficient is reduced to a very low value.

Conca and Wright (1990 [DIRS 101582]) have concluded that this picture is consistent with their measurements of crushed tuff.

A moisture retention relation proposed by Campbell (1985 [DIRS 100565], pp. 45-47) is used to develop the moisture potential relation for the crushed tuff invert. The relationship between moisture potential, ψ (J kg^{-1}), and volumetric moisture content, θ (percent), is the soil moisture retention curve, described by the function (Campbell 1985 [DIRS 100565], p. 43):

$$\psi = \psi_e (\theta / \theta_s)^{-b}, \qquad \text{(Eq. 6.6.5.1-2)}$$

where ψ_e is the air-entry moisture potential (i.e., water potential at which the largest water-filled pore in the soil will drain) (J kg^{-1}), θ_s is the saturated moisture content (percent), and b is the slope (dimensionless) of the $\ln\psi$ versus $\ln\theta$ curve. As the mean pore diameter becomes smaller, the air-entry moisture potential decreases (becomes more negative). The b parameter increases as the standard deviation σ_g (mm) of the pore size increases. Campbell studied the relationships between geometric particle diameter, d_g (mm), geometric standard deviation, σ_g (mm), and air entry potential, ψ_e (J kg^{-1}). By fitting Equation 6.6.5.1-2 to measured data, he obtained the following approximate relationships for soils (Campbell 1985 [DIRS 100565], p. 45) having a bulk density of 1,300 kg m^{-3}:

$$\psi_{es} = -0.5 d_g^{-1/2}, \qquad \text{(Eq. 6.6.5.1-3)}$$

$$b = -2\psi_{es} + 0.2\sigma_g, \qquad \text{(Eq. 6.6.5.1-4)}$$

where ψ_{es} is the air-entry moisture potential (J kg^{-1}); the subscript *es* refers to the bulk density of 1,300 kg m^{-3}. The geometric standard deviation depends on the soil texture. The geometric standard deviation can be estimated from a soil texture diagram as equal to 1 for coarse sand particles and 5 for fine-grained material (Campbell 1985 [DIRS 100565], Figure 2.1).

The results for the Campbell retention relation for crushed tuff of 0.45 bulk porosity and grain sizes ranging from 0.317 mm to 20 mm (BSC 2004 [DIRS 169565], Appendix X) are shown in Table 6.6-3. Table 6.6-3 also shows the associated range of the critical bulk moisture content in Equation 6.6.5.1-1.

Table 6.6-3. Parameters Developed for Crushed Tuff

Parameter				
Grain Size (mm)[a]	0.317	3	10	20
Bulk Porosity[b]	0.45	0.45	0.45	0.45
Standard Deviation, σ_g (mm)[c]	5	1	1	1
Slope of the Campbell retention curve, *b*	2.78	0.777	0.516	0.424
Critical bulk moisture content, 2.2*b* (%)	6.12	1.71	1.14	0.932

[a] BSC 2004 [DIRS 169565], Appendix X, Section X.4.
[b] BSC 2004 [DIRS 169565], Appendix X, Section X.3.
[c] Campbell 1985 [DIRS 100565], Figure 2.1.

Figure 6.6-6 shows the corresponding range in the diffusion coefficient evaluated according to Equation 6.6.5.1-1. In general, the invert will include a distribution of tuff grain sizes. Therefore, the determination of the critical bulk moisture content is made by sampling from a uniform distribution between 0.932 percent and 6.12 percent. This corresponds to the range of tuff grain sizes from 20 mm to 0.317 mm, as shown in Table 6.6-3; a uniform distribution is appropriate for covering the range for an initial analysis of an alternative conceptual model. The corresponding diffusion coefficient would then be evaluated for this sampled moisture content according to Equation 6.6.5.1-1.

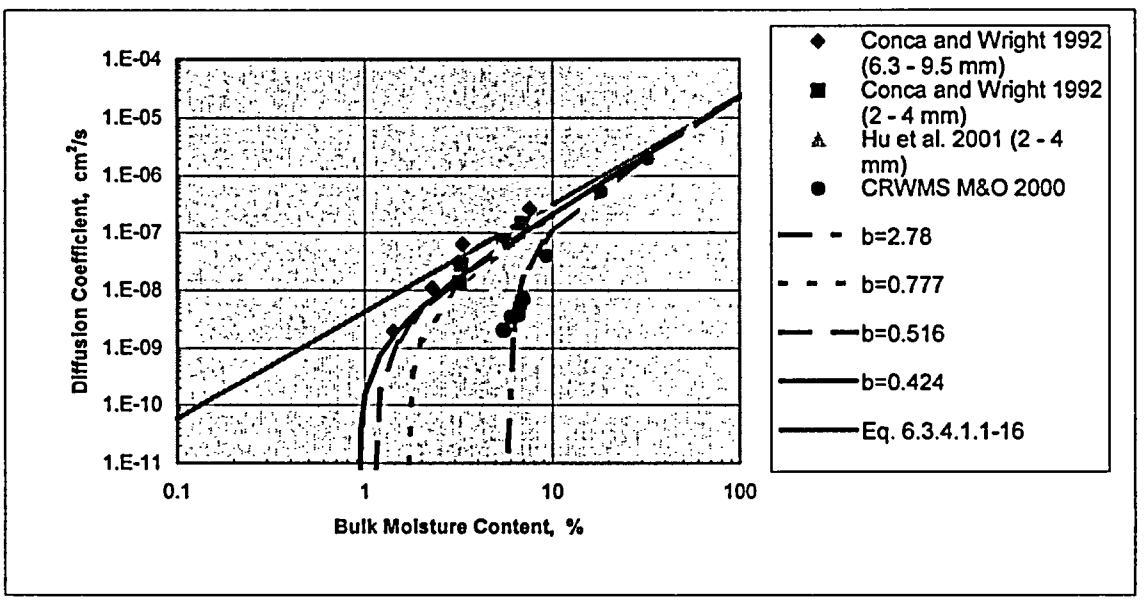

Source: Conca and Wright 1992 [DIRS 100436]; CRWMS M&O 2000 [DIRS 156680]; Hu et al. 2001 [DIRS 161623].

Figure 6.6-6. Range of the Bulk Diffusion Coefficients for Crushed Tuff

For conditions in which advective flow does not occur in the crushed tuff, observations indicate that the intergranular moisture content will generally be negligible. Conca and Wright (1990 [DIRS 101582]) observed that tuff gravel samples allowed to stand for several hours in the presence of 100 percent relative humidity reached moisture contents between 0.5 and 1.5 percent and negligible surface moisture. The measured diffusion coefficients were found in these cases to be below their measurement limit of 1.03×10^{-11} $cm^2 s^{-1}$. Therefore, in the portion of the invert in which there is no flow, the diffusion coefficient is expected to be negligible.

For conditions in which flow does occur in the crushed tuff, the bulk diffusion coefficient can be directly evaluated from Equation 6.6.5.1-1 as described above. This uncertainty is accounted for by expressing the threshold in terms of the critical bulk moisture content:

$$D = 0.0045 D_0 \theta \frac{(\theta - \theta_C)}{(100\phi - \theta_C)}, \qquad \theta \geq \theta_C$$
$$D = 0, \qquad \theta < \theta_C, \qquad \text{(Eq. 6.6.5.1-5)}$$

where θ is the bulk moisture content (percent), given by Equation 6.5.3.3-11, and θ_C is the critical value of the bulk moisture content, $0.022b$ (percent). The critical bulk moisture content is selected by sampling a uniform distribution between 0.932 percent and 6.12 percent, as discussed earlier in this section.

Diffusion coefficients of crushed tuff have been estimated using the ultracentrifuge technique and measurements of electrical resistivity. Conca and Wright (1992 [DIRS 100436]) and Conca et al. (1993 [DIRS 170709]) measured the bulk diffusion coefficients for a variety of granular materials, including crushed tuff, as a function of moisture content. Figure 6.6-6 shows the results of their measurements of crushed tuff samples with tuff grains sizes between 6.3 mm and 9.5 mm, and between 2 mm and 4 mm. Diffusion coefficients for crushed tuff with grain sizes between 2 mm and 4 mm have also been measured by Hu et al. (2001 [DIRS 161623]); these results are also shown in Figure 6.6-6. Finally, the diffusion coefficient measured for samples with a wide distribution of grain sizes (CRWMS M&O 2000 [DIRS 156680]) are also shown in Figure 6.6-6. Comparison of all of these measurements for crushed tuff indicates that the model provides a reasonable representation of the diffusion coefficient for these measured moisture contents (1.4 to 55 percent).

6.6.5.2 Alternative Dual-Continuum Invert Diffusion Coefficient Model

In general, the literature supports a dual continuum picture of the diffusive conductance by the invert granular material. For example, Roberts and Lin (1997 [DIRS 101710]) observed multiple conduction pathways in their measurements of the electrical conductance of unsaturated tuff samples. Their measurements indicated conduction by adsorbed water on the solid surfaces of the tuff samples and conduction by water within the tuff rock. These measurements support a dual continuum picture of the tuff samples in which the water on the surface of the samples corresponds to the intergranular continuum and the water within the samples corresponds to the intragranular continuum.

Other observations also support this picture. Porter et al. (1960 [DIRS 123115]) studied the way in which chloride ions move through soil and the effect of the moisture content of the soil on this movement. These characteristics were interpreted in terms of diffusion within the soil grains and diffusion on the solid surfaces of those grains. Nye (1979 [DIRS 167377]) concluded that, to a first approximation at least, diffusion can be considered to occur through two independent pathways in soil: through moisture between the soil grains and through the grains themselves. In this picture, the bulk diffusion coefficient, D, is represented by:

$$D = D_{inter}\phi_{inter} + D_{intra}(1-\phi_{inter}), \qquad \text{(Eq. 6.6.5.2-1)}$$

where D_{inter} is the diffusion coefficient for the intergranular continuum determined by the moisture films on the surfaces of the grains, D_{intra} is the diffusion coefficient for the intragranular continuum determined by the moisture within the grains, and ϕ_{inter} is the intergranular porosity of the material.

In this picture, the bulk diffusion coefficient is dominated by the intergranular diffusion coefficient above the critical bulk moisture content, while below this critical value, the intragranular diffusion coefficient dominates. That is, Equation 6.6.5.2-1 becomes:

$$\begin{aligned} D &\approx D_{inter}(\theta)\phi_{inter}, & \theta \geq \theta_C \\ D &= D_{intra}(1-\phi_{inter}), & \theta < \theta_C, \end{aligned} \qquad \text{(Eq. 6.6.5.2-2)}$$

where θ_C is the critical moisture content (percent). In this picture, the intergranular diffusion coefficient is represented by the model in Equation 6.6.5.1-1, divided by the intergranular porosity:

$$\begin{aligned} D_{inter} &= 0.45D_0\left(\frac{\theta}{100\phi_{inter}}\right)\left(\frac{\theta-\theta_C}{100\phi_I-\theta_C}\right), & \theta \geq \theta_C \\ D_{inter} &= D_{limit}, & \theta < \theta_C. \end{aligned} \qquad \text{(Eq. 6.6.5.2-3)}$$

D_{limit} is the measurement limit, 10^{-12} cm^2 s^{-1}, ϕ_I is the bulk porosity of the invert, $\phi_I = \phi_{inter} + (1-\phi_{inter})\phi_{intra}$ (fraction), and θ_C corresponds to $2.2b$ in Equation 6.6.5.1-1.

The intragranular diffusion coefficient is determined by the following considerations.

Reimus et al. (2002 [DIRS 163008]) measured diffusion coefficients for saturated whole rock samples of tuff. The measured values for the samples ranged from 1.5×10^{-7} cm^2 s^{-1} to 2×10^{-5} cm^2 s^{-1}. From these measurements, Reimus et al. (2002 [DIRS 163008]) developed a correlation between the saturated diffusion coefficient, D_{ms}, and the porosity, ϕ_m, and intrinsic permeability, k_m, of the tuff rock matrix:

$$\log_{10} D_{ms} = -3.49 + 1.38\phi_m + 0.165\log_{10} k_m. \qquad \text{(Eq. 6.6.5.2-4)}$$

The tuff samples were from Pahute Mesa, Nevada, but many of them are similar to tuff rocks at Yucca Mountain. To evaluate the flow characteristics of the drift invert, matrix porosity and intrinsic permeability for tuff from two different Topopah Spring welded tuff units, TSw35 and TSw36, were identified (DTN: LB0207REVUZPRP.002 [DIRS 159672]; Spreadsheet: Matrix_Props.xls, Row 20, Column C). These properties are summarized in Table 6.6-4. Using the correlation in Equation 6.6.5.2-4, the diffusion coefficient for saturated tuff whole rock with a saturated moisture content of 10.3 percent is 3.69×10^{-7} cm^2 s^{-1}, and the diffusion coefficient for a saturated moisture content of 13.1 percent is 6.73×10^{-7} cm^2 s^{-1}.

Table 6.6-4. Tuff Matrix Properties for TSw35 and TSw36

Parameter	TSw36	TSw35
Porosity of the rock matrix in an individual granule, ϕ_m	0.103	0.131
Intrinsic Permeability, k_m (m^2)	2.00×10^{-19}	4.48×10^{-18}
Saturated diffusion coefficient (from Equation 6.6.5.2-4), D_{ms} (cm^2 s^{-1})	3.69×10^{-7}	6.73×10^{-7}

DTN: LB0208UZDSCPMI.002 [DIRS 161243]; Spreadsheet "drift-scale calibrated properties for mean infiltration2.xls," Rows 17-18, Columns B-C.

A laser ablation microprofiling technique has been used to estimate the diffusion characteristics for an unsaturated whole tuff rock sample (Hu et al. 2001 [DIRS 161623]). Hu et al. (2001 [DIRS 161623], p. 25) found that, for a measured moisture content of the sample of 8.9 percent, the internal diffusion coefficients were on the order of 10^{-12} cm^2 s^{-1} (Hu et al. 2001 [DIRS 161623], p. 25). This result indicates a very low intragranular diffusion coefficient for tuff at intragranular saturations below about 80 percent.

The model developed for the intragranular diffusion coefficient considering this information is the following. For intragranular moisture content, θ_{intra}, below 8.9 percent, a value of 10^{-12} cm^2 s^{-1} is used to represent the diffusion coefficient. For saturated conditions ($\frac{\theta_{intra}}{100} = \phi_{intra}$, the intragranular porosity), the diffusion coefficient is set to a value corresponding to Equation 6.6.5.2-4. For unsaturated grains with moisture content above 8.9 percent, a power-law extrapolation from the saturated value is used. The overall model proposed for the intragranular diffusion coefficient is the following power law model:

$$D_{intra} = D_{ms}\left(\frac{\left(\frac{\theta_{intra}}{100}\right)}{\phi_{intra}}\right)^p, \qquad \theta_{intra} \geq \theta_{min} \qquad \text{(Eq. 6.6.5.2-5)}$$

$$D_{intra} = D_{limit}, \qquad \theta_{intra} < \theta_{min},$$

where θ_{intra} is the intragranular moisture content (percent), ϕ_{intra} is the intragranular porosity (fraction), D_{limit} is the measurement limit, 10^{-12} cm^2 s^{-1}, and θ_{min} is equal to 8.9 percent.

The exponent p is the slope of Equation 6.6.5.2-5 in a plot of $\log_{10}(D_{intra})$ versus $\log_{10}(\theta_{intra})$. This plot is a straight line between points $\left(D_{limit}, \frac{\theta_{min}}{100}\right)$ and (D_{ms}, ϕ_{intra}). Thus, p is given by:

$$p = \frac{\log_{10}(D_{limit}) - \log_{10}(D_{ms})}{\log_{10}\left(\frac{\theta_{min}}{100}\right) - \log_{10}(\phi_{intra})}. \qquad \text{(Eq. 6.6.5.2-6)}$$

The dual porosity model for the invert diffusion coefficient follows by specifying values for the intergranular and intragranular diffusion coefficients. The intergranular diffusion coefficient is evaluated from Equation 6.6.5.1-5 and dividing by the intergranular porosity. The intragranular diffusion coefficient is evaluated from Equation 6.6.5.2-5. The effective bulk diffusion coefficient is determined from Equation 6.6.5.2-2.

6.7 DESCRIPTION OF BARRIER CAPABILITY

6.7.1 Analyses of Engineered Barrier Capability

This section discusses the ability of barriers to prevent or delay the movement of water or radioactive materials and deals specifically with the engineered barriers addressed in this report – the drip shield, the waste package, and the invert. In assessing these barriers, a number of assumptions are made (see Section 5).

The drip shield prevents groundwater seepage that enters the drift from dripping onto the waste package. It will be completely effective until it is breached, and it is partially effective thereafter. Condensation on the underside of the drip shield has been screened out due to low consequence (BSC 2004 [DIRS 169898], Section 6.2.41). In this case, the presence of the drip shield can potentially increase the amount of water that contacts the waste package, but the effect is negligible. This report presents an algorithm to determine the fraction of seepage entering the drift that passes through a breached drip shield, based on the number and size of breaches (Section 6.3.2.4). In the case where no groundwater seepage or dripping of drift-wall condensation into the drift occurs, there will be no water flux through the drip shield. The flux of water into the waste package is equal to the groundwater and dripping condensation flux passing through the drip shield, less the fraction that is diverted by intact portions of the waste package. In this way, the effectiveness of the drip shield as a barrier can be quantified.

The waste package outer corrosion barrier consists of corrosion-resistant material that will prevent and delay water from entering the waste package. Once breaches occur, water may enter the waste package, dissolve radionuclides, and flow out, thereby generating advective releases of radionuclides. This report presents an algorithm to determine the fraction of the water flux impinging on the waste package (having passed through drip shield breaches) that enters the waste package, depending on the size and number of breaches, as well as the total water flux through the waste package (Section 6.3.3.2). Flow is modeled as steady state and passing through the waste package without accumulating. Submodels not detailed in this report provide the concentration of radionuclides that are dissolved in the water flowing through the waste package (BSC 2004 [DIRS 169425]) and the behavior of colloids (BSC 2004 [DIRS 170025]).

Sorption and retardation characteristics of radionuclides inside the waste package are discussed in this report (Section 6.3.4.2). When there is no advective transport, diffusive releases may still occur; a submodel for diffusion inside the waste package is presented (Section 6.5.1.2.1). With these models implemented in TSPA-LA, the effectiveness of the waste package as a barrier can be quantified.

The invert consists of crushed tuff that can delay releases of radionuclides to the unsaturated zone. The invert provides a diffusive barrier. A simple model for computing the diffusion coefficient of the invert as a function of the porosity and water saturation is presented in this report (Section 6.3.4.1). This enables the effectiveness of the invert as a barrier to be quantified when implemented in TSPA-LA.

6.7.2 Summary of Natural and Engineered Barrier Capability

Table 6.7-1 summarizes the performance function of natural and engineered barriers. Only engineered barriers are analyzed in this report; the performance of natural barriers is outside the scope of this report and is included in this table for completeness.

Table 6.7-1. Summary of Barrier and Performance Functions for a Yucca Mountain Repository

Barrier	Barrier Performance Function
Surficial soils and topography	Reduce the amount of water entering the unsaturated zone by surficial processes (e.g., precipitation lost to runoff, evaporation, and plant uptake).
Unsaturated rock layers overlying the repository and host unit	Reduce the amount of water entering emplacement drifts by natural subsurface processes including lateral diversion of flow, flow in fractures around emplacement drifts, reduction in seepage due to capillary pressure in the unsaturated zone, reduction in dripping onto waste packages due to film flow. In the repository, induced coupled thermal-hydrologic processes also reduce the amount of water available to contact waste packages through enhanced evaporation near emplacement drifts (and drainage through pillars), remobilization of water by boiling and condensate shedding in pillars (for higher temperature operating modes). Also, in the physical/chemical environment in the unsaturated zone at Yucca Mountain (mildly oxidizing, pH near neutral), the vast majority of radionuclides are present in thermodynamically stable forms (metal oxides or ceramics) that are not geochemically mobile, and therefore are unlikely to move.
Unsaturated rock layers below the repository	Delay radionuclide movement and decrease radionuclide concentrations in the groundwater aquifer because of water residence time (flow rates), matrix diffusion, precipitation, dispersion, sorption.
Saturated zone volcanic tuff and alluvial deposits below the water table from the repository to a point of compliance approximately 18 km south	Delay radionuclide movement to the receptor location and reduce radionuclide concentrations by water residence time, matrix diffusion, sorption, dispersion, and dilution.
Drip shield around the waste packages	Prevent water contacting the waste package and waste form by diverting water flow around the waste package, limiting advective transport through the invert.
Waste package	Prevent water from contacting the waste form for the effective life of the package. Limit advective and diffusive transport of radionuclides from failed waste packages by sorption onto steel internal component corrosion products.

Table 6.7-1. Summary of Barrier and Performance Functions for a Yucca Mountain Repository (*Continued*)

Barrier	Barrier Performance Function
Cladding	Delay and/or limit liquid water contacting SNF after waste packages have degraded (Note no cladding exists for High-Level Radioactive Waste.).
Waste form (CSNF, DOE SNF, DOE high-level radioactive waste)	Limit radionuclide release rates as a result of low degradation rates for the waste forms, and low radionuclide solubilities.
Invert	Limit diffusive transport of radionuclides out of the engineered barriers by maintaining unsaturated conditions under the waste package. Limit advective and diffusive transport of radionuclides by sorption onto crushed tuff.

INTENTIONALLY LEFT BLANK

7. VALIDATION

Model validation for the *EBS Radionuclide Transport Abstraction* was performed in accordance with AP-2.27Q, *Planning for Science Activities*, and AP-SIII.10Q, *Models*, and follows the validation guidelines in the *Technical Work Plan for: Near-Field Environment and Transport: Engineered Barrier System: Radionuclide Transport Abstraction Model Report Integration* (BSC 2004 [DIRS 170775]).

AP-SIII.10Q, *Models*, requires that TSPA-LA model components be validated for their intended purpose and stated limitations, and to the level of confidence required by the relative importance of the component to the potential performance of the repository system. Three levels of model validation are defined in AP-2.27Q, *Planning for Science Activities*, Attachment 3, with the level of validation increasing with an increasing level of model importance ranging from low to moderate to high. Models whose variation could lead to a potentially large effect on the estimate of mean annual dose (e.g., a change greater than 1 mrem yr^{-1}) should receive a high or Level III model validation. Models whose variation could lead to moderate effect on the estimate of mean annual dose (less than 1 mrem yr^{-1}, but greater than 0.1 mrem yr^{-1}) should receive Level II model validation. Level I validation is sufficient for models of less importance to the estimate of mean annual dose.

The levels of confidence required for the models of the *EBS RT Abstraction*, as stated in Section 2.2.2 of the TWP, are given as follows.

The required level of confidence for radionuclide transport from the waste package to the drift wall through the invert is Level I (also specified in Table 1 of AP-2.27Q, *Planning for Science Activities*). The EBS-UZ interface submodel of the *EBS RT Abstraction* provides input to the unsaturated zone radionuclide transport model as described in *Particle Tracking Model and Abstraction of Transport Processes* (BSC 2004 [DIRS 170041]). The appropriate level of confidence identified for unsaturated zone radionuclide transport is Level II. Therefore, Level II also represents appropriate level of confidence for the EBS-UZ interface submodel of the *EBS RT Abstraction.*

Confidence Building During Model Development to Establish Scientific Basis and Accuracy for Intended Use

For Level I validation, Section 2.2.3 of *Technical Work Plan for: Near-Field Environment and Transport: Engineered Barrier System: Radionuclide Transport Abstraction Model Report Integration* (BSC 2004 [DIRS 170775]) cites Attachment 3 of AP-2.27Q as guidance for documenting a discussion of decisions and activities for confidence building during model development. Additionally, the development of the model will be documented in accordance with the requirements of Section 5.3.2(b) of AP-SIII.10Q. The development of the *EBS RT Abstraction* model has been conducted according to these requirements and the requisite criteria have been met as discussed below:

1. *Selection of input parameters and/or input data, and a discussion of how the selection process builds confidence in the model. [AP-SIII.10 Q 5.3.2(b) (1) and AP-2.27Q Attachment 3 Level I (a)]*

The inputs to the *EBS RT Abstraction* have been obtained from appropriate sources as described in Section 4.1. All the data are qualified project data developed by or for the Yucca Mountain Project. Tables 4.1-1 through 4.1-17 describe the input parameters, the values of the parameters and the source of the information. Inputs were selected because they are expected to represent conditions at the repository and therefore build confidence in the model. Thus, this requirement can be considered satisfied.

2. *Description of calibration activities, initial boundary condition runs, run convergences, simulation conditions set up to span the range of intended use and avoid inconsistent outputs, and a discussion of how the activity or activities build confidence in the model. Inclusion of a discussion of impacts of any non-convergence runs [(AP-SIII.10Q 5.3.2(b)(2) and AP-2.27Q Attachment 3 Level I (e)].*

   A detailed discussion of the computational implementation of the *EBS RT Abstraction* is described in Section 6.5.3. The discretization and development of the computational cell network of the sub-model domains is described in Section 6.5.3.5. Section 6.5.3.6 provides special emphasis and discussion of the EBS-UZ boundary condition. Simulation conditions account for both seepage or no seepage boundary conditions and the flux splitting algorithm accounts for the eight key flow pathways in the engineered barrier system. Discussion about non-convergence runs is not relevant for this model report. Thus, this requirement can also be considered satisfied.

3. *Discussion of the impacts of uncertainties to the model results including how the model results represent the range of possible outcomes consistent with important uncertainties.[(AP-SIII.10 Q 5.3.2(b)(3) and AP-2.27Q Attachment 3 Level 1 (d) and (f)].*

   Data uncertainty is addressed in Section 6 and parameter uncertainties are summarized in Table 6.5-13. In particular, corrosion rates of carbon and stainless steels are listed as model input with ranges and distributions determined from the data in Table 4.1-1. Sorption coefficient distribution ranges are summarized in Tables 4.1-11 and 4.1-12 and sampling correlations are given in Table 4.1-13. Table 4.1-8 provides uncertainty for unsaturated zone parameters. The breached drip shield experimental test data in Tables 4.1-2 through 4.1-6 and Figure 4.1-1 are evaluated in Section 6.5.1, resulting in uncertain model input parameters listed in Table 6.5-13 (Flux_Split_DS_Uncert and Flux_Split_WP_Uncert).

   Model uncertainty is addressed through the evaluation of alternative conceptual models. In considering alternative conceptual models for radionuclide release rates and solubility limits (Sections 6.4. and 6.6), the EBS radionuclide transport abstraction uses models and analyses that are sensitive to the processes modeled for both natural and engineering systems.

   Conceptual model uncertainties are defined and documented, and effects on conclusions regarding performance are assessed. The fundamental relationships, e.g., mass balance and flow equations, upon which the *EBS RT Abstraction* is based, are well-established with a long history of use in the scientific community and as such are not subject to significant uncertainty. In addition, the alternative conceptual models have

been screened out (Section 6.4), thereby increasing confidence in the selected conceptual model. Other sources of uncertainty involve modeling choices (e.g., assumptions, geometry) that, because of their conservative nature, effectively bound uncertainty. Therefore this requirement can be considered satisfied.

4. *Formulation of defensible assumptions and simplifications. [AP-2.27Q Attachment 3 Level I (b)].*

   A discussion of assumptions is provided in Section 5. The conceptual model for *EBS RT Abstraction* are documented in Section 6.3.1. and the simplifications necessary for implementation bases on EBS design details and failure mechanisms are presented in Sections 6.3.3 and 6.3.4. Thus, this requirement can also be considered satisfied.

5. *Consistency with physical principles, such as conservation of mass, energy, and momentum. [AP-2.27Q Attachment 3 Level I (c)]*

   Consistency with physical principles is demonstrated by the development of the mass balance mathematical formulations in Section 6.5.1. Thus, this requirement can also be considered satisfied.

Confidence Building After Model Development to Support the Scientific Basis of the Model

Level II validation includes the above Level I criteria and a single post development model validation method described in Paragraph 5.3.2c of AP-SIII.10Q, *Models*, consistent with a model of moderate importance to mean annual dose. The post development model validation method selected for the EBS-UZ interface submodel, as delineated in the TWP, consists of: corroboration by comparison to an alternative mathematical model developed for a closely comparable description of the relevant EBS-UZ features. This validation approach is consistent with Paragraph 5.3.2c (2) of AP-SIII.10Q, *Models*, which lists corroboration of results with alternative mathematical models as one of the validation methods for Level II validation. The comparison is documented in Section 7.3.1.

To build further confidence in the *EBS RT Abstraction*, an independent model validation technical review was conducted as specified by the TWP (BSC 2004 [DIRS 170775], Sections 2.2.3 and 2.2.4) for the EBS flow model, the EBS transport model, and the EBS-UZ interface submodel. This approach is based on requirements of AP-SIII.10Q, Section 5.3.2 c), where independent technical review is listed as an appropriate method for model validation. Validation is achieved if the review determines that the questions/criteria for this model, listed in Section 2.2.4 of the TWP, are met. Qualifications of and review tasks to be completed by the independent technical reviewer are described in Section 2.2.4 of the TWP. The model validation criteria are described as follows (BSC 2004 [DIRS 170775], Section 2.2.4).

EBS Flow Model Validation Criteria

Criteria that the validation of the EBS flow model is met are as follows. Each shall be confirmed by the independent model validation technical reviewer.

a) The approach and algorithms described in the document and provided to the TSPA capture all known flow pathways into and from EBS components.

b) Modeling assumptions are clearly defined, discussed, and justified as appropriate for the intended use of the model.

c) Uncertainties in parameters, processes, and assumptions are sufficiently described, and impacts of these uncertainties discussed.

d) The overall technical credibility of the approach, including assumptions, parameters, equations, and the TSPA implementation, are sufficient for the model's intended use.

EBS Transport Model Validation Criteria

Criteria that the validation of the EBS transport model is met are as follows. Each shall be confirmed by the independent model validation technical reviewer.

a) The approach and algorithms described in the document and provided to TSPA address all known modes of radionuclide transport within and from the EBS components.

b) Modeling assumptions are clearly defined, discussed, and justified as appropriate for the intended use of the model.

c) Uncertainties in parameters, processes, and assumptions are sufficiently described, and impacts of these uncertainties discussed.

d) The overall technical credibility of the approach, including assumptions, parameters, equations, and the TSPA implementation, are sufficient for the model's intended use.

EBS-UZ Interface Submodel Validation Criteria

The criterion that the validation of the EBS-UZ interface submodel is met shall consist of concurrence by an independent technical reviewer that the invert fracture-matrix partitioning results obtained using this model compare favorably with the fracture-matrix partitioning cumulative distribution function obtained using a discrete fracture model described in the *Drift-Scale Radionuclide Transport* model (BSC 2004 [DIRS 170040]). Results of the comparison shall show qualitative agreement between the two methods. The report shall document equivalent trends and correlations between input parameter variation and predicted results, identification of differences between the model results, and a discussion of the reasons and potential significance of these differences, and shall also demonstrate that the EBS-UZ interface submodel provided to TSPA does not underestimate radionuclide transport from the EBS to the UZ.

The results of the independent model validation technical review for the flow and transport models demonstrate that the appropriate criteria from above have been met, and are presented in Section 7.2.3. The results of the EBS-UZ interface submodel review demonstrate that the appropriate criteria listed above have been met, and are presented in Section 7.3.2.

The validation guidelines in the *Technical Work Plan for: Near-Field Environment and Transport: Engineered Barrier System: Radionuclide Transport Abstraction Model Report Integration* (BSC 2004 [DIRS 170775]) also state that the Subject Matter Expert (author) may elect, as deemed appropriate, to provide additional validation in the form of:

- Corroboration of model results with data previously acquired from laboratory experiments or other relevant observations
- Corroboration of model results with results of alternative models.

Additional validation of the flux splitting portion of the flow model was performed through corroboration of model results of experimental data. The results of that validation exercise are presented in Section 7.1.1.

Additional validation of the in-package diffusion portion of the transport model was performed through corroboration with alternative models. The results of that validation exercise are presented below in Section 7.2.

7.1 EBS FLOW MODEL

The EBS flow is modeled as a one-dimensional, steady advective flow through the components of the EBS. The sources of flow to the model include a seepage flux from the roof of the drift, condensation on the walls of the drift above the drift shield, and an imbibition flux from the unsaturated zone into the crushed tuff invert. The output of the flow model includes an advective flux from the invert into the unsaturated zone.

The conceptual model divides the EBS components into three domains: waste form, waste package corrosion products, and the invert. Flow and transport in these domains are treated separately. The output of the waste form domain feeds into the corrosion products domain. The output of the corrosion products domain in turn feeds the invert.

The flow through the EBS may occur along eight pathways: (1) dripping flux, (2) flux through the drip shield, (3) diversion around the drip shield, (4) flux through the waste package, (5) diversion around the waste package, (6) total flux into the invert, (7) imbibition flux from the unsaturated zone matrix to the invert, and (8) flux from the invert to the unsaturated zone fractures.

The magnitude of seepage fluid passing through the drip shield and the waste package is accounted for using the flux splitting submodel. This submodel determines how much water flows through the drip shield or waste package and how much is diverted around these components. Below is the validation of the submodel and validation criteria for both the drip shield and waste package applications. Further discussions relevant to the validation of the flow model can be found in Sections 5, 6.3.2, 6.3.3, 6.5.1.1.1, 6.5.1.1.2, and 6.5.1.1.3.

7.1.1 Flux Splitting Submodel

The EBS flux splitting submodel, which is part of the *EBS RT Abstraction* flow model, determines the fraction of total dripping flux that will flow through the drip shield and/or waste package. This submodel is directly related to the waste isolation attribute (i.e., the limited release of radionuclides from engineered barriers). The amount of water flowing through engineered barriers, when combined with radionuclide solubility limits and diffusive transport, defines the mass flux of radionuclides that is mobilized for transport through the EBS to the unsaturated zone.

Level I validation is appropriate for the flux splitting submodel, because it is part of the process for radionuclide transport from waste package to the drift wall through the invert (see Section 7 above). In addition, the flux splitting submodel has the following features:

- The submodel is not extrapolated over large distances, spaces or time.
- The submodel has large uncertainties because of the chaotic nature of the flow of droplets or rivulets on corroded, roughened surfaces.
- Sensitivity analyses in the prioritization report *Risk Information to Support Prioritization of Performance Assessment Models* (BSC 2003 [DIRS 168796], Sections 3.3.6 through 3.3.11) show that the flux splitting abstraction will not have a large impact on dose in the first 10,000 years.
- The flux splitting submodel plays a minor role in TSPA-LA. In the nominal scenario class, neither the drip shield nor the waste package fails due to general corrosion within the 10,000-year regulatory period, and when the drip shield does fail, it is modeled as failing completely in a single time step (BSC 2004 [DIRS 169996], Section 6.3). In the igneous scenario class, neither the drip shield nor the waste package survives an igneous intrusion, so the flux splitting submodel is not used. Thus, the flux splitting submodel is actually applied only in the seismic scenario class when seismic damage occurs to the waste package.

This flux splitting submodel is validated through comparison to experimental data. A work plan entitled *Test Plan for: Atlas Breached Waste Package Test and Drip Shield Experiments* (BSC 2002 [DIRS 158193]) defines the experiments used for validation of this flux splitting submodel.

The flux splitting submodel is applied to two components of the EBS–the drip shield and the waste package–and is validated for each. Validation is achieved through comparison of the models developed in this document (based in part on the qualified experimental data) to other qualified data collected during associated testing. This comparison is limited because the validation experiments are based on flow measurements from a single fixed source for dripping, whereas the abstraction is based on randomly located drips relative to multiple patches on the drip shield. In this situation, the appropriate criterion for model validation is that the predictions of the abstraction bound the experimental measurements made on the rough drip shield surface. This criterion is appropriate because of the large spread of the experimental data.

The rough drip shield surface experiments replicate the smooth drip shield surface experiments and constitute a consistent set of data that can be compared with and serve as validation for the smooth drip shield surface data. The rough surface would be expected to yield results (specifically, the flux splitting uncertainty factors) that differ from those obtained for the smooth surface. However, because the only difference in the experiments is the surface texture, the trends in the data and the values obtained for the uncertainty factors should be similar, which validates the flux splitting submodel.

Experimental data used to develop the flux splitting submodel include the splash radius, the rivulet spread distance or angle, and the fraction of dripping flux that flowed into breaches. For the drip shield and waste package flux splitting submodels, data from smooth drip shield experiments were used (DTNs: MO0207EBSATBWP.022 [DIRS 163400]; MO0207EBSATBWP.023 [DIRS 163402]; MO0207EBSATBWP.024 [DIRS 163401]; MO0207EBSATBWP.025 [DIRS 163403]). For validation of the models, data from the rough drip shield experiments are used (DTNs: MO0207EBSATBWP.021 [DIRS 163399]; MO0208EBSATBWP.027 [DIRS 163404]; MO0208EBSATBWP.028 [DIRS 163405]). Each of the types of data used is discussed below, first for the drip shield submodel validation and then for the waste package flux splitting submodel validation.

7.1.1.1 Drip Shield Flux Splitting Submodel

Splash radius data for dripping onto the crown of the rough drip shield surface are listed in Table 7.1-1. The data are analyzed in the Microsoft Excel spreadsheet: Flux Splitting Validation, Worksheet: Splash Rad vs Number, which is documented in Appendix E. As shown in Figure 7.1-1, the splash radius tends to increase as the number of drips increases. The inner cluster radius is of interest because it is used to define the effective length of the drip shield in developing the flux splitting submodel (see Section 6.5.1.1.2). While the data do not indicate that a maximum splash radius was achieved, it stands to reason that a maximum must exist, simply because the distance a splashed droplet can travel is finite, limited by the kinetic energy of a falling drop. The uncertain parameter in the drip shield flux splitting submodel, f'_{DS}, was based on the maximum splash distance observed for the inner cluster of droplets on a smooth drip shield, 48 cm (see Section 6.5.1.1.2.4 for a discussion of the development of f'_{DS} based on the 48-cm maximum inner cluster splash radius). For the rough drip shield tests, the maximum inner cluster splash radius for dripping onto the crown was again 48 cm. Another approach is to use the splash radius at which rivulets begin to flow from coalesced droplets. In Splash Radius Test #1, rivulet flow began after 143 drips; in Test #2, after 145 drips; and in Test #3, after 133 drips (DTN: MO0207EBSATBWP.021 [DIRS 163399]), for an average of 140 drips. Using the Microsoft Excel Trendline application (least squares fitting routine) for the inner cluster data in Figure 7.1-1, the splash radius when rivulets began to flow was 31 cm. The minimum splash radius was about 3.5 cm for more than 20 drips (see Table 7.1-1). The range of uncertainty is bounded using the extreme values of splash radius (3.5 – 48 cm). Since the value of splash radius at which rivulets begin to flow (31 cm) is between those extremes, an estimate of uncertainty based on that value will not affect the estimated bounds on uncertainty.

The flux splitting submodel also depends on the rivulet spread angle. These data are analyzed in the Microsoft Excel spreadsheet: Flux Splitting Validation, Worksheet: Rough DS, which is

documented in Appendix E. For the smooth drip shield, the spread angle from crown drip locations ranged from 8.9° to 17.3° (± one standard deviation from the mean of 13.2°; see Section 6.5.1.1.2.4). For drip locations on the crown, the rough drip shield surface had a mean rivulet spread angle of 7.3°, with a range of 0° to 14.4° (± one standard deviation from the mean). Rivulet spread data for the rough surface are shown in Table 7.1-2. In Table 7.1-4, the spread angle calculation results are shown.

The amount of water dripped onto the crown and water flow into breaches on the rough drip shield surface are listed in Table 7.1-3. The fraction of the dripping flux that flowed into the pertinent breach, f_{expt}, is shown along with the rivulet spread angle for each particular test in Table 7.1-4.

Table 7.1-1. Atlas Breached Drip Shield Experiments on Rough Drip Shield Surface – Dripping on Crown – Splash Radius Tests

No. Drips	Splash Radius (cm)		Comments
	Left	Right	
Splash Radius Test #1			
10	2.0	2.0	Measured inner cluster (bulk)
10	15.0	25.5	Measured outer fringe
21	5.0	4.0	Measured inner cluster (bulk)
21	15.0	42.5	Measured outer fringe
60	18.0	22.0	Measured inner cluster (bulk)
60	72.5	75.5	Measured outer fringe
143	35.0	48.0	Measured inner cluster (bulk)
143	54.0	82.5	Measured outer fringe
203	35.0	48.0	Measured inner cluster (bulk)
203	79.5	106.5	Measured outer fringe
Splash Radius Test #2			
21	3.5	4.0	Measured inner cluster (bulk)
21	37.5	7.0	Measured outer fringe
82	10.5	19.0	Measured inner cluster (bulk)
82	63.0	32.0	Measured outer fringe
149	31.5	30.0	Measured inner cluster (bulk)
207	45.0	40.0	Measured inner cluster (bulk)
Splash Radius Test #3			
30	7.5	9.0	Measured inner cluster (bulk)
82	19.0	17.5	Measured inner cluster (bulk)
137	28.0	27.5	Measured inner cluster (bulk)
205	29.0	28.0	Measured inner cluster (bulk)

DTN: MO0207EBSATBWP.021 [DIRS 163399].

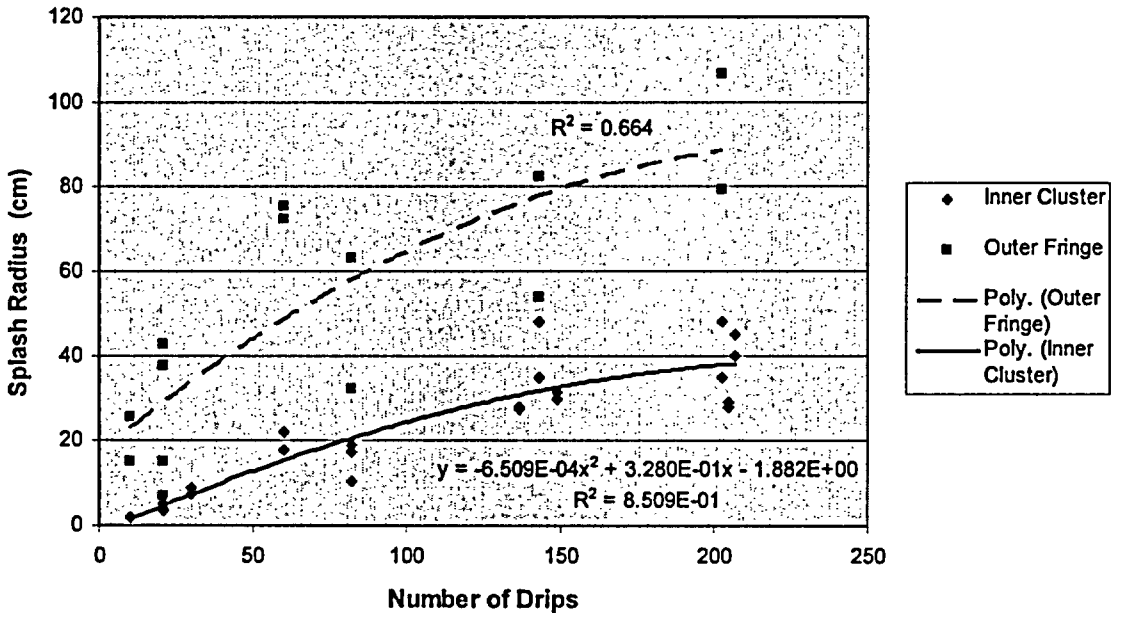

Figure 7.1-1. Splash Radius Dependence on Number of Drips for Rough Drip Shield Tests

Table 7.1-2. Atlas Breached Drip Shield Experiments on Rough Drip Shield Surface – Dripping on Crown – Rivulet Spread Data – 33° from Crown

Drip Location	Left (cm)	Right (cm)	Relevant Patch
Multiple Patch Tests (DTN: MO0208EBSATBWP.027 [DIRS 163404])			
81 cm left of drip shield center	32.5	17.5	4
27 cm left of drip shield center	21.5	18.0	4
27 cm right of drip shield center	10.0	10.0	5
27 cm right of drip shield center	1.0	0	5
81 cm right of drip shield center	17.0	34.0	5
Bounding Flow Rate Tests (DTN: MO0208EBSATBWP.028 [DIRS 163405])			
54 cm left of drip shield center (High Flow Rate)	2	0	4
27 cm left of drip shield center (High Flow Rate)	15	15	4
27 cm right of drip shield center (High Flow Rate)	6	6	5
27 cm right of drip shield center (Low Flow Rate)	50.0	16.0	5
27 cm right of drip shield center (Low Flow Rate)	—	1.0	5
27 cm left of drip shield center (Low Flow Rate)	25.5	12.0	4
54 cm left of drip shield center (Low Flow Rate)	0	0	4

Table 7.1-3. Atlas Breached Drip Shield Experiments on Rough Drip Shield Surface – Dripping on Crown – Flow into Breaches

Drip Location	Drip Location Relative to:		Water Input (g)	Water Collected In:	
	Breach B4 (cm)	Breach B5 (cm)		Breach B4 (g)	Breach B5 (g)
Multiple Patch Tests (DTN: MO0208EBSATBWP.027 [DIRS 163404])					
81 cm left of drip shield center	-27	-135	292.35	0.27	0.00
27 cm left of drip shield center	27	-81	288.45	5.27	0.00
27 cm right of drip shield center	81	-27	291.62	0.00	0.08
27 cm right of drip shield center	81	-27	294.13	0.00	0.27
81 cm right of drip shield center	135	27	290.10	0.00	1.01
Bounding Flow Rate Tests (DTN: MO0208EBSATBWP.028 [DIRS 163405])					
54 cm left of drip shield center (High Flow Rate)	0	-108	330.74	193.87	0.00
27 cm left of drip shield center (High Flow Rate)	27	-81	328.65	0.63	0.00
27 cm right of drip shield center (High Flow Rate)	81	-27	306.65	0.00	0.35
27 cm right of drip shield center (Low Flow Rate)	81	-27	545.14	0.00	11.11
27 cm right of drip shield center (Low Flow Rate)	81	-27	70.80	0.00	0.00
27 cm left of drip shield center (Low Flow Rate)	27	-81	113.32	1.36	0.00
54 cm left of drip shield center (Low Flow Rate)	0	-108	118.10	0.00	0.00

Table 7.1-4. Atlas Breached Drip Shield Experiments on Rough Drip Shield Surface – Dripping on Crown – Fraction of Dripping That Flowed into Breaches and Rivulet Spread Angle

Drip Location	Breach Collecting Flow	f_{expt}	Spread Angle (degree)	
			Left	Right
81 cm left of drip shield center	4	0.0018	32.5	17.5
27 cm left of drip shield center	4	0.0365	21.5	18
27 cm right of drip shield center	5	0.0005	10	10
27 cm right of drip shield center	5	0.0018	0	1
81 cm right of drip shield center	5	0.0070	17	34
54 cm left of drip shield center (High Flow Rate)	4	1.1723	2	0
27 cm left of drip shield center (High Flow Rate)	4	0.0038	15	15
27 cm right of drip shield center (High Flow Rate)	5	0.0023	6	6
27 cm right of drip shield center (Low Flow Rate)	5	0.0408	50	16
27 cm right of drip shield center (Low Flow Rate)	5	0.0110	—	1

Table 7.1-4. Atlas Breached Drip Shield Experiments on Rough Drip Shield Surface – Dripping on Crown – Fraction of Dripping That Flowed into Breaches and Rivulet Spread Angle (Continued)

Drip Location	Breach Collecting Flow	f_{expt}	Spread Angle (degree)	
			Left	Right
27 cm left of drip shield center (Low Flow Rate)	4	0.0240	25.5	12
54 cm left of drip shield center (Low Flow Rate)	4	0.0	0	0
Mean	—	0.108	7.25	
Standard Deviation	—	0.335	7.18	
Median	—	0.005	6.29	

NOTES: — = no measurement.
Mean, standard deviation, and median for spread angle are for all (left and right) measurements.

Following the approach used in Section 6.5.1.1.2.4, the "inner cluster" splash diameter is used for the effective length of the drip shield in the validation of the flux splitting algorithm, which is given by Equations 6.3.2.4-4 and 6.3.2.4-6 (or 6.5.1.1.2-35). The form of the equation is:

$$F = \frac{N_b \ell}{L_{DS}}\left(1 + \frac{\tan\alpha}{2}\right) f_{VD}, \qquad \text{(Eq. 7.1.1.1-1)}$$

where F is the fraction of dripping flux that flows through breaches, ℓ is one-half the width of a breach or patch, L_{DS} is the effective length of the drip shield (i.e., the length over which dripping or splattering occurs), α is the rivulet spread angle, and f_{VD} is the uncertainty factor for the drip shield developed for validation, corresponding to the drip shield uncertainty factor, f_{DS}. For the validation tests, the number of breaches, N_b, is one.

The splash diameter is used for the effective length, L_{DS}. As shown in Table 7.1-1, the "inner cluster" splash radius on the rough drip shield surface ranged from 3.5 cm to 48 cm (for more than 20 drops), giving a range for L_{DS} of 7 cm to 96 cm. The spread angle ranged (one standard deviation from the mean) from zero to 14.4°. For a drip shield patch width of 27 cm, ℓ = 13.5 cm. Then, as shown in Table 7.1-5, $F/f_{VD} = \frac{N_b \ell}{L_{DS}}\left(1 + \frac{\tan\alpha}{2}\right)$ ranges from 0.141 to 2.17.

Table 7.1-5. Range of Estimates for F/f_{VD}

L_{DS} (cm)	Drip Shield F/f_{VD}	
	$\alpha = 0°$	$\alpha = 14.4°$
7	1.93	2.17
96	0.141	0.158

The fraction of dripping flux, f_{expt}, that entered breaches in 12 rough drip shield experiments ranged from zero to 1.17, with a mean of 0.108 and a median of 0.0054. The wide range of

uncertainty and randomness in the experiments is demonstrated in two of the tests having the same drip location (54 cm to the left of the drip shield center). The high drip rate test yielded the highest flow into a breach with a negligible spread, which is the expected result. The low drip rate test at the same drip location, which had zero rivulet spread, unexpectedly resulted in no flow into the breach. Statistics for f_{expt} are compared in Table 7.1-6 between the smooth drip shield surface experimental results (Table 6.5-2) and the rough surface results discussed in this section.

Table 7.1-6. Comparison of f_{expt} Statistics for Smooth and Rough Drip Shield Surfaces

Experiments	Mean f_{expt}	Minimum f_{expt}	Maximum f_{expt}	Median f_{expt}
Drip Shield (Smooth Surface)	0.111	0.013	0.275	0.049
Drip Shield Validation (Rough Surface)	0.108	0.0	1.17	0.0054

The rough surface experimental results are now used to calibrate the drip shield flux splitting submodel that is developed for validation purposes, yielding the uncertainty factor f_{VD}:

$$f_{VD} = \frac{f_{expt}}{\frac{\ell}{L_{DS}}\left(1+\frac{\tan\alpha}{2}\right)}. \qquad \text{(Eq. 7.1.1.1-2)}$$

f_{VD} is at a minimum using the minimum value for L_{DS} (7 cm) and the maximum value for α (14.4°), resulting in $f_{VD} = 0.46 f_{expt}$. The maximum for f_{VD} is obtained using the maximum value for L_{DS} (96 cm) and the minimum value for α (0°), resulting in $f_{VD} = 7.1 f_{expt}$. Using the mean value for f_{expt} (0.108) results in a range for f_{VD} of 0.050 to 0.77. The drip shield flux splitting algorithm developed in Section 6.5.1.1.2.4 produced the corresponding factor f_{DS} ranging from about 0.36 to 0.73. These factors (f_{VD} and f_{DS}) actually represent the estimates of the upper bound on the uncertainty, since a lower bound is necessarily zero (i.e., no flow through a breach). Using the actual measured range of f_{expt} (0.0 to 1.17) instead of the mean increases the range estimated for f_{VD} to 0.0 to (7.1)(1.17) = 8.3. The corresponding range for f_{DS}, using the measured range of f_{expt} (0.013 to 0.275) (Table 6.5-2) for the smooth surface tests instead of the mean (0.111), is 0.013/0.31 = 0.041 (for $L_{DS} = 50\,\text{cm}$, $\alpha = 17.3°$) to 0.275/0.152 = 1.8 (for $L_{DS} = 96\,\text{cm}$, $\alpha = 8.9°$). Thus, using the extreme values of f_{expt} for estimating f_{DS} and f_{VD}, the upper bound on f_{VD} actually spans the uncertainty in the upper bound estimate of f_{DS}, as summarized in Table 7.1-7.

Table 7.1-7. Summary of f_{DS} and f_{VD} Values

	Based on Mean f_{expt}		Based on Minimum f_{expt}	Based on Maximum f_{expt}
	Minimum	Maximum	Minimum	Maximum
f_{DS}	0.36	0.73	0.041	1.8
f_{VD}	0.050	0.77	0	8.3

Based on mean values for the experimentally measured fraction of the dripping flux that flows through a breach, the rough drip shield surface factor shows that less of the dripping flux will flow through a breach, compared with the smooth surface results used to develop the drip shield flux splitting submodel. The rough surface data validate the drip shield submodel by confirming an estimate of the upper bound on the uncertainty of 0.77, based on mean values for f_{expt}. The range on the estimate for f_{VD} is also about 0.7, which is comparable (about a factor of 2) to the uncertainty in f_{DS}. While the upper bound on the uncertainty factor is about the same for both the smooth and rough surfaces (0.73 vs. 0.77), the lower bound is much higher for the smooth surface (0.36 vs. 0.05). A random sampling from these ranges will give a mean value of about 0.54 for the smooth surface versus about 0.42 for the rough surface. So the smooth surface range will, on average, overestimate the flux through the drip shield compared to the rough surface range. Both the smooth surface and the rough surface results include a wide range of variability that is incorporated in the sampled uncertainty parameter f_{DS} for the drip shield flux splitting submodel. The rough drip shield surface data provide confirmation that the drip shield submodel will generally overestimate the flux through that barrier.

A final comparison is made between f'_{DS}, which lumps the uncertainty in the rivulet spread angle into f_{DS}, and a corresponding parameter for the rough drip shield surface, f'_{VD}, is derived, where

$$f'_{VD} = \left(1 + \frac{\tan\alpha}{2}\right) f_{VD}. \qquad \text{(Eq. 7.1.1.1-3)}$$

Since α ranges from 0° to 14.4°, applying the maximum value for α will result in the range for f'_{VD} of 0 to 0.87, based on the mean value of f_{expt} (0.054) that gives a range of 0.050 to 0.77 for f_{VD}. For comparison, f'_{DS} was estimated to range from 0 to 0.85. The nearly-identical ranges for f'_{DS} and f'_{VD} validate the drip shield flux splitting submodel.

7.1.1.2 Waste Package Flux Splitting Submodel

Using off-crown drip location data for the rough drip shield surface (Table 7.1-8), the rivulet spread angle was found to depend strongly on the drip rate. These data are analyzed in the Microsoft Excel spreadsheet: Flux Splitting Validation, Worksheet: Rough off crown WP model, which is documented in Appendix E. The high drip rate resulted in an average spread angle of 27.1°; the nominal drip rate had a mean spread angle of 20.6°; and the low drip rate had a mean spread angle of 3.1°. However, to be consistent with the development of the spread angle for the waste package submodel, and to incorporate the real possibility of widely varying drip rates, all 50 data points are combined. The mean spread angle for the rough drip shield surface with off-crown drip locations is therefore 9.4°, with a range (± one standard deviation of 9.6°) of 0° to 19.0°.

In the off-crown splash radius tests #4 and #5 (Table 7.1-9) (Microsoft Excel spreadsheet: Flux Splitting Validation, Worksheet: Splash Radius, which is documented in Appendix E), the drip

location was 33° and 16.5° off the crown. The mean splash radius was 8.9 cm, with a measured range of 3.0 cm to 15.0 cm. This gives an effective waste package length of about 6 cm to 30 cm for the tests.

Table 7.1-8. Atlas Breached Drip Shield Experiments on Rough Drip Shield Surface – Dripping off Crown – Rivulet Spread Data

Drip Location	Spread at 33°		Spread at Transition		Relevant Patch
	Left (cm)	Right (cm)	Left (cm)	Right (cm)	
Multiple Patch Tests (DTN: MO0208EBSATBWP.027 [DIRS 163404])					
81 cm right of drip shield center, 16.5°	—[a]	—	—	—	5
27 cm right of drip shield center, 16.5°	8	12	6	8	5
27 cm left of drip shield center, 16.5°	21	19	12	13	4
81 cm left of drip shield center, 16.5°	16	22	14	12	4
81 cm right of drip shield center, 33°	—	—	2	2	5
27 cm right of drip shield center, 33°	—	—	3	1	5
27 cm left of drip shield center, 33°	—	—	2	1	4
81 cm left of drip shield center, 33°	—	—	3	4	4
Bounding Flow Rate Tests (DTN: MO0208EBSATBWP.028 [DIRS 163405])					
54 cm left of drip shield center, 33° (Low Flow Rate)	—	—	—	—	4
54 cm left of drip shield center, 33° (High Flow Rate)	—	—	—	—	4
27 cm left of drip shield center, 33° (High Flow Rate)	6[b]	9[b]	8	14	4
27 cm right of drip shield center, 33° (High Flow Rate)	5[b]	3[b]	12	11	5
27 cm right of drip shield center, 33° (Low Flow Rate)	—	—	2.5	2.5	5
27 cm right of drip shield center, 16.5° (High Flow Rate)	16	15	17	10	5
27 cm left of drip shield center, 16.5° (High Flow Rate)	26	32	13	34	4
54 cm left of drip shield center, 16.5° (High Flow Rate)	25	20	26	19	4
54 cm left of drip shield center, 16.5° (Low Flow Rate)	3	6	—	—	4
27 cm left of drip shield center, 16.5° (Low Flow Rate)	3	2	1	0	4
27 cm right of drip shield center, 16.5° (Low Flow Rate)	0	0	0	0	5
27 cm left of drip shield center, 33° (Low Flow Rate)	—	—	6	4.5	4

[a] — = rivulet spread not measured.
[b] These data are ignored due to inconsistent behavior – rivulet spread should not occur at the drip location.

Table 7.1-9. Atlas Breached Drip Shield Experiments on Rough Drip Shield Surface – Dripping off Crown – Splash Radius Tests

No. Drips	Splash Radius (cm)		Comments
	Left	Right	
Splash Radius Test #4 (33°) (DTN: MO0207EBSATBWP.021 [DIRS 163399])			
31	3.0	3.5	Measured inner cluster (bulk)
82	5.5	6.0	Measured inner cluster (bulk)
158	6.5	6.5	Measured inner cluster (bulk)
Splash Radius Test #5 (16.5°) (DTN: MO0207EBSATBWP.021 [DIRS 163399])			
22	9.0	10.0	Measured inner cluster (bulk)
82	13.0	14.5	Measured inner cluster (bulk)
156	14.0	15.0	Measured inner cluster (bulk)

The experimentally measured fraction of the drip flux (Table 7.1-10) that flowed into all breaches (f_{expt}) from off-crown drip locations had a mean of 0.12, with a standard deviation of 0.23. The measured minimum fraction was 0.0 and the maximum was 0.621.

Following the approach used in Section 6.5.1.1.3, the "inner cluster" splash diameter is used for the effective length of the waste package in the validation of the flux splitting algorithm, which is given by Equations 6.3.3.2-1 (or 6.5.1.1.3-2) and 6.3.3.2-3 (or 6.5.1.1.3-1). The form of the equation is:

$$F = \frac{N_b \ell}{L_{WP}}\left(1 + \frac{\tan\alpha}{2}\right) f_{VW}, \qquad \text{(Eq. 7.1.1.2-1)}$$

where F is the fraction of dripping flux that flows through breaches, ℓ is one-half the width of a breach or patch, L_{WP} is the effective length of the waste package (i.e., the length over which dripping or splattering occurs), α is the rivulet spread angle, and f_{VW} is the uncertainty factor for the waste package developed for validation, corresponding to the waste package uncertainty factor, f_{WP}. For the validation tests, the number of breaches, N_b, is one. f_{VW} is obtained by inserting f_{expt}, the measured fraction of the dripping flux that flowed into breaches, for F in Equation 7.1.1.2-1:

$$f_{VW} = \frac{f_{expt}}{\frac{N_b \ell}{L_{WP}}\left(1 + \frac{\tan\alpha}{2}\right)}. \qquad \text{(Eq. 7.1.1.2-2)}$$

Table 7.1-10. Atlas Breached Drip Shield Experiments on Rough Drip Shield Surface – Dripping off Crown – Flow into Breaches

Drip Location	Water Input (g)	Breach 4 Inflow (g)	Breach 4 f_{expt}	Breach 5 Inflow (g)	Breach 5 f_{expt}
81 cm right of drip shield center, 16.5°	282.96	0	0	0.76	**0.0027**
27 cm right of drip shield center, 16.5°	316.74	0	0	0.35	**0.0011**
27 cm left of drip shield center, 16.5°	309.57	0.48	**0.0016**	0.44	0.0014
81 cm left of drip shield center, 16.5°	242.56	0.94	**0.0039**	0	0
81 cm right of drip shield center, 33°	109.4	0	0	0.22	**0.0020**
27 cm right of drip shield center, 33°	108.44	0	0	0.30	**0.0028**
27 cm left of drip shield center, 33°	107.33	0.33	**0.0031**	0	0
81 cm left of drip shield center, 33°	106.75	0.01	**0.0001**	0	0
54 cm left of drip shield center, 33° (Low Flow Rate)	123.13	53.27	**0.4326**	0	0
54 cm left of drip shield center, 33° (High Flow Rate)	330.03	204.99	**0.6211**	0	0
27 cm left of drip shield center, 33° (High Flow Rate)	339.24	0.06	**0.0002**	0	0
27 cm right of drip shield center, 33° (High Flow Rate)	330.22	0.10	0.0003	1.23	**0.0037**
27 cm right of drip shield center, 33° (Low Flow Rate)	112.36	0	0	0.80	**0.0071**
27 cm right of drip shield center, 16.5° (High Flow Rate)	313.82	0	0	1.14	**0.0036**
27 cm left of drip shield center, 16.5° (High Flow Rate)	322.07	1.34	**0.0042**	0.19	0.00059
54 cm left of drip shield center, 16.5° (High Flow Rate)	328.27	197.92	**0.6029**	0	0
54 cm left of drip shield center, 16.5° (Low Flow Rate)	94.41	57.18	**0.6056**	0	0
27 cm left of drip shield center, 16.5° (Low Flow Rate)	115.97	0.34	**0.0029**	0.45	0.0039
27 cm right of drip shield center, 16.5° (Low Flow Rate)	119.76	0	0	0.09	**0.0008**
27 cm left of drip shield center, 33° (Low Flow Rate)	115.81	0.36	**0.0031**	0	0

DTNs: MO0208EBSATBWP.027 [DIRS 163404], MO0208EBSATBWP.028 [DIRS 163405].

NOTE: For all fexpt values in bold: mean = 0.115; standard deviation = 0.234; median = 0.0031; minimum = 0.00014; maximum = 0.621.

Statistics for f_{expt} are compared in Table 7.1-11 between the smooth drip shield surface experimental results used for the waste package flux splitting submodel (Appendix D) and the rough surface results discussed in this section (Table 7.1-10).

Table 7.1-11. Comparison of f_{expt} Statistics for Smooth and Rough Drip Shield Surfaces

Experiments	Mean f_{expt}	Minimum f_{expt}	Maximum f_{expt}	Median f_{expt}
Waste Package (Smooth Surface)	0.295	0.0	1.066	0.0142
WP Validation (Rough Surface)	0.115	0.0001	0.621	0.0031

WP = waste package

With the values for the breach flow fraction (f_{expt}), the effective waste package length (L_{WP}), and the spread angle (α) as determined above using off-crown rough drip shield surface test data, the range for f_{VW} is be determined. The half-width of the patch used in the experiments ($\ell = 13.5$ cm) is used to evaluate f_{VW}. The minimum for f_{VW} is obtained using the minimum effective waste package length ($L_{WP} = 6.0$ cm) and the maximum spread angle ($\alpha = 19.0°$), resulting in $f_{VW} = 0.379 f_{expt}$. The maximum for f_{VW} is obtained using the maximum effective waste package length ($L_{WP} = 30$ cm) and the minimum spread angle ($\alpha = 0°$), resulting in $f_{VW} = 2.22 f_{expt}$. Using the mean value of f_{expt} (0.115), f_{VW} for the waste package ranges from 0.044 to 0.26. Over the measured range of f_{expt} (0 to 0.621), f_{VW} ranges from 0.0 to (2.22)(0.621) = 1.38. The range obtained for f_{WP} (0.909 to 2.00), based on the mean smooth drip shield surface value of f_{expt} (0.295), is higher. When the measured range of smooth surface f_{expt} values (0.0 to 1.066; see Figure D-10) for the waste package flux splitting analysis is used instead of the mean, f_{WP} ranges from 0.0 to 3.28. The waste package flux splitting submodel overestimates flow through breaches compared to the model validation estimates, which in turn overestimates the advective releases of radionuclides compared to the model validation estimates. The estimated values for f_{WP} and f_{VW} are summarized in Table 7.1-12.

Table 7.1-12. Summary of f_{WP} and f_{VW} Values

	Based on Mean f_{expt}		Based on Minimum f_{expt}	Based on Maximum f_{expt}
	Minimum	Maximum	Minimum	Maximum
f_{WP}	0.909	2.001	0.0	3.28
f_{VW}	0.044	0.26	0.0	1.38

As with the drip shield submodel, a final comparison is between f'_{WP}, which lumps the uncertainty in the rivulet spread angle into f_{WP}, and a corresponding parameter for the rough drip shield surface, f'_{VW}, where

$$f'_{VW} = \left(1 + \frac{\tan\alpha}{2}\right) f_{VW}. \qquad \text{(Eq. 7.1.1.2-3)}$$

For the rough drip shield surface, α ranges from 0° to 19.0°. Applying the maximum value for α results in the range for f'_{VW} of 0 to 0.30, based on the mean value of f_{expt}. For comparison,

f'_{WP} was estimated to range from 0 to 2.41. The wider range for f'_{WP} means that the drip shield flux splitting submodel tends to overestimate the flow through breaches in the drip shield. The overlapping ranges for f'_{WP} and f'_{VW} validate the waste package flux splitting submodel.

Sections 7.1.1.1 and 7.1.1.2 have demonstrated that the drip shield and waste package flux splitting submodels overestimate fluxes when compared to the experimental data presented. The validations discussed uncertainties in relevant parameters. Based on these validation results, the EBS flow model is adequate for its intended use.

7.1.2 Results of Independent Model Validation Technical Review of the EBS Flow Model

The results of the independent model validation technical review of the EBS flow model are given in a memo (Jin 2004 [DIRS 170952]) presented in Section 7.2.3 that combines the technical reviews of the EBS flow and transport models.

7.2 EBS TRANSPORT MODEL

The transport of radionuclides through the EBS is modeled, using assumptions in Section 5, as a combination of advective and diffusive transport including retardation between a series of three domains:

- Waste form domain
- Corrosion products domain
- Invert domain.

Advective transport is considered when water enters the waste form domain and is able to flow through the EBS and enter the UZ. The EBS flow model (Section 7.1) calculates the water flux between each domain and a separate model provides radionuclide concentrations.

Diffusive transport between each of the domains occurs regardless of whether water is flowing though the EBS. Diffusive transport between each domain is modeled in one dimension and therefore is dependent upon the following parameters that can vary as a function of time and according to the specific transport pathway:

- Effective diffusion coefficient
- Diffusive area
- Diffusion length.

The effective diffusion coefficient is calculated from Archie's law and is dependent upon the free water diffusion coefficient, porosity, and saturation in each domain. Additionally a temperature correction is made for diffusion in the invert domain. Porosity is either assumed to be constant or is provided by a separate model (e.g., BSC 2004 [DIRS 170023]). Saturation varies with relative humidity. The diffusive area is calculated differently for each domain, but is either a function of the number of breaches in the waste package (corrosion patches or stress corrosion cracks) or it is calculated from the geometry of the different components of the EBS. The diffusive area of breaches also depends on the scenario class being modeled. The diffusion length is either calculated from EBS geometry or is sampled, depending upon the domain.

As stated in Section 7, the level of confidence required for the EBS transport model is Level I. Level I validation is described in Section 7. In Sections 6.3 and 6.5, a detailed explanation and justification is presented on the formulation of the transport model. These sections include a great amount of information that is relevant to Level I validation. In addition, the following sections include auxiliary information aimed to validate further certain components of the transport model. In some cases these descriptions and comparisons go beyond Level I validation criteria, but are included for completeness.

Section 7.2.1 describes a comparison between the in-package diffusion submodel and two similar, independently developed models of transport from a waste package to the invert. The comparison shows that although each model uses a different set of assumptions, the assumptions used and the final diffusion coefficients calculated by each model generally agree and thus the transport model is valid for its intended purpose.

Section 7.2.2 compares the invert diffusion coefficient of free water diffusivity for radionuclides at different temperatures and with other cations and anions and shows that the self-diffusion coefficient of water at 25°C is an upper bound.

7.2.1 In-Package Diffusion Submodel

Diffusive transport within the waste package will limit the release of radionuclides for those waste packages in a no-seep environment. The in-package diffusion submodel is directly related to the waste isolation attribute, limited release of radionuclides from the engineered barriers, because the model predicts delays in the release of mass from the waste package in comparison to the TSPA-SR model, which immediately mobilized radionuclides at the external surface of the waste package.

Level I validation is appropriate for the in-package diffusion submodel, as it is part of the mechanisms for radionuclide transport from waste package to the drift wall through the invert (see Section 7 above). In addition, the in-package diffusion submodel has the following features:

- The in-package diffusion submodel is not extrapolated over large distances or spaces. There is an inherent time extrapolation in the model.

- The in-package diffusion submodel bounds the uncertainties by considering two bounding states. In the first state, the waste package internal components are considered to be in their intact, as-emplaced condition. For the second state, the iron-based waste package internal components are considered to be completely degraded to a porous material. Although these are two bounding end states, uncertainties exist in the time- and spatially-dependent intermediate conditions.

- The in-package diffusion submodel has a modest impact on dose time history in the first 10,000 years, based on sensitivity calculations performed for the prioritization report *Risk Information to Support Prioritization of Performance Assessment Models* (BSC 2003 [DIRS 168796], Sections 3.3.6 through 3.3.11). Those studies indicate that the estimate of mean annual dose in the first 10,000 years has only a minor dependence on in-package conditions that impact diffusion.

The in-package diffusion submodel is validated by comparison to two other models:

- Electric Power Research Institute (EPRI) *Phase 5* report (EPRI 2000 [DIRS 154149])
- A model by Lee et al. (1996 [DIRS 100913]) for diffusive releases from waste package containers with multiple perforations.

The in-package diffusion submodel is based on the one-dimensional diffusion equation, Fick's first law of diffusion (Bird et al. 1960 [DIRS 103524], p. 503):

$$\frac{q_i}{A} = -D\frac{\partial C_i}{\partial x}. \qquad \text{(Eq. 7.2.1-1)}$$

That is, the fundamental process being modeled is diffusion through a porous medium, a process that is well understood and fully accepted throughout the scientific and engineering community.

Certain underlying assumptions need to be addressed. It is assumed that the bulk of the corrosion products inside a waste package is hematite, Fe_2O_3, based simply on the predominance of iron in the composition of internal non-waste form components. This assumption is also used in the EPRI report (EPRI 2000 [DIRS 154149], p. 6-22), based on cited studies (EPRI 2000 [DIRS 154149], p. 6-31) of corrosion products of carbon steel in humid, oxidizing environments that indicate that in the presence of an abundant supply of oxygen, iron would be expected to exist as Fe_2O_3, or FeOOH or $Fe(OH)_3$.

The specific surface area of hematite has been measured by numerous investigators. The range of values obtained varies widely, depending on the morphology of the sample. As can be seen in the expressions for effective saturation and diffusion coefficient, Equations 6.5.1.2.1-27 and 6.5.1.2.1-28, the diffusion coefficient is proportional to the square of the specific surface area, which from Table 6.5-6 varies by about a factor of about 12. This uncertainty is accounted for in the uncertain parameter, Surface_Area_CP (Table 6.5-13), which ranges from 1.0 to 22 $m^2\ g^{-1}$.

The water adsorption isotherm used for the in-package diffusion submodel is compared with another measured isotherm (McCafferty and Zettlemoyer 1971 [DIRS 154378], Figure 3) in Figure 7.2-1, which shows the close agreement between independent investigators. In addition, Figure 6.5-4 shows that hematite over-predicts the amount of water adsorbed compared to nickel oxide, which is one of the other major components of stainless steel (DTN: MO0003RIB00076.000 [DIRS 153044]) that would comprise the products of corrosion of the waste package internal components.

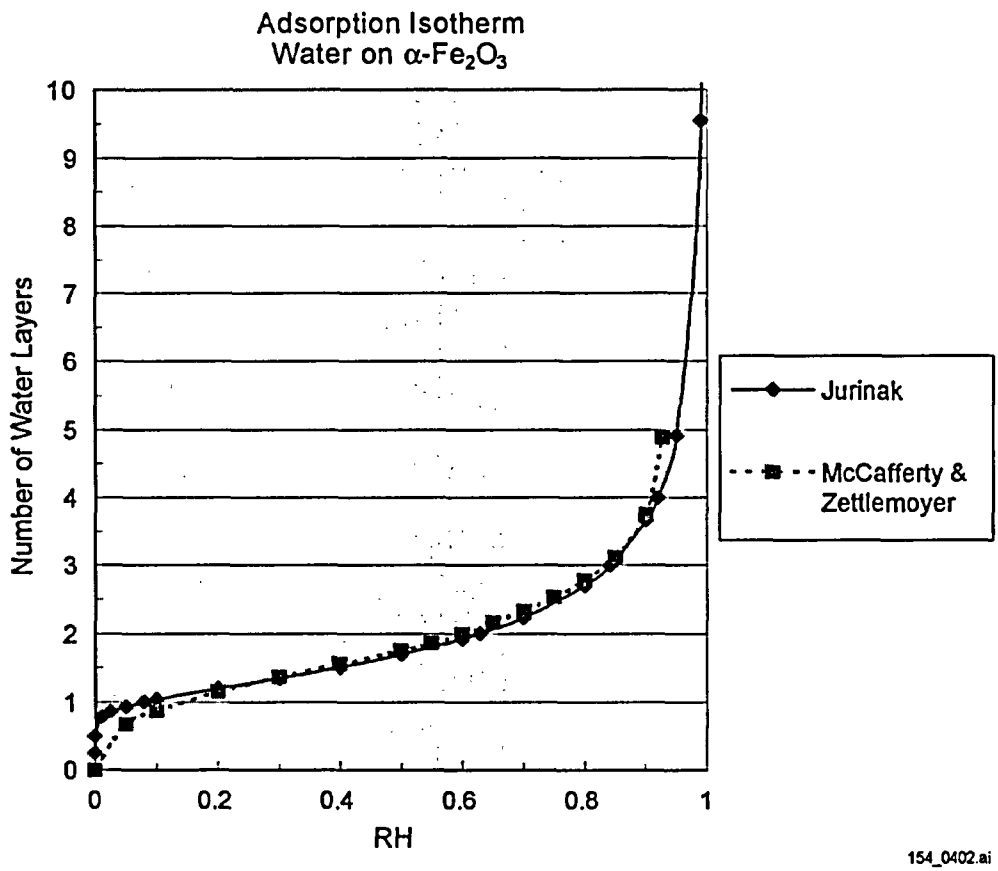

Source: Jurinak curve: Jurinak 1964 [DIRS 154381]; McCafferty and Zettlemoyer curve: McCafferty and Zettlemoyer 1971 [DIRS 154378].

Figure 7.2-1. Adsorption Isotherms for Water Vapor on α- Fe_2O_3

7.2.1.1 Comparison with Electric Power Research Institute 2000

Validation of the in-package diffusion submodel is provided in part by qualitative comparison with a similar model developed independently by a reputable performance assessment program (EPRI 2000 [DIRS 154149]).

The EPRI source-term model, COMPASS2000, implements five compartments–Waste, Corrosion Products, Canister, Invert, Near-Field Rock–of which two (Corrosion Products and Canister) are analogous to portions of the in-package diffusion submodel. The Corrosion Products compartment represents the porous material that is formed after the basket materials are corroded. The Canister compartment represents the failed metal canisters. As with the GoldSim TSPA-LA model, each compartment is treated as a mixing cell in which radionuclide concentrations are assumed to be uniform. Mass balances in each compartment account for the various processes that comprise the model, including transport by diffusion and advection, radioactive decay and ingrowth, sorption, dissolution, and precipitation.

In the EPRI model, EBS transport parameters are assigned fixed values. Both the Corrosion Products and corroded Canister compartments have a porosity of 0.42 (EPRI 2000 [DIRS 154149], p. 6-21), less than the initial porosity of a CSNF waste package, 0.54, as estimated in Section 6.5.1.2.1.3. The EPRI value accounts for the volume occupied by the oxide. A lower value for porosity overestimates releases of radionuclides. However, in the in-package diffusion submodel (Equation 6.5.1.2.1-28), the higher value of porosity increases the estimated diffusion coefficient by only a factor of 1.5, which is small compared to other uncertainties in the model.

The EPRI model assumes a fixed water saturation of 0.35 in both the Corrosion Products and corroded Canister compartments (EPRI 2000 [DIRS 154149], p. 6-21). This value is appropriate for scenarios involving advective transport, but overestimates releases of radionuclides for the expected large fraction of the repository that has no seepage flux, where the only water present is adsorbed water. The in-package diffusion submodel specifically applies to those regions and provides a more realistic estimate of saturation as a function of relative humidity.

The EPRI model uses a fixed value for effective diffusion coefficient of 4.645×10^{-4} m^2 yr^{-1} in both the Corrosion Products and corroded Canister compartments (EPRI 2000 [DIRS 154149], p. 6-22). This converts to 1.472×10^{-7} cm^2 s^{-1} or to 1.472×10^{-11} m^2 s^{-1}. For diffusion through a fully degraded waste package (Equation 6.5.1.2.1-27), this corresponds to a relative humidity of 97.9 percent. Thus, when the humidity is high, the EPRI model and the in-package diffusion submodel agree well. In contrast, the in-package diffusion submodel provides humidity-dependent diffusion coefficient values.

The EPRI model also specifies fixed diffusive lengths, which are defined as the distance from the center of the compartment to the interface of the two contacting compartments. For the Corrosion Products compartment, the diffusion length is 0.046 m; for the Canister compartment, the diffusion length is 0.025 m (EPRI 2000 [DIRS 154149], p. 6-22). In a well-degraded waste package, these are reasonable values, comparable to those used in the in-package diffusion submodel. However, the in-package diffusion submodel accounts for the uncertainty in diffusion lengths at all times, and provides special treatment at early times when large masses of corrosion products are not yet formed.

For the conditions assumed in the EPRI model, namely, at later times when the waste package is extensively corroded, the in-package diffusion submodel agrees quite well with the EPRI model. The primary differences are that the in-package diffusion submodel accounts for a wider range of conditions, including times just after breaches first appear in the waste package. In addition, the in-package diffusion submodel accounts explicitly for the relative humidity, which realistically is the only source of water when seepage does not occur. And finally, in contrast to the EPRI model, the in-package diffusion submodel accounts for uncertainty in diffusive path lengths. Thus, there is agreement between the models, and where differences occur, it is primarily to increase the realism of the diffusive release calculation and to account for uncertainty.

7.2.1.2 Comparison with Lee et al. 1996

Validation of the in-package diffusion submodel is provided in part by comparison with a similar model developed independently and published in technical literature (Lee et al. 1996 [DIRS 100913]).

Lee et al. (1996 [DIRS 100913]) developed a model for steady-state and "quasi-transient" diffusive releases from waste packages into the invert. In this model, perforations in the package are assumed to be cylindrical in shape. The diffusion path consists of the approach to the opening of the perforation from the waste form side; the path through the cylindrical portion of the perforation, which is filled with corrosion products; and the path through the exit disk separating the perforation from the invert. The waste is assumed to be distributed uniformly inside the waste container. The package is approximated by an equivalent spherical configuration, and the underlying invert is represented by a spherical shell surrounding the package.

The model of Lee et al. (1996 [DIRS 100913]) is suitable for the late stages of package degradation, when the waste form has become a mass of porous corrosion products. Although Lee et al. (1996 [DIRS 100913]) assumed the packages failed by localized corrosion, this model should be equally applicable to failure by general corrosion.

The assumption of Lee et al. (1996 [DIRS 100913]) that the waste (i.e., the radionuclide source) is uniformly distributed inside the waste package restricts the applicability of the model and comparison to the in-package diffusion submodel to the times when the waste package has extensively corroded. The object of the in-package diffusion submodel is to provide more realism at earlier and intermediate times, when the waste cannot yet be considered a uniform porous medium. (In the in-package diffusion submodel, the dependence of the diffusive properties of the waste package on the extent of degradation is computed explicitly as a function of time; see Sections 6.5.1.2.1.3.2 and 6.5.3.2.) On the other hand, the fundamental assumption that diffusive releases are controlled by diffusion through breaches that are filled with porous corrosion products may be valid over much of the waste package lifetime, including early times, when stress corrosion cracks are the first breaches to appear. Lee et al. (1996 [DIRS 100913], p. 5-67) assume that the porosity of the perforations is $\phi_{CP} = 0.4$, and the volumetric water content is $\Phi = 10$ percent (so the water saturation in the perforations is a constant $S_w = \Phi/(100\phi_{CP}) = 0.25$). Based on data by Conca and Wright (1990 [DIRS 101582]; 1992 [DIRS 100436]), Lee et al. compute a diffusion coefficient, D ($cm^2\ s^{-1}$), for the porous corrosion products filling the perforations (Lee et al. 1996 [DIRS 100913], p. 5-67):

$$\log_{10} D = -8.255(\pm 0.0499) + 1.898(\pm 0.0464)\log_{10}\Phi, \qquad \text{(Eq. 7.2.1.2-1)}$$

where the numbers in parentheses are one standard deviation. For $\Phi = 10$ percent (the assumed volumetric water content of the perforations), $D = 4.4 \times 10^{-7}\ cm^2\ s^{-1}$. Lee et al. assume that the diffusion coefficient inside the waste package (as opposed to the perforations) is $10^{-5}\ cm^2\ s^{-1}$ (Lee et al. 1996 [DIRS 100913], p. 5-67). As a comparison, the self-diffusion coefficient for water is $2.299 \times 10^{-5}\ cm^2\ s^{-1}$ (Mills 1973 [DIRS 133392], Table III), and for many actinides the diffusion coefficient in water is roughly $5 \times 10^{-6}\ cm^2\ s^{-1}$ (Table 7.2-11). The value for D given

by Equation 7.2.1.2-1 accounts for porosity and saturation, and so is comparable to the value for D_s given by Equation 6.5.1.2.1-28.

Using Equation 7.2.1.2-1 to obtain $D = 4.4 \times 10^{-7}$ cm^2 s^{-1} (for $\Phi = 10$ percent) and dividing this value by the self-diffusion coefficient for water, D_0 (2.299×10^{-5} cm^2 s^{-1}), gives $D/D_0 = 1.91 \times 10^{-2}$. This is greater than the largest value in Table 6.5-10, indicating that the Lee et al. (1996 [DIRS 100913]) model for D represents high relative humidity and high surface area if adsorption is the sole mechanism for water appearing in the corrosion products. If no advection takes place, the assumption of a water saturation of $S_w = 0.25$ is excessive. Using the lower saturations obtained from adsorption isotherms brings the diffusion coefficient from Equation 7.2.1.2-1 into closer agreement with the values in Table 6.5-11. For example, if $S_w = 10^{-5}$, then Equation 7.2.1.2-1 would give $D/D_0 = 8.59 \times 10^{-11}$.

A more detailed calculation can be performed to estimate the surface area of corrosion patches, the amount of water adsorbed at various relative humidity values, the resulting water saturation of the patches, and obtain a diffusion coefficient using Equation 6.5.1.2.1-28 or Equation 7.2.1.2-1. Alternatively, the diffusion coefficient can be obtained using Equation 7.2.1.2-1, in which

$$\Phi = 100 S_{we,CP} \phi_{CP} = 1.194(-\ln RH)^{-0.408}. \qquad \text{(Eq. 7.2.1.2-2)}$$

This equation uses a porosity of $\phi_{CP} = 0.4$, but obtains the effective water saturation from Equation 6.5.1.2.1-27, which is based on the assumption that all water comes from adsorption of water vapor onto hematite having a specific surface area of 9.1 m^2 g^{-1}. Then

$$\begin{aligned} \log_{10} D &= -8.255 + 1.898 \log_{10} \Phi \\ &= -8.255 + 1.898[0.07707 - 0.408 \log_{10}(-\ln RH)] \qquad \text{(Eq. 7.2.1.2-3)} \\ &= -8.109 - 0.775 \log_{10}(-\ln RH). \end{aligned}$$

For example, at $RH = 0.95$, and using $D_0 = 2.299 \times 10^{-9}$ m^{2}s^{-1} (self-diffusion coefficient for water), the effective diffusion coefficient for the patch using Archie's law (Equation 6.5.1.2.1-28) is $D_s = 7.03 \times 10^{-12}$ m^2 s^{-1}, whereas using Equation 7.2.1.2-3, the diffusion coefficient for the corrosion patch is $D = 7.77 \times 10^{-12}$ m^2 s^{-1}. For comparison with Table 6.5-10, $D_s / D_0 = 3.06 \times 10^{-3}$ and 3.38×10^{-3} for these respective cases.

Thus, for those cases where the release rate is controlled by diffusion through porous corrosion products, the in-package diffusion submodel agrees well with the model of Lee et al. (1996 [DIRS 100913]).

The in-package diffusion submodel provides a means for quantifying the uncertainty in diffusion coefficients for diffusion of radionuclides from within the waste form to the invert. Whereas other models consider only the times when the waste package is largely degraded, the in-package diffusion submodel presented here also considers earlier times, starting from the time of the initial waste package breach. The time period between initial breach and complete degradation

of the internal components may span many thousands of years. Thus, the in-package diffusion submodel fills a major time gap in modeling diffusive releases from a waste package. In effect, it provides a rationale for interpolating between essentially a zero diffusion coefficient (due to the absence of water) when a waste package is first breached to a value at a time when porous corrosion products can be expected to fill the waste package with a degree of water saturation capable of transporting radionuclides. The in-package diffusion submodel is considered validated based on corroborating data for input parameters such as water adsorption isotherms and specific surface areas, and based on the agreement with two other waste package diffusion models in areas where these models apply.

7.2.2 Invert Diffusion Submodel

Level I validation is appropriate for the invert diffusion submodel, as it is part of the mechanisms for radionuclide transport from waste package to the drift wall through the invert (see Section 7). In addition, the invert diffusion submodel has the following features:

- Diffusive release from the engineered barrier system does not result in significant releases from the repository system. Under expected conditions, there is a small probability of waste package breaching, and only limited release at all is likely. Therefore, the diffusion properties of the invert that might affect this release are expected to play a small role in the estimate of performance of the system under these conditions. The invert diffusion coefficient is also expected to play a small role for disruptive conditions under which more significant breaching of the waste package might occur. In this case, transport through the invert would be dominated by advection, and diffusion would therefore provide only a minor contribution. Therefore, the diffusion submodel is not expected to play a major role in the assessment of system performance.

- In addition to the above, the invert diffusion properties submodel is not extrapolated beyond the conditions and distances considered in the development of the model. The model applies only on the scale of the EBS and is not applied to larger scales, for example to the unsaturated zone rock.

The invert diffusion coefficient abstraction considers the free water diffusivity for radionuclides as an upper bound. The validation of each of these factors is considered in the following sections.

Section 6.3.4.1.2 describes modification of the self-diffusion coefficient due to temperature. The modification is based on established principles of diffusion in fluids and thus no validation is necessary. The temperature modification is based on the relationship between diffusion and viscosity and temperature (Cussler 1997 [DIRS 111468], p. 114). The relationship between temperature and viscosity of water is available in text books. Thus, it is straightforward to establish a direct relationship between diffusion coefficient and temperature.

7.2.2.1 Self-Diffusion Coefficient of Water

The self-diffusion coefficient of water at 25°C, 2.299×10^{-5} cm^2 s^{-1} (Mills 1973 [DIRS 133392], Table III), provides an upper bound for the diffusion of ionic and neutral inorganic, and

organo-metal species that may be released from a waste package. This assertion is based on the following points, which are discussed in the text following this list:

1. A survey of compiled diffusion coefficients at 25°C shows that simple cation and anion species (excluding the proton and hydroxyl species, which are not appropriate analogs to diffusing radionuclide species) have diffusion coefficients that are smaller than that of water.

2. The self-diffusion coefficient for water at 90°C is larger than compiled diffusion coefficients for simple inorganic species at 100°C.

3. Diffusion coefficients for simple lanthanide and actinide cations are much smaller than the self-diffusion coefficient of water and are expected to be even smaller for their hydroxyl and carbonate complexes.

In a compilation of diffusion coefficients for 97 ionic species , only 3 species, H^+, OH^-, and OD^- have diffusion coefficients at 25°C that are larger than the self-diffusion of water at 25°C (Mills and Lobo 1989 [DIRS 138725], Appendix A, Tables 1.1 to 1.6, pages 314 to 319). Of the 33 ionic species for which Mills and Lobo list diffusion coefficients at 100°C in Tables 1.1 through Table 1.7, only 2 species, H^+ and OH^-, have diffusion coefficients larger than the self-diffusion of water ($H_2{}^{18}O$) at 90°C (Mills and Lobo 1989 [DIRS 138725]; Table 1, page 17). The fact that the self-diffusion of $H_2{}^{18}O$ is less than that of H_2O, and that the self-diffusion of H_2O at 90°C would be greater than that of various ionic species at 100°C, further supports the contention that the self-diffusion of water at 25°C is bounding.

The compilation below (Table 7.2-1) lists a selection of diffusion coefficients for some trivalent lanthanides and actinides. Table 7.2-1 also includes some anions not listed in most compilations but relevant and/or analogous to those expected for radionuclides released from the waste package. The listing shows that the diffusion coefficients for these species are all smaller than the self-diffusion of water, by factors ranging from 1.6 to 14.7. In the case of uranium, the carbonate complexes of the metal species have even smaller diffusion coefficients. Based on the Stokes-Einstein equation (Bird et al. 1960 [DIRS 103524], p. 514, Equation 16.5-4), the diffusivity of a solute in a liquid is inversely proportional to the radius of the diffusing particles. It is therefore expected that other carbonate and hydroxyl complexes, on the basis of the greater size of the complexes relative to the metal species, will also have smaller diffusion coefficients than the metal species listed in Table 7.2-1.

As an alternative, four diffusion coefficients could be used. One coefficient could be used for each charge (mono-, di-, and tri-valent species) and one for the hydroxyl and carbonate complexes of the actinides and lanthanides. At 25°C, the mono-, di-, and trivalent species have bounding values of 2.2×10^{-5} cm^2 s^{-1}, 1.2×10^{-5} cm^2 s^{-1}, 0.7×10^{-5} cm^2 s^{-1}, respectively, as shown in Figure 7.2-2. Although this alternative model is not used for TSPA-LA, it provides further evidence that the use of the self-diffusion coefficient of water bounds the diffusion coefficients of diffusing radionuclide species in the EBS.

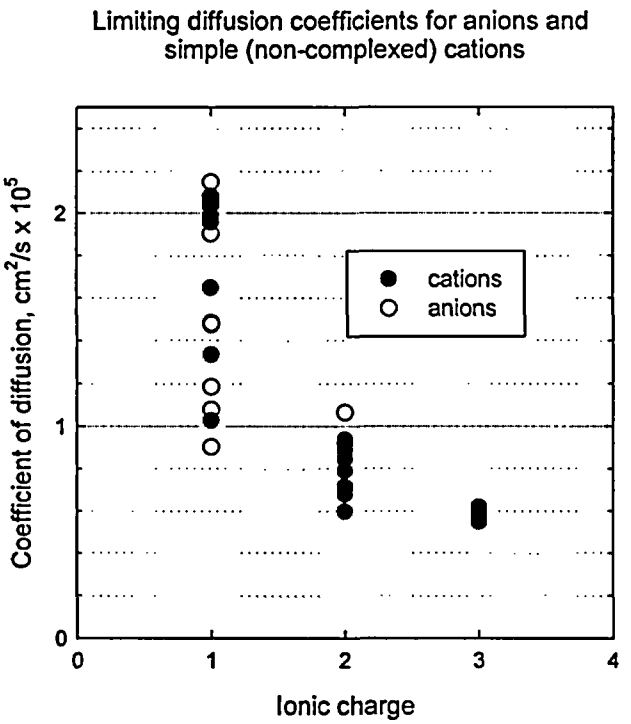

Source: Selected from Mills and Lobo 1989 [DIRS 138725], Appendix I, Tables 1.1 to 1.6; pp. 314 to 319.

Figure 7.2-2. Limiting Diffusion Coefficients for Anions and Simple (Non-Complexed) Cations

Table 7.2-1. Compilation of Diffusion Coefficients for Yttrium, Technetium, Molecular Iodine, and Lanthanide and Actinide Species

Species	D^*, $cm^2\ s^{-1}$	Comments	Reference
Y^{3+}	$5.7 \pm 0.06 \times 10^{-6}$	25°C	Mills and Lobo 1989 [DIRS 138725], p. 220.
TcO_4^-	$1.48 \pm 0.01 \times 10^{-5}$	25°C	Mills and Lobo 1989 [DIRS 138725], p. 105.
I_2^-	$1.36 \pm 0.04 \times 10^{-5}$	25°C; 0.075 M H_2SO_4	Cantrel et al. 1997 [DIRS 138551], Table 5.
La^{3+}	5.42×10^{-6}	25°C; 0.1 M $NaClO_4$; $u = 6.33\ cm^2\ s^{-1}\ V^{-1}$	Rosch and Khalkin 1990 [DIRS 138739], calculated from mobility data reported in Table 1, p. 103.[a]
La^{3+}	$6.18 \pm 0.06 \times 10^{-6}$	25°C	Mills and Lobo 1989 [DIRS 138725], p. 93.
Ce(III)-carbonate	$2.68 \pm 0.12 \times 10^{-6}$	5.5 M K_2CO_3, pH 13, presumably at 25°C.	Haltier et al. 1990 [DIRS 138643], p. 111.
Ce(IV)-carbonate	$1.56 \pm 0.07 \times 10^{-6}$	5.5 M K_2CO_3, pH 13, presumably at 25°C.	Haltier et al. 1990 [DIRS 138643], p. 111.
Eu^{3+}	4.38×10^{-6}	25°C; 0.1 M $NaClO_4$; $u = 5.12\ cm^2\ s^{-1}\ V^{-1}$	Rosch and Khalkin 1990 [DIRS 138739]; calculated from mobility data reported in Table 1, p. 103.[a]
Gd^{3+}	5.24×10^{-6}	25°C; 0.1 M $NaClO_4$; $u = 6.12\ cm^2\ s^{-1}\ V^{-1}$	Rosch and Khalkin 1990 [DIRS 138739]; calculated from mobility data reported in Table 1, p. 103.[a]

Table 7.2-1. Compilation of Diffusion Coefficients for Yttrium, Technetium, Molecular Iodine, and Lanthanide and Actinide Species (Continued)

Species	D^*, $cm^2 s^{-1}$	Comments	Reference
Tb^{3+}	5.01×10^{-6}	25°C; 0.1 M $NaClO_4$; $u = 5.85\ cm^2 s^{-1} V^{-1}$	Rosch and Khalkin 1990 [DIRS 138739]; calculated from mobility data reported in Table 1, p. 103.[a]
Tm^{3+}	5.10×10^{-6}	25°C; 0.1 M $NaClO_4$; $u = 5.96\ cm^2 s^{-1} V^{-1}$	Rosch and Khalkin 1990 [DIRS 138739], calculated from mobility data reported in Table 1; p. 103.[a]
Yb^{3+}	5.23×10^{-6}	25°C; 0.1 M $NaClO_4$; $u = 6.11\ cm^2 s^{-1} V^{-1}$	Rosch and Khalkin 1990 [DIRS 138739], calculated from mobility data reported in Table 1; p. 103.[a]
Lu^{3+}	5.01×10^{-6}	25°C; 0.1 M $NaClO_4$; $u = 5.85\ cm^2 s^{-1} V^{-1}$	Rosch and Khalkin 1990 [DIRS 138739], calculated from mobility data reported in Table 1; p. 103.[a]
$UO_2(CO_3)_3^{4-}$	3.6×10^{-6}	1 M total carbonate, 22°C	Perry et al. 1988 [DIRS 138732], p. 302.
$UO_2(CO_3)_3^{4-}$	$3.0 \pm 0.7 \times 10^{-6}$	0.2 M total carbonate, pH 9.8, 25°C	Perry et al. 1988 [DIRS 138732], p. 302.
$UO_2(CO_3)_3^{5-}$	$3.81 \pm 0.26 \times 10^{-6}$	0.75 M Na_2CO_3, 0.6 M $NaClO_4$, pH 11.5, presumably at 25°C	Haltier et al. 1990 [DIRS 138643], p. 110.
UO_2^{++}	6.8×10^{-6}	25°C	Millard and Hedges 1996 [DIRS 138677], p. 2141.
UO_2-carbonate	1.9×10^{-6}	Calculated using Stokes-Einstein with a radius of 8 Å at 10°C	Millard and Hedges 1996 [DIRS 138677], p. 2141.
Np(V)-carbonate	7×10^{-6}	Calculated using Stokes-Einstein with a radius of 3.4 Å at 25°C	Tsukamoto et al. 1994 [DIRS 138747]; p. 469.
Am^{3+}	5.78×10^{-6}	25°C; 0.1 M $NaClO_4$; $u = 6.75\ cm^2 s^{-1} V^{-1}$	Rosch and Khalkin 1990 [DIRS 138739]; calculated from mobility data reported in Table 1; p. 103.[a]
Am^{3+}	$5.95 \pm 0.06 \times 10^{-6}$	25°C, in 0.0002 M $Nd(ClO_4)_3$	Mills and Lobo 1989 [DIRS 138725]; p. 131.
Cf^{3+}	4.39×10^{-6}	25°C; 0.1 M $NaClO_4$; $u = 5.13\ cm^2 s^{-1} V^{-1}$	Rosch and Khalkin 1990 [DIRS 138739]; calculated from mobility data reported in Table 1; p. 103.[a]
Cf^{3+}	$5.50 \pm 0.06 \times 10^{-6}$	25°C, in 0.0002 M $Nd(ClO_4)_3$	Mills and Lobo 1989 [DIRS 138725]; p. 132.
Es^{3+}	$5.50 \pm 0.06 \times 10^{-6}$	25°C, in 0.0002 M $Nd(ClO_4)_3$	Mills and Lobo 1989 [DIRS 138725]; p. 132.

[a] Calculation of diffusion coefficients from reported ionic mobilities (Rosch and Khalkin 1990 [DIRS 138739]; Table 1). The mobilities (u) were measured in 0.1 M NaClO4 at various pHs (below the pH of hydrolysis) and were slightly larger at pHs greater than 5, and these are the data that were used for the calculation. The equation used to calculate the diffusion coefficient is: $D^* = (kT/(|z|e))\ u$, where k is Boltzmann constant ($J\ K^{-1}$), T is the temperature (K), z is the valence of the ion, e is the elementary charge (C), and u is the mobility ($cm^2\ s^{-1}\ V^{-1}$) (Atkins 1990 [DIRS 111464], Box 25.1, Einstein relation, p. 765).

7.2.2.2 Modification for Porosity and Saturation

Validation of the dependence of invert diffusion coefficient on porosity and saturation is provided by comparison with measured data obtained independently of the data used for model development. Data used for validation are obtained from diffusivity measurements for crushed tuff using electrical conductivity measurements (CRWMS M&O 2000 [DIRS 156680]) and from direct measurements of diffusivity between machined cubes of tuff (Hu et al. 2001 [DIRS 161623]).

Conca and Wright (1992 [DIRS 100436]) and Conca et al. (1993 [DIRS 170709]) obtained diffusion coefficients from electrical conductivity measurements for various granular materials, including tuff, with volumetric moisture content ranging from 0.5 percent to 66.3 percent. A statistical fit of the data (Conca and Wright 1992 [DIRS 100436], Figure 2; Conca et al. 1993 [DIRS 170709], Figure 2; listed in Table 4.1-14) ranging from 1.5 percent to 66.3 percent volumetric moisture content, based on Archie's law, results in the model used in TSPA-LA (Section 6.3.4.1.1 and Appendix G):

$$\begin{aligned} D &= D_0 \phi^{1.863} S_w^{1.863} 10^{ND(\mu=0.033,\sigma=0.218)} \\ &= D_0 \theta^{1.863} 10^{ND(\mu=0.033,\sigma=0.218)}, \end{aligned} \qquad \text{(Eq. 7.2.2.2-1)}$$

where $\theta = \phi S_w$ is the volumetric moisture content (fraction: m^3 water m^{-3} rock). The object of this validation is to show that the diffusion coefficient given by Equation 7.2.2.2-1 obtained from the electrical conductivity measurements of Conca and Wright (1992 [DIRS 100436]) and Conca et al. (1993 [DIRS 170709]) tends to overestimate the diffusivity of invert materials.

The diffusion coefficient has also been determined specifically for tuff, also using electrical conductivity measurements (CRWMS M&O 2000 [DIRS 156680], Tables A-1 and A-2). These data are listed in Table 7.2-2 and are plotted in Figure 7.2-3, along with the mean value and plus and minus three standard deviations from Equation 7.2.2.2-1. This plot shows that the fit to the measured diffusion coefficient data (Equation 7.2.2.2-1) overestimates the diffusion coefficient relative to *The Determination of Diffusion Coefficient of Invert Materials* (CRWMS M&O 2000 [DIRS 156680], Tables A-1 and A-2). This plot was created using Microsoft Excel; see Appendix G, Worksheet: Validation, p. VII-10.

The electrical conductivity measurements by Conca and Wright (1992 [DIRS 100436]) and Conca et al. (1993 [DIRS 170709]) use conductivity as an analog for diffusivity. While the analog is known to be valid in fully saturated media, its application to unsaturated media, particularly at low moisture contents, is questionable due to the difficulty in preparing samples and in making reliable electrical contact between the electrical leads and the samples. To avoid these problems, Hu et al. (2001 [DIRS 161623]) measured diffusive tracer concentrations in tuff cubes directly using laser ablation coupled with inductively coupled plasma-mass spectrometry (LA-ICP-MS), rather than relying on electrical analogs.

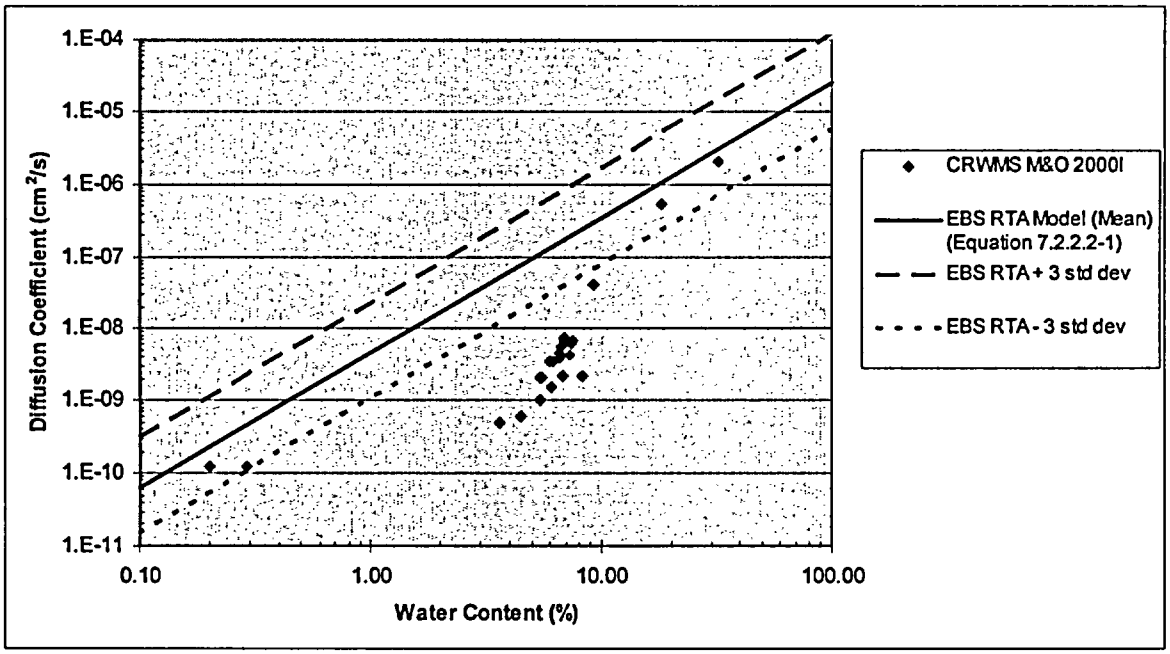

Source: CRWMS M&O 2000 [DIRS 156680].

Figure 7.2-3. Comparison of EBS Radionuclide Transport Abstraction Invert Diffusion Submodel (Equation 7.2.2.2-1) with Measured Diffusion Coefficients for Tuff

Table 7.2-2. Diffusion Coefficient of Crushed Tuff Invert Materials

Sample	Volumetric Moisture Content (%)	Diffusion Coefficient ($cm^2 s^{-1}$)
1	32.13	2.02×10^{-6}
2	18.15	5.40×10^{-7}
3	9.26	4.05×10^{-8}
4	7.03	6.75×10^{-9}
5	6.97	7.45×10^{-9}
6	6.89	6.73×10^{-9}
7	6.75	5.42×10^{-9}
8	6.63	4.39×10^{-9}
9	6.63	3.76×10^{-9}
10	6.23	3.40×10^{-9}
11	6.00	3.43×10^{-9}
12	5.55	2.04×10^{-9}
13	5.46	2.04×10^{-9}
14	8.29	2.24×10^{-9}

Table 7.2-2. Diffusion Coefficient of Crushed Tuff Invert Materials (Continued)

Sample	Volumetric Moisture Content (%)	Diffusion Coefficient ($cm^2 s^{-1}$)
15	7.54	6.81×10^{-9}
16	7.36	6.21×10^{-9}
17	7.22	4.38×10^{-9}
18	6.84	2.19×10^{-9}
19	6.11	1.55×10^{-9}
20	5.41	9.97×10^{-10}
21	4.45	6.19×10^{-10}
22	3.64	5.00×10^{-10}
23	0.29	1.24×10^{-10}
24	0.20	1.25×10^{-10}

Source: CRWMS M&O 2000 [DIRS 156680], Tables A-1 and A-2.

LA-ICP-MS has recently evolved as a powerful analytical tool for solid samples (Russo et al. 2000 [DIRS 155697]). It can simultaneously determine a large number of chemical elements with low detection limits. Laser ablation uses an intense burst of energy delivered by a short laser pulse to vaporize a minute sample (in the range of nanograms) from a small area. Several spot sizes can be selected (from 25 μm to 200 μm in diameter), allowing a choice of appropriate spot size for different applications. A smaller spot size will sample less solid material, leading to lower analytical precision, but allowing more heterogeneity to be observed. A single laser pulse reveals surface compositions, while multiple pulses allows compositions to measured at various depths below the surface, with the crater depth proportional to the number of laser pulses applied. For example, two pulses reach about 4 μm into the tuff matrix (Hu et al. 2001 [DIRS 161623], p. 22), and 50 pulses ablates to a depth of about 35 μm (Hu et al. 2001 [DIRS 161623], Figure 6).

In the approach of Hu et al. (2001 [DIRS 161623]), a machined 1.5-cm tuff cube containing a tracer was placed in contact with a cube not containing the tracer, both under the same thermodynamic conditions. The tracer is allowed to diffuse from the tracer-containing cube to the other. Tracers were chosen based on their chemical similarity to radionuclides of interest. The source cube was vacuum-saturated with a tracer solution mixture of NaBr, $NaReO_4$, CsBr, and RbBr; both Br^- and perrhenate (ReO_4^-) act as nonsorbing tracers. The sink cube was also vacuum-saturated, but had no tracers. Source and sink cubes were separately placed inside a humidity chamber within an incubator maintained at 22°C until the cubes equilibrated to a constant weight (13 days). The cubes were then clamped together in the relative humidity (*RH*) chamber to start the diffusion test. After 87 days, the diffusion test was stopped by separating the source and sink cubes. The surface and depth distribution of the tracer was then mapped using LA-ICP-MS. The mapping was done on the interface, the far side face (opposite side from the interface), and along the side perpendicular to the interface.

Measurements along the outside surface of the sink cube indicated that a nonsorbing tracer (ReO_4^-) diffused along the surface at a rate similar to its aqueous diffusion rate in bulk water (Hu et al. 2001 [DIRS 161623], pp. 21 and 22). This result was reasonable because the tuff cubes were located in the high-RH chamber, with the likely presence on the outside of the cube

of a thick water film that behaves like bulk water. These measurements provided a bounding value for the diffusivity of the tracer, comparable to the diffusion coefficient of 1.48×10^{-5} cm^2 s^{-1} (Table 7.2-1) for its analog, TcO_4^-. In other words, in regions on the tuff samples that were saturated or at least had high water saturation, the direct diffusivity measurements agreed with theoretical predictions.

Hu et al. also measured tracer concentrations at greater depths into the cube by using the laser ablation technique to probe into the surface. They found that internal diffusion coefficients, at depths of 60-410 μm, were on the order of 10^{-12} cm^2 s^{-1} (Hu et al. 2001 [DIRS 161623], p. 22). The measured volumetric water content of the tuff matrix was 8.9 percent (Hu et al. 2001 [DIRS 161623], p. 25). The mean diffusion coefficient predicted by the invert diffusion properties submodel (Equation 7.2.2.2-1) would then be 2.6×10^{-7} cm^2 s^{-1}. This is a factor of 10^5 larger than the measurement. Thus, the diffusion coefficient throughout most of a grain of crushed tuff is lower than that predicted by the invert diffusion properties submodel. This provides corroborating evidence that the invert diffusion properties submodel overestimates releases of radionuclides from the EBS. These data also show that the overestimation of diffusivities in the invert diffusion properties submodel may be excessive. However, insufficient data exist to reduce the uncertainty in this model, and, if this additional uncertainty were included in the invert diffusion submodel, estimated releases of radionuclides from the EBS would be reduced and no longer be bounding. Because the model has a low impact on repository performance, the degree of uncertainty in this model is acceptable for TSPA-LA.

The study by Hu et al. (2001 [DIRS 161623]) was primarily a development of the technique for using LA-ICP-MS of microscale profiling of the distribution of diffusing tracers. However, in the process, some preliminary data were obtained that can be used to corroborate the electrical conductivity measurements of Conca and Wright (1992 [DIRS 100436]) and Conca et al. (1993 [DIRS 170709]).

Sections 7.2.1 and 7.2.2 have demonstrated that the component models of the EBS transport model meet Level I validation. Based on the validation results, the EBS transport model is adequate for its intended use.

7.2.3 Results of Independent Model Validation Technical Review of the EBS Flow and Transport Models

An independent model validation technical review of the EBS flow and transport models was conducted, as specified in the TWP (BSC 2004 [DIRS 170775], Section 2.2.3). This model validation approach is justified based on requirements of AP-SIII.10Q, Section 5.3.2 c), where independent technical review is listed as an appropriate method for model validation. The results of the independent model validation technical review of the EBS flow and transport models are presented in a memo (Jin 2004 [DIRS 170952]), a verbatim copy of which follows.

MEMO

Date: July 22, 2004

To: James Schreiber, Cliff Howard, and Kathryn Knowles, Yucca Mountain Project

From: Minquan Jin, INTERA Inc., Austin, Texas

RE: **Independent Model Validation Technical Review of the EBS Flow and Transport Sub-Models of the Radionuclide Transport Abstraction Model for the Yucca Mountain Project**

Pursuant to your request to perform an independent model validation, a technical review is being conducted of three sub-models of the Engineered Barrier System (EBS) Radionuclide Transport Abstraction model as documented in ANL-WIS-PA-000001 Rev 01K, I have performed and documented the following review. This review is being conducted consistent with the requirements of the Technical Work Plan TWP-MGR-PA-000020 Rev 00. The three sub-models are the EBS flow sub-model, EBS transport sub-model, and EBS UZ interface sub-model. This memo describes the results of my review of the EBS flow sub-model and EBS transport sub-model only.

Review Qualifications

Section 2.2.4 of the Technical Work Plan TWP-MGR-PA-000020 Rev 00 describes the qualifications and responsibilities of the independent model validation technical reviewer. Based on the evaluation of the information provided in the document, I qualify to perform the work described for the following reasons. (1). I have not contributed to the development of the model assumptions, parameters, or implementing algorithms documented in ANL-WIS-PA-000001 Rev 01K, (2). I have a PhD degree in Petroleum and Geosystems Engineering and am a Licensed Professional Engineer in the State of Texas, and (3). I have more than ten years of professional expertise in modeling fluid flow and transport in porous media. More detailed information regarding my credentials can be found in the resume attached.

Appropriateness and Adequacy of the Conceptual Model

Document ANL-WIS-PA-000001 Rev 01K describes the conceptual model used to determine the rate of radionuclide release from EBS to the unsaturated zone. This model consists of two main components—a flow model and a transport model. The flow model defines the pathways for water flow in the EBS and specifies how the flow rate is computed for each pathway. The transport model considers the transport of radionuclide through each pathway. Sections 6.1, 6.3.1.1, 6.3.2, and 6.3.3 of the document provide a complete and clear description of the fundamental bases of the conceptual flow model. Sections 6.3.1.2 and 6.3.4 provide detailed

MEMO (Continued)

description of the fundamental bases of the conceptual transport model. In addition to the conceptual models developed, several alternative conceptual models are also considered and presented in Section 6.4. These alternative models are screened out in analysis and the rationales are summarized in Table 27. Based on the review of these sections and other related sections of the document, it is my professional judgment that both the flow model and the transport model incorporate the important design features, physical phenomena, and the relevant mechanisms that have a significant effect on the flow and transport of radionuclide in EBS.

The conceptual flow sub-model logically divides the EBS components into three domains: the waste form, the waste package corrosion products, and the invert. As a result, flow and transport in these domains is treated separately. The output of the waste form domain feeds into the corrosion products domain. The output of the corrosion products domain, in turn, feeds into the invert. Separation of domain makes it easier to identify the eight unique pathways of water flow through EBS. This approach and the algorithms therefore capture all known flow pathways into and from the EBS components and simplify a complicated problem. The magnitude of seepage fluid passing through the drip shield and the waste package is accounted for using the flux splitting sub-model.

The transport sub-model consists of the same three domains as the flow sub-model, the waste form, the waste package corrosion products, and the invert. The waste form is the source of all radionuclides where degradation processes occur. Dissolved radionuclide species are transported by advection and/or diffusion to the waste package corrosion products domain. Radionuclide species released from the corrosion products domain are then transported to the invert domain and interact with the crushed tuff in the invert by adsorption processes. Advective transport is considered when water enters the waste form domain and is able to flow through the EBS. Diffusive transport between each of the domains occurs regardless of whether water is flowing though the EBS. The properties that affect the rate of transport of radionuclides through each domain include the volume, porosity, water saturation, sorption, temperature, diffusion cross sectional area, and diffusive path length. These properties are well defined and discussed in details in the document. The concentration of each radionuclide during transport is limited by the sum of its solubility limit and the presence of any colloidal particles that may act as reversible or irreversible carriers for the radionuclide.

In general, the document sufficiently describes the uncertainties in model parameters, processes, and assumptions. The potential impacts of these uncertainties are discussed. In addition to the description of the conceptual model, the modeling assumptions are clearly defined, discussed, and justified as appropriate for the intended use of the two sub-models. This is done in a separate section (Section 5). Based on the review of the sections of the document described above, it is my professional judgment that the conceptual flow model and the conceptual transport model developed for water flow and radionuclide transport through the EBS are appropriate and adequate for their intended use.

Appropriateness of the Mathematical Representation of the Conceptual Model

Section 6.5 of the report provides a complete and clear description of the mathematic representation of the conceptual flow model and the conceptual transport model. As with any engineering mathematical model, assumptions and simplifications have been made in the development of the mathematical representations of the conceptual EBS flow sub-model and the transport sub-model. Review of the document indicates that the mathematical formulations developed provide justifiable representations of the technically important mechanisms identified in the conceptual models. Assumptions which are used to formulate models are justified and have a defensible technical basis (Section 5). The important parameters for the mathematical models are

MEMO (Continued)

derived from experimental data and by comparison of the experimental data to model calculations (Sections 6.5.1.1 and 6.5.1.2). Uncertainties associated with experimental data are quantified. For

the parameters with high uncertainty, assumptions are made such that the parameters used would predict a higher radionuclide release rate through the system. Based on review of this information, I conclude that both mathematical representations of the flow model and the transport model are appropriate for their intended use.

Appropriateness of the Key Model Assumptions

In Section 5 of the document, a number of key assumptions are identified and discussed in detail. The table below presents an assessment of the assumptions.

Assumptions	Comments
1. All seepage into the drift falls on the crown of the drip shield, and, in the absence of a drip shield, all seepage falls on the crown of the waste package.	I agree with the assumption and assessment as provided by the author. The assumption is reasonable and appropriate.
2. There is no evaporation of seepage water from the surface of the drip shield.	This assumption will overestimate water flow, since water evaporation will occur upon contact with a hot object. Nevertheless, this assumption has no adverse effect on the model results and only maximizes the water flux through the EBS.
3. Evaporation of water from the surface or interior of a waste package does not occur.	Same comments as item #2 above.
4. Chemical reactions in the EBS neither produce nor consume water and therefore do not affect water mass balance in the EBS	I concur with the author. This is a very reasonab assumption. In general, the consumption or production of water tends to be negligible.
5. A thin film of adsorbed water is assumed to always exist on the surfaces of internal waste package components and corrosion products in a breached waste package	I agree with the assumption and assessment as provided by the author. The assumption allows radionuclides to diffuse through the waste package interior and through corrosion products under no liquid flux condition. This assumption maximizes the rate of radionuclide transport through the EBS.
6. The products of the corrosion of all internal waste package components, except for the fuel rods and spent nuclear fuel, are Fe_2O_3 (hematite).	I concur with the author. The assumption is reasonable in the absence of detailed compositional data, corrosion process information, and adsorption isotherms for the numerous other potential steel corrosion products. The limited experimental data presented in the report also appear to support the validity of this assumption.

MEMO (Continued)

Assumptions	Comments
7. The void volume of a waste package remains constant as the internal components degrade.	I agree with the assumption and assessment as provided by the author. Reduction of void volume due to corrosion is a time-dependent variable and difficult to quantify. Nevertheless, a reduction in void volume can only reduce the diffusive releases of radionuclides. This assumption therefore maximizes the rate of radionuclide release through the EBS.
8. No corrosion products exist in the invert.	This is a reasonable assumption. It reduces the potential effectiveness of the invert as a transport barrier, and therefore, maximizes the rate of radionuclide release through the EBS.

As stated in the table above, the assumptions used for model development and application are appropriate. This is standard practice and is appropriate.

Evaluation of Model Validation

Documentation of the flow sub-model validation is presented in Section 7.1 and was performed in accordance with AP-2.27Q, *Planning for Science Activities*, and AP-SIII.10Q according to the author. Validation is achieved through comparison of the model calculation results to qualified experimental data collected during associated testing. The method of model validation by comparison of model calculation results to that of the experimental data is standard practice and therefore the model validation method used here is appropriate. Because of the large spread of the experimental data and the uncertainties associated with the chaotic nature of the flow of droplets on a corroded surface, the model validation criterion is that the predictions of the abstraction bound the experimental measurements. This is also standard practice and is appropriate. The results documented in the report demonstrate that the drip shield and waste package flux splitting sub-models bound the experimental data. Calculations could not be checked for accuracy because of their complexity. The calculations do, however, appear to be reasonable and consistent with the methodology. Review of the document indicates to me that the validation calculation of the flow sub-model is adequate and appropriate.

Documentation of the transport sub-model validation is presented in Section 7.2. Validation is achieved through comparison of the model calculation results to qualified literature data. The method of model validation by comparison of model calculation results to that of the literature data is standard practice and therefore the model validation method used here is also appropriate. Section 7.2.1 describes a comparison of the in-package diffusion sub-model to the model reported by Electric Power Research Institute Phase 5 report (EPRI 2000) and a model by Lee et al. (1996). The comparison shows that the final diffusion coefficients calculated by each model generally agree. Section 7.2.2 provides a compilation of literature data to show that the use of self-diffusion coefficient of water at 25°C for radionuclide species in the invert diffusion sub-model as an upper bound is appropriate. A comparison of the mean diffusion coefficient predicted by the invert diffusion sub-model with experimental data reported by Conca and Wright (1992) and by Hu et al. (2001) indicates that the invert diffusion sub-model significantly overestimates releases of radionuclides from the EBS. It is recommended that further studies be conducted to reduce the uncertainties of this model predication. Nevertheless, this overestimation has no adverse effect on the model results and only maximizes the release of radionuclides through the EBS. Review of the document indicates to me that the model validation meets Level I validation criteria and the model developed is therefore adequate for its intended use.

MEMO (Continued)

Evaluation of Model Validation Criteria

In Section 2.2.4 of Technical Work Plan TWP-MGR-PA-000020 Rev 00, a number of model validation criteria are identified. The tables below present an assessment of these criteria.

Evaluation of Flow Sub-model Validation Criteria

Criteria	Criteria met?	Response
a) The approach and algorithms described in the document and provided to the TSPA capture all known flow pathways into and from EBS components.	Yes	Section 6.3 of the document provides detailed information on the approach and algorithms of the flow model and Table 21 summarizes all known flow pathways and related parameters.
b) Modeling assumptions are clearly defined, discussed, and justified as appropriate for the intended use of the model.	Yes	Section 5 of the document presents a clear and complete description of the model assumptions and justifications.
c) Uncertainties in parameters, processes, and assumptions are sufficiently described, and impacts of these uncertainties discussed.	Yes	Input parameters are documented in Section 4. Uncertainties are discussed throughout the document whenever the related parameters are used.
d) The overall technical credibility of the approach, including assumptions, parameters, equations, and the TSPA implementation, are sufficient for the model's intended use.	Yes	The conceptual model is well presented and documented. Some of the assumptions are made such that the model would overestimate flow rate and therefore the model is well suited for its intended use.

Evaluation of Transport Sub-model Validation Criteria

Criteria	Criteria met?	Response
a) The approach and algorithms described in the document and provided to TSPA address all known modes of radionuclide transport within and from the EBS components.	Yes	The detailed explanation on the approach and algorithms of the transport model developed is presented in Sections 6.3 and 6.5 of the document. All known transport modes and related parameters are summarized in Table 22.
b) Modeling assumptions are clearly defined, discussed, and justified as appropriate for the intended use of the model.	Yes	Section 5 of the document presents a clear and complete description of the model assumptions and justifications.

MEMO (Continued)

Criteria	Criteria met?	Response
c) Uncertainties in parameters, processes, and assumptions are sufficiently described, and impacts of these uncertainties discussed.	Yes	Input parameters are documented in Section 4. Uncertainties are discussed throughout the document whenever the related parameters are used.
d) The overall technical credibility of the approach, including assumptions, parameters, equations, and the TSPA implementation, are sufficient for the model's intended use.	Yes	A great amount of information is given in the development, formulation and validation of the conceptual model. Review of the document indicates to me that EBS transport sub-model is adequate for its intended use.

Conclusions

The EBS flow sub-model and transport sub-model documented in report ANL-WIS-PA-000001 Rev 01K incorporate important design features, physical phenomena, and appropriate assumptions. Sufficient technical bases and justifications are provided for the model development and mathematical representation. Assumptions are well documented and justified and some of the model assumptions are made such that the model would overestimate water flow rate and radionuclide release through the EBS. Uncertainties are adequately and realistically bounded. Model validations are performed either by comparison of the model calculation results to the experimental data or by comparison to the literature values. It is my professional judgment that both EBS flow sub-model and EBS transport sub-model are adequate for their intended use.

References

Conca, J.L. and Wright, J. 1992. "Diffusion and Flow in Gravel, Soil and Whole Rock." Applied Hydrogeology, 1, 5-24. Hanover, Germany: Verlag Heinz Heise GmbH. TIC: 224081.

EPRI (Electric Power Research Institute) 2000. Evaluation of the Candidate High-Level Radioactive Waste Repository at Yucca Mountain Using Total System Performance Assessment, Phase 5. 1000802. Palo Alto, California: Electric Power Research Institute. TIC: 249555.

Hu, Q.; Kneafsey, T.; Wang, J.S.Y.; Roberts, J.; and Carlson, S. 2001. Summary Report on [Phase I] Feasibility Study of In-Drift Diffusion. LBNL-49063. Berkeley, California: Lawrence Berkeley National Laboratory. ACC: MOL.20030225.0125.

Lee, J.H.; Chambré, P.L.; and Andrews, R.W. 1996. "Mathematical Models for Diffusive Mass Transfer from Waste Package Container with Multiple Perforations." Proceedings of the 1996 International Conference on Deep Geological Disposal of Radioactive Waste, September 16-19, 1996, Winnipeg, Manitoba, Canada. Pages 5 61 - 5 72. Toronto, Ontario, Canada: Canadian Nuclear Society. TIC: 233923.

7.3 EBS-UZ INTERFACE SUBMODEL

The output of the invert domain feeds into the unsaturated zone through the EBS-UZ interface submodel. In the *EBS RT Abstraction*, the invert is modeled as a single-continuum porous medium whereas the adjacent UZ is modeled as a dual continuum fracture-matrix medium. The model is described in detail in Section 6.5.3.6.

The mass flux from the invert flows into the top layer of the middle zone in the UZ. The portion of the advective flux from the invert that is attributable to the seepage flux (F_1) flows into the UZ fractures. The imbibition flux into the invert (F_7) flows out of the invert into the UZ matrix. The diffusive flux from the invert can go into both UZ continua based on the concentration gradient and effective diffusion coefficient. The diffusive area remains the same because they are overlapping continua. The advective flux flowing through the UZ fracture cells in the middle zone is given by the greater of the advective flux out of the invert and the steady state UZ fracture flux. The advective flux in the two outer zones is given by the steady state UZ flow in each continuum at the repository horizon; the drift shadow effects are ignored.

For TSPA-LA, a semi-infinite zero concentration boundary condition is used for the EBS-UZ interface. This is approximated by applying an effective zero-concentration boundary at approximately three drift diameters below the invert-UZ boundary into the UZ. By moving the zero concentration boundary some distance below the invert, a more realistic diffusive gradient through the invert is achieved.

The EBS-UZ interface submodel of the *EBS RT Abstraction* provides input to the unsaturated zone radionuclide transport model in *Particle Tracking Model and Abstraction of Transport Processes* (BSC 2004 [DIRS 170041]). The appropriate level of confidence identified for unsaturated zone radionuclide transport is Level II. Therefore, Level II also represents appropriate level of confidence for the EBS-UZ interface submodel of the *EBS RT Abstraction.*

Section 7.3.1.1 describes the semi-analytical fracture-matrix partitioning model that is used to validate the EBS-UZ interface submodel of the *EBS RT Abstraction.* Section 7.3.1.2 compares the two interface models, and Section 7.3.1.3 provides an evaluation of differences between the two models and discussion of the applicability and suitability of the EBS-UZ interface submodel for TSPA-LA transport modeling.

7.3.1 Validation of EBS-UZ Boundary Condition Implementation in TSPA-LA

In this section, the predictions of the analytical fracture-matrix partitioning model developed in *Drift-Scale Radionuclide Transport* (BSC 2004 [DIRS 170040]) are compared with the fracture-matrix partitioning at the EBS-UZ boundary predicted by the *EBS RT Abstraction* (Section 6.5.3.6). Because the two models are conceptually different, exact agreement in their results is not expected. The objective of the validation is to demonstrate qualitative agreement, i.e., that the trends and general qualitative behavior of the EBS-UZ boundary condition implementation in the *EBS RT Abstraction* are also seen in a model that has been independently developed and uses a completely different solution approach.

7.3.1.1 Description of Fracture-Matrix Partitioning Model

The fracture-matrix partitioning model, described in *Drift-Scale Radionuclide Transport* (BSC 2004 [DIRS 170040]), is developed for the case where there is no seepage inside the drift. It may be used to compute the relative fraction of the radionuclide mass entering the UZ matrix and UZ fracture from the invert by the process of diffusion. The fracture-matrix partitioning model is extended to the case where there is seepage through the drift by specifying that all mass leaving the invert by advection enters the UZ fractures, i.e., there is no partitioning in this case.

The fracture-matrix partitioning model considers only that part of the invert that is directly underneath the waste package, and effectively treats the invert as a single continuum by assuming zero saturation in the intergranular pores of the invert and a fully saturated intragranular invert continuum, in order to compute a single continuum (or bulk) water content. A rectangular geometry is used for the invert, with a vertical length sampled from a uniform distribution whose maximum is the maximum thickness of the invert directly under the package and whose minimum is the thickness of the invert under the projected edges of the package. The invert width is defined to be equal to the half-fracture spacing in the UZ, which is the reciprocal of the sampled value of the fracture frequency. The model assumes two-dimensional steady state diffusion in a homogeneous invert material. The governing mass transport equation is the Laplace equation:

$$\nabla^2 C_I(x,y) = 0. \qquad \text{(Eq. 7.3.1.1-1)}$$

Both lateral boundaries are considered lines of symmetry and treated as no-flow boundaries (BSC 2004 [DIRS 170040], Section 6.4.1 and Figure 6-10). Along the top of the invert, a constant concentration boundary condition is imposed. At the bottom of the invert, two flux boundary conditions are imposed – one across the interface between the invert and the saturated width of the single UZ fracture (i.e., the water film thickness), and one for the interface of the invert with UZ matrix. The model only considers a single fracture in the UZ, located directly under the left boundary of the invert. The remaining width (the half fracture spacing minus the fracture water film thickness) interfaces with the UZ matrix. Within the single UZ fracture, only diffusive transport is allowed for a vertical distance below the invert that is sampled uniformly between zero and the fracture spacing. Beneath that point, only advective transport in the fracture is allowed. The imposed boundary condition is such that the diffusive flux in the fracture is equal to the downward advective flux in the fracture at this sampled transition point between diffusion and advection. For the UZ matrix, only advective transport is allowed, and the boundary condition is such that the diffusive flux from the invert to the UZ matrix is equal to the UZ matrix advective mass flux.

The fracture-matrix partitioning first formulates the above partial differential equation for concentration with boundary conditions in dimensionless form, which is then solved analytically by infinite series expansion in cosines and hyperbolic tangent functions. The flux to the fracture is then determined by integration at the invert-UZ boundary of the gradient of the concentration. The integral over the UZ fracture portion of the UZ represents the flux to the UZ fracture, while integration of the concentration gradient over the UZ matrix portion of the boundary provides the flux to the UZ matrix.

7.3.1.2 Comparison of Results from Fracture-Matrix Partitioning Model with Results from the Modified *EBS RT Abstraction*

The two models are compared for the predictions of the fraction of mass of radionuclides released to fractures of the unsaturated zone. The comparison is based on the results of the Fracture-Matrix Partitioning Model reported in Section 6.4.6 of the *Drift-Scale Radionuclide Transport* (BSC 2004 [DIRS 170040]). In that report, calculations are done for the three infiltration rates (lower, mean and upper) of the glacial transition climate. The calculations include parameter uncertainty. The EBS-UZ interface submodel is modified, as discussed below, to allow comparison of the two models without changing the conceptual design or solution algorithm. GoldSim V8.01 (Golder Associates 2003 [DIRS 166572]) is used for the *EBS RT Abstraction* calculations.

In order to compare the *EBS RT Abstraction* with the fracture-matrix partitioning model, all sampled and time-varying parameters in the EBS and UZ in the TSPA-LA system model are made consistent with the parameters used in the fracture-matrix partitioning model. Additional modifications made to the *EBS RT Abstraction* are listed below:

1. Delete the upstream waste form and corrosion products domains.

2. Apply uniform concentration at the top of the invert domain.

3. Set the seepage flux entering the invert domain to zero, so that the only transport mechanism is via diffusion.

4. Set the water saturation of invert intragranular continuum to 1.0 (fully saturated) and the water saturation of the intergranular continuum to zero. For the single continuum representation of the invert, the bulk water content is computed.

5. Turn off the imbibition flux entering the invert domain.

6. Change the diffusive property of the invert domain to match Equation E-1 of *Drift-Scale Radionuclide Transport* (BSC 2004 [DIRS 170040]).

7. Change the free water diffusion coefficient (D_0) to a lognormal distribution with the mean of $\log D_0$ of 4.69 $mm^2\ yr^{-1}$ ($1.49 \times 10^{-9}\ cm^2\ s^{-1}$) and standard deviation of $\log D_0$ of 0.150 $mm^2\ yr^{-1}$ ($4.8 \times 10^{-11}\ cm^2\ s^{-1}$), consistent with the approach adopted in *Drift-Scale Radionuclide Transport* (BSC 2004 [DIRS 170040], p. E-2 of Appendix E).

8. Change the diffusive thickness in the invert to a uniform distribution between 0.675 m and 0.806 m, as shown in *Drift-Scale Radionuclide Transport* (BSC 2004 [DIRS 170040], Appendix G, p. G-8).

9. Set the diffusive outflow area of the UZ matrix cells to zero, consistent with the boundary conditions imposed by the fracture-matrix partitioning model *Drift-Scale Radionuclide Transport* (BSC 2004 [DIRS 170040], Section 6.4.1). As a result, only

diffusive transport occurs from invert domain to the UZ matrix continuum, and only advective transport occurs in the UZ matrix continuum.

10. The distance where the flow occurs in the UZ fracture is uniformly sampled between 0 m and the fracture spacing (inverse of fracture frequency). For the UZ matrix, the flow occurs immediately under the invert.

11. Set the diffusive mass transfer term between the UZ matrix and fracture continuum to zero.

12. Ignore the transverse diffusion to the side UZ matrix and fracture cells from the UZ cells in the middle zone (These zones and cells in the EBS-UZ interface submodel are described in Section 6.5.3.6 and Figure 6.5-5).

Figure 7.3-1 (shown below) compares the fraction of the radionuclide mass released to the fractures as predicted by the fracture-matrix partitioning model (labeled as "F-M Partitioning Model" in Figure 7.3-1) with the fraction predicted by the EBS-UZ boundary condition implementation for TSPA-LA in the modified *EBS RT Abstraction* (labeled as "EBS RT Model" in Figure 7.3-1). The cumulative distribution function from the *EBS RT Abstraction* (thick red and green curves) is based on 100 realizations, while that for fracture-matrix partitioning model is based on 24 random samples selected for each infiltration case, as discussed in Section 6.4.6 of *Drift-Scale Radionuclide Transport* (BSC 2004 [DIRS 170040]). The 24 samples are the minimum required to ensure sampling of hydrologic parameters from each of the four host rock units (TSw33, TSw34, TSw35, and TSw36). Based on this sample size, it is estimated that for 95 percent confidence limit, the sample mean is within $\pm 0.41\sigma_s$ of the population mean, where σ_s is the sample standard deviation. Increasing the sample size narrows the estimated spread around the true mean and improves the accuracy of estimation. For the 100 realizations performed by the modified *EBS RT Abstraction*, the estimate of the sample mean for 95 percent confidence limit is within $\pm 0.2\sigma_s$ of the population mean. The uncertain parameters for the 100 realizations are sampled using the Latin Hypercube Sampling methodology employed by GoldSim.

The results for the fracture-matrix partitioning model for the three infiltration cases have been combined (weighted by the probability of each infiltration case) into a single curve (thick blue curve – "Combined Infiltration") for comparison with the EBS-UZ boundary condition implementation for TSPA-LA *EBS RT Abstraction*. The thick red curve shows the results for the modified *EBS RT Abstraction* using the single continuum representation of the invert, which is the base case model used in TSPA-LA. (Though not pertinent to model validation, the modified *EBS RT Abstraction* was also run using the dual continuum representation of the invert, an alternative conceptual model; results are shown as the thick green curve. These thick red and green curves virtually overlap showing little effect on the mass fraction released to fractures.)

In general, the modified *EBS RT Abstraction* predicts less mass fraction released to fracture compared to the fracture-matrix partitioning model. The difference is due to the fact that the two models are conceptually different with regard to the placement of fracture and matrix medium underneath the invert and in computing the flux out of the invert. The fracture-matrix

partitioning model solves the transport equation semi-analytically, whereas the modified *EBS RT Abstraction* model uses a finite difference approach. Because of these differences, a perfect match between the two models is not expected. Nevertheless, the comparison shows a similar qualitative and quantitative behavior between the two models.

The modified *EBS RT Abstraction* and the fracture-matrix partitioning model (combined infiltration curve) agree within a factor of three for the median and lower quantile values. At higher quantiles, the modified *EBS RT Abstraction* tends to agree more closely with the high infiltration case, in which releases are smaller than for lower infiltration cases because of the larger advective flux in the matrix (BSC 2004 [DIRS 170040], Section 6.4.6). The median matrix flux for the high infiltration case is more than a factor of four greater than the median matrix fluxes for the low and mean infiltration cases, which in turn are similar and therefore have similar fractions released to fractures in Figure 7.3-1 (BSC 2004 [DIRS 170040], Section 6.4.6). The uncertainty in the three infiltration curves, shown as error bars in Figures 6-26 and 6-28 of *Drift-Scale Radionuclide Transport* (BSC 2004 [DIRS 170040]), is bounded by the "Upper Error margin" and "Lower Error margin" curves in Figure 7.3-1. The thick red (or green) curve generally falls within the "error margins" of the individual infiltration case curves, indicating a close match between the modified *EBS RT Abstraction* and the fracture-matrix partitioning model, considering the uncertainties in the infiltration curves.

Although conceptual differences exist between the fracture-matrix partitioning model and the EBS-UZ interface submodel in the *EBS RT Abstraction,* with appropriate modifications to bring them into closer conceptual alignment, the two models display similar qualitative and quantitative behavior. The similarity in the results gives confidence that the EBS-UZ interface submodel is valid for use in TSPA-LA.

7.3.1.3 Applicability of EBS-UZ Interface Submodel in TSPA-LA in Comparison with Fracture-Matrix Partitioning Model

The EBS-UZ interface submodel of the *EBS RT Abstraction* is more suitable for TSPA-LA compared to the fracture-matrix partitioning model for the following reasons:

- The fracture-matrix partitioning model assumes steady state mass transport and is solved with a semi-analytic solution to the Laplace equation, assuming a constant concentration boundary at the top of the invert and a variable flux boundary at the bottom. This approach is restrictive compared to the *EBS RT Abstraction,* wherein the radionuclide concentrations will be varying with time. Thus, important transient effects related to fuel degradation, thermal-hydrology, in-drift chemistry, and seepage are captured in the *EBS RT Abstraction,* but may not be captured adequately in the fracture-matrix partitioning model.

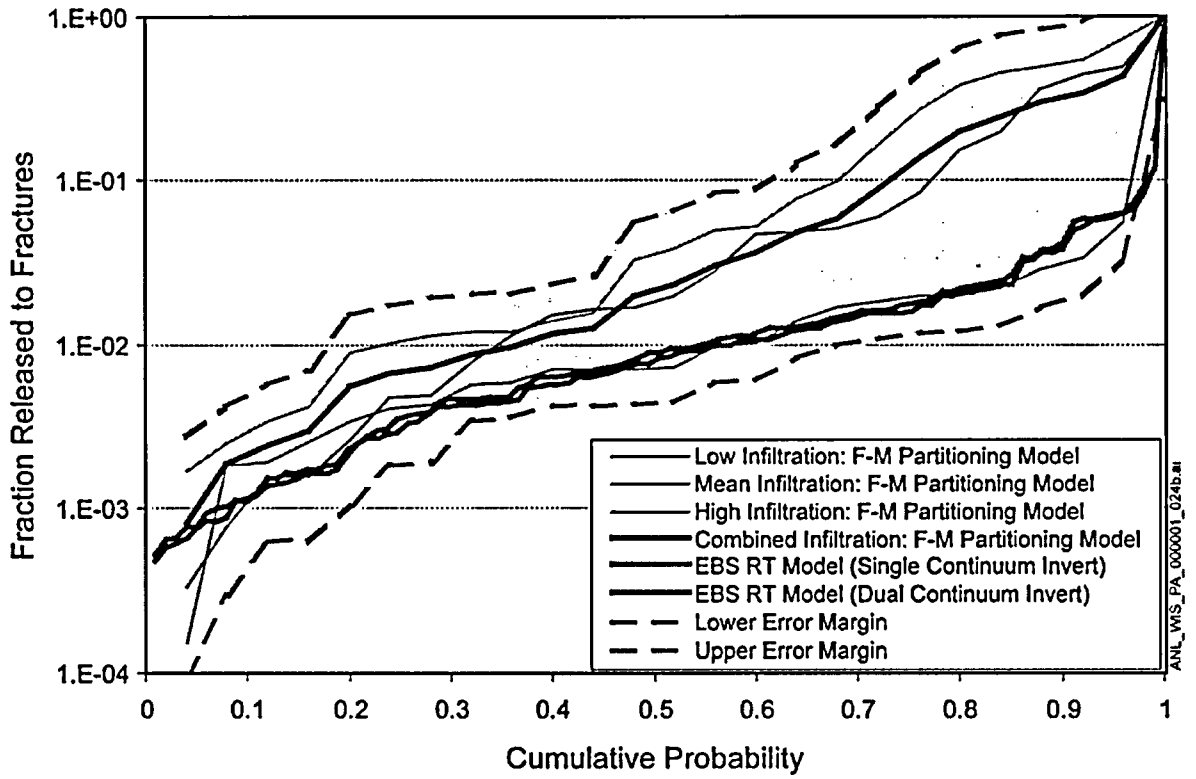

Fracture-Matrix Partitioning Model: BSC 2004 [DIRS 170040], Figures 6-26b and 6-28b.

Figure 7.3-1. Fracture-Matrix Partitioning for No Seepage Case

- The *EBS RT Abstraction* is a finite difference type model that treats the EBS processes and the near-field UZ processes as a coupled system. The upstream boundary condition is provided by a specified mass flux based on the degradation rate of the waste form and the radionuclide solubility limits, while the downstream boundary is provided by assuming a zero concentration boundary at some distance (~3 drift diameters) from the invert in the UZ. Consequently, the mass flux of radionuclides from the waste package to the invert and from the invert to the UZ is based on solving the coupled system of differential equations with realistic boundary conditions. Since the mass flux from the invert to the UZ is based on the EBS-UZ boundary condition implementation for TSPA-LA in the *EBS RT Abstraction*, to be consistent, the mass flux partitioning into the far-field UZ transport model (FEHM) should also be based on the *EBS RT Abstraction*, rather than on the fracture-matrix partitioning model.

- The fracture-matrix partitioning model assumes a discrete fracture network with no coupling between the fracture and matrix domains. In contrast, the EBS-UZ boundary condition implementation for TSPA-LA in the *EBS RT Abstraction* treats the UZ as a dual continuum (overlapping UZ fracture and matrix continua), with diffusive mass transfer capability between the two continua. This dual continuum modeling approach is consistent with the various process-level UZ flow and transport models created for the YMP.

- The imbibition flux from the surrounding host rock into the intragranular continuum is modeled in the *EBS RT Abstraction*, whereas its contribution in the fracture-matrix partitioning model is ignored. This flux could potentially carry some radionuclide mass into the UZ matrix that could lower the partitioning to the fracture continuum, which is realistic. The fracture-matrix partitioning model may overestimate the fraction released to the fractures where imbibition flux is significant.

- In the regions of the repository where water seeps through the drift, the fracture-matrix partitioning model arbitrarily proposes putting all the mass from the invert into the UZ fracture. This is a bounding approach and ignores the matrix pathway, which occupies most of the area under the invert. The EBS-UZ boundary condition implementation for TSPA-LA in the *EBS RT Abstraction*, however, applies a more realistic approach, computing the fracture-matrix partitioning based on the appropriate set of boundary conditions in drifts with seepage and including transport in the UZ matrix, as discussed in item (b) above. Sections 6.5.3.5 and 6.5.3.6 discuss how the advective flux from the invert is apportioned between fractures and matrix in the UZ.

The above comparisons of the results of the two models and their comparative suitability for TSPA-LA have demonstrated that the EBS-UZ interface submodel meets Level II validation criteria. Based on the validation results, the EBS-UZ interface submodel is suitable for its intended use.

7.3.2 Results of Independent Model Validation Technical Review of the EBS-UZ Interface Submodel

An independent model validation technical review of the EBS-UZ interface submodel was conducted, as specified in the TWP (BSC 2004 [DIRS 170775], Section 2.2.3). This model validation approach is justified based on requirements of AP-SIII.10Q, Section 5.3.2 c), where independent technical review is listed as an appropriate method for model validation. The results of the independent model validation technical review of the EBS-UZ interface submodel are presented in a memo (Baker and Grisak 2004 [DIRS 170953]), a verbatim copy of which follows.

MEMO

Date: July 27, 2004

To: James Schreiber and Cliff Howard, Yucca Mountain Project

Cc:

From: Noreen A. Baker, Gerald E. Grisak, INTERA Inc., Austin, Texas

RE: **Independent Model Validation Technical Review of the EBS-UZ Interface Sub-Model of the Radionuclide Transport Abstraction Model for the Yucca Mountain Project**

MEMO (Continued)

Pursuant to your request to perform an independent model validation technical review of three sub-models of the Engineered Barrier System (EBS) Radionuclide Transport Abstraction (RTA) model as documented in ANL-WIS-PA-000001 Rev 01K, we have performed and documented the review consistent with the requirements of the Technical Work Plan TWP-MGR-PA-000020 Rev 00. We reviewed the EBS-UZ interface sub-model of the EBS RTA report, and the results of the review are provided in this memo.

Review Qualifications

Section 2.2.4 of the Technical Work Plan TWP-MGR-PA-000020 Rev 00 describes the qualifications and responsibilities the independent model validation technical reviewer. We are qualified to perform the work described for the following reasons. (1). we have not contributed to the development of the model assumptions, parameters, or implementing algorithms documented in ANL-WIS-PA-000001 Rev 01K, (2). Noreen A. Baker has a BS and MS degree in Geology with specialties in Engineering Geology and Hydrogeology, respectively, with more than ten years of professional experience modeling fluid flow and transport in geologic media (3) G. E. Grisak has BS (Geology) and MS (Hydrogeology) degrees, and over 30 years experience evaluating and modeling fluid flow and transport in geologic media, including several publications on fracture/matrix flow and transport, (3) Both N. A. Baker and G. E. Grisak are licensed Professional Geoscientists in the State of Texas. More detailed information regarding credentials can be found in the resumes attached.

Appropriateness and Adequacy of the EBS-UZ Interface Sub-Model Conceptual Model

Discussion of the EBS-UZ interface sub-model is provided in Section 6.5.3.6. Discussion of the EBS-UZ interface sub-model is provided in Section 6.5.3.6. In the EBS-UZ interface sub-model, the near-field UZ is modeled as a dual continuum of overlapping UZ-matrix and UZ-fracture media. This approach is consistent with current technical approaches to modeling flow and ransport in fractured geologic media (Liu et al., 1998; Nitao, 1991). The matrix and fracture continua are represented by a two dimensional vertical array of cells oriented parallel to a cross section of a drift and located immediately beneath a drift. The array consists of three vertical zones, with each zone containing both a fracture cell and a matrix cell. The vertical zones are four layers deep in the vertical direction. The invert is in direct communication with the center zone of UZ matrix/fracture cells. A semi-infinite zero concentration boundary condition at the EBS-UZ interface is approximated by setting a zero concentration boundary at a distance of 3 drift diameters below the invert-UZ boundary.

The mass flux from the invert flows into the top layer of the middle zone in the UZ. The mass flux from the invert is routed to both the fracture cell and the matrix cell in the center zone beneath the invert, with the advective flux routed to the fracture and matrix cells in a manner that is consistent with physical reality. That is, the advective flux coming out of the invert, which is attributable to the dripping flux is routed to the fracture cell in the middle zone, while the imbibition flux is routed to the matrix. The diffusive flux is allowed to enter both the matrix and the fracture cells. The advective flux in the fractures is taken as the larger of the steady-state advective flux in the fractures and the advective flux out of the invert.

The mass flux that enters the center zone cells in the UZ below the invert is then transported by advection and diffusion throughout the modeled area. The advective flux in the two outer zones is given by the steady state UZ flow in the fractures and the matrix at the repository horizon. Advection occurs downward only, from the fracture cell of one layer to the fracture cell of the underlying layer in the same zone, and from the matrix cell of one layer to the matrix cell of the underlying layer in the same zone. Advection does not occur across zones. The fracture and

MEMO (Continued)

matrix cells of each zone interact via diffusion. The entire modeled area interacts through thematrix cells via diffusion, with the matrix cells of one zone interacting via diffusion with the matrix cells of adjacent zones, and the matrix cells of one layer in a zone interacting with adjacent overlying and underlying matrix cells in the same zone.

The conceptual model of how the EBS and UZ interface is well captured by the EBS-UZ interface model. The conceptual model recognizes the physical reality by considering both an advective and diffusive flux and by treating the UZ as a dual-permeability medium with both fracture and matrix continua. This modeling approach is consistent with the manner in which dual-permeability continua are modeled (Pruess, 2003). The conceptual model is appropriate for describing the interconnection between the EBS and the UZ because it considers the important components of mass flux out of the EBS and it conserves all the mass flux from the EBS and transfers it to the UZ. The mass transfer to the UZ also captures temporal variations, which may be due to variable radionuclide concentrations in the waste, production of corrosion products, or varying water flux through the EBS. The mass is distributed to the fractures and the matrix in the EBS-UZ interface sub-model in a manner that is conceptually logical. The mass is finally gathered from the EBS-UZ interface sub-model into a collector cell for delivery to the UZ transport model. The delivery from the collector cell to the UZ transport model retains the relative fractions of mass in the fractures and the matrix that is determined within the EBS-UZ interface sub-model.

Appropriateness of the Mathematical Representation of the EBS-UZ Interface Sub-Model

The EBS-UZ interface sub-model represents the UZ immediately below the invert as a dual continuum of UZ matrix and UZ fracture media. The dual permeability modeling approach is an appropriate way to model transport in fractured media. Mass is tracked and accounted for in the model in both fracture and matrix cells and the fracture and matrix cells have physical dimensions which adequately approximate the physical hydrogeologic system. The mathematical formulation of the dual permeability modeling approach is described in *Particle Tracking Model and Abstraction of Transport Processes* (BSC 2003w).

EBS-UZ Interface Sub-Model Assumptions and Boundary Conditions

The EBS-UZ sub-model assumptions and comments are provided below.

Assumptions/Boundary Condition	Comments
1. A semi-infinite zero concentration boundary condition is used for the EBS-UZ interface. The boundary condition is set at a distance of 3 drift diameters below the invert-UZ boundary.	We agree with the boundary condition and with the manner in which it is implemented. Placing the boundary condition at the interface would result in an unrealistically high diffusive flux from the invert to the UZ.
2. With respect to the advective flux in the outer two zones of cells, drift shadow effects are ignored.	We agree with the assumption. Drift shadow effects would increase the advective flux in the two outer zones and result in dilution of radionuclide concentrations entering the UZ immediately below the invert.

Evaluation of Model Validation

Documentation of the model validation is presented in Section 7.3.1. The EBS-UZ sub-model is validated by comparison with an alternative mathematical model developed for a closely

MEMO (Continued)

comparable description of the EBS-UZ interface. The alternative model used for the comparison is the fracture-matrix partitioning model described in *Drift-Scale Radionuclide Transport* (BSC 2004m). The primary validation criterion is corroboration of the model results with an alternative mathematical model, as described in TWP-MGR-PA-000020 Rev 00. This is a common approach to model validation where site specific or generic field or laboratory data or experiments do not adequately capture the processes involved. The EBS-UZ interface sub-model involves coupling the porous medium invert to the dual-permeability UZ with a numerical solution of a discretized model. In the fracture-matrix partitioning model, the coupling is accomplished by formulating the problem as a partial differential equation for concentration and deriving an analytical solution to the problem. In order to compare the two models, all sampled and time-varying parameters in the EBS-UZ interface sub-model are made consistent with the parameters used in the fracture-matrix partitioning model. Additionally, other changes to the EBS-UZ interface sub-model were made to more closely approximate conditions in the fracture-matrix partitioning model. The EBS-UZ interface sub-model was also run using an alternative conceptualization for the invert as a dual continuum. The results of the CDFs of the fraction released to fractures are then compared. This is a technically reasonable and appropriate approach to model validation.

Evaluation of Model Validation Criteria

In Section 2.2.4 of Technical Work Plan TWP-MGR-PA-000020 Rev 00, provides validation criteria for the EBS-UZ interface sub-model. The table below provides our assessment of these criteria.

Criteria	Criteria met?	Response
1. The results of the UBS-UZ interface sub-model shall show qualitative agreement with the results of the fracture-matrix partitioning model.	Yes	The two models display similar qualitative results, and in addition are reasonably similar quantitatively, in that the results of the EBS-UZ interface sub-model fall within the shadow of the error bars of the low, mean and high infiltration cases of the fracture-matrix partitioning model.
2. The report shall document equivalent trends and correlations between input parameter variation and predicted results	Yes	Equivalent trends and correlations between input parameter variations and predicted results are visually obvious on the graphical comparison between the two methods. Either the single or dual continuum representation of the invert by the EBS-UZ interface sub-model is adequate.
3. Identification of differences between model results.	Yes	Differences between model results and the reasons for the differences are provided in section 7.3.1.2
4. Demonstrate that the EBS-UZ interface sub-model does not underestimate radionuclide transport from the EBS to the UZ.	Yes	The suitability and applicability of the EBS-UZ interface sub-model is discussed and justified in Section 7.3.1.3. The sub-model is suitable for its intended use.

MEMO (Continued)

Conclusions

The EBS-UZ interface sub-model documented in report ANL-WIS-PA-000001 Rev 01K incorporates all the significant aspects contributing to mass flux from the invert to the UZ. The sub-model is validated against an alternative model developed for similar purposes and the results are comparable. The advective flux is the primary uncertainty in the mass flux to the fractures, and this uncertainty has been adequately and realistically bounded by the low, mean and high infiltration cases used in the fracture-matrix partitioning model in the validation comparison. It is our professional judgment that the EBS flow sub-model is appropriate for use in the Radionuclide Transport Abstraction.

References

Liu, H.H., C. Doughty and G.S. Bodvarsson, 1998, "An active fracture model for unsaturated flow and transport in fractured rock," Water Resources Research, vol. 34, no. 10, pages 2633-2646.

Nitao, J.J., 1991, "Theory of matrix and fracture flow regimes in unsaturated, fractured media," Proc., Second International High Level Radioactive Waste Management Conference, Las Vegas, NV, April 29-May 3, 1991.

Pruess, K. (editor), 2003, Proceedings, TOUGH Symposium 2003, Lawrence Berkeley National Laboratory, CA, May 12-14.

7.4 VALIDATION SUMMARY

The *EBS RT Abstraction* has been validated by applying acceptance criteria based on an evaluation of the model's relative importance to the potential performance of the repository system. All validation requirements defined in the *Technical Work Plan for: Near-Field Environment and Transport: Engineered Barrier System: Radionuclide Transport Abstraction Model Report Integration* (BSC 2004 [DIRS 170775]), Sections 2.2.1, 2.2.2, and 2.2.3 have been fulfilled. Requirements for confidence building during model development have also been satisfied. The model development activities and post-development validation activities described establish the scientific bases for the *EBS RT Abstraction*. Based on this, the *EBS RT Abstraction* is considered to be sufficiently accurate and adequate for the intended purpose and to the level of confidence required by the model's relative importance to the performance of the proposed repository system.

INTENTIONALLY LEFT BLANK

8. CONCLUSIONS

This abstraction defines the conceptual model used to determine the rate of release of radionuclides from the EBS to the unsaturated zone in the TSPA-LA given the assumptions listed in Section 5. The *EBS RT Abstraction* includes algorithms used in the TSPA-LA for computing the flow of water and the transport of radionuclides through the EBS and specifies how parameters used in the model are calculated or from what other models they are obtained. This model is reasonably bounding because it overestimates flow through the drip shield and into the waste package and transport out of the EBS. At the same time, wherever possible, it is realistic, not just bounding, within the appropriate range of uncertainty for TSPA-LA calculations.

8.1 CONCEPTUAL MODEL SUMMARY

This section summarizes the conceptual model for transport of radionuclides from the EBS as modeled in TSPA-LA. Radionuclide transport out of the waste form and waste package, through the invert, and into the unsaturated zone is dependent on a complex series of events in the repository. After the waste packages are emplaced, radioactive decay of the waste will heat the drifts and locally perturb the normal percolation of water through the mountain. As the drifts cool, some of the water percolating through the mountain may drip into the drifts and subsequently contact some of the drip shields. Over time, the drip shield, waste package, and other components of the EBS are expected to degrade, leading to contact between the water and the waste form, resulting in the mobilization and transport of radionuclides through the EBS to the unsaturated zone. The primary transport medium through the EBS is anticipated to be water. Either a thin film of water or moving water is necessary for radionuclides to be transported out of the waste package and through the invert to the unsaturated zone.

A number of key factors will affect the mobilization and transport of radionuclides through the EBS, including barrier effectiveness and transport behavior:

- Performance of the drip shields
- Performance of the waste packages
- Protection provided by cladding
- Waste form degradation rates
- Entry and movement of water through waste packages
- Solubilities of radionuclides
- Transport of radionuclides through and out of the waste packages
- Transport of radionuclides through the invert below the waste packages
- Colloidal transport of radionuclides.

Once the drip shield is breached, water may contact the waste packages. Once a waste package is breached, water may enter the package as water vapor or as drips. If the cladding around spent fuel rods or the canister around a vitrified waste form is also breached, radionuclides may start to dissolve in the water. The concentration of each radionuclide mobilized from the waste form cannot exceed the radionuclide solubility limit, unless suspended colloids are included. Colloids are important for two reasons: they may potentially increase the release of radionuclides from the waste package, and they may potentially increase the transport velocity of radionuclides.

Radionuclides mobilized in water as dissolved species or in association with colloidal species may then be transported by advection and/or diffusion from the waste form, through the waste package, and out of breaches in the waste packages. Once outside the package, the radionuclides may be transported through the invert predominantly by diffusion, if water is not flowing through the invert, or by advection, if water is flowing through the invert.

The conceptual model for flow of water through the EBS identifies eight key flow pathways. These pathways and their relationships are summarized in the following list and in Table 8.1-1. Sections 6.3.1.1, 6.3.2, 6.3.3, and 6.5.1.1 contain detailed technical discussions of the EBS flow abstraction portion of the *EBS RT Abstraction.*

- **Seepage Flux**–This is the input flux or boundary condition; it is a time- and location-dependent input to this model provided by *Abstraction of Drift Seepage* (BSC 2004 [DIRS 169131]). Any condensation that may occur on the walls of the drift above the drip shield is included in the seepage flux.
- **Through the Drip Shield to the Waste Package**–Flux through the drip shield is proportional to the ratio of the axial lengths of breaches in the drip shield to the total axial length of the drip shield, multiplied by a sampled factor that accounts for uncertainty in the fraction of the flux that is diverted by the drip shield. This flux splitting submodel for the drip shield should only be applied when there is a time-varying failure of the drip shield.
- **Drip Shield to Invert (Diversion around the Drip Shield)**–Any seepage flux that does not go through the drip shield flows directly into the invert.
- **Through the Waste Package to the Waste Form**–Flux into the waste package is proportional to the product of the flux through the drip shield and the ratio of the lengths of breaches in the waste package to the total axial length of the waste package, multiplied by a sampled factor that accounts for uncertainty in the fraction of the flux that is diverted by the waste package. The number of patches in the waste package is calculated by the waste package degradation model, *WAPDEG Analysis of Waste Package and Drip Shield Degradation* (BSC 2004 [DIRS 169996]).
- **Waste Package to Invert (Diversion around the Waste Package)**–Flow that does not go through the waste package is diverted directly to the invert.
- **Waste Package to Invert**–All of the flux from the waste package flows directly to the invert, independent of breach location on the waste package. The presence of the emplacement pallet, which maintains an air gap between the waste package and the invert and could potentially interfere with flow to the invert, is ignored in order to bound the water flow through this pathway.
- **Imbibition to Invert**–Water can be imbibed from the host rock matrix into the invert.
- **Invert to Unsaturated Zone**–All of the flux into the invert is released into the unsaturated zone.

In the conceptual model of radionuclide transport through the EBS, the waste form is the source of all radionuclides in the repository system. Radionuclides can be transported downward,

through corrosion products in the waste package, through the invert, and into the unsaturated zone. Transport can occur through advection when there is a liquid flux through the waste package, and by diffusion through any water present in the waste package. Diffusion can occur in a seep environment, when advective transport also takes place, as well as in a no-seep environment where no advective transport occurs; thin films of water are assumed to be present on all surfaces. If the only breaches in a waste package are stress corrosion cracks, advective transport does not occur, but diffusion of radionuclides out of the waste package can still take place. The concentration of each radionuclide during transport is limited by the sum of its solubility limit and the presence of any colloidal particles that may act as reversible or irreversible carriers for the radionuclide. The transport pathways and transport processes (advection or diffusion) are summarized in Table 8.1-2. Sections 6.3.4, 6.5.1.2, and 6.5.3 contain a detailed technical discussion of the EBS transport abstraction.

Table 8.1-1. Summary of EBS Flow Abstraction

Flow Pathway, Pathway Flux	Flow Parameters	Data Sources & Notes
1. Total dripping flux, F_1	Total dripping flux is a function of fracture properties, rock properties, and the percolation flux.	*Abstraction of Drift Seepage* (BSC 2004 [DIRS 169131]) provides time- and location-dependent values of total dripping flux.
2. Flux through the drip shield, F_2	L_{DS_Patch} is axial half-length of each patch due to general corrosion of Ti. L_{DS} is axial length of the drip shield. N_{bDS} is number of corrosion patches of length L_{DS_Patch} in the drip shield. f'_{DS} is sampled uncertain parameter, Flux_Split_DS_Uncert. $F_2 = \min[F_1 N_{bDS} L_{DS\_Patch} f'_{DS}/L_{DS}, F_1]$	This flux splitting submodel for the drip shield should only be applied when there is a time-varying failure of the drip shield. For the seismic scenario, the opening area is computed based on the drip shield damage fraction multiplied by the area of the drip shield.
3. Diversion around drip shield, F_3	$F_3 = F_1 - F_2$.	Continuity of liquid flux.
4. Flux into the WP, F_4	L_{WP_Patch} is axial half-length of each patch due to general corrosion of Alloy 22. L_{WP} is axial length of the WP. N_{bWP} is number of corrosion patches in the waste package. f'_{WP} is sampled uncertain parameter, Flux_Split_WP_Uncert. $F_4 = \min[F_2 N_{bWP} L_{WP\_Patch} f'_{WP}/L_{WP}, F_2]$	WAPDEG (BSC 2004 [DIRS 169996]) provides the number of patches and stress corrosion cracks on the WP. No flow through stress corrosion cracks due to plugging (BSC 2004 [DIRS 172203], Section 6.3.7). Steady state flow through WP (outflow = inflow in steady state; this is bounding for release).
5. Diversion around the WP, F_5	$F_5 = F_2 - F_4$	Continuity of liquid flux.
6. Flux to the invert, F_6	$F_6 = F_5 + F_4 + F_3$ $= F_1$	All advective flux enters the invert. Only F_4 can transport radionuclides into the invert.
7. Imbibition flux from the host rock matrix into the invert, F_7	F_7 is an input to the EBS flow model.	Imbibition flux is provided by *Multiscale Thermohydrologic Model* calculations (BSC 2004 [DIRS 169565]).

Table 8.1-1. Summary of EBS Flow Abstraction (Continued)

Flow Pathway, Pathway Flux	Flow Parameters	Data Sources & Notes
8. Flux from the invert into to the unsaturated zone, F_8	$F_8 = F_6 + F_7$ $= F_1 + F_7$	Total dripping flux portion (F_1) of advective flux from the invert flows into the UZ fractures, imbibition flux (F_7) flows into the UZ matrix.

Output DTN: SN0410T0507703.018.

WP = waste package

In the transport abstraction, the EBS is modeled as consisting of three domains. The first domain is the source (i.e., SNF or HLW). The second domain consists of corrosion products from the degradation of steel waste package internal components. The third domain is the invert. The physical and chemical properties and conditions are uniform throughout each domain, as though the contents of the domain were thoroughly and continuously stirred.

Parameters that define the size of the two waste package domains, specifically the volumes and diffusive path lengths, are summarized in Table 8.2-1. Parameter values that are provided by other models are identified there. The path length for diffusion through the invert is set to the average thickness of the invert, 0.597 m.

The mass of corrosion products is a function of time and depends on the corrosion rates of carbon steel and stainless steel, which are uncertain parameters with values that are sampled in TSPA-LA. In a seep environment, the corrosion products are fully saturated with water. In a no-seep environment for CSNF, the water saturation is based on the amount of water adsorbed onto iron oxide surfaces, which is a function of the relative humidity. The RH is an input to the transport model that depends on time and location in the repository. Calculation of corrosion products mass and saturation is discussed in Section 6.5.3.2.

The diffusion coefficient in the corrosion products is based on the self-diffusion coefficient of water at 25°C as a bounding value for all radionuclides, modified for the porosity and time-dependent water saturation.

The diffusion coefficient in the invert is also based on the self-diffusion coefficient of water at 25°C as a bounding value for all radionuclides. The effects of porosity and time-dependent saturation in the invert are incorporated, based on experimental data. The effect of temperature is also incorporated into the abstraction for the diffusion coefficient. The diffusion coefficient for colloids is assumed to be $1/100^{th}$ of the diffusion coefficient for a dissolved species (Section 6.3.4.4).

Sorption of radionuclides may occur on corrosion products in the waste package and on crushed tuff in the invert. Values for sorption distribution coefficients on corrosion products and on crushed tuff for all radionuclides of interest are determined in Section 6.3.4.2. K_d values for sorption on corrosion products are summarized in Table 8.2-2, with the uncertainty in each value represented by a specified range and distribution.

Table 8.1-2. Summary of EBS Transport Abstraction

Transport Pathway	Transport Modes	Transport Parameters and Data Sources
1. Waste form and corrosion products domains	Diffusion through stress corrosion cracks (no advective transport through stress corrosion cracks). Diffusion and advection through patches.	No lateral or forward dispersion. Colloidal particles will transport radionuclides. Diffusive area for each stress corrosion crack is 7.7×10^{-6} m^2 (see Section 6.3.3.1.2.1). Diffusion coefficient (all radionuclides): • Free water diffusion coefficient: 2.299×10^{-5} cm^2 s^{-1} at 25°C (Mills 1973 [DIRS 133392], Table III) • Modified for porosity and saturation (see Section 6.5.1.2.1.4) • Reduced by a factor of 100 if radionuclide is bound to a colloid (see Section 6.3.4.4). The cross-sectional area for radionuclide transport is dependent on the scenario class (see Sections 6.5.3.1.1 and 6.5.3.1.2). Transport of radionuclides is retarded by sorption onto corrosion products; time-dependent mass of corrosion products available for sorption is calculated based on corrosion rates of carbon and stainless steels. See Section 6.5.3 for further details.
2. Invert	Diffusion and advection (F_6) from corrosion products domain into the invert.	Liquid flux for advection = F_6 = F_5 (diverted by WP) + F_4 (flux through WP) + F_3 (diverted by drip shield). Diffusion coefficient (all radionuclides): • Free water diffusion coefficient: 2.299×10^{-5} cm^2 s^{-1} at 25°C (Mills 1973 [DIRS 133392], Table III) • Modified for porosity and saturation (see Section 6.3.4.1) • Temperature modification defined in Section 6.3.4.1.2; invert temperature is provided by *Multiscale Thermohydrologic Model* calculations (BSC 2004 [DIRS 169565] • Reduced by a factor of 100 if radionuclide is bound to a colloid (see Section 6.3.4.4). The cross-sectional area for radionuclide transport is the width of the invert times the waste package length. Transport of radionuclides is retarded by sorption onto crushed tuff in invert. See Section 6.5.3 for further details.
3. Invert-UZ interface	Advection from the invert to UZ fractures (F_6) and UZ matrix (F_7); total flux is F_8. Diffusion from the invert to UZ fractures and matrix.	The invert diffusion calculation uses radionuclide concentrations in the WP corrosion products domain as the boundary condition at the top of the invert and a series of unsaturated zone computational cells below the invert that provide a gradient to a zero radionuclide concentration at some distance from the bottom of the invert. See Section 6.5.3.6.

Output DTN: SN0410T0507703.018.

WP = waste package

8.2 MODEL OUTPUTS

Table 8.2-1 summarizes parameters that define the three-domain EBS transport abstraction, which is described in more detail in Section 6.5.3. These domains are comprised of:

- *The waste form.* In the case of CSNF waste packages, this consists of fuel rods. In codisposal waste packages, the waste form is a composite of HLW glass and DSNF; however, only HLW is modeled in this domain, because DSNF mass is added to the corrosion product domain due to near-instantaneous degradation. Transport processes that occur in this domain are dissolution of radionuclides in the waste form and diffusion from the waste form domain to the corrosion products domain.

- *Corrosion products inside the waste package.* These are the result of corrosion of steel internal waste package components such as baskets, HLW canisters, and the inner stainless steel vessel. The stationary iron-oxide-based corrosion products are strong sorbers of many radionuclides. In addition, radionuclides sorb onto colloidal materials released from the corrosion products and onto groundwater colloids. These sorption processes, both reversible and irreversible, are modeled as occurring in the corrosion products domain. Precipitation and dissolution can also take place in this domain. Diffusion transports radionuclides into this domain from the waste form domain and from this domain to the invert domain. In a codisposal waste package, the degraded DSNF is conceptualized to be in a powdered form that is commingled with steel corrosion products and is thus included in the corrosion product domain for purposes of calculating the mass of corrosion products and the volume of water in the domain.

- *Invert.* Advection and diffusion transport radionuclides into this domain from the corrosion products domain and from this domain to the unsaturated zone. Because the chemical environment of the invert may be different from the corrosion products domain, colloid stability may be affected and dissolution or precipitation of radionuclides may take place. The submodel for transport through the invert is summarized in transport pathway 3 of the transport abstraction summary, Table 8.1-2.

Transport is affected by the parameters that define the physicochemical environment, including the porosity and pore volume, water saturation, interfacial diffusive areas, diffusive path lengths, and diffusion coefficients. These diffusive transport parameters are discussed in Section 6.5.3.

Output from the *EBS RT Abstraction*, including algorithms and parameters, is summarized in final output DTN: SN0410T0507703.018. In addition, two preliminary output DTNs were created prior to final approval of this report: DTNs: SN0403T0507703.015 and SN0409T0507703.017. The DTNs consist of the tables found in Sections 8.1 and 8.2 of the *EBS RT Abstraction.* Differences between the preliminary and final DTNs are described in Appendix I. Both of the preliminary DTNs that were developed have been superseded by the final output DTN SN0410T0507703.018. The two preliminary output DTNs are discussed in Appendix I solely to provide transparency and traceability for TSPA-LA applications that were initially developed based on the preliminary DTNs. These two DTNs are not intended for any other application.

Table 8.2-1. Parameters for EBS Transport Abstraction

Waste Type	Transport Mode	Seep Case	No-Seep Case
Waste Form Domain (Fuel Rods, HLW)			
CSNF	Advection	Rind and water volume • Provided by *Clad Degradation – Summary and Abstraction for LA* (BSC 2004 [DIRS 170023])	• Same as Seep Case
	Diffusion	Diffusive area of Waste Form Domain: • Total exposed surface area of all failed (axially split) fuel rods, limited to the total surface area of the waste package. • Provided by *Clad Degradation – Summary and Abstraction for LA* (BSC 2004 [DIRS 170023]) Diffusion path length: • Thickness of rind; function of time. • Provided by *Clad Degradation – Summary and Abstraction for LA* (BSC 2004 [DIRS 170023]) Diffusion coefficient in Waste Form Domain, D_{WF}: • Archie's law: $D_{WF} = \phi^{1.3} S_w^2 D_0$ • ϕ = porosity of rind (BSC 2004 [DIRS 170023]) • S_w = water saturation in rind = 1.0 • D_0 = free water diffusion coefficient (Note the D_{WF} is an effective value defined in the same manner as D_s in Equation 6.5.1.2.1-12.)	• Same as Seep Case
Waste Form Domain (Fuel Rods, HLW)			
Codisposal	Advection	Volume of rind: • Provided as function of time by *Defense HLW Glass Degradation Model* (BSC 2004 [DIRS 169988], Section 6.7, Eq. 56) • Porosity provided by *Defense HLW Glass Degradation Model* (BSC 2004 [DIRS 169988], Table 8-1) • S_w = water saturation = 1.0	• Same as Seep Case

Table 8.2-1. Parameters for EBS Transport Abstraction (Continued)

Waste Type	Transport Mode	Seep Case	No-Seep Case
	Diffusion	Diffusive area: • Total initial surface area of 5 glass logs • Provided by *Defense HLW Glass Degradation Model* (BSC 2004 [DIRS 169988], Section 8.1) Diffusion path length: • Thickness of degraded glass layer; function of time. • Provided by *Defense HLW Glass Degradation Model* (BSC 2004 [DIRS 169988], Section 6.7, Eq. 56) Diffusion coefficient in Waste Form Domain, D_{WF}: • Archie's law: $D_{WF} = \phi^{1.3} S_w^2 D_0$ • ϕ = porosity of degraded glass layer (BSC 2004 [DIRS 169988], Table 8-1) • S_w = water saturation = 1.0 • D_0 = free water diffusion coefficient (Note the D_{WF} is an effective value defined in the same manner as D_s in Equation 6.5.1.2.1-12.)	• Same as Seep Case
Corrosion Product Domain			
CSNF	Advection	Volume of corrosion products, V_{CP}: • Mass of corrosion products, m_{CP}, is function of time, Table 8.2-5, Equation 8-7 • Porosity ϕ_{CP} = 0.4 • V_{CP} from Table 8.2-5, Equation 8-6	• Same as Seep Case
		Volume of water: • S_w = water saturation in CP = 1.0 • Water volume = $S_w V_{CP}$	Volume of water: • $S_{we,CP}$ = effective water saturation in CP from adsorbed water (in-package diffusion submodel); Table 8.2-5, Equation 8-5 • $S_{we,CP}$ function of RH and sampled specific surface area of CP CP_Spec_Surf_Area • Water volume = $S_{we,CP} V_{CP}$
	Diffusion	Diffusive area: • Total area of all waste package breaches	• Same as Seep Case
		Diffusion path length: • Sampled parameter Diff_Path_Length_CP_CSNF	• Same as Seep Case

Table 8.2-1. Parameters for EBS Transport Abstraction (Continued)

Waste Type	Transport Mode	Seep Case	No-Seep Case
		Diffusion coefficient in corrosion products, D_{CP}: • Archie's law: $D_{CP} = \phi_{CP}^{1.3} S_w^2 D_0$ • ϕ_{CP} = porosity of CP = 0.4 • S_w = water saturation in CP = 1.0 • D_0 = free water diffusion coefficient (Note the D_{CP} is an effective value defined in the same manner as D_s in Equation 6.5.1.2.1-12.)	Diffusion coefficient in corrosion products, D_{CP}: • $S_{we,CP}$ = effective water saturation in CP from adsorbed water (in-package diffusion submodel); Table 8.2-5, Equation 8-5 • $S_{we,CP}$ function of RH and sampled specific surface area of CP CP_Spec_Surf_Area • ϕ_{CP} = porosity of CP = 0.4 • D_0 = free water diffusion coefficient
Codisposal	Advection	Volume of corrosion products, V_{CP}: • Same as for CSNF drip case • ϕ_{CP} = porosity of CP = 0.4 • S_w = water saturation in CP = 1.0 Volume of degraded DSNF, V_{DSNF} • V_{DSNF} = 1 m^3 • ϕ_{DSNF} = porosity of DSNF = 0.2 • S_w = water saturation in DSNF = 1	• Same as Seep Case
		Volume of water: • Water volume = $\max[S_w V_{CP}, S_w \phi_{DSNF} V_{DSNF}]$	• Same as Seep Case
	Diffusion	Diffusive area: • Same as for CSNF drip case Diffusion path length: • Sampled parameter Diff_Path_Length_CP_CDSP Diffusion coefficient in corrosion products, D_{CP}: • Archie's law: $D_{CP} = \phi_{CP}^{1.3} S_w^2 D_0$ • ϕ_{CP} = porosity of CP = 0.4 • S_w = water saturation = 1.0 • D_0 = free water diffusion coefficient (Note the D_{CP} is an effective value defined in the same manner as D_s in Equation 6.5.1.2.1-12.)	• Same as Seep Case

Output DTN: SN0410T0507703.018.

DSNF = defense spent nuclear fuel

Table 8.2-2 summarizes the range and distribution of radionuclide sorption distribution coefficients for retardation in the waste package corrosion products. These parameter values are discussed in Section 6.3.4.2.

The ranges and distributions of radionuclide sorption distribution coefficients for sorption on devitrified unsaturated zone tuff given in Table 4.1-12 (DTNs: LA0408AM831341.001 [DIRS 171584]) are assigned to K_d values on crushed tuff in the invert. Correlations for sampling sorption distribution coefficient probability distributions for devitrified UZ tuff given in Table 4.1-13 (DTN: LA0311AM831341.001 [DIRS 167015]) are assigned to invert crushed tuff. The value for actinium sorption distribution coefficient for sorption on crushed tuff in the invert is set equal to the sampled americium K_d value on crushed tuff in the invert.

Table 8.2-2. Summary of Sorption Distribution Coefficient (K_d) Ranges and Distributions for Sorption on Waste Package Corrosion Products

Input Name	Element	Minimum K_d (ml g^{-1})	Maximum K_d (ml g^{-1})	Distribution Type
Kd_Ac_FeOx_CP	Actinium	100	5,000	Log-Uniform
Kd_Am_FeOx_CP	Americium	100	5,000	Log-Uniform
Kd_C_FeOx_CP	Carbon	10	100	Uniform
Kd_Cs_FeOx_CP	Cesium	0	300	Beta $E(x)$=30; $\sigma(x)$=30
Kd_I_FeOx_CP	Iodine	0	0.6	Uniform
Kd_Np_FeOx_CP	Neptunium	1	1,000	Log-Uniform
Kd_Pu_FeOx_CP	Plutonium	100	5,000	Log-Uniform
Kd_Pa_FeOx_CP	Protactinium	100	1,000	Uniform
Kd_Ra_FeOx_CP	Radium	0	500	Beta $E(x)$=30; $\sigma(x)$=30
Kd_Sr_FeOx_CP	Strontium	0	20	Beta $E(x)$=10; $\sigma(x)$=2.5
Kd_Tc_FeOx_CP	Technetium	0	0.6	Uniform
Kd_Th_FeOx_CP	Thorium	100	5,000	Log-Uniform
Kd_U_FeOx_CP	Uranium	100	1,000	Log-Uniform

Output DTN: SN0410T0507703.018.

NOTES: E(x) = Expected value
σ(x) = Standard deviation

Table 8.2-3 summarizes various sampled parameters to be used in the EBS radionuclide transport abstraction, with the range and distribution of each parameter provided. This table is itself a summary of Table 6.5-13, which, along with the rest of Section 6.5.2, gives further details about each parameter and the location in this document where the parameter is developed. A summary of fixed, single-value parameters to be used in the EBS radionuclide transport abstraction is given in Table 8.2-4. Equations used to compute various parameters in the EBS radionuclide transport abstraction are shown in Table 8.2-5.

Table 8.2-3. Sampled Model Inputs Used in the EBS Radionuclide Transport Abstraction

Input Name	Input Description	Range	Distribution
Invert_Diff_Coeff_Uncert	Invert diffusion coefficient uncertainty; Table 8.2-5, Equation 8-1	Range: $10^{\mu \pm 3\sigma}$ (dimensionless) Mean: $\mu = 0.033$; Std. Dev. $\sigma = 0.218$	10ND
SS_Corrosion_Rate	Stainless steel corrosion rate (DTN: MO0409SPAACRWP.000 [DIRS 172059]; Spreadsheet "ECDF_metals2.xls"; Worksheet "316 ss", Columns L & M, Rows 5–15); cumulative distribution function	**Rate (μm yr^{-1})** 0.03699 0.037 0.1016 0.109 0.1524 0.154 0.1778 0.2032 0.2286 0.254 0.2794 0.51	**CDF** 0.000 0.063 0.125 0.188 0.250 0.313 0.375 0.438 0.563 0.750 0.813 1.000
CS_Corrosion_Rate	Carbon steel corrosion rate (DTN: MO0409SPAACRWP.000 [DIRS 172059]; Spreadsheet "ECDF_metals2.xls"; Worksheet "A516-Carbon Steel", Columns B & C, Rows 5-30);cumulative distribution function	**Rate (μm yr^{-1})** 65.76 65.77 66.75 69.84 70.00 71.25 72.21 72.64 72.87 72.89 73.47 74.29 74.51 74.60 75.41 77.31 79.29 80.00 80.87 83.26 83.66 83.74 85.68 90.97 106.93	**CDF** 0.000 0.042 0.083 0.125 0.167 0.208 0.250 0.292 0.333 0.375 0.417 0.458 0.500 0.542 0.583 0.625 0.667 0.708 0.750 0.792 0.833 0.875 0.917 0.958 1.000
Diff_Path_Length_CP_CSNF	Diffusive path length through corrosion products domain for CSNF packages	0.02 – 0.859 m	Uniform
Diff_Path_Length_CP_CDSP	Diffusive path length through corrosion products domain for codisposal packages	0.025 – 1.063 m	Uniform
CP_Spec_Surf_Area	Specific surface area of Fe_2O_3 corrosion products	1.0 – 22 m^2 g^{-1}	Uniform
DS_Flux_Uncertainty	Drip shield flux splitting uncertainty factor	0 – 0.85 (dimensionless)	Uniform

Table 8.2-3. Sampled Model Inputs Used in the EBS Radionuclide Transport Abstraction (Continued)

Input Name	Input Description	Range	Distribution
WP_Flux_Uncertainty	Waste package flux splitting uncertainty factor	0 – 2.41 (dimensionless)	Uniform
Fracture_Frequency	Unsaturated zone fracture frequency (BSC 2004 [DIRS 170040], Appendix A, Table A-1)	Mean=3.16 m^{-1} Std. Dev.=2.63 m^{-1}	Log-normal
UZ_Fracture_Fraction	Unsaturated zone fracture porosity (BSC 2004 [DIRS 170040], Appendix D, Table D-1)	0 – 1 (fraction); $E(x)=9.6 \times 10^{-3}$; $\sigma(x)=2.82 \times 10^{-3}$	Beta
UZ_Matrix_Porosity	Unsaturated zone matrix porosity (BSC 2004 [DIRS 170040], Appendix D, Table D-1)	0 – 1 (fraction); $E(x)=0.131$; $\sigma(x)=0.031$	Beta
Fracture_Saturation	Unsaturated zone fracture saturation (DTN: LB0307FMRADTRN.001 [DIRS 165451])	Uniform sampling from 433 locations for each infiltration case	Provided in source DTN
Fracture_Residual_Sat	Unsaturated zone fracture residual saturation (DTN: LB0307FMRADTRN.001 [DIRS 165451])	Uniform sampling from 433 locations	Provided in source DTN
Fracture_Percolation_Flux	Unsaturated zone fracture percolation flux (DTN: LB0307FMRADTRN.001 [DIRS 165451])	Uniform sampling from 433 locations for each infiltration case	Provided in source DTN
Flow_Focus_Factor	Unsaturated zone fracture percolation flow-focusing factor (DTN: LB0307FMRADTRN.001 [DIRS 165451])	Uniform sampling from 433 locations for each infiltration case	Provided in source DTN
UZ_Matrix_Saturation	Unsaturated zone matrix saturation (DTN: LB0307FMRADTRN.001 [DIRS 165451])	Uniform sampling from 433 locations for each infiltration case	Provided in source DTN
Matrix_Percolation_Flux	Unsaturated zone matrix percolation flux (DTN: LB0307FMRADTRN.001 [DIRS 165451])	Uniform sampling from 433 locations for each infiltration case	Provided in source DTN
Matrix_Rel_Perm_Low, Matrix_Rel_Perm_Mean, Matrix_Rel_Perm_High	Unsaturated zone matrix relative permeability for all three infiltration cases (DTN: LB0307FMRADTRN.001 [DIRS 165451])	Uniform sampling from 433 locations for each infiltration case	Provided in source DTN

Output DTN: SN0410T0507703.018.

NOTES: ND = Truncated normal distribution
$E(x)$ = Expected value
$\sigma(x)$ = Standard deviation
CDF = cumulative distribution function

Table 8.2-4. Fixed Model Inputs Used in the EBS Radionuclide Transport Abstraction

Input Name	Input Description	Source, or Developed in *EBS RT Abstraction*	Value
Max_Mass_CP_CSNF	Mass of corrosion products in CSNF waste package	Developed: Table 6.3-4	19,440 kg
Max_Mass_CP_HLW	Mass of corrosion products in CDSP waste package	Developed: Table 6.3-4	14,230 kg
Max_Thick_CS	Maximum thickness of carbon steel waste package internal components	IED BSC 2004 [DIRS 169472]	10 mm
Max_Thick_SS	Maximum thickness of stainless steel waste package internal components	IED BSC 2004 [DIRS 167394]	50.8 mm
DS_Total_Length	Length of drip shield	IED BSC 2004 [DIRS 169220], Table 1	5,805 mm
Density_CP	Density of corrosion products	Weast 1985 [DIRS 111561]	5,240 kg m^{-3}
Porosity_CP	Porosity of corrosion products	Developed: Section 6.5.1.2.1.3.2	0.4 (fraction)
Width_Invert	Width of invert	Developed: Equation 6.5.3.3-1	4.00 m
Thick_Invert	Average thickness of invert (flow and diffusive path length)	Developed: Equation 6.5.3.3-5	0.597 m
Vert_Cross_Sect_Area_Invert	Vertical cross sectional area of invert	Developed: Equation 6.5.3.3-2	2.39 m^2
Density_Water	Water density at 25°C	Weast 1985 [DIRS 111561]	997.0449 kg m^{-3}
Viscosity_Water	Water viscosity at 25°C	Lide 2000 [DIRS 162229]	0.890×10^{-3} Pa s (0.000890 kg m^{-1} s^{-1})
Intergranular_Porosity_Invert	Porosity of crushed tuff invert ballast	BSC 2004 [DIRS 169565], Appendix X	0.45 (fraction)
Invert_Viscosity_Ref_Temp	Reference temperature for viscosity giving temperature dependence of invert diffusion coefficient	Reference temperature for free water diffusion coefficient (25°C)	298.15 K
Interface_Scale_Factor	Scale factor used in numerical approximation for computing mass flux distribution from single-continuum to dual-continuum medium	Developed: Section 6.5.3.5	1×10^{-6} (dimensionless)
Intragranular_Porosity_Invert	Porosity of TSw35 tuff rock matrix (used in dual-continuum invert alternative conceptual model)	DTN: LB0207REVUZPRP.002 [DIRS 159672], Spreadsheet "Matrix_Props.xls", Row 20, Column C	0.131 (fraction)
Fracture_Aperture	Unsaturated zone fracture aperture	DTN: LB0205REVUZPRP.001 [DIRS 159525], Spreadsheet "FRACTURE_PROPERTY .xls," Row 20, Column L	1.5×10^{-4} m

Table 8.2-4. Fixed Model Inputs Used in the EBS Radionuclide Transport Abstraction (Continued)

Input Name	Input Description	Source, or Developed in *EBS RT Abstraction*	Value
Fracture_Interface_Area	Unsaturated zone fracture interface area	DTN: LB0205REVUZPRP.001 [DIRS 159525], Spreadsheet "FRACTURE_PROPERTY .xls," Row 20, Column R	9.68 m^2 m^{-3}
Active_Fracture_Parameter	Unsaturated zone active fracture parameter for TSw35 for all three infiltration cases	DTN: LB03013DSSCP3I.001 [DIRS 162379]	Low=0.476 Mean=0.569 High=0.570 (dimensionless)
Matrix_Perm_TSW33	Unsaturated zone matrix permeability for TSw33 for all three infiltration cases	DTNs: LB0208UZDSCPLI.002 [DIRS 161788]	Low=1.60 × 10^{-18} m^2
		LB0208UZDSCPMI.002 [DIRS 161243]	Mean=6.57 × 10^{-18} m^2
		LB0302UZDSCPUI.002 [DIRS 161787]	High=2.39 × 10^{-17} m^2
Matrix_Perm_TSW34	Unsaturated zone matrix permeability for TSw34 for all three infiltration cases	DTNs: LB0208UZDSCPLI.002 [DIRS 161788];	Low=1.38 × 10^{-19} m^2
		LB0208UZDSCPMI.002 [DIRS 161243]	Mean=1.77 × 10^{-19} m^2
		LB0302UZDSCPUI.002 [DIRS 161787]	High=2.96 × 10^{-19} m^2
Matrix_Perm_TSW35	Unsaturated zone matrix permeability for TSw35 for all three infiltration cases	DTNs: LB0208UZDSCPLI.002 [DIRS 161788]	Low=2.33 × 10^{-18} m^2
		LB0208UZDSCPMI.002 [DIRS 161243]	Mean=4.48 × 10^{-18} m^2
		LB0302UZDSCPUI.002 [DIRS 161787]	High=8.55 × 10^{-18} m^2
Matrix_Perm_TSW36	Unsaturated zone matrix permeability for TSw36 for all three infiltration cases	DTNs: LB0208UZDSCPLI.002 [DIRS 161788]	Low=5.58 × 10^{-19} m^2
		LB0208UZDSCPMI.002 [DIRS 161243]	Mean=2.00 × 10^{-19} m^2
		LB0302UZDSCPUI.002 [DIRS 161787]	High=7.41 × 10^{-19} m^2
UZ_Matrix_Density	Unsaturated zone dry matrix density for TSw35	DTN: SN0404T0503102.011 [DIRS 169129]	1,980 kg m^{-3}

Output DTN: SN0410T0507703.018.

IED = information exchange drawing

Table 8.2-5. Calculated Model Inputs Used in the EBS Radionuclide Transport Abstraction

Input Description	Input Equation and Parameter Description
Equation 8-1 Invert diffusion coefficient (Equation 6.3.4.1.1-16)	$D = D_0 \phi^{1.863} S_w^{1.863} 10^{ND(\mu=0.033,\sigma=0.218)}$ D = invert diffusion coefficient ($cm^2\ s^{-1}$) D_0 = free water diffusion coefficient ($cm^2\ s^{-1}$) ϕ = invert bulk porosity (fraction) S_w = invert water saturation (fraction) ND = truncated normal distribution (±3 standard deviations from the mean) μ = mean σ = standard deviation (Note that D is an effective value that includes the effects from porosity, saturation, and tortuosity.)
Equation 8-2 Temperature modification for invert diffusion coefficient (Equation 6.3.4.1.2-4)	$D_T = D_{T_0} \frac{T}{T_0} 10^{\left[\frac{1.3272(293.15-T_0)-0.001053(T_0-293.15)^2}{T_0-168.15}\right]-\left[\frac{1.3272(293.15-T)-0.001053(T-293.15)^2}{T-168.15}\right]}$ D_T = invert diffusion coefficient at temperature T ($cm^2\ s^{-1}$) D_{T_0} = invert diffusion coefficient at temperature T_0 ($cm^2\ s^{-1}$) T = temperature (K); valid range: 293.15 K ≤ T ≤ 373.15 K T_0 = reference temperature (K) (Invert_Viscosity_Ref_Temp)
Equation 8-3 Diffusion coefficient of unsaturated zone matrix and fractures (Equation 6.5.3.6-2)	$\log_{10} D_{ms} = -3.49 + 0.0138\theta_m + 0.165 \log_{10} k_{me}$ D_{ms} = diffusion coefficient of unsaturated zone matrix ($cm^2\ s^{-1}$) θ_m = unsaturated zone matrix water content (percent) k_{me} = effective permeability of unsaturated zone matrix (m^2) (Note that D_{ms} is an effective value that includes the effects from porosity, saturation, and tortuosity in the rock matrix.)
Equation 8-4 Effective permeability of unsaturated zone matrix (Equation 6.5.3.6-3)	$k_{me} = k_{rm} k_m$ k_{me} = effective permeability of unsaturated zone tuff matrix (m^2) k_{rm} = relative permeability of unsaturated zone tuff matrix (dimensionless) k_m = intrinsic permeability of unsaturated zone tuff matrix (m^2) (Matrix_Perm_TSWxx, xx = 33, 34, 35, 36)
Equation 8-5 Effective water saturation of corrosion products (Equation 6.5.1.2.1-27)	$S_{we,CP} = 3.28 \times 10^{-6} \bar{s}_{CP} (-\ln RH)^{-1/2.45}$ $S_{we,CP}$ = effective water saturation of corrosion products $\bar{s}_{CP}$ = specific surface area of corrosion products ($m^2\ kg^{-1}$) (CP_Spec_Surf_Area) RH = relative humidity

Table 8.2-5. Calculated Model Inputs Used in the EBS Radionuclide Transport Abstraction (Continued)

Input Description	Input Equation and Parameter Description
Equation 8-6 Pore volume of corrosion products (Equation 6.5.3.1.1-1)	$V_{CP} = \frac{m_{CP}}{\rho_{FeOx}}\left(\frac{\phi_{CP}}{1-\phi_{CP}}\right)$ V_{CP} = pore volume of corrosion products (m^3) m_{CP} = mass of corrosion products (kg) ρ_{FeOx} = density of corrosion products (kg m^{-3}) (Density_CP) ϕ_{CP} = porosity of corrosion products (m^3 void m^{-3} bulk volume) (Porosity_CP)
Equation 8-7 Mass of corrosion products (Equations 6.5.3.2-1 to 6.5.3.2-5)	$m_{CP}(t) = m_{CP1} + m_{CP2}$ m_{CP} = mass of corrosion products (kg) t = time since waste package emplacement (yr) t_0 = time when waste package breach occurs (yr) $m_{CP1} = \begin{cases} \left(\frac{t-t_0}{t_{f1}}\right)\frac{1}{3}m_{CPf}, & t-t_0 \le t_{f1} \\ \frac{1}{3}m_{CPf}, & t-t_0 > t_{f1} \end{cases}$ m_{CPf} = mass of corrosion products when internal components are fully degraded (kg) (Max_Mass_CP_CSNF or Max_Mass_CP_HLW) t_{f1} = lifetime of carbon steel (yr) $= \frac{1000\,(\text{Max\_Thick\_CS})}{r_1}$ r_1 = corrosion rate of carbon steel (μm yr^{-1}) (CS_Corrosion_Rate) $m_{CP2} = \begin{cases} \left(\frac{t-t_0}{t_{f2}}\right)\frac{2}{3}m_{CPf}, & t-t_0 \le t_{f2} \\ \frac{2}{3}m_{CPf}, & t-t_0 > t_{f2} \end{cases}$ t_{f2} = lifetime of stainless steel (yr) $= \frac{1000\,(\text{Max\_Thick\_SS})}{r_2}$ r_2 = corrosion rate of stainless steel (μm yr^{-1}) (SS_Corrosion_Rate)

Output DTN: SN0410T0507703.018.

Input parameters for the dual-continuum invert alternative conceptual model are listed in Table 8.2-6. Equations for calculating the intergranular and intragranular diffusion coefficients are listed in Table 8.2-7.

Table 8.2-6. Invert Diffusion Coefficient Alternative Conceptual Model Parameters

Input Name	Input Description	Where Developed in *EBS RT Abstraction*	Value
Invert_Geometry_Coef	Dimensionless geometry-dependent coefficient for intergranular-intragranular mass transfer coefficient	Section 6.6.4.1	8 - 21 (dimensionless) Uniform
Diff_Length_Inv_Inter_Intra	Characteristic length of the matrix structure	Section 6.6.4.1	5 mm
Crit_Moisture_Content_Intra	Critical moisture content of invert intragranular continuum	Section 6.6.5.1	0.089 (fraction)
Crit_Moisture_Content_Inter	Critical moisture content of invert intergranular continuum	Section 6.6.5.1	0.00932 – 0.0612 Uniform
Diff_Threshold_Invert	Threshold value of diffusion coefficient in intragranular invert continuum	Section 6.6.5.2	1×10^{-12} cm^2 s^{-1}
Sat_Diff_Coeff_Matrix	Diffusion coefficient in saturated UZ matrix	Section 6.6.5.2	9.24×10^{-7} cm^2 s^{-1}

Output DTN: SN0410T0507703.018.

Table 8.2-7. Calculated Model Inputs Used in the EBS Radionuclide Transport Abstraction Invert Diffusion Coefficient Alternative Conceptual Model

Input Description	Input Equation and Parameter Description
Equation 8-8 Invert intergranular continuum diffusion coefficient (Equation 6.6.5.2-3)	$D_{inter} = 0.45 D_0 \left(\frac{\theta}{100\phi_{inter}}\right)\left(\frac{\theta - \theta_C}{100\phi_I - \theta_C}\right), \quad \theta \geq \theta_C$ $D_{inter} = D_{limit}, \quad \theta < \theta_C$ D_0 = free water diffusion coefficient (cm^2 s^{-1}) D_{inter} = invert intergranular continuum diffusion coefficient (cm^2 s^{-1}) $\phi_I = \phi_{inter} + (1 - \phi_{inter})\phi_{intra}$ = bulk porosity of invert (fraction) ϕ_{inter} = invert intergranular continuum porosity (fraction) (Intergranular_Porosity_Invert) ϕ_{intra} = invert intragranular continuum porosity (fraction) (Intragranular_Porosity_Invert) θ = invert bulk moisture content (percent) θ_C = invert intergranular continuum critical moisture content (percent) (Crit_Moisture_Content_Inter)

Table 8.2-7. Calculated Model Inputs Used in the EBS Radionuclide Transport Abstraction Invert Diffusion Coefficient Alternative Conceptual Model (Continued)

Input Description	Input Equation and Parameter Description
Equation 8-9 Invert intragranular continuum diffusion coefficient (Equations 6.6.5.2-5 and 6.6.5.2-6)	$D_{intra} = D_{ms}\left(\frac{\theta_{intra}}{100\phi_{intra}}\right)^{p}, \quad \theta_{intra} \geq \theta_{min}$ $D_{intra} = D_{limit}, \quad \theta_{intra} < \theta_{min}$ D_{intra} = invert intragranular continuum diffusion coefficient ($cm^2\ s^{-1}$) D_{ms} = tuff matrix saturated diffusion coefficient ($cm^2\ s^{-1}$) (Sat_Diff_Coeff_Matrix) D_{limit} = threshold value of diffusion coefficient in intragranular invert continuum ($cm^2\ s^{-1}$) (Diff_Threshold_Invert) θ_{intra} = invert intragranular continuum moisture content (percent) ϕ_{intra} = invert intragranular continuum porosity (fraction) (Intragranular_Porosity_Invert) $p = \frac{\log_{10} D_{limit} - \log_{10} D_{ms}}{\log_{10}\left(\frac{\theta_{min}}{100}\right) - \log_{10} \phi_{intra}}$ θ_{min} = critical moisture content of invert intragranular continuum (percent) (Crit_Moisture_Content_Intra)

Output DTN: SN0410T0507703.018.

8.3 EVALUATION OF YUCCA MOUNTAIN REVIEW PLAN CRITERIA

This model report documents the abstraction model for flow of liquid and transport of radionuclides through the EBS. This section provides responses to the *Yucca Mountain Review Plan, Final Report* acceptance criteria applicable to this model report. Being conceptual in nature, it is not possible to evaluate quantitatively many of the *Yucca Mountain Review Plan, Final Report* (NRC 2003 [DIRS 163274]) acceptance criteria in Section 4.2.1.

The relevance of this model report to *Yucca Mountain Review Plan, Final Report* (NRC 2003 [DIRS 163274], Section 2.2.1.3.3) criteria for "Quantity and Chemistry of Water Contacting Engineered Barriers and Waste Forms," which are based on meeting the requirements of 10 CFR 63.114(a)–(c) and (e)–(g) [DIRS 158535], is as follows:

Acceptance Criterion 1–System Description and Model Integration are Adequate.

(1) Total system performance assessment adequately incorporates important design features, physical phenomena, and couplings, and uses consistent and appropriate assumptions throughout the quantity and chemistry of water contacting engineered barriers and waste forms abstraction process.

Response: The EBS radionuclide transport abstraction incorporates important design features, physical phenomena, and couplings, and uses consistent assumptions throughout the evaluation of the quantity of water contacting engineered barriers and waste forms. Sections 6.3.2 and 6.3.3 describe the conceptual model for water flux through the EBS. Section 6.5.1 describes the mathematical description of the EBS flow model. These sections provide information on seepage, effectiveness of the EBS components and mechanisms for breach or failure of the drip shield and waste package. Important general technical information related to water flow through the EBS can also be found throughout Section 6.

(2) The abstraction of the quantity and chemistry of water contacting engineered barriers and waste forms uses assumptions, technical bases, data, and models, that are appropriate and consistent with other related U.S. Department of Energy abstractions. For example, the assumptions used for the quantity and chemistry of water contacting engineered barriers and waste forms are consistent with the abstractions of "Degradation of Engineered Barriers" (NRC 2003 [DIRS 163274], Section 2.2.1.3.1); "Mechanical Disruption of Engineered Barriers" (NRC 2003 [DIRS 163274], Section 2.2.1.3.2); "Radionuclide Release Rates and Solubility Limits" (Section 2.2.1.3.4); "Climate and Infiltration" (NRC 2003 [DIRS 163274], Section 2.2.1.3.5); and "Flow Paths in the Unsaturated Zone" (NRC 2003 [DIRS 163274], Section 2.2.1.3.6). The descriptions and technical bases provide transparent and traceable support for the abstraction of quantity and chemistry of water contacting engineered barriers and waste forms.

Response: The EBS radionuclide transport abstraction uses assumptions, technical bases, data, and models that are consistent with other related U.S. Department of Energy abstractions. Sections 6.3.2, 6.3.3 and 6.5.1 of this model report provide descriptions and technical bases to support the quantity-related portion of the abstraction of quantity and chemistry of water contacting engineered barriers and waste forms. Section 5 provides assumptions that are relevant to the EBS flow model.

(3) Important design features, such as waste package design and material selection, drip shield, ground support, thermal loading strategy, and degradation processes, are considered during the determination of initial and boundary conditions for calculations of the quantity of water contacting engineered barriers and waste forms.

Response: Sections 6.3 and 6.5 provide the technical bases and details of model features for the EBS flow model. Section 6.3.2 describes drip shield design, effectiveness and breaching. Section 6.3.3 describes waste package design, breaching and impact of heat generation. Sections 6.3.3 and 6.5.3 provide invert model features.

(4) The U.S. Department of Energy reasonably accounts for the range of environmental conditions expected inside breached waste packages and in the engineered barrier environment surrounding the waste package. For example, the U.S. Department of Energy should provide a description and sufficient technical bases for its abstraction of changes in hydrologic properties in the near field, caused by coupled thermal-hydrologic-mechanical-chemical processes.

Response: Spatial and temporal abstractions address physical couplings (thermal-hydrologic-mechanical-chemical). Sections 6.3 and 6.5 provide descriptions of coupled effects for the flow model. These effects include heat generation inside the waste package and condensation on the drip shield surface. The seepage and imbibition fluxes are also the product of coupled thermal-hydrologic-mechanical-chemical processes.

(5) Sufficient technical bases and justification are provided for total system performance assessment assumptions and approximations for modeling coupled thermal-hydrologic mechanical-chemical effects on seepage and flow, the waste package chemical environment, and the chemical environment for radionuclide release. The effects of distribution of flow on the amount of water contacting the engineered barriers and waste forms are consistently addressed, in all relevant abstractions.

Response: The technical bases and justification are provided for total system performance assessment assumptions and approximations for modeling coupled thermal-hydrologic-mechanical-chemical effects on flow and radionuclide release throughout Sections 5 and 6. The effects of distribution of flow on the amount of water contacting the engineered barriers and waste forms are consistently addressed in Sections 6.3 and 6.5.

(6) The expected ranges of environmental conditions within the waste package emplacement drifts, inside of breached waste packages, and contacting the waste forms and their evolution with time are identified.

Response: These are provided in Sections 6.3, 6.5 and 6.7. Examples include the effects of the drip shield on the quantity of water (Sections 6.3.2 and 6.5.1); conditions that promote corrosion of engineered barriers and degradation of waste forms (Sections 6.3 and 6.5); wet and dry cycles; and size and distribution of penetrations of engineered barriers.

(7) The model abstraction for quantity and chemistry of water contacting engineered barriers and waste forms is consistent with the detailed information on engineered barrier design and other engineered features. For example, consistency is demonstrated for: (i) dimensionality of the abstractions; (ii) various design features and site characteristics; and (iii) alternative conceptual approaches. Analyses are adequate to demonstrate that no deleterious effects are caused by design or site features that the U.S. Department of Energy does not take into account in this abstraction.

Response: The EBS radionuclide transport abstraction is consistent with detailed information on engineered barrier design and other engineered features. Analysis discussions in Section 6 demonstrate that no deleterious effects are caused by design or site features that are not taken into account in this abstraction. Section 6.7 provides a summary discussion on the capability of the engineered barriers.

(8) Adequate technical bases are provided, including activities such as independent modeling, laboratory or field data, or sensitivity studies, for inclusion of any thermal-hydrologic-mechanical-chemical couplings and features, events, and processes.

Response: Technical bases are provided, including activities such as independent modeling, laboratory or field data, or sensitivity studies, for inclusion of any thermal-hydrologic-mechanical-chemical couplings and features, events, and processes. These are provided throughout Sections 6 and 7.

(9) Performance-affecting processes that have been observed in thermal-hydrologic tests and experiments are included into the performance assessment. For example, the U.S. Department of Energy either demonstrates that liquid water will not reflux into the underground facility or incorporates refluxing water into the performance assessment calculation, and bounds the potential adverse effects of alteration of the hydraulic pathway that result from refluxing water.

Response: Performance-affecting processes that have been observed in thermal-hydrologic tests and experiments are included primarily through the inputs (e.g., seepage values from *Abstraction of Drift Seepage* (BSC 2004 [DIRS 169131]), described in Section 6.3.2 of this model report, required to implement the EBS radionuclide transport abstraction.

Acceptance Criterion 2–Data are Sufficient for Model Justification.

(1) Geological, hydrological, and geochemical values used in the license application are adequately justified. Adequate description of how the data were used, interpreted, and appropriately synthesized into the parameters is provided.

Response: The EBS radionuclide transport abstraction provides the technical justification for geological, hydrological, and geochemical values used. There is also a description of how the data were used, interpreted, and synthesized into associated parameter values. Section 6.5.2 provides a summary discussion on the use and interpretation of data used in the EBS flow and transport models. The discussion includes the range, distribution and uncertainty of model data. Detailed description of data and technical justification of values used are provided throughout Sections 6.3 and 6.5.

(2) Sufficient data were collected on the characteristics of the natural system and engineered materials to establish initial and boundary conditions for conceptual models of thermal-hydrologic-mechanical-chemical coupled processes, that affect seepage and flow and the engineered barrier chemical environment.

Response: Data and sources of data are provided in Section 4.1 on the characteristics of the natural system and engineered materials needed to establish initial and boundary conditions for conceptual models of thermal-hydrologic-mechanical-chemical coupled processes that affect flow. Collection of input data used in this model report was done using acceptable techniques under the YMP quality assurance plan; specific techniques are provided in Sections 4.1.1 to 4.1.3.

(4) Sufficient information to formulate the conceptual approach(es) for analyzing water contact with the drip shield, engineered barriers, and waste forms is provided.

Response: Information required to formulate the conceptual approaches for analyzing water contact with the drip shield, engineered barriers, and waste forms is provided in Sections 6.3 and 6.5. Sections 6.3.2, 6.3.3 and 6.5.1 present the conceptual models used for water flux through the Engineered Barrier System, together with information on drip shield effectiveness, drip shield and waste package breaching, seepage and imbibition flux from the unsaturated zone matrix.

Acceptance Criterion 3–Data Uncertainty Is Characterized and Propagated Through the Model Abstraction.

(1) Models use parameter values, assumed ranges, probability distributions, and bounding assumptions that are technically defensible, reasonably account for uncertainties and variabilities, and do not result in an under representation of the risk estimate.

Response: The EBS radionuclide transport abstraction uses parameter values, assumed ranges, probability distributions, and bounding assumptions that account for uncertainties and variabilities, and that do not result in an under-representation of the risk estimate. Section 4.1 lists the data and parameters used, together with their sources. Section 6.5.2 provides a summary of the base case model inputs together with associated uncertainties.

(2) Parameter values, assumed ranges, probability distributions, and bounding assumptions used in the total system performance assessment calculations of quantity and chemistry of water contacting engineered barriers and waste forms are technically defensible and reasonable, based on data from the Yucca Mountain region (e.g., results from large block and drift-scale heater and niche tests), and a combination of techniques that may include laboratory experiments, field measurements, natural analog research, and process-level modeling studies.

Response: Parameter values, assumed ranges, probability distributions, and bounding assumptions used in the total system performance assessment calculations of quantity of water contacting engineered barriers and waste forms are based on data from the Yucca Mountain region, laboratory experiments, field measurements, natural analog research, and process-level modeling studies. Section 4.1 lists the data and parameters used, together with their sources. Section 6.5.2 provides a summary of the base case model inputs together with associated uncertainties.

(3) Input values used in the total system performance assessment calculations of quantity and chemistry of water contacting engineered barriers (e.g., drip shield and waste package) are consistent with the initial and boundary conditions and the assumptions of the conceptual models and design concepts for the Yucca Mountain site. Correlations between input values are appropriately established in the U.S. Department of Energy total system performance assessment. Parameters used to define initial conditions, boundary conditions, and computational domain in sensitivity analyses involving coupled thermal-hydrologic-mechanical-chemical effects on seepage and flow, the waste package chemical environment, and the chemical environment for radionuclide release, are consistent with available data. Reasonable or conservative ranges of parameters or functional relations are established.

Response: Input values used in the total system performance assessment calculations of quantity of water contacting engineered barriers (e.g., drip shield and waste package) are consistent with the initial and boundary conditions and the assumptions of the conceptual models and design concepts for the Yucca Mountain site. Reasonable or conservative ranges of parameters or functional relations have been established. Section 4.1 lists the data and parameters used, together with their sources. Section 6.5.2 provides a summary of the base case model inputs together with associated uncertainties.

(4) Uncertainty is adequately represented in parameter development for conceptual models, process models, and alternative conceptual models considered in developing the abstraction of radionuclide release rates and solubility limits, either through sensitivity analyses or use of bounding analyses.

Response: Adequate representation of uncertainties in the characteristics of the natural system and engineered materials is provided in parameter development for conceptual models, process-level models, and alternative conceptual models. In some instances, uncertainty is constrained using conservative limits. Parameter development for the models described in this model report is provided throughout Sections 6.3, 6.4, 6.5 and 6.6.

Acceptance Criterion 4–Model Uncertainty Is Characterized and Propagated Through the Model Abstraction.

(1) Alternative modeling approaches of features, events, and processes are considered and are consistent with available data and current scientific understanding, and the results and limitations are appropriately considered in the abstraction.

Response: Alternative modeling approaches of features, events, and processes are considered in Sections 6.4 and 6.6 and are consistent with available data and current scientific understanding, and the results and limitations are considered.

(2) Alternative modeling approaches are considered and the selected modeling approach is consistent with available data and current scientific understanding. A description that includes a discussion of alternative modeling approaches not considered in the final analysis and the limitations and uncertainties of the chosen model is provided.

Response: Alternative modeling approaches are considered in Sections 6.4 and 6.6. The selected modeling approach is consistent with available data and current scientific understanding. A description that includes a discussion of alternative modeling approaches not considered in the final analysis and the limitations and uncertainties of the chosen model is provided.

(3) Consideration of conceptual model uncertainty is consistent with available site characterization data, laboratory experiments, field measurements, natural analog information and process-level modeling studies; and the treatment of conceptual model uncertainty does not result in an under-representation of the risk estimate.

Response: Consideration of conceptual model uncertainty is consistent with available site characterization data, laboratory experiments, field measurements, natural analog information and process-level modeling studies. The fundamental relationships, e.g., mass balance and flow equations, upon which the EBS radionuclide transport abstraction is based, are well-established with a long history of use in the scientific community and as such are not subject to significant uncertainty. In addition, the alternative conceptual models have been screened out (Section 6.4), thereby increasing confidence in the selected conceptual model. Other sources of uncertainty involve modeling choices (e.g., assumptions, geometry) that, because of their conservative nature, effectively bound uncertainty. This treatment of conceptual model uncertainty does not result in an under-representation of the risk estimate.

(4) Adequate consideration is given to effects of thermal-hydrologic-mechanical-chemical coupled processes in the assessment of alternative conceptual models. These effects may include: (i) thermal-hydrologic effects on gas, water, and mineral chemistry; (ii) effects of microbial processes on the engineered barrier chemical environment and the chemical environment for radionuclide release; (iii) changes in water chemistry that may result from the release of corrosion products from the engineered barriers and interactions between engineered materials and ground water; and (iv) changes in boundary conditions (e.g., drift shape and size) and hydrologic properties, relating to the response of the geomechanical system to thermal loading.

Response: Consideration is given in Sections 6.4 and 6.6 to effects of thermal-hydrologic-mechanical-chemical coupled processes in the assessment of alternative conceptual models.

Acceptance Criterion 5–Model Abstraction Output Is Supported by Objective Comparisons.

(1) The models implemented in this total system performance assessment abstraction provide results consistent with output from detailed process-level models and/or empirical observations (laboratory and field testings and/or natural analogs).

Response: The models implemented in this total system performance assessment abstraction provide results consistent with output from detailed process-level models and/or empirical observations (laboratory testings). For example, Sections 6.5.1 and 7.1 provide comparison of the drip shield and waste package flux splitting models with breached drip shield and waste package experiments.

(2) Abstracted models for coupled thermal-hydrologic-mechanical-chemical effects on seepage and flow and the engineered barrier chemical environment, as well as on the chemical environment for radionuclide release, are based on the same assumptions and approximations demonstrated to be appropriate for process-level models or closely analogous natural or experimental systems. For example, abstractions of processes, such as thermally induced changes in hydrological properties, or estimated diversion of percolation away from the drifts, are adequately justified by comparison to results of process-level modeling, that are consistent with direct observations and field studies.

Response: Abstracted models for coupled thermal-hydrologic-mechanical-chemical effects on flow and radionuclide release are based on the same assumptions and approximations demonstrated to be appropriate for process-level models or closely analogous natural or experimental systems, as demonstrated throughout Sections 5 and 6.

(3) Accepted and well-documented procedures are used to construct and test the numerical models that simulate coupled thermal-hydrologic-mechanical-chemical effects on seepage and flow, engineered barrier chemical environment, and the chemical environment for radionuclide release. Analytical and numerical models are appropriately supported. Abstracted model results are compared with different mathematical models, to judge robustness of results.

Response: The EBS radionuclide transport abstraction uses accepted and well-documented procedures to construct and test the numerical models that simulate coupled thermal-hydrologic-mechanical-chemical effects on flow and radionuclide release, as provided throughout Sections 6 and 7. Technical support is presented for analytical and numerical models.

The relevance of this model report to the *Yucca Mountain Review Plan* criteria for "Radionuclide Release Rates and Solubility Limits" (NRC 2003 [DIRS 163274], Section 2.2.1.3.4), which are based on meeting the requirements of 10 CFR 63.114(a)–(c) and (e)–(g) [DIRS 158535], is as follows:

Acceptance Criterion 1–System Description and Model Integration Are Adequate.

(1) Total system performance assessment adequately incorporates important design features, physical phenomena, and couplings, and uses consistent and appropriate assumptions throughout the radionuclide release rates and solubility limits abstraction process.

Response: Total system performance assessment adequately incorporates important design features, physical phenomena, and couplings, and uses consistent and appropriate assumptions throughout the radionuclide release rates and solubility limits abstraction process. Section 6.3.4 describes the conceptual model for EBS transport model. Sections 6.5.1 and 6.5.3 describe the mathematical description of the EBS transport model components. These sections provide information on diffusion, retardation, transport through stress corrosion cracks and EBS-UZ boundary condition implementation. Important general technical information related to radionuclide transport through the EBS can also be found throughout Section 6.

(2) The abstraction of radionuclide release rates uses assumptions, technical bases, data, and models that are appropriate and consistent with other related U.S. Department of Energy abstractions. For example, the assumptions used for this model abstraction are consistent with the abstractions of "Degradation of Engineered Barriers" (NRC 2003 [DIRS 163274], Section 2.2.1.3.1); "Mechanical Disruption of Engineered Barriers" (NRC 2003 [DIRS 163274], Section 2.2.1.3.2); "Quantity and Chemistry of Water Contacting Engineered Barriers and Waste Forms" (NRC 2003 [DIRS 163274], Section 2.2.1.3.3); "Climate and Infiltration" (NRC 2003 [DIRS 163274], Section 2.2.1.3.5); and "Flow Paths in the Unsaturated Zone" (NRC 2003

[DIRS 163274], Section 2.2.1.3.6). The descriptions and technical bases provide transparent and traceable support for the abstraction of radionuclide release rates.

Response: The EBS radionuclide transport abstraction uses assumptions, technical bases, data, and models consistent with other related U.S. Department of Energy abstractions. The descriptions and technical bases described in Sections 6.3.4, 6.5.1, and 6.5.3 provide support for the abstraction of radionuclide release rates. Section 5 provides assumptions that are relevant to the EBS transport model.

(3) The abstraction of radionuclide release rates provides sufficient, consistent design information on waste packages and engineered barrier systems. For example, inventory calculations and selected radionuclides are based on the detailed information provided on the distribution (both spatially and by compositional phase) of the radionuclide inventory, within the various types of high-level radioactive waste.

Response: The EBS radionuclide transport abstraction provides consistent design information on waste packages and engineered barrier systems (Section 4.1 and throughout Section 6). Selected radionuclides are based on the detailed information provided on the distribution (both spatially and by compositional phase) of the radionuclide inventory, within the various types of high-level radioactive waste. Input data on radionuclides are provided in Section 4.1 and 6.5.2.

(4) The U.S. Department of Energy reasonably accounts for the range of environmental conditions expected inside breached waste packages and in the engineered barrier environment surrounding the waste package. For example, the U.S. Department of Energy should provide a description and sufficient technical bases for its abstraction of changes in hydrologic properties in the near field, caused by coupled thermal-hydrologic-mechanical-chemical processes.

Response: The EBS radionuclide transport abstraction accounts for the range of environmental conditions expected inside breached waste packages and in the engineered barrier environment surrounding the waste package. Sections 6.3 and 6.5 describe provisions for thermal, chemical, and hydrologic conditions inside and surrounding the waste package.

(5) The description of process-level conceptual and mathematical models is sufficiently complete, with respect to thermal-hydrologic processes affecting radionuclide release from the emplacement drifts. For example, if the U.S. Department of Energy uncouples coupled processes, the demonstration that uncoupled model results bound predictions of fully coupled results is adequate.

Response: The description of process-level conceptual and mathematical models, with respect to thermal-hydrologic processes affecting radionuclide release from the emplacement drifts is provided in Section 6.5.

(6) Technical bases for inclusion of any thermal-hydrologic-mechanical-chemical couplings and features, events, and processes in the radionuclide release rates and solubility Review Plan for Safety Analysis Report limits model abstraction are adequate. For example, technical bases may include activities, such as independent modeling, laboratory or field data, or sensitivity studies.

Response: Technical bases for inclusion of thermal-hydrologic-mechanical-chemical couplings and the disposition of features, events, and processes in the EBS radionuclide transport abstraction are summarized in Section 6.2.

Acceptance Criterion 2–Data Are Sufficient for Model Justification.

(1) Geological, hydrological, and geochemical values used in the license application are adequately justified. Adequate description of how the data were used, interpreted, and appropriately synthesized into the parameters is provided.

Response: Technical justification for the geological, hydrological, and geochemical values used in the EBS radionuclide transport abstraction is provided. There is also a discussion of how the data are used, interpreted, and synthesized into associated parameters values. Section 6.5.2 provides a summary discussion on the use and interpretation of data used in the EBS flow and transport models. The discussion includes the range, distribution and uncertainty of model data. Detailed descriptions of data and technical justification of values used are provided throughout Sections 6.3 and 6.5.

(2) Sufficient data have been collected on the characteristics of the natural system and engineered materials to establish initial and boundary conditions for conceptual models and simulations of thermal-hydrologic-chemical coupled processes. For example, sufficient data should be provided on design features, such as the type, quantity, and reactivity of materials, that may affect radionuclide release for this abstraction.

Response: Section 4.1 provides data on characteristics of the natural system and engineered materials needed to establish initial and boundary conditions for the EBS radionuclide transport abstraction conceptual models and simulations of thermal-hydrologic-chemical coupled processes.

(4) The corrosion and radionuclide release testing program for high-level radioactive waste forms intended for disposal provides consistent, sufficient, and suitable data for the in-package and in-drift chemistry used in the abstraction of radionuclide release rates and solubility limits. For expected environmental conditions, the U.S. Department of Energy provides sufficient justification for the use of test results, not specifically collected from the Yucca Mountain site, for engineered barrier components, such as high-level radioactive waste forms, drip shield, and backfill.

Response: The corrosion and radionuclide release testing program for HLW forms intended for disposal provides data for the in-package and in-drift chemistry used in the EBS radionuclide transport abstraction (Section 4.1). For expected environmental conditions, the EBS radionuclide transport abstraction provides justification for the use of test results, not specifically collected from the Yucca Mountain site, for engineered barrier components, such as HLW forms and drip shield (Sections 6.3 and 6.5).

Acceptance Criterion 3–Data Uncertainty Is Characterized and Propagated Through the Model Abstraction.

(1) Models use parameter values, assumed ranges, probability distributions, and bounding assumptions that are technically defensible, reasonably account for uncertainties and variabilities, and do not result in an under representation of the risk estimate.

Response: The EBS radionuclide transport abstraction uses parameter values, assumed ranges, probability distributions, and/or bounding assumptions that account for uncertainties and variabilities, and that do not cause an under-representation of the risk estimate. Section 4.1 lists the data and parameters used, together with their sources. Section 6.5.2 provides a summary of the base case model inputs together with associated uncertainties.

(2) Parameter values, assumed ranges, probability distributions, and bounding assumptions used in the abstractions of radionuclide release rates and solubility limits in the total system performance assessment are technically defensible and reasonable based on data from the Yucca Mountain region, laboratory tests, and natural analogs. For example, parameter values, assumed ranges, probability distributions, and bounding assumptions adequately reflect the range of environmental conditions expected inside breached waste packages.

Response: Parameter values, assumed ranges, probability distributions, and bounding assumptions used in the abstractions of radionuclide release rates and solubility limits in the total system performance assessment are based on data from the Yucca Mountain region, laboratory tests, and natural analogs. Parameter values, assumed ranges, probability distributions, and bounding assumptions reflect the range of environmental conditions expected inside breached waste packages. Section 4.1 lists the data and parameters used, together with their sources. Section 6.5.2 provides a summary of the base case model inputs together with associated uncertainties.

(3) DOE uses reasonable or conservative ranges of parameters or functional relations to determine effects of coupled thermal-hydrologic-chemical processes on radionuclide release. These values are consistent with the initial and boundary conditions and the assumptions for the conceptual models and design concepts for natural and engineered barriers at the Yucca Mountain site. If any correlations between the input values exist, they are adequately established in the total system performance assessment. For example, estimations are based on a thermal loading and ventilation strategy; engineered barrier system design (including drift liner, backfill, and drip-shield); and natural system masses and fluxes that are consistent with those used in other abstractions.

Response: The EBS radionuclide transport abstraction uses reasonable or conservative ranges of parameters or functional relations to determine effects of coupled thermal-hydrologic-chemical processes on radionuclide release. These values are consistent with the initial and boundary conditions and the assumptions for the conceptual models and design concepts for natural and engineered barriers at the Yucca Mountain site. Section 4.1 lists the data and parameters used, together with their sources. Section 6.5.2 provides a summary of the base case model inputs together with associated uncertainties.

(4) Uncertainty is adequately represented in parameter development for conceptual models, process models, and alternative conceptual models considered in developing the abstraction of radionuclide release rates and solubility limits, either through sensitivity analyses or use of bounding analyses.

Response: Uncertainty is represented in parameter development for conceptual models, process models, and alternative conceptual models considered in developing the abstraction of radionuclide release rates and solubility limits. Parameter development for the models described in this model report is provided throughout Sections 6.3, 6.4, 6.5, and 6.6.

(5) Parameters used to describe flow through and out of the engineered barrier, sufficiently bound the effects of backfill, excavation-induced changes, and thermally induced mechanical changes that affect flow.

Response: The EBS radionuclide transport abstraction considers the uncertainties, in the characteristics of the natural system and engineered materials, such as the type, quantity, and reactivity of material, in establishing initial and boundary conditions for conceptual models and simulations of thermal-hydrologic-chemical coupled processes that affect radionuclide release. Parameter development for the models described in this model report is provided throughout Sections 6.3, 6.4, 6.5, and 6.6.

(8) DOE adequately considers the uncertainties, in the characteristics of the natural system and engineered materials, such as the type, quantity, and reactivity of material, in establishing initial and boundary conditions for conceptual models and simulations of thermal-hydrologic-chemical coupled processes that affect radionuclide release.

Response: Parameters used to describe flow through and out of the engineered barrier bound the effects of excavation-induced changes and thermally induced mechanical changes that affect flow.

Acceptance Criterion 4–Model Uncertainty Is Characterized and Propagated Through the Model Abstraction.

(1) Alternative modeling approaches of features, events, and processes are considered and are consistent with available data and current scientific understanding, and the results and limitations are appropriately considered in the abstraction.

Response: Alternative modeling approaches of features, events, and processes are considered in Section 6.4 and are consistent with available data and current scientific understanding, and the results and limitations are considered.

(2) In considering alternative conceptual models for radionuclide release rates and solubility limits, DOE uses appropriate models, tests, and analyses that are sensitive to the processes modeled for both natural and engineering systems. Conceptual model uncertainties are adequately defined and documented, and effects on conclusions regarding performance are properly assessed. For example, in modeling flow and radionuclide release from the drifts, DOE represents significant discrete features, such as fault zones, separately, or demonstrates that their inclusion in the equivalent continuum model produces a conservative effect on calculated performance.

Response: In considering alternative conceptual models for radionuclide release rates and solubility limits (Sections 6.4. and 6.6), the EBS radionuclide transport abstraction uses models and analyses that are sensitive to the processes modeled for both natural and engineering systems. Conceptual model uncertainties are defined and documented, and effects on conclusions regarding performance are assessed. The fundamental relationships, e.g., mass balance and flow equations, upon which the EBS radionuclide transport abstraction is based, are well-established with a long history of use in the scientific community and as such are not subject to significant uncertainty. In addition, the alternative conceptual models have been screened out (Section 6.4), thereby increasing confidence in the selected conceptual model. Other sources of uncertainty involve modeling choices (e.g., assumptions, geometry) that, because of their conservative nature, effectively bound uncertainty.

(3) Consideration of conceptual model uncertainty is consistent with available site characterization data, laboratory experiments, field measurements, natural analog information and process-level modeling studies; and the treatment of conceptual model uncertainty does not result in an under-representation of the risk estimate.

Response: Consideration of conceptual model uncertainty is consistent with available site characterization data, laboratory experiments, field measurements, natural analog information and process-level modeling studies; and the treatment of conceptual model uncertainty does not result in an under-representation of the risk estimate, as discussed throughout Section 6. Section 6.5.2 provides discussions on parameter uncertainty.

(4) The effects of thermal-hydrologic-chemical coupled processes that may occur in the natural setting, or from interactions with engineered materials, or their alteration products, on radionuclide release, are appropriately considered.

Response: The effects of thermal-hydrologic-chemical coupled processes that may occur in the natural setting or from interactions with engineered materials or their alteration products, on radionuclide release, are considered in Section 6. For example, the effect of corrosion products on the transport of radionuclides is provided in Sections 6.3.4, 6.5.1, and 6.5.3.

Acceptance Criterion 5–Model Abstraction Output Is Supported by Objective Comparisons.

(1) The models implemented in this total system performance assessment abstraction provide results consistent with output from detailed process-level models and/or empirical observations (laboratory and field testings and/or natural analogs).

Response: The models implemented in this total system performance assessment abstraction provide results consistent with output from detailed process-level models and/or empirical observations (laboratory testings), as described in Sections 6.3, 6.5, and 7. Section 7 provides comparisons of models developed in this model report with other models and experimental results.

(3) DOE adopts well-documented procedures that have been accepted by the scientific community to construct and test the numerical models, used to simulate coupled thermal-hydrologic-chemical effects on radionuclide release. For example, DOE demonstrates that the numerical models used for high-level radioactive waste degradation and dissolution, and radionuclide release from the engineered barrier system, are adequate representations; include consideration of uncertainties; and are not likely to underestimate radiological exposures to the reasonably maximally exposed individual and releases of radionuclides into the accessible environment.

Response: The EBS radionuclide transport abstraction uses well-documented procedures in Section 6.5 that have been accepted by the scientific community to construct and test the numerical models used to simulate radionuclide release. The abstraction demonstrates that the numerical models used for radionuclide release from the EBS include consideration of uncertainties and are not likely to underestimate radiological exposures to the reasonably maximally exposed individual and releases of radionuclides into the accessible environment.

8.4 RESTRICTIONS FOR SUBSEQUENT USE

This abstraction was developed specifically for application in TSPA-LA. Assumptions and approximations are made in order to integrate with and be consistent with other models and abstractions incorporated in TSPA-LA. Therefore, individual submodels should not be used independently outside of the TSPA-LA framework. This abstraction must be reevaluated if any models that feed into it are modified.

Use of the two preliminary output DTNs: SN0403T0507703.015 and SN0409T0507703.017 is restricted to providing traceability in TSPA-LA. For any other application, the final output DTN: SN0410T0507703.018 is to be used. Differences between the preliminary and final DTNs are described in Appendix I.

INTENTIONALLY LEFT BLANK

9. INPUTS AND REFERENCES

The following is a list of references cited in this document. Column 2 represents the unique six digit identifier numerical identifier (the Document Input Reference System number), which is placed in the text following the reference callout (e.g., BSC 2002 [DIRS 160819]). The purpose of these numbers is to assist in locating a specific reference. Within the reference list, multiple sources by the same author (e.g., BSC 2002) are sorted alphabetically by title.

9.1 DOCUMENTS CITED

Anderson, M.J. 2004. "Mass for Nickel Gadolinium Neutron Absorber for Commercial Spent Nuclear Fuel (CSNF) Waste Packages--Initial Calculations (Not Yet Approved)." Interoffice memorandum from M.J. Anderson (BSC) to C. Howard, September 14, 2004, 0914043170, with enclosure. ACC: MOL.20040928.0325. 171637

Anderson, M.P. and Woessner, W.W. 1992. *Applied Groundwater Modeling, Simulation of Flow and Advective Transport.* San Diego, California: Academic Press. TIC: 103227. 123665

Atkins, P.W. 1990. *Physical Chemistry.* 4th Edition. New York, New York: W. H. Freeman and Company. TIC: 245483. 111464

Baker, N.A.; and Grisak, G.E. 2004. "Independent Model Validation Technical Review of the EBS-UZ Interface Sub-Model of the Radionuclide Transport Abstraction Model for the Yucca Mountain Project." Memo from N.A. Baker (INTERA) and G.E. Grisak (INTERA) to J. Schreiber (YMP) and C. Howard (YMP), July 27, 2004. ACC: MOL.20040730.0182. 170953

Balsley, S.D.; Brady, P.V.; Krumhansl, J.L.; and Anderson, H.L. 1998. "Anion Scavengers for Low-Level Radioactive Waste Repository Backfills." *Journal of Soil Contamination, 7,* (2), 125-141. Boca Raton, Florida: Lewis Publishers. TIC: 249779. 154439

Bear, J. 1988. *Dynamics of Fluids in Porous Media.* New York, New York: Dover Publications. TIC: 217568. 101379

Bethke, C.M.; and Brady, P.V. 2000. "How the Kd Approach Undermines Ground Water Cleanup." *Ground Water, 38,* (3), 435-443. Westerville, Ohio: National Ground Water Association. TIC: 249781. 154437

Bird, R.B.; Stewart, W.E.; and Lightfoot, E.N. 1960. *Transport Phenomena.* New York, New York: John Wiley & Sons. TIC: 208957. 103524

Brady, P.V.; Spalding, B.P.; Krupka, K.M.; Waters, R.D.; Zhang, P.; Borns, D.J.; and Brady, W.D. 1999. *Site Screening and Technical Guidance for Monitored Natural Attenuation at DOE Sites.* SAND99-0464. Albuquerque, New Mexico: Sandia National Laboratories. TIC: 249720. 154421

Briand, L.E.; Hirt, A.M.; and Wachs, I.E. 2001. "Quantitative Determination of the Number of Surface Active Sites and the Turnover Frequencies for Methanol Oxidation over Metal Oxide Catalysts: Application to Bulk Metal Molybdates and Pure Metal Oxide Catalysts." *Journal of Catalysis, 202,* ([2]), 268-278. New York, New York: Academic Press. TIC: 253845 161617

Brown, R.L.; and Richards, J.C. 1970. *Principles of Powder Mechanics, Essays on the Packing and Flow of Powders and Bulk Solids.* Pages 17-20. New York, New York: Pergamon Press. TIC: 245119. 131479

BSC (Bechtel SAIC Company) 2001. *Committed Material in Repository Drift.* CAL-GCS-GE-000002 REV 00. Las Vegas, Nevada: Bechtel SAIC Company. ACC: MOL.20010412.0157. 154441

BSC 2001. *Unsaturated Zone and Saturated Zone Transport Properties (U0100).* ANL-NBS-HS-000019 REV 00 ICN 02. Las Vegas, Nevada: Bechtel SAIC Company. ACC: MOL.20020311.0017. 160828

BSC 2002. *Test Plan for: Atlas Breached Waste Package Test and Drip Shield Experiments.* SITP-02-EBS-005 REV 00. Las Vegas, Nevada: Bechtel SAIC Company. ACC: MOL.20020314.0181. 158193

BSC 2002. *The Enhanced Plan for Features, Events, and Processes (FEPs) at Yucca Mountain.* TDR-WIS-PA-000005 REV 00. Las Vegas, Nevada: Bechtel SAIC Company. ACC: MOL.20020417.0385. 158966

BSC 2003. *Atlas Breached Waste Package and Drip Shield Experiments: Breached Drip Shield Tests.* TDR-EBS-MD-000025 REV 00. Las Vegas, Nevada: Bechtel SAIC Company. ACC: DOC.20030619.0001. 163406

BSC 2003. *Design and Engineering, Naval Long Waste Package Configuration.* 000-MW0-DNF0-00103-000-00A. Las Vegas, Nevada: Bechtel SAIC Company. ACC: ENG.20030929.0004. 165159

BSC 2003. *Risk Information to Support Prioritization of Performance Assessment Models.* TDR-WIS-PA-000009 REV 01 ICN 01, Errata 001. Las Vegas, Nevada: Bechtel SAIC Company. ACC: MOL.20021017.0045; DOC.20031014.0003. 168796

BSC 2004. *Abstraction of Drift Seepage.* MDL-NBS-HS-000019 REV 01. Las Vegas, Nevada: Bechtel SAIC Company. ACC: DOC.20041103.0003. 169131

BSC 2004. *Clad Degradation – Summary and Abstraction for LA.* ANL-WIS-MD-000021 REV 01. Las Vegas, Nevada: Bechtel SAIC Company. ACC: DOC.20041004.0002. 170023

BSC 2004. *CSNF Waste Form Degradation: Summary Abstraction.* ANL-EBS-MD-000015 REV 02. Las Vegas, Nevada: Bechtel SAIC Company. ACC: DOC.20040908.0001. 169987

BSC 2004. *D&E / PA/C IED Emplacement Drift Configuration and Environment.* 800-IED-MGR0-00202-000-00B. Las Vegas, Nevada: Bechtel SAIC Company. ACC: ENG.20040503.0001. 170559

BSC 2004. *D&E / PA/C IED Interlocking Drip Shield and Emplacement Pallet.* 800-IED-WIS0-00401-000-00D. Las Vegas, Nevada: Bechtel SAIC Company. ACC: ENG.20040503.0018. 169220

BSC 2004. *D&E/PA/C IED Typical Waste Package Components Assembly.* 800-IED-WIS0-00202-000-00B. Las Vegas, Nevada: Bechtel SAIC Company. ACC: ENG.20040202.0010. 167207

BSC 2004. *D&E/PA/C IED Typical Waste Package Components Assembly.* 800-IED-WIS0-00202-000-00C. Las Vegas, Nevada: Bechtel SAIC Company. ACC: ENG.20040517.0008. 169472

BSC 2004. *Defense HLW Glass Degradation Model.* ANL-EBS-MD-000016 REV 02. Las Vegas, Nevada: Bechtel SAIC Company. ACC: DOC.20041020.0015. 169988

BSC 2004. *Design & Engineering, 5 DHLW/DOE SNF - Short Waste Package Configuration.* 000-MW0-DS00-00102-000-00A. Las Vegas, Nevada: Bechtel SAIC Company. ACC: ENG.20040121.0002. 166946

BSC 2004. *Design & Engineering, 5 DHLW/DOE SNF - Short Waste Package Configuration.* 000-MW0-DS00-00103-000-00A. Las Vegas, Nevada: Bechtel SAIC Company. ACC: ENG.20040121.0003. 166947

BSC 2004. *Design and Engineering, 21-PWR Waste Package Configuration.* 000-MW0-DSU0-00402-000-00B. Las Vegas, Nevada: Bechtel SAIC Company. ACC: ENG.20040119.0004. 166953

BSC 2004. *Design and Engineering, 21-PWR Waste Package Configuration.* 000-MW0-DSU0-00403-000-00C. Las Vegas, Nevada: Bechtel SAIC Company. ACC: ENG.20040202.0024. 167394

BSC 2004. *21-PWR Waste Package Configuration.* 000-MW0-DSU0-00403-000-00D. Las Vegas, Nevada: Bechtel SAIC Company. ACC: ENG.20040708.0005. 170710

BSC 2004. *Design and Engineering, 44-BWR Waste Package Configuration.* 000-MW0-DSU0-00503-000-00B. Las Vegas, Nevada: Bechtel SAIC Company. ACC: ENG.20040213.0006. 167555

BSC 2004. *44-BWR Waste Package Configuration.* 000-MW0-DSU0-00503-000-00C. Las Vegas, Nevada: Bechtel SAIC Company. ACC: ENG.20040708.0007. 170838

BSC 2004. *Design and Engineering, Drip Shield Connector Guide.* 000-M00-SSE0-02001-000-00A. Las Vegas, Nevada: Bechtel SAIC Company. ACC: ENG.20040309.0011. 168326

BSC 2004. *Design and Engineering, Interlocking Drip Shield Configuration.* 000-M00-SSE0-00101-000-00B. Las Vegas, Nevada: Bechtel SAIC Company. ACC: ENG.20040305.0020. 168275

BSC 2004. *Design and Engineering, Interlocking Drip Shield Configuration.* 000-M00-SSE0-00102-000-00B. Las Vegas, Nevada: Bechtel SAIC Company. ACC: ENG.20040305.0021. 168067

BSC 2004. *Dissolved Concentration Limits of Radioactive Elements.* ANL-WIS-MD-000010, Rev. 03. Las Vegas, Nevada: Bechtel SAIC Company. ACC: DOC.20041109.0006. 169425

BSC 2004. *Drift-Scale Radionuclide Transport.* MDL-NBS-HS-000016 REV 01. Las Vegas, Nevada: Bechtel SAIC Company. ACC: DOC.20040927.0031. 170040

BSC 2004. *DSNF and Other Waste Form Degradation Abstraction.* ANL-WIS-MD-000004 REV 03. Las Vegas, Nevada: Bechtel SAIC Company. ACC: DOC.20040928.0003. 167618

BSC 2004. *Engineered Barrier System Features, Events, and Processes.* ANL-WIS-PA-000002 REV 03. Las Vegas, Nevada: Bechtel SAIC Company. 169898

BSC 2004. *Engineered Barrier System: Physical and Chemical Environment Model.* ANL-EBS-MD-000033, Rev. 03. Las Vegas, Nevada: Bechtel SAIC Company. 169860

BSC 2004. *Estimation of Mechanical Properties of Crushed Tuff for Use as Ballast Material in Emplacement Drifts.* 800-CYC-SSE0-00100-000-00A. Las Vegas, Nevada: Bechtel SAIC Nevada. ACC: ENG.20040309.0023. 168138

BSC 2004. *General Corrosion and Localized Corrosion of Waste Package Outer Barrier.* ANL-EBS-MD-000003 REV 02. Las Vegas, Nevada: Bechtel SAIC Company. ACC: DOC.20041004.0001. 169984

BSC 2004. *Igneous Intrusion Impacts on Waste Packages and Waste Forms.* MDL-EBS-GS-000002 REV 01. Las Vegas, Nevada: Bechtel SAIC Company. ACC: DOC.20040421.0002. 168960

BSC 2004. *In-Drift Natural Convection and Condensation.* MDL-EBS-MD-000001 REV 00. Las Vegas, Nevada: Bechtel SAIC Company. ACC: DOC.20041025.0006. 164327

BSC 2004. *In-Drift Precipitates/Salts Model.* ANL-EBS-MD-000045 REV 02. Las Vegas, Nevada: Bechtel SAIC Company. ACC: DOC.20041111.0002. 169863

BSC 2004. *Multiscale Thermohydrologic Model.* ANL-EBS-MD-000049 REV 02. Las Vegas, NV: Bechtel SAIC Company. ACC: DOC.20041014.0008. 169565

BSC 2004. *Particle Tracking Model and Abstraction of Transport Process.* MDL-NBS-HS-000020, Rev. 01. Las Vegas, Nevada: Bechtel SAIC Company. ACC: DOC.20041020.0016. 170041

BSC 2004. *Q-List.* 000-30R-MGR0-00500-000-000 REV 00. Las Vegas, Nevada: Bechtel SAIC Company. ACC: ENG.20040721.0007. 168361

BSC 2004. *Repository Subsurface Emplacement Drifts Steel Invert Structure Plan & Elevation.* 800-SS0-SSE0-00101-000-00B. Las Vegas, Nevada: Bechtel SAIC Company. ACC: ENG.20040520.0004. 169503

BSC 2004. *Repository Subsurface Emplacement Drifts Steel Invert Structure Sect. & Committed Materials.* 800-SS0-SSE0-00102-000-00B. Las Vegas, Nevada: Bechtel SAIC Company. ACC: ENG.20040520.0005. 169776

BSC 2004. *Seepage Model for PA Including Drift Collapse.* MDL-NBS-HS-000002 REV 03. Las Vegas, Nevada: Bechtel SAIC Company. ACC: DOC.20040922.0008. 167652

BSC 2004. *Seismic Consequence Abstraction.* MDL-WIS-PA-000003 Rev. 01. Las Vegas, Nevada: Bechtel SAIC Company. ACC: DOC.20041025.0004. 169183

BSC 2004. *Stress Corrosion Cracking of the Drip Shield, the Waste Package Outer Barrier, and the Stainless Steel Structural Material.* ANL-EBS-MD-000005 REV 02. Las Vegas, Nevada: Bechtel SAIC Company. ACC: DOC.20041028.0008. 172203

BSC 2004. *Technical Management Review Board (TMRB) Decision Proposal.* TMRB-2004-088. Las Vegas, Nevada: Bechtel SAIC Company. ACC: MOL.20041027.0228. 172219

BSC 2004. *Technical Work Plan for: Near-Field Environment and Transport: Engineered Barrier System: Radionuclide Transport Abstraction Model Report Integration.* TWP-MGR-PA-000020 REV 00. Las Vegas, Nevada: Bechtel SAIC Company. ACC: DOC.20040714.0001. 170775

BSC 2004. *UZ Flow Models and Submodels.* MDL-NBS-HS-000006 REV 02. Las Vegas, Nevada: Bechtel SAIC Company. ACC: DOC.20041101.0004. 169861

BSC 2004. *WAPDEG Analysis of Waste Package and Drip Shield Degradation.* ANL-EBS-PA-000001, Rev. 02. Las Vegas, Nevada: Bechtel SAIC Company. ACC: DOC.20041004.0005. 169996

BSC 2004. *Waste Form and In-Drift Colloids-Associated Radionuclide Concentrations: Abstraction and Summary.* MDL-EBS-PA-000004 REV 01. Las Vegas, Nevada: Bechtel SAIC Company. ACC: DOC.20041028.0007. 170025

Campbell, A.N.; and Smith, N.O. 1951. *The Phase Rule and its Applications.* 9th Edition. New York, New York: Dover Publications. TIC: 254360. 163817

Campbell, G.S. 1985. *Soil Physics with BASIC Transport Models for Soil-Plant Systems.* Developments in Soil Science 14. Amsterdam, The Netherlands: Elsevier. TIC: 214477. 100565

Canori, G.F.; and Leitner, M.M. 2003. *Project Requirements Document.* TER-MGR-MD-000001 REV 02. Las Vegas, Nevada: Bechtel SAIC Company. ACC: DOC.20031222.0006. 166275

Cantrel, L.; Chaouche, R.; and Chopin-Dumas, J. 1997. "Diffusion Coefficients of Molecular Iodine in Aqueous Solutions." *Journal Chemical Engineering Data, 42,* 216-220. Washington, D.C.: American Chemical Society. TIC: 246757. 138551

Choi, H. and Corapcioglu, M.Y. 1997. "Transport of a Non-volatile Contaminant in Unsaturated Porous Media in the Presence of Colloids." *Journal of Contaminant Hydrology, 25,* ([3-4]), 299-324. New York, New York: Elsevier. TIC: 253843. 161621

Conca, J.L.; and Wright, J. 1990. "Diffusion Coefficients in Gravel Under Unsaturated Conditions." *Water Resources Research, 26,* (5), 1055-1066. Washington, D.C.: American Geophysical Union. TIC: 237421. 101582

Conca, J.L. and Wright, J. 1992. "Diffusion and Flow in Gravel, Soil, and Whole Rock." *Applied Hydrogeology, 1,* 5-24. Hanover, Germany: Verlag Heinz Heise GmbH. TIC: 224081. 100436

Conca, J.L.; Apted, M.; and Arthur, R. 1993. "Aqueous Diffusion in Repository and Backfill Environments." *Scientific Basis for Nuclear Waste Management XVI, Symposium held November 30-December 4, 1992, Boston, Massachusetts.* Interrante, C.G. and Pabalan, R.T., eds. *294,* 395-402. Pittsburgh, Pennsylvania: Materials Research Society. TIC: 208880. 170709

Corapcioglu, Y.M.; and Jiang, S. 1993. "Colloid-Facilitated Groundwater Contaminant Transport," *Water Resources Research, 29* (7), 2215 - 2226. Washington, D.C.: American Geophysical Union. TIC: 222362. 105761

Corapcioglu, Y.M.; and Wang, S. 1999. "Dual-Porosity Groundwater Contaminant Transport in the Presence of Colloids," *Water Resources Research, 35* (11), 3261 - 3273. Washington, D.C.: American Geophysical Union. TIC: 255571. 167464

Coughtrey, P.J.; Jackson, D.; and Thorne, M.C. 1983. *Radionuclide Distribution and Transport in Terrestrial and Aquatic Ecosystems, A Critical Review of Data.* Six volumes. Rotterdam, The Netherlands: A.A. Balkema. TIC: 240299. 132164

CRWMS (Civilian Radioactive Waste Management System) M&O (Management and Operating Contractor) 1997. *Criticality Evaluation of Degraded Internal Configurations for the PWR AUCF WP Designs.* BBA000000-01717-0200-00056 REV 00. Las Vegas, Nevada: CRWMS M&O. ACC: MOL.19971231.0251. 102824

CRWMS M&O 2000. *Abstraction of Models for Stainless Steel Structural Material Degradation.* ANL-EBS-PA-000005 REV 00. Las Vegas, Nevada: CRWMS M&O. ACC: MOL.20000526.0337. 135968

CRWMS M&O 2000. *Clad Degradation–Local Corrosion of Zirconium and Its Alloys Under Repository Conditions.* ANL-EBS-MD-000012 REV 00. Las Vegas, Nevada: CRWMS M&O. ACC: MOL.20000405.0479. 136058

CRWMS M&O 2000. *The Determination of Diffusion Coefficient of Invert Materials.* TDR-EBS-MD-000002 REV 00. Las Vegas, Nevada: CRWMS M&O. ACC: MOL.20000124.0320. 156680

CRWMS M&O 2000. *Total System Performance Assessment for the Site Recommendation.* TDR-WIS-PA-000001 REV 00 ICN 01. Las Vegas, Nevada: CRWMS M&O. ACC: MOL.20001220.0045. 153246

CRWMS M&O 2000. *WAPDEG Analysis of Waste Package and Drip Shield Degradation.* ANL-EBS-PA-000001 REV 00 ICN 01. Las Vegas, Nevada: CRWMS M&O. ACC: MOL.20001208.0063. 151566

Cussler, E.L. 1997. *Diffusion: Mass Transfer in Fluid Systems.* 2nd Edition. Cambridge, United Kingdom: Cambridge University Press. TIC: 241150. 111468

Davis, J.A. and Kent, D.B. 1990. "Surface Complexation Modeling in Aqueous Geochemistry." *Mineral-Water Interface Geochemistry.* Hochella, M.F., Jr. and White, A.F., eds. Reviews in Mineralogy Volume 23. Pages 177-260. Washington, D.C.: Mineralogical Society of America. TIC: 224085. 143280

Davis, J.A.; Coston, J.A.; Kent, D.B.; and Fuller, C.C. 1998. "Application of the Surface Complexation Concept to Complex Mineral Assemblages." *Environmental Science and Technology, 32,* (19), 2820-2828. Washington, D.C.: American Chemical Society. TIC: 249656. 154436

Dillmann, Ph.; Mazaudier,F.; and Hœrlé, S. 2004. "Advances in Understanding Atmospheric Corrosion of Iron. I. Rust Characterisation of Ancient Ferrous Artefacts Exposed to Indoor Atmospheric Corrosion." *Corrosion Science 46*, 1401 – 1429. New York, New York: Elsevier. TIC: 256483. 171480

DOE (U.S. Department of Energy) 1992. *Characteristics of Potential Repository Wastes*. DOE/RW-0184-R1. Four volumes. Washington, D.C.: U.S. Department of Energy, Office of Civilian Radioactive Waste Management. ACC: HQO.19920827.0001; HQO.19920827.0002; HQO.19920827.0003; HQO.19920827.0004. 102588

DOE 1998. *Deficiency Report VAMO-98-D-132*. Washington, D.C.: U.S. Department of Energy, Office of Civilian Radioactive Waste Management. ACC: MOL.19991029.0063. 123628

DOE 2001. *Yucca Mountain Science and Engineering Report*. DOE/RW-0539. Washington, D.C.: U.S. Department of Energy, Office of Civilian Radioactive Waste Management. ACC: MOL.20010524.0272. 153849

EPA (U.S. Environmental Protection Agency) 1999. *Review of Geochemistry and Available K_d Values for Cadmium, Cesium, Chromium, Lead, Plutonium, Radon, Strontium, Thorium, Tritium (H^3), and Uranium.* Volume II of *Understanding Variation in Partition Coefficient, K_d, Values.* EPA 402-R-99-004B. Washington, D.C.: U.S. Environmental Protection Agency, Office of Radiation and Indoor Air. ACC: MOL.20040628.0034. 170376

EPA 2004. "Review of Geochemistry and Available K_d Values for Americium, Arsenic, Curium, Iodine, Neptunium, Radium, and Technetium." Volume III of *Understanding the Variation in Partition Coefficient, K_d, Values.* EPA 402-R-04-002C. Washington, D.C.: U.S. Environmental Protection Agency. ACC: MOL.20041102.0060. 172215

EPRI (Electric Power Research Institute) 1997. *The Technical Basis for the Classification of Failed Fuel in the Back-End of the Fuel Cycle.* EPRI TR-108237. Palo Alto, California: Electric Power Research Institute. TIC: 236839. 100444

EPRI 2000. *Evaluation of the Candidate High-Level Radioactive Waste Repository at Yucca Mountain Using Total System Performance Assessment, Phase 5.* 1000802. Palo Alto, California: Electric Power Research Institute. TIC: 249555. 154149

Faruque, M. 1993. *LWR Fuel Assemblies PC Database (VA-M04-20004.015.C032 602465).* Canyon Lake, Texas: Knowledge Dynamics. ACC: MOL.19990816.0229. 170706

Freeze, G.A.; Brodsky, N.S.; and Swift, P.N. 2001. *The Development of Information Catalogued in REV00 of the YMP FEP Database*. TDR-WIS-MD-000003 REV 00 ICN 01. Las Vegas, Nevada: Bechtel SAIC Company. ACC: MOL.20010301.0237. 154365

Freeze, R.A.; and Cherry, J.A. 1979. *Groundwater*. Englewood Cliffs, New Jersey: Prentice-Hall. TIC: 217571. 101173

Gerke, H.H. and van Genuchten, M.Th. 1996. "Macroscopic Representation of Structural Geometry for Simulating Water and Solute Movement in Dual-Porosity Media." *Advances in Water Resources, 19,* (6), 343-357. New York, New York: Elsevier. TIC: 255572. 167466

Gertsch, R.E.; Fjeld, A.; Asbury, B.; and Ozdemir, L. 1993. *Construction Applications for TSw2 TBM Cuttings at Yucca Mountain*. Golden, Colorado: Colorado School of Mines. ACC: NNA.19940317.0013. 107880

GoldSim Technology Group. 2002. *GoldSim Contaminant Transport Module, User's Guide*. Version 1.30. Redmond, Washington: Golder Associates. TIC: 253562. 160579

Graf, W.L. 1994. *Plutonium and the Rio Grande Environmental Change and Contamination in the Nuclear Age*. New York, New York: Oxford University Press. TIC: 249730. 154419

Gray, D.E., ed. 1972. *American Institute of Physics Handbook*. 3rd Edition. New York, New York: McGraw-Hill Book Company. TIC: 247425. 138541

Gregg, S.J.; and Sing, K.S.W. 1982. *Adsorption, Surface Area and Porosity*. 2nd Edition. 4th Printing 1997. San Diego, California: Academic Press. TIC: 249076. 153010

Haltier, E.; Fourest, B.; and David, F. 1990. "Spectroelectrochemical Study of Uranium and Cerium in Carbonate Media." *Radiochimica Acta, 51*, 107-112. München, Germany: R. Oldenbourg Verlag. TIC: 246868. 138643

Hiemenz, P.C. 1986. *Principles of Colloid and Surface Chemistry*. 2nd Edition, Revised and Expanded. Undergraduate Chemistry Volume 9. Lagowski, J.J., ed. New York, New York: Marcel Dekker. TIC: 246392. 117358

Holmes, H.F.; Fuller, E.L., Jr.; and Beh, R.A. 1974. "Adsorption of Argon, Nitrogen, and Water Vapor on Zirconium Oxide." *Journal of Colloid and Interface Science, 47*, (2), 365-371. New York, New York: Academic Press. TIC: 249666. 154379

Howard, C.L. 2002. Breached Waste Package Test and Drip Shield Experiments. Scientific Notebook SN-M&O-SCI-043-V1. ACC: MOL. 20021219.0022. 161516

Howard, C.L. 2002. Breached Waste Package Test and Drip Shield Experiments. Scientific Notebook SN-M&O-SCI-043-V2. ACC: MOL.20021219.0023. 161522

Hu, Q.; Kneafsey, T.; Wang, J.S.Y.; Roberts, J.; and Carlson, S. 2001. *Summary Report on Phase I Feasibility Study of In-Drift Diffusion.* LBNL-49063. Berkeley, California: Lawrence Berkeley National Laboratory. ACC: MOL.20030225.0125. 161623

Jin, M. 2004. "Independent Model Validation Technical Review of the EBS Flow and Transport Sub-Models of the Radionuclide Transport Abstraction Model for the Yucca Mountain Project." Memo from M. Jin (INTERA) to J. Schreiber, C. Howard, and K. Knowles, July 22, 2004. ACC: MOL.20040730.0179. 170952

Jurinak, J.J. 1964. "Interaction of Water with Iron and Titanium Oxide Surfaces: Goethite, Hematite, and Anatase." *Journal of Colloid Science, 19,* 477-487. New York, New York: Academic Press. TIC: 249667. 154381

Keller, G.V.; and Frischknecht, F.C. 1966. *Electrical Methods in Geophysical Prospecting.* Volume 10 of *International Series in Electromagnetic Waves.* Cullen, A.L.; Fock, V.A.; and Wait, J.R., eds. New York, New York: Pergamon Press. TIC: 230941. 111470

Kersting, A.B.; Efurd, D.W.; Finnegan, D.L.; Rokop, D.J.; Smith, D.K.; and Thompson, J.L. 1999. "Migration of Plutonium in Ground Water at the Nevada Test Site." *Nature, 397,* (6714), 56-59. London, England: Macmillan Journals]. TIC: 243597. 103282

Knight, B. 1982. "Why Do Some Iron Objects Break Up In Store?" *Conservation of Iron.* Clarke, R.W. and Blackshaw, S.M., eds. Maritime Monographs and Reports 53-1982. Pages 50-51. London, England: National Maritime Museum. TIC: 241006. 106733

Kügler, A. 1991. Special Sheet and Plate – Do the Job All Over the World. Mürzzuschlag, Austria: Böhler Bleche GmbH. TIC: 250553. 155761

Kügler, A. 1996. *Böhler Neutronit A976 Sheet and Plate for Nuclear Engineering.* Mürzzuschlag, Austria: Böhler Bleche GmbH. TIC: 240558. 107760

Langmuir, D. 1997. *Aqueous Environmental Geochemistry.* Upper Saddle River, New Jersey: Prentice Hall. TIC: 237107. 100051

Lee, J.H.; Chambré, P.L.; and Andrews, R.W. 1996. "Mathematical Models for Diffusive Mass Transfer from Waste Package Container with Multiple Perforations." *Proceedings of the 1996 International Conference on Deep Geological Disposal of Radioactive Waste, September 16-19, 1996, Winnipeg, Manitoba, Canada.* Pages 5-61 - 5-72. Toronto, Ontario, Canada: Canadian Nuclear Society. TIC: 233923. 100913

Lee, S. 1994. *Report to TRW on Contract No. DX 1456KP2L, Adsorption Studies of Water on Gold, Copper, Nickel and Iron Using the Quartz-Crystal Microbalance Technique.* Minneapolis, Minnesota: University of Minnesota. ACC: NNA.19940428.0129. 154380

Lide, D.R., ed. 2000. *CRC Handbook of Chemistry and Physics.* 81st Edition. Boca Raton, Florida: CRC Press. TIC: 253056. 162229

Lide, D.R., ed. 2002. *CRC Handbook of Chemistry and Physics.* 83rd Edition. Boca Raton, Florida: CRC Press. TIC: 253582. 160832

Liu, H.H.; Doughty, C.; and Bodvarsson, G.S. 1998. "An Active Fracture Model for Unsaturated Flow and Transport in Fractured Rocks." *Water Resources Research, 34,* (10), 2633-2646. Washington, D.C.: American Geophysical Union. TIC: 243012. 105729

Matsuda, T.; Taguchi, H.; and Nagao, M. 1992. "Energetic Properties of NiO Surface Examined by Heat-of-Adsorption Measurement." *Journal of Thermal Analysis, 38,* 1835 - 1845. Chichester, England: John Wiley & Sons. TIC: 249669. 154383

McCafferty, E. and Zettlemoyer, A.C. 1970. "Entropy of Adsorption and the Mobility of Water Vapour on α-Fe_2O_3." *Journal of Colloid and Interface Science, 34,* (3), 452-460. New York, New York: Academic Press. TIC: 249668. 154382

McCafferty, E.; and Zettlemoyer, A.C. 1971. "Adsorption of Water Vapour on α-Fe_2O_3." *Discussions of the Faraday Society, 52,* 239-263. London, England: Gurney and Jackson. TIC: 249665. 154378

Meijer, A. 1990. *Yucca Mountain Project Far-Field Sorption Studies and Data Needs.* LA-11671-MS. Los Alamos, New Mexico: Los Alamos National Laboratory. ACC: MOL.19980508.1113. 100780

Millard, A.R. and Hedges, R.E.M. 1996. "A Diffusion-Adsorption Model of Uranium Uptake by Archaeological Bone." *Geochimica et Cosmochimica Acta, 60,* (12), 2139-2152. New York, New York: Pergamon Press. TIC: 246791. 138677

Mills, R. 1973. "Self-Diffusion in Normal and Heavy Water in the Range 1-45°." *Journal of Physical Chemistry, 77,* (5), 685-688. Washington, D.C.: American Chemical Society. TIC: 246404. 133392

Mills, R. and Lobo, V.M.M. 1989. *Self-Diffusion in Electrolyte Solutions, A Critical Examination of Data Compiled from the Literature.* Physical Sciences Data 36. Pages 314-319. New York, New York: Elsevier. TIC: 248026. 138725

Mohanty, S.; Cragnolino, G.; Ahn, T.; Dunn, D.S.; Lichtner, P.C.; Manteufel, R.D.; and Sridhar, N. 1996. *Engineered Barrier System Performance Assessment Code: Ebspac Version 1.0B Technical Description and User's Manual.* CNWRA 96-011. San Antonio, Texas: Center for Nuclear Waste Regulatory Analyses. TIC: 233382. 130419

Morimoto, T.; Nagao, M.; and Tokuda, F. 1969. "The Relation between the Amounts of Chemisorbed and Physisorbed Water on Metal Oxides." *The Journal of Physical Chemistry, 73,* (1), 243 – 248. Washington, D.C.: American Chemical Society. TIC: 254165. 162877

Nagao, M.; Kumashiro, R.; Matsuda, T.; and Kuroda, Y. 1995. "Calorimetric Study of Water Two-Dimensionally Condensed on the Homogeneous Surface of a Solid." *Thermochimica Acta, 253,* (1-2), 221-233. New York, New York: Elsevier. TIC: 254099. 162878

NRC (U.S. Nuclear Regulatory Commission) 2003. *Yucca Mountain Review Plan, Final Report.* NUREG-1804, Rev. 2. Washington, D.C.: U.S. Nuclear Regulatory Commission, Office of Nuclear Material Safety and Safeguards. TIC: 254568. 163274

Nye, P.H. 1979. "Diffusion of Ions and Uncharged Solutes in Soils and Soil Clays." *Advances in Agronomy, 31,* 225-272. New York, New York: Academic Press. TIC: 255345. 167377

Olesen, T.; Moldrup, P.; and Gamst, J. 1999. "Solute Diffusion and Adsorption in Six Soils along a Soil Texture Gradient." *Soil Science Society of America Journal, 63,* (3), 519-524. Madison, Wisconsin: Soil Science Society of America. TIC: 249743. 154588

Olesen, T.; Moldrup, P.; Henricksen, K.; and Petersen, L.W. 1996. "Modeling Diffusion and Reaction in Soils: IV. New Models for Predicting Ion Diffusivity." *Soil Science, 161,* (10), 633 – 645. Baltimore, Maryland: Williams & Wilkins. TIC: 250477. 155700

Onishi, Y.; Serne, R.J.; Arnold, E.M.; Cowan, C.E.; and Thompson, F.L. 1981. *Critical Review: Radionuclide Transport, Sediment Transport, and Water Quality Mathematical Modeling; and Radionuclide Adsorption/Desorption Mechanisms.* NUREG/CR-1322. Washington, D.C.: U.S. Nuclear Regulatory Commission. TIC: 249732. 154420

Perry, D.L.; Phillips, S.L.; and Chung, J.D. 1988. "Potentiostatic Measurement of the Diffusion Coefficient of UO_2^{2+} in Carbonate Media." *Inorganica Chimica Acta, 149,* 301-304. Lausanne, Switzerland: Elsevier. TIC: 246806. 138732

Perry, R.H.; Chilton, C.H.; and Kirkpatrick, S.D., eds. 1963. *Chemical Engineers' Handbook.* 4th Edition. New York, New York: McGraw-Hill. TIC: 237828. 119529

Perry, R.H.; and Chilton, C.H., eds. 1973 . *Chemical Engineers' Handbook.* 5th Edition. New York, New York: McGraw-Hill. TIC: 242591. 104946

Philip, J.R.; Knight, J.H.; and Waechter, R.T. 1989. "Unsaturated Seepage and Subterranean Holes: Conspectus, and Exclusion Problem for Circular Cylindrical Cavities." *Water Resources Research, 25,* (1), 16-28. Washington, D.C.: American Geophysical Union. TIC: 239117. 105743

Pirson, S.J. 1963. *Handbook of Well Log Analysis for Oil and Gas Formation Evaluation.* Englewood Cliffs, New Jersey: Prentice-Hall. TIC: 245393. 111477

Porter, L.K.; Kemper, W.D.; Jackson, R.D.; and Stewart, B.A. 1960. "Chloride Diffusion in Soils as Influenced by Moisture Content." *Soil Science Society of America Proceedings, 24,* (5), 460-463. Danville, Illinois: Soil Science Society of America. TIC: 246854. 123115

Reardon, E.J. 1981. "Kd's – Can They be Used to Describe Reversible Ion Sorption Reactions in Contaminant Migration?" *Ground Water, 19,* (3), 279-286. Worthington, Ohio: Water Well Journal Publishing Company. TIC: 249726. 154434

Reimus, P.W.; Ware, S.D.; Benedict, F.C.; Warren, R.G.; Humphrey, A.; Adams, A.; Wilson, B.; and Gonzales, D. 2002. *Diffusive and Advective Transport of H^3, C^{14}, and Tc^{99} in Saturated, Fractured Volcanic Rocks from Pahute Mesa, Nevada.* LA-13891-MS. Los Alamos, New Mexico: Los Alamos National Laboratory. TIC: 253905. 163008

Roberts, J. J.; and Lin, W. 1997. "Electrical Properties of Partially Saturated Topopah Spring Tuffs: Water Distribution as a Function of Saturation." *Water Resources Research, 33*(4), 577-587. Washington, D.C.: American Geophysical Union. TIC: 239736. 101710

Rosch, F.; and Khalkin, V.A. 1990. "Ion mobilities of Trivalent f-Elements in Aqueous Electrolytes." *Radiochimica Acta, 51,* 101-106. Munich, Germany: R. Oldenbourg Verlag. TIC: 246710. 138739

Russo, R.E.; Mao, X.; Borisov, O.V.; and Liu, H. 2000. "Laser Ablation in Atomic Spectroscopy." *Encyclopedia of Analytical Chemistry.* Meyers, R.A., ed. Pages 9485-9506. Chichester, England: John Wiley & Sons. TIC: 250479. 155697

Šimůnek, J.; Jarvis, N.J.; van Genuchten, M.Th.; and Gardenas, A. 2003. "Review and Comparison of Models for Describing Non-Equilibrium and Preferential Flow and Transport in the Vadose Zone." *Journal of Hydrology, 272,* (1-4), 14-35. New York, New York: Elsevier. TIC: 255570. 167469

Singh, A.K.; Singh, H.; Singh, S.P.; and Sawhney, R.L. 2002. "Numerical Calculation of Psychrometric Properties on a Calculator." *Building and Environment, 37,* (4), 415-419. New York, New York: Elsevier. TIC: 253846. 161624

So, H.B.; and Nye, P.H. 1989. "The Effect of Bulk Density, Water Content and Soil Type on the Diffusion of Chloride in Soil." *Journal of Soil Science 40* (4), 743-749. Oxford, England: Blackwell Scientific. TIC: 255392. 170588

Stumm, W. 1992. *Chemistry of the Solid-Water Interface, Processes at the Mineral-Water and Particle-Water Interface in Natural Systems.* New York, New York: John Wiley & Sons. TIC: 237213. 141778

Tada, H.; Paris, P.C.; and Irwin, G.R. 1973. *The Stress Analysis of Cracks Handbook.* St. Louis, Missouri: Del Research Corporation. TIC: 247050. 118706

Tamura, H.; Tanaka, A.; Mita, K.; and Furuichi, R. 1999. "Surface Hydroxyl Site Densities on Metal Oxides as a Measure for the Ion-Exchange Capacity." *Journal of Colloid and Interface Science, 209,* (1), 225-231. New York, New York: Academic Press. TIC: 253844. 161625

Tsukamoto, M.; Ohe, T.; Fujita, T.; Hesbol, R.; and Hermansson, H-P. 1994. "Diffusion of Neptunium(V) in Loosely Compacted Sodium Bentonite." *Radiochimica Acta, 66/67,* 397-403. München, Germany: R. Oldenbourg Verlag. TIC: 246893. 138747

Wan, J.; and Wilson, J.L. 1994. "Visualization of the Role of the Gas-Water Interface on the Fate and Transport of Colloids in Porous Media," *Water Resources Research, 30* (1), 11 - 23. Washington, D.C.: American Geophysical Union. TIC: 246300. 124994

Weast, R.C.; and Astle, M.J., eds. 1981. *CRC Handbook of Chemistry and Physics.* 62nd Edition. Boca Raton, Florida: CRC Press. TIC: 240722. 100833

Weast, R.C., ed. 1985. *CRC Handbook of Chemistry and Physics.* 66th Edition. Boca Raton, Florida: CRC Press. TIC: 216054. 111561

YMP (Yucca Mountain Site Characterization Project) 1998. *Disposal Criticality Analysis Methodology Topical Report.* YMP/TR-004Q, Rev. 00. Las Vegas, Nevada: Yucca Mountain Site Characterization Office. ACC: MOL.19990210.0236. 104441

9.2 CODES, STANDARDS, REGULATIONS, AND PROCEDURES

10 CFR 63. 2002. Energy: Disposal of High-Level Radioactive Wastes in a Geologic Repository at Yucca Mountain, Nevada. Readily available. 158535

ASM (American Society for Metals) 1979. *Properties and Selection: Nonferrous Alloys and Pure Metals.* Volume 2 of *Metals Handbook.* 9th Edition. Metals Park, Ohio: American Society for Metals. TIC: 209800. 154085

ASTM (American Society for Testing and Materials) A 20/A20M-99a. 1999. *Standard Specification for General Requirements for Steel Plates for Pressure Vessels.* West Conshohocken, Pennsylvania: American Society for Testing and Materials. TIC: 247403. 147578

ASTM A 588/A 588M-01. 2001. *Standard Specification for High-Strength Low-Alloy Structural Steel with 50 ksi [345 MPa] Minimum Yield Point to 4-in. [100-mm] Thick.* West Conshohocken, Pennsylvania: American Society for Testing and Materials. TIC: 253998. 162724

ASTM A 759-00. 2001. *Standard Specification for Carbon Steel Crane Rails.* West Conshohocken, Pennsylvania: American Society for Testing and Materials. TIC: 253176. 159971

ASTM B 932-04. 2004. *Standard Specification for Low-Carbon Nickel-Chromium-Molybdenum-Gadolinium Alloy Plate, Sheet, and Strip.* West Conshohocken, Pennsylvania: American Society for Testing and Materials. TIC: 255846. 168403

ASTM G 1-90 (Reapproved 1999). 1999. *Standard Practice for Preparing, Cleaning, and Evaluating Corrosion Test Specimens.* West Conshohocken, Pennsylvania: American Society for Testing and Materials. TIC: 238771. 103515

AP-2.22Q, Rev. 1, ICN 1. *Classification Analyses and Maintenance of the Q-List.* Washington, D.C.: U.S. Department of Energy, Office of Civilian Radioactive Waste Management. ACC: DOC.20040714.0002.

AP-2.27Q, Rev. 1, ICN 5. *Planning for Science Activities.* Washington, D.C.: U.S. Department of Energy, Office of Civilian Radioactive Waste Management. ACC: DOC.20041014.0001.

AP-SIII.2Q, Rev. 1, ICN 2. *Qualification of Unqualified Data.* Washington, D.C.: U.S. Department of Energy, Office of Civilian Radioactive Waste Management. ACC: DOC.20040127.0008.

AP-SIII.10Q, Rev. 2, ICN 7. *Models.* Washington, D.C.: U.S. Department of Energy, Office of Civilian Radioactive Waste Management. ACC: DOC.20040920.0002.

LP-SI.11Q-BSC, Rev. 0, ICN 01. *Software Management.* Washington, D.C.: U.S. Department of Energy, Office of Civilian Radioactive Waste Management. ACC: DOC.20041005.0008

9.3 SOURCE DATA, LISTED BY DATA TRACKING NUMBER (DTN)

LA0003AM831341.001. Probability Distributions for Sorption Coefficients (Kds). Submittal date: 03/29/2000. 148751

LA0311AM831341.001. Correlation Matrix for Sampling of Sorption Coefficient Probability Distributions. Submittal date: 11/06/2003. 167015

LA0408AM831341.001. Unsaturated Zone Distribution Coefficients (Kds) for U, Np, Pu, Am, Pa, Cs, Sr, Ra, and Th. Submittal date: 08/24/2004. 171584

LB0205REVUZPRP.001. Fracture Properties for UZ Model Layers Developed from Field Data. Submittal date: 05/14/2002. 159525

LB0207REVUZPRP.002. Matrix Properties for UZ Model Layers Developed from Field and Laboratory Data. Submittal date: 07/15/2002. 159672

LB0208UZDSCPLI.002. Drift-Scale Calibrated Property Sets: Lower Infiltration Data Summary. Submittal date: 08/26/2002. 161788

LB0208UZDSCPMI.002. Drift-Scale Calibrated Property Sets: Mean Infiltration Data Summary. Submittal date: 08/26/2002. 161243

LB03013DSSCP3I.001. 3-D Site Scale Calibrated Properties: Data Summaries. Submittal date: 01/27/2003. 162379

LB0302UZDSCPUI.002. Drift-Scale Calibrated Property Sets: Upper Infiltration Data Summary. Submittal date: 02/05/2003. 161787

LB0307FMRADTRN.001. Fracture-Matrix Partitioning Model: Spreadsheet Calculations. Submittal date: 07/31/2003. 165451

MO0003RIB00076.000. Physical and Chemical Characteristics of Type 316N Grade. Submittal date: 03/14/2000. 153044

MO0107TC239753.000. ASME Boiler and Pressure Vessel Code, Sec II B SB-575 Specification for Low-Carbon Nickel-Molybdenum-Chromium, Low-Carbon. Submittal date: 07/23/2004. 169973

MO0107TC240032.000. Standard Specification for Pressure Vessel Plates, Carbon Steel, for Moderate- and-Lower-Temperature Service. Submittal date: 07/19/2001. 169970

MO0207EBSATBWP.021. Atlas Breached Waste Package and Drip Shield Experiments: Initial Tests for Rough Drip Shield Surface. Submittal date: 07/31/2002. 163399

MO0207EBSATBWP.022. Atlas Breached Waste Package and Drip Shield Experiments: Initial Tests for Smooth Drip Shield Surface. Submittal date: 07/31/2002. 163400

MO0207EBSATBWP.023. Atlas Breached Waste Package and Drip Shield Experiments: Single Patch Q(Splash) and Q(Film) Tests on the Smooth Drip Shield Surface. Submittal date: 07/31/2002. 163402

MO0207EBSATBWP.024. Atlas Breached Waste Package and Drip Shield Experiments: Multiple Patch Tests for Smooth Drip Shield Surface. Submittal date: 07/31/2002. 163401

MO0207EBSATBWP.025. Atlas Breached Waste Package and Drip Shield Experiments: Bounding Flow Rate Tests on the Smooth Drip Shield Surface. Submittal date: 07/31/2002. 163403

MO0208EBSATBWP.027. Atlas Breached Waste Package and Drip Shield Experiments: Multiple Patch Tests on the Rough Drip Shield Surface. Submittal date: 08/13/2002. 163404

MO0208EBSATBWP.028. Atlas Breached Waste Package and Drip Shield Experiments: Bounding Flow Rate Tests on the Rough Drip Shield Surface. Submittal date: 08/13/2002. 163405

MO0302UCC034JC.003. Graphical X-Ray Diffractometer Data and Mineral Analysis of Filtered Solids from Effluent Solution During Miniature Waste Package Corrosion. Submittal date: 02/10/2003. 162871

MO0312SPAPCEML.003. EBS P&CE Model Longevity of Materials Evaluation. Submittal date: 12/18/2003. 167409

MO0407SEPFEPLA.000. LA FEP List. Submittal date: 07/20/2004. 170760

MO0409SPAACRWP.000. Aqueous Corrosion Rates for Non-Waste Form Waste Package Materials. Submittal date: 09/16/2004. 172059

SN0306T0504103.006. Revised Sorption Partition Coefficients (Kd Values) for Selected Radionuclides Modeled in the TSPA (Total System Performance Assessment). Submittal date: 06/30/2003. 164131

SN0309T0504103.010. Updated Iron Oxyhydroxide Colloid Concentration Parameters, Specific Surface Area (SA) of Iron Oxyhydroxide Colloids, Target Flux Out Ratio (FRN) and Forward Rate Constant (K) for Pu & Am Sorption to Iron Oxyhydroxide Colloids & Stationary Corrosion. Submittal date: 09/18/2003. 165540

SN0310T0505503.004. Initial Radionuclide Inventories for TSPA-LA. Submittal date: 10/27/2003. 168761

SN0404T0503102.011. Thermal Conductivity of the Potential Repository Horizon Rev 3. Submittal date: 04/27/2004. 169129

9.4 OUTPUT DATA, LISTED BY DATA TRACKING NUMBER (DTN)

SN0403T0507703.015. Model Inputs Used in Engineered Barrier System (EBS) Radionuclide Transport Abstraction, Version 1. Submittal date: 03/12/2004. (Preliminary developed data).

SN0409T0507703.017. Model Inputs Used in Engineered Barrier System (EBS) Radionuclide Transport Abstraction. Submittal date: 09/27/2004. (Preliminary developed data).

SN0410T0507703.018. Engineered Barrier System (EBS) Radionuclide Transport Abstraction Model Inputs. Submittal date: 11/03/2004.

9.5 SOFTWARE CODES

Golder Associates 2003. *Software Code: GoldSim.* V8.01 Service Pack 1. PC, Windows 2000. 10344-8.01 SP1-00. 166572

APPENDIX A
MICROSOFT EXCEL SPREADSHEET "MASSES OF MATERIALS"

MICROSOFT EXCEL SPREADSHEET "MASSES OF MATERIALS"

In this spreadsheet, the mass of iron and the equivalent mass of Fe_2O_3 is calculated for four waste packages. The results are reported in Table 6.3-4. The calculation is done: 21-PWR (absorber plate), 44-BWR (absorber plate), 5-DHLW/DOE Short, and Naval Long.

The procedure for determining the equivalent mass of Fe_2O_3 is to calculate the total mass of each type of iron-containing alloy, calculate the mass of iron in all components of each alloy based on the iron content of the alloy, sum the mass of iron in the waste package, and convert the iron mass to Fe_2O_3 mass using the stoichiometry and molecular weights. Only the components within the outer corrosion barrier are included in the calculation; the outer corrosion barrier is considered to be inert.

For a 21-PWR waste package, the mass and number of each component are listed in Figures A-1 and A-2 as shown in Table 4.1-17 (BSC 2004 [DIRS 169472], Table 2). This calculation uses the previous waste package design in which the absorber plates are composed of Neutronit, rather than the current design with Ni-Gd absorber plates (BSC 2004 [DIRS 170710]). The impact of using the previous design is discussed in Section 6.3.4.2.3, where it is shown that the differences in absorber plate design should have negligible net effect on radionuclides transport from the EBS. In Column E (Figure A-1), the total mass of the components is computed (e.g., E2=C2*D2). The total mass of all components is summed in Cell E23. The calculation is repeated for a 44-BWR waste package (BSC 2004 [DIRS 169472], Table 3) in Column K (Figure A-1), for a 5 –DHLW/DOE Short waste package (BSC 2004 [DIRS 167207], Table 5) in Column Q (Figure A-2), and for a Naval Long waste package (BSC 2004 [DIRS 169472], Table 4) in Column W (Figure A-2). Consistent with the treatment for the 21-PWR waste package, the previous design with Neutronit absorber plates is considered for a 44-BWR waste package rather than the current design (BSC 2004 [DIRS 170838]). For the 5 DHLW/DOE Short waste package, a mass of 1 kg is erroneously used for the Interface Ring (Column O, Row 5 in Figure A-2); the correct mass is 44.6 kg (BSC 2004 [DIRS 167207], Table 5).

	A	B	C	D	E	F	G	H	I	J	K	L
1	21-PWR	Component Name	Mass, kg	Quantity	Total Mass kg		44-BWR	Component Name	Mass, kg	Quantity	Total Mass kg	
2	A516 CS	Basket -Side Guide	24.9	16	398.4		A516 CS	Basket -Side Guide	31.5	16	504	
3	A516 CS	Basket -Side Guide Stiffener	0.615	32	19.68		A516 CS	Basket Side Guide Stiffener	0.487	32	15.584	
4	A516 CS	Basket -End Side Guide	32.7	32	1046.4		A516 CS	Basket Corner Guide	43.4	32	1388.8	
5	A516 CS	Basket End Side Guide Stiffener	1.36	64	86.32		A516 CS	Basket Corner Guide Stiffener	8.23	64	142.72	
6	A516 CS	Basket Corner Guide	40.1	16	641.6		A516 CS	Fuel Basket Tube	108	44	4752	
7	A516 CS	Basket Corner Guide Stiffener	3.07	22	68.24		Neutronit A 978	Fuel Basket A - Plate	60.7	4	242.8	
8	A516 CS	Fuel Basket Tube	183	81	3335		Neutronit A 978	Fuel Basket B - Plate	60.7	12	728.4	
9	Neutronit A 978	Fuel Basket A - Plate	84.8	8	694.4		Neutronit A 978	Fuel Basket C - Plate	47.8	16	764.8	
10	Neutronit A 978	Fuel Basket B - Plate	84.8	8	694.4		Neutronit A 978	Fuel Basket D - Plate	60.7	8	485.6	
11	Neutronit A 978	Fuel Basket C - Plate	41.8	16	732.8		Neutronit A 978	Fuel Basket E - Plate	47.8	16	764.8	
12	Al 6061	Fuel Basket D - Plate	27.4	8	219.2		Al 6061	Fuel Basket F - Plate	20.4	8	163.2	
13	Al 6061	Fuel Basket E - Plate	27.4	8	219.2		Al 6061	Fuel Basket G - Plate	20.4	8	163.2	
14	316NG SS	Inner Vessel w/o Guides	8320	1	8320		316NG SS	Inner Vessel w/o Guides	10200	1	10200	
15	316NG SS	Inner Lid w/ LLF	733	1	733		316NG SS	Inner Lid w/ LLF	776	1	776	
16	316NG SS	Interface Ring	35.6	1	35.6		316NG SS	Interface Ring	36.4	1	36.4	
17	316NG SS	Spread Ring	25.3	1	25.3		316NG SS	Spread Ring	25.9	1	25.9	
18	316NG SS	Total 316 Welds	61	1	61		316NG SS	Total 316 Welds	63	1	63	
19	Alloy 22	OCB with transom sleeves	5730	1	5730		Alloy 22	OCB with transom sleeves	5650	1	5650	
20	Alloy 22	Middle Lid w/ LLF	226	1	226		Alloy 22	Middle Lid w/ LLF	237	1	237	
21	Alloy 22	Outer Lid w/ LLF	445	1	445		Alloy 22	Outer Lid w/ LLF	467	1	467	
22	Alloy 22	Total Alloy 22 Welds	51.8	1	51.8		Alloy 22	Total Alloy 22 Welds	53	1	53	
23		VP Total			29413.34			VP Total			27884.284	

Figure A-1. Spreadsheet "Masses of Materials;" Calculation of Mass of 21-PWR and 44-BWR Waste Package Components

	L	M	N	O	P	Q	R	S	T	U	V	V
1		5-DHLW	Component Name	Mass kg	Quantity	Total Mass, kg		Naval SNF	Component Name	Mass kg	Quantity	Total Mass, kg
2		A516 CS	Divider Plate Assembly	3720	1	3720		316NG SS	Inner Vessel	13300	1	13300
3		316NG SS	Inner Vessel	8860	1	8860		316NG SS	Inner Lid w/ LLF	962	1	962
4		316NG SS	Inner Lid w/ LLF	1170	1	1170		316NG SS	Interface Ring	40.5	1	40.5
5		316NG SS	Interface Ring	1	1	1		316NG SS	Spread Ring	28.9	1	28.9
6		316NG SS	Spread Ring	31.9	1	31.9		316NG SS	Total 316 Welds	92.2	1	92.2
7		316NG SS	Total 316 Welds	102	1	102		Alloy 22	OCB with trunnion sleeves	6360	1	6360
8		Alloy 22	OCB with trunnion sleeves	6540	1	6540		Alloy 22	Middle Lid w/ LLF	230	1	230
9		Alloy 22	Middle Lid w/ LLF	350	1	350		Alloy 22	Outer Lid w/ LLF	573	1	573
10		Alloy 22	Outer Lid w/ LLF	633	1	633		Alloy 22	Total Alloy 22 Welds	58.6	1	58.6
11		Alloy 22	Total Alloy 22 Welds	64.2	1	64.2			VP Total			24305.2
12			VP Total			21532.1						
13								316NG SS	Inner Vessel	13300	1	13300
14		A516 CS	Divider Plate Assembly	3720	1	3720		316NG SS	Inner Lid w/ LLF	962	1	962
15		A516 CS	Total			3720		316NG SS	Interface Ring	40.5	1	40.5
16								316NG SS	Spread Ring	28.9	1	28.9
17		316NG SS	Inner Vessel	8860	1	8860		316NG SS	Total 316 Welds	92.2	1	92.2
18		316NG SS	Inner Lid w/ LLF	1170	1	1170		316NG SS	Total			14423.6
19		316NG SS	Interface Ring	1	1	1						
20		316NG SS	Spread Ring	31.9	1	31.9		Alloy 22	OCB with trunnion sleeves	6360	1	6360
21		316NG SS	Total 316 Welds	102	1	102		Alloy 22	Middle Lid w/ LLF	230	1	230
22		316NG SS	Total			9864.9		Alloy 22	Outer Lid w/ LLF	573	1	573
23								Alloy 22	Total Alloy 22 Welds	58.6	1	58.6
24		Alloy 22	OCB with trunnion sleeves	6540	1	6540		Alloy 22	Total			8661.6
25		Alloy 22	Middle Lid w/ LLF	350	1	350						
26		Alloy 22	Outer Lid w/ LLF	633	1	633						
27		Alloy 22	Total Alloy 22 Welds	64.2	1	64.2						
28		Alloy 22	Total			7647.2						
29												
30												

Figure A-2. Spreadsheet "Masses of Materials;" Calculation of Mass of 5-DHLW and Naval Long Waste Package Components and Materials

In Rows 25-32, the calculation (Figure A-3) is repeated for a 21-PWR waste package for A 516 carbon steel components only. The total mass of carbon steel components is shown in Cell E32. Similarly, the calculation is repeated in Rows 34-37 (Figure A-3) for Neutronit, with the total Neutronit mass shown in Cell E37; in Rows 43-48 for 316 SS, with the total 316 SS mass shown in Cell E48. The masses of Al 6061 and Alloy 22 are also calculated, but this information is not used because the aluminum alloy contains a negligible amount of iron, and the Alloy 22 is considered to be inert. The calculation is repeated for a 44-BWR waste package in Column K (Figure A-3), for a 5-DHLW Short waste package in Column Q (Figure A-2), and for a Naval Long waste package in Column W (Figure A-2).

	A	B	C	D	E	F	G	H	I	J	K	L
24												
25	A516 CS	Basket -Side Guide	84.8	16	398.4		A516 CS	Basket -Side Guide	31.5	16	504	
26	A516 CS	Basket -Side Guide Stiffener	0.515	32	16.48		A516 CS	Basket Side Guide Stiffener	0.497	32	15.904	
27	A516 CS	Basket -End Side Guide	32.7	32	1046.4		A516 CS	Basket Corner Guide	43.4	32	1388.8	
28	A516 CS	Basket End Side Guide Stiffener	1.34	64	85.32		A516 CS	Basket Corner Guide Stiffener	2.23	64	142.72	
29	A516 CS	Basket Corner Guide	40.1	16	641.6		A516 CS	Fuel Basket Tube	108	44	4752	
30	A516 CS	Basket Corner Guide Stiffener	2.07	32	66.24		A516 CS	Total			6883.184	
31	A516 CS	Fuel Basket Tube	159	21	3339							
32	A516 CS	Total			5599.84		Neutronit A 978	Fuel Basket A - Plate	50.1	4	242.8	
33							Neutronit A 978	Fuel Basket B - Plate	50.1	12	728.4	
34	Neutronit A 978	Fuel Basket A - Plate	66.8	8	534.4		Neutronit A 978	Fuel Basket C - Plate	47.8	16	764.8	
35	Neutronit A 978	Fuel Basket B - Plate	66.8	8	534.4		Neutronit A 978	Fuel Basket D - Plate	50.1	8	485.6	
36	Neutronit A 978	Fuel Basket C - Plate	45.8	16	732.8		Neutronit A 978	Fuel Basket E - Plate	47.8	16	764.8	
37	Neutronit A 978	Total			2121.6		Neutronit A 978	Total			2986.4	
38												
39	Al 6061	Fuel Basket D - Plate	27.4	8	219.2		Al 6061	Fuel Basket F - Plate	20.4	8	163.2	
40	Al 6061	Fuel Basket E - Plate	27.4	8	219.2		Al 6061	Fuel Basket G - Plate	20.4	8	163.2	
41	Al 6061	Total			438.4		Al 6061	Total			326.4	
42												
43	316NG SS	Inner Vessel w/o Guides	8520	1	8520							
44	316NG SS	Inner Lid w/ LLF	739	1	739		316NG SS	Inner Vessel w/o Guides	10200	1	10200	
45	316NG SS	Interface Ring	35.6	1	35.6		316NG SS	Inner Lid w/ LLF	776	1	776	
46	316NG SS	Spread Ring	25.3	1	25.3		316NG SS	Interface Ring	36.4	1	36.4	
47	316NG SS	Total 316 Welds	81	1	81		316NG SS	Spread Ring	25.9	1	25.9	
48	316NG SS	Total			9400.9		316NG SS	Total 316 Welds	83	1	83	
49							316NG SS	Total			11121.3	
50	Alloy 22	OCB with trunnion sleeves	5730	1	5730							
51	Alloy 22	Middle Lid w/ LLF	226	1	226		Alloy 22	OCB with trunnion sleeves	5850	1	5850	
52	Alloy 22	Outer Lid w/ LLF	445	1	445		Alloy 22	Middle Lid w/ LLF	237	1	237	
53	Alloy 22	Total Alloy 22 Welds	51.6	1	51.6		Alloy 22	Outer Lid w/ LLF	447	1	447	
54	Alloy 22	Total			6452.6		Alloy 22	Total Alloy 22 Welds	53	1	53	
55							Alloy 22	Total			6647	
56												
57			Fe content (%)	Total Mass (kg)	Fe Mass (kg)				Fe content (%)	Total Mass (kg)	Fe Mass (kg)	
58		316NG SS	61.935	10861	6690			316NG SS	61.935	11121	6888	
59		A516 CS	98.37	5600	5508			A516 CS	98.37	6883	6692	
60		Neutronit A 978	56.08	2122	1462			Neutronit A 978	56.08	2986	1973	
61				18522	13659	73.4				20911	15553	74.4
62		Equivalent Fe_2O_3 mass (kg)			19443			Equivalent Fe_2O_3 mass (kg)			22236	
63												

Figure A-3. Spreadsheet "Masses of Materials;" Calculation of Mass of 21-PWR and 44-BWR Waste Package Materials and Equivalent Mass of Fe_2O_3

In Row 78, Columns C-E (Figure A-4), the iron content is calculated for the three alloys of interest (316 stainless steel, A 516 carbon steel, and Neutronit A 978, respectively). The iron content of these alloys is specified as "Balance" (see Table 4.1-10). It is calculated by summing the content of all nonferrous components of the alloys (Row 77, Columns C-E) and subtracting from 100 percent.

	A	B	C	D	E	F
64						
65						
66		Element	316NG Stainless Steel[a]	A 516 Carbon Steel[b]	Neutronit A 978[c]	
67		Mo	3	0	2.2	
68		Cr	18	0	18.5	
69		Ni	14	0	13	
70		Co	0	0	0.2	
71		Mn	2	1.3	0	
72		C	0.08	0.26	0.04	
73		P	0.045	0.035	0	
74		S	0.03	0.035	0	
75		Si	0.75	0	0	
76		N	0.16	0	0	
77		Total Non-Fe	38.065	1.63	33.94	
78		Fe	61.935	98.37	66.06	
79						
80		[a]DTN: MO0003RIB00076.000.				
81		[b]DTN: MO0107TC240032.000.				
82		[c]Kügler 1991, p. 15.				
83						

DTN: MO0003RIB00076.000 [DIRS 153044]; DTN: MO0107TC240032.000 [DIRS 169970].

Source: Kügler 1991 [DIRS 155761], p.15.

Figure A-4. Spreadsheet "Masses of Materials;" Elemental Weight Percent Compositions used in Calculation of Iron Content in Three Steel Alloys

In Figure A-3, the total masses of 316 SS (from E48), of A 516 CS (from E32), and of Neutronit A 978 (from E37) in all 21-PWR components are listed in Column D, Rows 58-60, respectively. The iron content of all components for each alloy is calculated in Column E (e.g., E58=C58*D58/100). The total iron content in the three alloys is summed in Cell E61. The average iron content of all components constructed of these three alloys is calculated in Cell F61 (F61=E61*100/D61); this information is not used.

The equivalent mass of Fe_2O_3 is computed in Cell E62 (Figure A-3) using the formula shown in Footnote d of Table 6.3-4: E62=E61*0.15969/0.055847/2. The results of these calculations (Rows 58-62, Columns C-F) are presented in Table 6.3-4 for a 21-PWR. These calculations are repeated for a 44-BWR waste package (Rows 58-62, Columns I-L; see Figure A-3), a 5-DHLW waste package (Rows 58-62, Columns O-R; Figure A-5), and for a Naval Long waste package (Rows 58-62, Columns U-X; Figure A-5).

	M	N	O	P	Q	R	S	T	U	V	W	X
56												
57			Fe content (%)	Total Mass (kg)	Fe Mass (kg)				Fe content (%)	Total Mass (kg)	Fe Mass (kg)	
58		316NG SS	61.935	10165	6296			316NG SS	61.935	14424	8933	
59		A516 CS	98.37	3729	3669			A516 CS	98.37	0	0	
60		Neutronit A 978	66.06	0	0			Neutronit A 978	66.06	0	0	
61				13895	9955	71.7				14424	8933	61.9
62		Equivalent Fe_2O_3 mass (kg)			14233			Equivalent Fe_2O_3 mass (kg)			12772	

Figure A-5. Spreadsheet "Masses of Materials;" Calculation of Equivalent Mass of Fe_2O_3 in 5-DHLW and Naval Long Waste Packages

INTENTIONALLY LEFT BLANK

APPENDIX B
IMPLEMENTATION OF RADIONUCLIDE SORPTION ONTO COLLOIDAL AND STATIONARY PHASES WITH FINITE DIFFERENCE SOLUTION

IMPLEMENTATION OF RADIONUCLIDE SORPTION ONTO COLLOIDAL AND STATIONARY PHASES WITH FINITE DIFFERENCE SOLUTION

CONCEPTUAL MODEL

This colloid model accounts for both reversible and irreversible sorption onto the iron oxyhydroxide (designated FeO) mobile colloids and the immobile FeO corrosion products together with reversible sorption onto both waste form and groundwater (GW) colloids within the engineered barrier system (EBS). Figure B-1 shows the conceptual model of radionuclide sorption onto the iron oxy-hydroxide colloidal and stationary phases. The upstream domain is considered to be degraded fuel rods, including secondary mineral phases, in equilibrium with the aqueous phase at the radionuclide solubility limit predicted by the solubility limits model (BSC 2004 [DIRS 169425]). The radionuclides of concern are the Pu and Am isotopes. Since the material balance equations are written as a mass balance, the equations are valid for any solute species. Certain system parameters, such as solubility, decay rate, and partition coefficients, will be dependent on the species. In this appendix, the species used for subsequent analysis and discussion is Pu.

There is no sorption considered in the upstream domain. Pu at its solubility limit is considered to transport by both advection and diffusion downstream into the corrosion product domain, where it can be involved in six separate reactions:

- Reversible Pu sorption onto FeO colloidal particles
- Reversible Pu sorption onto the stationary phase FeO corrosion products
- Irreversible Pu sorption onto FeO colloidal particles
- Irreversible Pu sorption onto the stationary phase FeO corrosion products
- Reversible Pu sorption onto waste form colloids
- Reversible Pu sorption onto GW colloids.

Denote the concentrations (kg Pu m^{-3} water) for the Pu in the seven possible states as

c_{Pu_aq} = concentration of Pu in aqueous solution

$c_{Pu\_FeO\_c}$ = concentration of Pu in the FeO colloid state from reversible sorption

$c_{Pu\_FeO\_CP}$ = concentration of Pu in the stationary FeO corrosion product state from reversible sorption

$c_{Irrv\_Pu\_FeO\_c}$ = concentration of Pu in the FeO colloid state from irreversible sorption

$c_{Irrv\_Pu\_FeO\_CP}$ = concentration of Pu in the stationary FeO corrosion products state from irreversible sorption

$c_{Pu\_WF\_c}$ = concentration of Pu in the waste form colloid state from reversible sorption

$c_{Pu\_GW\_c}$ = concentration of Pu in the GW colloid state from reversible sorption

and let

c_s = Pu solubility (concentration at the solubility limit) (kg Pu m^{-3} water).

The concentrations (kg colloid m^{-3} water) of all colloids and stationary corrosion products are:

c_{FeO_c} = concentration of FeO in the colloid state

c_{FeO_CP} = concentration of FeO in the corrosion product state

c_{WF_c} = concentration of waste form in the colloid state

c_{GW_c} = concentration of GW in the colloid state.

As indicated in Figure B-1, the mass in the fluid exiting the corrosion-product domain (reaction mixing cell) is expected to be proportioned such that the mass of Pu sorbed onto FeO colloids is some fraction of the total mass of Pu exiting the system in all forms—aqueous, reversibly sorbed, and irreversibly sorbed. Observations in nature, such as the transport of Pu from the Benham test site (Kersting et al. 1999 [DIRS 103282]) suggest that this fraction is about 95 percent. This is expressed as:

$$\Omega = \frac{\text{colloid mass flux out}}{\text{total mass flux out}} = 0.95 . \qquad \text{(Eq. B-1)}$$

This value of 95 percent is uncertain with an uncertainty range of 0.90 to 0.99 associated with it (BSC 2004 [DIRS 170025], Table 6-12, p. 6-72). It also may be a function of time, since the observation time for the Benham test is only about 50 years.

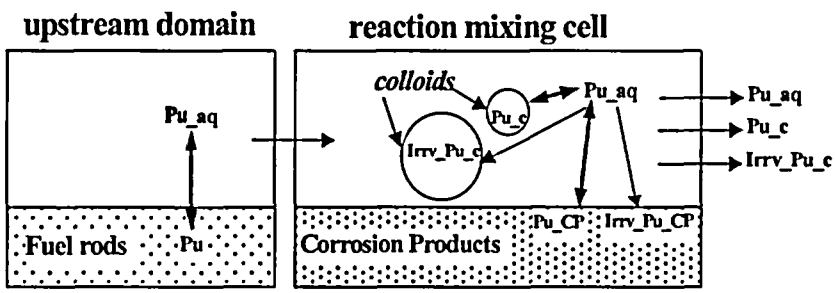

Figure B-1. Conceptual Model Schematic

Also of interest is the ratio of the mass flux leaving the mixing cell to the mass flux entering the mixing cell. This ratio of mass out to mass in is given by:

$$\Psi = \frac{\text{mass flux out}}{\text{mass flux in}} , \qquad \text{(Eq. B-2)}$$

and is a measure of the retardation due to sorption on the stationary corrosion products. The model is set up is such a way that most of the Pu mass entering the mixing cell is expected to be

sorbed onto the stationary FeO phase and only a small fraction of it flows downstream to the unsaturated zone.

REACTIONS

The reactions considered in this model are as follows, where R_i, represents the bulk reaction rate of Pu for the ith reaction, in units (kg Pu m^{-3} yr^{-1}):

$$R_1: \quad \mathrm{Pu(aq)} \rightarrow \mathrm{Pu(FeO_{col}^{irrev})} \qquad \text{(Eq. B-3)}$$

$$R_2: \quad \mathrm{Pu(aq)} \rightarrow \mathrm{Pu(FeO_{CP}^{irrev})} \qquad \text{(Eq. B-4)}$$

$$R_3: \quad \mathrm{Pu(aq)} \leftrightarrow \mathrm{Pu(FeO_{col}^{rev})} \qquad \text{(Eq. B-5)}$$

$$R_4: \quad \mathrm{Pu(aq)} \leftrightarrow \mathrm{Pu(FeO_{CP}^{rev})} \qquad \text{(Eq. B-6)}$$

$$R_5: \quad \mathrm{Pu(aq)} \leftrightarrow \mathrm{Pu(WF_{col}^{rev})} \qquad \text{(Eq. B-7)}$$

$$R_6: \quad \mathrm{Pu(aq)} \leftrightarrow \mathrm{Pu(GW_{col}^{rev})} \qquad \text{(Eq. B-8)}$$

Note that the reactions in Equations B-5 through B-8 are reversible equilibrium reactions, therefore their reaction rates are undefined and not included in subsequent mass balance equations. Equilibrium mass-action relationships are imposed instead, for these four reactions.

KINETIC REACTIONS

The ith irreversible reaction rate (where $i = 1$ or 2), R_i (kg Pu m^{-3} bulk-volume yr^{-1}), is expressed in terms of the ith bulk surface area for the mineral phase involved in the reaction, S_i (m^2 FeO m^{-3} bulk-volume), and the ith intrinsic (or surface) reaction rate, r_i (kg Pu m^{-2} FeO yr^{-1}):

$$R_i = S_i r_i . \qquad \text{(Eq. B-9)}$$

The irreversible reaction of Pu onto FeO colloids is then

$$R_1 = S_{FeO\_c} r_1 \qquad \text{(Eq. B-10)}$$

and for the irreversible reaction of Pu onto FeO corrosion products

$$R_2 = S_{FeO\_CP} r_2 . \qquad \text{(Eq. B-11)}$$

The bulk surface area (m^2 FeO m^{-3} bulk-volume) for FeO colloids and corrosion products are, respectively,

$$S_{FeO\_c} = \hat{S}_{FeO\_c} c_{FeO\_c} \phi S_w \qquad \text{(Eq. B-12)}$$

$$S_{FeO\_CP} = \hat{S}_{FeO\_CP} c_{FeO\_CP} \phi S_w \qquad \text{(Eq. B-13)}$$

where ϕ is the porosity of the FeO matrix, S_w is the water saturation and

$\hat{S}_{FeO\_c}$ = specific surface area of FeO colloids (m^2 FeO-colloid kg^{-1} FeO-colloid)

$\hat{S}_{FeO\_CP}$ = specific surface area of FeO corrosion products (m^2 FeO-CP kg^{-1} FeO-CP).

The intrinsic or surface reaction rate (i.e., rate per unit mineral surface area) is considered to be the same for the colloidal and stationary phases, i.e., $r_1 = r_2 \equiv r$, and it only has a forward component, since the reaction is irreversible. Further, suppose that the reactions are first order in the solution concentration c_{Pu_aq}:

$$r = kc_{Pu\_aq}, \qquad \text{(Eq. B-14)}$$

where

k = forward rate constant, (m^3 water-volume m^{-2} FeO yr^{-1}).

The two irreversible reaction rates on a water volume basis are then

$$\frac{R_1}{\phi S_w} = \hat{S}_{FeO\_c} c_{FeO\_c} k c_{Pu\_aq} = \overline{R}_1 c_{Pu\_aq} \qquad \text{(Eq. B-15)}$$

$$\frac{R_2}{\phi S_w} = \hat{S}_{FeO\_CP} c_{FeO\_CP} k c_{Pu\_aq} = \overline{R}_2 c_{Pu\_aq}, \qquad \text{(Eq. B-16)}$$

where $\overline{R}_1 = \hat{S}_{FeO\_c} c_{FeO\_c} k$ and $\overline{R}_2 = \hat{S}_{FeO\_CP} c_{FeO\_CP} k$ are reaction rate constants (yr^{-1}) for colloids and corrosion products, respectively.

EQUILIBRIUM REACTIONS

The four chemical species, $Pu(FeO_{col}^{rev})$, $Pu(FeO_{CP}^{rev})$, $Pu(WF_{col}^{rev})$ and $Pu(GW_{col}^{rev})$, involved in reversible equilibrium sorption reactions, Equations B-5, B-6, B-7, and B-8, follow the law of mass action according to

$$K_3^{eq} = \frac{[Pu(FeO_{col}^{rev})]}{[Pu(aq)]} \qquad \text{(Eq. B-17)}$$

$$K_4^{eq} = \frac{[Pu(FeO_{CP}^{rev})]}{[Pu(aq)]} \qquad \text{(Eq. B-18)}$$

$$K_5^{eq} = \frac{[Pu(WF_{col}^{rev})]}{[Pu(aq)]} \qquad \text{(Eq. B-19)}$$

$$K_6^{eq} = \frac{[\mathrm{Pu(GW_{col}^{rev})}]}{[\mathrm{Pu(aq)}]} \qquad \text{(Eq. B-20)}$$

where [Pu(j)] represents the thermodynamic activity of Pu in the jth phase (aqueous, colloidal, or corrosion product). Normally, these relationships are expressed for dilute solutions as a simple linear (K_d) (water volume/mass FeO) type of isotherm in terms of concentrations:

$$\hat{c}_{Pu\_FeO\_c} = K_{d\_FeO\_c} c_{Pu\_aq} \qquad \text{(Eq. B-21)}$$

$$\hat{c}_{Pu\_FeO\_CP} = K_{d\_FeO\_CP} c_{Pu\_aq} \qquad \text{(Eq. B-22)}$$

$$\hat{c}_{Pu\_WF\_c} = K_{d\_WF\_c} c_{Pu\_aq} \qquad \text{(Eq. B-23)}$$

$$\hat{c}_{Pu\_GW\_c} = K_{d\_GW\_c} c_{Pu\_aq} \qquad \text{(Eq. B-24)}$$

where

$\hat{c}_{Pu\_FeO\_c}$ = mass ratio of Pu sorbed onto FeO colloids (kg Pu kg^{-1} FeO-colloid)

$\hat{c}_{Pu\_FeO\_CP}$ = mass ratio of Pu sorbed onto FeO corrosion products (kg Pu kg^{-1} FeO-CP)

$\hat{c}_{Pu\_WF\_c}$ = mass ratio of Pu sorbed onto waste form colloids (kg Pu kg^{-1} WF-colloid)

$\hat{c}_{Pu\_GW\_c}$ = mass ratio of Pu sorbed onto GW colloids (kg Pu kg^{-1} GW-colloid).

The mass ratio for these reversible sorption reactions can be converted to water volume concentrations by the following:

$$c_{Pu\_FeO\_c} = c_{FeO\_c} \hat{c}_{Pu\_FeO\_c} \qquad \text{(Eq. B-25)}$$

$$c_{Pu\_FeO\_CP} = c_{FeO\_CP} \hat{c}_{Pu\_FeO\_CP} \qquad \text{(Eq. B-26)}$$

$$c_{Pu\_WF\_c} = c_{WF\_c} \hat{c}_{Pu\_WF\_c} \qquad \text{(Eq. B-27)}$$

$$c_{Pu\_GW\_c} = c_{GW\_c} \hat{c}_{Pu\_GW\_c} \qquad \text{(Eq. B-28)}$$

The reversible Pu equilibrium is expressed by the partition coefficients relating the aqueous state and the two reversible states given by Equations B-25 to B-28 as

$$c_{Pu\_FeO\_c} = c_{FeO\_c} K_{d\_FeO\_c} c_{Pu\_aq} = \overline{K}_{d\_FeO\_c} c_{Pu\_aq} \qquad \text{(Eq. B-29)}$$

$$c_{Pu\_FeO\_CP} = c_{FeO\_CP} K_{d\_FeO\_CP} c_{Pu\_aq} = \overline{K}_{d\_FeO\_CP} c_{Pu\_aq} \qquad \text{(Eq. B-30)}$$

$$c_{Pu\_WF\_c} = c_{WF\_c} K_{d\_WF\_c} c_{Pu\_aq} = \overline{K}_{d\_WF\_c} c_{Pu\_aq} \qquad \text{(Eq. B-31)}$$

$$c_{Pu\_GW\_c} = c_{GW\_c} K_{d\_GW\_c} c_{Pu\_aq} = \overline{K}_{d\_GW\_c} c_{Pu\_aq} \qquad \text{(Eq. B-32)}$$

where $\overline{K}_{d\_FeO\_c}$, $\overline{K}_{d\_FeO\_CP}$, $\overline{K}_{d\_WF\_c}$ and $\overline{K}_{d\_GW\_c}$ are dimensionless partition coefficients.

QUANTIFICATION OF CORROSION PRODUCTS

The corrosion products are generated from the degradation of the waste packages. It is the corrosion product mass that provides the porous matrix for the transport of nuclides in the reaction mixing cell. The amount of corrosion products is time dependent. As modeled, the corrosion product density (kg m^{-3} solid) and mass (kg) are known. Let

ρ_{FeO_CP} = corrosion product density

m_{FeO_CP} = mass of corrosion product.

The volume of corrosion products (kg m^{-3} solid) is then

$$V_{FeO\_CP} = \frac{m_{FeO\_CP}}{\rho_{FeO\_CP}}.$$

If the porosity of the corrosion product mass is specified as

$$\phi = \frac{V_{pore}}{V_{bulk}},$$

then

$$1-\phi = \frac{V_{FeO\_CP}}{V_{bulk}}.$$

The bulk volume is computed from

$$V_{bulk} = \frac{V_{FeO\_CP}}{1-\phi}$$

and the pore volume is

$$V_{pore} = \phi V_{bulk} = \frac{\phi}{1-\phi}\frac{m_{FeO\_CP}}{\rho_{FeO\_CP}}.$$

The stationary corrosion products concentration is defined as

$$c_{FeO\_CP} = \frac{mass_{FeO\_CP}}{V_{pore}}.$$

TRANSPORT EQUATIONS

The mass balance equation for the Pu contained in the aqueous state, the reversible colloid state and the reversible corrosion product state with radionuclide decay (neglecting ingrowth) is (see development in Section 6.5.1.2):

$$\begin{aligned}
&\frac{\partial \phi S_w (c_{Pu_aq} + c_{Pu_FeO_c} + c_{Pu_FeO_CP} + c_{Pu_WF_c} + c_{Pu_GW_c})}{\partial t} \\
&+ u \frac{\partial (c_{Pu_aq} + c_{Pu_FeO_c} + c_{Pu_WF_c} + c_{Pu_GW_c})}{\partial x} - \frac{\partial}{\partial x}\left(\phi S_w D_{aq} \frac{\partial c_{Pu_aq}}{\partial x} \right) \\
&- \frac{\partial}{\partial x}\left(\phi S_w D_{colloid} \frac{\partial (c_{Pu_FeO_c} + c_{Pu_WF_c} + c_{Pu_GW_c})}{\partial x} \right) \\
&= -R_1 - R_2 - \lambda \phi S_w (c_{Pu_aq} + c_{Pu_FeO_c} + c_{Pu_FeO_CP} + c_{Pu_WF_c} + c_{Pu_GW_c})
\end{aligned} \qquad \text{(Eq. B-33)}$$

where ϕ is the porosity of the FeO matrix, S_w is the water saturation, u is the Darcy velocity of the water ($\mathrm{m\,yr^{-1}}$), D_{aq} is the diffusivity ($\mathrm{m^2\,yr^{-1}}$) of the Pu in solution, $D_{colloid}$ is the colloid diffusivity ($\mathrm{m^2\,yr^{-1}}$), and λ is the radionuclide decay rate ($\mathrm{yr^{-1}}$). Now impose the reversible equilibrium of the Pu mass between the aqueous, colloid and corrosion products (Equations B-29 and B-32) together with representing the irreversible reactions as functions of the aqueous phase Pu concentration (Equations B-15 and B-16). The mass balance (Equation B-33) on a bulk volume basis can be expressed in terms of the concentration in the aqueous state:

$$\begin{aligned}
&(1 + \overline{K}_{d_FeO_c} + \overline{K}_{d_FeO_CP} + \overline{K}_{d_WF_c} + \overline{K}_{d_GW_c}) \frac{\partial \phi S_w c_{Pu_aq}}{\partial t} \\
&+ u(1 + \overline{K}_{d_FeO_c} + \overline{K}_{d_WF_c} + \overline{K}_{d_GW_c}) \frac{\partial c_{Pu_aq}}{\partial x} \\
&- \frac{\partial}{\partial x}\left(\phi S_w D_{aq} \frac{\partial c_{Pu_aq}}{\partial x} \right) \\
&- \frac{\partial}{\partial x}\left(\phi S_w D_{colloid} (\overline{K}_{d_FeO_c} + \overline{K}_{d_WF_c} + \overline{K}_{d_GW_c}) \frac{\partial c_{Pu_aq}}{\partial x} \right) \\
&= -\phi S_w (\overline{R}_1 + \overline{R}_2) c_{Pu_aq} \\
&- \lambda \phi S_w (1 + \overline{K}_{d_FeO_c} + \overline{K}_{d_FeO_CP} + \overline{K}_{d_WF_c} + \overline{K}_{d_GW_c}) c_{Pu_aq}.
\end{aligned} \qquad \text{(Eq. B-34)}$$

The mass balance equations for the irreversible Pu in the colloid and corrosion product states are, respectively,

$$\begin{aligned}
&\frac{\partial \phi S_w c_{Irrv_Pu_FeO_c}}{\partial t} + u \frac{\partial c_{Irrv_Pu_FeO_c}}{\partial x} - \frac{\partial}{\partial x}\left(\phi S_w D_{colloid} \frac{\partial c_{Irrv_Pu_FeO_c}}{\partial x} \right) \\
&= \phi S_w \overline{R}_1 c_{Pu_aq} - \lambda \phi S_w c_{Irrv_Pu_FeO_c}
\end{aligned} \qquad \text{(Eq. B-35)}$$

and

$$\frac{\partial \phi S_w c_{Irrv\_Pu\_FeO\_CP}}{\partial t} = \phi S_w \overline{R}_2 c_{Pu\_aq} - \lambda \phi S_w c_{Irrv\_Pu\_FeO\_CP} \cdot \qquad \text{(Eq. B-36)}$$

The boundary conditions require the upstream (left boundary cell, if flow is from left to right) conditions

$$\begin{aligned} c_{Pu\_aq} &= c_s \\ c_{Pu\_WF\_c} &= \overline{K}_{d\_WF\_c} c_s \end{aligned} \qquad \text{(Eq. B-37)}$$

$$c_{Pu\_FeO\_c} = c_{Pu\_FeO\_CP} = c_{Irrv\_Pu\_FeO\_c} = c_{Irrv\_Pu\_FeO\_CP} = c_{Pu\_GW\_c} = 0, \qquad \text{(Eq. B-38)}$$

where c_s is the Pu solubility as defined earlier. In this model, no FeO or groundwater colloids exit in the upstream waste form cell. The solubility at the upstream location is dependent on the CO_2 fugacity and pH at the upstream location (BSC 2004 [DIRS 169425], Section 8.1) and in general is time dependent: $c_s = c_s(t)$. The right boundary cell is a free flow boundary with concentrations fixed at zero. For diffusion calculations it is required to specify down stream diffusion parameters (porosity, diffusivity, diffusive length and diffusive area). The initial conditions within the mixing cell are zero for all Pu concentrations.

Both the colloid and corrosion product concentrations are chosen to be time dependent:

$$\begin{aligned} c_{FeO\_c} &= c_{FeO\_c}(t) \\ c_{FeO\_CP} &= c_{FeO\_CP}(t) \\ c_{WF\_c} &= c_{WF\_c}(t) \\ c_{GW\_c} &= c_{GW\_c}(t) \end{aligned} \qquad \text{(Eq. B-39)}$$

but are independent of the Pu concentrations. This implies that the reaction rates $\overline{R}_1$ and $\overline{R}_2$ are also time dependent.

The mass balance equations are solved numerically by finite difference method. The calculation sequence for a time step is to solve Equation B-34 for c_{Pu_aq}. Reversible equilibrium Equations B-29 through B-32 then give $c_{Pu\_FeO\_c}$, $c_{Pu\_FeO\_CP}$, $c_{Pu\_WF\_c}$ and $c_{Pu\_GW\_c}$. With c_{Pu_aq} known the mass balance Equations B-35 and B-36 for the irreversible components are solved.

DIMENSIONLESS FORM OF TRANSPORT EQUATIONS

In order to express the governing equations in dimensionless form, define dimensionless length, time and concentration, respectively,

$$\chi = x / L$$

$$\tau = \frac{ut}{\phi S_w L} = \frac{\bar{u}t}{L}$$

$$\bar{c} = c / c_s,$$

where L is the characteristic length (m) and $\bar{u} = \frac{u}{\phi S_w}$ is the average linear advective velocity (m yr^{-1}). The characteristic length would be the interval length or, for a finite difference solution, the grid block cell length. Make the change of variables to dimensionless space and time in the mass balance equations. If the colloid/corrosion product concentrations are taken to be constant (Equations B-39), then the Pu mass balance equation in the aqueous state is:

$$\begin{aligned}
&(1+\bar{K}_{d_FeO_c}+\bar{K}_{d_FeO_CP}+\bar{K}_{d_WF_c}+\bar{K}_{d_GW_c})\frac{\partial \bar{c}_{Pu_aq}}{\partial \tau} \\
&+(1+\bar{K}_{d_FeO_c}+\bar{K}_{d_WF_c}+\bar{K}_{d_GW_c})\frac{\partial \bar{c}_{Pu_aq}}{\partial \chi} \\
&-\left[\Delta_{aq}+\Delta_{colloid}\left(\bar{K}_{d_FeO_c}+\bar{K}_{d_WF_c}+\bar{K}_{d_GW_c}\right)\right]\frac{\partial^2 \bar{c}_{Pu_aq}}{\partial \chi^2} \\
&=-(\Theta_1+\Theta_2)\bar{c}_{Pu_aq}-(1+\bar{K}_{d_FeO_c}+\bar{K}_{d_FeO_CP}+\bar{K}_{d_WF_c}+\bar{K}_{d_GW_c})\Lambda\bar{c}_{Pu_aq}
\end{aligned} \qquad \text{(Eq. B-40)}$$

where

$$\Delta_{aq} = \frac{\frac{D_{aq}}{L}}{\frac{\bar{u}}{L}} = \frac{\text{diffusive rate in water}}{\text{advective rate}}, \qquad \text{(Eq. B-41)}$$

$$\Delta_{collid} = \frac{\frac{D_{colloid}}{L^2}}{\frac{\bar{u}}{L}} = \frac{\text{diffusive rate of colloids}}{\text{advective rate}}, \qquad \text{(Eq. B-42)}$$

$$\Theta_1 = \frac{\bar{R}_1}{\frac{\bar{u}}{L}} = \frac{\text{reaction rate to colloids}}{\text{advective rate}}, \qquad \text{(Eq. B-43)}$$

$$\Theta_2 = \frac{\bar{R}_2}{\frac{\bar{u}}{L}} = \frac{\text{reaction rate to corrosion products}}{\text{advective rate}}, \qquad \text{(Eq. B-44)}$$

$$\Lambda = \frac{\lambda}{\frac{\bar{u}}{L}} = \frac{\text{decay rate}}{\text{advective rate}}. \qquad \text{(Eq. B-45)}$$

The dimensionless form of the mass balance for the irreversible Pu concentrations (Equations B-5 and B-36) are:

$$\frac{\partial \bar{c}_{Irrv\_Pu\_FeO\_c}}{\partial \tau} + \frac{\partial \bar{c}_{Irrv\_Pu\_FeO\_c}}{\partial \chi} - \Delta_{colloid} \frac{\partial^2 \bar{c}_{Irrv\_Pu\_FeO\_c}}{\partial \chi^2} = \Theta_1 \bar{c}_{Pu\_aq} - \Lambda \bar{c}_{Irrv\_Pu\_FeO\_c} \qquad \text{(Eq. B-46)}$$

$$\frac{\partial \bar{c}_{Irrv\_Pu\_FeO\_CP}}{\partial \tau} = \Theta_2 \bar{c}_{Pu\_aq} - \Lambda \bar{c}_{Irrv\_Pu\_FeO\_CP}. \qquad \text{(Eq. B-47)}$$

DIFFERENCE SOLUTION OF TRANSPORT EQUATIONS

Consider a finite difference approximation of the governing mass balance equations. The discretization uses three spatial cells. The left or first cell represents the upstream boundary conditions. The second cell represents the mixing cell with reactions. The third or right cell represents the down stream boundary conditions. Since cells one and three represent boundary conditions, this discretization is a 0-dimensional or single cell representation of the processes. Let time step length be Δt. Let superscript n, for example $c^n_{Pu\_aq}$, denote the concentration at the nth time step. The discretization uses a first order backward difference approximation for the time derivative and the advective transport term. The diffusive flux uses a second order approximation. This discretization is consistent with GoldSim (GoldSim Technology Group 2002 [DIRS 160579]). In this model, diffusion of dissolved mass and waste form colloids occurs at the left boundary, and at the right boundary, diffusion of both dissolved mass and all colloids occur. In addition, the porosity and water saturation are time-independent but may vary spatially. If the discretization is fully implicit in concentrations and time dependent velocity, irreversible reactions and solubility, then the discrete form of Equation B-34 is solved for $c^{n+1}_{Pu\_aq}$ as:

$$c^{n+1}_{Pu\_aq} = \frac{\bar{K}_1 c^n_{Pu\_aq} + \left[\bar{U}^{n+1}\left(1+\bar{K}_{d\_WF\_c}\right) + \bar{D}_{left\_aq} + \bar{D}_{left\_col}\bar{K}_{d\_WF\_c}\right] c^{n+1}_s \Delta t}{\bar{K}_1 + \left(\bar{U}^{n+1}\bar{K}_2 + \bar{D}_{left\_aq} + \bar{D}_{left\_col}\bar{K}_{d\_WF\_c} + \bar{D}_{right\_aq} + \bar{D}_{right\_col}\bar{K}_3 + \bar{R}^{n+1}_1 + \bar{R}^{n+1}_2 + \lambda \bar{K}_1\right)\Delta t} \qquad \text{(Eq. B-48)}$$

where

$$\frac{u\Delta t}{\phi S_w L} = \frac{U\Delta t}{V_{water}} = \bar{U}\Delta t$$

is the Courant number (dimensionless), L is the characteristic length (m), V_{water} is the volume of water in the cell (m^3), U is the volumetric water flux ($m^3\ yr^{-1}$), and $\overline{U}$ is the advective rate constant (yr^{-1}). Further,

$$\overline{K}_1 = 1 + \overline{K}_{d\_FeO\_c} + \overline{K}_{d\_FeO\_CP} + \overline{K}_{d\_WF\_c} + \overline{K}_{d\_GW\_c}$$

$$\overline{K}_2 = 1 + \overline{K}_{d\_FeO\_c} + \overline{K}_{d\_WF\_c} + \overline{K}_{d\_GW\_c}$$

$$\overline{K}_3 = \overline{K}_{d\_FeO\_c} + \overline{K}_{d\_WF\_c} + \overline{K}_{d\_GW\_c}$$

and

$$\overline{D} = \frac{H\left(\frac{\phi S_w D}{L}\right)}{V_{water}} A_s$$

is the diffusive rate constant with respect to either the solution or colloid mass at either the right or left cell interface. Here, A_s is the cross sectional area for diffusion (m^2), and V_{pore} is the pore volume of the cell (m^3). $H\left(\frac{\phi S_w D}{L}\right)$ is the harmonic average:

$$H\left(\frac{\phi S_w D}{L}\right) = \frac{1}{\frac{L_1}{\phi_1 S_{w1} D_1} + \frac{L_2}{\phi_2 S_{w2} D_2}}$$

at Cell 1 and Cell 2 interface, where L_1 and L_2 are the half-lengths (m) of Cells 1 and 2, respectively. The harmonic average of $\frac{\phi S_w D}{L}$ guarantees the continuity of the diffusive flux at the cell interface. The diffusive rate constant subscript left or right refers to the left or right diffusive boundary conditions, while the subscript aq or colloid refers to diffusion of the dissolved mass or colloid mass, respectively.

The reversible concentrations are determined from Equations B-29 through B-32

$$c^{n+1}_{Pu\_FeO\_c} = \overline{K}_{d\_FeO\_c} c^{n+1}_{Pu\_aq} \qquad \text{(Eq. B-49)}$$

$$c^{n+1}_{Pu\_FeO\_CP} = \overline{K}_{d\_FeO\_CP} c^{n+1}_{Pu\_aq} \qquad \text{(Eq. B-50)}$$

$$c^{n+1}_{Pu\_WF\_c} = \overline{K}_{d\_WF\_c} c^{n+1}_{Pu\_aq} \qquad \text{(Eq. B-51)}$$

$$c^{n+1}_{Pu\_GW\_c} = \overline{K}_{d\_GW\_c} c^{n+1}_{Pu\_aq}. \qquad \text{(Eq. B-52)}$$

The discretization of the balance Equation B-35 for irreversible Pu mass on the colloids yields

$$c^{n+1}_{Irrv\_Pu\_FeO\_c} = \frac{c^{n}_{Irrv\_Pu\_FeO\_c} + \overline{R}_1^{n+1}\Delta t c^{n+1}_{Pu\_aq}}{1+(\overline{U}^{n+1} + \overline{D}_{right\_col} + \lambda)\Delta t} \qquad \text{(Eq. B-53)}$$

and for irreversible Pu mass on the corrosion products, Equation B-36 yields

$$c^{n+1}_{Irrv\_Pu\_FeO\_CP} = \frac{c^{n}_{Irrv\_Pu\_FeO\_CP} + \overline{R}_2^{n+1}\Delta t c^{n+1}_{Pu\_aq}}{1+\lambda\Delta t}. \qquad \text{(Eq. B-54)}$$

SAMPLE CALCULATION WITH TSPA REPRESENTATIVE PARAMETERS

A sample calculation is performed to demonstrate the solution technique and illustrate the types of behavior that might be expected in this model. Parameter values that are representative of the TSPA-LA are used in this sample calculation and are given in Table B-1. Let the solubility, flow velocity, and irreversible reaction parameters be constant over time.

For this set of parameters, the irreversible reactive rates, advective rate, diffusive rates, decay rate and the dimensionless colloids and corrosion product partition coefficients are:

$$\begin{aligned}
\overline{R}_1 &= 0.02000\ \text{yr}^{-1} \\
\overline{R}_2 &= 786\ \text{yr}^{-1} \\
\overline{U} &= 0.04367\ \text{yr}^{-1} \\
\overline{D}_{left_aq} &= 0.09127\ \text{yr}^{-1} \\
\overline{D}_{right_aq} &= 2.229\times10^{-3}\ \text{yr}^{-1} \\
\overline{D}_{right_col} &= 2.229\times10^{-5}\ \text{yr}^{-1} \\
\lambda &= 2.875\times10^{-5}\ \text{yr}^{-1} \\
\overline{K}_{d_FeO_c} &= 0.20 \\
\overline{K}_{d_FeO_CP} &= 1.965\times10^{4} \\
\overline{K}_{d_WF_c} &= 0.60 \\
\overline{K}_{d_GW_c} &= 0.020.
\end{aligned}$$

The simulation for the mixing cell (Cell 2) concentrations over a 1000-year time interval is shown in Figure B-2. The dominant rate constant, by several orders of magnitude, is the irreversible rate constant of the corrosion products, $\overline{R}_2 = 786\ \text{yr}^{-1}$. This is a result of the large mass of corrosion products and results in a relative large concentration of irreversibly sorbed Pu on the corrosion products, $c_{Irrv\_Pu\_FeO\_CP}$. For this simulation, the amount of corrosion product mass is representative of the total mass of corrosion products in a waste package, and all the corrosion products are available at initial time. In the TSPA abstraction model, the corrosion product mass is time dependent and a function of the corrosion rates for the carbon and stainless

steel (see Section 6.5.3.2). A large mass of Pu is reversibly sorbed onto the corrosion products. This is a result of the large reversible partition coefficient for the corrosion products, $\overline{K}_{d\_FeO\_CP} = 19650$, which again is a result of the large corrosion product mass. For this simulation, almost all of the mass is sorbed onto the corrosion products. Only a small amount of mass remains in solution or is sorbed onto the colloids. The qualitative behavior of the concentrations in Figure B-2 shows the concentrations approach a limiting value, with the exception of the irreversibly sorbed mass on the corrosion products. This behavior is discussed in the next section, where the concentrations are expressed analytically as solutions of difference equations, and their asymptotic in time values are determined.

Table B-1. Representative Parameter Values for Sample Calculation

Parameter	Value	Units	Description
c_s	1.0	mg l^{-1}	Solubility
S_w	1.0	dimensionless	Water saturation
ϕ_1	1.0	dimensionless	Porosity of Cell 1
ϕ_2	0.4	dimensionless	Porosity of Cell 2
ϕ_3	0.3	dimensionless	Porosity of Cell 3
U	0.1	m^3 yr^{-1}	Volumetric water flux
$K_{d\_FeO\_c}$	1×10^4	ml g^{-1}	Colloid partition coefficient
$K_{d\_FeO\_CP}$	2.5×10^3	ml g^{-1}	Corrosion product partition coefficient
$K_{d\_WF\_c}$	2×10^5	ml g^{-1}	Waste form colloids partition coefficient
$K_{d\_GW\_c}$	2×10^5	ml g^{-1}	Groundwater colloids partition coefficient
$\hat{S}_{FeO\_c}$	100	m^2 g^{-1}	Specific surface area of FeO colloids
$\hat{S}_{FeO\_CP}$	10	m^2 g^{-1}	Specific surface area of FeO corrosion products
c_{FeO_c}	20	mg l^{-1}	Concentration of FeO colloids
c_{FeO_CP}	7.86×10^6	mg l^{-1}	Concentration of FeO corrosion products
c_{WF_c}	3.0	mg l^{-1}	Concentration of waste form colloids
c_{GW_c}	0.1	mg l^{-1}	Concentration of groundwater colloids
k	0.001	cm yr^{-1}	Forward sorption rate constant
V_{pore}	2.290	m^3	Pore volume
A_{s12}	36.0	m^2	Diffusive area between Cell 1 and Cell 2
A_{s23}	1.068	m^2	Diffusive area between Cell 2 and Cell 3
L_1	0.001	m	Half-length of Cell 1 diffusive path
L_2	5.0	m	Half-length of Cell 2 diffusive path

Table B-1. Representative Parameter Values for Sample Calculation (Continued)

Parameter	Value	Units	Description
L_3	0.806	m	Half-length of Cell 3 diffusive path
D_{aq}	2.3×10^{-9}	$m^2\ s^{-1}$	Aqueous diffusivity
$D_{colloid}$	2.3×10^{-11}	$m^2\ s^{-1}$	Colloid diffusivity
λ	2.875×10^{-5}	yr^{-1}	Radionuclide decay rate

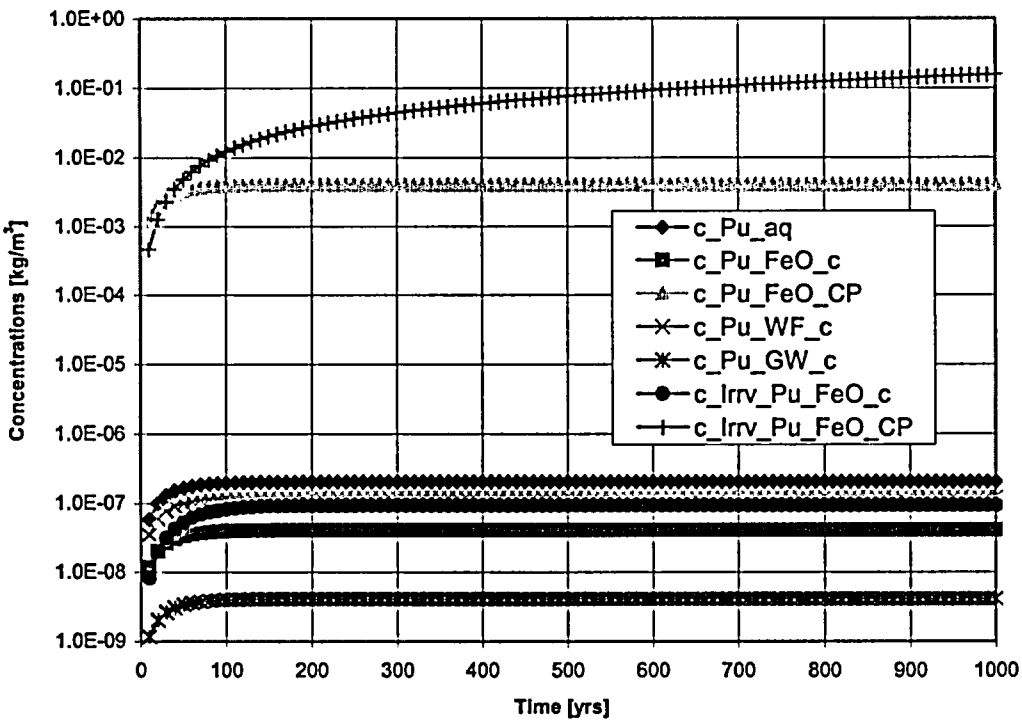

Figure B-2. Concentrations with Respect to Pore Volume

CLOSED FORM SOLUTIONS OF THE DIFFERENCE EQUATIONS

If the solubility, advective flux, saturation, and irreversible rates are chosen to be constant over time, then the mass balance equation for the aqueous Pu, Equation B-48, is a first order linear constant coefficient nonhomogeneous difference equation. This equation is of the form

$$c_{Pu\_aq}^{n+1} = a_1 c_{Pu\_aq}^{n} + a_2 \quad \text{(Eq. B-55)}$$

where

$$a_1 = \frac{\overline{K}_1}{\overline{K}_1 + \left(\overline{U}\,\overline{K}_2 + \overline{D}_{left\_aq} + \overline{D}_{left\_col}\overline{K}_{d\_WF\_c} + \overline{D}_{right\_aq} + \overline{D}_{right\_col}\overline{K}_3 + \overline{R}_1 + \overline{R}_2 + \lambda\overline{K}_1\right)\Delta t}$$

$$a_2 = \frac{\left(\overline{U}(1+\overline{K}_{d\_WF\_c}) + \overline{D}_{left\_aq} + \overline{D}_{left\_col}\overline{K}_{d\_WF\_c}\right)\Delta t c_s}{\overline{K}_1 + \left(\overline{U}\,\overline{K}_2 + \overline{D}_{left\_aq} + \overline{D}_{left\_col}\overline{K}_{d\_WF\_c} + \overline{D}_{right\_aq} + \overline{D}_{right\_col}\overline{K}_3 + \overline{R}_1 + \overline{R}_2 + \lambda\overline{K}_1\right)\Delta t}.$$

The difference equation (Equation B-55) with initial condition of zero concentration has the solution

$$c^n_{Pu\_aq} = \frac{a_2(1-a_1^n)}{1-a_1}. \qquad \text{(Eq. B-56)}$$

Since the condition $0 < a_1 < 1$ is guaranteed, the solution $c^n_{Pu\_aq}$ for large time is asymptotic to

$$\begin{aligned}\lim_{n\to\infty} c^n_{Pu\_aq} &= \frac{a_2}{1-a_1} \\ &= \frac{\left(\overline{U}(1+\overline{K}_{d\_WF\_c}) + \overline{D}_{left\_aq} + \overline{D}_{left\_col}\overline{K}_{d\_WF\_c}\right)c_s}{\overline{U}\,\overline{K}_2 + \overline{D}_{left\_aq} + \overline{D}_{left\_col}\overline{K}_{d\_WF\_c} + \overline{D}_{right\_aq} + \overline{D}_{right\_col}\overline{K}_3 + \overline{R}_1 + \overline{R}_2 + \lambda\overline{K}_1}.\end{aligned} \qquad \text{(Eq. B-57)}$$

The terms in this expression represent the effects of advection, diffusion, decay, and reversible and irreversible sorption reactions.

The difference equation for the irreversible colloid concentration (Equation B-53) is first order linear and is written as:

$$c^{n+1}_{Irrv\_Pu\_FeO\_c} = b_1 c^n_{Irrv\_Pu\_FeO\_c} + b_2 c^{n+1}_{Pu\_aq} \qquad \text{(Eq. B-58)}$$

where

$$b_1 = \frac{1}{1+\left(\overline{U} + \overline{D}_{right\_col} + \lambda\right)\Delta t} \qquad \text{(Eq. B-59)}$$

$$b_2 = \frac{\overline{R}_1 \Delta t}{1+\left(\overline{U} + \overline{D}_{right\_col} + \lambda\right)\Delta t} \qquad \text{(Eq. B-60)}$$

and $c^{n+1}_{Pu\_aq}$ is given by Equation B-56. The difference Equation B-58 with initial condition zero has solution

$$c^n_{Irrv\_Pu\_FeO\_c} = \frac{a_2 b_2}{1-a_1}\left[\frac{1-b_1^{n+1}}{1-b_1} - \frac{a_1^{n+1} - b_1^{n+1}}{a_1 - b_1}\right]. \qquad \text{(Eq. B-61)}$$

Since $0 < a_1 < 1$ and $0 < b_1 < 1$, this solution has asymptotic behavior

$$\lim_{n\to\infty} c^n_{Irrv\_Pu\_FeO\_c} = \frac{a_2 b_2}{(1-a_1)(1-b_1)}. \qquad \text{(Eq. B-62)}$$

Thus

$$\lim_{n\to\infty} c^n_{Irrv\_Pu\_FeO\_c} = \frac{b_2}{1-b_1}\lim_{n\to\infty} c^n_{Pu\_aq} = \frac{\overline{R}_1}{\overline{U}+\overline{D}_{right\_col}+\lambda}\lim_{n\to\infty} c^n_{Pu\_aq}. \qquad \text{(Eq. B-63)}$$

The difference equation for the concentration of the irreversible mass on the corrosion products is first order linear and is written as

$$c^{n+1}_{Irrv\_Pu\_FeO\_CP} = e_1 c^n_{Irrv\_Pu\_FeO\_CP} + e_2 c^{n+1}_{Pu\_aq} \qquad \text{(Eq. B-64)}$$

where

$$e_1 = \frac{1}{1+\lambda\Delta t} \qquad \text{(Eq. B-65)}$$

$$e_2 = \frac{\overline{R}_2 \Delta t}{1+\lambda\Delta t}. \qquad \text{(Eq. B-66)}$$

If $\lambda > 0$, Equation B-64 with initial concentration of zero has solution

$$c^n_{Irrv\_Pu\_FeO\_CP} = \frac{a_2 e_2}{1-a_1}\left[\frac{1-e_1^{n+1}}{1-e_1} - \frac{a_1^{n+1}-e_1^{n+1}}{a_1-e_1}\right]. \qquad \text{(Eq. B-67)}$$

If $\lambda = 0$, Equation B-64 with initial concentration of zero has solution

$$c^n_{Irrv\_Pu\_FeO\_CP} = \frac{a_2 e_2}{1-a_1}\left[n+1-\frac{1-a_1^{n+1}}{1-a_1}\right]. \qquad \text{(Eq. B-68)}$$

The solution Equation B-67 has asymptotic value

$$\lim_{n\to\infty} c^n_{Irrv\_Pu\_FeO\_CP} = \frac{e_2}{1-e_1}\lim_{n\to\infty} c^n_{Pu\_aq} = \frac{\overline{R}_2}{\lambda}\lim_{n\to\infty} c_{Pu\_aq}, \qquad \text{(Eq. B-69)}$$

while the solution Equation B-68 does not have a limiting value, but is unbounded as a function of the time index n.

BOUNDARY FLUXES

Now consider the two boundary flux conditions given in Equations B-1 and B-2. The left or upstream boundary flux accounts for advection/diffusion of Pu mass in solution (Pu_aq) and Pu mass sorbed to waste form colloids. In this analysis, upstream diffusion of colloids is ignored, although the TSPA-LA implementation does account for upstream colloid diffusion. The mass flux rates (kg yr^{-1}) at this upstream left boundary for the nth time step are:

Advective_Pu_aq (kg yr^{-1}) $= \overline{U} V_{pore} c_s$

Diffusive_Pu_aq (kg yr^{-1}) $= \overline{D}_{left\_aq} V_{pore} (c_s - c^n_{Pu\_aq})$

Advective_Pu_WF_c (kg yr^{-1}) $= \overline{U} V_{pore} \overline{K}_{d\_WF\_c} c_s$

Diffusive_Pu_WF_c (kg yr^{-1}) $= \overline{D}_{left\_col} V_{pore} \overline{K}_{d\_WF\_c} (c_s - c^n_{Pu\_aq})$.

The right or downstream boundary flux has contributions from advection/diffusion of Pu in solution and colloid together with advection/diffusion of Irrv_Pu on colloids. There is no advective or diffusive flux associated with the immobile corrosion products. The mass flux rates (kg yr^{-1}) at the right boundary assuming zero downstream concentrations are:

Advective_Pu_aq (kg yr^{-1}) $= \overline{U} V_{pore} c^n_{Pu\_aq}$

Diffusive_Pu_aq (kg yr^{-1}) $= \overline{D}_{right\_aq} V_{pore} c^n_{Pu\_aq}$

Advective_Pu_FeO_c (kg yr^{-1}) $= \overline{U} V_{pore} \overline{K}_{d\_FeO\_c} c^n_{Pu\_aq}$

Diffusive_Pu_FeO_c (kg yr^{-1}) $= \overline{D}_{right\_col} V_{pore} \overline{K}_{d\_FeO\_c} c^n_{Pu\_aq}$

Advective_Irrv_Pu_FeO_c (kg yr^{-1}) $= \overline{U} V_{pore} c^n_{Irrv\_Pu\_FeO\_c}$

Diffusive_Irrv_Pu_FeO_c (kg yr^{-1}) $= \overline{D}_{right\_col} V_{pore} c^n_{Irrv\_Pu\_FeO\_c}$

Advective_Pu_WF_c (kg yr^{-1}) $= \overline{U} V_{pore} \overline{K}_{d\_WF\_c} c^n_{Pu\_aq}$

Diffusive_Pu_WF_c (kg yr^{-1}) $= \overline{D}_{right\_col} V_{pore} \overline{K}_{d\_WF\_c} c^n_{Pu\_aq}$

Advective_Pu_GW_c (kg yr^{-1}) $= \overline{U} V_{pore} \overline{K}_{d\_GW\_c} c^n_{Pu\_aq}$

Diffusive_Pu_GW_c (kg yr^{-1}) $= \overline{D}_{right\_col} V_{pore} \overline{K}_{d\_GW\_c} c^n_{Pu\_aq}$.

The total flux at the left boundary (upstream) at the nth time step, $F^n_{left\_bddy\_total}$, is

$$F^n_{left\_bddy\_total} = \overline{U} V_{pore} c_s + \overline{D}_{left\_aq} V_{pore} (c_s - c^n_{Pu\_aq})$$
$$+ \overline{U} V_{pore} \overline{K}_{d\_WF\_c} c_s + \overline{D}_{left\_col} V_{pore} \overline{K}_{d\_WF\_c} (c_s - c^n_{Pu\_aq}).$$

The condition discussed in Equation B-1 considers the ratio of the colloid mass to total mass flux out the right boundary. The right boundary colloidal flux, $F^n_{right\_bddy\_colloid}$, due to both reversibly and irreversibly sorbed Pu is:

$$F^n_{right\_bddy\_colloid} = \overline{U}V_{pore}\overline{K}_{d\_FeO\_c}c^n_{Pu\_aq} + \overline{U}V_{pore}c^n_{Irrv\_Pu\_FeO\_c}$$

$$+\overline{U}V_{pore}\overline{K}_{d\_WF\_c}c^n_{Pu\_aq} + \overline{U}V_{pore}\overline{K}_{d\_GW\_c}c^n_{Pu\_aq}$$

$$+\overline{D}_{right\_col}V_{pore}\overline{K}_{d\_FeO\_c}c^n_{Pu\_aq} + \overline{D}_{right\_col}V_{pore}c^n_{Irrv\_Pu\_FeO\_c}$$

$$+\overline{D}_{right\_col}V_{pore}\overline{K}_{d\_WF\_c}c^n_{Pu\_aq} + \overline{D}_{right\_col}V_{pore}\overline{K}_{d\_GW\_c}c^n_{Pu\_aq}.$$

The total Pu flux at the right boundary, $F^n_{right\_bddy\_total}$, is

$$F^n_{right\_bddy\_total} = F^n_{right\_bddy\_colloid} + \overline{U}V_{pore}c^n_{Pu\_aq} + \overline{D}_{right\_aq}V_{pore}c^n_{Pu\_aq}.$$

The right boundary ratio of colloid flux out to total flux out at time level n is

$$\Omega_n = \frac{F^n_{right\_bddy\_colloid}}{F^n_{right\_bddy\_total}}.$$

Then

$$\Omega_n = \frac{\overline{K}_3 + \dfrac{c^n_{Irrv\_Pu\_c}}{c^n_{Pu\_aq}}}{\dfrac{\overline{U}\,\overline{K}_2 + \overline{D}_{right\_aq} + \overline{D}_{right\_col}\overline{K}_3}{\overline{U} + \overline{D}_{right\_col}} + \dfrac{c^n_{Irrv\_Pu\_c}}{c^n_{Pu\_aq}}}.$$

Now from Equation B-61

$$\lim_{n\to\infty}\frac{c^n_{Irrv\_Pu\_c}}{c^n_{Pu\_aq}} = \frac{\overline{R}_1}{\overline{U} + \overline{D}_{right\_col} + \lambda}.$$

The limiting value for the right boundary ratio of colloid flux to total flux is

$$\Omega = \lim_{n\to\infty}\Omega_n = \frac{\overline{K}_3 + \dfrac{\overline{R}_1}{\overline{U} + \overline{D}_{right\_col} + \lambda}}{\dfrac{\overline{U}\,\overline{K}_2 + \overline{D}_{right\_aq} + \overline{D}_{right\_col}\overline{K}_3}{\overline{U} + \overline{D}_{right\_col}} + \dfrac{\overline{R}_1}{\overline{U} + \overline{D}_{right\_col} + \lambda}}$$

or

$$\Omega = \frac{\overline{K}_3\left(\overline{U} + \overline{D}_{right\_col} + \lambda\right) + \overline{R}_1}{\left(\overline{U}\,\overline{K}_2 + \overline{D}_{right\_aq} + \overline{D}_{right\_col}\overline{K}_3\right)\left(\dfrac{\overline{U} + \overline{D}_{right\_col} + \lambda}{\overline{U} + \overline{D}_{right\_col}}\right) + \overline{R}_1}. \qquad \text{(Eq. B-70)}$$

This can be written as

$$\Omega = \frac{p_1 + \overline{R}_1}{p_2 + \overline{R}_1} \qquad \text{(Eq. B-71)}$$

where

$$p_1 = \overline{K}_3\left(\overline{U} + \overline{D}_{right\_col} + \lambda\right)$$

$$p_2 = \left(\overline{U}\,\overline{K}_2 + \overline{D}_{right\_aq} + \overline{D}_{right\_col}\overline{K}_3\right)\left(\frac{\overline{U} + \overline{D}_{right\_col} + \lambda}{\overline{U} + \overline{D}_{right\_col}}\right).$$

Note the limiting flux out ratio Ω satisfies

$$0 < \frac{\overline{K}_3(\overline{U} + \overline{D}_{right\_col})}{\overline{U}\,\overline{K}_2 + \overline{D}_{right\_aq} + \overline{D}_{right\_col}\overline{K}_3} < \Omega < 1,$$

where the lower bound on Ω is obtained when $\overline{R}_1 = 0$. Qualitatively, if the advective, diffusive, and decay rates dominate the reactive rate constant $\overline{R}_1$, then Ω is close to the minimum value. However, if the reactive rate constant dominates, then Ω is close to one. The latter is the expected qualitative behavior of the system as alluded to in the introduction of this appendix.

For the parameter values given in Table B-1, the minimum value $\Omega = 0.4384$ is obtained with $\overline{R}_1 = 0$. The limiting flux out ratio for Table B-1 parameter values is $\Omega = 0.5487$; in other words, about 55 percent of the total Pu mass exiting the cell is sorbed onto colloids. Figure B-3 shows the dependence of the flux out ratio Ω on the irreversible linear reaction rate constant *k*, where $\overline{R}_1 = \hat{S}_{FeO\_c} c_{FeO\_c} k$. The point obtained with the Table B-1 parameter values is also shown in Figure B-3. An increase of the irreversible linear reaction rate, *k*, of approximately one and a half orders of magnitude would increase the flux out ratio to approximately 95 percent.

In the expression for irreversible sorption to colloids, $\overline{R}_1 = \hat{S}_{FeO\_c} c_{FeO\_c} k$, consider the irreversible linear reaction rate k a fitting parameter to match a specified flux out ratio Ω. Then the solution of Equation B-71 for k is:

$$k = \frac{p_2 \Omega - p_1}{(1-\Omega)\hat{S}_{FeO\_c} c_{FeO\_c}}. \qquad \text{(Eq. B-72)}$$

The result in Equation B-72 provides the fitting parameter, k, given a target flux ratio Ω. From the parameter values in Table B-1 and with $\Omega = 0.95$, the irreversible linear reaction rate is determined from Equation B-72 as $k = 0.04184$ cm yr^{-1}. The fitting parameter curve together with this point is shown in Figure B-4.

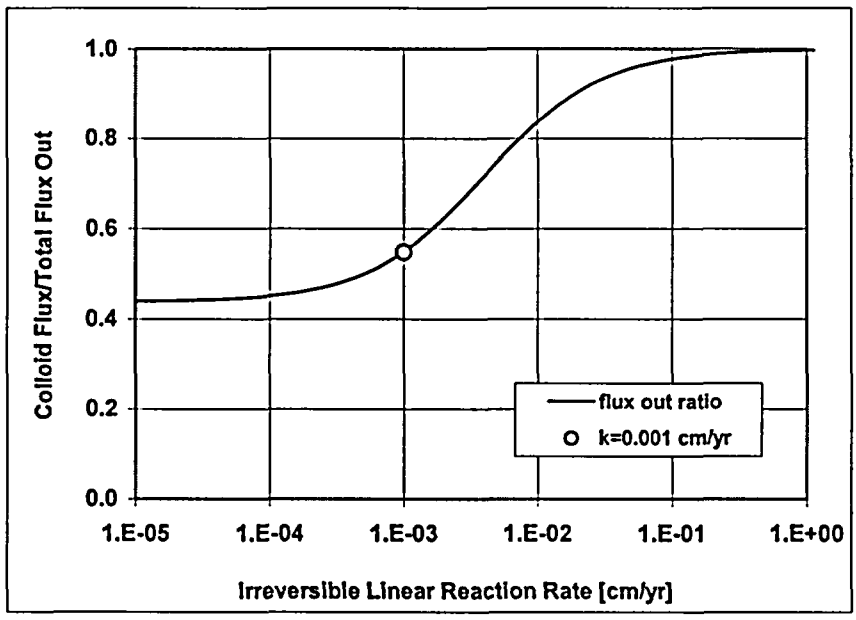

Source: Worksheet: K-surface in Appendix F.

Figure B-3. Limiting Flux Out Ratio as a Function of Irreversible Reaction Rate

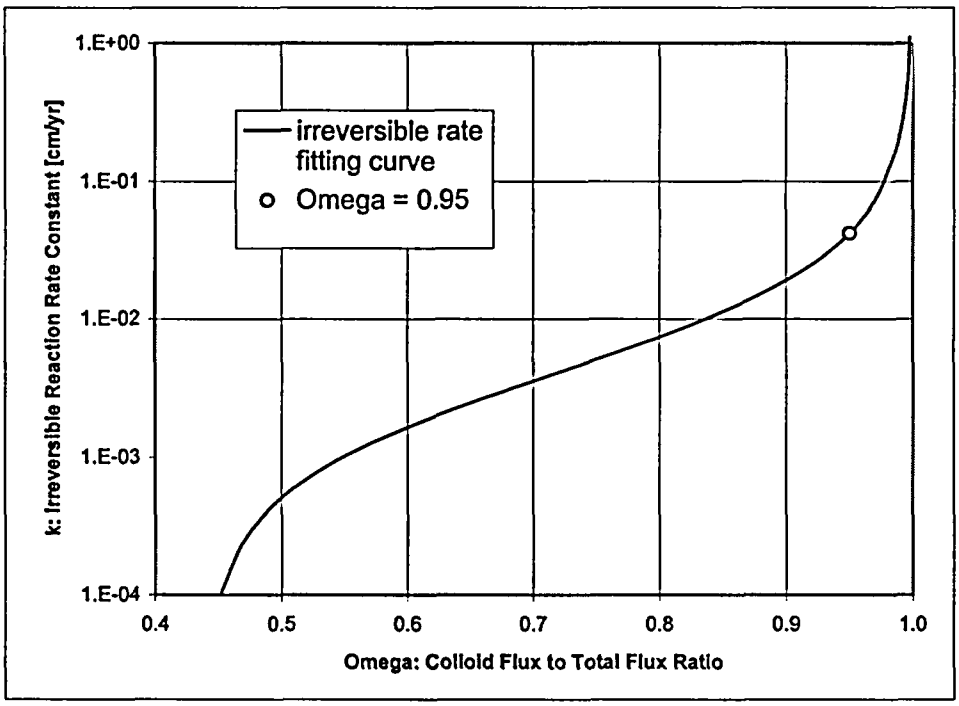

Source: Worksheet: adv_diff_decay in Appendix F.

Figure B-4. Linear Reaction Rate from Colloid to Total Flux Out Ratio

The ratio of the total flux out (right boundary) to total flux in (left boundary) at time level n is

$$\Psi_n = \frac{\left(\overline{U}\,\overline{K}_2 + \overline{D}_{right\_aq} + \overline{D}_{right\_col}\overline{K}_3\right)c^n_{Pu\_aq} + \left(\overline{U} + \overline{D}_{right\_col}\right)c^n_{Irrv\_Pu\_FeO\_c}}{\left(\overline{U}\left(1+\overline{K}_{d\_WF\_c}\right) + \overline{D}_{left\_aq} + \overline{D}_{left\_col}\overline{K}_{d\_WF\_c}\right)c_s - \left(\overline{D}_{left\_aq} + \overline{D}_{left\_col}\overline{K}_{d\_WF\_c}\right)c^n_{Pu\_aq}}.$$

This flux ratio has limiting value

$$\Psi = \frac{p_2 + \overline{R}_1}{p_2 + \left(\dfrac{\overline{U} + \overline{D}_{right\_col} + \lambda}{\overline{U} + \overline{D}_{right\_col}}\right)\left(\overline{R}_1 + \overline{R}_2 + \lambda\overline{K}_1\right)}. \qquad \text{(Eq. B-73)}$$

The mass flux ratio Ψ is calculated from Equation B-73 for the Table B-1 parameter values, but with irreversible linear reaction rate k = 0.04184 cm yr^{-1} obtained from the fit to $\Omega = 0.95$. Equation B-73 gives

$$\Psi = 1.293 \times 10^{-4},$$

which demonstrates that most of the Pu mass is reacted both reversibly and irreversibly to the corrosion products.

CONVERGENCE ESTIMATES FOR CLOSED FORM SOLUTIONS

Consider the convergence of the concentration in the aqueous state given by Equation B-56:

$$c^n_{Pu\_aq} = \frac{a_2}{1-a_1}\left(1-a_1^n\right)$$

with limit value (Equation B-57)

$$\lim_{n\to\infty} c^n_{Pu\_aq} = \frac{a_2}{1-a_1}.$$

The relative error estimate with tolerance ε is given by

$$\left|\frac{\lim\limits_{n\to\infty} c^n_{Pu\_aq} - c^n_{Pu\_aq}}{\lim\limits_{n\to\infty} c^n_{Pu\_aq}}\right| < \varepsilon.$$

Then the error estimate is

$$\left|\frac{\dfrac{a_2}{1-a_1} - \dfrac{a_2}{1-a_1}\left(1-a_1^n\right)}{\dfrac{a_2}{1-a_1}}\right| = a_1^n < \varepsilon.$$

The bounds $0 < a_1 < 1$ implies $\log_{10} a_1 < 0$ and the error estimate holds for

$$n > \frac{\log_{10}\varepsilon}{\log_{10} a_1}$$

or

$$\text{time} = n\Delta t > \frac{\log_{10}\varepsilon}{\log_{10} a_1}\Delta t. \qquad \text{(Eq. B-74)}$$

The time to converge to a given relative error tolerance for all reversible sorbed Pu concentrations is the same as the estimate for the aqueous concentration, inequality Equation B-74, since the reversibly sorbed concentration is a constant multiple of the aqueous concentration.

Now consider the convergence of the irreversible Pu concentration on colloids, $c^n_{Irrv\_Pu\_c}$. An estimate of the relative error is given by

$$\left|\frac{c^n_{Irrv\_Pu\_c} - \lim_{n\to\infty} c^n_{Irrv\_Pu\_c}}{\lim_{n\to\infty} c^n_{Irrv\_Pu\_c}}\right| = \left|\frac{\frac{a_2 b_2}{1-a_1}\left[\frac{1-b_1^{n+1}}{1-b_1} - \frac{a_1^{n+1}-b_1^{n+1}}{a_1-b_1}\right] - \frac{a_2 b_2}{(1-a_1)(1-b_1)}}{\frac{a_2 b_2}{(1-a_1)(1-b_1)}}\right|$$

$$= \left|(1-b_1)\left(\frac{-b_1^{n+1}}{1-b_1} - \frac{a_1^{n+1}-b_1^{n+1}}{a_1-b_1}\right)\right|$$

$$= \left|\frac{(1-a_1)b_1^{n+1}}{a_1-b_1} - \frac{(1-b_1)a_1^{n+1}}{a_1-b_1}\right|$$

$$\le \left|\frac{1-a_1}{a_1-b_1}\right| b_1^{n+1} + \left|\frac{1-b_1}{a_1-b_1}\right| a_1^{n+1} < \varepsilon.$$

This estimate holds if

$$b_1^{n+1} < \left|\frac{a_1-b_1}{1-a_1}\right|\frac{\varepsilon}{2} = \delta_1 \text{ and } a_1^{n+1} < \left|\frac{a_1-b_1}{1-b_1}\right|\frac{\varepsilon}{2} = \delta_2.$$

These two estimates are satisfied if

$$n+1 \ge \text{Integer}\left[\max\left(\frac{\log_{10}\delta_1}{\log_{10} b_1}, \frac{\log_{10}\delta_2}{\log_{10} a_1}\right)\right] + 1$$

or

$$\text{time} = n\Delta t \ge \text{Integer}\left[\max\left(\frac{\log_{10}\delta_1}{\log_{10} b_1}, \frac{\log_{10}\delta_2}{\log_{10} a_1}\right)\right]\Delta t. \qquad \text{(Eq. B-75)}$$

For a relative error tolerance of 1 percent ($\varepsilon = 0.01$) and the parameter values in Table B-1, Figure B-5 shows the time to converge for time step size 0.1 to 1000 years for both the aqueous Pu concentration and irreversible colloid Pu concentration. For example, if the time step is small, say 10 years, the number of years to converge within the given tolerance for the aqueous phase concentration is 137 years, whereas the time to converge for the irreversible colloid concentration is 240 years. If the time step is increased to 100 years, then the time to converge to the aqueous phase concentration is 286 years (three time steps), whereas the time to converge to the irreversible colloid concentration is 500 years (5 time steps).

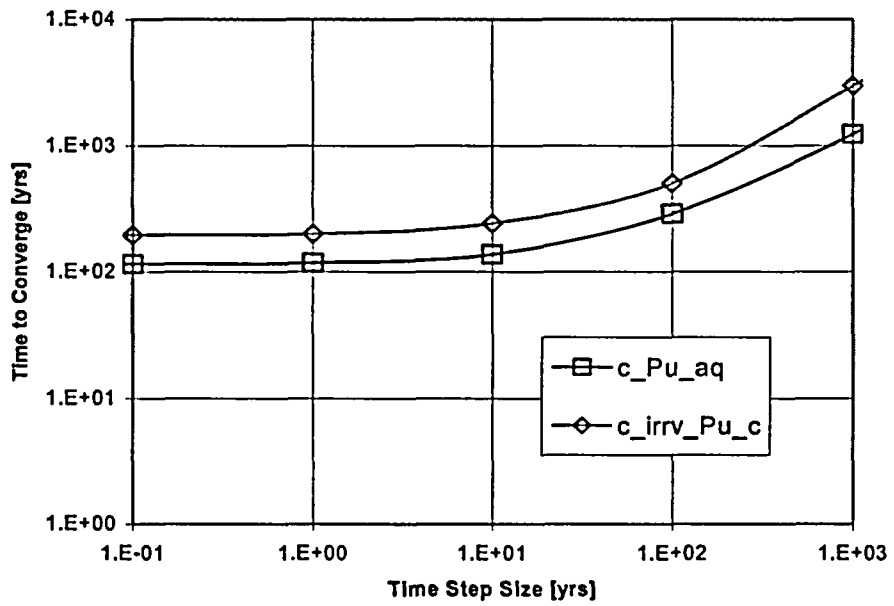

Source: Spreadsheet: time_to_conv.xls, Worksheet: plot_time_to_conv in Appendix F.

Figure B-5. Time for Concentration to Converge with 1 Percent Relative Error Tolerance

ESTIMATED SORPTION CAPACITY OF CORROSION MATERIALS

It is important to know if the radionuclide mass is capable of saturating the sorption sites available on the FeO. Let

$\hat{S}_{FeO\_CP}$ = specific surface area of FeO (m^2 FeO kg^{-1} FeO)
ρ_{site} = adsorption site density (sites m^{-2} FeO)
N_A = Avogadro's number (sites mol^{-1})
M_{Pu} = Pu molecular weight (g mol^{-1}).

Use the following values in this calculation:

$\hat{S}_{FeO\_CP}$ = 10 m^2 g^{-1} (representative, from Table B-1)
ρ_{site} = 2.3×10^{18} sites m^{-2} (Davis and Kent 1990 [DIRS 143280])
N_A = 6×10^{23} sites mol^{-1} (Lide 2002 [DIRS 160832], p. 1-7)
M_{Pu} = 239 g mol^{-1} (Weast 1985 [DIRS 111561], p. B-125).

Then the radionuclide mass (represented by Pu) that will be sorbed per unit mass of FeO is:

$$\frac{\hat{S}_{FeO}\rho_{site}M_{Pu}}{N_A} = \frac{\left(10\,\frac{\mathrm{m}^2}{\mathrm{g\ FeO}}\right)\left(2.3\times10^{18}\,\frac{\mathrm{sites}}{\mathrm{m}^2}\right)\left(239\,\frac{\mathrm{g\ Pu}}{\mathrm{mol}}\right)}{6\times10^{23}\,\frac{\mathrm{sites}}{\mathrm{mol}}}$$

$$= 9.16\ \mathrm{g\ Pu\ kg^{-1}\ FeO.}$$

The mass of FeO in a 21-PWR is estimated to be (Table 6.3-4):

$$m_{FeO} = 19440\ \mathrm{kg}$$

and the radionuclide mass that can be sorbed is

$$\text{Radionuclide mass sorbed} = \left(9.16\,\frac{\mathrm{g\ Pu}}{\mathrm{kg\ FeO}}\right)(19440\ \mathrm{kg\ FeO})$$

$$= 178\ \mathrm{kg\ Pu.}$$

This sorption capacity of the corrosion materials is dependent on the variability of the specific surface area, $\hat{S}_{FeO}$. The inventory mass of elements and their isotopes that is available to sorb irreversibly (Pu and Am) is estimated to be 83.6 kg per CSNF waste packages (DTN: SN0310T0505503.004 [DIRS 168761]). This estimate using representative parameter values shows that the mass of corrosion products is capable of sorbing all of the available radionuclide inventory.

INTENTIONALLY LEFT BLANK

APPENDIX C
MICROSOFT EXCEL SPREADSHEET "FLUX SPLIT DRIP SHIELD MODEL"

MICROSOFT EXCEL SPREADSHEET "FLUX SPLIT DRIP SHIELD MODEL"

SPREADSHEET "FLUX SPLIT DRIP SHIELD MODEL" WORKSHEET "F CALCULATIONS"

Breach Flow Fraction Calculation using Smooth Drip Shield Data, On-Crown Tests

Source Data / Calculated results

The spread angles are the mean, 1-sigma, and 1-sigma, calculated on the "Spread Anges" sheet

This cell performs a conditional test, comparing y to Ya, Yb, Yc, Yd, and 1 to determine which case applies

DTN: MO0207EBSATBWP.023

For α = 0.6788 degrees

These are the Y values calculated, given α, l, and α, for each measurement. Note that Yb and Yc are different depending on the

	A	B	C	D	E	F	G	H	I	J	K	L	M	N	O	P
8		Drip Location (Test Description)	Breach No.	y, Drip Location Relative to Breach Center (cm)	z, Vertical Distance from Crown (drip) to Top of Breach (cm)	l, Patch half-width (cm)	Drip Flux (g)	Flow into Breach (g)	f_meas	f_TAN(α)	Model Case #	Ya	Yb	Yc	Yd	Fractio n Case #
9		8 cm right of Patch 4 centerline [Q(film) Test]	4	8	136.5	13.5	178.2	22.02	0.2471	21.3040	2	-39.0180	-7.8040	7.8040	39.0180	5
10		Patch 5 centerline [Q(film) Test]	5	0	86	13.5	163.74	21.12	0.2580	13.4223	1	-31.1363	-0.0777	0.0777	31.1363	4
11		4 cm left of Patch 5 centerline [Q(film) Test]	5	-4	86	13.5	133.79	9.1	0.1360	13.4223	1	-31.1363	-0.0777	0.0777	31.1363	3
12		Patch 4 centerline [Q(film) Test]	4	0	136.5	13.5	189.63	22.25	0.2359	21.3040	2	-39.0180	-7.8040	7.8040	39.0180	4
13		27 cm right of DS center (Multiple Patch	5	27	86	13.5	276.14	4.49	0.0325	13.4223	1	-31.1363	-0.0777	0.0777	31.1363	2
14		27 cm left of DS center (Multiple patch test)	4	27	136.5	13.5	278.83	2.83	0.0190	21.3040	2	-39.0180	-7.8040	7.8040	39.0180	6
15		81 cm left of DS center (Multiple Patch Test)	4	-27	136.5	13.5	226.22	3.45	0.0305	21.3040	2	-39.0180	-7.8040	7.8040	39.0180	2
16		81 cm right of DS center (Multiple Patch Test)	5	27	86	13.5	221.12	3.54	0.0320	13.4223	1	-31.1363	-0.0777	0.0777	31.1363	6
17		54 cm left of DS center (High Flow Rate Test)	4	0	136.5	13.5	337.72	46.41	0.2748	21.3040	2	-39.0180	-7.8040	7.8040	39.0180	4
18		54 cm left of DS center (Low Flow Rate Test)	4	0	136.5	13.5	89.83	7.88	0.1773	21.3040	2	-39.0180	-7.8040	7.8040	39.0180	4
19		27 cm left of DS center (High Flow Rate Test)	4	27	136.5	13.5	332.69	3.35	0.0201	21.3040	2	-39.0180	-7.8040	7.8040	39.0180	6
20		27 cm left of DS center (Low Flow Rate Test)	4	27	136.5	13.5	100.95	0.65	0.0129	21.3040	2	-39.0180	-7.8040	7.8040	39.0180	6
21		27 cm right of DS center (High Flow Rate	5	-27	86	13.5	378.73	2.45	0.0129	13.4223	1	-31.1363	-0.0777	0.0777	31.1363	2
22		center (Low Flow Rate Test)	5	-27	86	13.5	137.72	4.45	0.0646	13.4223	1	-31.1363	-0.0777	0.0777	31.1363	2

DTN: MO0207EBSATBWP.024

DTN: MO0207EBSATBWP.025

DTN: MO0207EBSATBWP.023 [DIRS 163402]; DTN: MO0207EBSATBWP.024 [DIRS 163401]; DTN: MO0207EBSATBWP.025 [DIRS 163403].

Figure C-1. Spreadsheet "Flux Split Drip Shield Model," Worksheet "f calculations;" Calculation of Experimental Breach Flow Fractions and Model Flow Fractions for Mean Minus One Standard Deviation Rivulet Spread Angle

The purpose of this spreadsheet is to develop the drip shield flux splitting submodel using experimental data from the breached drip shield experiments. The data are analyzed to estimate an average and range of the rivulet spread angle, α. The disparity between measured fraction of dripping flux that enters a breach and the fraction calculated using the model (with the measured range of the rivulet spread angle) is then used to establish a range of uncertainty in the model.

All descriptions for this worksheet (Figures C-1 to C-4) pertain to Rows 9–22. Equations in spreadsheet format are illustrated using Row 9.

Column B: Drip location as indicated for each test in the designated DTN (Figure C-1).

Column C: Breach or patch number most pertinent to this particular test, for which flow is analyzed in this row of the spreadsheet.

Column D: Drip location, y, relative to the center of the breach listed in Column C.

Column E: Vertical distance, x, from the drip shield crown to the top of the breach.

Column F: Half-width, ℓ, of the breach–13.5 cm, same for all breaches.

Column G: Measured mass of water, F_1, dripped onto the drip shield during the test. It is assumed that half of the water that dripped onto the drip shield, $F_1/2$, flowed down the side that contained the breach.

Column H: Measured mass of water, F_2, that flowed into the breach during the test.

Column I: Fraction of water dripped onto the drip shield that flowed into the breach:

$$f_{expt} = \frac{F_2}{F_1/2} = \frac{2F_2}{F_1}.$$

I9=H9*2/G9

Column J: $x \tan\alpha$, where x is from Column E, and α is the spread angle. For Columns J-X, the value used for α is 8.8708° (Cell $M$7), which is one standard deviation less than the mean measured spread angle for these tests (see Worksheet "Spread angles").

J9=$E9*TAN(RADIANS($M$7))

Column K: Case number as described in Sections 6.5.1.1.2.1 and 6.5.1.1.2.2. For Case 1, $\ell > x\tan\alpha$; for Case 2, $\ell < x\tan\alpha$; x is from Column E, and the half-width of the breach, ℓ, is from Column F.

K9=IF($F9>J9,1,2)

Column L: Value of y_A (Point A) as described in Sections 6.5.1.1.2.1 and 6.5.1.1.2.2, corresponding to the leftmost point from which the edge of the fan from the rivulet can enter the left side of the breach:

$$y_A = -\ell - (x + 2\ell)\tan\alpha$$

L9=-$F9-($E9+2*$F9)*TAN(RADIANS($M$7))

Column M: Value of y_B (Point B) as described in Sections 6.5.1.1.2.1 and 6.5.1.1.2.2, corresponding to the leftmost point from which rivulets will enter the top edge of the breach. The value of y_B depends on the Model Case number (Column K):

$$y_B = -\ell + x\tan\alpha \qquad \text{Case 1.}$$

$$y_B = \ell - x\tan\alpha \qquad \text{Case 2.}$$

```
M9=IF(K9=1,(-$F9+$E9*TAN(RADIANS($M$7))),
      ($F9-$E9*TAN(RADIANS($M$7))))
```

Column N: Value of y_C (Point C) as described in Sections 6.5.1.1.2.1 and 6.5.1.1.2.2, corresponding to the rightmost point from which rivulets will enter the top edge of the breach. The value of y_C depends on the Model Case number (Column K):

$$y_C = \ell - x\tan\alpha \qquad \text{Case 1.}$$

$$y_C = -\ell + x\tan\alpha \qquad \text{Case 2.}$$

```
N9=IF(K9=1,($F9-$E9*TAN(RADIANS($M$7))),
      (-$F9+$E9*TAN(RADIANS($M$7))))
```

Column O: Value of y_D (Point D) as described in Sections 6.5.1.1.2.1 and 6.5.1.1.2.2, corresponding to the rightmost point from which the edge of the fan from the rivulet can enter the right side of the breach:

$$y_D = \ell + (x + 2\ell)\tan\alpha$$

```
O9=$F9+($E9+2*$F9)*TAN(RADIANS($M$7))
```

Column P: Determines which region (designated as Fraction Case #) along the crown where the drip is located:

1. $y \le y_A$
2. $y_A < y \le -\ell$
3. $-\ell < y < y_B$
4. $y_B \le y \le y_C$
5. $y_C < y < \ell$
6. $\ell \le y < y_D$
7. $y \ge y_D$

```
P9=IF(D9<=L9,1,IF(D9<=-F9,2,IF(D9<M9,3,
IF(D9<=N9,4,IF(D9<F9,5,IF(D9<O9,6,IF(D9>=O9,7)))))))
```

Crown Tests

The spread angles are the mean, 1-sigma, and 1-sigma, calculated on the "Spread Anges" sheet

This cell performs a conditional test, comoparing g to Ya, Yb, Yc, Yd, and l to determine which case applies

This cell is the f value determined by the appropriate case of the 7

For α = 8.8708 degrees

These are the Y values calculated, given α, l, and α, for each measurement. Note that Yb and Yc are different depending on the

These are the calculations that represent the 7 different fraction cases in the model. Some are constants (1 or 0)

	I	J	K	L	M	N	O	P	Q	R	S	T	U	V	W	X
8	f_{expt}	tan(α)	Model Case #	Ya	Yb	Yc	Yd	Fraction Case #	f_{calc}	f1	f2	f3	f4	f5	f6	f7
9	0.2471	21.3040	2	-39.0180	-7.8040	7.8040	39.0180	6	0.6291	0.0000	0.9213	1.0046	0.6337	0.6291	0.6078	0.0000
10	0.2580	13.4223	1	-31.1363	-0.0777	0.0777	31.1363	4	1.0000	0.0000	0.8827	1.0029	1.0000	1.0029	0.8827	0.0000
11	0.1360	13.4223	1	-31.1363	-0.0777	0.0777	31.1363	3	0.8539	0.0000	0.7693	0.8539	1.0000	1.1519	0.3961	0.0000
12	0.2359	21.3040	2	-39.0180	-7.8040	7.8040	39.0180	4	0.6337	0.0000	0.7645	0.8168	0.6337	0.8168	0.7645	0.0000
13	0.0325	13.4223	1	-31.1363	-0.0777	0.0777	31.1363	2	0.1173	0.0000	0.1173	-0.0029	1.0000	2.0087	1.6482	0.0000
14	0.0190	21.3040	2	-39.0180	-7.8040	7.8040	39.0180	6	0.2355	0.0000	1.2936	1.4505	0.6337	0.1832	0.2355	0.0000
15	0.0305	21.3040	2	-39.0180	-7.8040	7.8040	39.0180	2	0.2355	0.0000	0.2355	0.1832	0.6337	1.4505	1.2936	0.0000
16	0.0320	13.4223	1	-31.1363	-0.0777	0.0777	31.1363	6	0.1173	0.0000	1.6482	2.0087	1.0000	-0.0029	0.1173	0.0000
17	0.2748	21.3040	2	-39.0180	-7.8040	7.8040	39.0180	4	0.6337	0.0000	0.7645	0.8168	0.6337	0.8168	0.7645	0.0000
18	0.1773	21.3040	2	-39.0180	-7.8040	7.8040	39.0180	4	0.6337	0.0000	0.7645	0.8168	0.6337	0.8168	0.7645	0.0000
19	0.0201	21.3040	2	-39.0180	-7.8040	7.8040	39.0180	6	0.2355	0.0000	1.2936	1.4505	0.6337	0.1832	0.2355	0.0000
20	0.0129	21.3040	2	-39.0180	-7.8040	7.8040	39.0180	6	0.2355	0.0000	1.2936	1.4505	0.6337	0.1832	0.2355	0.0000
21	0.0129	13.4223	1	-31.1363	-0.0777	0.0777	31.1363	2	0.1173	0.0000	0.1173	-0.0029	1.0000	2.0087	1.6482	0.0000
22	0.0646	13.4223	1	-31.1363	-0.0777	0.0777	31.1363	2	0.1173	0.0000	0.1173	-0.0029	1.0000	2.0087	1.6482	0.0000
23																

Figure C-2. Spreadsheet "Flux Split Drip Shield Model," Worksheet "f calculations;" Calculation of Model Flow Fractions for Mean Minus One Standard Deviation Rivulet Spread Angle

Columns R though X (Figure C-2) compute the fraction of dripping flux f_{calc} that is predicted to flow into a breach, assuming the drip location is within each of seven regions along the crown. Although f_{calc} is computed for all seven regions, it is valid in only one of the regions. The correct valid region is determined in Column P (Fraction Case #), and the appropriate value from Columns R through X is entered in Column Q.

Column Q: f_{calc} is the fraction of dripping flux onto the drip shield that is predicted by the drip shield flux splitting submodel, Equations 6.5.1.1.2-2 through 6.5.1.1.2-6 or 6.5.1.1.2-19 through 6.5.1.1.2-23, for Cases 1 and 2, respectively. f_{calc} is intended to be compared with f_{expt} (Column I). The value of f_{calc} is selected from Columns R through X, depending on the appropriate Fraction Case # (Column P).

```
Q9=IF(P9=1,R9,IF(P9=2,S9,IF(P9=3,T9,IF(P9=4,U9,
    IF(P9=5,V9,IF(P9=6,W9,IF(P9=7,X9)))))))
```

Column R: Value of f_{calc} in region 1 ($y \le y_A$), where $f_{calc} = 0$.

R9=0

Column S: Value of f_{calc} in region 2 ($y_A < y \le -\ell$):

$$f_{calc} = \frac{y + \ell + (x + 2\ell)\tan\alpha}{2(x + 2\ell)\tan\alpha}$$

S9=(D9+F9+(E9+2*F9)*TAN(RADIANS($M$7)))/
(2*(E9+2*F9)*TAN(RADIANS($M$7)))

Column T: Value of f_{calc} in region 3 ($-\ell < y < y_B$):

$$f_{calc} = \frac{y + \ell + x\tan\alpha}{2x\tan\alpha}$$

T9=(D9+F9+E9*TAN(RADIANS($M$7)))/(2*E9*TAN(RADIANS($M$7)))

Column U: Value of f_{calc} in region 4 ($y_B \le y \le y_C$):

$$f_{calc} = \frac{2\ell}{2x\tan\alpha}$$

U9=IF(K9=1,1,(2*$F9/(2*$E9*TAN(RADIANS($M$7)))))

Column V: Value of f_{calc} in region 5 ($y_C < y < \ell$):

$$f_{calc} = \frac{-y + \ell + x\tan\alpha}{2x\tan\alpha}$$

V9=(-D9+F9+E9*TAN(RADIANS($M$7)))/(2*E9*TAN(RADIANS($M$7)))

Column W: Value of f_{calc} in region 6 ($\ell \le y < y_D$):

$$f_{calc} = \frac{-y + \ell + (x + 2\ell)\tan\alpha}{2(x + 2\ell)\tan\alpha}$$

W9=(-D9+F9+(E9+2*F9)*TAN(RADIANS($M$7)))/
(2*(E9+2*F9)*TAN(RADIANS($M$7)))

Column X: Value of f_{calc} in region 7 ($y \ge y_D$) where $f_{calc} = 0$:

X9=0

	Y	Z	AA	AB	AC	AD	AE	AF	AG	AH	AI	AJ	AK	AL	AM
1															
2															
3															
4															
5															
6															
7	For α = 13.1527 degrees														
8	y*tan(α)	Mode Case #	Y3	Y3	Y4	Y4	Fraction Case #	f	f1	f2	f3	f4	f5	f6	f7
9	31.8968	2	-51.7061	-18.3968	18.3968	51.7061	4	0.4232	0.0000	0.7814	0.8370	0.4232	0.5862	0.5720	0.0000
10	20.0962	2	-39.9054	-6.5962	6.5962	39.9054	4	0.6718	0.0000	0.7556	0.8359	0.6718	0.8359	0.7556	0.0000
11	20.0962	2	-39.9054	-6.5962	6.5962	39.9054	2	0.6799	0.0000	0.6799	0.7364	0.6718	0.9354	0.8314	0.0000
12	31.8968	2	-51.7061	-18.3968	18.3968	51.7061	4	0.4232	0.0000	0.6767	0.7116	0.4232	0.7116	0.6767	0.0000
13	20.0962	2	-39.9054	-6.5962	6.5962	39.9054	2	0.2444	0.0000	0.2444	0.1641	0.6718	1.5077	1.2669	0.0000
14	31.8968	2	-51.7061	-18.3968	18.3968	51.7061	6	0.3233	0.0000	1.0300	1.1349	0.4232	0.2884	0.3233	0.0000
15	31.8968	2	-51.7061	-18.3968	18.3968	51.7061	2	0.3233	0.0000	0.3233	0.2884	0.4232	1.1349	1.0300	0.0000
16	20.0962	2	-39.9054	-6.5962	6.5962	39.9054	6	0.2444	0.0000	1.2669	1.5077	0.6718	0.1641	0.2444	0.0000
17	31.8968	2	-51.7061	-18.3968	18.3968	51.7061	4	0.4232	0.0000	0.6767	0.7116	0.4232	0.7116	0.6767	0.0000
18	31.8968	2	-51.7061	-18.3968	18.3968	51.7061	4	0.4232	0.0000	0.6767	0.7116	0.4232	0.7116	0.6767	0.0000
19	31.8968	2	-51.7061	-18.3968	18.3968	51.7061	6	0.3233	0.0000	1.0300	1.1349	0.4232	0.2884	0.3233	0.0000
20	31.8968	2	-51.7061	-18.3968	18.3968	51.7061	6	0.3233	0.0000	1.0300	1.1349	0.4232	0.2884	0.3233	0.0000
21	20.0962	2	-39.9054	-6.5962	6.5962	39.9054	2	0.2444	0.0000	0.2444	0.1641	0.6718	1.5077	1.2669	0.0000
22	20.0962	2	-39.9054	-6.5962	6.5962	39.9054	2	0.2444	0.0000	0.2444	0.1641	0.6718	1.5077	1.2669	0.0000

Figure C-3. Spreadsheet "Flux Split Drip Shield Model," Worksheet "f calculations;" Calculation of Model Flow Fractions for Mean Rivulet Spread Angle

Columns Y though AM (Figure C-3) repeat the calculations done in Columns J though X using the mean rivulet spread angle of $\alpha = 13.1527°$ (Cell $AB$7). For Row 9, the spreadsheet equations are as follows:

```
Y9=$E9*TAN(RADIANS($AB$7))

Z9=IF($F9>Y9,1,2)

AA9=-$F9-($E9+2*$F9)*TAN(RADIANS($AB$7))

AB9=IF(Z9=1,(-$F9+$E9*TAN(RADIANS($AB$7))),($F9-$E9*TAN(RADIANS($AB$7))))

AC9=IF(Z9=1,($F9-$E9*TAN(RADIANS($AC$7))),(-$F9+$E9*TAN(RADIANS($AB$7))))

AD9=$F9+($E9+2*$F9)*TAN(RADIANS($AB$7))

AE9=IF(D9<=AA9,1,IF(D9<=-
      U9,2,IF(D9<AB9,3,IF(D9<=AC9,4,IF(D9<U9,5,IF(D9<AD9,6,IF(D9>=AD9,7)))))))

AF9=IF(AE9=1,AG9,IF(AE9=2,AH9,IF(AE9=3,AI9,IF(AE9=4,AJ9,IF(AE9=5,AK9,IF(AE9
      =6,AL9,IF(AE9=7,AM9)))))))
```

```
AG9=0
AH9=(D9+F9+(E9+2*F9)*TAN(RADIANS($AB$7)))/
      (2*(E9+2*F9)*TAN(RADIANS($AB$7)))
AI9=(D9+F9+E9*TAN(RADIANS($AB$7)))/(2*E9*TAN(RADIANS($AB$7)))
AJ9=IF(Z9=1,1,(2*$F9/(2*$E9*TAN(RADIANS($AB$7)))))
AK9=(-D9+F9+E9*TAN(RADIANS($AB$7)))/(2*E9*TAN(RADIANS($AB$7)))
AL9=(-D9+F9+(E9+2*F9)*TAN(RADIANS($AB$7)))/
      (2*(E9+2*F9)*TAN(RADIANS($AB$7)))
AM9=0
```

Columns AN though BB (Figure C-1) repeat the calculations done in Columns J though X using a rivulet spread angle of $\alpha = 17.2903°$ (Cell $AQ$7), which is one standard deviation greater than the mean rivulet spread angle. For Row 9, the spreadsheet equations are as follows:

```
AN9=$E9*TAN(RADIANS($AQ$7))
AO9=IF($F9>AN9,1,2)
AP9=-$F9-($E9+2*$F9)*TAN(RADIANS($AQ$7))
AQ9=IF(AO9=1,(-$F9+$E9*TAN(RADIANS($AQ$7))),($F9-
      $E9*TAN(RADIANS($AQ$7))))
AR9=IF(AO9=1,($F9-$E9*TAN(RADIANS($AQ$7))),
      (-$F9+$E9*TAN(RADIANS($AQ$7))))
AS9=$F9+($E9+2*$F9)*TAN(RADIANS($AQ$7))
AT9=IF(AH9<=AP9,1,IF(AH9<=-AJ9,2,IF(AH9<AQ9,3,IF(AH9<=AR9,4,
      IF(AH9<AJ9,5,IF(AH9<AS9,6,IF(AH9>=AS9,7)))))))
AU9=IF(AT9=1,AV9,IF(AT9=2,AW9,IF(AT9=3,AX9,IF(AT9=4,AY9,IF(AT9=5,AZ9,IF
      (AT9=6,BA9,IF(AT9=7,BB9)))))))
AV9=0
AW9=(D9+F9+(E9+2*F9)*TAN(RADIANS($AQ$7)))/
      (2*(E9+2*F9)*TAN(RADIANS($AQ$7)))
AX9=(D9+F9+E9*TAN(RADIANS($AQ$7)))/(2*E9*TAN(RADIANS($AQ$7)))
AY9=IF(AO9=1,1,(2*$F9/(2*$E9*TAN(RADIANS($AQ$7)))))
AZ9=(-D9+F9+E9*TAN(RADIANS($AQ$7)))/(2*E9*TAN(RADIANS($AQ$7)))
BA9=(-D9+F9+(E9+2*F9)*TAN(RADIANS($AQ$7)))/
      (2*(E9+2*F9)*TAN(RADIANS($AQ$7)))
BB9=0
```

	AN	AO	AP	AQ	AR	AS	AT	AU	AV	AW	AX	AY	AZ	BA	BB
1															
2															
3															
4															
5															
6															
7	For α = 88888 degrees														
8	Tan(α)	Mode 1 Case #	Y0	Y1	Y2	Y3	Fract on Case #	f calc	f1	f2	f3	f4	f5	f6	f7
9	42.4896	2	-64.3942	-28.9896	28.9896	64.3942	4	0.3177	0.0000	0.7112	0.7530	0.3177	0.5647	0.5540	0.0000
10	26.7700	2	-48.6746	-13.2700	13.2700	48.6746	4	0.5043	0.0000	0.6919	0.7521	0.5043	0.7521	0.6919	0.0000
11	26.7700	2	-48.6746	-13.2700	13.2700	48.6746	4	0.5043	0.0000	0.6350	0.6774	0.5043	0.8269	0.7488	0.0000
12	42.4896	2	-64.3942	-28.9896	28.9896	64.3942	4	0.3177	0.0000	0.6326	0.6589	0.3177	0.6589	0.6326	0.0000
13	26.7700	2	-48.6746	-13.2700	13.2700	48.6746	4	0.5043	0.0000	0.3081	0.2479	0.5043	1.2564	1.0757	0.0000
14	42.4896	2	-64.3942	-28.9896	28.9896	64.3942	4	0.3177	0.0000	0.8979	0.9766	0.3177	0.3411	0.3674	0.0000
15	42.4896	2	-64.3942	-28.9896	28.9896	64.3942	4	0.3177	0.0000	0.3674	0.3411	0.3177	0.9766	0.8979	0.0000
16	26.7700	2	-48.6746	-13.2700	13.2700	48.6746	4	0.5043	0.0000	1.0757	1.2564	0.5043	0.2479	0.3081	0.0000
17	42.4896	2	-64.3942	-28.9896	28.9896	64.3942	4	0.3177	0.0000	0.6326	0.6589	0.3177	0.6589	0.6326	0.0000
18	42.4896	2	-64.3942	-28.9896	28.9896	64.3942	4	0.3177	0.0000	0.6326	0.6589	0.3177	0.6589	0.6326	0.0000
19	42.4896	2	-64.3942	-28.9896	28.9896	64.3942	4	0.3177	0.0000	0.8979	0.9766	0.3177	0.3411	0.3674	0.0000
20	42.4896	2	-64.3942	-28.9896	28.9896	64.3942	4	0.3177	0.0000	0.8979	0.9766	0.3177	0.3411	0.3674	0.0000
21	26.7700	2	-48.6746	-13.2700	13.2700	48.6746	4	0.5043	0.0000	0.3081	0.2479	0.5043	1.2564	1.0757	0.0000
22	26.7700	2	-48.6746	-13.2700	13.2700	48.6746	4	0.5043	0.0000	0.3081	0.2479	0.5043	1.2564	1.0757	0.0000

Figure C-4. Spreadsheet "Flux Split Drip Shield Model," Worksheet "f calculations;" Calculation of Model Flow Fractions for Mean Plus One Standard Deviation Rivulet Spread Angle

Rivulet spread measurements are listed in Column D, Rows 6-31 (Figure C-5), for 26 tests described in the indicated DTNs. The sketch to the right shows the relationships between measured rivulet spread ("1/2 spread") and the "1/2 spread angle," α. The average, μ_r, of the 26 spread measurements (Cell D33) is 20.096 cm, with a standard deviation, σ, of 6.674 cm. The uncertainty in the spread angle is incorporated into the drip shield flux splitting submodel by assigning a range for the rivulet spread of $\mu_r \pm 1\sigma$. The mean rivulet spread and $\mu_r \pm 1\sigma$ are shown in Cells K6–K8. The rivulet spread is converted to spread angle in Cells L6-L8 using the relation shown in the sketch that defines α:

$$\alpha = \tan^{-1}\left(\frac{w_r}{x}\right),$$

where w_r is the rivulet "1/2 spread" (cm), and x is the distance from the crown to the spread measurement location (cm). The Microsoft Excel equation for the mean spread angle is:

L6=DEGREES(ATAN(K6/($N$4)))

where $N$4 = x = 86 cm for these tests. The Microsoft Excel function ATAN returns a value in radians, which must be converted to degrees using the DEGREES function.

Also included in this worksheet is a sketch (Figure C-6) showing the dimensions and locations of breaches in the drip shield mockup used in the experiments. The sketch appears in the scientific notebook from the experiments (Howard 2002 [DIRS 161516], p. 14), and is also shown in Figure 4.1-1, Section 4.1.1.

SPREADSHEET "FLUX SPLIT DRIP SHIELD MODEL" WORKSHEET "SPREAD ANGLES"

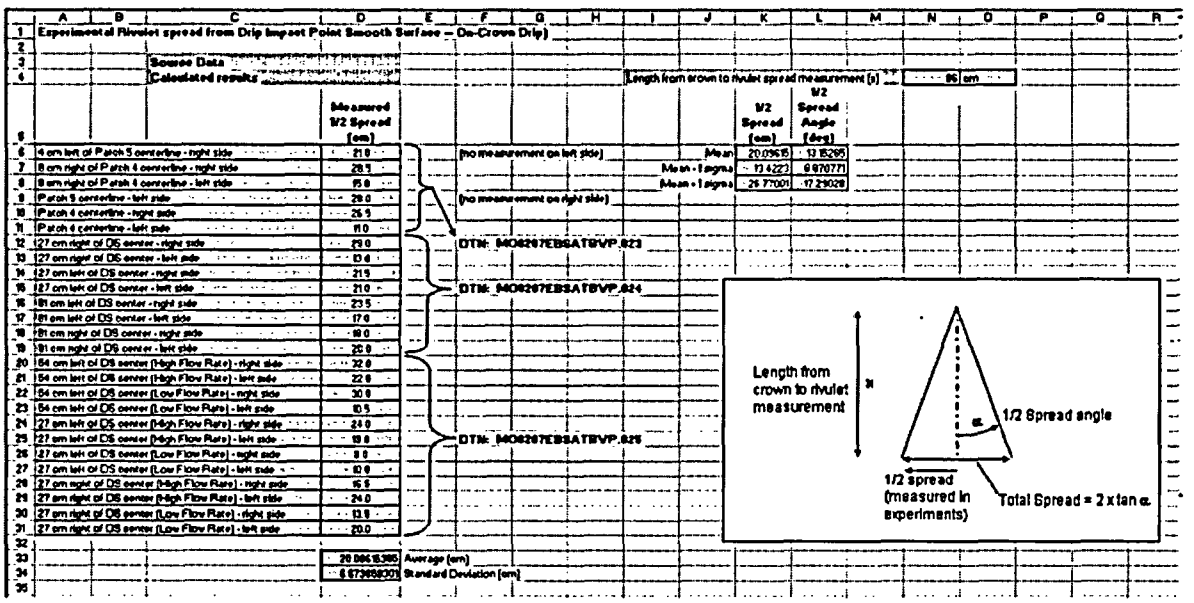

DTN: MO0207EBSATBWP.023 [DIRS 163402]; DTN: MO0207EBSATBWP.024 [DIRS 163401]; DTN: MO0207EBSATBWP.025 [DIRS 163403].

Figure C-5. Spreadsheet "Flux Split Drip Shield Model," Worksheet "Spread angles;" Calculation of Rivulet Spread Angle

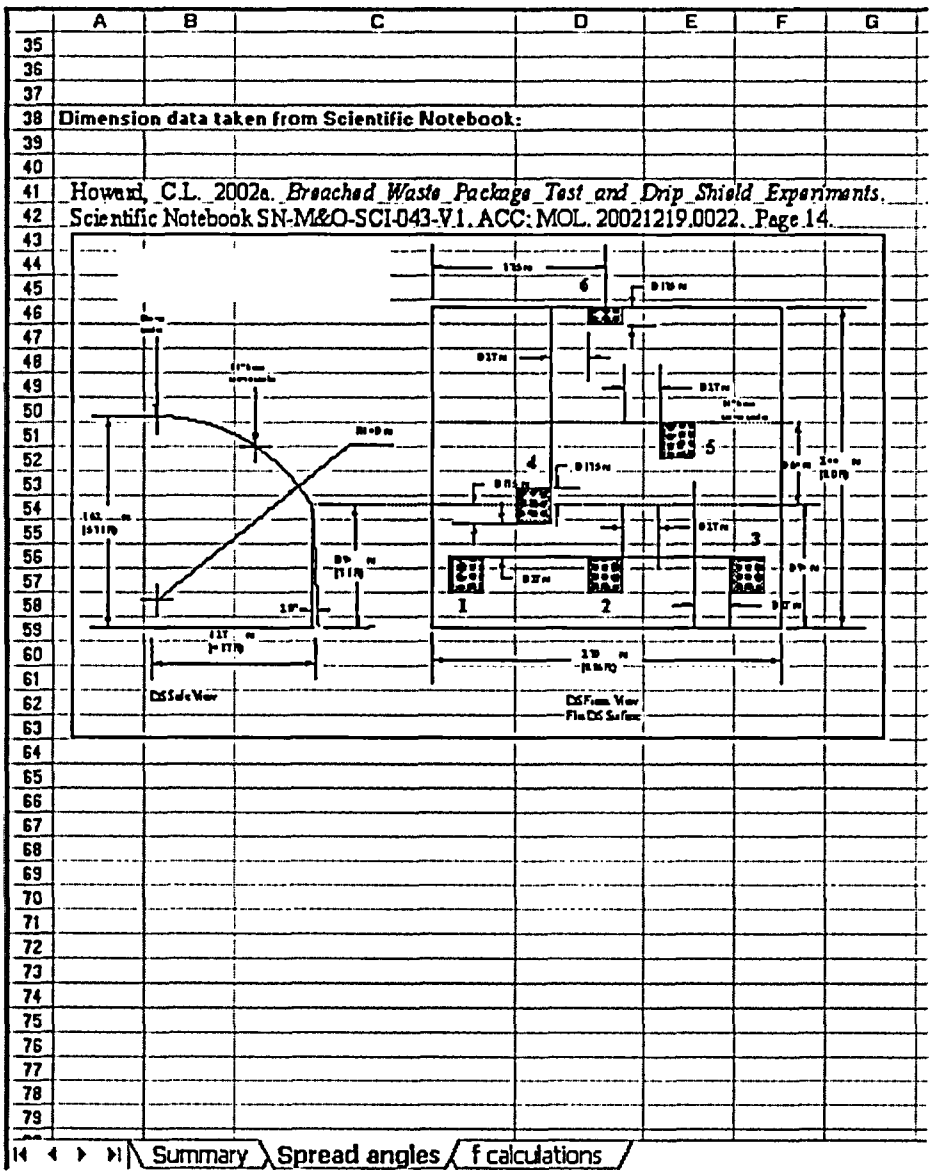

Source: Howard 2002 [DIRS 161516], p. 14.

Figure C-6. Spreadsheet "Flux Split Drip Shield Model," Worksheet "Spread Angles;" Dimensions and Locations of Breaches in Drip Shield Mockup Used in Breached Drip Shield Experiments

SPREADSHEET "FLUX SPLIT DRIP SHIELD MODEL" WORKSHEET "SUMMARY"

	A	B	C	D	E	F	G	H	I	J	K
1											
2		Drip Shield Model: Comparison of Measured and Modeled Fraction of Drip Seepage Flowing into a Breach									
3											
4											
5											
6		This spreadsheet compares results from the "Atlas Breached Waste Package and Drip Shield Experiments: Breached Drip Shield Tests" (documented in BSC 2003: TDR-EBS-MD-000025 REV 00) with the model developed in the "EBS Radionuclide Transport Abstraction" (BSC 2003: ANL-WIS-PA-000001 REV 01). Test data are taken directly from the TDMS for this comparison.									
7											
8		Methodology:									
9		1. Spreading angles are calculated from the test data in the sheet titled *Spread angles*									
10		2. Given spread angle and test geometry, seepage fractions are calculated for both the test data and the model in the worksheet *f calculations* :									
11			a. Geometric data for each measurement (x,y,l) and the spread angle are used to determine which of 7 cases the measurement corresponds to								
12			b. For each test result the appropriate case model is applied to calculate the seepage flow fraction f								
13		3. The seepage fractions calculated from both the test and model are listed and compared in the two tables listed below in this *Summary* worksheet									
14											
15		Notes:									
16		Source data DTNs are noted where source data is used									
17		Model equations are provided on the calculational sheets									
18		Data in tables below are linked directly to the calculational worksheets									
19											

Source: BSC 2003 [DIRS 163406].

Figure C-7. Spreadsheet "Flux Split Drip Shield Model," Worksheet "Summary;" Summary of Drip Shield Flux Splitting Submodel

This worksheet, beginning with Figure C-7, summarizes the calculations in worksheets "Spread angles" and "f calculations."

The first table (Figure C-8), "Measured Breach Flow Fractions and Calculated Breach Flow Fractions," Rows 25-43, Columns B-I, is identical to Table 6.5-2. Columns B-E are identical to the same respective columns described earlier for worksheet "f calculations." Column F is identical to Column I in worksheet "f calculations." Columns G-I summarize the calculated fraction of the dripping flux that the flux splitting submodel predicts should flow into the breach, for the minimum, mean, and maximum spread angles. The minimum spread angle is specified to be one standard deviation less than the mean of the measured spread angles. The maximum spread angle is specified to be one standard deviation greater than the mean of the measured spread angles. Column G is identical to Column Q of worksheet "f calculations." Column H is identical to Column AF of worksheet "f calculations." Column I is identical to Column AU of worksheet "f calculations."

Rows 39–43, Columns F–I, show the results of Microsoft Excel functions "AVERAGE," "STDEVA," "MEDIAN," "MIN", and "MAX," respectively, as applied to Rows 25-38.

	A	B	C	D	E	F	G	H	I
19									
20		*Measured Breach Flow Fractions and Calculated Breach Flow Fractions*							
21									
22				y, Drip Location Relative to Breach Center (cm)	z, Vertical Distance from Crown (drip) to Top of Breach (cm)		f_{calc}		
23							α (deg)	α (deg)	α (deg)
24		Drip Location (Test Description)	Breach No.			f_{expt}	8.87	13.15	17.29
25		8 cm right of Patch 4 centerline [Q(film) Test]	4	8	136.5	0.2471	0.6291	0.4232	0.3177
26		Patch 5 centerline [Q(film) Test]	5	0	86.0	0.2580	1.0000	0.6718	0.5043
27		4 cm left of Patch 5 centerline [Q(film) Test]	5	-4	86.0	0.1360	0.8539	0.6799	0.5043
28		Patch 4 centerline [Q(film) Test]	4	0	136.5	0.2359	0.6337	0.4232	0.3177
29		27 cm right of DS center (Multiple Patch Test)	5	-27	86.0	0.0325	0.1173	0.2444	0.5043
30		27 cm left of DS center (Multiple patch test)	4	27	136.5	0.0190	0.2355	0.3233	0.3177
31		81 cm left of DS center (Multiple Patch Test)	4	-27	136.5	0.0305	0.2355	0.3233	0.3177
32		81 cm right of DS center (Multiple Patch Test)	5	27	86.0	0.0320	0.1173	0.2444	0.5043
33		54 cm left of DS center (High Flow Rate Test)	4	0	136.5	0.2748	0.6337	0.4232	0.3177
34		54 cm left of DS center (Low Flow Rate Test)	4	0	136.5	0.1773	0.6337	0.4232	0.3177
35		27 cm left of DS center (High Flow Rate Test)	4	27	136.5	0.0201	0.2355	0.3233	0.3177
36		27 cm left of DS center (Low Flow Rate Test)	4	27	136.5	0.0129	0.2355	0.3233	0.3177
37		27 cm right of DS center (High Flow Rate Test)	5	-27	86.0	0.0129	0.1173	0.2444	0.5043
38		27 cm right of DS center (Low Flow Rate Test)	5	-27	86.0	0.0646	0.1173	0.2444	0.5043
39		Mean				0.1110	0.4139	0.3797	0.3977
40		Std. Dev.				0.1055	0.3048	0.1438	0.0958
41		Median				0.0486	0.2355	0.3233	0.3177
42		Minimum				0.0129	0.1173	0.2444	0.3177
43		Maximum				0.2748	1.0000	0.6799	0.5043
44									

Figure C-8. Spreadsheet "Flux Split Drip Shield Model," Worksheet "Summary;" Summary of Drip Shield Flux Splitting Submodel

The second table (Figure C-9), "Comparison of Measured and Calculated Breach Flows," is identical to Table 6.5-3. Column K is again the drip location. Column L is the fraction of dripping flux that flowed into a breach as measured experimentally; this is identical to Column F of the preceding table, or Column I in worksheet "f calculations." The next three columns (M-O) show the difference between the predicted breach flow fraction, f_{calc}, and the measured fraction, f_{expt}, for the minimum, mean, and maximum rivulet spread angle. Columns P-R show the ratio f_{calc} / f_{expt} for the minimum, mean, and maximum rivulet spread angle.

Rows 39-43, Columns L-R, show the results of Microsoft Excel functions "AVERAGE," "STDEVA," "MEDIAN," "MIN," and "MAX," respectively, as applied to Rows 25-38.

	J	K	L	M	N	O	P	Q	R
19									
20									
21		*Comparison of Measured and Calculated Breach Flows*							
22				$f_{calc} - f_{expt}$			f_{calc} / f_{expt}		
23				α (deg)	α (deg)	α (deg)	α (deg)	α (deg)	α (deg)
24		**Drip Location (Test Description)**	f_{expt}	**8.87**	**13.15**	**17.29**	**8.87**	**13.15**	**17.29**
25		8 cm right of Patch 4 centerline [Q(film) Test]	0.2471	0.3819	0.1761	0.0706	2.5455	1.7126	1.2856
26		Patch 5 centerline [Q(film) Test]	0.2580	0.7420	0.4138	0.2463	3.8764	2.6041	1.9549
27		4 cm left of Patch 5 centerline [Q(film) Test]	0.1360	0.7179	0.5439	0.3683	6.2770	4.9979	3.7071
28		Patch 4 centerline [Q(film) Test]	0.2359	0.3978	0.1873	0.0818	2.6861	1.7941	1.3468
29		27 cm right of DS center [Multiple Patch Test]	0.0325	0.0847	0.2119	0.4718	3.6060	7.5145	15.5074
30		27 cm left of DS center [Multiple patch test]	0.0190	0.2165	0.3043	0.2987	12.3932	17.0164	16.7216
31		81 cm left of DS center [Multiple Patch Test]	0.0305	0.2050	0.2928	0.2872	7.7203	10.6004	10.4168
32		81 cm right of DS center [Multiple Patch Test]	0.0320	0.0852	0.2124	0.4723	3.6624	7.6321	15.7500
33		54 cm left of DS center [High Flow Rate Test]	0.2748	0.3588	0.1484	0.0429	2.3056	1.5399	1.1560
34		54 cm left of DS center [Low Flow Rate Test]	0.1773	0.4564	0.2459	0.1404	3.5741	2.3872	1.7920
35		27 cm left of DS center [High Flow Rate Test]	0.0201	0.2153	0.3032	0.2976	11.6928	16.0548	15.7767
36		27 cm left of DS center [Low Flow Rate Test]	0.0129	0.2226	0.3104	0.3048	18.2860	25.1075	24.6725
37		27 cm right of DS center [High Flow Rate Test]	0.0129	0.1043	0.2314	0.4914	9.0637	18.8879	38.9779
38		27 cm right of DS center [Low Flow Rate Test]	0.0646	0.0526	0.1797	0.4397	1.8146	3.7814	7.8035
39		Mean	0.1110	0.3029	0.2687	0.2867	6.3931	8.6879	11.2049
40		Std. Dev.	0.1055	0.2210	0.1065	0.1550	4.8845	7.6717	11.0326
41		Median	0.0486	0.2195	0.2387	0.2982	3.7694	6.2562	9.1102
42		Minimum	0.0129	0.0526	0.1484	0.0429	1.8146	1.5399	1.1560
43		Maximum	0.2748	0.7420	0.5439	0.4914	18.2860	25.1075	38.9779

Figure C-9. Spreadsheet "Flux Split Drip Shield Model," Worksheet "Summary;" Summary of Drip Shield Flux Splitting Submodel Comparing Measured and Calculated Breach Flows

Finally, a plot in worksheet "Summary" (Figure C-10) compares the calculated f_{calc} with the measured f_{expt} (Column F) for the minimum, mean, and maximum spread angles (Columns G, H, and I, respectively); the f_{expt} and f_{calc} values that are plotted in Figure C-10 are shown in Figure C-8. The diagonal line in the plot represents $f_{calc} = f_{expt}$. All values of f_{calc} lie above the line $f_{calc} = f_{expt}$, indicating that the drip shield flux splitting submodel overestimates the flow into breaches.

	A	B	C	D	E	F	G	H	I	J
39		Mean				0.1110	0.4139	0.3797	0.3977	
40		Std. Dev.				0.1055	0.3048	0.1438	0.0958	
41		Median				0.0486	0.2355	0.3233	0.3177	
42		Minimum				0.0129	0.1173	0.2444	0.3177	
43		Maximum				0.2748	1.0000	0.6799	0.5043	

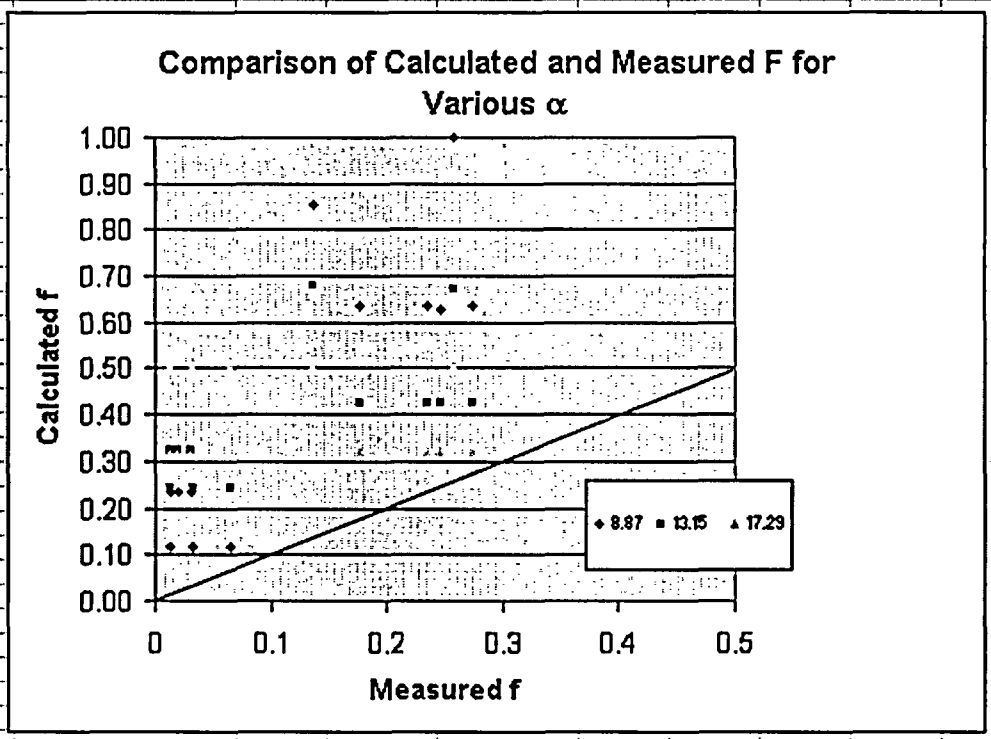

Summary / Spread angles / f calculations

Figure C-10. Spreadsheet "Flux Split Drip Shield Model," Worksheet "Summary;" Comparison of Calculated and Measured Breach Flow Fractions for Drip Shield Flux Splitting Submodel for Minimum (8.87°), Mean (13.15°), and Maximum (17.29°) Rivulet Spread Angles

APPENDIX D
MICROSOFT EXCEL SPREADSHEET "FLUX SPLIT WASTE PACKAGE MODEL"

MICROSOFT EXCEL SPREADSHEET "FLUX SPLIT WASTE PACKAGE MODEL"

SPREADSHEET "FLUX SPLIT WASTE PACKAGE MODEL"–WORKSHEET "F CALCULATIONS"

Breach Flow Fraction Calculation using Smooth Drip Shield Data, Off-Crown Tests

The Model Case depends on whether the breach is wider (case 1) or narrower (case 2) than the spread at the breach. So the patch width is compared to a tan(α).

Single Patch Tests (DTN: MO0207EBSATBVP.023)

Source Data (Calculated results)

	A	B	C	D	E	F	G	H	I	J	K	L	M	N
8		Test Type	Test Date	Drip Location (Test Description)	Breach No.	Location of Drip Relative to DS Centerline (cm)	Location of Breach Relative to DS Centerline (cm)	y, Drip Location Relative to Breach Center (cm)	s, Vertical Distance from Drip to Top of Breach (cm)	L, Patch half-width (cm)	Drip Flux (g)	Flow Into Breach (g)	f_{exp}	$x^*\tan(\alpha)$
9		Q(splash)	5/17/2002	P5, 17.5 cm left of center, 33"	4			-17.5	50.5	13.5	85.77	0	0.0000	4.8659
10		Q(splash)	5/20/2002	P4, center, 33"	4			0.0	50.5	13.5	127.21	103.84	0.8005	4.8659
11		Q(splash)	5/20/2002	P4, 17.5 cm right of center, 33"	4			17.5	50.5	13.5	131.42	0.96	0.0032	4.8659
12		Q(splash)	5/21/2002	P4, 17.5 cm right of center, 15.5"	4			17.5	93.5	13.5	150.76	1.79	0.0119	9.0092
13		Q(splash)	5/21/2002	P4, centerline, 15.5"	4			0.0	93.5	13.5	138.9	84.35	0.6029	9.0092
14		Q(splash)	5/21/2002	P5, 17.5 cm left of center, 15.5"	5			-17.5	43	13.5	187.5	2.68	0.0142	4.1432
15		Q(splash)	5/21/2002	P5, 35.5 cm left of center, 15.5"	4			18.5	93.5	13.5	142.28	0.22	0.0015	9.0092
16		Q(splash)	5/22/2002	P5, centerline, 15.5"	5			0.0	43	13.5	124.74	90.54	0.7260	4.1432
17		Q(splash)	5/22/2002	P5, 35.5 cm left of center, between crown and 15.5"	4			17.5	115	13.5	129.27	6.63	0.0513	11.0608
18		Q(film)	5/31/2002	P4, 6 cm right of center, 15.5"	4			0.0	93.5	13.5	172.38	92.93	0.5389	9.0092
19		Q(film)	5/31/2002	P2, center, 15.5"	4			54.0	93.5	13.5	242.49	151.86	0.6254	9.0092
20		Q(film)	5/31/2002	P2, 15 cm right of center, 15.5"	5			-39.0	43	13.5	177.22	0.39	0.0022	4.1432
21		Q(film)	5/31/2002	P5, 4 cm left of center, 15.5"	5			-4.0	43	13.5	173.17	184.54	1.0657	4.1432
22		Q(film)	6/1/2002	P4, 6 cm right of center, 15.5"	4			0.0	93.5	13.5	137.44	107.38	0.7813	9.0092
23		Bounding	6/18/2002	54 cm left of DS center, 15.5"	4	-54	-54	0.0	93.5	13.5	353.43	163.77	0.4633	9.0092
24		Bounding	6/19/2002	54 cm left of DS center, 15.5"	4	-54	-54	0.0	93.5	13.5	107.01	84.95	0.7901	9.0092
25		Bounding	6/16/2002	27 cm left of DS center, 15.5"	5	-27	54	-81.0	43	13.5	121.76	0.58	0.0049	4.1432
26		Bounding	6/20/2002	27 cm left of DS center, 15.5"	5	-27	54	-81.0	43	13.5	370.41	1.16	0.0031	4.1432
27		Bounding	6/20/2002	27 cm right of DS center, 15.5"	5	27	54	-27.0	43	13.5	339.74	4.24	0.0125	4.1432
28		Bounding	6/20/2002	27 cm right of DS center, 15.5"	5	27	54	-27.0	43	13.5	95.41	0.78	0.0082	4.1432
29		Bounding	6/20/2002	27 cm left of DS center, 33"	4	-27	-54	27.0	50.5	13.5	367.11	0.96	0.0026	4.8659
30		Bounding	6/20/2002	27 cm right of DS center, 33"	4	27	-54	81.0	50.5	13.5	317.8	0.62	0.0020	4.8659
31		Bounding	6/20/2002	54 cm left of DS center, 33"	4	-54	-54	0.0	50.5	13.5	329.85	188.05	0.5692	4.8659
32		Bounding	6/21/2002	54 cm left of DS center, 33"	4	-54	-54	0.0	50.5	13.5	101.13	83.1	0.8217	4.8659
33		Bounding	6/24/2002	27 cm left of DS center, 33"	4	-27	-54	27.0	50.5	13.5	96.21	1.18	0.0123	4.8659
34		Bounding	6/24/2002	27 cm right of DS center, 33"	4	27	-54	81.0	50.5	13.5	96.75	0	0.0000	4.8659
35														
36														
37														

Bounding Flow Rate Tests (DTN: MO0207EBSATBVP.025)

Summary / Spread angles / f calculations

DTN: MO0207EBSATBWP.023 [DIRS 163402]; DTN: MO0207EBSATBWP.025 [DIRS 163403].

Figure D-1. Spreadsheet "Flux Split Waste Package Model," Worksheet "f calculations;" Calculation of Experimental Breach Flow Fractions and Model Flow Fractions for Mean Minus One Standard Deviation Rivulet Spread Angle

The purpose of this spreadsheet is to develop the waste package flux splitting submodel using experimental data from the breached drip shield experiments. The data are analyzed to estimate an average and range of the rivulet spread angle, α. The disparity between measured fraction of dripping flux that enters a breach and the fraction calculated using the model (with the measured range of the rivulet spread angle) is then used to establish a range of uncertainty in the model. Whereas the drip shield submodel is based on data from on-crown drip locations, the waste package submodel uses off-crown drip data, for which the drip location is some distance away from the crown of the drip shield mockup.

All descriptions for this worksheet pertain to Rows 9-34. Equations in spreadsheet format are illustrated using Row 9.

Column B: Test type. The first three columns (B-D) help identify uniquely each test as described in the designated DTN.

Column C: Test date.

Column D: Drip location as indicated for each test in the designated DTN.

Column E: Breach or patch number most pertinent to this particular test, for which flow is analyzed in this row of the spreadsheet.

Column F: Drip location relative to drip shield center. Applies only to Bounding tests, further defining the drip location as specified in the DTN.

Column G: Breach location relative to drip shield center. Applies only to Bounding tests, further defining the breach location as specified in the DTN.

Column H: Drip location, y, relative to the center of the breach listed in Column E.

Column I: Vertical distance, x, from the drip location to the top of the breach.

Column J: Half-width, ℓ, of the breach–13.5 cm, same for all breaches.

Column K: Measured mass of water, F_1, dripped onto the drip shield during the test. For the on-crown drips, it is assumed that half of the water that dripped onto the drip shield, $F_1/2$, flowed down the side that contained the breach. For these off-crown tests, the full dripping flux is assumed to flow down the side where the drip is located.

Column L: Measured mass of water, F_2, that flowed into the breach during the test.

Column M: Fraction of water dripped onto the drip shield that flowed into the breach:

$$f_{expt} = \frac{F_2}{F_1}.$$

M9=L9/K9

Columns N through AB perform calculations that result in f_{calc}, the fraction of dripping flux that is predicted by the model to flow into a breach.

Column N: $x \tan\alpha$, where x is from Column I, and α is the spread angle. For Columns N-AB, the value used for α is 5.5037° (Cell $Q$7), which is one standard deviation less than the mean measured spread angle for these tests (see Worksheet "Spread angles").

N9=$I9*TAN(RADIANS($Q$7))

Column O: Case number as described in Sections 6.5.1.1.2.1 and 6.5.1.1.2.2. For Case 1, $\ell > x\tan\alpha$; for Case 2, $\ell < x\tan\alpha$; x is from Column I, and the half-width of the breach, ℓ, is from Column J.

O9=IF($J9>N9,1,2)

Column P: Value of y_A (Point A) as described in Sections 6.5.1.1.2.1 and 6.5.1.1.2.2, corresponding to the leftmost point from which the edge of the fan from the rivulet can enter the left side of the breach:

$$y_A = -\ell - (x + 2\ell)\tan\alpha$$

P9=-$J9-($I9+2*$J9)*TAN(RADIANS($Q$7))

Column Q: Value of y_B (Point B) as described in Sections 6.5.1.1.2.1 and 6.5.1.1.2.2, corresponding to the leftmost point from which rivulets will enter the top edge of the breach. The value of y_B depends on the Model Case number (Column O):

$$y_B = -\ell + x\tan\alpha \qquad \text{Case 1.}$$
$$y_B = \ell - x\tan\alpha \qquad \text{Case 2.}$$

Q9=IF(O9=1,(-$J9+$I9*TAN(RADIANS($Q$7))),
($J9-$I9*TAN(RADIANS($Q$7))))

Column R: Value of y_C (Point C) as described in Sections 6.5.1.1.2.1 and 6.5.1.1.2.2, corresponding to the rightmost point from which rivulets will enter the top edge of the breach. The value of y_C depends on the Model Case number (Column O):

$$y_C = \ell - x\tan\alpha \qquad \text{Case 1.}$$
$$y_C = -\ell + x\tan\alpha \qquad \text{Case 2.}$$

R9=IF(O9=1,($J9-$I9*TAN(RADIANS($Q$7))),
(-$J9+$I9*TAN(RADIANS($Q$7)))),

Column S: Value of y_D (Point D) as described in Sections 6.5.1.1.2.1 and 6.5.1.1.2.2, corresponding to the rightmost point from which the edge of the fan from the rivulet can enter the right side of the breach:

$$y_D = \ell + (x + 2\ell)\tan\alpha$$

S9=$J9+($I9+2*$J9)*TAN(RADIANS($Q$7))

Column T: Determines which region (designated as Fraction Case #) along the drip shield relative to the center of the breach where the drip is located:

1. $y \le y_A$
2. $y_A < y \le -\ell$
3. $-\ell < y < y_B$
4. $y_B \le y \le y_C$
5. $y_C < y < \ell$
6. $\ell \le y < y_D$
7. $y \ge y_D$

T9=IF($H9<=P9,1,IF($H9<=-$J9,2,IF($H9<Q9,3,
IF($H9<=R9,4,IF($H9<$J9,5,IF($H9<S9,6,IF($H9>=S9,7)))))))

The spread angles are the mean, 1-sigma, and 1-sigma, calculated on the "Spread Angles" sheet

This cell performs a conditional test, comoparing y to Ya, Yb, Yc, Yd, and l to determine which case applies

This cell is the f value determined by the appropriate case of the 7 possible.

For α = 5.5037 degrees

These are the Y values calculated, given z, l, and α, for each measurement. Note that Yb and Yc are different depending on the Model Case #

These are the calculations that represent the 7 different fraction cases in the model. Some are constants (1 or 0)

	N	O	P	Q	R	S	T	U	V	W	X	Y	Z	AA	AB
8	x*tan(α)	Model Case #	Ya	Yb	Yc	Yd	Fraction Case #	f_{calc}	f1	f2	f3	f4	f5	f6	f7
9	4.8659	1	-20.9675	-8.6341	8.6341	20.9675	2	0.2322	0.0000	0.2322	0.0890	1.0000	3.6854	2.5757	0.0000
10	4.8659	1	-20.9675	-8.6341	8.6341	20.9675	4	1.0000	0.0000	1.4039	1.8872	1.0000	1.8872	1.4039	0.0000
11	4.8659	1	-20.9675	-8.6341	8.6341	20.9675	6	0.2322	0.0000	2.5757	3.6854	1.0000	0.0890	0.2322	0.0000
12	9.0092	1	-25.1107	-4.4908	4.4908	25.1107	6	0.3277	0.0000	1.8350	2.2205	1.0000	0.2780	0.3277	0.0000
13	9.0092	1	-25.1107	-4.4908	4.4908	25.1107	4	1.0000	0.0000	1.0814	1.2492	1.0000	1.2492	1.0814	0.0000
14	4.1432	1	-20.2448	-8.3568	8.3568	20.2448	2	0.2035	0.0000	0.2035	0.0173	1.0000	4.2410	2.7981	0.0000
15	9.0092	1	-25.1107	-4.4908	4.4908	25.1107	6	0.2847	0.0000	1.8780	2.2760	1.0000	0.2226	0.2847	0.0000
16	4.1432	1	-20.2448	-8.3568	8.3568	20.2448	4	1.0000	0.0000	1.5008	2.1292	1.0000	2.1292	1.5008	0.0000
17	11.0808	1	-27.1923	-2.4192	2.4192	27.1923	6	0.3538	0.0000	1.8328	1.8988	1.0000	0.3195	0.3538	0.0000
18	9.0092	1	-25.1107	-4.4908	4.4908	25.1107	6	0.8052	0.0000	1.4259	1.6932	1.0000	0.8052	0.7369	0.0000
19	9.0092	1	-25.1107	-4.4908	4.4908	25.1107	7	0.0000	0.0000	3.4068	4.2462	1.0000	-1.7477	-1.2441	0.0000
20	4.1432	1	-20.2448	-8.3568	8.3568	20.2448	1	0.0000	0.0000	-1.3903	-2.5773	1.0000	6.8356	4.3919	0.0000
21	4.1432	1	-20.2448	-8.3568	8.3568	20.2448	4	1.0000	0.0000	1.2042	1.6464	1.0000	2.6119	1.7973	0.0000
22	9.0092	1	-25.1107	-4.4908	4.4908	25.1107	6	0.8052	0.0000	1.4259	1.6932	1.0000	0.8052	0.7369	0.0000
23	9.0092	1	-25.1107	-4.4908	4.4908	25.1107	4	1.0000	0.0000	1.0814	1.2492	1.0000	1.2492	1.0814	0.0000
24	9.0092	1	-25.1107	-4.4908	4.4908	25.1107	4	1.0000	0.0000	1.0814	1.2492	1.0000	1.2492	1.0814	0.0000
25	4.1432	1	-20.2448	-8.3568	8.3568	20.2448	1	0.0000	0.0000	-4.5039	-7.6458	1.0000	11.9041	7.5054	0.0000
26	4.1432	1	-20.2448	-8.3568	8.3568	20.2448	1	0.0000	0.0000	-4.5039	-7.6458	1.0000	11.9041	7.5054	0.0000
27	4.1432	1	-20.2448	-8.3568	8.3568	20.2448	1	0.0000	0.0000	-0.5009	-1.1292	1.0000	6.3875	3.5023	0.0000
28	4.1432	1	-20.2448	-8.3568	8.3568	20.2448	1	0.0000	0.0000	-0.5009	-1.1292	1.0000	6.3875	3.5023	0.0000
29	4.8659	1	-20.9675	-8.6341	8.6341	20.9675	7	0.0000	0.0000	3.2119	4.6616	1.0000	-0.8872	-0.4039	0.0000
30	4.8659	1	-20.9675	-8.6341	8.6341	20.9675	7	0.0000	0.0000	6.8274	10.2104	1.0000	-6.4360	-4.0196	0.0000
31	4.8659	1	-20.9675	-8.6341	8.6341	20.9675	4	1.0000	0.0000	1.4039	1.8872	1.0000	1.8872	1.4039	0.0000
32	4.8659	1	-20.9675	-8.6341	8.6341	20.9675	4	1.0000	0.0000	1.4039	1.8872	1.0000	1.8872	1.4039	0.0000
33	4.8659	1	-20.9675	-8.6341	8.6341	20.9675	7	0.0000	0.0000	3.2119	4.6616	1.0000	-0.8872	-0.4039	0.0000
34	4.8659	1	-20.9675	-8.6341	8.6341	20.9675	7	0.0000	0.0000	6.8274	10.2104	1.0000	-6.4360	-4.0196	0.0000

Figure D-2. Spreadsheet "Flux Split Waste Package Model," Worksheet "f calculations;" Calculation of Model Flow Fractions for Mean Minus One Standard Deviation Rivulet Spread Angle

Columns V though AB compute the fraction of dripping flux f_{calc} that is predicted to flow into a breach, assuming the drip location is within each of seven regions listed above under Column T. Although f_{calc} is computed for all seven regions, it is valid in only one of the regions. The

correct valid region is determined in Column T (Fraction Case #), and the appropriate value from Columns V–AB is entered in Column U.

Column U: f_{calc} is the fraction of dripping flux onto the drip shield that is predicted by the drip shield flux splitting submodel, Equations 6.5.1.1.2-2 through 6.5.1.1.2-6 or 6.5.1.1.2-19 through 6.5.1.1.2-23, for Cases 1 and 2, respectively. f_{calc} is intended to be compared with f_{expt} (Column M). The value of f_{calc} is selected from Columns V through AB, depending on the appropriate Fraction Case # (Column T).

```
U9 =IF(T9=1,V9,IF(T9=2,W9,IF(T9=3,X9,IF(T9=4,Y9,
    IF(T9=5,Z9,IF(T9=6,AA9,IF(T9=7,AB9)))))))
```

Column V: Value of f_{calc} in region 1 ($y \le y_A$), where $f_{calc} = 0$.

```
V9=0
```

Column W: Value of f_{calc} in region 2 ($y_A < y \le -\ell$):

$$f_{calc} = \frac{y + \ell + (x + 2\ell)\tan\alpha}{2(x + 2\ell)\tan\alpha}$$

```
W9 =(H9+J9+(I9+2*J9)*TAN(RADIANS($Q$7)))/
    (2*(I9+2*J9)*TAN(RADIANS($Q$7)))
```

Column X: Value of f_{calc} in region 3 ($-\ell < y < y_B$):

$$f_{calc} = \frac{y + \ell + x\tan\alpha}{2x\tan\alpha}$$

```
X9=(H9+J9+I9*TAN(RADIANS($Q$7)))/(2*I9*TAN(RADIANS($Q$7)))
```

Column Y: Value of f_{calc} in region 4 ($y_B \le y \le y_C$):

$$f_{calc} = \frac{2\ell}{2x\tan\alpha}$$

```
Y9=IF(O9=1,1,(2*$J9/(2*$I9*TAN(RADIANS($Q$7)))))
```

Column Z: Value of f_{calc} in region 5 ($y_C < y < \ell$):

$$f_{calc} = \frac{-y + \ell + x\tan\alpha}{2x\tan\alpha}$$

```
Z9=(-H9+J9+I9*TAN(RADIANS($Q$7)))/(2*I9*TAN(RADIANS($Q$7)))
```

Column AA: Value of f_{calc} in region 6 ($\ell \le y < y_D$):

$$f_{calc} = \frac{-y+\ell+(x+2\ell)\tan\alpha}{2(x+2\ell)\tan\alpha}$$

AA9=(-H9+J9+I9*TAN(RADIANS($Q$7)))/
(2*I9*TAN(RADIANS(AA9$Q$7)))

Column AB: Value of f_{calc} in region 7 ($y \ge y_D$) where $f_{calc} = 0$:

AB9=0

	AC	AD	AE	AF	AG	AH	AI	AJ	AK	AL	AM	AN	AO	AP	AQ
1															
2															
3															
4															
5															
6															
7			For α =	13.7326	degrees										
8	x*tan(α)	Model Case #	Ya	Yb	Yc	Yd	Fraction Case #	f_{calc}	f1	f2	f3	f4	f5	f6	f7
9	12.3410	1	-32.4391	-1.1590	1.1590	32.4391	2	0.3944	0.0000	0.3944	0.3379	1.0000	1.7560	1.3184	0.0000
10	12.3410	1	-32.4391	-1.1590	1.1590	32.4391	4	1.0000	0.0000	0.8564	1.0470	1.0000	1.0470	0.8564	0.0000
11	12.3410	1	-32.4391	-1.1590	1.1590	32.4391	6	0.3944	0.0000	1.3184	1.7560	1.0000	0.3379	0.3944	0.0000
12	22.8491	2	-42.9473	-9.3491	9.3491	42.9473	6	0.4321	0.0000	1.0284	1.1784	0.5908	0.4125	0.4321	0.0000
13	22.8491	2	-42.9473	-9.3491	9.3491	42.9473	4	0.5908	0.0000	0.7292	0.7954	0.5908	0.7954	0.7292	0.0000
14	10.5082	1	-30.6063	-2.9918	2.9918	30.6063	2	0.3831	0.0000	0.3831	0.3097	1.0000	1.9750	1.4061	0.0000
15	22.8491	2	-42.9473	-9.3491	9.3491	42.9473	6	0.4151	0.0000	1.0433	1.2002	0.5908	0.3906	0.4151	0.0000
16	10.5082	1	-30.6063	-2.9918	2.9918	30.6063	4	1.0000	0.0000	0.8948	1.1424	1.0000	1.1424	0.8948	0.0000
17	26.1032	2	-48.2014	-14.6032	14.6032	48.2014	6	0.4424	0.0000	0.9467	1.0515	0.4804	0.4288	0.4424	0.0000
18	22.8491	2	-42.9473	-9.3491	9.3491	42.9473	4	0.5908	0.0000	0.8651	0.9705	0.5908	0.8204	0.5934	0.0000
19	22.8491	2	-42.9473	-9.3491	9.3491	42.9473	7	0.0000	0.0000	1.6461	1.8771	0.5908	-0.3862	-0.1877	0.0000
20	10.5082	1	-30.6063	-2.9918	2.9918	30.6063	1	0.9000	0.0000	-0.2453	-0.7133	1.0000	2.9981	2.0345	0.0000
21	10.5082	1	-30.6063	-2.9918	2.9918	30.6063	3	0.9520	0.0000	0.7777	0.8520	1.0000	1.3327	1.0115	0.0000
22	22.8491	2	-42.9473	-9.3491	9.3491	42.9473	4	0.5908	0.0000	0.8651	0.9705	0.5908	0.8204	0.5934	0.0000
23	22.8491	2	-42.9473	-9.3491	9.3491	42.9473	4	0.5908	0.0000	0.7292	0.7954	0.5908	0.7954	0.7292	0.0000
24	22.8491	2	-42.9473	-9.3491	9.3491	42.9473	4	0.5908	0.0000	0.7292	0.7954	0.5908	0.7954	0.7292	0.0000
25	10.5082	1	-30.6063	-2.9918	2.9918	30.6063	1	0.0000	0.0000	-1.4730	-2.7118	1.0000	4.9965	3.2621	0.0000
26	10.5082	1	-30.6063	-2.9918	2.9918	30.6063	1	0.0000	0.0000	-1.4730	-2.7118	1.0000	4.9965	3.2621	0.0000
27	10.5082	1	-30.6063	-2.9918	2.9918	30.6063	2	0.1054	0.0000	0.1054	-0.1424	1.0000	2.4271	1.6838	0.0000
28	10.5082	1	-30.6063	-2.9918	2.9918	30.6063	2	0.1054	0.0000	0.1054	-0.1424	1.0000	2.4271	1.6838	0.0000
29	12.3410	1	-32.4391	-1.1590	1.1590	32.4391	6	0.1436	0.0000	1.5692	2.1409	1.0000	-0.0470	0.1436	0.0000
30	12.3410	1	-32.4391	-1.1590	1.1590	32.4391	7	0.0000	0.0000	2.9948	4.3287	1.0000	-2.2348	-1.2820	0.0000
31	12.3410	1	-32.4391	-1.1590	1.1590	32.4391	4	1.0000	0.0000	0.8564	1.0470	1.0000	1.0470	0.8564	0.0000
32	12.3410	1	-32.4391	-1.1590	1.1590	32.4391	4	1.0000	0.0000	0.8564	1.0470	1.0000	1.0470	0.8564	0.0000
33	12.3410	1	-32.4391	-1.1590	1.1590	32.4391	6	0.1436	0.0000	1.5692	2.1409	1.0000	-0.0470	0.1436	0.0000
34	12.3410	1	-32.4391	-1.1590	1.1590	32.4391	7	0.0000	0.0000	2.9948	4.3287	1.0000	-2.2348	-1.2820	0.0000

Figure D-3. Spreadsheet "Flux Split Waste Package Model," Worksheet "f calculations;" Calculation of Model Flow Fractions for Mean Rivulet Spread Angle

Columns AC though AQ repeat the calculations done in Columns N though AB using the mean rivulet spread angle of $\alpha = 13.7326°$ (Cell $AF$7). For Row 9, the spreadsheet equations are as follows:

AC9=$I9*TAN(RADIANS($AF$7))

```
AD9=IF($J9>AC9,1,2)

AE9=-$J9-($I9+2*$J9)*TAN(RADIANS($AF$7))

AF9=IF(AD9=1,(-$J9+$I9*TAN(RADIANS($AF$7))),($J9-$I9*TAN(RADIANS($AF$7))))

AG9=IF(AD9=1,($J9-$I9*TAN(RADIANS($AF$7))),(-$J9+$I9*TAN(RADIANS($AF$7))))

AH9=$J9+($I9+2*$J9)*TAN(RADIANS($AF$7))

AI9=IF($H9<=AE9,1,IF($H9<=-$J9,2,IF($H9<AF9,3,
      IF($H9<=AG9,4,IF($H9<$J9,5,IF($H9<AH9,6,IF($H9>=AH9,7)))))))

AJ9=IF(AI9=1,AK9,IF(AI9=2,AL9,IF(AI9=3,AM9,IF(AI9=4,AN9,IF(AI9=5,AO9,IF(AI9=6,A
      P9,IF(AI9=7,AQ9)))))))

AK9=0

AL9=(H9+J9+(I9+2*J9)*TAN(RADIANS($AF$7)))/
      (2*(I9+2*J9)*TAN(RADIANS($AF$7)))

AM9=(H9+J9+I9*TAN(RADIANS($AF$7)))/(2*I9*TAN(RADIANS($AF$7)))

AN9=IF(AD9=1,1,(2*$J9/(2*$I9*TAN(RADIANS($AF$7)))))

AO9=(-H9+J9+I9*TAN(RADIANS($AF$7)))/(2*I9*TAN(RADIANS($AF$7)))

AP9=(-H9+J9+(I9+2*J9)*TAN(RADIANS($AF$7)))/
      (2*(I9+2*J9)*TAN(RADIANS($AF$7)))

AQ9=0
```

Columns AR though BF (next page) repeat the calculations done in Columns N though AB using a rivulet spread angle of $\alpha = 21.9614°$ (Cell $AU$7), which is one standard deviation greater than the mean rivulet spread angle. For Row 9, the spreadsheet equations are as follows:

```
AR9=$I9*TAN(RADIANS($AU$7))

AS9=IF($J9>AR9,1,2)

AT9=-$J9-($I9+2*$J9)*TAN(RADIANS($AU$7))

AU9=IF(AS9=1,(-$J9+$I9*TAN(RADIANS($AU$7))),($J9-$I9*TAN(RADIANS($AU$7))))

AV9=IF(AS9=1,(-$J9+$I9*TAN(AV9RADIANS($AU$7))),($J9-
      $I9*TAN(RADIANS($AU$7))))

AW9=$J9+($I9+2*$J9)*TAN(RADIANS($AU$7))

AX9=IF($H9<=AT9,1,IF($H9<=-$J9,2,IF($H9<AU9,3,IF($H9<=AV9,4,
      IF($H9<$J9,5,IF($H9<AW9,6,IF($H9>=AW9,7)))))))

AY9=IF(AX9=1,AZ9,IF(AX9=2,BA9,IF(AX9=3,BB9,IF(AX9=4,BC9,IF(AX9=5,BD9,IF
      (AX9=6,BE9,IF(AX9=7,BF9)))))))

AZ9=0
```

BA9=(H9+J9+(I9+2*J9)*TAN(RADIANS($AU$7)))/
(2*(I9+2*J9)*TAN(RADIANS($AU$7)))

BB9=(H9+J9+I9*TAN(RADIANS($AU$7)))/(2*I9*TAN(RADIANS($AU$7)))

BC9=IF(AS9=1,1,(2*$J9/(2*$I9*TAN(RADIANS($AU$7)))))

BD9=(-H9+J9+I9*TAN(RADIANS($AU$7)))/(2*I9*TAN(RADIANS($AU$7)))

BE9=(-H9+J9+(I9+2*J9)*TAN(RADIANS($AU$7)))/
(2*(I9+2*J9)*TAN(RADIANS($AU$7)))

BF9=0

	AR	AS	AT	AU	AV	AW	AX	AY	AZ	BA	BB	BC	BD	BE	BF
1															
2															
3															
4															
5															
6															
7	For α = 21.9614 degrees														
8	x*tan(α)	Model Case #	Ya	Yb	Yc	Yd	Fraction Case #	f_{avg}	f1	f2	f3	f4	f5	f6	f7
9	20.3638	2	-44.7513	-6.8638	6.8638	44.7513	2	0.4360	0.0000	0.4360	0.4018	0.6629	1.2612	0.9960	0.0000
10	20.3638	2	-44.7513	-6.8638	6.8638	44.7513	4	0.6629	0.0000	0.7160	0.8315	0.6629	0.8315	0.7160	0.0000
11	20.3638	2	-44.7513	-6.8638	6.8638	44.7513	6	0.4360	0.0000	0.9960	1.2612	0.6629	0.4018	0.4360	0.0000
12	37.7032	2	-62.0907	-24.2032	24.2032	62.0907	4	0.3581	0.0000	0.8190	0.9111	0.3581	0.4470	0.4588	0.0000
13	37.7032	2	-62.0907	-24.2032	24.2032	62.0907	4	0.3581	0.0000	0.6389	0.6790	0.3581	0.6790	0.6389	0.0000
14	17.3394	2	-41.7270	-3.8394	3.8394	41.7270	2	0.4291	0.0000	0.4291	0.3847	0.7786	1.3939	1.0491	0.0000
15	37.7032	2	-62.0907	-24.2032	24.2032	62.0907	4	0.3581	0.0000	0.8293	0.9244	0.3581	0.4337	0.4485	0.0000
16	17.3394	2	-41.7270	-3.8394	3.8394	41.7270	4	0.7786	0.0000	0.7391	0.8893	0.7786	0.8893	0.7391	0.0000
17	46.3729	2	-70.7605	-32.8729	32.8729	70.7605	4	0.2911	0.0000	0.7707	0.8342	0.2911	0.4569	0.4651	0.0000
18	37.7032	2	-62.0907	-24.2032	24.2032	62.0907	4	0.3581	0.0000	0.7212	0.7851	0.3581	0.5729	0.5566	0.0000
19	37.7032	2	-62.0907	-24.2032	24.2032	62.0907	6	0.0833	0.0000	1.1946	1.3951	0.3581	-0.0371	0.0833	0.0000
20	17.3394	2	-41.7270	-3.8394	3.8394	41.7270	2	0.8483	0.0000	0.0483	-0.2353	0.7786	2.0139	1.4300	0.0000
21	17.3394	2	-41.7270	-3.8394	3.8394	41.7270	3	0.7739	0.0000	0.6683	0.7739	0.7786	1.0046	0.8100	0.0000
22	37.7032	2	-62.0907	-24.2032	24.2032	62.0907	4	0.3581	0.0000	0.7212	0.7851	0.3581	0.5729	0.5566	0.0000
23	37.7032	2	-62.0907	-24.2032	24.2032	62.0907	4	0.3581	0.0000	0.6389	0.6790	0.3581	0.6790	0.6389	0.0000
24	37.7032	2	-62.0907	-24.2032	24.2032	62.0907	4	0.3581	0.0000	0.6389	0.6790	0.3581	0.6790	0.6389	0.0000
25	17.3394	2	-41.7270	-3.8394	3.8394	41.7270	1	0.0000	0.0000	-0.6957	-1.4464	0.7786	3.2250	2.1739	0.0000
26	17.3394	2	-41.7270	-3.8394	3.8394	41.7270	1	0.0000	0.0000	-0.6957	-1.4464	0.7786	3.2250	2.1739	0.0000
27	17.3394	2	-41.7270	-3.8394	3.8394	41.7270	2	0.2609	0.0000	0.2609	0.1107	0.7786	1.6679	1.2174	0.0000
28	17.3394	2	-41.7270	-3.8394	3.8394	41.7270	2	0.2609	0.0000	0.2609	0.1107	0.7786	1.6679	1.2174	0.0000
29	20.3638	2	-44.7513	-6.8638	6.8638	44.7513	6	0.2840	0.0000	1.1480	1.4944	0.6629	0.1695	0.2840	0.0000
30	20.3638	2	-44.7513	-6.8638	6.8638	44.7513	7	0.0000	0.0000	2.0119	2.8203	0.6629	-1.1574	-0.5800	0.0000
31	20.3638	2	-44.7513	-6.8638	6.8638	44.7513	4	0.6629	0.0000	0.7160	0.8315	0.6629	0.8315	0.7160	0.0000
32	20.3638	2	-44.7513	-6.8638	6.8638	44.7513	4	0.6629	0.0000	0.7160	0.8315	0.6629	0.8315	0.7160	0.0000
33	20.3638	2	-44.7513	-6.8638	6.8638	44.7513	6	0.2840	0.0000	1.1480	1.4944	0.6629	0.1695	0.2840	0.0000
34	20.3638	2	-44.7513	-6.8638	6.8638	44.7513	7	0.0000	0.0000	2.0119	2.8203	0.6629	-1.1574	-0.5800	0.0000

Figure D-4. Spreadsheet "Flux Split Waste Package Model," Worksheet "f calculations;" Calculation of Model Flow Fractions for Mean Plus One Standard Deviation Rivulet Spread Angle

SPREADSHEET "FLUX SPLIT WASTE PACKAGE MODEL"–WORKSHEET "SPREAD ANGLES"

	A	B	C	D	E	F	G	H	I	J	K
1		Rivulet spread measurements for WP model: Drips at 16.5° and 33°, measurements at 33° and transition Smooth Drip Shield)									
2											
3					Source Data						
4					Calculated results						
5											
6					Rivulet Spread Measurements						
7					At 33°			At Transition			
8		Q(film)	(DTN: MO0207EBSATBVP.023)	Drop Location	x (distance from drop, cm)	Right (cm)	Left (cm)	x (distance from drop, cm)	Right (cm)	Left (cm)	
9		6/31/2002	P4, 8 cm right of center, 16.5°	16.5°	43	6.5	3.5	107.0	13.5		
10		6/31/2002	P2, center, 16.5°	16.5°	43	7.5	4.5	107.0	19.5	22.0	
11		6/31/2002	P2, 15 cm right of center, 16.5°	16.5°	43	11.5	9.0	107.0	18.0	15.0	
12		6/31/2002	P5, 4 cm left of center, 16.5°	16.5°	43	8.5	8.5	107.0			
13											
14		Bounding	(DTN: MO0207EBSATBVP.025)								
15		6/18/2002	54 cm left of DS center, 16.5°	16.5°	43	31.0	46.0	107.0	35.0	46.0	
16		6/19/2002	54 cm left of DS center, 16.5°	16.5°	43	8.5	10.0	107.0	18.0	27.0	
17		6/16/2002	27 cm left of DS center, 16.5°	16.5°	43	6.0	8.0	107.0	17.0	16.0	
18		6/20/2002	27 cm left of DS center, 16.5°	16.5°	43	18.0	24.0	107.0	22.0	19.0	
19		6/20/2002	27 cm right of DS center, 16.5°	16.5°	43	13.0	27.0	107.0	14.0	23.0	
20		6/20/2002	27 cm right of DS center, 16.5°	16.5°	43	12.0	17.0	107.0	16.0	13.0	
21		6/20/2002	27 cm left of DS center, 33°	33°				64.0	11.0	17.0	
22		6/20/2002	27 cm right of DS center, 33°	33°				64.0	16.0	17.0	
23		6/20/2002	54 cm left of DS center, 33°	33°				64.0	17.0	17.0	
24		6/24/2002	27 cm left of DS center, 33°	33°				64.0	8.0	8.5	
25		6/24/2002	27 cm right of DS center, 33°	33°				64.0	8.5	10.0	
26											

DTN: MO0207EBSATBWP.023 [DIRS 163402]; DTN: MO0207EBSATBWP.025 [DIRS 163403].

Figure D-5. Spreadsheet "Flux Split Waste Package Model," Worksheet "Spread angles;" Calculation of Rivulet Spread Angle

In this worksheet, the mean and range of the rivulet spread angle α is determined from spread measurements. The drip locations are off-crown, at the 16.5° and 33° positions on the drip shield mockup. These angles are the angular distances from the crown about the center of curvature of the drip shield; thus, the crown is at 0°, and the transition from the curved top surface to the vertical side of the drip shield is located about 60° from vertical. The actual distance (arc length) from the crown to the 16.5° line is 43 cm; from the crown to the 33° line the distance is 86 cm; and from the crown to the transition line the distance is 150 cm. The distance x from the drip location to the spread measurement location (the 33° line or the transition line) is shown in Columns E and H, respectively.

Columns B and C identify the pertinent tests as described in the designated DTNs. In each test, the spread of rivulets to the right and to the left of the drip location was measured. The spread distance measured at the 33° line is listed in Columns F and G. The spread distance measured at the transition line is listed in Columns I and J. For drips at the 33° location, no rivulet spread was measured, although splattering upslope may have resulted in some rivulets appearing at the drip location.

The sketch below from the scientific notebook for the experiments (Howard 2002 [DIRS 161516], p. 14) indicates the dimensions and locations of breaches on the drip shield mockup used in the tests. This sketch is also shown in Figure 4.1-1, Section 4.1.1.

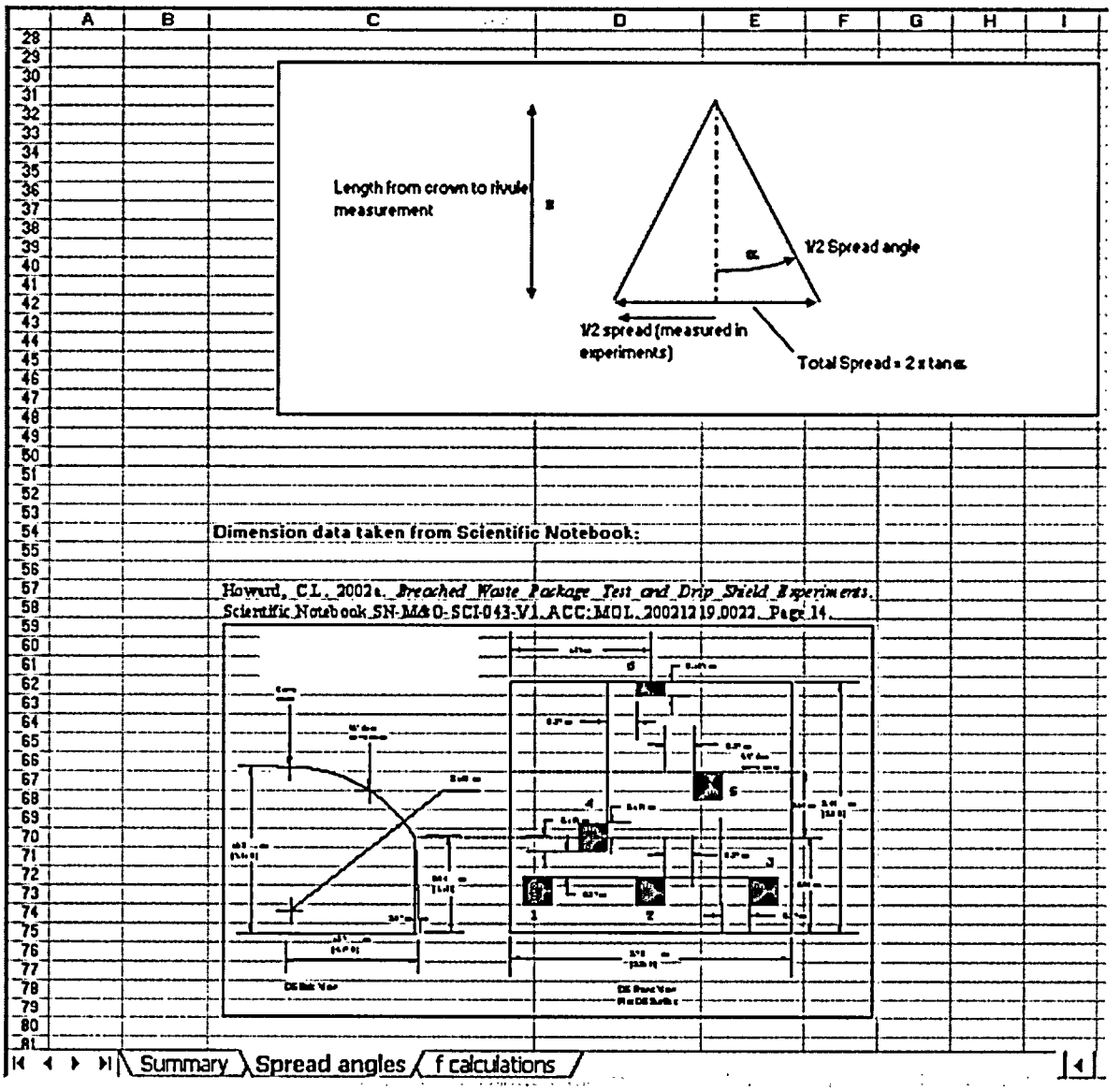

Source: Howard 2002 [DIRS 161516], p. 14.

Figure D-6. Spreadsheet "Flux Split Waste Package Model," Worksheet "Spread angles;" Dimensions and Locations of Breaches in Drip Shield Mockup Used in Breached Drip Shield Experiments

	L	M	N	O	P	Q	R	S	T	U
1										
2										
3										
4										
5										
6										
7										
8		Measurement (cm)	x (distance from drop to measure ment,	Spread angle (degrees)						
9		5.5	43	7.2890						
10		7.5	43	9.8939						
11		11.5	43	14.9729						
12		8.5	43	11.1818						
13		3.5	43	4.6534						
14		4.5	43	5.9743						
15		9.0	43	11.8215						
16		8.5	43	11.1818		Drip at 16.5°.			All Measurements	
17		31.0	43	35.7890		Spread Angle			Spread Angle	
18		8.5	43	11.1818		No. of mea	20		No. of meas.	47
19		6.0	43	7.9435		Mean	17.0218		Mean	13.7326
20		18.0	43	22.7144		Std. Dev.	11.17224		Std. Dev.	8.228837
21		13.0	43	16.8214					Mean - 1σ	5.5037
22		12.0	43	15.5928					Mean + 1σ	21.9614
23		46.0	43	46.9306						
24		10.0	43	13.0919						
25		8.0	43	10.5392						
26		24.0	43	29.1676						
27		27.0	43	32.1250						
28		17.0	43	21.5713						
29										

Figure D-7. Spreadsheet "Flux Split Waste Package Model," Worksheet "Spread angles;" Calculation of Rivulet Spread Angles and Statistical Measures

In Column M, Rows 9–28 (Figure D-7), all of the spread measurements (right and left) at the 33° line are listed for the 16.5° drip location from the Q(film) and Bounding tests. In Rows 31-47 (Figure D-7), the spread from 16.5° drips measured at the transition are listed for the Q(film) and Bounding tests. In Rows 50–59, the spread from 33° drips measured at the transition are listed for the Bounding tests. In Column N, the distance, x, from the drip location to the measurement location is listed. In Column O, the spread angle, α, is computed from the rivulet spread, w_r (cm):

$$\alpha = \tan^{-1}\left(\frac{w_r}{x}\right),$$

The spreadsheet equation for Row 9 is:

O9=DEGREES(ATAN(M9/N9))

In Column R (Figures D-7 and D-8), the mean spread angle and standard deviation are shown for comparison for three groups of data–drip location at 16.5° measured at 33°, drip location at 16.5° measured at the transition line, and drip location at 33° measured at the transition line. The statistics for all measurements are computed in Column U. The mean rivulet spread angle (Cell U19) and the bounds on the range for spread angle as defined by the mean minus one standard deviation (Cell U21) and the mean minus one standard deviation (Cell U22) are used in Worksheet "f calculations" as the basis of the waste package flux splitting submodel to compute the predicted fraction of dripping flux that flows into a breach, f_{calc}.

	L	M	N	O	P	Q	R	S	T	U
29										
30										
31		13.5	107	7.1909						
32		19.5	107	10.3284						
33		18.0	107	9.5491						
34		22.0	107	11.6185						
35		15.0	107	7.9801						
36		35.0	107	18.1131						
37		19.0	107	10.0691		Drip at 16.5°.				
38		17.0	107	9.0276		Spread Angle				
39		22.0	107	11.6185		No. of mea	17			
40		14.0	107	7.4543		Mean	11.1561			
41		16.0	107	8.5046		Std. Dev.	4.110299			
42		46.0	107	23.2632						
43		27.0	107	14.1622						
44		16.0	107	8.5046						
45		19.0	107	10.0691						
46		23.0	107	12.1313						
47		19.0	107	10.0691						
48										
49										
50		11.0	64	9.7524						
51		15.0	64	13.1906						
52		17.0	64	14.8757		Drip at 33°.				
53		9.0	64	8.0047		Spread Angle				
54		8.5	64	7.5653		No. of mea	10			
55		17.0	64	14.8757		Mean	11.5340			
56		17.0	64	14.8757		Std. Dev.	3.255512			
57		17.0	64	14.8757						
58		9.5	64	8.4432						
59		10.0	64	8.8807						

Figure D-8. Spreadsheet "Flux Split Waste Package Model," Worksheet "Spread angles;" Calculation of Rivulet Spread Angles

SPREADSHEET "FLUX SPLIT WASTE PACKAGE MODEL"–WORKSHEET "SUMMARY"

	A	B	C	D	E	F	G	H	I	J	K
1											
2											
3											
4		Waste Package Model: Comparison of Measured and Modeled Fraction of Drip Seepage Flowing Into a Breach									
5											
6		This spreadsheet compares results from the "Atlas Breached Waste Package and Drip Shield Experiments: Breached Drip Shield Tests" (documented in BSC 2003: TDR-EBS-MD-000025-00 REV 00) with the model developed in the "EBS Radionuclide Transport Abstraction" (BSC 2003: ANL-WIS-PA-000001 REV 01). Test data are taken directly from the TDMS for this comparison.									
7											
8		Methodology:									
9		1. Spreading angles are calculated from the test data in the sheet titled *Spread angles*									
10		2. Given spread angle and test geometry, seepage fractions are calculated for both the test data and the model in the worksheet *f calculations* :									
11			a. Geometric data for each measurement (x,y,l) and the spread angle are used to determine which of 7 cases the measurement corresponds to								
12			b. For each test result the appropriate case model is applied to calculate the seepage flow fraction f								
13		3. The seepage fractions calculated from both the test and model are listed and compared in the two tables listed below in this *Summary* worksheet									
14		Notes:									
15		Source data DTNs are noted where source data is used									
16		Model equations are provided on the calculational sheets									
17		Data in tables below are linked directly to the calculational worksheets									
18											
19											

Source: BSC 2003 [DIRS 163406].

Figure D-9. Spreadsheet "Flux Split Waste Package Model," Worksheet "Summary;" Summary of Waste Package Flux Splitting Submodel

This worksheet, beginning with Figure D-9, summarizes the calculations in Worksheets "Spread angles" and "f calculations."

In the first table (Figure D-10), "Measured Breach Flow Fractions and Calculated Breach Flow Fractions," Columns B, C, D, and E are identical to Columns D, E, H, and I described earlier for Worksheet "f calculations." Column F (f_{expt}) is identical to Column M in Worksheet "f calculations." Columns G–I summarize the calculated fraction of the dripping flux that the flux splitting submodel predicts should flow into the breach, for the minimum, mean, and maximum spread angles. The minimum spread angle is specified to be one standard deviation less than the mean of the measured spread angles. The maximum spread angle is specified to be one standard deviation greater than the mean of the measured spread angles. Column G is identical to Column U of Worksheet "f calculations." Column H is identical to Column AJ of Worksheet "f calculations." Column I is identical to Column AY of Worksheet "f calculations."

Rows 50–54, Columns F–I, show the results of Microsoft Excel functions "AVERAGE," "STDEVA," "MEDIAN," "MIN," and "MAX," respectively, as applied to Rows 25-49.

	A	B	C	D	E	F	G	H	I
19									
20		Measured Breach Flow Fractions and Calculated Breach Flow Fractions							
21									
22				y, Drip Location Relative to Breach Center (cm)	z, Vertical Distance from Drip to Top of Breach (cm)		f_{calc}		
23							∝ (deg)	∝ (deg)	∝ (deg)
24		Drip Location (Test Description)	Breach No.			f_{expt}	5.50	13.73	21.96
25		P5, 17.5 cm left of center, 33°	4	-17.5	50.5	0.0000	0.2322	0.3944	0.4360
26		P4, center, 33°	4	0	50.5	0.0005	1.0000	1.0000	0.6629
27		P4, 17.5 cm right of center, 33°	4	17.5	50.5	0.0642	0.2322	0.3944	0.4360
28		P4, 17.5 cm right of center, 16.5°	4	17.5	93.5	0.0119	0.3277	0.4321	0.3501
29		P4, centerline, 16.5°	4	0	93.5	0.6029	1.0000	0.5900	0.3501
30		P5, 17.5 cm left of center, 16.5°	5	-17.5	43.0	0.0142	0.2035	0.3931	0.4291
31		P6, 35.5 cm left of center, 16.5°	4	10.5	93.5	0.0015	0.2847	0.4151	0.3501
32		P5, centerline, 16.5°	5	0	43.0	0.7260	1.0000	1.0000	0.7786
33		P6, 36.5 cm left of center, between crown and 16.5°	4	17.5	115.0	0.0513	0.3530	0.4424	0.2911
34		P4, 0 cm right of center, 16.5°	4	0	93.5	0.5360	0.0052	0.5900	0.3501
35		P2, 15 cm right of center, 16.5°	5	-39	43.0	0.0022	0.0000	0.0000	0.0403
36		P5, 4 cm left of center, 16.5°	5	-4	43.0	1.0657	1.0000	0.9520	0.7739
37		P4, 0 cm right of center, 16.5°	4	0	93.5	0.7013	0.0052	0.5900	0.3501
38		54 cm left of DS center, 16.5°	4	0	93.5	0.4003	1.0000	0.5900	0.3501
39		54 cm left of DS center, 16.5°	4	0	93.5	0.7901	1.0000	0.5900	0.3501
40		27 cm left of DS center, 16.5°	5	-81	43.0	0.0040	0.0000	0.0000	0.0000
41		27 cm left of DS center, 16.5°	5	-81	43.0	0.0031	0.0000	0.0000	0.0000
42		27 cm right of DS center, 16.5°	5	-27	43.0	0.0125	0.0000	0.1054	0.2609
43		27 cm right of DS center, 16.5°	5	-27	43.0	0.0002	0.0000	0.1054	0.2609
44		27 cm left of DS center, 33°	4	27	50.5	0.0026	0.0000	0.1436	0.2040
45		27 cm right of DS center, 33°	4	81	50.5	0.0020	0.0000	0.0000	0.0000
46		54 cm left of DS center, 33°	4	0	50.5	0.5602	1.0000	1.0000	0.6629
47		54 cm left of DS center, 33°	4	0	50.5	0.0217	1.0000	1.0000	0.6629
48		27 cm left of DS center, 33°	4	27	50.5	0.0123	0.0000	0.1436	0.2040
49		27 cm right of DS center, 33°	4	81	50.5	0.0000	0.0000	0.0000	0.0000
50		Mean				0.2947	0.4490	0.4346	0.3511
51		Std. Dev.				0.3693	0.4426	0.3539	0.2316
52		Median				0.0142	0.2847	0.4151	0.3501
53		Minimum				0.0000	0.0000	0.0000	0.0000
54		Maximum				1.0657	1.0000	1.0000	0.7786
55									

Summary / Spread angles / f calculations

Figure D-10. Spreadsheet "Flux Split Waste Package Model," Worksheet "Summary;" Summary of Waste Package Flux Splitting Submodel

In the second table (Figure D-11), "Comparison of Measured and Calculated Breach Flows," Column K is again the drip location. Column L is the fraction of dripping flux (f_{expt}) that flowed into a breach as measured experimentally; this is identical to Column F of the preceding table, or Column M in Worksheet "f calculations." The next three columns (M-O) show the difference between the predicted breach flow fraction, f_{calc}, and the measured fraction, f_{expt}, for the minimum, mean, and maximum rivulet spread angle. Columns P-R show the ratio f_{calc} / f_{expt} for the minimum, mean, and maximum rivulet spread angle.

Rows 50-54, Columns L-R, show the results of Microsoft Excel functions "AVERAGE," "STDEVA," "MEDIAN," "MIN," and "MAX," respectively, as applied to Rows 25-49.

	J	K	L	M	N	O	P	Q	R
19									
20		Comparison of Measured and Calculated Breach Flow							
21									
22				f calc - f meas			f calc / f meas		
23				α (deg)	α (deg)	α (deg)	α (deg)	α (deg)	α (deg)
24		Drip Location (Test Description)	f meas	5.50	13.73	21.96	5.50	13.73	21.96
25		P5, 17.5 cm left of center, 33°	0.0000	0.2322	0.3944	0.4360			
26		P4, center, 33°	0.0005	0.1995	0.1995	-0.1376	1.2492	1.2492	0.0291
27		P4, 17.5 cm right of center, 33°	0.0602	0.1640	0.3262	0.3670	3.4054	5.7640	6.3950
28		P4, 17.5 cm right of center, 16.5°	0.0119	0.3159	0.4202	0.3462	27.6039	36.3914	30.1570
29		P4, centerline, 16.5°	0.6029	0.3971	-0.0121	-0.2449	1.6586	0.9799	0.5939
30		P5, 17.5 cm left of center, 16.5°	0.0142	0.1493	0.3609	0.4150	14.3420	27.0031	30.2499
31		P6, 35.5 cm left of center, 16.5°	0.0015	0.2031	0.4136	0.3545	104.1115	268.4501	231.5671
32		P5, centerline, 16.5°	0.7260	0.2740	0.2740	0.0526	1.3774	1.3774	1.0724
33		P6, 36.5 cm left of center, between crown and 16.5°	0.0513	0.3025	0.3911	0.2390	6.0900	6.6251	5.6761
34		P4, 0 cm right of center, 16.5°	0.5360	0.2605	0.0541	-0.1787	1.5001	1.1007	0.6671
35		P2, 15 cm right of center, 16.5°	0.0022	-0.0022	-0.0022	0.0461	0.0000	0.0000	21.9501
36		P5, 4 cm left of center, 16.5°	1.0657	-0.0657	-0.1136	-0.2917	0.9384	0.9934	0.7263
37		P4, 0 cm right of center, 16.5°	0.7913	0.0240	-0.1905	-0.4232	1.0307	0.7562	0.4503
38		54 cm left of DS center, 16.5°	0.4803	0.5197	0.1105	-0.1223	2.0818	1.2300	0.7454
39		54 cm left of DS center, 16.5°	0.7961	0.2099	-0.1993	-0.4321	1.2656	0.7476	0.4532
40		27 cm left of DS center, 16.5°	0.0040	-0.0040	-0.0040	-0.0040	0.0000	0.0000	0.0000
41		27 cm left of DS center, 16.5°	0.0031	-0.0031	-0.0031	-0.0031	0.0000	0.0000	0.0000
42		27 cm right of DS center, 16.5°	0.0125	-0.0125	0.0929	0.2404	0.0000	0.4461	20.9026
43		27 cm right of DS center, 16.5°	0.0002	-0.0002	0.0972	0.2527	0.0000	12.0936	31.9094
44		27 cm left of DS center, 33°	0.0026	-0.0026	0.1410	0.2014	0.0000	54.9116	100.6060
45		27 cm right of DS center, 33°	0.0020	-0.0020	-0.0020	-0.0020	0.0000	0.0000	0.0000
46		54 cm left of DS center, 33°	0.5602	0.4310	0.4310	0.0940	1.7600	1.7600	1.1660
47		54 cm left of DS center, 33°	0.0217	0.1703	0.1703	-0.1590	1.2170	1.2170	0.0060
48		27 cm left of DS center, 33°	0.0123	-0.0123	0.1313	0.2717	0.0000	11.7079	23.1564
49		27 cm right of DS center, 33°	0.0000	0.0000	0.0000	0.0000			
50		Mean	0.2947	0.1551	0.1399	0.0564	10.0007	19.3710	22.5256
51		Std Dev.	0.3593	0.1670	0.1939	0.2596	30.2601	56.0050	51.4010
52		Median	0.0142	0.1703	0.1105	0.0461	1.2492	1.2492	1.0724
53		Minimum	0.0000	-0.0657	-0.1992	-0.4321	0.0000	0.0000	0.0000
54		Maximum	1.0657	0.5197	0.4310	0.4360	104.1115	268.4501	231.5671
55									

Summary / Spread angles / f calculations

Figure D-11. Spreadsheet "Flux Split Waste Package Model," Worksheet "Summary;" Summary of Waste Package Flux Splitting Submodel Comparing Measured and Calculated Breach Flows

Lastly, a plot in Worksheet "Summary" (Figure D-12) compares the calculated f_{calc} with the measured f_{expt} for the minimum, mean, and maximum spread angles; the f_{expt} and f_{calc} values that are plotted in Figure D-12 are shown in Figure D-10. The diagonal line in the plot represents $f_{calc} = f_{expt}$. Most values of f_{calc} lie above the line $f_{calc} = f_{expt}$, indicating that the waste package flux splitting submodel tends to overestimate the flow into breaches.

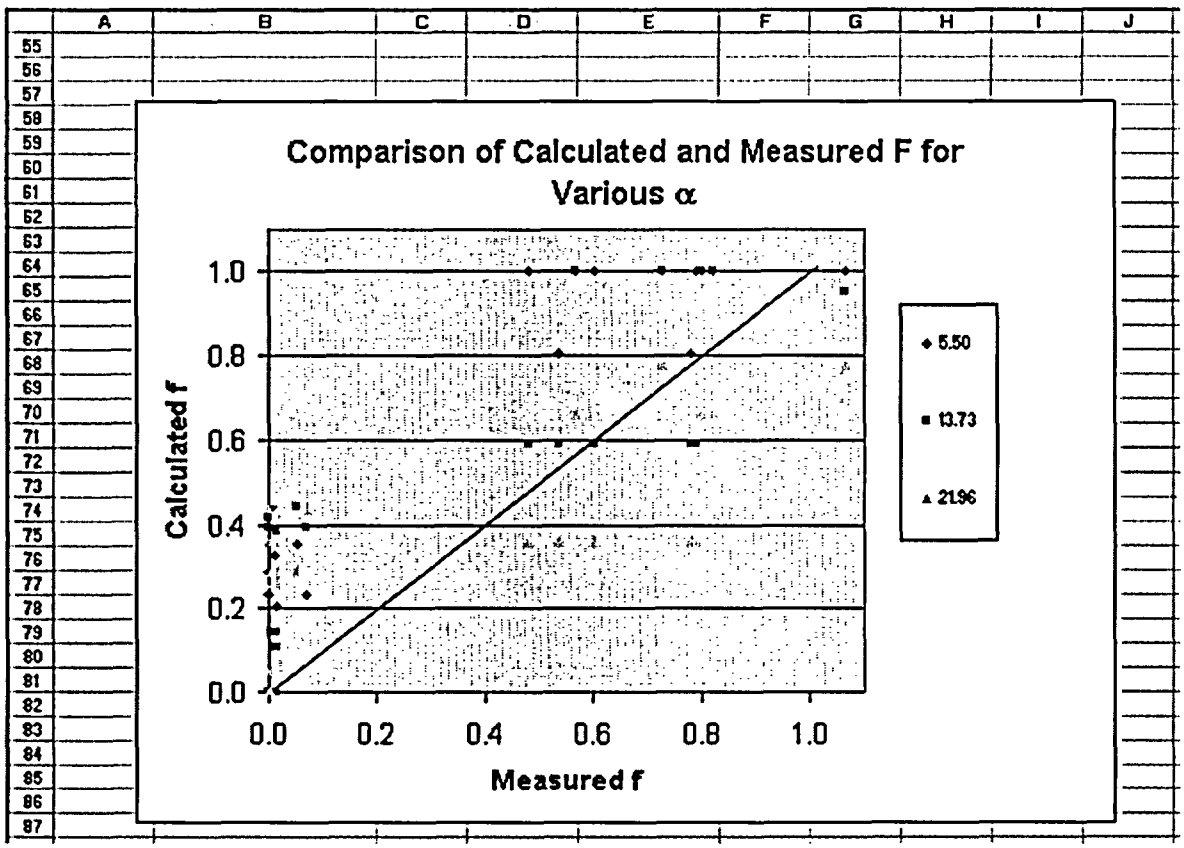

Figure D-12. Spreadsheet "Flux Waste Package Shield Model," Worksheet "Summary;" Comparison of Calculated and Measured Breach Flow Fractions for Waste Package Flux Splitting Submodel for Minimum (5.50°), Mean (13.73°), and Maximum (21.96°) Rivulet Spread Angles

APPENDIX E
MICROSOFT EXCEL SPREADSHEET "FLUX SPLITTING VALIDATION"

MICROSOFT EXCEL SPREADSHEET "FLUX SPLITTING VALIDATION"

SPREADSHEET "FLUX SPLITTING VALIDATION"–WORKSHEET "SPLASH RAD VS NUMBER"

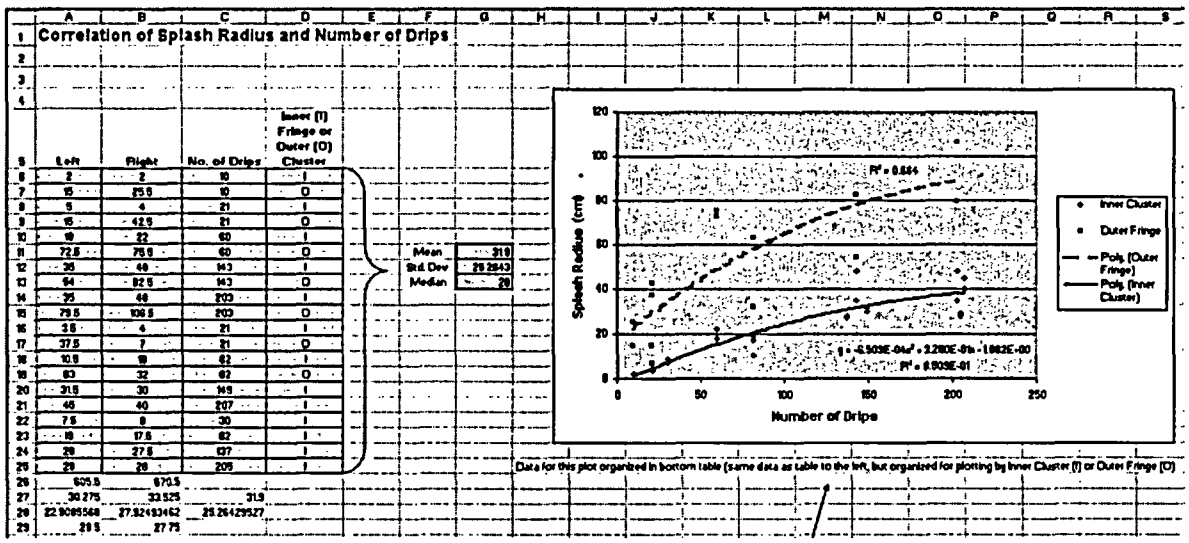

Figure E-1. Spreadsheet "Flux Splitting Validation"–Worksheet "Splash Rad vs Number;" Effect of Number of Drips on Splash Radius

In this worksheet (Figures E-1 to E-3), the effect of the number of drips on the splash radius is analyzed using data from dripping on the crown in the rough drip shield tests. This analysis is used for validation of the drip shield flux splitting submodel. The splash distance or radius (cm) to the left and to the right of the drip location are listed in Columns A and B, respectively. The number of drips in each test is given in Column C. The type of measurement–inner cluster (I) or outer fringe (O)–is indicated in Column D. These data and the DTN from which they were obtained (MO0207EBSATBWP.021 [DIRS 163399]) are also presented in Table 7.1-1. In Row 26, the sum of the splash radii is shown. Rows 27, 28, and 29 give the mean, standard deviation, and median for each column. The mean, standard deviation, and median for all 40 splash radius measurements are listed in Column G, Rows 11, 12, and 13, respectively.

The plot to the right in Figure E-1, which is reproduced as Figure 7.1-1, shows the dependence of splash radius on the number of drips. As indicated beneath the figure, the data are the same as in the table, but organized by type of measurement further down in this worksheet. The Trendline tool in Microsoft Excel is used to fit a quadratic curve to the inner cluster and outer fringe data. The correlation coefficient is shown for each curve, and the correlation equation is shown for the inner cluster curve. A second degree polynomial was chosen for the Trendline in order to display the expected behavior–the splash radius should increase with the number of drips, but eventually reach a maximum. A functional form such as $y = y_{\max}\left(1 - e^{-ax}\right)$ may be more appropriate, but because this is nonlinear in the fitting parameter a, a simple linear least squares fit using Trendline is not possible. Since the object is simply to demonstrate a correlation, a more accurate fit to the data is not necessary.

In Figure E-2, the experimental data from the top of the worksheet are reorganized by type of measurement and, in Figure E-3, all left and right measurements are consolidated for plotting in the plot at the top of the worksheet (shown in Figure E-1).

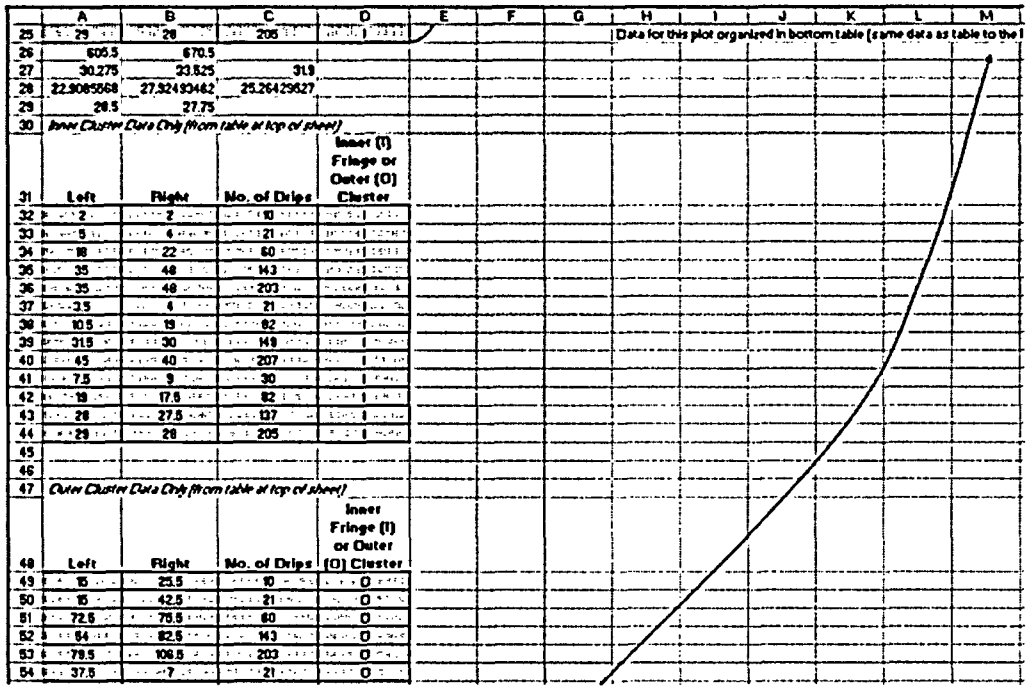

	A	B	C	D
25	29	28	205	
26	606.5	670.5		
27	30.275	33.525	31.9	
28	22.9085568	27.32493462	25.26429627	
29	28.5	27.75		
30	*Inner Cluster Data Only (from table at top of sheet)*			
31	Left	Right	No. of Drips	Inner (I) Fringe or Outer (O) Cluster
32	2	2	10	I
33	5	6	21	I
34	18	22	60	I
35	35	48	143	I
36	35	48	203	I
37	3.5	4	21	I
38	10.5	19	62	I
39	31.5	30	149	I
40	45	40	207	I
41	7.5	9	30	I
42	19	17.5	82	I
43	28	27.5	137	I
44	29	28	205	I
45				
46				
47	*Outer Cluster Data Only (from table at top of sheet)*			
48	Left	Right	No. of Drips	Inner Fringe (I) or Outer (O) Cluster
49	15	23.5	10	O
50	15	42.5	21	O
51	72.5	76.5	60	O
52	64	82.5	143	O
53	79.5	109.5	203	O
54	37.5	7	21	O

Figure E-2. Spreadsheet "Flux Splitting Validation"–Worksheet "Splash Rad vs Number;" Effect of Number of Drips on Splash Radius; Data Organized by Type of Measurement

	A	B	C	D
56				
57				
58				
59				
60				
61				
62	*Recordered List for Plotting (data from table at top of sheet)*			
63				
64	Inner Cluster		Outer Fringe	
65	# of Drips	Radius cm	# of Drips	Radius cm
66	10	2	10	15
67	21	5	21	15
68	60	19	60	72.5
69	143	35	143	84
70	203	35	203	79.5
71	21	3.5	21	37.5
72	82	10.5	82	63
73	149	31.5	10	25.5
74	207	45	21	42.5
75	30	7.5	60	75.5
76	82	19	143	82.5
77	137	28	203	106.5
78	205	29	21	7
79	10	2	82	32
80	21	4		
81	60	22		
82	143	48		
83	203	48		
84	21	4		
85	82	19		
86	149	30		
87	207	40		
88	30	9		
89	82	17.5		
90	137	27.5		
91	205	28		
92				

Figure E-3. Spreadsheet "Flux Splitting Validation"–Worksheet "Splash Rad vs Number;" Effect of Number of Drips on Splash Radius; All Left and Right Measurements Are Consolidated

SPREADSHEET "FLUX SPLITTING VALIDATION"–WORKSHEET "SPLASH RADIUS"

For validation of the drip shield and waste package flux splitting submodels, splash radius data are analyzed for measurements on the rough drip shield surface, with dripping on the crown and at off-crown locations. Data for crown drip locations are used for the drip shield submodel validation, and off-crown drip locations are used for the waste package submodel validation. The statistics (mean, standard deviation, median, mean plus one standard deviation, and mean minus one standard deviation) are shown in Column I, Rows 19–23 for crown drip locations, and in Rows 37-41 for off-crown locations. The data actually used in the model validation are the minimum and maximum values for more than 20 drips, Cells H11 and I9, respectively, for crown locations, and Cells H31 and I36, respectively, for off-crown locations.

	A	B	C	D	E	F	G	H	I	J	K	L	M	N
1	**Splash Radius Determination, Rough Drip Shield Surface, Dripping on Crown**													
2														
3	**Source Data**													
4	**Calculated results**													
5							# Drips	Left (cm)	Right (cm)					
6	Splash Radius Test #1 - Rough DS Surface - Crown						10	2.0	2.0					
7							21	5.0	4.0					
8							60	18.0	22.0					
9							143	35.0	48.0					
10							203	35.0	48.0					
11	Splash Radius Test #2 - Rough DS Surface - Crown						21	3.5	4.0					
12							82	10.5	19.0					
13							149	31.5	30.0					
14							207	45.0	40.0					
15	Splash Radius Test #3 - Rough DS Surface - Crown						30	7.5	9.0					
16							82	19.0	17.5					
17							137	28.0	27.5					
18							205	29.0	28.0					
19								Mean	21.8					
20								Std. Dev.	14.8228					
21								Median	20.5					
22								Mean-SD	7.023354					
23								Mean+SD	36.66895					
24														
25														
26	**Splash Radius Determination, Rough Drip Shield Surface, Dripping off Crown**													
27														
28	**Source Data**													
29	**Calculated results**													
30							# Drips	Left (cm)	Right (cm)					
31	Splash Radius Test #4 - Rough DS Surface - 33 degrees						31	3	3.5					
32							82	5.5	6					
33							158	6.5	6.5		DTN: MO0207EBSATBWP.021			
34	Splash Radius Test #5 - Rough DS Surface - 16.5 degrees						22	9	10					
35							82	13	14.5					
36							156	14	15					
37								Mean	8.875					
38								Std. Dev.	4.349112					
39								Median	7.75					
40								Mean-SD	4.525888					
41								Mean+SD	13.22411					
42														

Splash Rad vs Number | Splash Radius | Rough DS | Rough off crown WP model

DTN: MO0207EBSATBWP.021 [DIRS 163399].

Figure E-4. Spreadsheet "Flux Splitting Validation"–Worksheet "Splash Radius;" Splash Radius Determination

SPREADSHEET "FLUX SPLITTING VALIDATION"–WORKSHEET "ROUGH DS"

This worksheet provides calculations for validation of the drip shield flux splitting submodel based on data from rough drip shield surface tests. An overall view of the worksheet is shown in Figure E-5 to show the layout of the worksheet, and individual tables are then presented more legibly and described in detail on following pages.

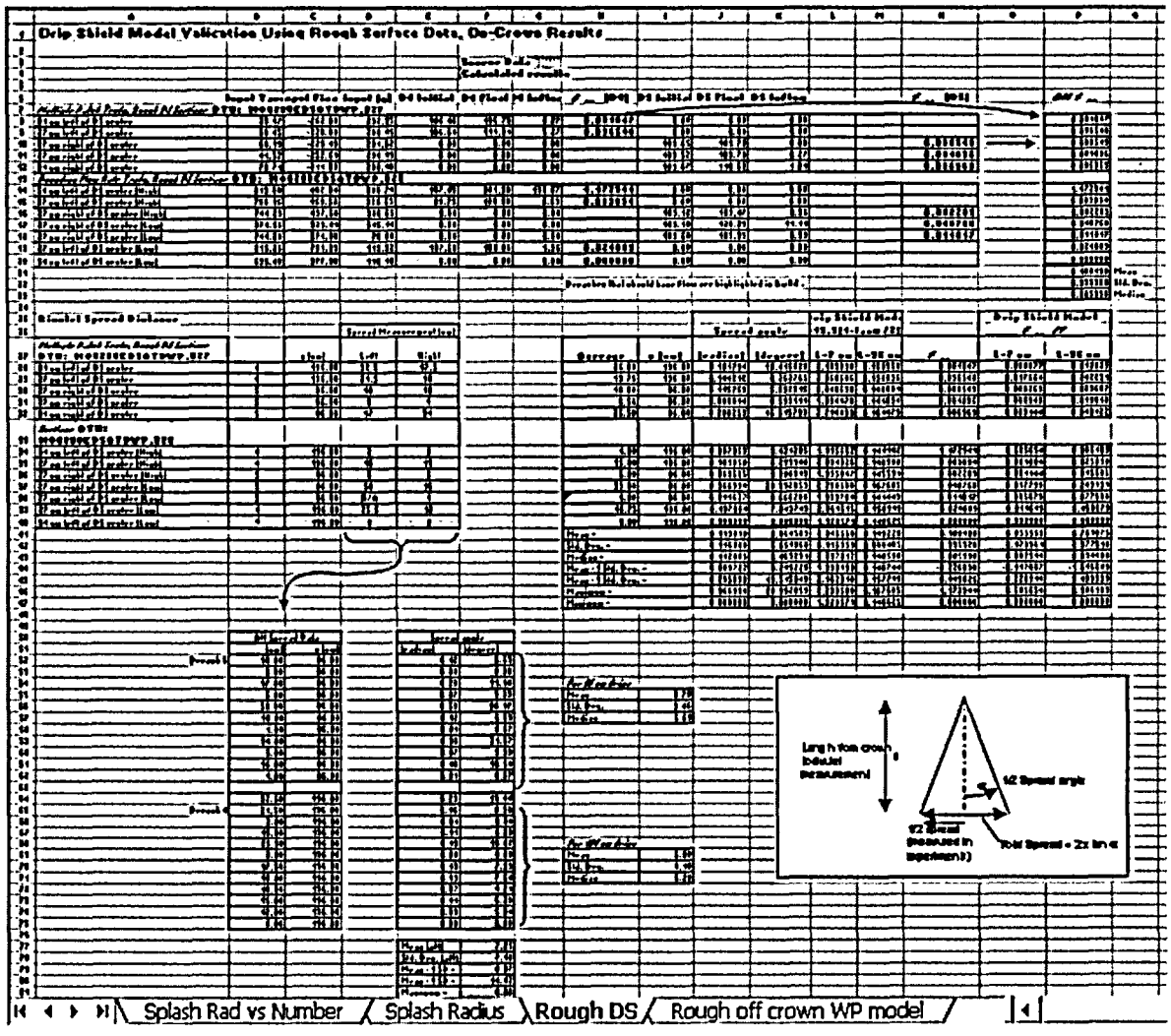

DTN: MO0208EBSATBWP.027 [DIRS 163404]; DTN: MO0208EBSATBWP.028 [DIRS 163405].

Figure E-5. Spreadsheet "Flux Splitting Validation"–Worksheet "Rough DS;" Worksheet Overview

	A	B	C	D	E	F	G	H
1	**Drip Shield Model Valication Using Rough Surface Data, On-Crown Results**							
2								
3						Source Data		
4						Calculated results		
5								
6		Input Tare	Input Final	Input (g)	B4 Initial	B4 Final	B4 Inflow	f_{exp} (B4)
7	*Multiple Patch Tests, Rough DS Surface* DTN: MO0208EBSATBWP.027							
8	81 cm left of DS center	29.47	-262.68	292.35	106.46	106.73	0.27	**0.001847**
9	27 cm left of DS center	68.45	-220.00	288.45	106.64	111.91	5.27	**0.036540**
10	27 cm right of DS center	68.19	-223.43	291.62	0.00	0.00	0.00	
11	27 cm right of DS center	41.52	-252.61	294.13	0.00	0.00	0.00	
12	81 cm right of DS center	78.71	-211.39	290.10	0.00	0.00	0.00	
13	*Bounding Flow Rate Tests, Rough DS Surface* DTN: MO0208EBSATBWP.028							
14	54 cm left of DS center (High)	813.08	482.34	330.74	107.43	301.30	193.87	**1.172341**
15	27 cm left of DS center (High)	788.15	459.50	328.65	99.75	100.38	0.63	**0.003834**
16	27 cm right of DS center (High)	744.25	437.60	306.65	0.00	0.00	0.00	
17	27 cm right of DS center (Low)	874.55	329.41	545.14	0.00	0.00	0.00	
18	27 cm right of DS center (Low)	744.80	674.00	70.80	0.00	0.00	0.00	
19	27 cm left of DS center (Low)	815.25	701.93	113.32	107.50	108.86	1.36	**0.024003**
20	54 cm left of DS center (Low)	695.48	577.38	118.10	0.00	0.00	0.00	**0.000000**
21								
22								Breaches that sho
23								

DTN: MO0208EBSATBWP.027 [DIRS 163404]; DTN: MO0208EBSATBWP.028 [DIRS 163405].

Figure E-6. Spreadsheet "Flux Splitting Validation"–Worksheet "Rough DS;" Calculation of Experimental Breach Flow Fractions

	H	I	J	K	L	M	N	O	P	Q
1										
2										
3										
4										
5										
6	f_{exp} (B4)	B5 Initial	B5 Final	B5 Inflow			f_{exp} (B5)		Δf_{exp}	
7										
8	**0.001847**	0.00	0.00	0.00					0.001847	
9	**0.036540**	0.00	0.00	0.00					0.036540	
10		109.65	109.73	0.08			**0.000549**	→	0.000549	
11		109.52	109.79	0.27			**0.001836**		0.001836	
12		109.67	110.68	1.01			**0.006963**		0.006963	
13										
14	**1.172341**	0.00	0.00	0.00					1.172341	
15	**0.003834**	0.00	0.00	0.00					0.003834	
16		109.12	109.47	0.35			**0.002283**		0.002283	
17		109.18	120.29	11.11			**0.040760**		0.040760	
18		109.60	109.99	0.39			**0.011017**		0.011017	
19	**0.024003**	0.00	0.00	0.00					0.024003	
20	**0.000000**	0.00	0.00	0.00					0.000000	
21									0.108498	Mean
22	Breaches that should have flow are highlighted in **bold**.								0.335328	Std. Dev.
23									0.005398	Median

Figure E-7. Spreadsheet "Flux Splitting Validation"–Worksheet "Rough DS;" Summary of Experimental Breach Flow Fractions

Tests are identified in Figure E-6 in Column A. Columns B and C are raw data–the initial and final water mass in the input water container. Column D is the difference between Columns B and C (e.g., D8=B8-C8), giving the mass of water dripped onto the drip shield. Columns E and F are the initial and final masses of water in the Breach B4 collection vessel. The difference, in Column G (e.g., G8=F8-E8), is the mass of water that flowed into B4. In Column H (Figure E-7), the fraction of the dripping flux that flowed into B4, f_{expt} (B4), is calculated for tests in which the flow into B4 was greater than zero (e.g., H8=2*G8/D8). Because the dripping was onto the crown, it is assumed that only half of the total input (i.e., D8/2) flowed down the side of the drip shield where B4 was located.

Columns I and J are the initial and final masses of water in the Breach B5 collection vessel. The difference, in Column G (e.g., K8=J8-I8), is the mass of water that flowed into B5. In Column N, the fraction of the dripping flux that flowed into B5, f_{expt} (B5), is calculated for tests in which the flow into B5 was greater than zero (e.g., N10=2*K10/D10). Because the drip location was the crown, it is assumed that only half of the total input (i.e., D10/2) flowed down the side of the drip shield where B5 was located.

The input water mass and flows into Breaches B4 and B5 are summarized in Table 7.1-3.

In Column P, all values of f_{expt} are consolidated. The mean, standard deviation, and median for the 12 data values are given in Rows 21, 22, and 23, respectively. The values of f_{expt} are listed in Table 7.1-4.

24										
25	Rivulet Spread Distance									
26				Spread Measurement (cm)					Spread angle	
27	*Multiple Patch Tests, Rough DS Surface* DTN: MO0208EBSATBWP.027		s (cm)	Left	Right		Average	s (cm)	(radian)	(degree)
28	61 cm left of DS center	4	136.00	32.5	17.5		25.00	136.00	0.181734	10.416028
29	27 cm left of DS center	4	136.00	21.5	18		19.75	136.00	0.144212	8.262765
30	27 cm right of DS center	5	86.00	10	10		10.00	86.00	0.115759	6.632515
31	27 cm right of DS center	5	86.00	0	1		0.50	86.00	0.005814	0.333111
32	61 cm right of DS center	5	86.00	17	34		25.50	86.00	0.294253	16.515703
33	*Bounding Flow Rate Tests, Rough DS Surface* DTN: MO0208EBSATBWP.028									
34	54 cm left of DS center (High)	4	136.00	2	0		1.00	136.00	0.007353	0.421295
35	27 cm left of DS center (High)	4	136.00	15	15		15.00	136.00	0.109850	6.293948
36	27 cm right of DS center (High)	5	86.00	6	6		6.00	86.00	0.069858	3.930913
37	27 cm right of DS center (Low)	5	86.00	50	16		33.00	86.00	0.366394	20.992853
38	27 cm right of DS center (Low)	5	86.00	N/A	1		1.00	86.00	0.011627	0.666200
39	27 cm left of DS center (Low)	4	136.00	25.5	12		18.75	136.00	0.137004	7.849749
40	54 cm left of DS center (Low)	4	136.00	0	0		0.00	136.00	0.000000	0.000000
41							Mean =		0.119810	6.864589
42							Std Dev =		0.116088	6.651060
43							Median =		0.112805	6.463231
44							Mean - 1 Std Dev =		0.003722	0.213229
45							Mean + 1 Std Dev =		0.235898	13.515949
46							Maximum =		0.366394	20.992853
47							Minimum =		0.000000	0.000000
48										
49										
50		All Spread Data			Spread angle					

DTN: MO0208EBSATBWP.027 [DIRS 163404]; DTN: MO0208EBSATBWP.028 [DIRS 163405].

Figure E-8. Spreadsheet "Flux Splitting Validation"–Worksheet "Rough DS;" Rivulet Spread Distances

Rivulet spread distances for each test are listed in Figure E-8, Columns D and E, Rows 28-40, for drips originating on the crown of the rough drip shield surface. The spread data are reorganized in Column B, starting in Row 52 (see Figure E-9). All spread data measured 86 cm from the drip

location are listed first, followed by all data measured 136 cm from the drip location. The corresponding x-distance is listed in Column C, starting in Row 52. In Column E, the spread distances, w_r, are converted to spread angles using the formula:

$$\alpha = \tan^{-1}\left(\frac{w_r}{x}\right).$$

In Cell E52, for example, the Microsoft Excel equation is: E52=ATAN(B52/C52). The result is the spread angle in radians, which is converted to degrees in Column F (e.g., F52=DEGREES(E52)). The mean spread angle for 86-cm drips is given in Cell I55 (I55=AVERAGE(F52:F63)) and for 136-cm drips in Cell I69 (I69=AVERAGE(F65:F75)). Statistics are computed for all individual spread angle data in Column F, Rows 77-82:

F77=AVERAGE(F52:F75)

F78=STDEVA(F52:F75)

F79=F77-F78

F80=F77+F78

F81=MIN(F52:F75)

F82=MAX(F52:F75)

As shown in F79 and F80, the range for the spread angle is zero (rounding down) to 14.4°.

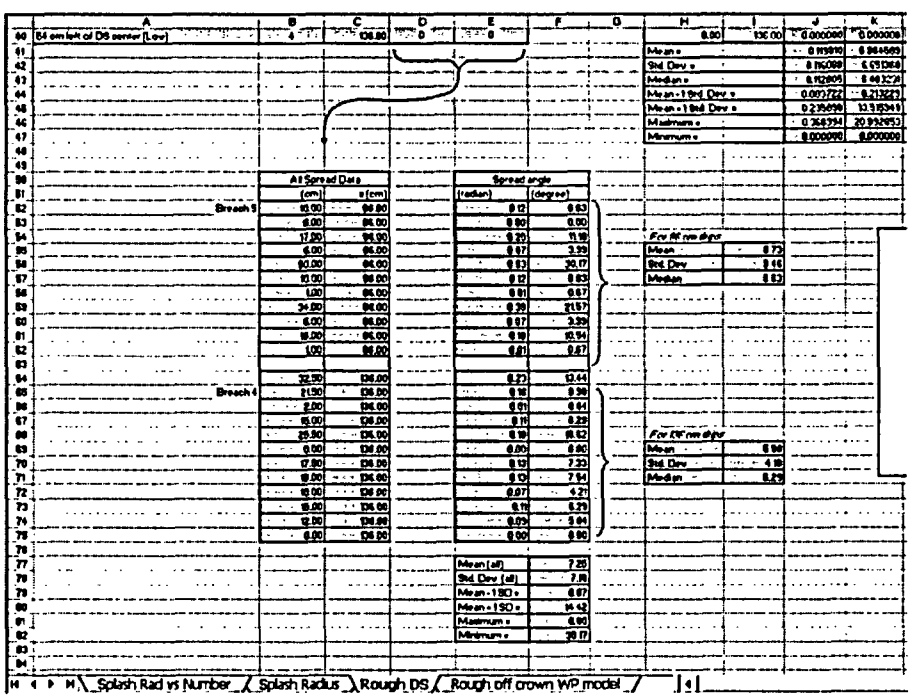

Figure E-9. Spreadsheet "Flux Splitting Validation"–Worksheet "Rough DS;" Rivulet Spread Data Reorganized

	G	H	I	J	K	L	M	N	O	P	Q
24											
25						Drip Shield Mode			Drip Shield Model		
26				Spread angle		F=13.5(1+tanα/2)/			f_{crit} AF		
27		Average	x (cm)	(radian)	(degree)	L=7 cm	L=96 cm	f_{crit}	L=7 cm	L=96 cm	
28		25.00	136.00	0.181794	10.416028	2.105830	0.153550	0.001847	0.000877	0.012029	
29		19.75	136.00	0.144212	8.262765	2.068606	0.150836	0.036540	0.017664	0.242251	
30		10.00	86.00	0.115759	6.632515	2.040698	0.148801	0.000549	0.000269	0.003687	
31		0.50	86.00	0.005814	0.333111	1.934178	0.141034	0.001836	0.000949	0.013018	
32		25.50	86.00	0.288253	16.515703	2.214493	0.161473	0.006963	0.003144	0.043122	
33											
34		1.00	136.00	0.007353	0.421285	1.935662	0.141142	1.172341	0.605654	8.306109	
35		15.00	136.00	0.109850	6.293948	2.034926	0.148380	0.003834	0.001884	0.025838	
36		6.00	86.00	0.069655	3.990913	1.995847	0.145531	0.002283	0.001144	0.015686	
37		33.00	86.00	0.366394	20.992853	2.298588	0.167605	0.040760	0.017733	0.243191	
38		1.00	86.00	0.011627	0.666200	1.939784	0.141443	0.011017	0.005679	0.077890	
39		18.75	136.00	0.137004	7.849749	2.061515	0.150319	0.024003	0.011643	0.159679	
40		0.00	136.00	0.000000	0.000000	1.928571	0.140625	0.000000	0.000000	0.000000	
41		Mean =		0.119810	6.864589	2.046558	0.149228	0.108498	0.055553	0.761875	
42		Std. Dev. =		0.116088	6.651360	0.116359	0.008485	0.335328	0.173361	2.377518	
43		Median =		0.112805	6.463231	2.037812	0.148590	0.005398	0.002514	0.034480	
44		Mean - 1 Std. Dev. =		0.003722	0.213229	1.930199	0.140744	-0.226830	-0.117807	-1.615643	
45		Mean + 1 Std. Dev. =		0.235898	13.515949	2.162918	0.157713	0.443825	0.228914	3.139393	
46		Maximum =		0.366394	20.992853	2.298588	0.167605	1.172341	0.605654	8.306109	
47		Minimum =		0.000000	0.000000	1.928571	0.140625	0.000000	0.000000	0.000000	
48											
49											
50											
51											
52											
53											
54		*For 86 cm drips*									
55		Mean	8.73								
56		Std. Dev.	9.46								
57		Median	6.63								
58											
59											
60											
61											
62											
63											
64											
65											
66											
67											
68		*For 136 cm drips*									
69		Mean	5.88								
70		Std. Dev.	4.18								
71		Median	6.29								
72											
73											
74											

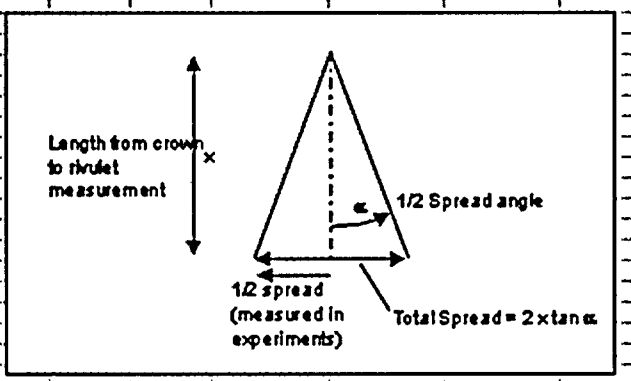

Splash Rad vs Number | Splash Radius | Rough DS | Rough off crown WP model

Figure E-10. Spreadsheet "Flux Splitting Validation"–Worksheet "Rough DS;" Calculation of Rivulet Spread Angles

In Column H, Rows 28-40 (see Figure E-10), the average rivulet spread is computed for each experiment (e.g., H28=(D28+E28)/2). Column I is the distance from the crown to the point where the rivulet spread was measured (identical to Column C). The spread angle is computed in Column J, Rows 28-40, (e.g., J28=ATAN(H28/I28)). In Column K, Rows 28-40, the

average spread angle in radians is converted to degrees (e.g., K28=DEGREES(J28)). In Worksheet "Splash Rad vs Number," the minimum splash radius for tests using 20 or more drips was 3.5 cm, for a total splash distance of 7 cm. This is used as the effective drip shield length in Column L, where f_{calc} is obtained using the formula

$$f_{calc} = \frac{\ell}{L}\left(1+\frac{\tan\alpha}{2}\right)$$
$$= \frac{13.5}{7}\left(1+\frac{\tan\alpha}{2}\right)$$

L28=13.5*(1+TAN(J28)/2)/7

The maximum splash radius tests using 20 or more drips was 48 cm in Worksheet "Splash Rad vs. Number," giving a total splash distance of 96 cm. This is used as the effective drip shield length in Column M,

$$f_{calc} = \frac{\ell}{L}\left(1+\frac{\tan\alpha}{2}\right)$$
$$= \frac{13.5}{96}\left(1+\frac{\tan\alpha}{2}\right)$$

M28=13.5*(1+TAN(J28)/2)/96

The values of f_{calc} in Columns L and M are the same as F/f_{VD} following Equation 7.2.1-1. As shown in the statistics (Rows 46–47), F/f_{VD} ranges from 0.147 to 2.078.

In Column N, Rows 28–40, the values of f_{expt} are transferred from Column P, Rows 9–20. In Column O, the ratio f_{expt}/f_{calc} is computed (e.g., O28=N28/L28) for the minimum effective drip shield length of 7 cm. In Column P, the ratio f_{expt}/f_{calc} is computed (e.g., P28=N28/M28) for the maximum effective drip shield length of 96 cm. This ratio is identical to the uncertainty factor f_{DV} in Equation 7.2.1-2. As shown in the statistics (Rows 46–47), F/f_{VD} for the experimental data ranges from 0.0 to 8.306

SPREADSHEET "FLUX SPLITTING VALIDATION"–WORKSHEET "ROUGH OFF CROWN WP MODEL"

This worksheet provides calculations for validation of the waste package flux splitting submodel based on data from the rough drip shield surface tests. An overall view of the worksheet is shown in Figure E-11, and individual tables are then described in detail.

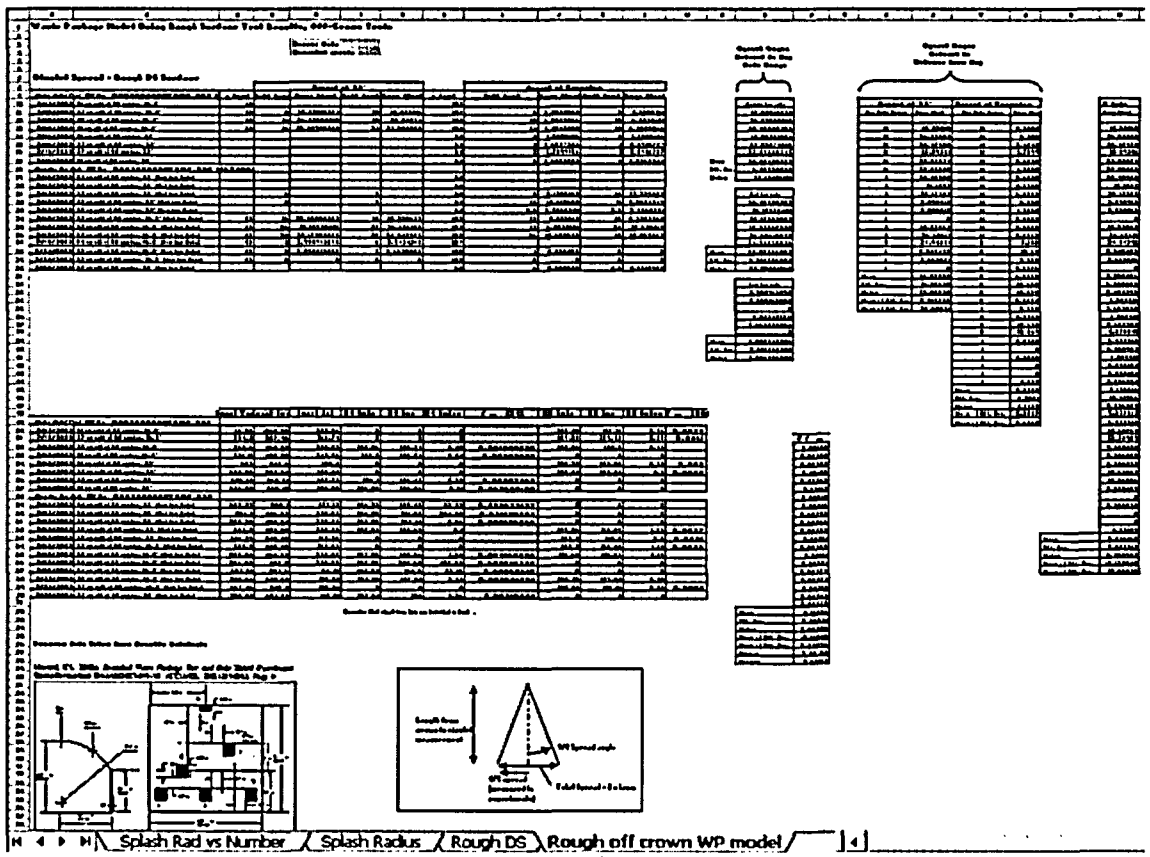

Figure E-11. Spreadsheet "Flux Splitting Validation"–Worksheet "Rough off crown WP model;" Worksheet Overview

	A	B	C	D	E	F	G	H	I	J	K	L
1	Waste Package Model Using Rough Surface Test Results, Off-Crown Tests											
2												
3					Source Data							
4					Calculated results							
5												
6												
7	Rivulet Spread - Rough DS Surface											
8				Spread at 33°					Spread at Transition			
9	*Multiple Patch Test* DTN: MO0208EBSATBWP.027		x [cm]	Left [cm]	Angle [deg]	Right [cm]	Angle [deg]	x [cm]	Left [cm]	Angle [deg]	Right [cm]	Angle [deg]
10	7/16/2002	81 cm right of DS center, 16 ß	43					107				
11	7/16/2002	27 cm right of DS center, 16 ß	43	6	8.5298373	12	15.88291094	107	5	3.208486278	9	4.276941115
12	7/16/2002	27 cm left of DS center, 16 ß	43	21	26.02995218	19	23.83874014	107	12	6.398956427	13	6.827248126
13	7/16/2002	81 cm left of DS center, 16 ß	43	16	20.40868245	23	27.89568249	107	14	7.454298813	12	6.398956427
14	7/16/2002	81 cm right of DS center, 33°						64	2	1.789510638	2	1.789510638
15	7/16/2002	27 cm right of DS center, 33°						64	3	2.683775159	9	8.695173711
16	7/16/2002	27 cm left of DS center, 33°						64	2	1.789510638	9	8.695173711
17	7/16/2002	81 cm left of DS center, 33°						64	3	2.683775159	4	3.576354375
18	*Bounding Flow Rate* DTN: MO0208EBSATBWP.028											
19	7/16/2002	54 cm left of DS center, 33° (Low Flow Rate)						64				
20	7/17/2002	54 cm left of DS center, 33° (High Flow Rate)						64				
21	7/17/2002	27 cm left of DS center, 33° (High Flow Rate)		6		5		64	8	7.125018348	14	12.23508729
22	7/17/2002	27 cm right of DS center, 33° (High Flow Rate)		6		3		64	12	10.61455528	8	8.752142942
23	7/17/2002	27 cm right of DS center, 33° (Low Flow Rate)						64	2.5	2.236979063	2.5	2.236979063
24	7/18/2002	27 cm right of DS center, 16 ß (High Flow Rate)	43	15	20.10988293	16	19.23047239	107	17	8.027652951	10	5.359256804
25	7/18/2002	27 cm left of DS center, 16 ß (High Flow Rate)	43	28	31.15135451	22	26.55158472	107	13	6.827248126	34	17.82807037
26	7/18/2002	54 cm left of DS center, 16 ß (High Flow Rate)	43	25	30.07263023	20	24.94359258	107	26	13.65764251	19	10.06906271
27	7/18/2002	54 cm left of DS center, 16 ß (Low Flow Rate)	43	3	3.890913096	8	7.943471811	107				
28	7/24/2002	27 cm left of DS center, 16 ß (Low Flow Rate)	43	3	3.890913096	2	2.543000766	107	1	0.8954958586	0	0
29	7/24/2002	27 cm right of DS center, 16 ß (Low Flow Rate)	43	0	0	0	0	107	0	0	0	0
30	7/25/2002	27 cm left of DS center, 33° (Low Flow Rate)						64	5	5.365825043	4.5	4.829843077
31												

DTN: MO0208EBSATBWP.027 [DIRS 163404]; DTN: MO0208EBSATBWP.028 [DIRS 163405].

Figure E-12. Spreadsheet "Flux Splitting Validation"–Worksheet "Rough off crown WP model;" Calculation of Rivulet Spread Angles

In Figure E-12, Columns A and B, Rows 10–30, identify the tests reported in indicated DTNs. In Columns C and H, the value of x, the distance from the drip location to the measurement point, is listed. Rivulet spread measured to the left and right of the drip location is shown in Columns D and F, respectively, for measurements at the 33° line. Measurements at the transition line are listed in Columns I and K. Portions of this table are reproduced in Table 7.1-8.

The spread distance, w_r, is converted to spread angle, α, in Columns E, G, J, and L:

$$\alpha = \tan^{-1}\left(\frac{w_r}{x}\right).$$

An example of the Microsoft Excel equation used for this calculation is:

E11=DEGREES(ATAN(D11/C11))

where the DEGREES function converts the result of the inverse tangent function ATAN from radians to degrees.

In Figure E-13, Column O, Rows 11–38, the spread angles measured at the 33° line are ordered by drip rate. The "nominal" drip rate is that used in the Multiple Patch tests, and the high and low drip rates were used in the Bounding Flow Rate tests. The mean, standard deviation, and median are computed for each of the three drip rates.

In Column S, the spread angles from Column O are repeated, and statistics (mean, standard deviation, median, and mean plus or minus one standard deviation) are computed for the entire set in Rows 31–35. The drip rate is indicated in Column R, where "M" indicates the nominal drip rate.

In Column U, the spread angles from Columns J and L are consolidated for measurements at the transition line. The drip rate used in each test is indicated in Column T. (The values in this column are currently incorrect, since they are just copies of the incorrect results in Column L and incorrectly recalculated values from Column J, where the actual Column J values are correct.)

All 50 spread angle measurements are compiled in Column W, with statistics (mean, standard deviation, median, and mean plus or minus one standard deviation) computed for the entire set in Rows 63-67 (Figure E-14). The mean plus or minus one standard deviation are used as the spread angle range in Section 7.1.1.2 for determination of the uncertainty in the waste package flux splitting submodel validation.

	M	N	O	P	Q	R	S	T	U	Y	W
1											
2											
3											
4			Spread Angles								
5			Ordered by Drip Rate				Spread Angles				
6			Range				Ordered by Distance				
7							from Drip				
8											
9											
10			Nominal drip rate			Spread at 33°		Spread at Transition			All data
11			10.53918373			Drip Rate Range	Angle (deg)	Drip Rate Range	Angle (deg)		Angle (deg)
12			26.02955219								
13			20.40988283			M	10.5391837	M	3.20949		10.5391837
14			15.59281094			M	26.0295922	M	6.39896		26.0295922
15			23.83874018			M	20.4098828	M	-7.4543		20.4098828
16			27.09555249			M	15.5928109	M	1.78991		15.5928109
17		Mean	20.58429373			M	23.8387402	M	2.68378		23.8387402
18		Std. Dev.	6.45737938			M	27.0955525	M	1.78991		27.0955525
19		Median	22.12431151			H	20.4098828	M	2.68378		20.4098828
20						H	31.1533045	M	4.27584		31.1533045
21			High drip rate			H	30.17352	M	6.82722		30.17352
22			20.40988283			L	3.9909131	M	6.39896		3.9909131
23			31.16930451			L	3.9909131	M	1.78991		3.9909131
24			30.17352003			L	0	M	0.89517		0
25			19.23067238			H	19.2306724	M	0.89517		19.2306724
26			36.65610842			H	36.6561084	M	3.57633		36.6561084
27			24.94390526			H	24.9439053	H	7.12502		24.9439053
28		Mean	27.09556557			L	7.94347181	H	10.6197		7.94347181
29		Std. Dev.	6.761306057			L	2.66300077	L	2.23698		2.66300077
30		Median	27.55871265			L	0	H	9.02761		0
31						Mean	16.8259697	H	6.82722		3.20948632
32			Low drip rate			Std. Dev.	11.7062451	H	13.6576		6.39895663
33			3.990913098			Median	19.8202776	H	12.3391		7.45429881
34			3.990913098			Mean - 1 Std. Dev.	5.21972461	H	9.75242		1.78991061
35			0			Mean + 1 Std. Dev.	28.6322148	L	2.23698		2.68377516
36			7.943471811					H	5.33924		1.78991061
37			2.663000766					H	17.628		2.68377516
38			0					H	10.0691		4.27584111
39		Mean	3.098049796					L	0.53546		6.92721813
40		Std. Dev.	2.981865758					L	0		6.39895663
41		Median	3.326956932					L	5.36583		1.78991061
42								L	0		0.89517371
43								L	0		0.89517371
44								L	4.02199		3.57633437
45								Mean	5.23878		7.12501635
46								Std. Dev.	4.38812		10.6196553
47								Median	4.14832		2.23697306
48	(B5)							Mean + 1 Std. Dev.	0.85066		9.02761295
49								Mean - 1 Std. Dev.	9.6269		6.92721813
50	0.0026853										13.6576425
51	0.001105										12.3390873
52				0.0015505							9.75242494

Splash Rad vs Number | Splash Radius | Rough DS | Rough off crown WP model

Figure E-13. Spreadsheet "Flux Splitting Validation"–Worksheet "Rough off crown WP model;" Additional Calculations of Rivulet Spread Angles

	S	T	U	V	W
45		Mean	5.23878		7.12501635
46		Std. Dev.	4.38812		10.6196553
47		Median	4.14892		2.23697906
48		Mean - 1 Std. Dev.	0.85066		9.02761295
49		Mean + 1 Std. Dev.	9.6269		6.92721813
50					13.6576425
51					12.3390873
52					9.75242494
53					2.23697906
54					5.3392368
55					17.6280194
56					10.0690627
57					0.53545899
58					0
59					5.35582504
60					0
61					0
62					4.02199018
63				Mean	9.4461677
64				Std. Dev.	9.68321235
65				Median	6.39895663
66				Mean - 1 Std. Dev.	-0.1370447
67				Mean + 1 Std. Dev.	19.02938

Figure E-14. Spreadsheet "Flux Splitting Validation"–Worksheet "Rough off crown WP model;" Statistics of Rivulet Spread Angles

	A	B	C	D	E	F	G	H	I
47									
48			Input Tare	Input Final	Input (g)	B4 Initial	B4 Final	B4 Inflow	f_{expt} (B4)
49	*Multiple Drip Test* DTN: MO0208EBSATBVP.027								
50	7/12/2002	81 cm right of DS center, 16.5	16.98	-265.58	282.56	0	0	0	
51	7/15/2002	27 cm right of DS center, 16.5	824.2	507.46	316.74	0	0	0	
52	7/15/2002	27 cm left of DS center, 16.5	763.6	450.03	309.57	105.86	106.34	0.48	0.001550538
53	7/15/2002	81 cm left of DS center, 16.5	731.11	488.55	242.56	105.9	108.84	0.94	0.00387533
54	7/16/2002	81 cm right of DS center, 33	652	542.6	109.4	0	0	0	
55	7/16/2002	27 cm right of DS center, 33	690.98	582.54	108.44	0	0	0	
56	7/16/2002	27 cm left of DS center, 33	676.14	568.81	107.33	106.1	106.43	0.33	0.00307463
57	7/16/2002	81 cm left of DS center, 33	636.92	530.17	106.75	106.05	106.06	0.01	9.36768E-05
58	*Bounding Flow Rate* DTN: MO0208EBSATBVP.028								
59	7/16/2002	54 cm left of DS center, 33 (Low Flow Rate)	682.23	559.1	123.13	106.22	159.49	53.27	0.432632177
60	7/17/2002	54 cm left of DS center, 33 (High Flow Rate)	776.1	446.07	330.03	106.09	311.08	204.99	0.621125352
61	7/17/2002	27 cm left of DS center, 33 (High Flow Rate)	798.78	459.54	339.24	107.55	107.61	0.06	0.000176866
62	7/17/2002	27 cm right of DS center, 33 (High Flow Rate)	803.2	472.98	330.22	107.52	107.62	0.1	
63	7/17/2002	27 cm right of DS center, 33 (Low Flow Rate)	661.79	549.43	112.36	0	0	0	
64	7/18/2002	27 cm right of DS center, 16.5 (High Flow Rate)	759.3	445.48	313.82	0	0	0	
65	7/18/2002	27 cm left of DS center, 16.5 (High Flow Rate)	780.84	458.77	322.07	107.52	108.86	1.34	0.004160586
66	7/18/2002	54 cm left of DS center, 16.5 (High Flow Rate)	755.07	427.8	328.27	107.77	305.69	197.92	0.602918329
67	7/18/2002	54 cm left of DS center, 16.5 (Low Flow Rate)	627.01	532.6	94.41	107.32	164.5	57.18	0.60565618
68	7/24/2002	27 cm left of DS center, 16.5 (Low Flow Rate)	795.66	679.69	115.97	107.58	107.92	0.34	0.002931793
69	7/24/2002	27 cm right of DS center, 16.5 (Low Flow Rate)	667.46	547.7	119.76	0	0	0	
70	7/25/2002	27 cm left of DS center, 33 (Low Flow Rate)	798.53	682.72	115.81	107.64	108	0.36	0.00310854
71									
72						Breaches that should have flow are highlighted in bold.			

DTN: MO0208EBSATBWP.027 [DIRS 163404]; DTN: MO0208EBSATBWP.028 [DIRS 163405].

Figure E-15. Spreadsheet "Flux Splitting Validation"–Worksheet "Rough off crown WP model;" Calculation of Experimental Breach Flow Fractions

For the tests identified in Columns A and B, Rows 50–70 (Figure E-15), the initial and final water mass in the input water container are listed in Columns C and D, and the amount of water dripped onto the drip shield is calculated in Column E (e.g., E50=C50-D50). The initial and final mass of water in the Breach B4 collection vessel is listed in Columns F and G, respectively, and the amount of water collected from flow into Breach B4 is calculated in Column H (e.g., H52=G52-F52). The fraction of water dripped onto the drip shield that flowed into Breach B4, f_{expt} (B4), is computed in Column I for the tests in which the inflow was greater than zero (e.g., I52=H52/E52).

	J	K	L	M	N	O	P
47							
48	B5 Initial	B5 Final	B5 Inflow	f_{expt} (B5)			
49							
50	109.45	110.21	0.76	0.00268589			
51	109.08	109.43	0.35	0.00110501			All f_{expt}
52	109.06	109.5	0.44				0.001550538
53	0	0	0				0.00387533
54	109.33	109.55	0.22	0.00201097			0.00307463
55	109.44	109.74	0.3	0.00276651			9.36768E-05
56	0	0	0				0.432632177
57	0	0	0				0.621125352
58							0.000176866
59	0	0	0				0.004160586
60	0	0	0				0.602918329
61	0	0	0				0.60565618
62	109.36	110.59	1.23	0.00372479			0.002931793
63	109.7	110.5	0.8	0.00711997			0.00310854
64	109.3	110.44	1.14	0.00363266			0.002685892
65	101.63	101.82	0.19				0.001105007
66	0	0	0				0.002010969
67	0	0	0				0.002766507
68	109.49	109.94	0.45				0.00372479
69	109.92	110.01	0.09	0.0007515			0.007119972
70	0	0	0				0.003632656
71							0.000751503
72						Mean	0.115255065
73						Std. Dev.	0.233709623
74						Median	0.003091585
75						Mean - 1 Std. Dev.	-0.11845456
76						Mean + 1 Std. Dev.	0.348964688
77						Minimum	9.36768E-05
78						Maximum	0.621125352

Figure E-16. Spreadsheet "Flux Splitting Validation"–Worksheet "Rough Off Crown WP Model;" Summary of Experimental Breach Flow Fractions

The initial and final mass of water in the Breach B5 collection vessel is listed in Figure E-16, Columns I and J, respectively, and the amount of water collected from flow into Breach B5 is calculated in Column L (e.g., L50=K50-J50). The fraction of water dripped onto the drip shield that flowed into Breach B5, f_{expt} (B5), is computed in Column M for the tests in which the inflow was greater than zero (e.g., M50=L50/E50).

The 20 values of f_{expt} are compiled in Column P, with statistics (mean, standard deviation, median, and mean plus or minus one standard deviation) presented in Rows 73-76.

The input water, breach inflows, and f_{expt} for each breach are reproduced in Table 7.1-10.

INTENTIONALLY LEFT BLANK

APPENDIX F
MICROSOFT EXCEL SPREADSHEETS "TRANSPORT_CALC_ALL_COLLOIDS," "FLUX_OUT_RATIO.XLS," AND "TIME_TO_CONV.XLS"

MICROSOFT EXCEL SPREADSHEETS "TRANSPORT_CALC_ALL_COLLOIDS," "FLUX_OUT_RATIO.XLS," AND "TIME_TO_CONV.XLS"

SPREADSHEET "TRANSPORT_CALC_ALL_COLLOIDS.XLS"

The purpose of this spreadsheet is to implement the colloid model that represents the sorption of radionuclides onto the oxy-hydroxide (designated FeO) corrosion material within the engineered barrier system (EBS). The model accounts for both reversible and irreversible sorption onto the FeO mobile colloids and the immobile corrosion products together with reversible sorption onto both waste form and groundwater (GW) colloids. This description refers to equations in Appendix B, "Implementation of Radionuclide Sorption onto Colloidal and Stationary Phases with Finite Difference Solution."

Description of Input Values

The first 29 rows of the worksheet (see Figure F-1 for an image of the worksheet) contain parameter input values. Column D contains the typical values input from the GoldSim model. Column B contains values from Column D that are scaled appropriately for the current calculations.

Row 2: c_s [kg/m^3],

c_s = Pu solubility

$B$2=$D$2/1000

Row 3: phi_1

ϕ_cell1, $\phi = \frac{V_{pore}}{V_{bulk}}$, porosity of the upstream boundary

$B$3=$D$3

Row 4: phi_2

ϕ_cell2, $\phi = \frac{V_{pore}}{V_{bulk}}$, porosity of the corrosion product mass

$B$4=$D$4

Row 5: phi_3

ϕ_cell3, $\phi = \frac{V_{pore}}{V_{bulk}}$, porosity of the downstream boundary

$B$5=$D$5

Row 6: u [m^3/yr]

volumetric water flux, U Table B-1

$B$6=$D$6

Row 7: Kd_FeO_c [m^3/kg]

partition coefficient in the FeO colloid state

$B$7=$D$7/1000

Row 8: Kd_FeO_CP [m^3/kg]

partition coefficient in the stationary FeO corrosion product state

$B$8=$D$8/1000

Row 9: Kd_WF_c [m^3/kg]

partition coefficient in the waste form colloid state

$B$9=$D$9/1000

	A	B	C	D
1	Input for Excel sreadsheet		Input from GoldSim	
2	c_s [kg/m^3]	0.001	c_s [mg/L]	1
3	phi_1	1	phi_1	1
4	phi_2	0.4	phi_2	0.4
5	phi_3	0.3	phi_3	0.3
6	u [m^3/yr]	0.1	u [m^3/yr]	0.1
7	Kd_FeO_c [m^3/kg]	1.00000E+01	Kd_FeO_c [ml/g]	1.00000E+04
8	Kd_FeO_CP [m^3/kg]	2.50000E+00	Kd_FeO_CP [ml/g]	2.50000E+03
9	Kd_WF_c [m^3/kg]	2.00000E+02	Kd_WF_c [ml/g]	2.00000E+05
10	Kd_GW_c [m^3/kg]	2.00000E+02	Kd_GW_c [ml/g]	2.00000E+05
11	mass_FeO_CP [kg]	1.80000E+04	mass_FeO_CP [g]	1.80000E+07
12	V_pore [m^3]	2.29008E+00	V_pore [L]	2.29008E+03
13	c_FeO_c [kg/m^3]	2.00000E-02	c_FeO_c [mg/L]	2.00000E+01
14	c_FeO_CP [kg/m^3]	7.86000E+03	c_FeO_CP [mg/L]	7.86000E+06
15	c_WF_c [kg/m^3]	3.00000E-03	c_WF_c [mg/L]	3.00000E+00
16	c_GW_c [kg/m^3]	1.00000E-04	c_GW_c [mg/L]	1.00000E-01
17	rate [m/yr]	1.00000E-05	rate [cm/yr]	1.00000E-03
18	S_FeO_c [m^2/kg]	1.00000E+05	S_FeO_c[m^2/g]	1.00000E+02
19	S_FeO_CP [m^2/kg]	1.00000E+04	S_FeO_CP [m^2/g]	1.00000E+01
20	d_FeO [kg/m^3]	5.24000E+03	den FeO [kg/m^3]	5.24000E+03
21	diffus_aq [m^2/yr]	7.25834E-02	diffus_aq [m^2/s]	2.30000E-09
22	diffus_colloid [m^2/yr]	7.25834E-04	diffus_colloid [m^2/	2.30000E-11
23	diff_length_1 [m]	1.00000E-03	diff_length_1 [m]	1.00000E-03
24	diff_length_2 [m]	5.00000E+00	diff_length_2 [m]	5.00000E+00
25	diff_length_3 [m]	8.06000E-01	diff_length_3 [m]	8.06000E-01
26	diff_area_1_2 [m^2]	3.60000E+01	diff_area_1_2 [m^2]	3.60000E+01
27	diff_area_2_3 [m^2]	1.06800E+00	diff_area_2_3 [m^2]	1.06800E+00
28	decay [1/yr]	2.87494E-05	decay [1/yr]	2.87494E-05
29	delt [yr]	10	delt [yr]	10

Figure F-1. Spreadsheet "Transport_Calc_all_colloids.xls;" Summary of Inputs

Row 10: Kd_GW_c [m^3/kg]

partition coefficient in the GW colloid state

$B$10=$D$10/1000

Row 11: mass_FeO_CP [kg]

m_{FeO_CP} = mass of corrosion product

$B$11=$D$11/1000

Row 12: V_pore [m^3]

$V_{pore} = \phi V_{bulk} = \frac{\phi}{1-\phi}\frac{m_{FeO\_CP}}{\rho_{FeO\_CP}}$, pore volume

$B$12=$D$12/1000

Row 13: c_FeO_c [kg/m^3]

$c_{Pu\_FeO\_c}$, concentration of Pu in the FeO colloid state from reversible sorption

$B$13=$D$13/1000

Row 14: c_FeO_CP [kg/m^3]

$c_{Pu\_FeO\_CP}$, concentration of Pu in the stationary FeO corrosion product state from reversible sorption

$B$14=$D$14/1000

Row 15: c_WF_c [kg/m^3]

$c_{Pu\_WF\_c}$, concentration of Pu in the waste form colloid state from reversible sorption

$B$15=$D$15/1000

Row 16: c_GW_c [kg/m^3]

$c_{Pu\_GW\_c}$, concentration of Pu in the GW colloid state from reversible sorption

$B$16=$D$16/1000

Row 17: rate [m/yr]

k, forward rate constant (m^3 water m^{-2} FeO yr^{-1})

$B$17=$D$17/100

Row 18: S_FeO_c [m^2/kg]

$\hat{S}_{FeO}$ = specific surface area of FeO (m^2 kg^{-1}) in the colloid state

$B$18=$D$18*1000

Row 19: S_FeO_CP [m^2/kg]

$\hat{S}_{FeO}$ = specific surface area of FeO (m^2 kg^{-1}) in the corrosion product state

$B$19=$D$19*1000

Row 20: d_FeO [kg/m^3]

ρ_{FeO_CP} = corrosion product (FeO) density (kg m^{-3})

$B$20=$D$20

Row 21: diffus_aq [m^2/yr]

D_{aq} = aqueous diffusivity (m^2 yr^{-1})

$B$21=$D$21*31558000

Row 22: diffus_colloid [m^2/yr]

$D_{colloid}$ = colloid diffusivity (m^2 yr^{-1})

$B$22=$D$22*31558000

Row 23: diff_length_1 [m]

L_1 = diffusive length for cell_1

$B$23=$D$23

Row 24: diff_length_2 [m]

L_2 = diffusive length for cell_2

$B$24=$D$24

Row 25: diff_length_3 [m]

L_3 = diffusive length for cell_3

$B$25=$D$25

Row 26: diff_area_1_2 [m^2]

A_{s12} = diffusive area at cell_1 and cell_2 interface

$B$26=$D$26

Row 27: diff_area_2_3 [m^2]

A_{s23} = diffusive area at cell_2 and cell_3 interface

$B$27=$D$27

Row 28: decay [1/yr]

λ, decay rate (yr^{-1})

$B$28=$D$28

Row 29: delt [yr]

Δt, time step length

$B$29=$D$29

Rows 30 through 53 contain additional derived parameters for the mixing cell colloid model.

	A	B	C	D	E	F	G
30	R_bar_1 [1/yr]	2.00000E-02					
31	R_bar_2 [1/yr]	7.86000E+02					
32	U_bar [1/yr]	4.36667E-02					
33	Kd_bar_FeO_c	2.00000E-01					
34	Kd_bar_FeO_CP	1.96500E+04					
35	Kd_bar_WF_c	6.00000E-01					
36	Kd_bar_GW_c	2.00000E-02					
37	K_bar_1	1.96518E+04					
38	K_bar_2	1.82000E+00					
39	K_bar_3	8.20000E-01					
40	Diff_left_aq	9.12736E-02					
41	Diff_left_c	9.12736E-04					
42	Diff_right_aq	2.22893E-03		limiting values			
43	Diff_right_colloid	2.22893E-05		p_1	3.58485E-02		
44	denom_a_1_2	2.75194E+04		p_2	8.17743E-02	tolerence =	1.00000E-02
45	a_1	7.14108E-01		lim c_Pu_aq	2.05511E-07	Pu_aq time [yr]	137
46	a_2	5.87541E-08		lim c_irr_c	9.40175E-08	delta_1	3.2004E-04
47	b_1	6.95808E-01		lim c_rev_c	4.11023E-08	delta_2	3.0078E-04
48	b_2	1.39162E-01		lim c_irr_CP	5.61862E+00	t_1	22
49	e_1	9.99713E-01		lim c_rev_CP	4.03830E-03	t_2	24
50	e_2	7.85774E+03		flux out ratio	5.48749E-01	irrv_Pu_c time [yr]	240
51	Omega	9.5000E-01		flux out/flux in	1.29289E-04		
52	k_fit_Omega [cm/yr]	4.1837E-02		irrv_col/rev_col	5.57903E-01		
53	p1/p2	4.3838E-01					
54							
55							

Figure F-2. Spreadsheet "Transport_Calc_all_colloids.xls;" Additional Derived Parameters

Row 30: R_bar_1 [1/yr]

$\overline{R}_1 = \hat{S}_{FeO\_c} c_{FeO\_c} k$, reaction rate for colloids

$B$30=$B$18*$B$13*$B$17

Row 31: R_bar_2 [1/yr]

$\overline{R}_2 = \hat{S}_{FeO\_CP} c_{FeO\_CP} k$, reaction rate constants for corrosion products

$B$31=$B$19*$B$14*$B$17

Row 32: U_bar [1/yr]

$\overline{U}$ is the advective rate constant

$B$32=$B$6/$B$12

Row 33: Kd_bar_FeO_c

advective dimensionless partition coefficient in the FeO colloid state

$B$33=$B$13*$B$7

Row 34: Kd_bar_FeO_CP

advective dimensionless partition coefficient in the FeO corrosion product state

$B$34=$B$14*$B$8

Row 35: Kd_bar_WF_c

advective dimensionless partition coefficient in the waste form colloid state

$B$35=$B$15*$B$9

Row 36: Kd_bar_GW_c

advective dimensionless partition coefficient in the GW colloid state

$B$36=$B$16*$B$10

Row 37: K_bar_1

$\overline{K}_1 = 1 + \overline{K}_{d\_FeO\_c} + \overline{K}_{d\_FeO\_CP} + \overline{K}_{d\_WF\_c} + \overline{K}_{d\_GW\_c}$, combination of dimensionless partition coefficients

$B$37=1+$B$33+$B$34+$B$35+$B$36

Row 38: K_bar_2

$\overline{K}_2 = 1 + \overline{K}_{d\_FeO\_c} + \overline{K}_{d\_WF\_c} + \overline{K}_{d\_GW\_c}$, combination of dimensionless partition coefficients

$B$38=1+$B$33+$B$35+$B$36

Row 39: K_bar_3

$\overline{K}_3 = \overline{K}_{d\_FeO\_c} + \overline{K}_{d\_WF\_c} + \overline{K}_{d\_GW\_c}$, combination of dimensionless partition coefficients

$B$39=$B$33+$B$35+$B$36

Row 40: Diff_left_aq

aqueous diffusive rate constant for left diffusive boundary condition

$B$40=($B$26/($B$23/($B$3*$B$21)+$B$24/($B$4*$B$21)))/$B$12

Row 41: Diff_left_c

colloid diffusive rate constant for left diffusive boundary condition

$B$41=($B$26/($B$23/($B$3*$B$22)+$B$24/($B$4*$B$22)))/$B$12

Row 42: Diff_right_aq

aqueous diffusive rate constant for right diffusive boundary condition

$B$42=($B$27/($B$24/($B$4*$B$21)+$B$25/($B$5*$B$21)))/$B$12

Row 43: Diff_right_colloid

colloid diffusive rate constant for right diffusive boundary condition

$B$43=($B$27/($B$24/($B$4*$B$22)+$B$25/($B$5*$B$22)))/$B$12

Row 44: denom_a_1_2

denominator of a_1 in Equation B-55 (see Row 45)

$B$44=$B$37+($B$32*$B$38+$B$40+$B$41*$B$35+$B$42+$B$43*$B$39
+$B$30+$B$31+$B$28*$B$37)*$B$29

Row 45: a_1

first order linear constant coefficient for Equation B-55,

$$a_1 = \frac{\overline{K}_1}{\overline{K}_1 + \left(\overline{U}\overline{K}_2 + \overline{D}_{left\_aq} + \overline{D}_{left\_col}\overline{K}_{d\_WF\_c} + \overline{D}_{right\_aq} + \overline{D}_{right\_col}\overline{K}_3 + \overline{R}_1 + \overline{R}_2 + \lambda\overline{K}_1\right)\Delta t}$$

B$45=$B$37/$B$44

Row 46: a_2

first order linear constant coefficient for Equation B-55,

$$a_2 = \frac{\left(\overline{U}(1+\overline{K}_{d\_WF\_c}) + \overline{D}_{left\_aq} + \overline{D}_{left\_col}\overline{K}_{d\_WF\_c}\right)\Delta t c_s}{\overline{K}_1 + \left(\overline{U}\overline{K}_2 + \overline{D}_{left\_aq} + \overline{D}_{left\_col}\overline{K}_{d\_WF\_c} + \overline{D}_{right\_aq} + \overline{D}_{right\_col}\overline{K}_3 + \overline{R}_1 + \overline{R}_2 + \lambda\overline{K}_1\right)\Delta t}$$

$B$46=(($B$32*(1+$B$35)+$B$40+$B$41*$B$35)*$B$29*$B$2)/$B$44

Row 47: b_1

irreversible colloid coefficient (Equation B-59) for Equation B-58,

$$b_1 = \frac{1}{1+\left(\overline{U}+\overline{D}_{right\_col}+\lambda\right)\Delta t}$$

$B$47=1/(1+($B$32+$B$43+$B$28)*$B$29)

Row 48: b_2

irreversible colloid coefficient (Equation B-60) for Equation B-58,

$$b_2 = \frac{\overline{R}_1\Delta t}{1+\left(\overline{U}+\overline{D}_{right\_col}+\lambda\right)\Delta t}$$

$B$48=($B$30*$B$29)*$B$47

Row 49: e_1

irreversible corrosion products coefficient (Equation B-65) for Equation B-64,

$$e_1 = \frac{1}{1+\lambda\Delta t}$$

$B$49=1/(1+$B$28*$B$29)

Row 50: e_2

irreversible corrosion products coefficient (Equation B-66) for Equation B-64,

$$e_2 = \frac{\overline{R}_2\Delta t}{1+\lambda\Delta t}$$

$B$50=($B$31*$B$29)*$B$49

Row 51: Omega

$$\Omega = \frac{\text{colloid mass flux out}}{\text{total mass flux out}} = 0.95 \text{ (Equation B-1)}$$

$B$51=0.95

Row 52: k_fit_Omega [cm/yr]

$k = \dfrac{p_2\Omega - p_1}{(1-\Omega)\hat{S}_{FeO\_c}c_{FeO\_c}}$, fitting parameter, k, given a target flux ratio Ω, Equation B-72

$B$52=100*($E$44*$B$51-$E$43)/((1-$B$51)*$B$18*$B$13)

Row 53: p1/p2

$$\Omega = \frac{p_1 + \overline{R}_1}{p_2 + \overline{R}_1} \qquad \text{(Equation B-71)}$$

$B$53=$E$43/$E$44

The values of parameters in Column E & G Rows 43 through 52 under the heading "limiting values" pertain to the equations and discussion in Section "Boundary Fluxes" in Appendix B.

Row 43, Column E: p_1

$$p_1 = \overline{K}_3\left(\overline{U} + \overline{D}_{right\_col} + \lambda\right)$$

$E$43=$B$39*($B$32+$B$43+$B$28)

Row 44, Column E: p_2

$$p_2 = \left(\overline{UK}_2 + \overline{D}_{right\_aq} + \overline{D}_{right\_col}\overline{K}_3\right)\left(\frac{\overline{U} + \overline{D}_{right\_col} + \lambda}{\overline{U} + \overline{D}_{right\_col}}\right)$$

$E$44=($B$32*$B$38+$B$42+$B$43*$B$39)*($B$32+$B$43+$B$28)/($B$32+$B$43)

Row 45, Column E: lim c_Pu_aq

$$\lim_{n\to\infty} c^n_{Pu\_aq} = \frac{a_2}{1-a_1}$$

$E$45=$B$46/(1-$B$45)

Row 46, Column E: lim c_irr_c

$$\lim_{n\to\infty} c^n_{Irrv\_Pu\_FeO\_c} = \frac{a_2 b_2}{(1-a_1)(1-b_1)}$$

$E$46=($B$30*$E$45)/($B$32+$B$43+$B$28)

Row 47, Column E: lim c_rev_c

$$\lim_{n\to\infty} c^n_{Pu\_FeO\_c} = \overline{K}_{d\_FeO\_c} \lim_{n\to\infty} c^n_{Pu\_aq}$$

$E$47=$B$33*$E$45

Row 48, Column E: lim c_irr_CP

$$\lim_{n\to\infty} c^n_{Irrv\_Pu\_FeO\_CP} = \frac{e_2}{1-e_1} \lim_{n\to\infty} c^n_{Pu\_aq} = \frac{\overline{R}_2}{\lambda} \lim_{n\to\infty} c^n_{Pu\_aq}$$

$E$48=$E$45*$B$31/$B$28

Row 49, Column E: lim c_rev_CP

$$\lim_{n\to\infty} c^n_{Pu\_FeO\_CP} = \overline{K}_{d\_FeO\_CP} \lim_{n\to\infty} c^n_{Pu\_aq}$$

$E$49=$B$34*$E$45

Row 50, Column E: flux out ratio

$$\Omega = \frac{p_1 + \overline{R}_1}{p_2 + \overline{R}_1}$$

$E$50=($E$43+$B$30)/($E$44+$B$30)

Row 51, Column E: flux out/flux in

$$\Psi = \frac{p_2 + \overline{R}_1}{p_2 + \left(\frac{\overline{U} + \overline{D}_{right\_col} + \lambda}{\overline{U} + \overline{D}_{right\_col}}\right)\left(\overline{R}_1 + \overline{R}_2 + \lambda \overline{K}_1\right)}$$

$E$51=($E$44+$B$30)/($E$44+($B$32+$B$43+$B$28)*($B$30+$B$31+$B$28*$B$37)/($B$32+$B$43))

Row 52, Column E: irrv_col/rev_col

$$0 < \frac{\overline{K}_3(\overline{U} + \overline{D}_{right\_col})}{\overline{U}\overline{K}_2 + \overline{D}_{right\_aq} + \overline{D}_{right\_col}\overline{K}_3} < \Omega < 1$$

$E$52=($B$32+$B$43)*$E$46/(($B$32+$B$43)*$B$39*$E$45)

Row 44, Column G: tolerance

relative error estimate with tolerance ε

$G$44 =G44

Row 45, Column G: Pu_aq time [yr]

$$time = n\Delta t > \frac{\log_{10} \varepsilon}{\log_{10} a_1} \Delta t \quad \text{(Equation B-74)}$$

$G$45 =$B$29*LOG10($G$44)/LOG10($B$45)

Row 46, Column G: delta_1

$$b_1^{n+1} < \left|\frac{a_1 - b_1}{1 - a_1}\right| \frac{\varepsilon}{2} = \delta_1$$

$G$46 =0.5*$G$44*ABS(($B$47-$B$45)/(1-$B$45))

Row 47, Column G: delta_2

$$a_1^{n+1} < \left|\frac{a_1 - b_1}{1 - b_1}\right| \frac{\varepsilon}{2} = \delta_2$$

$G$47 =0.5*$G$44*ABS(($B$47-$B$45)/(1-$B$47))

Row 48, Column G: t_1

$$\frac{\log_{10} \delta_1}{\log_{10} b_1}$$

$G$48 =LOG10($G$46)/LOG10($B$47)

Row 49, Column G: t_2

$$\frac{\log_{10} \delta_2}{\log_{10} a_1}$$

$G$49 =LOG10($G$47)/LOG10($B$45)

Row 50, Column G: irrv_Pu_c time [yr]

time to converge to a given relative error tolerance,

$$time = n\Delta t > \frac{\log_{10} \varepsilon}{\log_{10} a_1} \Delta t$$

$G$50 =INT(MAX($G$48,$G$49))*$B$29

Rows 58 thru 158 and Columns A through AC contain calculated solutions and equation terms, iterated in time, for the mixing cell colloid model. Images of this section of the spreadsheet are included at the end of this appendix (Figures F-3 through F-14).

A58 through A158 are the model times, time(n+1) = time(n)+delt, $A$59=$A58+$B$29

Column B: c_Pu_aq

B$59=$B$45*$B58+$B$46

Column C: c_Pu_FeO_c

C$59 =$B$33*$B59

Column D: c_Pu_FeO_CP

D$59 =$B$34*$B59

Column E: c_Pu_WF_c

E$59 =$B$35*$B59

Column F: c_Pu_GW_c

F$59 =$B$36*$B59

Column G: c_irrv_Pu FeO_c

G$59 =$B$47*$G58+$B$48*$B59

Column H: c_irrv_Pu FeO_CP

H$59 =$B$49*$H58+$B$50*$B59

Column I: c_Pu_Fluid1 [mg/L]

I$59 =1000*($B59+$C59+$E59+$F59)

Column J: c_Pu_FeO_c [g/kg]

J$59 =1000*$C59/$B$13

Column K: c_Pu_FeO_CP [g/kg]

K$59 =1000*$D59/$B$14

Column L: c_PU_WF_c [g/kg]

L$59 =1000*$E59/$B$15

Column M: c_Pu_GW_c [g/kg]

M$59 =1000*$F59/$B$16

Column N: c_Irrv_Pu_c [g/kg]

N$59 =1000*$G59/$B$13

Column O: c_Irrv_Pu_CP [g/kg]

O$59 =1000*$H59/$B$14

Column P: time

P$59 =$A59

Column Q: left_bddy_flux [kg]

$$F^n_{left\_bddy\_total} = \overline{U}V_{pore}c_s + \overline{D}_{left\_aq}V_{pore}(c_s - c^n_{Pu\_aq})$$
$$+\overline{U}V_{pore}\overline{K}_{d\_WF\_c}c_s + \overline{D}_{left\_col}V_{pore}\overline{K}_{d\_WF\_c}(c_s - c^n_{Pu\_aq})$$

Q$59=($B$32*(1+$B$35)*$B$2+($B$40+$B$41*$B$35)*($B$2-$B59))*$B$12*$B$29

Column R: right_bddy colloid flux [kg]

$$F^n_{right\_bddy\_colloid} = \overline{U}V_{pore}\overline{K}_{d\_FeO\_c}c^n_{Pu\_aq} + \overline{U}V_{pore}c^n_{Irrv\_Pu\_FeO\_c}$$
$$\overline{U}V_{pore}\overline{K}_{d\_WF\_c}c^n_{Pu\_aq} + \overline{U}V_{pore}\overline{K}_{d\_GW\_c}c^n_{Pu\_aq}$$
$$+\overline{D}_{right\_col}V_{pore}\overline{K}_{d\_FeO\_c}c^n_{Pu\_aq} + \overline{D}_{right\_col}V_{pore}c^n_{Irrv\_Pu\_FeO\_c}$$
$$\overline{D}_{right\_col}V_{pore}\overline{K}_{d\_WF\_c}c^n_{Pu\_aq} + \overline{D}_{right\_col}V_{pore}\overline{K}_{d\_GW\_c}c^n_{Pu\_aq}$$

R$59 =($B$32+$B$43)*($B$39*$B59+$G59)*$B$12*$B$29

Column S: right bddy total flux [kg]

$$F^n_{right\_bddy\_total} = F^n_{right\_bddy\_colloid} + \overline{U}V_{pore}c^n_{Pu\_aq} + \overline{D}_{right\_aq}V_{pore}c^n_{Pu\_aq}$$

S$59 =$R59+($B$32+$B$42)*$B59*$B$12*$B$29

Column T: col_out/total_out

$$\Omega_n = \frac{F^n_{right\_bddy\_colloid}}{F^n_{right\_bddy\_total}}$$

T$59 =$R59/$S59

Column U: flux_out/flux_in

U$59 =$S59/$Q59

Column V: change mass [kg]

V$59 =(($B59-$B58)+($C59-$C58)+($D59-$D58)+($E59-$E58)+($F59-$F58))*$B$12

Column W: in - out [kg]

W$59=$Q59-(($B$32+$B$43)*$B$39+$B$32+$B$42)*$B59*$B$12*$B$29

Column X: react/decay [kg]

X$59 =-($B$30+$B$31+$B$28*$B$37)*$B$12*$B$29*$B59

Column Y: PU mass balance

Y$59 =$V59-$W59-$X59

Column Z: change mass [kg]

Z$59 =(($G59-$G58)+($H59-$H58))*$B$12

Column AA: in-out [kg]

AA$59 =-($B$32+$B$43)*$G59*$B$12*$B$29

Column AB: react/decay [kg]

AB$59 =(($B$30+$B$31)*$B59-$B$28*($G59+$H59))*$B$12*$B$29

Column AC: Irrv_Pu mass balance

AC$59 =$Z59-$AA59-$AB59

	A	B	C	D	E	F	G	H	I
56			concentration are Pu mass per pore volume [kg/m^3]						
57	time	c_Pu_aq	c_Pu_FeO_c	c_Pu_FeO_CP	c_Pu_WF_c	c_Pu_GW_c	c_irrv_Pu FeO_c	c_irrv_Pu FeO_CP	c_Pu_Fluid1 [mg/L]
58	0.00	0	0	0	0	0	0	0	0
59	10.00	5.87541E-08	1.17508E-08	1.15452E-03	3.52525E-08	1.17508E-09	8.17633E-09	4.61675E-04	1.0693E-04
60	20.00	1.00711E-07	2.01422E-08	1.97897E-03	6.04266E-08	2.01422E-09	1.97043E-08	1.25290E-03	1.8329E-04
61	30.00	1.30673E-07	2.61345E-08	2.56772E-03	7.84036E-08	2.61345E-09	3.18950E-08	2.27933E-03	2.3782E-04
62	40.00	1.52068E-07	3.04137E-08	2.98814E-03	9.12411E-08	3.04137E-09	4.33549E-08	3.47359E-03	2.7676E-04
63	50.00	1.67347E-07	3.34695E-08	3.28838E-03	1.00408E-07	3.34695E-09	5.34551E-08	4.78757E-03	3.0457E-04
64	60.00	1.78258E-07	3.56516E-08	3.50277E-03	1.06955E-07	3.56516E-09	6.20012E-08	6.18690E-03	3.2443E-04
65	70.00	1.86050E-07	3.72099E-08	3.65588E-03	1.11630E-07	3.72099E-09	6.90320E-08	7.64705E-03	3.3861E-04
66	80.00	1.91614E-07	3.83227E-08	3.76521E-03	1.14968E-07	3.83227E-09	7.46983E-08	9.15050E-03	3.4874E-04
67	90.00	1.95587E-07	3.91174E-08	3.84328E-03	1.17352E-07	3.91174E-09	7.91939E-08	1.06847E-02	3.5597E-04
68	100.00	1.98424E-07	3.96849E-08	3.89904E-03	1.19055E-07	3.96849E-09	8.27169E-08	1.22408E-02	3.6113E-04
69	110.00	2.00450E-07	4.00901E-08	3.93885E-03	1.20270E-07	4.00901E-09	8.54501E-08	1.38124E-02	3.6482E-04
70	120.00	2.01897E-07	4.03795E-08	3.96726E-03	1.21138E-07	4.03795E-09	8.75533E-08	1.53949E-02	3.6745E-04
71	130.00	2.02931E-07	4.05861E-08	3.98759E-03	1.21758E-07	4.05861E-09	8.91605E-08	1.69850E-02	3.6933E-04
72	140.00	2.03668E-07	4.07337E-08	4.00208E-03	1.22201E-07	4.07337E-09	9.03815E-08	1.85805E-02	3.7068E-04
73	150.00	2.04195E-07	4.08391E-08	4.01244E-03	1.22517E-07	4.08391E-09	9.13044E-08	2.01797E-02	3.7164E-04
74	160.00	2.04572E-07	4.09143E-08	4.01983E-03	1.22743E-07	4.09143E-09	9.19989E-08	2.17814E-02	3.7232E-04
75	170.00	2.04840E-07	4.09681E-08	4.02511E-03	1.22904E-07	4.09681E-09	9.25195E-08	2.33847E-02	3.7281E-04
76	180.00	2.05032E-07	4.10064E-08	4.02888E-03	1.23019E-07	4.10064E-09	9.29085E-08	2.49891E-02	3.7316E-04
77	190.00	2.05169E-07	4.10338E-08	4.03157E-03	1.23102E-07	4.10338E-09	9.31902E-08	2.65941E-02	3.7341E-04
78	200.00	2.05267E-07	4.10534E-08	4.03350E-03	1.23160E-07	4.10534E-09	9.34134E-08	2.81994E-02	3.7359E-04
79	210.00	2.05337E-07	4.10674E-08	4.03487E-03	1.23202E-07	4.10674E-09	9.35729E-08	2.98047E-02	3.7371E-04
80	220.00	2.05387E-07	4.10774E-08	4.03585E-03	1.23232E-07	4.10774E-09	9.36908E-08	3.14100E-02	3.7380E-04
81	230.00	2.05422E-07	4.10845E-08	4.03655E-03	1.23253E-07	4.10845E-09	9.37778E-08	3.30152E-02	3.7387E-04
82	240.00	2.05448E-07	4.10896E-08	4.03705E-03	1.23269E-07	4.10896E-09	9.38419E-08	3.46200E-02	3.7392E-04
83	250.00	2.05466E-07	4.10932E-08	4.03741E-03	1.23280E-07	4.10932E-09	9.38890E-08	3.62246E-02	3.7396E-04
84	260.00	2.05479E-07	4.10958E-08	4.03766E-03	1.23287E-07	4.10958E-09	9.39236E-08	3.78288E-02	3.7397E-04
85	270.00	2.05488E-07	4.10977E-08	4.03785E-03	1.23293E-07	4.10977E-09	9.39489E-08	3.94326E-02	3.7399E-04
86	280.00	2.05495E-07	4.10990E-08	4.03798E-03	1.23297E-07	4.10990E-09	9.39675E-08	4.10360E-02	3.7400E-04
87	290.00	2.05500E-07	4.10999E-08	4.03807E-03	1.23300E-07	4.10999E-09	9.39810E-08	4.26389E-02	3.7401E-04

conc_plot / conc_plot_porevol / Implicit_FD

Figure F-3. Spreadsheet "Transport_Calc_all_colloids.xls;" Calculated Solutions and Equation Terms, Iterated in Time, for Mixing Cell Colloid Model, Time 0 – 290 Years

	J	K	L	M	N	O	P	Q	R	S	T
56											
57	c_Pu_FeO_c [g/kg]	c_Pu_FeO_C P [g/kg]	c_PU_WF_c [g/kg]	c_Pu_GW_c [g/kg]	c_Irrv_Pu_c [g/kg]	c_Irrv_Pu_CP [g/kg]	time	left_bddy_flux [kg]	right_bddy colloid flux [kg]	right bddy total flux [kg]	col_out/total_out
58	0	0			0	0					
59	5.8754E-04	1.4689E-04	1.1751E-02	1.1751E-02	4.0882E-04	5.8737E-05	10.00	3.70265E-03	5.63835E-08	1.18137E-07	4.77273E-01
60	1.0071E-03	2.5178E-04	2.0142E-02	2.0142E-02	9.8521E-04	1.5940E-04	20.00	3.70256E-03	1.02339E-07	2.08191E-07	4.91565E-01
61	1.3067E-03	3.2668E-04	2.6135E-02	2.6135E-02	1.5948E-03	2.8999E-04	30.00	3.70250E-03	1.39118E-07	2.76460E-07	5.03210E-01
62	1.5207E-03	3.8017E-04	3.0414E-02	3.0414E-02	2.1677E-03	4.4193E-04	40.00	3.70246E-03	1.68137E-07	3.27967E-07	5.12663E-01
63	1.6736E-03	4.1837E-04	3.3469E-02	3.3469E-02	2.6728E-03	6.0911E-04	50.00	3.70242E-03	1.90777E-07	3.66667E-07	5.20301E-01
64	1.7826E-03	4.4565E-04	3.5652E-02	3.5652E-02	3.1001E-03	7.8714E-04	60.00	3.70240E-03	2.08279E-07	3.95636E-07	5.26441E-01
65	1.8605E-03	4.6512E-04	3.7210E-02	3.7210E-02	3.4516E-03	9.7291E-04	70.00	3.70239E-03	2.21706E-07	4.17252E-07	5.31347E-01
66	1.9161E-03	4.7903E-04	3.8323E-02	3.8323E-02	3.7349E-03	1.1642E-03	80.00	3.70237E-03	2.31940E-07	4.33334E-07	5.35245E-01
67	1.9559E-03	4.8897E-04	3.9117E-02	3.9117E-02	3.9597E-03	1.3594E-03	90.00	3.70236E-03	2.39697E-07	4.45268E-07	5.38322E-01
68	1.9842E-03	4.9606E-04	3.9685E-02	3.9685E-02	4.1358E-03	1.5574E-03	100.00	3.70236E-03	2.45550E-07	4.54103E-07	5.40737E-01
69	2.0045E-03	5.0113E-04	4.0090E-02	4.0090E-02	4.2725E-03	1.7573E-03	110.00	3.70235E-03	2.49947E-07	4.60629E-07	5.42621E-01
70	2.0190E-03	5.0474E-04	4.0379E-02	4.0379E-02	4.3777E-03	1.9586E-03	120.00	3.70235E-03	2.53239E-07	4.65441E-07	5.44082E-01
71	2.0293E-03	5.0733E-04	4.0586E-02	4.0586E-02	4.4580E-03	2.1609E-03	130.00	3.70235E-03	2.55694E-07	4.68983E-07	5.45210E-01
72	2.0367E-03	5.0917E-04	4.0734E-02	4.0734E-02	4.5191E-03	2.3639E-03	140.00	3.70235E-03	2.57521E-07	4.71586E-07	5.46075E-01
73	2.0420E-03	5.1049E-04	4.0839E-02	4.0839E-02	4.5652E-03	2.5674E-03	150.00	3.70235E-03	2.58877E-07	4.73495E-07	5.46736E-01
74	2.0457E-03	5.1143E-04	4.0914E-02	4.0914E-02	4.5999E-03	2.7712E-03	160.00	3.70235E-03	2.59880E-07	4.74894E-07	5.47238E-01
75	2.0484E-03	5.1210E-04	4.0968E-02	4.0968E-02	4.6260E-03	2.9752E-03	170.00	3.70235E-03	2.60622E-07	4.75918E-07	5.47619E-01
76	2.0503E-03	5.1258E-04	4.1006E-02	4.1006E-02	4.6454E-03	3.1793E-03	180.00	3.70234E-03	2.61169E-07	4.76666E-07	5.47906E-01
77	2.0517E-03	5.1292E-04	4.1034E-02	4.1034E-02	4.6599E-03	3.3835E-03	190.00	3.70234E-03	2.61570E-07	4.77212E-07	5.48122E-01
78	2.0527E-03	5.1317E-04	4.1053E-02	4.1053E-02	4.6707E-03	3.5877E-03	200.00	3.70234E-03	2.61866E-07	4.77611E-07	5.48283E-01
79	2.0534E-03	5.1334E-04	4.1067E-02	4.1067E-02	4.6786E-03	3.7920E-03	210.00	3.70234E-03	2.62083E-07	4.77901E-07	5.48404E-01
80	2.0539E-03	5.1347E-04	4.1077E-02	4.1077E-02	4.6845E-03	3.9962E-03	220.00	3.70234E-03	2.62242E-07	4.78112E-07	5.48494E-01
81	2.0542E-03	5.1356E-04	4.1084E-02	4.1084E-02	4.6889E-03	4.2004E-03	230.00	3.70234E-03	2.62368E-07	4.78266E-07	5.48561E-01
82	2.0545E-03	5.1362E-04	4.1090E-02	4.1090E-02	4.6921E-03	4.4046E-03	240.00	3.70234E-03	2.62443E-07	4.78378E-07	5.48610E-01
83	2.0547E-03	5.1367E-04	4.1093E-02	4.1093E-02	4.6944E-03	4.6087E-03	250.00	3.70234E-03	2.62505E-07	4.78459E-07	5.48647E-01
84	2.0548E-03	5.1370E-04	4.1096E-02	4.1096E-02	4.6962E-03	4.8128E-03	260.00	3.70234E-03	2.62550E-07	4.78518E-07	5.48674E-01
85	2.0549E-03	5.1372E-04	4.1098E-02	4.1098E-02	4.6974E-03	5.0169E-03	270.00	3.70234E-03	2.62583E-07	4.78561E-07	5.48694E-01
86	2.0549E-03	5.1374E-04	4.1099E-02	4.1099E-02	4.6984E-03	5.2209E-03	280.00	3.70234E-03	2.62607E-07	4.78592E-07	5.48709E-01
87	2.0550E-03	5.1375E-04	4.1100E-02	4.1100E-02	4.6991E-03	5.4248E-03	290.00	3.70234E-03	2.62625E-07	4.78614E-07	5.48719E-01

conc_plot / conc_plot_porevol / Implicit_FD

Figure F-4. Spreadsheet "Transport_Calc_all_colloids.xls;" Additional Calculated Solutions and Equation Terms, Iterated in Time, for Mixing Cell Colloid Model, Time 0 – 290 Years

	U	V	W	X	Y	Z	AA	AB	AC
56		Pu mass balance				Irreversible Pu mass balance			
57	flux_out/flux_in	change mass [kg]	in - out [kg]	react/decay [kg]	PU mass balance	change mass [kg]	in-out [kg]	react/decay [kg]	Irrv_Pu mass balance
58									
59	3.19060E-05	2.64418E-03	3.70254E-03	-1.05836E-03	0.00000E+00	1.05729E-03	-8.18050E-09	1.05730E-03	0.00000E+00
60	5.62289E-05	1.88823E-03	3.70236E-03	-1.81415E-03	0.00000E+00	1.81200E-03	-1.97143E-08	1.81202E-03	0.00000E+00
61	7.46685E-05	1.34840E-03	3.70226E-03	-2.35386E-03	0.00000E+00	2.35063E-03	-3.19113E-08	2.35067E-03	0.00000E+00
62	8.85810E-05	9.62903E-04	3.70217E-03	-2.73927E-03	0.00000E+00	2.73497E-03	-4.33771E-08	2.73501E-03	0.00000E+00
63	9.90342E-05	6.87616E-04	3.70211E-03	-3.01449E-03	0.00000E+00	3.00912E-03	-5.34824E-08	3.00918E-03	0.00000E+00
64	1.06859E-04	4.91032E-04	3.70207E-03	-3.21104E-03	0.00000E+00	3.20459E-03	-6.20329E-08	3.20466E-03	0.00000E+00
65	1.12698E-04	3.50650E-04	3.70204E-03	-3.35139E-03	0.00000E+00	3.34388E-03	-6.90672E-08	3.34394E-03	0.00000E+00
66	1.17042E-04	2.50402E-04	3.70201E-03	-3.45161E-03	0.00000E+00	3.44303E-03	-7.47364E-08	3.44311E-03	0.00000E+00
67	1.20266E-04	1.78814E-04	3.70200E-03	-3.52318E-03	0.00000E+00	3.51354E-03	-7.92343E-08	3.51362E-03	4.33681E-18
68	1.22652E-04	1.27692E-04	3.70199E-03	-3.57430E-03	0.00000E+00	3.56359E-03	-8.27591E-08	3.56367E-03	0.00000E+00
69	1.24415E-04	9.11861E-05	3.70198E-03	-3.61079E-03	0.00000E+00	3.59902E-03	-8.54937E-08	3.59911E-03	4.77049E-18
70	1.25715E-04	6.51167E-05	3.70197E-03	-3.63686E-03	0.00000E+00	3.62402E-03	-8.75980E-08	3.62411E-03	0.00000E+00
71	1.26672E-04	4.65003E-05	3.70197E-03	-3.65547E-03	0.00000E+00	3.64157E-03	-8.92060E-08	3.64166E-03	0.00000E+00
72	1.27375E-04	3.32062E-05	3.70197E-03	-3.66876E-03	0.00000E+00	3.65380E-03	-9.04276E-08	3.65389E-03	1.04083E-17
73	1.27890E-04	2.37128E-05	3.70196E-03	-3.67825E-03	0.00000E+00	3.66223E-03	-9.13510E-08	3.66232E-03	6.07153E-18
74	1.28268E-04	1.69336E-05	3.70196E-03	-3.68503E-03	0.00000E+00	3.66795E-03	-9.20458E-08	3.66804E-03	0.00000E+00
75	1.28545E-04	1.20924E-05	3.70196E-03	-3.68987E-03	0.00000E+00	3.67173E-03	-9.25668E-08	3.67182E-03	1.08420E-17
76	1.28747E-04	8.63525E-06	3.70196E-03	-3.69333E-03	0.00000E+00	3.67413E-03	-9.29559E-08	3.67422E-03	7.80626E-18
77	1.28895E-04	6.16650E-06	3.70196E-03	-3.69579E-03	0.00000E+00	3.67554E-03	-9.32458E-08	3.67563E-03	0.00000E+00
78	1.29002E-04	4.40354E-06	3.70196E-03	-3.69756E-03	0.00000E+00	3.67624E-03	-9.34511E-08	3.67633E-03	3.90313E-18
79	1.29081E-04	3.14460E-06	3.70196E-03	-3.69882E-03	0.00000E+00	3.67644E-03	-9.36207E-08	3.67654E-03	1.21431E-17
80	1.29138E-04	2.24559E-06	3.70196E-03	-3.69971E-03	0.00000E+00	3.67628E-03	-9.37386E-08	3.67638E-03	8.67362E-18
81	1.29179E-04	1.60359E-06	3.70196E-03	-3.70036E-03	0.00000E+00	3.67587E-03	-9.38257E-08	3.67596E-03	5.20417E-18
82	1.29209E-04	1.14514E-06	3.70196E-03	-3.70081E-03	0.00000E+00	3.67527E-03	-9.38898E-08	3.67536E-03	0.00000E+00
83	1.29231E-04	8.17751E-07	3.70196E-03	-3.70114E-03	0.00000E+00	3.67454E-03	-9.39369E-08	3.67463E-03	3.46945E-18
84	1.29247E-04	5.83962E-07	3.70196E-03	-3.70138E-03	0.00000E+00	3.67372E-03	-9.39715E-08	3.67381E-03	9.54098E-18
85	1.29259E-04	4.17012E-07	3.70196E-03	-3.70154E-03	0.00000E+00	3.67283E-03	-9.39969E-08	3.67292E-03	1.34441E-17
86	1.29267E-04	2.97791E-07	3.70196E-03	-3.70166E-03	0.00000E+00	3.67189E-03	-9.40154E-08	3.67199E-03	0.00000E+00
87	1.29273E-04	2.12655E-07	3.70196E-03	-3.70175E-03	0.00000E+00	3.67092E-03	-9.40290E-08	3.67102E-03	0.00000E+00

conc_plot / conc_plot_porevol / Implicit_FD

Figure F-5. Spreadsheet "Transport_Calc_all_colloids.xls;" Final Calculated Solutions and Equation Terms, Iterated in Time, for Mixing Cell Colloid Model, Time 0 – 290 Years

	A	B	C	D	E	F	G	H	I
88	300.00	2.05503E-07	4.11006E-08	4.03813E-03	1.23302E-07	4.11006E-09	9.39910E-08	4.42415E-02	3.7402E-04
89	310.00	2.05505E-07	4.11011E-08	4.03818E-03	1.23303E-07	4.11011E-09	9.39982E-08	4.58436E-02	3.7402E-04
90	320.00	2.05507E-07	4.11014E-08	4.03822E-03	1.23304E-07	4.11014E-09	9.40035E-08	4.74452E-02	3.7402E-04
91	330.00	2.05508E-07	4.11017E-08	4.03824E-03	1.23305E-07	4.11017E-09	9.40073E-08	4.90464E-02	3.7403E-04
92	340.00	2.05509E-07	4.11019E-08	4.03826E-03	1.23306E-07	4.11019E-09	9.40101E-08	5.06472E-02	3.7403E-04
93	350.00	2.05510E-07	4.11020E-08	4.03827E-03	1.23306E-07	4.11020E-09	9.40121E-08	5.22474E-02	3.7403E-04
94	360.00	2.05510E-07	4.11021E-08	4.03828E-03	1.23306E-07	4.11021E-09	9.40136E-08	5.38473E-02	3.7403E-04
95	370.00	2.05511E-07	4.11021E-08	4.03828E-03	1.23306E-07	4.11021E-09	9.40147E-08	5.54466E-02	3.7403E-04
96	380.00	2.05511E-07	4.11022E-08	4.03829E-03	1.23307E-07	4.11022E-09	9.40155E-08	5.70456E-02	3.7403E-04
97	390.00	2.05511E-07	4.11022E-08	4.03829E-03	1.23307E-07	4.11022E-09	9.40160E-08	5.86440E-02	3.7403E-04
98	400.00	2.05511E-07	4.11022E-08	4.03829E-03	1.23307E-07	4.11022E-09	9.40164E-08	6.02420E-02	3.7403E-04
99	410.00	2.05511E-07	4.11022E-08	4.03830E-03	1.23307E-07	4.11022E-09	9.40167E-08	6.18396E-02	3.7403E-04
100	420.00	2.05511E-07	4.11023E-08	4.03830E-03	1.23307E-07	4.11023E-09	9.40169E-08	6.34366E-02	3.7403E-04
101	430.00	2.05511E-07	4.11023E-08	4.03830E-03	1.23307E-07	4.11023E-09	9.40171E-08	6.50333E-02	3.7403E-04
102	440.00	2.05511E-07	4.11023E-08	4.03830E-03	1.23307E-07	4.11023E-09	9.40172E-08	6.66294E-02	3.7403E-04
103	450.00	2.05511E-07	4.11023E-08	4.03830E-03	1.23307E-07	4.11023E-09	9.40173E-08	6.82251E-02	3.7403E-04
104	460.00	2.05511E-07	4.11023E-08	4.03830E-03	1.23307E-07	4.11023E-09	9.40173E-08	6.98204E-02	3.7403E-04
105	470.00	2.05511E-07	4.11023E-08	4.03830E-03	1.23307E-07	4.11023E-09	9.40174E-08	7.14152E-02	3.7403E-04
106	480.00	2.05511E-07	4.11023E-08	4.03830E-03	1.23307E-07	4.11023E-09	9.40174E-08	7.30095E-02	3.7403E-04
107	490.00	2.05511E-07	4.11023E-08	4.03830E-03	1.23307E-07	4.11023E-09	9.40174E-08	7.46034E-02	3.7403E-04
108	500.00	2.05511E-07	4.11023E-08	4.03830E-03	1.23307E-07	4.11023E-09	9.40175E-08	7.61968E-02	3.7403E-04
109	510.00	2.05511E-07	4.11023E-08	4.03830E-03	1.23307E-07	4.11023E-09	9.40175E-08	7.77897E-02	3.7403E-04
110	520.00	2.05511E-07	4.11023E-08	4.03830E-03	1.23307E-07	4.11023E-09	9.40175E-08	7.93822E-02	3.7403E-04
111	530.00	2.05511E-07	4.11023E-08	4.03830E-03	1.23307E-07	4.11023E-09	9.40175E-08	8.09743E-02	3.7403E-04
112	540.00	2.05511E-07	4.11023E-08	4.03830E-03	1.23307E-07	4.11023E-09	9.40175E-08	8.25659E-02	3.7403E-04
113	550.00	2.05511E-07	4.11023E-08	4.03830E-03	1.23307E-07	4.11023E-09	9.40175E-08	8.41570E-02	3.7403E-04
114	560.00	2.05511E-07	4.11023E-08	4.03830E-03	1.23307E-07	4.11023E-09	9.40175E-08	8.57476E-02	3.7403E-04
115	570.00	2.05511E-07	4.11023E-08	4.03830E-03	1.23307E-07	4.11023E-09	9.40175E-08	8.73379E-02	3.7403E-04
116	580.00	2.05511E-07	4.11023E-08	4.03830E-03	1.23307E-07	4.11023E-09	9.40175E-08	8.89276E-02	3.7403E-04
117	590.00	2.05511E-07	4.11023E-08	4.03830E-03	1.23307E-07	4.11023E-09	9.40175E-08	9.05169E-02	3.7403E-04
118	600.00	2.05511E-07	4.11023E-08	4.03830E-03	1.23307E-07	4.11023E-09	9.40175E-08	9.21057E-02	3.7403E-04
119	610.00	2.05511E-07	4.11023E-08	4.03830E-03	1.23307E-07	4.11023E-09	9.40175E-08	9.36941E-02	3.7403E-04
120	620.00	2.05511E-07	4.11023E-08	4.03830E-03	1.23307E-07	4.11023E-09	9.40175E-08	9.52821E-02	3.7403E-04
121	630.00	2.05511E-07	4.11023E-08	4.03830E-03	1.23307E-07	4.11023E-09	9.40175E-08	9.68695E-02	3.7403E-04

conc_plot / conc_plot_porevol / Implicit_FD

Figure F-6. Spreadsheet "Transport_Calc_all_colloids.xls;" Calculated Solutions and Equation Terms, Iterated in Time, for Mixing Cell Colloid Model, Time 300 – 630 Years

	J	K	L	M	N	O	P	Q	R	S	T
88	2.0550E-03	5.1376E-04	4.1101E-02	4.1101E-02	4.6995E-03	5.6287E-03	300.00	3.70234E-03	2.62637E-07	4.78630E-07	5.48727E-01
89	2.0551E-03	5.1376E-04	4.1101E-02	4.1101E-02	4.6999E-03	5.8325E-03	310.00	3.70234E-03	2.62647E-07	4.78642E-07	5.48733E-01
90	2.0551E-03	5.1377E-04	4.1101E-02	4.1101E-02	4.7002E-03	6.0363E-03	320.00	3.70234E-03	2.62653E-07	4.78650E-07	5.48737E-01
91	2.0551E-03	5.1377E-04	4.1102E-02	4.1102E-02	4.7004E-03	6.2400E-03	330.00	3.70234E-03	2.62658E-07	4.78657E-07	5.48740E-01
92	2.0551E-03	5.1377E-04	4.1102E-02	4.1102E-02	4.7005E-03	6.4437E-03	340.00	3.70234E-03	2.62662E-07	4.78661E-07	5.48743E-01
93	2.0551E-03	5.1377E-04	4.1102E-02	4.1102E-02	4.7006E-03	6.6473E-03	350.00	3.70234E-03	2.62664E-07	4.78664E-07	5.48744E-01
94	2.0551E-03	5.1378E-04	4.1102E-02	4.1102E-02	4.7007E-03	6.8508E-03	360.00	3.70234E-03	2.62666E-07	4.78667E-07	5.48745E-01
95	2.0551E-03	5.1378E-04	4.1102E-02	4.1102E-02	4.7007E-03	7.0543E-03	370.00	3.70234E-03	2.62667E-07	4.78668E-07	5.48746E-01
96	2.0551E-03	5.1378E-04	4.1102E-02	4.1102E-02	4.7008E-03	7.2577E-03	380.00	3.70234E-03	2.62668E-07	4.78669E-07	5.48747E-01
97	2.0551E-03	5.1378E-04	4.1102E-02	4.1102E-02	4.7008E-03	7.4611E-03	390.00	3.70234E-03	2.62669E-07	4.78670E-07	5.48747E-01
98	2.0551E-03	5.1378E-04	4.1102E-02	4.1102E-02	4.7008E-03	7.6644E-03	400.00	3.70234E-03	2.62670E-07	4.78671E-07	5.48748E-01
99	2.0551E-03	5.1378E-04	4.1102E-02	4.1102E-02	4.7008E-03	7.8676E-03	410.00	3.70234E-03	2.62670E-07	4.78671E-07	5.48748E-01
100	2.0551E-03	5.1378E-04	4.1102E-02	4.1102E-02	4.7008E-03	8.0708E-03	420.00	3.70234E-03	2.62670E-07	4.78672E-07	5.48748E-01
101	2.0551E-03	5.1378E-04	4.1102E-02	4.1102E-02	4.7009E-03	8.2740E-03	430.00	3.70234E-03	2.62670E-07	4.78672E-07	5.48748E-01
102	2.0551E-03	5.1378E-04	4.1102E-02	4.1102E-02	4.7009E-03	8.4770E-03	440.00	3.70234E-03	2.62671E-07	4.78672E-07	5.48748E-01
103	2.0551E-03	5.1378E-04	4.1102E-02	4.1102E-02	4.7009E-03	8.6800E-03	450.00	3.70234E-03	2.62671E-07	4.78672E-07	5.48748E-01
104	2.0551E-03	5.1378E-04	4.1102E-02	4.1102E-02	4.7009E-03	8.8830E-03	460.00	3.70234E-03	2.62671E-07	4.78672E-07	5.48749E-01
105	2.0551E-03	5.1378E-04	4.1102E-02	4.1102E-02	4.7009E-03	9.0859E-03	470.00	3.70234E-03	2.62671E-07	4.78672E-07	5.48749E-01
106	2.0551E-03	5.1378E-04	4.1102E-02	4.1102E-02	4.7009E-03	9.2887E-03	480.00	3.70234E-03	2.62671E-07	4.78672E-07	5.48749E-01
107	2.0551E-03	5.1378E-04	4.1102E-02	4.1102E-02	4.7009E-03	9.4915E-03	490.00	3.70234E-03	2.62671E-07	4.78672E-07	5.48749E-01
108	2.0551E-03	5.1378E-04	4.1102E-02	4.1102E-02	4.7009E-03	9.6942E-03	500.00	3.70234E-03	2.62671E-07	4.78672E-07	5.48749E-01
109	2.0551E-03	5.1378E-04	4.1102E-02	4.1102E-02	4.7009E-03	9.8969E-03	510.00	3.70234E-03	2.62671E-07	4.78672E-07	5.48749E-01
110	2.0551E-03	5.1378E-04	4.1102E-02	4.1102E-02	4.7009E-03	1.0100E-02	520.00	3.70234E-03	2.62671E-07	4.78672E-07	5.48749E-01
111	2.0551E-03	5.1378E-04	4.1102E-02	4.1102E-02	4.7009E-03	1.0302E-02	530.00	3.70234E-03	2.62671E-07	4.78672E-07	5.48749E-01
112	2.0551E-03	5.1378E-04	4.1102E-02	4.1102E-02	4.7009E-03	1.0505E-02	540.00	3.70234E-03	2.62671E-07	4.78673E-07	5.48749E-01
113	2.0551E-03	5.1378E-04	4.1102E-02	4.1102E-02	4.7009E-03	1.0707E-02	550.00	3.70234E-03	2.62671E-07	4.78673E-07	5.48749E-01
114	2.0551E-03	5.1378E-04	4.1102E-02	4.1102E-02	4.7009E-03	1.0909E-02	560.00	3.70234E-03	2.62671E-07	4.78673E-07	5.48749E-01
115	2.0551E-03	5.1378E-04	4.1102E-02	4.1102E-02	4.7009E-03	1.1112E-02	570.00	3.70234E-03	2.62671E-07	4.78673E-07	5.48749E-01
116	2.0551E-03	5.1378E-04	4.1102E-02	4.1102E-02	4.7009E-03	1.1314E-02	580.00	3.70234E-03	2.62671E-07	4.78673E-07	5.48749E-01
117	2.0551E-03	5.1378E-04	4.1102E-02	4.1102E-02	4.7009E-03	1.1516E-02	590.00	3.70234E-03	2.62671E-07	4.78673E-07	5.48749E-01
118	2.0551E-03	5.1378E-04	4.1102E-02	4.1102E-02	4.7009E-03	1.1718E-02	600.00	3.70234E-03	2.62671E-07	4.78673E-07	5.48749E-01
119	2.0551E-03	5.1378E-04	4.1102E-02	4.1102E-02	4.7009E-03	1.1920E-02	610.00	3.70234E-03	2.62671E-07	4.78673E-07	5.48749E-01
120	2.0551E-03	5.1378E-04	4.1102E-02	4.1102E-02	4.7009E-03	1.2122E-02	620.00	3.70234E-03	2.62671E-07	4.78673E-07	5.48749E-01
121	2.0551E-03	5.1378E-04	4.1102E-02	4.1102E-02	4.7009E-03	1.2324E-02	630.00	3.70234E-03	2.62671E-07	4.78673E-07	5.48749E-01

conc_plot / conc_plot_porevol / Implicit_FD

Figure F-7. Spreadsheet "Transport_Calc_all_colloids.xls;" Additional Calculated Solutions and Equation Terms, Iterated in Time, for Mixing Cell Colloid Model, Time 300 – 630 Years

	U	V	W	X	Y	Z	AA	AB	AC
88	1.29278E-04	1.51859E-07	3.70196E-03	-3.70181E-03	0.00000E+00	3.66993E-03	-9.40389E-08	3.67002E-03	0.00000E+00
89	1.29281E-04	1.08443E-07	3.70196E-03	-3.70185E-03	0.00000E+00	3.66892E-03	-9.40462E-08	3.66901E-03	8.23994E-18
90	1.29283E-04	7.74403E-08	3.70196E-03	-3.70188E-03	0.00000E+00	3.66789E-03	-9.40515E-08	3.66799E-03	1.60462E-17
91	1.29285E-04	5.53007E-08	3.70196E-03	-3.70190E-03	0.00000E+00	3.66686E-03	-9.40553E-08	3.66695E-03	9.97456E-18
92	1.29286E-04	3.94907E-08	3.70196E-03	-3.70192E-03	0.00000E+00	3.66582E-03	-9.40581E-08	3.66592E-03	1.47451E-17
93	1.29287E-04	2.82006E-08	3.70196E-03	-3.70193E-03	0.00000E+00	3.66478E-03	-9.40601E-08	3.66487E-03	9.97456E-18
94	1.29287E-04	2.01383E-08	3.70196E-03	-3.70194E-03	0.00000E+00	3.66373E-03	-9.40616E-08	3.66383E-03	2.03830E-17
95	1.29288E-04	1.43809E-08	3.70196E-03	-3.70194E-03	0.00000E+00	3.66269E-03	-9.40627E-08	3.66278E-03	6.07153E-18
96	1.29288E-04	1.02695E-08	3.70196E-03	-3.70195E-03	0.00000E+00	3.66164E-03	-9.40634E-08	3.66173E-03	1.43115E-17
97	1.29288E-04	7.33053E-09	3.70196E-03	-3.70195E-03	0.00000E+00	3.66059E-03	-9.40640E-08	3.66068E-03	1.64799E-17
98	1.29289E-04	5.23693E-09	3.70196E-03	-3.70195E-03	0.00000E+00	3.65954E-03	-9.40644E-08	3.65963E-03	1.73472E-17
99	1.29289E-04	3.73973E-09	3.70196E-03	-3.70196E-03	0.00000E+00	3.65849E-03	-9.40647E-08	3.65858E-03	6.93889E-18
100	1.29289E-04	2.67057E-09	3.70196E-03	-3.70196E-03	0.00000E+00	3.65744E-03	-9.40649E-08	3.65753E-03	0.00000E+00
101	1.29289E-04	1.90708E-09	3.70196E-03	-3.70196E-03	0.00000E+00	3.65639E-03	-9.40651E-08	3.65648E-03	7.37257E-18
102	1.29289E-04	1.36186E-09	3.70196E-03	-3.70196E-03	0.00000E+00	3.65534E-03	-9.40652E-08	3.65543E-03	-8.23994E-18
103	1.29289E-04	9.72513E-10	3.70196E-03	-3.70196E-03	0.00000E+00	3.65429E-03	-9.40653E-08	3.65438E-03	2.90566E-17
104	1.29289E-04	6.94479E-10	3.70196E-03	-3.70196E-03	0.00000E+00	3.65324E-03	-9.40653E-08	3.65333E-03	5.63785E-18
105	1.29289E-04	4.95933E-10	3.70196E-03	-3.70196E-03	0.00000E+00	3.65219E-03	-9.40654E-08	3.65228E-03	0.00000E+00
106	1.29289E-04	3.54150E-10	3.70196E-03	-3.70196E-03	0.00000E+00	3.65114E-03	-9.40654E-08	3.65123E-03	-4.77049E-18
107	1.29289E-04	2.52901E-10	3.70196E-03	-3.70196E-03	0.00000E+00	3.65009E-03	-9.40654E-08	3.65018E-03	5.20417E-18
108	1.29289E-04	1.80599E-10	3.70196E-03	-3.70196E-03	0.00000E+00	3.64904E-03	-9.40654E-08	3.64913E-03	2.16840E-17
109	1.29289E-04	1.28967E-10	3.70196E-03	-3.70196E-03	0.00000E+00	3.64799E-03	-9.40655E-08	3.64808E-03	1.25767E-17
110	1.29289E-04	9.20962E-11	3.70196E-03	-3.70196E-03	0.00000E+00	3.64694E-03	-9.40655E-08	3.64704E-03	1.55125E-17
111	1.29289E-04	6.57666E-11	3.70196E-03	-3.70196E-03	0.00000E+00	3.64589E-03	-9.40655E-08	3.64599E-03	3.20924E-17
112	1.29289E-04	4.69644E-11	3.70196E-03	-3.70196E-03	0.00000E+00	3.64485E-03	-9.40655E-08	3.64494E-03	3.90313E-18
113	1.29289E-04	3.35377E-11	3.70196E-03	-3.70196E-03	0.00000E+00	3.64380E-03	-9.40655E-08	3.64389E-03	3.07913E-17
114	1.29289E-04	2.39495E-11	3.70196E-03	-3.70196E-03	0.00000E+00	3.64275E-03	-9.40655E-08	3.64285E-03	-4.77049E-18
115	1.29289E-04	1.71025E-11	3.70196E-03	-3.70196E-03	0.00000E+00	3.64170E-03	-9.40655E-08	3.64180E-03	1.30104E-17
116	1.29289E-04	1.22130E-11	3.70196E-03	-3.70196E-03	0.00000E+00	3.64066E-03	-9.40655E-08	3.64075E-03	3.20924E-17
117	1.29289E-04	8.72143E-12	3.70196E-03	-3.70196E-03	0.00000E+00	3.63961E-03	-9.40655E-08	3.63971E-03	4.42354E-17
118	1.29289E-04	6.22804E-12	3.70196E-03	-3.70196E-03	0.00000E+00	3.63857E-03	-9.40655E-08	3.63866E-03	1.30104E-17
119	1.29289E-04	4.44749E-12	3.70196E-03	-3.70196E-03	0.00000E+00	3.63752E-03	-9.40655E-08	3.63761E-03	7.37257E-18
120	1.29289E-04	3.17599E-12	3.70196E-03	-3.70196E-03	0.00000E+00	3.63647E-03	-9.40655E-08	3.63657E-03	0.00000E+00
121	1.29289E-04	2.26800E-12	3.70196E-03	-3.70196E-03	0.00000E+00	3.63543E-03	-9.40655E-08	3.63552E-03	1.82146E-17

conc_plot / conc_plot_porevol \ Implicit_FD /

Figure F-8. Spreadsheet "Transport_Calc_all_colloids.xls;" Final Calculated Solutions and Equation Terms, Iterated in Time, for Mixing Cell Colloid Model, Time 300 – 630 Years

	A	B	C	D	E	F	G	H	I
122	640.00	2.05611E-07	4.11023E-08	4.03830E-03	1.23307E-07	4.11023E-09	9.40175E-08	9.84565E-02	3.7403E-04
123	650.00	2.05611E-07	4.11023E-08	4.03830E-03	1.23307E-07	4.11023E-09	9.40175E-08	1.00043E-01	3.7403E-04
124	660.00	2.05611E-07	4.11023E-08	4.03830E-03	1.23307E-07	4.11023E-09	9.40175E-08	1.01629E-01	3.7403E-04
125	670.00	2.05611E-07	4.11023E-08	4.03830E-03	1.23307E-07	4.11023E-09	9.40175E-08	1.03215E-01	3.7403E-04
126	680.00	2.05611E-07	4.11023E-08	4.03830E-03	1.23307E-07	4.11023E-09	9.40175E-08	1.04800E-01	3.7403E-04
127	690.00	2.05611E-07	4.11023E-08	4.03830E-03	1.23307E-07	4.11023E-09	9.40175E-08	1.06385E-01	3.7403E-04
128	700.00	2.05611E-07	4.11023E-08	4.03830E-03	1.23307E-07	4.11023E-09	9.40175E-08	1.07969E-01	3.7403E-04
129	710.00	2.05611E-07	4.11023E-08	4.03830E-03	1.23307E-07	4.11023E-09	9.40175E-08	1.09553E-01	3.7403E-04
130	720.00	2.05611E-07	4.11023E-08	4.03830E-03	1.23307E-07	4.11023E-09	9.40175E-08	1.11136E-01	3.7403E-04
131	730.00	2.05611E-07	4.11023E-08	4.03830E-03	1.23307E-07	4.11023E-09	9.40175E-08	1.12719E-01	3.7403E-04
132	740.00	2.05611E-07	4.11023E-08	4.03830E-03	1.23307E-07	4.11023E-09	9.40175E-08	1.14302E-01	3.7403E-04
133	750.00	2.05611E-07	4.11023E-08	4.03830E-03	1.23307E-07	4.11023E-09	9.40175E-08	1.15884E-01	3.7403E-04
134	760.00	2.05611E-07	4.11023E-08	4.03830E-03	1.23307E-07	4.11023E-09	9.40175E-08	1.17465E-01	3.7403E-04
135	770.00	2.05611E-07	4.11023E-08	4.03830E-03	1.23307E-07	4.11023E-09	9.40175E-08	1.19046E-01	3.7403E-04
136	780.00	2.05611E-07	4.11023E-08	4.03830E-03	1.23307E-07	4.11023E-09	9.40175E-08	1.20627E-01	3.7403E-04
137	790.00	2.05611E-07	4.11023E-08	4.03830E-03	1.23307E-07	4.11023E-09	9.40175E-08	1.22207E-01	3.7403E-04
138	800.00	2.05611E-07	4.11023E-08	4.03830E-03	1.23307E-07	4.11023E-09	9.40175E-08	1.23787E-01	3.7403E-04
139	810.00	2.05611E-07	4.11023E-08	4.03830E-03	1.23307E-07	4.11023E-09	9.40175E-08	1.25366E-01	3.7403E-04
140	820.00	2.05611E-07	4.11023E-08	4.03830E-03	1.23307E-07	4.11023E-09	9.40175E-08	1.26945E-01	3.7403E-04
141	830.00	2.05611E-07	4.11023E-08	4.03830E-03	1.23307E-07	4.11023E-09	9.40175E-08	1.28523E-01	3.7403E-04
142	840.00	2.05611E-07	4.11023E-08	4.03830E-03	1.23307E-07	4.11023E-09	9.40175E-08	1.30101E-01	3.7403E-04
143	850.00	2.05611E-07	4.11023E-08	4.03830E-03	1.23307E-07	4.11023E-09	9.40175E-08	1.31679E-01	3.7403E-04
144	860.00	2.05611E-07	4.11023E-08	4.03830E-03	1.23307E-07	4.11023E-09	9.40175E-08	1.33256E-01	3.7403E-04
145	870.00	2.05611E-07	4.11023E-08	4.03830E-03	1.23307E-07	4.11023E-09	9.40175E-08	1.34832E-01	3.7403E-04
146	880.00	2.05611E-07	4.11023E-08	4.03830E-03	1.23307E-07	4.11023E-09	9.40175E-08	1.36408E-01	3.7403E-04
147	890.00	2.05611E-07	4.11023E-08	4.03830E-03	1.23307E-07	4.11023E-09	9.40175E-08	1.37984E-01	3.7403E-04
148	900.00	2.05611E-07	4.11023E-08	4.03830E-03	1.23307E-07	4.11023E-09	9.40175E-08	1.39559E-01	3.7403E-04
149	910.00	2.05611E-07	4.11023E-08	4.03830E-03	1.23307E-07	4.11023E-09	9.40175E-08	1.41134E-01	3.7403E-04
150	920.00	2.05611E-07	4.11023E-08	4.03830E-03	1.23307E-07	4.11023E-09	9.40175E-08	1.42708E-01	3.7403E-04
151	930.00	2.05611E-07	4.11023E-08	4.03830E-03	1.23307E-07	4.11023E-09	9.40175E-08	1.44282E-01	3.7403E-04
152	940.00	2.05611E-07	4.11023E-08	4.03830E-03	1.23307E-07	4.11023E-09	9.40175E-08	1.45856E-01	3.7403E-04
153	950.00	2.05611E-07	4.11023E-08	4.03830E-03	1.23307E-07	4.11023E-09	9.40175E-08	1.47428E-01	3.7403E-04
154	960.00	2.05611E-07	4.11023E-08	4.03830E-03	1.23307E-07	4.11023E-09	9.40175E-08	1.49001E-01	3.7403E-04
155	970.00	2.05611E-07	4.11023E-08	4.03830E-03	1.23307E-07	4.11023E-09	9.40175E-08	1.50573E-01	3.7403E-04

conc_plot / conc_plot_porevol \ Implicit_FD /

Figure F-9. Spreadsheet "Transport_Calc_all_colloids.xls;" Calculated Solutions and Equation Terms, Iterated in Time, for Mixing Cell Colloid Model, Time 640 – 970 Years

	I	J	K	L	M	N	O	P	Q	R	S	T
122		2.0551E-03	5.1378E-04	4.1102E-02	4.1102E-02	4.7009E-03	1.2526E-02	640.00	3.70234E-03	2.62671E-07	4.78673E-07	5.48749E-01
123		2.0551E-03	5.1378E-04	4.1102E-02	4.1102E-02	4.7009E-03	1.2728E-02	650.00	3.70234E-03	2.62671E-07	4.78673E-07	5.48749E-01
124		2.0551E-03	5.1378E-04	4.1102E-02	4.1102E-02	4.7009E-03	1.2930E-02	660.00	3.70234E-03	2.62671E-07	4.78673E-07	5.48749E-01
125		2.0551E-03	5.1378E-04	4.1102E-02	4.1102E-02	4.7009E-03	1.3132E-02	670.00	3.70234E-03	2.62671E-07	4.78673E-07	5.48749E-01
126		2.0551E-03	5.1378E-04	4.1102E-02	4.1102E-02	4.7009E-03	1.3333E-02	680.00	3.70234E-03	2.62671E-07	4.78673E-07	5.48749E-01
127		2.0551E-03	5.1378E-04	4.1102E-02	4.1102E-02	4.7009E-03	1.3535E-02	690.00	3.70234E-03	2.62671E-07	4.78673E-07	5.48749E-01
128		2.0551E-03	5.1378E-04	4.1102E-02	4.1102E-02	4.7009E-03	1.3737E-02	700.00	3.70234E-03	2.62671E-07	4.78673E-07	5.48749E-01
129		2.0551E-03	5.1378E-04	4.1102E-02	4.1102E-02	4.7009E-03	1.3938E-02	710.00	3.70234E-03	2.62671E-07	4.78673E-07	5.48749E-01
130		2.0551E-03	5.1378E-04	4.1102E-02	4.1102E-02	4.7009E-03	1.4139E-02	720.00	3.70234E-03	2.62671E-07	4.78673E-07	5.48749E-01
131		2.0551E-03	5.1378E-04	4.1102E-02	4.1102E-02	4.7009E-03	1.4341E-02	730.00	3.70234E-03	2.62671E-07	4.78673E-07	5.48749E-01
132		2.0551E-03	5.1378E-04	4.1102E-02	4.1102E-02	4.7009E-03	1.4542E-02	740.00	3.70234E-03	2.62671E-07	4.78673E-07	5.48749E-01
133		2.0551E-03	5.1378E-04	4.1102E-02	4.1102E-02	4.7009E-03	1.4743E-02	750.00	3.70234E-03	2.62671E-07	4.78673E-07	5.48749E-01
134		2.0551E-03	5.1378E-04	4.1102E-02	4.1102E-02	4.7009E-03	1.4945E-02	760.00	3.70234E-03	2.62671E-07	4.78673E-07	5.48749E-01
135		2.0551E-03	5.1378E-04	4.1102E-02	4.1102E-02	4.7009E-03	1.5146E-02	770.00	3.70234E-03	2.62671E-07	4.78673E-07	5.48749E-01
136		2.0551E-03	5.1378E-04	4.1102E-02	4.1102E-02	4.7009E-03	1.5347E-02	780.00	3.70234E-03	2.62671E-07	4.78673E-07	5.48749E-01
137		2.0551E-03	5.1378E-04	4.1102E-02	4.1102E-02	4.7009E-03	1.5548E-02	790.00	3.70234E-03	2.62671E-07	4.78673E-07	5.48749E-01
138		2.0551E-03	5.1378E-04	4.1102E-02	4.1102E-02	4.7009E-03	1.5749E-02	800.00	3.70234E-03	2.62671E-07	4.78673E-07	5.48749E-01
139		2.0551E-03	5.1378E-04	4.1102E-02	4.1102E-02	4.7009E-03	1.5950E-02	810.00	3.70234E-03	2.62671E-07	4.78673E-07	5.48749E-01
140		2.0551E-03	5.1378E-04	4.1102E-02	4.1102E-02	4.7009E-03	1.6151E-02	820.00	3.70234E-03	2.62671E-07	4.78673E-07	5.48749E-01
141		2.0551E-03	5.1378E-04	4.1102E-02	4.1102E-02	4.7009E-03	1.6352E-02	830.00	3.70234E-03	2.62671E-07	4.78673E-07	5.48749E-01
142		2.0551E-03	5.1378E-04	4.1102E-02	4.1102E-02	4.7009E-03	1.6552E-02	840.00	3.70234E-03	2.62671E-07	4.78673E-07	5.48749E-01
143		2.0551E-03	5.1378E-04	4.1102E-02	4.1102E-02	4.7009E-03	1.6753E-02	850.00	3.70234E-03	2.62671E-07	4.78673E-07	5.48749E-01
144		2.0551E-03	5.1378E-04	4.1102E-02	4.1102E-02	4.7009E-03	1.6954E-02	860.00	3.70234E-03	2.62671E-07	4.78673E-07	5.48749E-01
145		2.0551E-03	5.1378E-04	4.1102E-02	4.1102E-02	4.7009E-03	1.7154E-02	870.00	3.70234E-03	2.62671E-07	4.78673E-07	5.48749E-01
146		2.0551E-03	5.1378E-04	4.1102E-02	4.1102E-02	4.7009E-03	1.7355E-02	880.00	3.70234E-03	2.62671E-07	4.78673E-07	5.48749E-01
147		2.0551E-03	5.1378E-04	4.1102E-02	4.1102E-02	4.7009E-03	1.7555E-02	890.00	3.70234E-03	2.62671E-07	4.78673E-07	5.48749E-01
148		2.0551E-03	5.1378E-04	4.1102E-02	4.1102E-02	4.7009E-03	1.7756E-02	900.00	3.70234E-03	2.62671E-07	4.78673E-07	5.48749E-01
149		2.0551E-03	5.1378E-04	4.1102E-02	4.1102E-02	4.7009E-03	1.7956E-02	910.00	3.70234E-03	2.62671E-07	4.78673E-07	5.48749E-01
150		2.0551E-03	5.1378E-04	4.1102E-02	4.1102E-02	4.7009E-03	1.8156E-02	920.00	3.70234E-03	2.62671E-07	4.78673E-07	5.48749E-01
151		2.0551E-03	5.1378E-04	4.1102E-02	4.1102E-02	4.7009E-03	1.8356E-02	930.00	3.70234E-03	2.62671E-07	4.78673E-07	5.48749E-01
152		2.0551E-03	5.1378E-04	4.1102E-02	4.1102E-02	4.7009E-03	1.8557E-02	940.00	3.70234E-03	2.62671E-07	4.78673E-07	5.48749E-01
153		2.0551E-03	5.1378E-04	4.1102E-02	4.1102E-02	4.7009E-03	1.8757E-02	950.00	3.70234E-03	2.62671E-07	4.78673E-07	5.48749E-01
154		2.0551E-03	5.1378E-04	4.1102E-02	4.1102E-02	4.7009E-03	1.8957E-02	960.00	3.70234E-03	2.62671E-07	4.78673E-07	5.48749E-01
155		2.0551E-03	5.1378E-04	4.1102E-02	4.1102E-02	4.7009E-03	1.9157E-02	970.00	3.70234E-03	2.62671E-07	4.78673E-07	5.48749E-01

conc_plot / conc_plot_porevol / Implicit_FD

Figure F-10. Spreadsheet "Transport_Calc_all_colloids.xls;" Additional Calculated Solutions and Equation Terms, Iterated in Time, for Mixing Cell Colloid Model, Time 640 – 970 Years

	U	V	W	X	Y	Z	AA	AB	AC
122	1.29289E-04	1.61959E-12	3.70196E-03	-3.70196E-03	0.00000E+00	3.63436E-03	-9.40655E-08	3.63448E-03	1.12757E-17
123	1.29289E-04	1.15657E-12	3.70196E-03	-3.70196E-03	0.00000E+00	3.63334E-03	-9.40655E-08	3.63343E-03	7.37257E-18
124	1.29289E-04	8.25913E-13	3.70196E-03	-3.70196E-03	0.00000E+00	3.63230E-03	-9.40655E-08	3.63239E-03	-5.20417E-18
125	1.29289E-04	5.89790E-13	3.70196E-03	-3.70196E-03	0.00000E+00	3.63125E-03	-9.40655E-08	3.63135E-03	2.08167E-17
126	1.29289E-04	4.21174E-13	3.70196E-03	-3.70196E-03	0.00000E+00	3.63021E-03	-9.40655E-08	3.63030E-03	2.55872E-17
127	1.29289E-04	3.00763E-13	3.70196E-03	-3.70196E-03	0.00000E+00	3.62916E-03	-9.40655E-08	3.62926E-03	1.99493E-17
128	1.29289E-04	2.14777E-13	3.70196E-03	-3.70196E-03	0.00000E+00	3.62812E-03	-9.40655E-08	3.62822E-03	3.98986E-17
129	1.29289E-04	1.53374E-13	3.70196E-03	-3.70196E-03	0.00000E+00	3.62708E-03	-9.40655E-08	3.62717E-03	0.00000E+00
130	1.29289E-04	1.09526E-13	3.70196E-03	-3.70196E-03	0.00000E+00	3.62604E-03	-9.40655E-08	3.62613E-03	-4.77049E-18
131	1.29289E-04	7.82126E-14	3.70196E-03	-3.70196E-03	0.00000E+00	3.62499E-03	-9.40655E-08	3.62509E-03	8.67362E-18
132	1.29289E-04	5.58527E-14	3.70196E-03	-3.70196E-03	0.00000E+00	3.62395E-03	-9.40655E-08	3.62405E-03	6.93889E-18
133	1.29289E-04	3.98851E-14	3.70196E-03	-3.70196E-03	0.00000E+00	3.62291E-03	-9.40655E-08	3.62300E-03	2.38524E-17
134	1.29289E-04	2.84826E-14	3.70196E-03	-3.70196E-03	0.00000E+00	3.62187E-03	-9.40655E-08	3.62196E-03	1.77809E-17
135	1.29289E-04	2.03379E-14	3.70196E-03	-3.70196E-03	0.00000E+00	3.62083E-03	-9.40655E-08	3.62092E-03	2.21177E-17
136	1.29289E-04	1.45254E-14	3.70196E-03	-3.70196E-03	0.00000E+00	3.61979E-03	-9.40655E-08	3.61988E-03	4.20670E-17
137	1.29289E-04	1.03735E-14	3.70196E-03	-3.70196E-03	0.00000E+00	3.61875E-03	-9.40655E-08	3.61884E-03	5.63785E-18
138	1.29289E-04	7.40570E-15	3.70196E-03	-3.70196E-03	0.00000E+00	3.61771E-03	-9.40655E-08	3.61780E-03	3.90313E-17
139	1.29289E-04	5.28809E-15	3.70196E-03	-3.70196E-03	0.00000E+00	3.61667E-03	-9.40655E-08	3.61676E-03	2.73219E-17
140	1.29289E-04	3.77834E-15	3.70196E-03	-3.70196E-03	0.00000E+00	3.61563E-03	-9.40655E-08	3.61572E-03	2.47198E-17
141	1.29289E-04	2.69569E-15	3.70196E-03	-3.70196E-03	0.00000E+00	3.61459E-03	-9.40655E-08	3.61468E-03	3.64292E-17
142	1.29289E-04	1.92691E-15	3.70196E-03	-3.70196E-03	0.00000E+00	3.61355E-03	-9.40655E-08	3.61364E-03	2.55872E-17
143	1.29289E-04	1.37665E-15	3.70196E-03	-3.70196E-03	0.00000E+00	3.61251E-03	-9.40655E-08	3.61261E-03	6.46184E-17
144	1.29289E-04	9.81335E-16	3.70196E-03	-3.70196E-03	0.00000E+00	3.61147E-03	-9.40655E-08	3.61157E-03	3.33934E-17
145	1.29289E-04	7.01238E-16	3.70196E-03	-3.70196E-03	0.00000E+00	3.61043E-03	-9.40655E-08	3.61053E-03	-3.90313E-18
146	1.29289E-04	5.00600E-16	3.70196E-03	-3.70196E-03	0.00000E+00	3.60940E-03	-9.40655E-08	3.60949E-03	7.37257E-18
147	1.29289E-04	3.57572E-16	3.70196E-03	-3.70196E-03	0.00000E+00	3.60836E-03	-9.40655E-08	3.60845E-03	3.94650E-17
148	1.29289E-04	2.55260E-16	3.70196E-03	-3.70196E-03	0.00000E+00	3.60732E-03	-9.40655E-08	3.60742E-03	4.77049E-17
149	1.29289E-04	1.82759E-16	3.70196E-03	-3.70196E-03	0.00000E+00	3.60629E-03	-9.40655E-08	3.60638E-03	3.33934E-17
150	1.29289E-04	1.29123E-16	3.70196E-03	-3.70196E-03	0.00000E+00	3.60525E-03	-9.40655E-08	3.60534E-03	3.72966E-17
151	1.29289E-04	9.33659E-17	3.70196E-03	-3.70196E-03	0.00000E+00	3.60421E-03	-9.40655E-08	3.60431E-03	7.97973E-17
152	1.29289E-04	6.55549E-17	3.70196E-03	-3.70196E-03	0.00000E+00	3.60318E-03	-9.40655E-08	3.60327E-03	2.99240E-17
153	1.29289E-04	4.76762E-17	3.70196E-03	-3.70196E-03	0.00000E+00	3.60214E-03	-9.40655E-08	3.60224E-03	-1.43115E-17
154	1.29289E-04	3.37706E-17	3.70196E-03	-3.70196E-03	0.00000E+00	3.60111E-03	-9.40655E-08	3.60120E-03	2.60209E-17
155	1.29289E-04	2.36381E-17	3.70196E-03	-3.70196E-03	0.00000E+00	3.60007E-03	-9.40655E-08	3.60017E-03	1.38778E-17

conc_plot / conc_plot_porevol / Implicit_FD

Figure F-11. Spreadsheet "Transport_Calc_all_colloids.xls;" Final Calculated Solutions and Equation Terms, Iterated in Time, for Mixing Cell Colloid Model, Time 640 – 970 Years

	A	B	C	D	E	F	G	H	I
156	980.00	2.05511E-07	4.11023E-08	4.03830E-03	1.23307E-07	4.11023E-09	9.40175E-08	1.52144E-01	3.7403E-04
157	990.00	2.05511E-07	4.11023E-08	4.03830E-03	1.23307E-07	4.11023E-09	9.40175E-08	1.53716E-01	3.7403E-04
158	1000.00	2.05511E-07	4.11023E-08	4.03830E-03	1.23307E-07	4.11023E-09	9.40175E-08	1.55286E-01	3.7403E-04
159									

Figure F-12. Spreadsheet "Transport_Calc_all_colloids.xls;" Calculated Solutions and Equation Terms, Iterated in Time, for Mixing Cell Colloid Model, Time 980 – 1000 Years

	J	K	L	M	N	O	P	Q	R	S	T
156	2.0551E-03	5.1378E-04	4.1102E-02	4.1102E-02	4.7009E-03	1.9357E-02	980.00	3.70234E-03	2.62671E-07	4.78673E-07	5.48749E-01
157	2.0551E-03	5.1378E-04	4.1102E-02	4.1102E-02	4.7009E-03	1.9557E-02	990.00	3.70234E-03	2.62671E-07	4.78673E-07	5.48749E-01
158	2.0551E-03	5.1378E-04	4.1102E-02	4.1102E-02	4.7009E-03	1.9757E-02	1000.00	3.70234E-03	2.62671E-07	4.78673E-07	5.48749E-01
159											

Figure F-13. Spreadsheet "Transport_Calc_all_colloids.xls;" Additional Calculated Solutions and Equation Terms, Iterated in Time, for Mixing Cell Colloid Model, Time 980 – 1000 Years

	U	V	W	X	Y	Z	AA	AB	AC
156	1.29289E-04	1.78786E-17	3.70196E-03	-3.70196E-03	0.00000E+00	3.59904E-03	-9.40655E-08	3.59913E-03	3.94650E-17
157	1.29289E-04	1.19191E-17	3.70196E-03	-3.70196E-03	0.00000E+00	3.59800E-03	-9.40655E-08	3.59810E-03	4.25007E-17
158	1.29289E-04	9.93245E-18	3.70196E-03	-3.70196E-03	0.00000E+00	3.59697E-03	-9.40655E-08	3.59706E-03	3.90313E-18
159									

Figure F-14. Spreadsheet "Transport_Calc_all_colloids.xls;" Final Calculated Solutions and Equation Terms, Iterated in Time, for Mixing Cell Colloid Model, Time 980 – 1000 Years

SPREADSHEET "FLUX_OUT_RATIO.XLS"

The purpose of this spreadsheet is to demonstrate the use of the irreversible linear reaction rate constant to fit a specified flux out ratio. The spreadsheet calculates and plots the figures "Limiting Flux Out Ratio as a function of Irreversible Reaction Rate" and "Linear reaction rate from colloid to total flux out ratio."

The calculations for flux out ratio as a function of k, linear irreversible reaction rate, are done in Worksheet "adv_diff_decay." The calculations for k as a function of flux out ratio are done in Worksheet "K-surface." This description refers to equations from Appendix B, "Implementation of Radionuclide Sorption onto Colloidal and Stationary Phases with Finite Difference Solution."

Description of Input Values

The first 29 rows of the worksheet contain the input data values with the exception of Row 12, where pore volume is computed. Column D contains input values typical of the TSPA-LA. Column B contains values from Column D that are scaled for unit conversion of mass (kg), length (m), and time (yr). An image of the first 31 rows of the Microsoft Excel spreadsheet is shown in Figure F-15.

<u>Row 2</u>: c_s [kg/m^3]

c_s (mg L^{-1}) = Pu solubility

$B$2=$D$2/1000

Row 3: phi_1

ϕ_1, porosity of the waste form cell_1

$B$3=$D$3

Row 4: phi_2

ϕ_2, porosity of the corrosion product mass in waste form cell_2

$B$4=$D$4

Row 5: phi_3

ϕ_3, porosity of the invert

$B$5=$D$5

Row 6: u [m^3/yr]

u, volumetric water flux

$B$6=$D$6

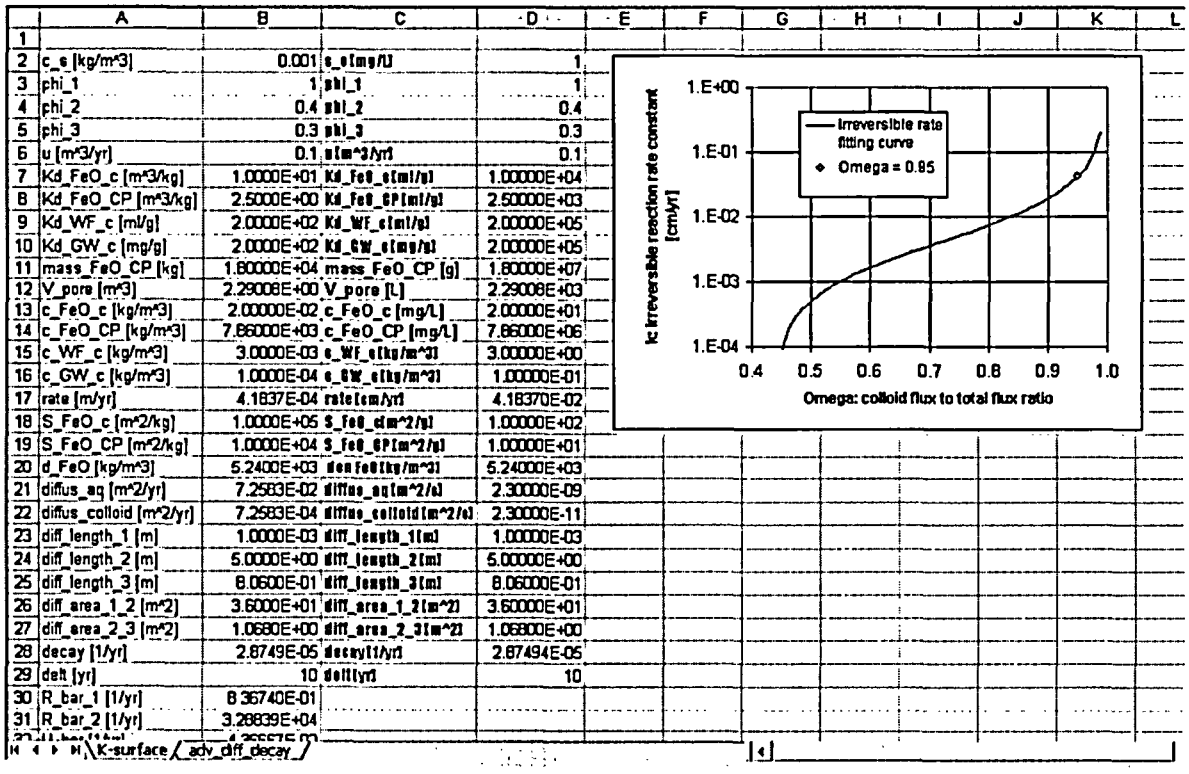

	A	B	C	D
1				
2	c_s [kg/m^3]	0.001	c_s [mg/l]	1
3	phi_1	1	phi_1	1
4	phi_2	0.4	phi_2	0.4
5	phi_3	0.3	phi_3	0.3
6	u [m^3/yr]	0.1	u [m^3/yr]	0.1
7	Kd_FeO_c [m^3/kg]	1.0000E+01	Kd_FeO_c [ml/g]	1.00000E+04
8	Kd_FeO_CP [m^3/kg]	2.5000E+00	Kd_FeO_CP [ml/g]	2.50000E+03
9	Kd_WF_c [ml/g]	2.0000E+02	Kd_WF_c [ml/g]	2.00000E+05
10	Kd_GW_c [mg/g]	2.0000E+02	Kd_GW_c [mg/g]	2.00000E+05
11	mass_FeO_CP [kg]	1.80000E+04	mass_FeO_CP [g]	1.80000E+07
12	V_pore [m^3]	2.29008E+00	V_pore [L]	2.29008E+03
13	c_FeO_c [kg/m^3]	2.00000E-02	c_FeO_c [mg/L]	2.00000E+01
14	c_FeO_CP [kg/m^3]	7.86000E+03	c_FeO_CP [mg/L]	7.86000E+06
15	c_WF_c [kg/m^3]	3.0000E-03	c_WF_c [kg/m^3]	3.00000E+00
16	c_GW_c [kg/m^3]	1.0000E-04	c_GW_c [kg/m^3]	1.00000E-01
17	rate [m/yr]	4.1837E-04	rate [cm/yr]	4.18370E-02
18	S_FeO_c [m^2/kg]	1.0000E+05	S_FeO_c [m^2/g]	1.00000E+02
19	S_FeO_CP [m^2/kg]	1.0000E+04	S_FeO_CP [m^2/g]	1.00000E+01
20	d_FeO [kg/m^3]	5.2400E+03	den FeO [kg/m^3]	5.24000E+03
21	diffus_aq [m^2/yr]	7.2583E-02	diffus_aq [m^2/s]	2.30000E-09
22	diffus_colloid [m^2/yr]	7.2583E-04	diffus_colloid [m^2/s]	2.30000E-11
23	diff_length_1 [m]	1.0000E-03	diff_length_1 [m]	1.00000E-03
24	diff_length_2 [m]	5.0000E+00	diff_length_2 [m]	5.00000E+00
25	diff_length_3 [m]	8.0600E-01	diff_length_3 [m]	8.06000E-01
26	diff_area_1_2 [m^2]	3.6000E+01	diff_area_1_2 [m^2]	3.60000E+01
27	diff_area_2_3 [m^2]	1.0680E+00	diff_area_2_3 [m^2]	1.06800E+00
28	decay [1/yr]	2.8749E-05	decay [1/yr]	2.87494E-05
29	delt [yr]	10	delt [yr]	10
30	R_bar_1 [1/yr]	8.36740E-01		
31	R_bar_2 [1/yr]	3.28839E+04		

Figure F-15. Spreadsheet "flux_out_ratio.xls," Worksheet "K-surface;" Summary of Inputs

Row 7: Kd_FeO_c [m^3/kg]

$K_{d\_FeO\_c}$, partition coefficient in the FeO colloid state

$B$7=$D$7/1000

Row 8: Kd_FeO_CP [m^3/kg]

$K_{d\_FeO\_CP}$, partition coefficient in the stationary FeO corrosion product state

$B$8=$D$8/1000

Row 9: Kd_WF_c [m^3/kg]

$K_{d\_WF\_c}$, partition coefficient in the waste form colloid state

$B$9=$D$9/1000

Row 10: Kd_GW_c [m^3/kg]

$K_{d\_GW\_c}$, partition coefficient in the GW colloid state

$B$10=$D$10/1000

Row 11: mass_FeO_CP [kg]

m_{FeO_CP}, mass of corrosion products

$B$11=$D$11/1000

Row 12: V_pore [m^3]

$V_{pore} = \phi V_{bulk} = \frac{\phi}{1-\phi}\frac{m_{FeO\_CP}}{\rho_{FeO\_CP}}$, pore volume

$B$12=$D$12/1000

$D$12=$D$4*$D$11/($D$20*(1-$D$4))

Row 13: c_FeO_c [kg/m^3]

$c_{Pu\_FeO\_c}$, concentration of FeO colloids

$B$13=$D$13/1000

Row 14: c_FeO_CP [kg/m^3]

$c_{Pu\_FeO\_CP}$, concentration of FeO corrosion product

$B$14=$D$14/1000

Row 15: c_WF_c [kg/m^3]

$c_{Pu\_WF\_c}$, concentration of waste form colloids

$B$15=$D$15/1000

Row 16: c_GW_c [kg/m^3]

$c_{Pu\_GW\_c}$, concentration of GW colloid state

$B$16=$D$16/1000

Row 17: k [m/yr]

k, intrinsic or surface reaction rate ($m^3\ m^{-2}\ yr^{-1}$)

$B$17=$D$17/100

Row 18: S_FeO_c [m^2/kg]

$\hat{S}_{FeO\_c}$ = specific surface area of FeO colloids ($m^2\ kg^{-1}$)

$B$18=$D$18*1000

Row 19: S_FeO_CP [m^2/kg]

$\hat{S}_{FeO\_CP}$ = specific surface area of FeO corrosion products ($m^2\ kg^{-1}$)

$B$19=$D$19*1000

Row 20: d_FeO [kg/m^3]

ρ_{FeO_CP} = density of FeO

$B$20=$D$20

Row 21: diffus_aq [m^2/yr]

D_{aq} = aqueous diffusivity

$B$21=$D$21*31558000

Row 22: diffus_colloid [m^2/yr]

$D_{colloid}$ = colloid diffusivity

$B$22=$D$22*31558000

Row 23: diff_length_1 [m]

L_1 = diffusive length for cell_1

$B$23=$D$23

Row 24: diff_length_2 [m]

L_2 = diffusive length for cell_2

$B$24=$D$24

Row 25: diff_length_3 [m]

L_3 = diffusive length for cell_3

$B$25=$D$25

Row 26: diff_area_1_2 [m^2]

A_{s12} = diffusive area at cell_1 and cell_2 interface

$B$26=$D$26

Row 27: diff_area_2_3 [m^2]

A_{s23} = diffusive area at cell_2 and cell_3 interface

$B$27=$D$27

Row 28: decay [1/yr]

λ, decay rate

$B$28=$D$28

Row 29: delt [yr]

Δt, time step length

$B$29=$D$29

Rows 30 through 51 contain additional derived parameters for the colloid model. Images of Rows 32 through 100 are shown at the end of the description of this spreadsheet.

Row 30: R_bar_1 [1/yr]

$\overline{R}_1 = \hat{S}_{FeO\_c} c_{FeO\_c} k$, reaction rate constant for colloids

$B$30=$B$18*$B$13*$B$17

Row 31: R_bar_2 [1/yr]

$\overline{R}_2 = \hat{S}_{FeO\_CP} c_{FeO\_CP} k$, reaction rate constant for corrosion products

$B$31=$B$19*$B$14*$B$17

Row 32: U_bar [1/yr]

$\overline{U}$ = advective rate constant

$B$32=$B$6/$B$12

Row 33: Kd_bar_FeO_c

dimensionless partition coefficient in the FeO colloid state

$B$33=$B$13*$B$7

Row 34: Kd_bar_FeO_CP

dimensionless partition coefficient in the FeO corrosion product state

$B$34=$B$14*$B$8

Row 35: Kd_bar_WF_c

dimensionless partition coefficient in the waste form colloid state

$B$35=$B$15*$B$9

Row 36: Kd_bar_GW_c

dimensionless partition coefficient in the GW colloid state

$B$36=$B$16*$B$10

Row 37: K_bar_1

$\overline{K}_1 = 1 + \overline{K}_{d\_FeO\_c} + \overline{K}_{d\_FeO\_CP} + \overline{K}_{d\_WF\_c} + \overline{K}_{d\_GW\_c}$, combination of dimensionless partition coefficients

$B$37=1+$B$33+$B$34+$B$35+$B$36

Row 38: K_bar_2

$\overline{K}_2 = 1 + \overline{K}_{d\_FeO\_c} + \overline{K}_{d\_WF\_c} + \overline{K}_{d\_GW\_c}$, combination of dimensionless partition coefficients

$B$38=1+$B$33+$B$35+$B$36

Row 39: K_bar_3

$\overline{K}_3 = \overline{K}_{d\_FeO\_c} + \overline{K}_{d\_WF\_c} + \overline{K}_{d\_GW\_c}$, combination of dimensionless partition coefficients

$B$39=$B$33+$B$35+$B$36

Row 40: Diff_left_aq [1/yr]

diffusive rate constant, left interface in water

$B$40=($B$26/($B$23/($B$3*$B$21)+$B$24/($B$4*$B$21)))/$B$12

Row 41: Diff_right_aq

diffusive rate constant, right interface in water

$B$41=($B$27/($B$24/($B$4*$B$21)+$B$25/($B$5*$B$21)))/$B$12

Row 42: Diff_right_colloid

diffusive rate constant, right interface colloids

$B$42=($B$27/($B$24/($B$4*$B$22)+$B$25/($B$5*$B$22)))/$B$12

Row 43: Omega

$$\Omega = \frac{\text{colloid mass flux out}}{\text{total mass flux out}}$$

$B$43=($B$44+$B$30)/($B$45+$B$30)

Row 44: p_1

$p_1 = \overline{K}_3\left(\overline{U} + \overline{D}_{right\_col} + \lambda\right)$

$B$44=$B$39*($B$32+$B$42+$B$28)

Row 45: p_2

$$p_2 = \left(\overline{UK}_2 + \overline{D}_{right\_aq} + \overline{D}_{right\_col}\overline{K}_3\right)\left(\frac{\overline{U} + \overline{D}_{right\_col} + \lambda}{\overline{U} + \overline{D}_{right\_col}}\right)$$

$B$45=($B$32*$B$38+$B$41+$B$42*$B$39)*($B$32+$B$42+$B$28)/($B$32+$B$42)

Row 46: delta

scale value for $k = 2.0$

Row 47: comments

Rows 48 through 81 are values for the flux out ratio calculated as a function of the irreversible forward reaction rate, Equation B-71. Column A contains the values of k, and Column B contains the corresponding values of flux out ratio.

$A$48=0
$A$49=1.E-5
$A50 = $B$46*$A49

Row 50 is dragged down through Row 81.

Then in Column B the flux out ratio, $\Omega = \frac{\text{colloid mass flux out}}{\text{total mass flux out}}$, is calculated as a function of the irreversible reaction rate value:

$B48 = ($B$44+$B$18*$B$13*$A48*0.01)/($B$45+$B$18*$B$13*$A48*0.01)

The factor 0.01 converts the irreversible reaction rate constant from units of cm yr^{-1} to m yr^{-1}. The above expression is then dragged down through Row 81.

Figure B-3 in Appendix B, "Limiting Flux Out Ratio as a Function of Irreversible Reaction Rate," is plotted, where:

x-axis: $A$49:$A$73
y-axis: $B$49:$B$73

The point $k = 0.001$ cm yr^{-1} is

x-axis: $D$17:$D$17
y-axis: $B$43:$B$43

In Worksheet "K-surface," Rows 1 through 46 are the same as for Worksheet "adv_diff_decay." In Worksheet "K-surface," Rows 48 through 100 (Figure F-16), values for the irreversible forward reaction rate, k, are calculated as a function of the flux out ratio, Ω, Equation B-72. Column A contains the values of flux out ratio, and Column B contains the corresponding values of k.

$A$48: minimum flux out ratio when k = 0, $\Omega = \frac{p_1}{p_2}$

$A$48 = $B$44/$B$45

$A49 to $A100: uniform spacing of omega values between the minimum and 1.
$A49 = $A48+(1-$A$48)/53.

$A49 is dragged down to row 100.

$B48 to $B101: irreversible reaction rate. $k = \frac{p_2\Omega - p_1}{(1-\Omega)\hat{S}_{FeO\_c}c_{FeO\_c}}$

$B48 = 100*($B$35*$A48-$B$44)/((1-$A48)*$B$18*$B$13)

(The factor of 100 is a conversion from meters to cm.)

$B$48 is dragged down through $B$100

Figure B-4 in Appendix B, "Linear Reaction Rate from Colloid to Total Flux Out Ratio," is the plot in Worksheet "K-surface," where

x-axis: $A$49:$A$100
y-axis: $B$49:$B$100

The point labeled "Omega = 0.95" is

x-axis: $B$43:$B$43
y-axis: $D$17:$D$17

	A	B	C
32	U_bar [1/yr]	4.36667E-02	
33	Kd_FeO_c_bar	2.00000E-01	
34	Kd_FeO_CP_bar	1.96500E+04	
35	Kd_WF_c_bar	6.00000E-01	
36	Kd_GW_c_bar	2.00000E-02	
37	K_1	1.96518E+04	
38	K_2	1.82000E+00	
39	K_3	8.20000E-01	
40	Diff_left_aq	9.12736E-02	
41	Diff_right_aq	2.22893E-03	
42	Diff_right_colloid	2.22893E-05	
43	Omega	9.50000E-01	
44	p_1	3.58465E-02	
45	p_2	8.17743E-02	
46	delta	2.00E+00	
47	Omega	k	
48	0.4384	0.0000E+00	
49	0.4490	7.8629E-05	
50	0.4596	1.6034E-04	
51	0.4702	2.4532E-04	
52	0.4808	3.3377E-04	
53	0.4914	4.2591E-04	
54	0.5020	5.2196E-04	
55	0.5126	6.2220E-04	
56	0.5232	7.2688E-04	
57	0.5338	8.3633E-04	
58	0.5443	9.5086E-04	
59	0.5549	1.0709E-03	
60	0.5655	1.1967E-03	
61	0.5761	1.3288E-03	
62	0.5867	1.4677E-03	
63	0.5973	1.6140E-03	
64	0.6079	1.7681E-03	
65	0.6185	1.9308E-03	

K-surface / adv_diff_decay

	A	B
66	0.6291	2.1028E-03
67	0.6397	2.2849E-03
68	0.6503	2.4780E-03
69	0.6609	2.6832E-03
70	0.6715	2.9017E-03
71	0.6821	3.1347E-03
72	0.6927	3.3838E-03
73	0.7033	3.6506E-03
74	0.7139	3.9373E-03
75	0.7245	4.2460E-03
76	0.7351	4.5794E-03
77	0.7457	4.9405E-03
78	0.7563	5.3331E-03
79	0.7669	5.7614E-03
80	0.7775	6.2304E-03
81	0.7881	6.7464E-03
82	0.7987	7.3166E-03
83	0.8093	7.9503E-03
84	0.8199	8.6585E-03
85	0.8305	9.4552E-03
86	0.8411	1.0358E-02
87	0.8516	1.1390E-02
88	0.8622	1.2581E-02
89	0.8728	1.3970E-02
90	0.8834	1.5611E-02
91	0.8940	1.7581E-02
92	0.9046	1.9989E-02
93	0.9152	2.2999E-02
94	0.9258	2.6869E-02
95	0.9364	3.2028E-02
96	0.9470	3.9252E-02
97	0.9576	5.0087E-02
98	0.9682	6.8145E-02
99	0.9788	1.0426E-01

K-surface / adv_diff_decay

	A	B
100	0.9894	2.1261E-01
101		

Figure F-16. Spreadsheet "flux_out_ratio.xls," Worksheet "K-surface;" Calculation of Irreversible Forward Reaction Rate, *k*, as Function of Flux Out Ratio, Ω

SPREADSHEET "TIME_TO_CONV.XLS"

The purpose of this spreadsheet is to demonstrate the time to converge for the Pu concentration in solution and the irreversible Pu concentration on colloids. The spreadsheet verifies the convergence estimate discussed in Section "Convergence Estimates For Closed Form Solutions" in Appendix B.

The calculations are done in Worksheet "time_to_conv," while the plot is in Worksheet "plot_time_to_conv." This description will refer to equations from Appendix B, "Implementation of Radionuclide Sorption onto Colloidal and Stationary Phases with Finite Difference Solution."

Description of Input Values

The first 29 rows of each worksheet contain the input data values, with the exception of Row 12, where pore volume is computed. Column D contains input values representative of TSPA-LA. Column B contains values from column D that are scaled for unit conversion of mass (kg), length (m), time (yr). An image of Rows 1 through 33 is shown on the next page.

Row 2: c_s [kg/m^3]

c_s (mg L^{-1}) = Pu solubility

$B$2=$D$2/1000

Row 3: phi_1

ϕ_1, porosity of the waste form cell_1

$B$3=$D$3

Row 4: phi_2

ϕ_2, porosity of the corrosion product mass in waste form cell_2

$B$4=$D$4

Row 5: phi_3

ϕ_3, porosity of the invert

$B$5=$D$5

Row 6: u [m^3/yr]

u = volumetric water flux (m^3 yr^{-1})

$B$6=$D$6

Row 7: Kd_FeO_c [m^3/kg]

$K_{d\_FeO\_c}$, partition coefficient in the FeO colloid state

$B$7=$D$7/1000

	A	B	C	D
1	Input for Excel sreadsheet		Input from GoldSim	
2	c_s [kg/m^3]	0.001	c_s[mg/L]	1
3	phi_1	1	phi_1	1
4	phi_2	0.4	phi_2	0.4
5	phi_3	0.3	phi_3	0.3
6	u [m^3/yr]	0.1	u[m^3/yr]	0.1
7	Kd_FeO_c [m^3/kg]	1.00000E+01	Kd_FeO_c [ml/g]	1.00000E+04
8	Kd_FeO_CP [m^3/kg]	2.50000E+00	Kd_FeO_CP [ml/g]	2.50000E+03
9	Kd_WF_c [m^3/kg]	2.00000E+02	Kd_WF_c [ml/g]	2.00000E+05
10	Kd_GW_c [m^3/kg]	2.00000E+02	Kd_GW_c [ml/g]	2.00000E+05
11	mass_FeO_CP [kg]	1.80000E+04	mass_FeO_CP [g]	1.80000E+07
12	V_pore [m^3]	2.29008E+00	V_pore [L]	2.29008E+03
13	c_FeO_c [kg/m^3]	2.00000E-02	c_FeO_c [mg/L]	2.00000E+01
14	c_FeO_CP [kg/m^3]	7.86000E+03	c_FeO_CP [mg/L]	7.86000E+06
15	c_WF_c [kg/m^3]	3.00000E-03	c_WF_c [mg/L]	3.00000E+00
16	c_GW_c [kg/m^3]	1.00000E-04	c_GW_c [mg/L]	1.00000E-01
17	rate [m/yr]	1.00000E-05	rate [cm/yr]	1.00000E-03
18	S_FeO_c [m^2/kg]	1.00000E+05	S_FeO_c[m^2/g]	1.00000E+02
19	S_FeO_CP [m^2/kg]	1.00000E+04	S_FeO_CP [m^2/g]	1.00000E+01
20	d_FeO [kg/m^3]	5.24000E+03	den FeO [kg/m^3]	5.24000E+03
21	diffus_aq [m^2/yr]	7.25834E-02	diffus_aq [m^2/s]	2.30000E-09
22	diffus_colloid [m^2/yr]	7.25834E-04	diffus_colloid [m^2/	2.30000E-11
23	diff_length_1 [m]	1.00000E-03	diff_length_1 [m]	1.00000E-03
24	diff_length_2 [m]	5.00000E+00	diff_length_2 [m]	5.00000E+00
25	diff_length_3 [m]	8.06000E-01	diff_length_3 [m]	8.06000E-01
26	diff_area_1_2 [m^2]	3.60000E+01	diff_area_1_2 [m^2]	3.60000E+01
27	diff_area_2_3 [m^2]	1.06800E+00	diff_area_2_3 [m^2]	1.06800E+00
28	decay [1/yr]	2.87494E-05	decay [1/yr]	2.87494E-05
29	delt [yr]	1.00000E+01	delt [yr]	10
30	R_bar_1 [1/yr]	2.00000E-02		
31	R_bar_2 [1/yr]	7.86000E+02		
32	U_bar [1/yr]	4.36667E-02		
33	Kd_bar_FeO_c	2.00000E-01		
34	Kd_bar_FeO_CP	1.86500E+04		

plot_time_to_conv | time_to_conv

Figure F-17. Spreadsheet "time_to_conv.xls," Worksheet "time_to_conv;" Summary of Inputs

Row 8: Kd_FeO_CP [m^3/kg]

$K_{d\_FeO\_CP}$, partition coefficient in the stationary FeO corrosion product state

$B$8=$D$8/1000

Row 9: Kd_WF_c [m^3/kg]

$K_{d\_WF\_c}$, partition coefficient in the waste form colloid state

$B$9=$D$9/1000

Row 10: Kd_GW_c [m^3/kg]

$K_{d\_GW\_c}$, partition coefficient in the GW colloid state

$B$10=$D$10/1000

Row 11: mass_FeO_CP [kg]

m_{FeO_CP} mass of corrosion products

$B$11=$D$11/1000

Row 12: V_pore [m^3]

$V_{pore} = \phi V_{bulk} = \frac{\phi}{1-\phi}\frac{m_{FeO\_CP}}{\rho_{FeO\_CP}}$, pore volume

$B$12=$D$12/1000

$D$12=$D$4*$D$11/($D$20*(1-$D$4))

Row 13: c_FeO_c [kg/m^3]

$c_{Pu\_FeO\_c}$, concentration of FeO colloids

$B$13=$D$13/1000

Row 14: c_FeO_CP [kg/m^3]

$c_{Pu\_FeO\_CP}$, concentration of FeO corrosion product

$B$14=$D$14/1000

Row 15: c_WF_c [kg/m^3]

$c_{Pu\_WF\_c}$, concentration of waste form colloids

$B$15=$D$15/1000

Row 16: c_GW_c [kg/m^3]

$c_{Pu\_GW\_c}$, concentration of GW colloid state

$B$16=$D$16/1000

Row 17: k [m/yr]

k, intrinsic or surface reaction rate (pore-vol/area-FeO/time)

$B$17=$D$17/100

Row 18: S_FeO_c [m^2/kg]

$\hat{S}_{FeO\_c}$ = specific surface area of FeO colloids ($m^2\ kg^{-1}$)

$B$18=$D$18*1000

Row 19: S_FeO_CP [m^2/kg]

$\hat{S}_{FeO\_CP}$ = specific surface area of FeO corrosion products ($m^2\ kg^{-1}$)

$B$19=$D$19*1000

Row 20: d_FeO [kg/m^3]

ρ_{FeO_CP} = density of FeO

$B$20=$D$20

Row 21: diffus_aq [m^2/yr]

D_{aq} = aqueous diffusivity

$B$21=$D$21*31558000

Row 22: diffus_colloid [m^2/yr]

$D_{colloid}$ = colloid diffusivity

$B$22=$D$22*31558000

Row 23: diff_length_1 [m]

L_1 = diffusive length for cell_1

$B$23=$D$23

Row 24: diff_length_2 [m]

L_2 = diffusive length for cell_2

$B$24=$D$24

Row 25: diff_length_3 [m]

L_3 = diffusive length for cell_3

$B$25=$D$25

Row 26: diff_area_1_2 [m^2]

A_{s12} = diffusive area at cell_1 and cell_2 interface

$B$26=$D$26

Row 27: diff_area_2_3 [m^2]

A_{s23} = diffusive area at cell_2 and cell_3 interface

$B$27=$D$27

Row 28: decay [1/yr]

λ, decay rate

$B$28=$D$28

Row 29: delt [yr]

Δt, time step length

$B$29=$D$29

Rows 30 through 51 contains additional derived parameters for the colloid model. An image of Rows 34 through 61 is shown in Figure F-18.

	A	B	C	D	E	F	G	H	I	J
34	Kd_bar_FeO_CP	1.96500E+04								
35	Kd_bar_WF_c	6.00000E-01								
36	Kd_bar_GW_c	2.00000E-02								
37	K_bar_1	1.96518E+04								
38	K_bar_2	1.82000E+00								
39	K_bar_3	8.20000E-01								
40	Diff_left_aq	9.12736E-02								
41	Diff_left_c	9.12736E-04								
42	Diff_right_aq	2.22693E-03								
43	Diff_right_colloid	2.22693E-05								
44	denom_a_1_2	2.75194E+04								
45	a_1	7.14108E-01								
46	a_2	5.87541E-08								
47	b_1	6.95808E-01								
48	b_2	1.39162E-01								
49	a_1	9.99713E-01								
50	a_2	7.85774E+03								
51	tolerance	1.00000E-02								
52										
53	delt_time	denom_a_1_2	a_1	time Pu_aq [yrs]	b_1	delta_1	delta_2	t_1	t_2	time [yrs]
54	1.0E-03	1.9653E+04	9.9996E-01	115	9.9996E-01	4.5993E-04	4.2119E-04	1.7578E+05	1.9415E+05	194
55	1.0E-02	1.9660E+04	9.9960E-01	115	9.9956E-01	4.5975E-04	4.2104E-04	1.7582E+04	1.9419E+04	194
56	1.0E-01	1.9730E+04	9.9601E-01	115	9.9565E-01	4.5795E-04	4.1952E-04	1.7626E+03	1.9463E+03	195
57	1.0E+00	2.0439E+04	9.6151E-01	117	9.5811E-01	4.4068E-04	4.0499E-04	1.8059E+02	1.9900E+02	199
58	1.0E+01	2.7519E+04	7.1411E-01	137	6.9581E-01	3.2004E-04	3.0078E-04	2.2188E+01	2.4083E+01	240
59	1.0E+02	9.8328E+04	1.9986E-01	286	1.8616E-01	8.5624E-05	8.4182E-05	5.5709E+00	5.8272E+00	500
60	1.0E+03	8.0641E+05	2.4370E-02	1240	2.2363E-02	1.0286E-05	1.0265E-05	3.0220E+00	3.0925E+00	3000
61	1.0E+04	7.8872E+06	2.4916E-03	7682	2.2822E-03	1.0497E-06	1.0495E-06	2.2633E+00	2.2965E+00	20000

Figure F-18. Spreadsheet "time_to_conv.xls," Worksheet "time_to_conv;" Additional Derived Parameters and Results for Colloid Model

Row 30: R_bar_1 [1/yr]

$\overline{R}_1 = \hat{S}_{FeO\_c} c_{FeO\_c} k$, reaction rate constant for colloids

$B$30=$B$18*$B$13*$B$17

Row 31: R_bar_2 [1/yr]

$\overline{R}_2 = \hat{S}_{FeO\_CP} c_{FeO\_CP} k$, reaction rate constant for corrosion products

$B$31=$B$19*$B$14*$B$17

Row 32: U_bar [1/yr]

$\overline{U}$ advective rate constant

$B$32=$B$6/$B$12

Row 33: Kd_bar_FeO_c

dimensionless partition coefficient in the FeO colloid state

$B$33=$B$13*$B$7

Row 34: Kd_bar_FeO_CP

dimensionless partition coefficient in the FeO corrosion product state

$B$34=$B$14*$B$8

Row 35: Kd_bar_WF_c

dimensionless partition coefficient in the waste form colloid state

$B$35=$B$15*$B$9

Row 36: Kd_bar_GW_c

dimensionless partition coefficient in the GW colloid state

$B$36=$B$16*$B$10

Row 37: K_bar_1

$\overline{K}_1 = 1 + \overline{K}_{d\_FeO\_c} + \overline{K}_{d\_FeO\_CP} + \overline{K}_{d\_WF\_c} + \overline{K}_{d\_GW\_c}$, combination of dimensionless partition coefficients

$B$37=1+$B$33+$B$34+$B$35+$B$36

Row 38: K_bar_2

$\overline{K}_2 = 1 + \overline{K}_{d\_FeO\_c} + \overline{K}_{d\_WF\_c} + \overline{K}_{d\_GW\_c}$, combination of dimensionless partition coefficients

$B$38=1+$B$33+$B$35+$B$36

Row 39: K_bar_3

$\overline{K}_3 = \overline{K}_{d\_FeO\_c} + \overline{K}_{d\_WF\_c} + \overline{K}_{d\_GW\_c}$, combination of dimensionless partition coefficients

$B$39=$B$33+$B$35+$B$36

Row 40: Diff_left_aq [1/yr]

diffusive rate constant, left interface in water

$B$40=($B$26/($B$23/($B$3*$B$21)+$B$24/($B$4*$B$21)))/$B$12

Row 41: Diff_left_colloid [1/yr]

diffusive rate constant, left interface colloids

$B$41=($B$26/($B$23/($B$3*$B$22)+$B$24/($B$4*$B$22)))/$B$12

Row 42: Diff_right_aq [1/yr]

diffusive rate constant, right interface in water

$B$41=($B$27/($B$24/($B$4*$B$21)+$B$25/($B$5*$B$21)))/$B$12

Row 43: Diff_right_colloid [1/yr]

diffusive rate constant, right interface colloids

$B$42=($B$27/($B$24/($B$4*$B$22)+$B$25/($B$5*$B$22)))/$B$12

Row 44: denom_a_1_2

denominator of Equation B-48

$B$44=$B$37+($B$32*$B$38+$B$40+$B$41*$B$35+$B$42+$B$43*$B$39
+$B$30+$B$31+$B$28*$B$37)*$B$29

Row 45: a_1

first coefficient for Equation B-55,

$$a_1 = \frac{\overline{K}_1}{\overline{K}_1 + \left(\overline{U}\overline{K}_2 + \overline{D}_{left\_aq} + \overline{D}_{left\_col}\overline{K}_{d\_WF\_c} + \overline{D}_{right\_aq} + \overline{D}_{right\_col}\overline{K}_3 + \overline{R}_1 + \overline{R}_2 + \lambda\overline{K}_1\right)\Delta t}$$

$B$45=$B$37/$B$44

Row 46: a_2

second coefficient for Equation B-55,

$$a_2 = \frac{\left(\overline{U}(1+\overline{K}_{d\_WF\_c}) + \overline{D}_{left\_aq} + \overline{D}_{left\_col}\overline{K}_{d\_WF\_c}\right)\Delta t c_s}{\overline{K}_1 + \left(\overline{U}\overline{K}_2 + \overline{D}_{left\_aq} + \overline{D}_{left\_col}\overline{K}_{d\_WF\_c} + \overline{D}_{right\_aq} + \overline{D}_{right\_col}\overline{K}_3 + \overline{R}_1 + \overline{R}_2 + \lambda\overline{K}_1\right)\Delta t}$$

$B$46=(($B$32*(1+$B$35)+$B$40+$B$41*$B$35)*$B$29*$B$2)/$B$44

Row 47: b_1

first coefficient for Equation B-58, $b_1 = \dfrac{1}{1+\left(\overline{U} + \overline{D}_{right\_col} + \lambda\right)\Delta t}$

$B$47=1/(1+($B$32+$B$43+$B$28)*$B$29)

Row 48: b_2

second coefficient for Equation B-58, $b_2 = \dfrac{\overline{R}_1\Delta t}{1+\left(\overline{U} + \overline{D}_{right\_col} + \lambda\right)\Delta t}$

$B$48=($B$30*$B$29)*$B$47

Row 49: e_1

first coefficient for Equation B-64, $e_1 = \dfrac{1}{1+\lambda\Delta t}$

$B$49=1/(1+$B$28*$B$29)

Row 50: e_2

second coefficient for Equation B-64, $e_2 = \dfrac{\overline{R}_2\Delta t}{1+\lambda\Delta t}$

$B$50=($B$31*$B$29)*$B$49

Row 51: convergence relative error tolerance 1% = 0.01.

Rows 54 through 61 calculates the times to converge to limit value for Pu_aq concentration and Irrv_Pu_c concentration as a function of time step size. The time step size (yr) varies by order of magnitude increments from 1×10^{-3} to 1×10^{4}.

Column A: delt_time

Row 54: assign time step value 1×10^{-3}

Rows 55: $A55 = 10*$A54

This value is dragged down through Row 61

Column B: denom_a_1_2

denominator in the calculation for a_1 and a_2 coefficients.

$B54=$B$37+($B$32*$B$38+$B$40+$B$41*$B$35+$B$42+$B$43*$B$39+$B$30+$B$31+$B$28*$B$37)*$A54

This value is dragged down through Row 61

Column C: a_1

coefficient in Pu_aq concentration Equation B-56.

Row 54: $C54 = $B$37/$B54

This result is dragged down through Row 61

Column D: time Pu_aq [yrs]

time for Pu_aq concentration to converge, estimate Equation B-74.

Row 54: $D54 = $A54*LOG10($B$51)/LOG10($C54)

This result is dragged down through Row 61

Column E: b_1

coefficient in Irrv_Pu_c concentration, Equation B-59.

Row 54: $E54 = 1/(1+($B$32+$B$43+$B$28)*$A54)

This result is dragged down through Row 61

Column F: delta_1

intermediate tolerance δ_1 in estimate for Irrv_Pu_c concentration convergence.

Row 54: $F54 = 0.5*$B$51*ABS(($E54-$C54)/(1-$C54))

This result is dragged down through Row 61

Column G:delta_2

intermediate tolerance δ_2 in estimate for Irrv_Pu_c concentration convergence.

Row 54: $G54 = 0.5*$B$51*ABS(($E54-$C54)/(1-$E54))

This result is dragged down through Row 61

Column H:t_1

intermediate result $\frac{\log_{10}(\delta_1)}{\log_{10}(b_1)}$ Equation B-75.

Row 54: $H54 = LOG10($F54)/LOG10($E54)

This result is dragged down through row 61

Column I: t_2

intermediate result $\frac{\log_{10}(\delta_2)}{\log_{10}(a_1)}$ Equation B-75.

Row 54: $G54 = LOG10($G54)/LOG10($C54)

This result is dragged down through Row 61

Column J: time [yrs]

time for Irrv_Pu_c concentration to converge to given tolerance, Equation B-75.

Row 54: $J54
=$A54*INT(MAX(LOG10($F54)/LOG10($E54),LOG10($G54)/LOG10($C54)))

This result is dragged down through Row 61.

The plot of the time to converge (shown in Figure F-19) is in Worksheet "plot_time_to_conv" and is Figure B-5 of Appendix B.

Time to converge for Pu_aq concentration is

x-axis: $A$54:$A$61
y-axis: $D$54:$D$61

Time to converge for Irrv_Pu_colloids is

x-axis: $A$54:$A$61
y-axis: $J$54:$J$61

Note that the *x*-axis scale is from 1×10^{-3} to 1×10^{3} years, so only Rows 54 through 60 are shown in the figure.

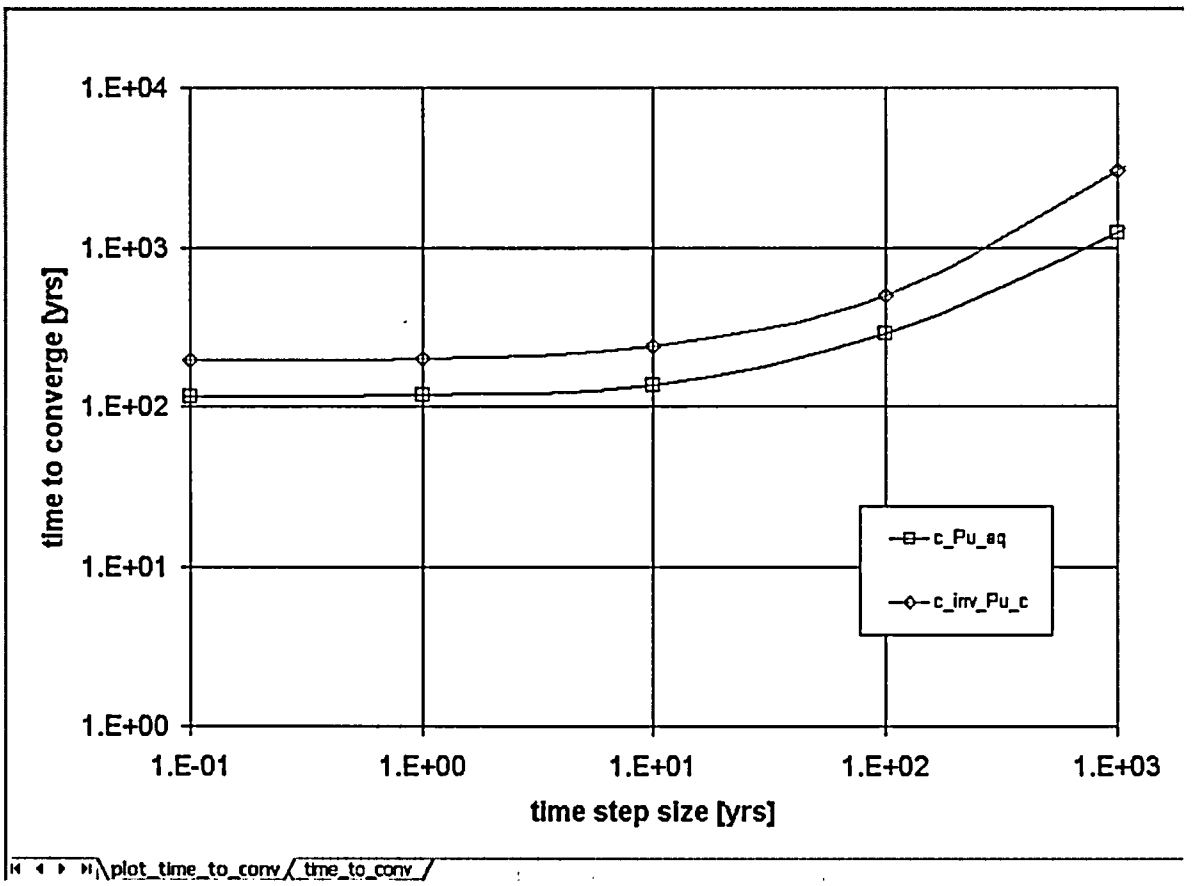

Figure F-19. Spreadsheet "time_to_conv.xls," Worksheet "plot_time_to_conv;" Plot of Colloid Model Results

INTENTIONALLY LEFT BLANK

APPENDIX G
MICROSOFT EXCEL SPREADSHEET "INVERT DIFFUSION COEFFICIENT"

MICROSOFT EXCEL SPREADSHEET "INVERT DIFFUSION COEFFICIENT"

SPREADSHEET "INVERT DIFFUSION COEFFICIENT" WORKSHEET "MODEL"

The purpose of this spreadsheet is to perform a statistical analysis of the dependence of diffusion coefficients, D ($cm^2 s^{-1}$), on volumetric moisture content, θ (percent, 100 m^3 water m^{-3} bulk volume), as described in Section 6.3.4.1.1. The diffusion data are fit to an equation of the form

$$D = D_0 \left(\frac{\theta}{100} \right)^n , \qquad \text{(Eq. G-1)}$$

where D_0 is the self-diffusion coefficient of water (2.299×10^{-5} $cm^2 s^{-1}$) (Mills 1973 [DIRS 133392], Table III), and the fitting parameter is the exponent, n. To perform a least squares fit of the data, this equation is linearized in terms of n:

$$\log_{10}\left(\frac{D}{D_0} \right) = n \log_{10}\left(\frac{\theta}{100} \right). \qquad \text{(Eq. G-2)}$$

Column A, Rows 1 through 125, of the spreadsheet, shown in Figures G-1 through G-4, contains the moisture content values, θ (percent) (Conca and Wright 1992 [DIRS 100436]; Conca et al. 1993 [DIRS 170709]), that are listed in Table 4.1-14. The corresponding diffusion coefficient values listed in Table 4.1-14 are in Column B, Rows 1 through 125. In Column C, the quantity $\theta/100$ is computed (e.g., C3=A3/100], and D/D_0 is computed in Column D (e.g., D3=B3/0.00002299). The log term on the right hand side of Equation G-2, containing the moisture content, is computed Column E (e.g., E3=LOG10(A3)-2). In Column F, the left-hand side of Equation G-2 is calculated (e.g., D3=LOG10(D3)).

The least squares fit of the data is done using the Microsoft Excel Trendline tool. In Figure G-5, the results in Column F are plotted on the y-axis against the corresponding values in Column E on the x-axis in the plot located between Rows 132 and 154 of the worksheet. The type of regression is linear. The Trendline features, "Set intercept = 0," "Display equation on chart," and "Display R-squared value on chart" are clicked on. In particular, the "Set intercept = 0" feature results in a fit to Equation G-2, in which the intercept is constrained to be zero.

As shown on the charts, the fitting parameter, n, has a value of 1.863. The correlation coefficient, R^2, is 0.915, indicating a strong correlation between the diffusion coefficient and the volumetric moisture content. The regression equation is:

$$D = D_0 \left(\frac{\theta}{100} \right)^{1.863} , \qquad \text{(Eq. G-3)}$$

In Column G, the error, or deviation of each data point from the fitted equation, is calculated (e.g., G3=F3-1.862899*E3)); i.e., for data point i, the calculation in Column G is the deviation ε_i:

$$\varepsilon_i = \log_{10}\left(\frac{D}{D_0}\right) - 1.863\log_{10}\left(\frac{\theta}{100}\right). \qquad \text{(Eq. G-4)}$$

In Cell G128, the average of the 125 values of ε_i is computed: G128=AVERAGE(G3:G127). The standard deviation of the ε_i, Cell G129 is computed: G129=STDEV(G3:G127).

	A	B	C	D	E	F	G
1	Water Content, θ	Diffusion Coefficient, D	$\theta/100$	D/D_0	$\log_{10}\theta - 2$	$\log_{10}(D/D_0)$	Error = $[\log_{10}(D/D_0) - 1.863(\log_{10}\theta - 2)]$
2	(%)	(cm²/s)					
3	1.50	1.39E-08	0.0150	6.046E-04	-1.824	-3.219	0.1792
4	1.70	6.60E-09	0.0170	2.871E-04	-1.770	-3.542	-0.2455
5	1.90	8.60E-09	0.0190	3.741E-04	-1.721	-3.427	-0.2205
6	2.17	2.77E-08	0.0217	1.205E-03	-1.664	-2.919	0.1799
7	2.20	3.63E-08	0.0220	1.579E-03	-1.658	-2.802	0.2863
8	2.29	1.09E-08	0.0229	4.741E-04	-1.640	-3.324	-0.2687
9	2.50	2.50E-08	0.0250	1.087E-03	-1.602	-2.964	0.0209
10	3.10	3.30E-08	0.0310	1.435E-03	-1.509	-2.843	-0.0326
11	3.14	3.06E-08	0.0314	1.331E-03	-1.503	-2.876	-0.0757
12	3.20	1.35E-08	0.0320	5.872E-04	-1.495	-3.231	-0.4465
13	3.27	2.79E-08	0.0327	1.214E-03	-1.485	-2.916	-0.1487
14	3.33	6.35E-08	0.0333	2.762E-03	-1.478	-2.559	0.1938
15	3.34	2.60E-08	0.0334	1.131E-03	-1.476	-2.947	-0.1965
16	3.57	3.37E-08	0.0357	1.466E-03	-1.447	-2.834	-0.1377
17	3.70	3.70E-08	0.0370	1.609E-03	-1.432	-2.793	-0.1260
18	3.70	6.60E-08	0.0370	2.871E-03	-1.432	-2.542	0.1253
19	4.00	5.22E-08	0.0400	2.271E-03	-1.398	-2.644	-0.0396
20	4.20	5.94E-08	0.0420	2.584E-03	-1.377	-2.588	-0.0230
21	4.60	6.21E-08	0.0460	2.701E-03	-1.337	-2.568	-0.0773
22	4.90	7.20E-08	0.0490	3.132E-03	-1.310	-2.504	-0.0642
23	5.10	1.32E-07	0.0510	5.742E-03	-1.292	-2.241	0.1667
24	5.30	2.40E-08	0.0530	1.044E-03	-1.276	-2.981	-0.6048
25	5.40	7.60E-08	0.0540	3.306E-03	-1.268	-2.481	-0.1193
26	5.51	7.68E-08	0.0551	3.341E-03	-1.259	-2.476	-0.1311
27	5.83	1.23E-07	0.0583	5.350E-03	-1.234	-2.272	0.0278
28	5.90	9.80E-08	0.0590	4.045E-03	-1.229	-2.393	-0.1033
29	6.00	8.92E-08	0.0600	3.880E-03	-1.222	-2.411	-0.1350
30	6.30	1.06E-07	0.0630	4.611E-03	-1.201	-2.336	-0.0995
31	6.90	6.00E-08	0.0690	2.610E-03	-1.161	-2.583	-0.4203
32	6.93	1.50E-07	0.0693	6.525E-03	-1.159	-2.185	-0.0259

Model / Validation / Sheet3

Figure G-1. Spreadsheet "Invert Diffusion Coefficient," Worksheet "Model;" Invert Diffusion Coefficient Input Data (Water Content 1.50 to 6.93 Percent)

	A	B	C	D	E	F	G
33	7.30	1.60E-07	0.0730	6.960E-03	-1.137	-2.157	-0.0399
34	7.40	2.50E-07	0.0740	1.087E-02	-1.131	-1.964	0.1429
35	7.60	2.60E-07	0.0760	1.131E-02	-1.119	-1.947	0.1384
36	7.60	1.10E-07	0.0760	4.785E-03	-1.119	-2.320	-0.2352
37	7.60	2.69E-07	0.0760	1.170E-02	-1.119	-1.932	0.1531
38	7.70	1.10E-07	0.0770	4.785E-03	-1.114	-2.320	-0.2458
39	8.00	1.98E-07	0.0800	8.612E-03	-1.097	-2.065	-0.0214
40	8.10	1.70E-07	0.0810	7.395E-03	-1.092	-2.131	-0.0977
41	8.32	4.10E-07	0.0832	1.783E-02	-1.080	-1.749	0.2629
42	8.35	2.15E-07	0.0835	9.352E-03	-1.078	-2.029	-0.0203
43	8.60	3.20E-07	0.0860	1.392E-02	-1.066	-1.856	0.1285
44	8.80	2.30E-07	0.0880	1.000E-02	-1.056	-2.000	-0.0335
45	9.24	2.55E-07	0.0924	1.109E-02	-1.034	-1.955	-0.0282
46	9.24	2.55E-07	0.0924	1.109E-02	-1.034	-1.955	-0.0282
47	9.56	3.00E-07	0.0956	1.305E-02	-1.020	-1.884	0.0149
48	9.64	3.07E-07	0.0964	1.335E-02	-1.016	-1.874	0.0182
49	9.75	3.20E-07	0.0975	1.392E-02	-1.011	-1.856	0.0270
50	10.10	3.51E-07	0.1010	1.527E-02	-0.996	-1.816	0.0386
51	10.10	3.62E-07	0.1010	1.575E-02	-0.996	-1.803	0.0520
52	10.20	3.54E-07	0.1020	1.540E-02	-0.991	-1.813	0.0343
53	10.20	3.30E-07	0.1020	1.435E-02	-0.991	-1.843	0.0039
54	10.30	3.34E-07	0.1030	1.453E-02	-0.987	-1.838	0.0012
55	10.30	2.10E-07	0.1030	9.134E-03	-0.987	-2.039	-0.2003
56	10.40	3.40E-07	0.1040	1.479E-02	-0.983	-1.830	0.0011
57	10.90	3.62E-07	0.1090	1.575E-02	-0.963	-1.803	-0.0097
58	11.10	3.72E-07	0.1110	1.618E-02	-0.955	-1.791	-0.0125
59	11.10	4.22E-07	0.1110	1.836E-02	-0.955	-1.736	0.0422
60	11.10	4.27E-07	0.1110	1.857E-02	-0.955	-1.731	0.0474
61	11.20	4.19E-07	0.1120	1.823E-02	-0.951	-1.739	0.0319
62	11.20	5.48E-07	0.1120	2.384E-02	-0.951	-1.623	0.1485
63	11.40	4.27E-07	0.1140	1.857E-02	-0.943	-1.731	0.0258
64	11.40	4.12E-07	0.1140	1.792E-02	-0.943	-1.747	0.0102
65	11.60	5.40E-07	0.1160	2.349E-02	-0.936	-1.629	0.1137

Model / Validation / Sheet3

Figure G-2. Spreadsheet "Invert Diffusion Coefficient," Worksheet "Model;" Invert Diffusion Coefficient Input Data (Water Content 7.30 to 11.60 Percent)

	A	B	C	D	E	F	G
65	11.60	5.40E-07	0.1160	2.349E-02	-0.936	-1.629	0.1137
66	11.70	2.60E-07	0.1170	1.131E-02	-0.932	-1.947	-0.2107
67	11.80	4.80E-07	0.1180	2.088E-02	-0.928	-1.680	0.0487
68	12.00	2.40E-07	0.1200	1.044E-02	-0.921	-1.981	-0.2659
69	12.00	4.47E-07	0.1200	1.944E-02	-0.921	-1.711	0.0042
70	12.20	4.09E-07	0.1220	1.779E-02	-0.914	-1.750	-0.0478
71	12.30	5.05E-07	0.1230	2.197E-02	-0.910	-1.658	0.0372
72	12.30	4.40E-07	0.1230	1.914E-02	-0.910	-1.718	-0.0227
73	12.30	3.60E-07	0.1230	1.566E-02	-0.910	-1.805	-0.1098
74	12.30	4.50E-07	0.1230	1.957E-02	-0.910	-1.708	-0.0129
75	12.50	2.90E-07	0.1250	1.261E-02	-0.903	-1.899	-0.2168
76	12.70	4.37E-07	0.1270	1.901E-02	-0.896	-1.721	-0.0515
77	12.70	4.90E-07	0.1270	2.131E-02	-0.896	-1.671	-0.0018
78	12.70	6.32E-07	0.1270	2.314E-02	-0.896	-1.636	0.0339
79	13.10	4.77E-07	0.1310	2.075E-02	-0.883	-1.683	-0.0386
80	13.90	5.39E-07	0.1390	2.344E-02	-0.857	-1.630	-0.0335
81	13.90	7.80E-07	0.1390	3.393E-02	-0.857	-1.469	0.1270
82	14.10	5.12E-07	0.1410	2.227E-02	-0.851	-1.652	-0.0674
83	14.20	5.52E-07	0.1420	2.401E-02	-0.848	-1.620	-0.0404
84	14.40	4.50E-07	0.1440	1.957E-02	-0.842	-1.708	-0.1404
85	14.40	5.20E-07	0.1440	2.262E-02	-0.842	-1.646	-0.0776
86	14.40	4.50E-07	0.1440	1.957E-02	-0.842	-1.708	-0.1404
87	14.60	6.82E-07	0.1460	2.967E-02	-0.836	-1.528	0.0290
88	14.70	9.00E-07	0.1470	3.915E-02	-0.833	-1.407	0.1439
89	14.80	6.54E-07	0.1480	2.845E-02	-0.830	-1.546	-0.0002
90	16.00	1.47E-06	0.1600	6.394E-02	-0.796	-1.194	0.2884
91	16.10	6.82E-07	0.1610	2.967E-02	-0.793	-1.528	-0.0502
92	16.50	5.45E-07	0.1650	2.371E-02	-0.783	-1.625	-0.1674
93	16.70	6.60E-07	0.1670	2.871E-02	-0.777	-1.542	-0.0940
94	17.00	1.20E-06	0.1700	5.220E-02	-0.770	-1.282	0.1512
95	17.10	8.20E-07	0.1710	3.567E-02	-0.767	-1.448	-0.0189
96	17.30	1.76E-06	0.1730	7.656E-02	-0.762	-1.116	0.3034
97	17.50	1.10E-06	0.1750	4.785E-02	-0.757	-1.320	0.0900

Model / Validation / Sheet3

Figure G-3. Spreadsheet "Invert Diffusion Coefficient," Worksheet "Model;" Invert Diffusion Coefficient Input Data (Water Content 11.60 to 17.50 Percent)

	A	B	C	D	E	F	G	H	I
97	17.50	1.10E-06	0.1750	4.785E-02	-0.757	-1.320	0.0900		
98	18.80	1.60E-06	0.1880	6.960E-02	-0.726	-1.157	0.1948		
99	18.90	8.19E-07	0.1890	3.562E-02	-0.724	-1.448	-0.1004		
100	19.40	9.89E-07	0.1940	4.302E-02	-0.712	-1.366	-0.0396		
101	20.40	4.19E-06	0.2040	1.823E-01	-0.690	-0.739	0.5468		
102	20.80	3.58E-06	0.2080	1.557E-01	-0.682	-0.808	0.4627		
103	21.00	2.84E-06	0.2100	1.018E-01	-0.678	-0.992	0.2703		
104	21.50	1.23E-06	0.2150	5.350E-02	-0.668	-1.272	-0.0280		
105	21.60	1.29E-06	0.2160	5.611E-02	-0.666	-1.251	-0.0111		
106	23.10	2.40E-06	0.2310	1.044E-01	-0.636	-0.981	0.2042		
107	23.10	1.90E-06	0.2310	8.264E-02	-0.636	-1.083	0.1027		
108	24.00	2.90E-06	0.2400	1.261E-01	-0.620	-0.899	0.2555		
109	25.30	5.82E-06	0.2530	2.532E-01	-0.597	-0.597	0.5153		
110	25.40	2.50E-06	0.2540	1.087E-01	-0.595	-0.964	0.1451		
111	25.70	9.26E-06	0.2570	4.028E-01	-0.590	-0.395	0.7043		
112	28.20	3.50E-06	0.2820	1.522E-01	-0.550	-0.817	0.2067		
113	28.50	1.00E-06	0.2850	4.350E-02	-0.545	-1.362	-0.3460		
114	30.90	1.51E-06	0.3090	6.568E-02	-0.510	-1.183	-0.2324		
115	31.70	1.23E-05	0.3170	5.350E-01	-0.499	-0.272	0.6578		
116	32.30	4.60E-06	0.3230	2.001E-01	-0.491	-0.699	0.2155		
117	33.80	1.34E-05	0.3380	5.829E-01	-0.471	-0.234	0.6431		
118	35.80	1.57E-05	0.3580	6.829E-01	-0.446	-0.166	0.6654		
119	38.50	4.33E-06	0.3850	1.883E-01	-0.415	-0.725	0.0472		
120	39.30	1.36E-05	0.3930	5.916E-01	-0.406	-0.228	0.5276		
121	39.50	1.13E-05	0.3950	4.915E-01	-0.403	-0.308	0.4430		
122	40.00	6.90E-06	0.4000	3.001E-01	-0.398	-0.523	0.2186		
123	42.00	5.80E-06	0.4200	2.523E-01	-0.377	-0.598	0.1037		
124	42.50	3.22E-06	0.4250	1.401E-01	-0.372	-0.854	-0.1614		
125	43.40	1.02E-05	0.4340	4.437E-01	-0.363	-0.353	0.3224		
126	49.00	6.09E-06	0.4900	2.649E-01	-0.310	-0.577	0.0002		
127	66.30	1.83E-05	0.6630	7.960E-01	-0.178	-0.099	0.2334		
128							0.0329	Average	
129							0.2181	Standard Deviation	

Model / Validation / Sheet3

Figure G-4. Spreadsheet "Invert Diffusion Coefficient," Worksheet "Model;" Invert Diffusion Coefficient Input Data (Water Content 17.50 to 66.30 Percent)

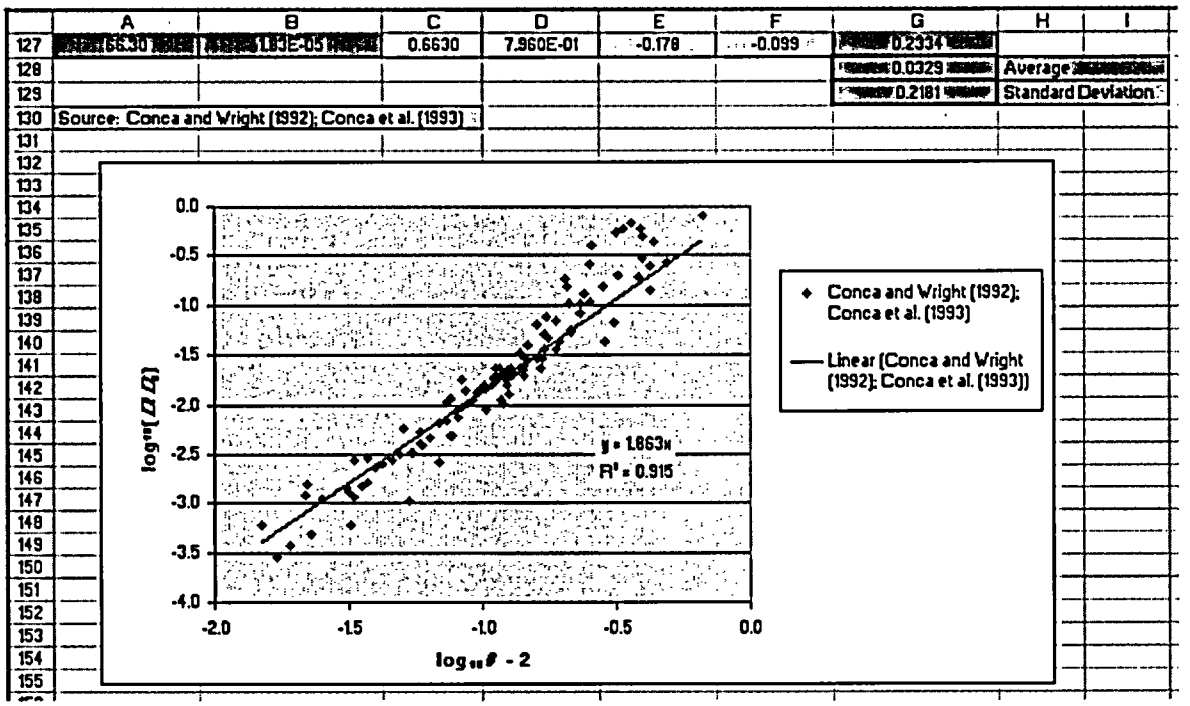

Source: Conca and Wright 1992 [DIRS 100436]; Conca et al. 1993 [DIRS 170709].

Figure G-5. Spreadsheet "Invert Diffusion Coefficient," Worksheet "Model;" Plot of Fitted Invert Diffusion Coefficient Data

In the plot in Figure G-6 between Rows 169 and 191, the lines for the mean and for the mean plus or minus three standard deviations are added to the plot shown earlier. The lines are drawn over the range of the data, i.e., for $\theta/100$ from 0.015 to 0.663 (Column C, Rows 159 to 166). The y-values for the Trendline fit are computed as $D/D_0 = (\theta/100)^{1.863}$ (e.g., D159=(C159^1.863)), and the values plotted are $\log_{10}(D/D_0)$ (e.g., G159=LOG10(D159)). For the mean curve, the y-values are computed as $D/D_0 = (\theta/100)^{1.863}10^{0.033}$ (e.g., D163=(C163^1.863)*10^(0.033)), and the values plotted are again $\log_{10}(D/D_0)$ (e.g., G163=LOG10(D163)). For the mean plus three standard deviations curve, the y-values are computed as $D/D_0 = (\theta/100)^{1.863}10^{0.033+3(0.218)}$ (e.g., G161=(C161^1.863)*10^(0.033+3*0.218)), and the values plotted are again $\log_{10}(D/D_0)$ (e.g., G161=LOG10(D161)). The mean minus three standard deviations curve is done similarly. This plot is shown as Figure 6.3-4 in Section 6.3.4.1.1.

	A	B	C	D	E	F	G	H	I
156									
157		Lines for plot at ± 3 standard deviations							
158		log10(q/100)	θ/100	$D/D_0=(\theta/100)^{1.863x}$			$\log_{10}(D/D_0)$		
159		-1.8239	0.015	4.000E-04	Trendline		-3.3979		
160		-0.1785	0.663	4.650E-01	Trendline		-0.3325		
161		-1.8239	0.015	1.946E-03	mean + 3 std dev		-2.7109		
162		-0.1785	0.663	2.262E+00	mean + 3 std dev		0.3545		
163		-1.8239	0.015	4.316E-04	mean		-3.3649		
164		-0.1785	0.663	5.017E-01	mean		-0.2995		
165		-1.8239	0.015	9.573E-05	mean - 3 std dev		-4.0189		
166		-0.1785	0.663	1.113E-01	mean - 3 std dev		-0.9535		
167									
168									
169									
170									
171									
172									
173									
174									
175									
176									
177									
178									
179									
180									
181									
182									
183									
184									
185									
186									
187									
188									
189									
190									
191									
192									
193									
194									
195									

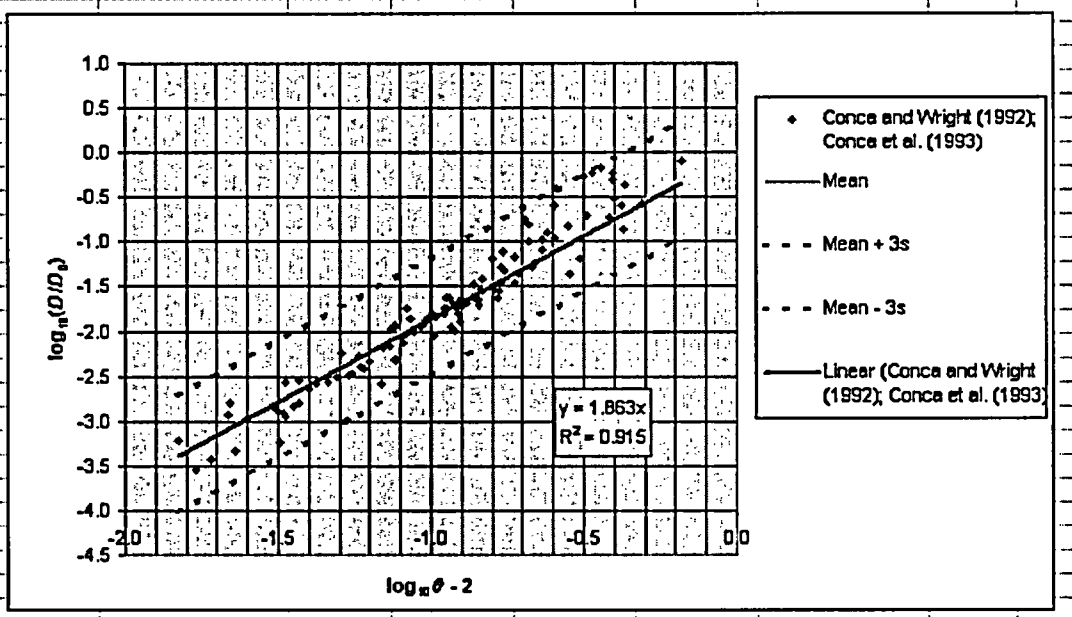

Model / Validation / Sheet3

Source: Conca and Wright 1992 [DIRS 100436]; Conca et al. 1993 [DIRS 170709].

Figure G-6. Spreadsheet "Invert Diffusion Coefficient," Worksheet "Model;" Plotted Results of Invert Diffusion Coefficient Data, Showing Uncertainty Range as Mean ±3 Standard Deviations

The data are further analyzed in Figure G-7 to demonstrate that the deviations approximately follow a normal distribution. Under the Microsoft Excel menu item Tools, Data Analysis... is clicked, and Histogram is selected under Analysis Tools. In the Histogram window, the error data (Column G, Rows 3 to 127) are entered for the Input Range. For the Bin Range, Column I, Rows 3 to 22, is entered. The frequency distribution is output in Column J, Rows 3 to 22. For comparison, a theoretical normal distribution is computed over the same range in Column M:

$$f(x;\mu,\sigma)=\frac{1}{\sigma\sqrt{2\pi}}e^{-(x-\mu)^2/2\sigma^2}, \qquad \text{(Eq. G-5)}$$

where x is the bin value, the mean $\mu \approx 0.033$, and the standard deviation $\sigma \approx 0.218$.

The Microsoft Excel formula is (for Cell M3, for example):

M3=EXP(-((I3-0.0329438386573088)^2)/(2*0.218121819319092^2))/
(0.218121819319092*(2*PI())^0.5)

	G	H	I	J	K	L	M	N	O	P
1	Error = [log10(D/D0)]									
2	1.863 [log10(3.2)]		Bin	Frequency	Bin	Frequency	Normal Distribution			
3	0.1792		-1	0	0	34	0.000025			
4	-0.2455		-0.9	0	0.1	24	0.000195			
5	-0.2205		-0.8	0	0.2	18	0.001246			
6	0.1799		-0.7	0	-0.1	14	0.006462			
7	0.2863		-0.6	1	-0.2	10	0.027149			
8	-0.2687		-0.5	0	0.3	10	0.092442			
9	0.0209		-0.4	2	0.6	3	0.255101			
10	-0.0326		-0.3	1	0.7	3	0.570522			
11	-0.0757		-0.2	10	-0.4	2	1.034069			
12	-0.4465		-0.1	14	0.4	2	1.518954			
13	-0.1487		0	34	0.5	2	1.808246			
14	0.1938		0.1	24	-0.6	1	1.744570			
15	-0.1965		0.2	18	-0.3	1	1.364071			
16	-0.1377		0.3	10	0.8	1	0.864377			
17	-0.1260		0.4	2	-1	0	0.443902			
18	0.1253		0.5	2	-0.9	0	0.184752			
19	-0.0396		0.6	3	-0.8	0	0.062317			
20	-0.0230		0.7	3	-0.7	0	0.017035			
21	-0.0773		0.8	1	-0.5	0	0.003774			
22	-0.0642		0.9	0	0.9	0	0.000678			
23	0.1667		1	0	1	0	0.000099			
24	-0.6048		More	0	More	0				
25	-0.1193									
26	-0.1311									
27	0.0278									
28	-0.1033									
29	-0.1350									
30	-0.0995									
31	-0.4203									
32	-0.0259									
33	-0.0399									
34	0.1429									
35	0.1384									
36	-0.2352									
37	0.1531									
38	-0.2458									
39	-0.0214									
40	-0.0977									
41	0.2629									
42	-0.0203									
43	0.1285									
44	-0.0335									
45	-0.0282									
46	-0.0282									

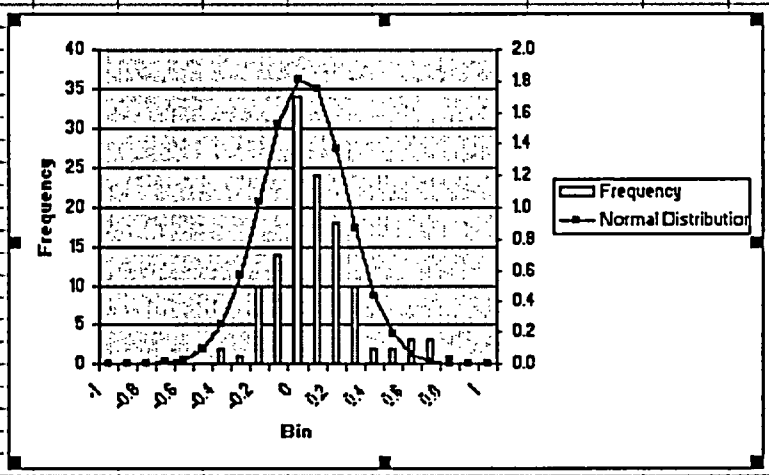

Model / Validation / Sheet3

Figure G-7. Spreadsheet "Invert Diffusion Coefficient," Worksheet "Model;" Further Analysis of Invert Diffusion Coefficient Data

SPREADSHEET "INVERT DIFFUSION COEFFICIENT" WORKSHEET "VALIDATION"

In this worksheet (Figure G-8), diffusion coefficient data (Column B) from Tables A-1 and A-2 of *The Determination of Diffusion Coefficient of Invert Materials* (CRWMS M&O 2000 [DIRS 156680]) are plotted against water content (Column A), along with the results of the analysis in Worksheet "Model." The purpose of this worksheet is partially to validate the diffusion coefficient submodel by showing that the model overestimates the value of the invert diffusion coefficient, thereby overestimating diffusive releases of radionuclides through the invert. The model curve fit (Equation 6.3.4.1.1-16), also shown on p. G-7 and in Figure 6.3-4 in Section 6.3.4.1.1, is reproduced in Columns D-G, Rows 3 and 4, and plotted in the figure below.

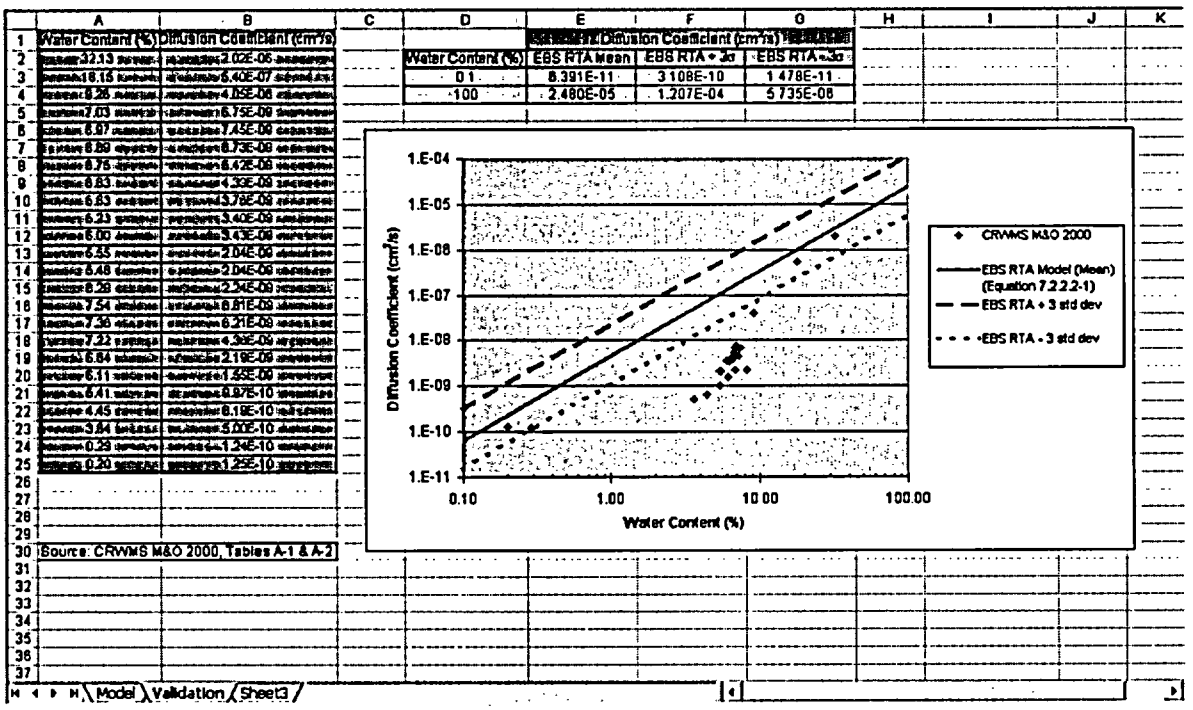

Source: CRWMS M&O 2000 [DIRS 156680], Tables A-1 and A-2.

Figure G-8. Spreadsheet "Invert Diffusion Coefficient," Worksheet "Validation;" Validation of Invert Diffusion Coefficient Data

INTENTIONALLY LEFT BLANK

APPENDIX H
QUALIFICATION OF DIFFUSION COEFFICIENT DATA

QUALIFICATION OF DIFFUSION COEFFICIENT DATA

DESCRIPTION OF DATA TO BE QUALIFIED

The data reported in Conca and Wright (1992 [DIRS 100436]) and Conca et al. (1993 [DIRS 170709]) consist of measured diffusion coefficients of unsaturated soil, gravel, bentonite, rock, and crushed tuff from Yucca Mountain, over a broad range of water contents. These data have been collected and analyzed using standard scientific practices. The diffusivity data for various granular media at volumetric moisture contents ranging between 1.5 percent and 66.3 percent are given in Section 4.1.2, Table 4.1-14. These measured data have been used to analyze the dependence of the diffusion coefficient on volumetric moisture content for a variety of granular materials (Section 6.3.4.1.1). These data are qualified in accordance with the data qualification plan included in this appendix.

CORROBORATING DATA

The diffusion coefficient data for crushed tuff materials from *The Determination of Diffusion Coefficient of Invert Materials* (CRWMS M&O 2000 [DIRS 156680]) are used to qualify the data reported by Conca and Wright (1992 [DIRS 100436]) and Conca et al. (1993 [DIRS 170709]). The diffusion coefficient data found in *The Determination of Diffusion Coefficient of Invert Materials* (CRWMS M&O 2000 [DIRS 156680]) were collected in the DOE Atlas Facility. The tests were performed by the EBS Testing Department under YMP-approved procedures using the Unsaturated Flow Apparatus. The Unsaturated Flow Apparatus method is reported to be an accurate and fast indirect method of determining diffusion coefficients in porous media (Conca and Wright 1992 [DIRS 100436], p. 7). The method uses measurements of electrical conductivity, at specified volumetric moisture content, which is converted to diffusion coefficient. *The Determination of Diffusion Coefficient of Invert Materials* (CRWMS M&O 2000 [DIRS 156680]) reports that the error on the reported data is within ±7 percent. The reported data are shown in Table H-1.

DATA EVALUATION CRITERIA

The diffusion coefficient data from Conca and Wright (1992 [DIRS 100436]) and Conca et al. (1993 [DIRS 170709]) will be considered qualified if they are within one order of magnitude of the values reported in *The Determination of Diffusion Coefficient of Invert Materials* (CRWMS M&O 2000 [DIRS 156680]); or if greater differences are observed, they result in more conservative results with regard to radionuclide releases.

COMPARISON OF THE DIFFUSION COEFFICIENT DATA IN CONCA AND WRIGHT (1992 [DIRS 100436]) AND CONCA ET AL. (1993 [DIRS 170709]) TO CRWMS M&O (2000 [DIRS 156680])

The data reported by Conca and Wright (1992 [DIRS 100436]) and Conca et al. (1993 [DIRS 170709]) (shown in Section 4.1.2, Table 4.1-14) consist of diffusion coefficient data for the range of 1.5 percent to 66.3 percent volumetric moisture content. The data from *The Determination of Diffusion Coefficient of Invert Materials* (CRWMS M&O 2000 [DIRS 156680]) ranges between 0.2 percent and 32.13 percent. Figure H-1 shows a plot of moisture content versus diffusion coefficient for data from both sources. The figure shows that

overall the Conca and Wright (1992 [DIRS 100436]) and Conca et al. (1993 [DIRS 170709]) data have higher diffusion coefficient values over the measured range of water content. The differences are highest at low water content. At water content values below 10 percent, the Conca and Wright (1992 [DIRS 100436]) and Conca et al. (1993 [DIRS 170709]) diffusion coefficient values are higher by as much as two orders of magnitude. For water content values above 10 percent, the Conca and Wright (1992 [DIRS 100436]) and Conca et al. (1993 [DIRS 170709]) diffusion coefficient data show higher but comparable values.

The differences in diffusion coefficient at low water content values can be partly attributed to the measurement technique. As discussed in Section 6 of *The Determination of Diffusion Coefficient of Invert Materials* (CRWMS M&O 2000 [DIRS 156680]), errors in measurement are higher at low diffusion coefficient values. Conca and Wright (1992 [DIRS 100436], p. 10) also reported that, at low water content, reductions in water content result in sharp declines in the measured diffusion coefficient as surface films become thin and discontinuous, and pendular water elements become small. Measurement differences could also be attributed to the different porous medium samples used. The Conca and Wright (1992 [DIRS 100436]) and Conca et al. (1993 [DIRS 170709]) data include various material samples whereas the determination report (CRWMS M&O 2000 [DIRS 156680]) data are for crushed tuff only. The data from both sources show some scatter. The diffusion coefficient data of Conca and Wright (1992 [DIRS 100436]) and Conca et al. (1993 [DIRS 170709]) are thus comparable to those of the determination report (CRWMS M&O 2000 [DIRS 156680]) for volumetric water content values above 10 percent. For low volumetric water content values, the differences are greater. However, the higher diffusion coefficient values of Conca and Wright (1992 [DIRS 100436]) and Conca et al. (1993 [DIRS 170709]) will result in predicted radionuclide releases being higher.

The Conca and Wright (1992 [DIRS 100436]) data have been published in a peer-reviewed journal (*Applied Hydrology*), and thus has undergone strict review. The data are shown plotted in Figure 2 of Conca and Wright (1992 [DIRS 100436]).

The Conca et al. (1993 [DIRS 170709]) data have been published in the proceedings of the *Scientific Basis for Nuclear Waste Management XVI Symposium* held November 30 to December 4, 1992. This symposium was organized by the Materials Research Society, which was formed in 1973. The most recent *Scientific Basis for Nuclear Waste Management XVI Symposium* is XXVII, the proceedings of which were published in 2004. Papers published in the proceedings undergo peer review prior to publication and must be presented at the meeting in order to be published.

SUMMARY OF QUALIFICATION

The diffusion coefficient data of Conca and Wright (1992 [DIRS 100436]) and Conca et al. (1993 [DIRS 170709]) have been evaluated in the context of their use in radionuclide transport modeling, and are considered qualified for use within this report per AP-SIII.2Q, *Qualification of Unqualified Data,* Attachment 3, on the basis of:

- Availability of corroborating data–The corroborating data are YMP-generated data using the same measurement technique.

- Reliability of data sources–The data are published in a peer-reviewed journal and in a peer-reviewed symposium proceedings.

- Data demonstrate properties of interest–The published data, diffusion coefficients in crushed rock, are the data required for the model of transport in the invert.

The above comparison of the diffusion coefficient data of Conca and Wright (1992 [DIRS 100436]) and Conca et al. (1993 [DIRS 170709]) with the corroborating data from CRWMS M&O 2000 [DIRS 156680] shows that the data evaluation criteria have been met. The data to be qualified are within one order of magnitude of the values in the corroborating source for volumetric water content values above 10 percent (Figure H-1). The differences between the two data sets are greater than one order of magnitude below 10 percent; however, the higher diffusion coefficient values of Conca and Wright (1992 [DIRS 100436]) and Conca et al. (1993 [DIRS 170709]) will result in predicted radionuclide releases being higher. Therefore, the Conca and Wright (1992 [DIRS 100436]) and Conca et al. (1993 [DIRS 170709]) diffusion coefficient data shown on Table 4.1-14 are judged to be qualified for use in this report. Use of these data in other applications would require a comparable evaluation for that specific use.

Table H-1. Diffusion Coefficient of Crushed Tuff Invert Materials

Sample	Volumetric Moisture Content (%)	Diffusion Coefficient ($cm^2 s^{-1}$)
1	32.13	2.02×10^{-6}
2	18.15	5.40×10^{-7}
3	9.26	4.05×10^{-8}
4	7.03	6.75×10^{-9}
5	6.97	7.45×10^{-9}
6	6.89	6.73×10^{-9}
7	6.75	5.42×10^{-9}
8	6.63	4.39×10^{-9}
9	6.63	3.76×10^{-9}
10	6.23	3.40×10^{-9}
11	6.00	3.43×10^{-9}
12	5.55	2.04×10^{-9}
13	5.46	2.04×10^{-9}
14	8.29	2.24×10^{-9}
15	7.54	6.81×10^{-9}
16	7.36	6.21×10^{-9}
17	7.22	4.38×10^{-9}
18	6.84	2.19×10^{-9}
19	6.11	1.55×10^{-9}
20	5.41	9.97×10^{-10}
21	4.45	6.19×10^{-10}
22	3.64	5.00×10^{-10}
23	0.29	1.24×10^{-10}
24	0.20	1.25×10^{-10}

Source: CRWMS M&O 2000 [DIRS 156680].

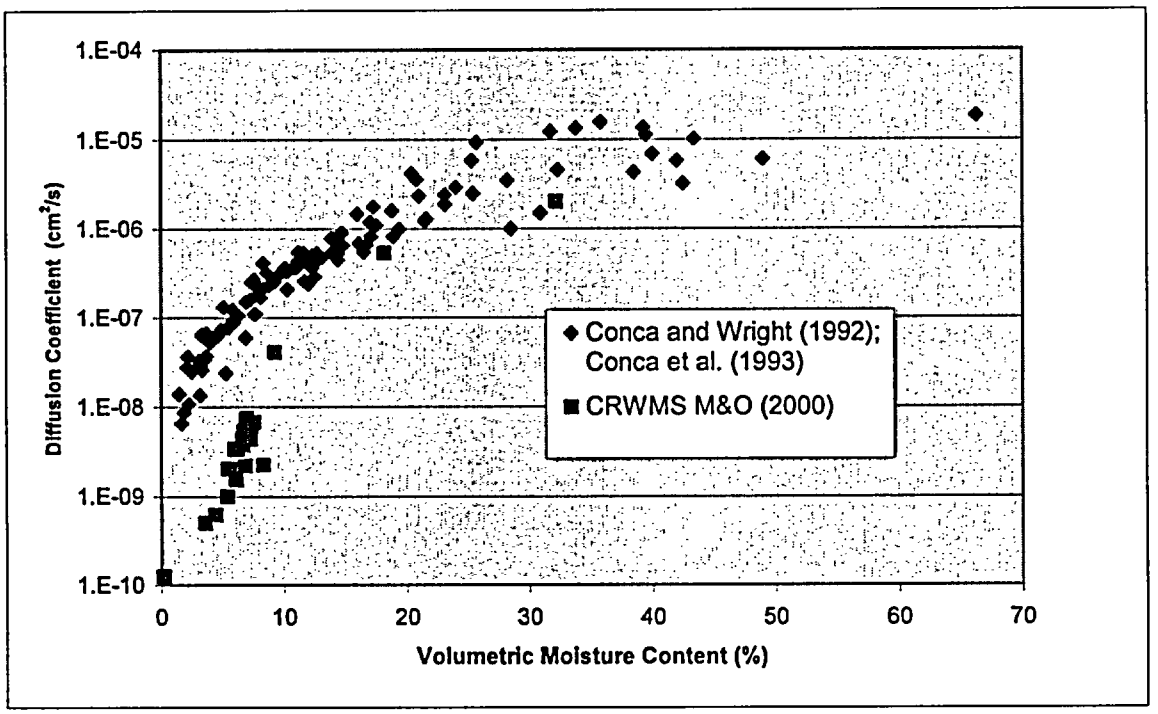

Source: Conca and Wright 1992 [DIRS 100436]; Conca et al. 1993 [DIRS 170709]; CRWMS M&O 2000 [DIRS 156680].

Figure H-1. Comparison of Diffusion Coefficients

DATA QUALIFICATION PLAN

A facsimile of the data qualification plan developed for the above qualification effort is provided in Figure H-2. The original is included in the records package for this model report.

BSC	DATA QUALIFICATION PLAN	QA: QA Page 1 of 1

Section I. Organizational Information

Qualification Title

QUALIFICATION OF DIFFUSION COEFFICIENT DATA

Requesting Organization

Near Field Environment and Transport

Section II. Process Planning Requirements

1. List of Unqualified Data to be Evaluated

Diffusion coefficient data reported in Conca and Wright (1992 [DIRS 100436]) and Conca et al. (1993 [DIRS 170709]). These data are shown on Table 4.1-14 of this report.

2. Type of Data Qualification Method(s) [including rationale for selection of method(s) (Attachment 3) and qualification attributes (Attachment 4)]

Qualification method, from Attachment 3 of AP-SIII.2Q, Rev 1, ICN 2: Corroborating Data. The diffusion coefficient data for crushed tuff materials from The Determination of Diffusion Coefficient of Invert Materials (CRWMS M&O 2000 [DIRS 156680]) are used to qualify the data reported by Conca and Wright (1992 [DIRS 100436]) and Conca et al. (1993 [DIRS 170709]).

Attributes used from Attachment 4: (3) The extent to whih the data demonstrate the properties of interest. (8) Prior peer or other professional review of the data and their results: and (10) Extent and quality of corroborating data .

3. Data Qualification Team and Additional Support Staff Required

Chairperson: James Schreiber, Sandia National Laboratories
Technically competant individual: Teklu Hadgu, Sandia National Laboratories

4. Data Evaluation Criteria

The diffusion coefficient data from Conca and Wright (1992 [DIRS 100436]) and Conca et al. (1993 [DIRS 170709]) will be considered qualified if they are within one order of magnitude of the values reported in CRWMS M&O 2000 [DIRS 156680]; or if greater differences are observed, they result in more conservative results with regard to radionuclide releases.

5. Identification of Procedures Used

AP-SIII.2Q, Qualification of Unqualified Data
AP-SIII.10Q, Models

Section III. Approval

Qualification Chairperson Printed Name	Qualification Chairperson Signature	Date
James Schreiber		11/17/04
Responsible Manager Printed Name	**Responsible Manager Signature**	**Date**
Ernest Hardin		11/17/04

AP-SIII.2Q PA_ASIII2-1 (Rev. 01/29/2004)

Figure H-2. Data Qualification Plan

INTENTIONALLY LEFT BLANK

APPENDIX I
COMPARISON OF OUTPUT DTNS

COMPARISON OF OUTPUT DTNs

The output from this report consists of two preliminary output DTNs: SN0403T0507703.015 and SN0409T0507703.017, and a final output DTN: SN0410T0507703.018. In this appendix, the differences between the two preliminary output DTNs are discussed. In addition, the final output DTN is compared with the second preliminary DTN. These comparisons provide traceability for TSPA-LA applications that were initially developed based on the preliminary output DTNs.

The output in these DTNs consists of the tables from Section 8 (Conclusions) of the *EBS RT Abstraction*. Each of these tables is compared in this appendix. Numerous editorial revisions were made in converting the first preliminary version of the DTN to the second preliminary version; because these editorial revisions have no impact on TSPA-LA results, they are not discussed in this appendix.

TABLE 57 (DTN: SN0403T0507703.015) VS. TABLE 8.1-1 (DTN: SN0409T0507703.017)

Table 57 (Summary of EBS Flow Abstraction) in DTN: SN0403T0507703.015 corresponds to Table 8.1-1 in DTN: SN0409T0507703.017. The key differences in this table between the two DTN versions are the expressions for the flux through the drip shield, F_2, and the flux into the waste package, F_4. In preliminary DTN: SN0403T0507703.015, F_2 is expressed as:

$$F_2 = F_1 L_{DS\_Patch} f_{DS}'/(2L_{DS}). \qquad \text{(Eq. I-1)}$$

The parameters are defined in the Table 57 in DTN: SN0403T0507703.015. This equation is technically correct, but it is expressed more completely in DTN: SN0409T0507703.017 as:

$$F_2 = \min[F_1 N_{bDS} L_{DS\_Patch} f'_{DS}/(2L_{DS}), F_1]. \qquad \text{(Eq. I-2)}$$

The parameters are defined in the Table 8.1-1 in DTN: SN0409T0507703.017. Equation I-2 replicates Equation 6.5.1.1.2-37 in the *EBS RT Abstraction*. Equations I-1 and I-2 give the same result when the number of corrosion patches in the drip shield, N_{bDS}, is one, which is the case in the WAPDEG model of drip shield failure (BSC 2004 [DIRS 169996], Section 6.3). The min function in Equation I-2 provides a numerical check to prevent an unrealistic result of $F_2 > F_1$ from being obtained if the parameter values used in the equation were to give that result.

The same discussion applies to the flux into the waste package. In DTN: SN0403T0507703.015, F_4, is expressed as:

$$F_4 = F_2 L_{WP\_Patch} f_{WP}'/(2L_{WP}). \qquad \text{(Eq. I-3)}$$

The parameters are defined in the Table 57 in DTN: SN0403T0507703.015.

This equation is technically correct, but it is expressed more completely in DTN: SN0409T0507703.017 as:

$$F_4 = \min[F_2 N_{bWP} L_{WP\_Patch} f'_{WP}/(2L_{WP}), F_2]. \qquad \text{(Eq. I-4)}$$

The parameters are defined in the Table 8-1 in DTN: SN0409T0507703.017. Equation I-4 replicates Equation 6.5.1.1.3-1 in the *EBS RT Abstraction*. The difference between Equations I-3 and I-4 is the definition of L_{WP_Patch}. In Equation I-3, L_{WP_Patch}, is the length of *all* corrosion patches in the waste package, whereas in Equation I-4, L_{WP_Patch} is the length of *each* corrosion patch; thus, the product $N_{bWP}L_{WP\_Patch}$ in Equation I-4 is equal to L_{WP_Patch} in Equation I-3. The min function in Equation I-4 provides a numerical check to prevent an unrealistic result of $F_4 > F_2$ from being obtained if the parameter values used in the equation were to give that result.

In the Flow Parameter column for Flow Pathway 8 in Table 57 in DTN: SN0403T0507703.015, a flux F_9 is erroneously included in the equation and is deleted in the final DTN. Since this flux does not exist, its inclusion in the preliminary DTN has no impact on the TSPA-LA calculation.

The references and comments in the Data Sources & Notes column in Table 8.1-1 in DTN: SN0409T0507703.017 are updated from Table 57 in DTN: SN0403T0507703.015; these updates have no impact on TSPA-LA calculations.

TABLE 58 (DTN: SN0403T0507703.015) VS. TABLE 8.1-2 (DTN: SN0409T0507703.017)

In DTN: SN0409T0507703.017, the cross-sectional area for radionuclide transport is clarified in Table 8.1-2, with references to sections in the report. In DTN: SN0403T0507703.015, the same parameter is referred to as the flow cross-sectional area in Table 58 and described in vague terms that prompted a revised description in the final DTN. References are updated in DTN: SN0409T0507703.017 Table 8.1-2. None of these changes has any impact on TSPA-LA calculations.

TABLE 59 (DTN: SN0403T0507703.015) VS. TABLE 8.2-1 (DTN: SN0409T0507703.017)

In Table 57 in DTN: SN0403T0507703.015, the lower end of the range on sampled parameter Diff_Path_Length_CP_CDSP is erroneously shown as 0.02 m; this error is also found in Table 63 in DTN: SN0403T0507703.015. Because the correct value, 0.025 m, is included in the database used for TSPA-LA, this error has no impact on TSPA-LA. In the corresponding table in DTN: SN0409T0507703.017, Table 8.2-1, the range for this parameter is not shown, since it is given correctly in Table 8.2-3.

References to parameter sources and sections in the *EBS RT Abstraction* are updated in DTN: SN0409T0507703.017. These changes have no impact on TSPA-LA calculations.

TABLE 60 (DTN: SN0403T0507703.015) VS. TABLE 8.2-2 (DTN: SN0409T0507703.017)

Table 8.2-2 in DTN: SN0409T0507703.017 (K_d values for corrosion products) is identical to Table 60 in DTN: SN0403T0507703.015. Therefore, there is no impact on TSPA-LA calculations.

TABLES 61 & 62 (DTN: SN0403T0507703.015) VS. TEXT (DTN: SN0409T0507703.017)

Tables 61 and 62 in DTN: SN0403T0507703.015 (K_d values and correlations for the invert) are replaced in DTN: SN0409T0507703.017 with text clarifying that TSPA-LA is to use UZ K_d values for the invert. This change has no impact on TSPA-LA calculations.

TABLE 63 (DTN: SN0403T0507703.015) VS. TABLE 8.2-3 (DTN: SN0409T0507703.017)

In Table 63 in DTN: SN0403T0507703.015, sampled parameter Diff_Path_Length_CP_CDSP is erroneously shown as having a lower end of the range of 0.02 m. Because the correct value, 0.025 m, is included in the database used for TSPA-LA, this error has no impact on TSPA-LA. The correct range is shown in Table 8.2-3 in DTN: SN0409T0507703.017. References are updated in Table 8.2-3 in DTN: SN0409T0507703.017. These changes have no impact on TSPA-LA calculations.

TABLE 64 (DTN: SN0403T0507703.015) VS. TABLE 8.2-4 (DTN: SN0409T0507703.017)

References are updated in Table 8.2-4 in DTN: SN0409T0507703.017. Three parameters were added to this table to provide a source for the values used in TSPA-LA: DS_Total_Length (5805 mm), Invert_Viscosity_Ref_Temp (298.15 K), and Interface_Scale_Factor (1×10^{-6}). These changes have no impact on TSPA-LA calculations. No other changes were made in converting Table 64 to Table 8.2-4.

TABLE 65 (DTN: SN0403T0507703.015) VS. TABLE 8.2-5 (DTN: SN0409T0507703.017)

The following changes were made to convert Table 65 to Table 8.2-5. References to the equations in the *EBS RT Abstraction* were added to the Input Description column. In the Parameter Description for Equation 8-1, clarification of the definition of *ND*, the truncated normal distribution, was added. In Equation 8-2, the range of validity was added to the definition of temperature. In Equation 8-3, the definition of θ_m was changed from fraction to percent, and the equation was modified accordingly by changing the term $0.138\theta_m$ to $0.00138\theta_m$. Equation 8-7 was completely revised in order to clarify the calculation of corrosion product mass as computed in TSPA-LA over each time interval, from t_0, when breach occurs, to t_{f1} and t_{f2}, the lifetimes of each type of steel. These changes have no impact on TSPA-LA calculations.

TABLE 66 (DTN: SN0403T0507703.015) VS. TABLE 8.2-6 (DTN: SN0409T0507703.017)

Table 8.2-6 DTN: SN0409T0507703.017 (Invert Diffusion Coefficient Alternative conceptual Model Parameters) is identical to Table 66 in DTN: SN0403T0507703.015. Therefore, there is no impact on TSPA-LA calculations.

TABLE 67 (DTN: SN0403T0507703.015) VS. TABLE 8.2-7 (DTN: SN0409T0507703.017)

Equation 8-8 was reformulated in the *EBS RT Abstraction* and revised accordingly in Table 8.2-7. Because this is an alternative conceptual model, this change has no impact on TSPA-LA calculations. Equation 8-9, the definitions of θ_{intra} and θ_{min} were changed from fractions to percent. This change has no impact on the results.

TABLE 8.1-1 (DTN: SN0410T0507703.018)VS. TABLE 8.1-1 (DTN: SN0409T0507703.017)

The differences in this table (Summary of EBS Flow Abstraction) between the two DTN versions are the expressions for the flux through the drip shield, F_2, and the flux into the waste package, F_4. In DTN: SN0409T0507703.017, F_2 is expressed as:

$$F_2 = \min\left[F_1 N_{bDS} L_{DS\_Patch} f'_{DS} / (2L_{DS}), F_1\right]. \qquad \text{(Eq. I-5)}$$

The parameters are defined in Table 8.1-1 in both DTNs. Because L_{DS_Patch} is defined as the axial *half*-length of each corrosion patch, the factor of 2 should not appear in the denominator. This equation is presented correctly in DTN: SN0410T0507703.018 as:

$$F_2 = \min\left[F_1 N_{bDS} L_{DS\_Patch} f'_{DS} / L_{DS}, F_1\right]. \qquad \text{(Eq. I-6)}$$

Similarly, in DTN: SN0409T0507703.017, F_4 is expressed in Table 8.1-1 as:

$$F_4 = \min\left[F_2 N_{bWP} L_{WP\_Patch} f'_{WP} / (2L_{WP}), F_2\right]. \qquad \text{(Eq. I-7)}$$

This equation is presented correctly in Table 8.1-1 in DTN: SN0410T0507703.018 as:

$$F_4 = \min\left[F_2 N_{bWP} L_{WP\_Patch} f'_{WP} / L_{WP}, F_2\right]. \qquad \text{(Eq. I-8)}$$

These differences have no impact because the correct equations (Equations I-6 and I-8) have been implemented in the TSPA.

TABLE 8.2-5 (DTN: SN0410T0507703.018)VS. TABLE 8.2-5 (DTN: SN0409T0507703.017)

The differences in this table (Calculated Model Inputs Used in the EBS Radionuclide Transport Abstraction) between the two DTN versions include Equation 8-5 for the effective water saturation of corrosion products. In DTN: SN0409T0507703.017, this equation is:

$$S_{we,CP} = 1.312 \times 10^{-6} \bar{s}_{CP} (-\ln RH)^{-1/2.45}. \qquad \text{(Eq. I-9)}$$

This equation, developed in an earlier draft of Section 6.5.1.2.1.4.2 as Equation 6.5.1.2.1-27, is incorrect. The correct equation (as shown in Section 6.5.1.2.1.4.2, Equation 6.5.1.2.1-27 of this report), is given in DTN: SN0410T0507703.018 as:

$$S_{we,CP} = 3.28 \times 10^{-6} \bar{s}_{CP} (-\ln RH)^{-1/2.45}. \qquad \text{(Eq. I-10)}$$

In addition, in DTN: SN0409T0507703.017, parameter $\bar{s}_{CP}$ is defined in Table 8.2-5 as having units of ($m^2\ g^{-1}$). The correct units for use in this parameter are given in DTN: SN0410T0507703.018 as ($m^2\ kg^{-1}$).

The impact of this correction has been assessed in a *Technical Management Review Board (TMRB) Decision Proposal* (BSC 2004 [DIRS 172219]). Because the water saturation in the waste package corrosion products is used to calculate the diffusion coefficient, this correction has a direct impact on dose estimates. In the preliminary assessment, using Equation I-10 instead of Equation I-9 increases the total peak mean annual dose from all scenario classes by 10 percent (BSC 2004 [DIRS 172219]).

INTENTIONALLY LEFT BLANK